



University of Bradford eThesis

This thesis is hosted in [Bradford Scholars](#) – The University of Bradford Open Access repository. Visit the repository for full metadata or to contact the repository team



© University of Bradford. This work is licenced for reuse under a [Creative Commons Licence](#).

**TENSILE AND FRACTURE BEHAVIOUR OF
ISOTROPIC AND DIE-DRAWN
POLYPROPYLENE-CLAY NANOCOMPOSITES**

A.S. AL-SHEHRI

PhD

University of Bradford

2010

TENSILE AND FRACTURE BEHAVIOUR OF ISOTROPIC AND
DIE-DRAWN POLYPROPYLENE-CLAY NANOCOMPOSITES

Compounding, processing, characterization and mechanical properties of isotropic
and die-drawn polypropylene/clay/polypropylene maleic anhydride composites

Abdulhadi S Al-Shehri

Submitted for the degree of
Doctor of Philosophy

School of Engineering, Design and Technology

University of Bradford

2010

Abstract

As a preliminary starting point for the present study, physical and mechanical properties of polypropylene nanocomposites (PPNCs) for samples received from Queen's University Belfast have been evaluated. Subsequently, polymer/clay nanocomposite material has been produced at Bradford. Mixing and processing routes have been explored, and mechanical properties for the different compounded samples have been studied. Clay intercalation structure has received particular attention to support the ultimate objective of optimising tensile and fracture behaviour of isotropic and die-drawn PPNCs. Solid-state molecular orientation has been introduced to PPNCs by the die-drawing process. Tensile stress-strain measurements with video-extensometry and tensile fracture of double edge-notched tensile specimens have been used to evaluate the Young's modulus at three different strain rates and the total work of fracture toughness at three different notch lengths. The polymer composite was analyzed by differential scanning calorimetry, thermogravimetric analysis, polarizing optical microscopy, wide angle x-ray diffraction, and transmission electron microscopy.

3% and 5% clay systems at various compatibilizer (PPMA) loadings were prepared by three different mixing routes for the isotropic sheets, produced by compression moulding, and tensile bars, produced by injection moulding process. Die-drawn oriented tensile bars were drawn to draw ratio of 2, 3 and 4.

The results from the Queen's University Belfast samples showed a decrement in tensile strength at yield. This might be explained by poor bonding, which refers to poor dispersion. Voids that can be supported by intercalated PP/clay phases might be responsible for improvement of elongation at break.

The use of PPMA and an intensive mixing regime with a two-step master batch process overcame the compatibility issue and achieved around 40% and 50% increase in modulus for 3% and 5% clay systems respectively. This improvement of the two systems was reduced after drawing to around 15% and 25% compared with drawn PP.

The work of fracture is increased either by adding nanoclay or by drawing to low draw ratio, or both. At moderate and high draw ratios, PPNCs may undergo either an increase in the size of microvoids at low clay loading or coalescence of microvoids at high clay loading, eventually leading to an earlier failure than with neat PP.

The adoption of PPMA loading using an appropriate mixing route and clay loading can create a balance between the PPMA stiffness effect and the degree of bonding between clay particles and isotropic or oriented polymer molecules. Spherulites size, d-spacing of silicate layers, and nanoparticles distribution of intercalated microtactoids with possible semi-exfoliated particles have been suggested to optimize the final PPNCs property.

Keywords

Tensile modulus, video-extensometer, fracture toughness, die-drawing, oriented polymers, polypropylene, nanocomposites, polypropylene maleic anhydrid

Sections of the work presented in this thesis have been reported in the following forms:

Conference paper

J Sweeney, A Alshehri, P E Spencer, P D Coates. Modelling polymer/clay nanocomposites using statistical and continuum approaches with experimental verification. 26th Annual meeting polymer processing society, Banff, Canada July (2010).

Conference abstract and presentations

J Sweeney, A Alshehri, P E Spencer, P D Coates. Modelling interfacial effects in polymer/clay nanocomposites with experimental verification. Plasticity 2010, Saint Kitts and Nevis, January (2010).

Contents

Abstract	i
List of Figures	vii
List of Tables	xii
Acknowledgements	xiv
1 Introduction	1
1.1 General	1
1.2 Objective	3
1.3 Scope and Content	4
2 Literature Review	7
2.1 Introduction	7
2.2 Polypropylene	7
2.2.1 Polypropylene general features	7
2.2.2 Polypropylene structure	7
2.2.3 Polypropylene properties	9
2.3 Surface-Modified Montmorillonite Clay	10
2.3.1 Structure of montmorillonite clay	10
2.3.2 Surface treatment	11
2.4 Compatibilizer	14
2.4.1 Molecular weight effect	16
2.4.2 Maleic Anhydride content effect	17
2.5 Polymer Nanocomposites	17
2.5.1 Polymer nanocomposites general features	17
2.5.2 Types of polymer nanocomposites	18
2.5.3 Thermodynamics and dispersion of PPNCs	19
2.5.4 Formation of Polypropylene nanocomposites	21
2.6 Processing of Polypropylene Nanocomposite	23
2.6.1 Effect of the base polymer on PPNCs processing	24
2.6.2 Effect of compounding conditions on PPNCs formation	25
2.7 Characterization and Morphology of Nanocomposite Structure	27
2.7.1 Wide angle x-ray diffraction and transmission electron microscopy	28
2.7.2 Scanning electron microscopy and wide angle x-ray diffraction	30
2.7.3 Small angle X-ray scattering and wide angle x-ray scattering	30
2.7.4 Nuclear magnetic resonance	32
2.8 Nanocomposite Properties	32
2.8.1 Crystallization Behaviour and Structure of PPNCs	33
2.8.2 Mechanical properties	36
2.8.3 Dynamic mechanical analysis	42
2.8.4 Thermal properties	43
2.8.5 Melt Rheology and Structure–Property Relationship	44
2.9 Conclusions and Recommendations	48
3 Tensile and Fracture Behaviour of Polymer	52
3.1 Introduction	52
3.2 The Definition of Stress	53
3.3 The Definition of Strain	54
3.4 The Definition of Modulus	55
3.5 Anisotropic Materials	57

3.5.1	Triaxial Symmetry Specimens	58
3.5.2	Uniaxial Symmetry Specimens	59
3.6	<i>Tensile Testing Graphs</i>	61
3.6.1	Nominal and true stresses	61
3.6.2	Cold drawing phenomenon	62
3.6.3	Definition of yield stress	66
3.7	<i>The Yield Criterion</i>	66
3.8	<i>Hot-Drawing Processes</i>	68
3.8.1	Hydrostatic extrusion process	68
3.8.2	Die-Drawing Process	69
3.9	<i>Fracture Toughness</i>	71
4	Experimental Work	78
4.1	<i>Introduction</i>	78
4.2	<i>Raw materials</i>	78
4.2.1	Polypropylene	78
4.2.2	Nano-clays (MMT)	79
4.2.3	Compatibilizer	81
4.3	<i>Compounding of Polypropylene Nanocomposite</i>	82
4.3.1	Compounding: the prism eurolab twin-screw extruder	82
4.3.2	Primary and secondary screw feeders	84
4.3.3	Sample preparation and production	85
4.3.4	Extruder processing conditions	86
4.4	<i>Processing and Sample Preparation of Polypropylene Nanocomposite</i>	90
4.4.1	Queen's University Belfast Samples	90
4.4.2	Compression moulding process	92
4.4.3	Injection moulding process	94
4.4.4	Die drawing apparatus	97
4.5	<i>Characterization of Polypropylene Nanocomposite</i>	102
4.5.1	Differential scanning calorimetry (DSC)	102
4.5.2	Thermal gravimetric analysis (TGA)	104
4.5.3	Polarizing optical microscopy	104
4.5.4	Wide-angle x-ray diffraction	107
4.5.5	Transmission electron microscopy	109
4.5.6	Video extensometer test	111
4.5.7	Fracture toughness test	115
5	Results and Discussion	119
5.1	<i>Introduction</i>	119
5.2	<i>Twin Screw Extruder Compounding Samples</i>	121
5.2.1	Crystallization results	121
5.2.2	Sample Thermal History	127
5.3	<i>Queen's University Belfast Samples</i>	130
5.3.1	Crystallization results	130
5.3.2	Tensile Testing	133
5.4	<i>Processing behaviour of PPNCs</i>	140
5.5	<i>Drawing Process Curves</i>	142
5.6	<i>Spherulitic Morphology</i>	147
5.6.1	Spherulitic morphology of undrawn PPNCs	147
5.6.2	Spherulitic morphology of drawn PPNCs	155
5.7	<i>Wide Angle X-ray Diffraction and Transmission Electron Micrographs</i>	159
5.7.1	WAXD and TEM micrographs of undrawn PPNCs	160
5.7.2	TEM micrographs of drawn PPNCs	166

5.7.3	TEM micrographs analyses of undrawn and drawn PPNCs	168
5.8	<i>Tensile Video Extensometer of PPNCs</i>	174
5.8.1	Tensile modulus of undrawn PPNCs	174
5.8.2	Tensile modulus of drawn PPNCs	189
5.9	<i>Fracture Toughness of PPNCs</i>	198
5.9.1	Load-displacement behaviour of undrawn 3% clay systems of PPNCs	202
5.9.2	Load-displacement behaviour of undrawn 5% clay systems of PPNCs	205
5.9.3	Load-displacement behaviour of drawn PPNCs tensile fracture	209
5.9.4	Total work of fracture of PPNCs	222
6	Conclusions, Recommendations and Suggestions for the Future Work	231
6.1	<i>DSC and TGA Results of PPNCs Compounding Samples</i>	231
6.1.1	DSC Results of PPNCs Compounding Samples	231
6.1.2	TGA Results of PPNCs Compounding Samples	232
6.2	<i>Queen's University Belfast Samples</i>	232
6.3	<i>Processing Behaviour of PPNCs</i>	233
6.4	<i>Drawing Process Curves of PPNCs</i>	234
6.5	<i>Spherulitic Morphology of PPNCs</i>	235
6.6	<i>WAXD and TEM Micrographs of PPNCs</i>	236
6.6.1	WAXD measurements of PPNCs	236
6.6.2	TEM images of undrawn PPNCs	237
6.6.3	TEM images of drawn PPNCs	238
6.6.4	WAXD and TEM images for different mixing routes	239
6.7	<i>Tensile Modulus of Undrawn PPNCs</i>	239
6.7.1	Effect of PPMA/clay ratio	240
6.7.2	Effect of orientation produced from different processing equipments	241
6.7.3	Effect of different strain rates	241
6.7.4	Effect of different mixing routes	241
6.8	<i>Tensile Modulus of drawn PPNCs</i>	242
6.8.1	Effect of low and high deformation systems	243
6.8.2	Effect of draw speed on modulus of drawn PPNCs	243
6.9	<i>Fracture Toughness of PPNCs</i>	244
6.9.1	Load-displacement behaviour for core and skin of undrawn samples	244
6.9.2	Effect of orientation of clay particles on the fracture behaviour	245
6.9.3	Total work of fracture	245
7	References	248
	Appendix A: Nomenclature	258
	Appendix B: Material Technical Data Sheets	260
	<i>Appendix B1: Polypropylene PPH 5060</i>	260
	<i>Appendix B2: Polypropylene PPH 5042</i>	261
	<i>Appendix B3: Southern Clay Cloisite® 15A</i>	262
	<i>Appendix B4: DuPont Fusabond® P M613 05</i>	264
	Appendix C: Twin Screw Configuration	266
	Appendix D: Modulus Measurement Program by Video Extensometer	267
	Appendix E: Tensile Graphs	268
	<i>Appendix E1: Original Extruded Sheets</i>	268
	<i>Appendix E2: PP/Clay Stretched Sheet - Instron Results</i>	270
	<i>Appendix E3: PP Clay Biaxial Machine Testing Results</i>	278

Appendix F: TEM Micrographs of PPNCs	280
<i>Appendix F1: TEM Micrographs of Undrawn PPNC</i>	280
<i>Appendix F2: TEM Micrographs of Drawn PPNCs</i>	284
Appendix G: Tensile Video Extensometer of Undrawn PPNCs	288
<i>Appendix G1: Tensile Video Extensometer for Compression Sheets</i>	288
<i>Appendix G2: Tensile Video Extensometer (Strain Rate Effect on Modulus) for Compression Sheets</i>	297
<i>Appendix G3: Tensile Video Extensometer for Injection Moulded bars</i>	298
<i>Appendix G4: Tensile Video Extensometer for Different Mixing Procedure Injection Bar Samples</i>	307
<i>Appendix G5: Tensile Video Extensometer for Pure PP Recycle</i>	309
<i>Appendix G6: Tensile Video Extensometer (Strain Rate Effect on Modulus) for Injection Moulded bars</i>	312
Appendix H: Tensile Video Extensometer of Drawn PPNCs	313
<i>Appendix H1: Tensile Video Extensometer of Different Draw Ratios</i>	313
<i>Appendix H2: Tensile Video Extensometer (Strain Rate Effect on Modulus) for Injection Moulded bars</i>	327
Appendix I: Tensile Fracture Stress-Strain Graphs of PPNCs	329
<i>Appendix I1: Stress-Strain Graphs of Undrawn PPNCs</i>	329
<i>Appendix I2: Stress-Strain Graphs of Drawn PPNCs</i>	331
Appendix J: Total Work of Fracture for Different Ligament Lengths of PPNCs	336

List of Figures

Figure 2.1: Schematic illustration of chains organization in PP spherulites	9
Figure 2.2: Schematic representation of the MMT chemical structure of 2:1 layered silicates (left) and the shape and dimensions of a clay platelet (right).	11
Figure 2.3: Schematic representation of clay surface treatment	12
Figure 2.4: Schematic representation of the clay dispersion process	15
Figure 2.5: Immiscible, intercalated and exfoliated PPNCs	19
Figure 2.6: Modelling of clay intercalation and exfoliation of polymers in the galleries between adjacent clay platelets in a stack.	21
Figure 2.7: The intercalation process between a polymer melt and silicate layer	24
Figure 2.8: Different orientations and crystallization structure measured by SAXS and WAXS	31
Figure 2.9: DSC curves of nonisothermal crystallization at different cooling rates: (a) PPMA and (b) PPNC.	34
Figure 2.10: Dynamic shear modulus of PPNCs (a) storage modulus and, (b) loss modulus.	46
Figure 2.11: TEM micrographs (a) and elongational viscosity with time variation (b) for elongated PPNCs at 150 °C	47
Figure 3.1: General types of stress-strain curves[109]	53
Figure 3.2: Typical stress-strain curve	53
Figure 3.3: The components of stress	54
Figure 3.4: Illustration of (a) extensional strain and (b) simple shear strain	55
Figure 3.5: Triaxial symmetry of polymer sheet	58
Figure 3.6: Uniaxial symmetry in drawn polymer film	60
Figure 3.7: Nominal stress and true stress in tensile testing graphs	62
Figure 3.8: Necking behaviour of nominal stress-strain graph	63
Figure 3.9: Schematic stress-strain curves for a semicrystalline polymer	64
Figure 3.10 Stress-strain curves for cold drawing polymer/clay system	64
Figure 3.11: Steps in the deformation of semicrystalline polymers	65
Figure 3.12: Yield stress definition	66
Figure 3.13: Hydrostatic extrusion process	69
Figure 3.14: Die drawing process	70
Figure 3.15: Plot of the flow energy versus the amount of crack extension [125]	73
Figure 3.16: The load- displacement curve of fracture	74
Figure 3.17: : Essential work of fracture test specimen diagram	75
Figure 3.18: Specific total work of fracture against ligament length [132]	76
Figure 4.1: Prism Eurolab 16 mm twin-screw extruder	83
Figure 4.2: Twin screw mixing sections of Prism Eurolab 16 mm TSE	84
Figure 4.3: Secondary screw feeder	85
Figure 4.4: Primary and secondary feeders	85
Figure 4.5: Processing conditions for different PPMA master batches compounding	87
Figure 4.6: Processing conditions for clay master batch and PP/PPMA/MMT compounding	88
Figure 4.7: Processing conditions for recycle Polypropylene pellets	89
Figure 4.8: ISO 527-2 dimension for tensile test specimen	90
Figure 4.9: Biaxial Grips of stretching testing machine	91
Figure 4.10: Compression moulding machine	92
Figure 4.11: Compression moulding process	93
Figure 4.12: ASTM D 638 type IV dimension for tensile test specimen	93
Figure 4.13: Injection Moulding Machine	94
Figure 4.14: Injection Moulded Tensile Specimen	95
Figure 4.15: ASTM D638 standard- type I specimen	95
Figure 4.16: The integrating area under the nozzle pressure-time curve	97
Figure 4.17: The nozzle pressure-time curve of PPNC (PP + 5% clay + 6% PPMA)	97
Figure 4.18: Photo of the die drawing process	98
Figure 4.19: Schematic diagram of die drawing process	99
Figure 4.20: A schema diagram of constant width small reg	100
Figure 4.21: Constant width small reg die photos	100
Figure 4.22: Attainable draw ratios at different haul-off speeds	101
Figure 4.23: Different obtained drawn samples from the drawing process ($\lambda=2, 3$ and 4)	102
Figure 4.24: Differential scanning calorimetry equipment	103

Figure 4.25: Thermal gravimetric analyzer	104
Figure 4.26: Hot-stage polarizing optical microscope (Leica DMRXP)	106
Figure 4.27: Image of calibration scale at 100x magnification used in the images	106
Figure 4.28: Schematic diagrams of WAXD principle	108
Figure 4.29: A photo of Panalytical X'Pert Pro X-Ray diffractometer	108
Figure 4.30: Transmission electron microscopy apparatus	109
Figure 4.31: Schematic structure of transmission electron microscopy	110
Figure 4.32: Leica microtome	110
Figure 4.33: Feret diameter	111
Figure 4.34: Loop of the modulus measurement program of video-extensometer experiment	112
Figure 4.35: Dimensions of undrawn and drawn samples prepared for tensile video-extensometer test	113
Figure 4.36: Video extensometer tensile test	114
Figure 4.37: Video extensometer test	114
Figure 4.38: A schema of the tensile fracture test	116
Figure 4.39: A photo of tensile fracture test	116
Figure 4.40: Dimensions of undrawn and drawn samples prepared for tensile fracture test	117
Figure 4.41: Keeton cutter machine used to dimension the length of the drawn samples	118
Figure 4.42: Perfecto sharper- cut machine	118
Figure 5.1: PPMA content effect on crystallization of PPNCs without clay	121
Figure 5.2: Clay content effect on crystallization of PPNCs without PPMA	122
Figure 5.3: Clay content effect on crystallization of PPNCs at constant PPMA loading level	123
Figure 5.4: PPMA content effect on crystallization of PPNCs at constant clay loading level	123
Figure 5.5: Clay content effect on nucleation of PPNCs without PPMA	124
Figure 5.6: PPMA content effect on nucleation of PPNCs without clay	124
Figure 5.7: Clay content effect on nucleation of PPNCs at constant PPMA loading level	125
Figure 5.8: PPMA content effect on nucleation of PPNCs at constant clay loading level	125
Figure 5.9: Clay content effect on melting temperature of PPNCs without PPMA	126
Figure 5.10: PPMA content effect on melting temperature of PPNCs without clay	126
Figure 5.11: Clay content effect on melting temperature of PPNCs at constant PPMA loading level	127
Figure 5.12: PPMA content effect on melting temperature of PPNCs at constant clay loading level	127
Figure 5.13: Thermal history effect on crystallization of PP, first PP recycle (R1), second PP recycle (R2) and third PP recycle (R3)	128
Figure 5.14: Thermal decomposition of the recycling PP, first PP recycle (R1), second PP recycle (R2) and third PP recycle (R3)	129
Figure 5.15: Tensile modulus of the recycling PP samples	129
Figure 5.16: Thermal decomposition of the PP and PPNCs samples	130
Figure 5.17: Clay content effect on crystallinity of PPQNCs without compatibilizer	132
Figure 5.18: Clay content effect on melting temperature of PPQNCs without compatibilizer	132
Figure 5.19: Clay content effect on crystallization temperature of PPQNCs without compatibilizer	132
Figure 5.20: Nominal stress-strain curve for a pure PP specimen	134
Figure 5.21: Tensile yield stress for the original extruded sheets (Instron results)	135
Figure 5.22: Tensile yield stress for the stretched sheets at room temperature (Instron results)	135
Figure 5.23: Tensile yield stress for the stretched sheets (Biaxial Testing Machine)	136
Figure 5.24: Tensile strength at break for the original extruded sheets (Instron results)	137
Figure 5.25: Tensile Elongation at break for the original extruded sheets (Instron results)	138
Figure 5.26: Tensile strength at break for the stretched sheets (Instron results)	138
Figure 5.27: Tensile elongation at break for the stretched sheets (Instron results)	139
Figure 5.28: Crystallinity and tensile yield stress correlation	140
Figure 5.29: Crystallization temperature and tensile yield stress correlation	140
Figure 5.30: In-line viscosity index measurement vs. PPMA contents of different PPNCs	142
Figure 5.31: Die drawing process curves of samples with PPMA ($\lambda = 2$)	143
Figure 5.32: Die drawing process curves of samples without PPMA ($\lambda = 2$)	143
Figure 5.33: Die drawing process curves of samples with PPMA ($\lambda = 3$)	144
Figure 5.34: Die drawing process curves of samples without PPMA ($\lambda = 3$)	144
Figure 5.35: Die drawing process curves of samples with PPMA ($\lambda = 4$)	145
Figure 5.36: Die drawing process curves of samples without PPMA ($\lambda = 4$)	145

Figure 5.37: Steady draw load vs. draw ratio of the drawing process of PPNCs without PPMA	146
Figure 5.38: Steady draw load vs. draw ratio of the drawing process of PPNCs with PPMA	146
Figure 5.39: Spherulitic morphology of PP at (a) 115 °C (b) room temperature	147
Figure 5.40: Spherulitic morphology of unoriented PPNCs at different temperatures	150
Figure 5.41: Spherulitic morphology of unoriented PPNCs with 3 % clay	151
Figure 5.42: Spherulitic morphology of unoriented PPNCs with 5% clay	152
Figure 5.43: Spherulitic size and crystallization start temperature of undrawn PPNCs with 3% clay	153
Figure 5.44: Spherulitic size and crystallization start temperature of undrawn PPNCs with 5% clay	153
Figure 5.45: Spherulitic size and crystallization start temperature of undrawn PPNCs without PPMA	154
Figure 5.46: Spherulitic size and crystallization start temperature of undrawn PPNCs with PPMA	154
Figure 5.47: Spherulitic morphology of oriented PPNCs without PPMA at different draw ratios	157
Figure 5.48: Spherulitic morphology of oriented PPNCs ($\lambda=4$)	158
Figure 5.49: WAXD and TEM of undrawn PPNCs with 3% clay	164
Figure 5.50: WAXD and TEM of undrawn PPNCs with 5% clay	165
Figure 5.51: TEM photos of drawn PPNCs (scale bar is 1 μm)	167
Figure 5.52: Feret diameter and number of particles per unit area at different PPMA contents of undrawn PPNCs with 3% clay	170
Figure 5.53: Feret diameter and number of particles per unit area at different PPMA contents of undrawn PPNCs with 5% clay	170
Figure 5.54: Feret diameter and number of particles per unit area vs. draw ratio of PPNCs with 3% clay	171
Figure 5.55: Feret diameter and number of particles per unit area vs. draw ratio of PPNCs with 5% clay	172
Figure 5.56: Feret diameter and number of particles per unit area vs. draw ratio of PPNCs with PPMA and 3% clay content	172
Figure 5.57: Feret diameter and number of particles per unit area vs. draw ratio of PPNCs with PPMA and 5% clay content	173
Figure 5.58: Feret diameter and number of particles per unit area vs. draw ratio of PPNCs prepared with different procedure of mixing	173
Figure 5.59: Stress-strain curve obtained using the video-extensometer at 0.0158 1/min strain rate	174
Figure 5.60: Tensile Modulus vs. PPMA contents for compression moulded sheets at 0.0053 1/min strain rate	177
Figure 5.61: Tensile Modulus vs. clay contents of compression moulded sheets at 0.0053 1/min strain rate	177
Figure 5.62: Tensile Modulus vs. PPMA contents of injection moulded bars at 0.0053 1/min strain rate	178
Figure 5.63: Tensile Modulus vs. clay contents of injection moulded bars at 0.0053 1/min strain rate	178
Figure 5.64: Tensile Modulus of compression moulded sheets vs. injection moulded bars at 0.0053 1/min strain rate	179
Figure 5.65: Tensile Modulus vs. PPMA contents of compression moulded sheets at 0.0105 1/min strain rate	180
Figure 5.66: Tensile Modulus vs. clay contents of compression moulded sheets at 0.0105 1/min strain rate	180
Figure 5.67: Tensile Modulus vs. PPMA contents of injection moulded bars at 0.0105 1/min strain rate	181
Figure 5.68: Tensile Modulus vs. clay contents of injection moulded bars at 0.0105 1/min strain rate	181
Figure 5.69: Tensile Modulus vs. PPMA contents of compression moulded sheets at 0.0158 1/min strain rate	182
Figure 5.70: Tensile Modulus vs. clay contents of compression moulded sheets at 0.0158 1/min strain rate	182
Figure 5.71: Tensile Modulus vs. PPMA contents of injection moulded bars at 0.0158 1/min strain rate	183

Figure 5.72: Tensile Modulus vs. clay contents of injection moulded bars at 0.0158 1/min strain rate	183
Figure 5.73: Tensile Modulus of 3% clay systems vs. PPMA/clay ratio of compression moulded sheets at different strain rates	184
Figure 5.74: Tensile Modulus of 3% clay systems vs. PPMA/clay ratio of injection moulded bars at different strain rates	185
Figure 5.75: Tensile Modulus of 5% clay systems vs. PPMA/clay ratio of compression moulded sheets at different strain rates	186
Figure 5.76: Tensile Modulus of 5% clay systems vs. PPMA/clay ratio of injection moulded bars at different strain rates	186
Figure 5.77: Tensile Modulus of 3% clay system with 3% PPMA for different mixing procedures at different strain rates	188
Figure 5.78: Tensile Modulus of drawn PPNCs ($\lambda=3$) vs. clay contents at different strain rates	193
Figure 5.79: Tensile Modulus of drawn PPNCs ($\lambda=2$) vs. clay contents at different strain rates	193
Figure 5.80: Tensile Modulus of drawn PPNCs ($\lambda=4$) vs. clay contents at different strain rates	194
Figure 5.81: Effect of draw ratio on tensile Modulus of different drawn PPNC samples at 0.0053 (1/min)	195
Figure 5.82: Effect of draw ratio on tensile Modulus of different drawn PPNC samples at 0.0105 (1/min)	196
Figure 5.83: Effect of draw ratio on tensile Modulus of different drawn PPNC samples at 0.0158 (1/min)	196
Figure 5.84: Effect of draw ratio on tensile Modulus of different mixing route of drawn PPNC samples at 0.0053 (1/min)	197
Figure 5.85: Effect of draw ratio on tensile Modulus of different mixing route of drawn PPNC samples at 0.0105 (1/min)	198
Figure 5.86: Effect of draw ratio on tensile Modulus of different mixing route of drawn PPNC samples at 0.0158 (1/min)	198
Figure 5.87: Thermal and video images taken during the fracture test showing general behaviours of undrawn and drawn PP and PPNCs	201
Figure 5.88: Load-displacement plot of 1.5 mm notch for the undrawn core PP and 3% clay systems of PPNCs	202
Figure 5.89: Load-displacement plot of 1.5 mm notch for the undrawn skin PP and 3% clay systems of PPNCs	203
Figure 5.90: Load-displacement plot of 2.0 mm notch for the undrawn core PP and 3% clay systems of PPNCs	203
Figure 5.91: Load-displacement plot of 2.0 mm notch for the undrawn skin PP and 3% clay systems of PPNCs	204
Figure 5.92: Load-displacement plot of 2.5 mm notch for the undrawn core PP and 3% clay systems of PPNCs	204
Figure 5.93: Load-displacement plot of 2.5 mm notch for the undrawn skin PP and 3% clay systems of PPNCs	205
Figure 5.94: Load-displacement plot of 1.5 mm notch for the undrawn core PP and 5% clay systems of PPNCs	205
Figure 5.95: Load-displacement plot of 1.5 mm notch for the undrawn skin PP and 5% clay systems of PPNCs	206
Figure 5.96: Load-displacement plot of 2.0 mm notch for the undrawn core PP and 5% clay systems of PPNCs	206
Figure 5.97: Load-displacement plot of 2.0 mm notch for the undrawn skin PP and 5% clay systems of PPNCs	207
Figure 5.98: Load-displacement plot of 2.5 mm notch for the undrawn core PP and 5% clay systems of PPNCs	207
Figure 5.99: Load-displacement plot of 2.5 mm notch for the undrawn skin PP and 5% clay systems of PPNCs	208
Figure 5.100: TEM micrographs for skin and core of undrawn (PP+ 5% clay+ 3% PPMA)	209
Figure 5.101: Thermal images taken during the fracture test for the first notch length just before the yielded ligament had fully ruptured	210
Figure 5.102: Thermal images taken during the fracture test for the second notch length just before the yielded ligament had fully ruptured	211
Figure 5.103: Thermal images taken during the fracture test for the third notch length just before the yielded ligament had fully ruptured	212

Figure 5.104: Load-displacement plot of the first notch for the drawn PP and 3% clay systems of PPNCs ($\lambda=2$)	213
Figure 5.105: Load-displacement plot of the first notch for the drawn PP and 5% clay systems of PPNCs ($\lambda=2$)	214
Figure 5.106: Load-displacement plot of the second notch for the drawn PP and 3% clay systems of PPNCs ($\lambda=2$)	214
Figure 5.107: Load-displacement plot of the second notch for the drawn PP and 5% clay systems of PPNCs ($\lambda=2$)	215
Figure 5.108: Load-displacement plot of the third notch for the drawn PP and 3% clay systems of PPNCs ($\lambda=2$)	215
Figure 5.109: Load-displacement plot of the third notch for the drawn PP and 5% clay systems of PPNCs ($\lambda=2$)	216
Figure 5.110: Load-displacement plot of the first notch for the drawn PP and 3% clay systems of PPNCs ($\lambda=3$)	217
Figure 5.111: Load-displacement plot of the first notch for the drawn PP and 5% clay systems of PPNCs ($\lambda=3$)	217
Figure 5.112: Load-displacement plot of the second notch for the drawn PP and 3% clay systems of PPNCs ($\lambda=3$)	218
Figure 5.113: Load-displacement plot of the second notch for the drawn PP and 5% clay systems of PPNCs ($\lambda=3$)	218
Figure 5.114: Load-displacement plot of the third notch for the drawn PP and 3% clay systems of PPNCs ($\lambda=3$)	219
Figure 5.115: Load-displacement plot of the third notch for the drawn PP and 5% clay systems of PPNCs ($\lambda=3$)	219
Figure 5.116: Load-displacement plot of the first notch for the drawn PP and 3% clay systems of PPNCs ($\lambda=4$)	220
Figure 5.117: Load-displacement plot of the first notch for the drawn PP and 5% clay systems of PPNCs ($\lambda=4$)	220
Figure 5.118: Load-displacement plot of the second notch for the drawn PP and 3% clay systems of PPNCs ($\lambda=4$)	221
Figure 5.119: Load-displacement plot of the second notch for the drawn PP and 5% clay systems of PPNCs ($\lambda=4$)	221
Figure 5.120: Load-displacement plot of the third notch for the drawn PP and 3% clay systems of PPNCs ($\lambda=4$)	222
Figure 5.121: Load-displacement plot of the third notch for the drawn PP and 5% clay systems of PPNCs ($\lambda=4$)	222
Figure 5.122: Effect of draw ratio on the total work of fracture of PP and 3% clay systems PPNCs at low notch length	224
Figure 5.123: Effect of draw ratio on the total work of fracture of PP and 5% clay systems PPNCs at low notch length	225
Figure 5.124: Effect of draw ratio on the total work of fracture of uncompatibilized 3% and 5% clay systems PPNCs at low notch length	226
Figure 5.125: Effect of draw ratio on the total work of fracture of PP and 3% clay systems PPNCs at medium notch length	227
Figure 5.126: Effect of draw ratio on the total work of fracture of PP and 5% clay systems PPNCs at medium notch length	227
Figure 5.127: Effect of draw ratio on the total work of fracture of uncompatibilized 3% and 5% clay systems PPNCs at medium notch length	228
Figure 5.128: Effect of draw ratio on the total work of fracture of PP and 3% clay systems PPNCs at high notch length	229
Figure 5.129: Effect of draw ratio on the total work of fracture of PP and 5% clay systems PPNCs at high notch length	229
Figure 5.130: Effect of draw ratio on the total work of fracture of uncompatibilized 3% and 5% clay systems PPNCs at high notch length	230

List of Tables

Table 4.1: TOTAL PPH 5042 & PPH 5060 Properties	79
Table 4.2: Southern Clay® Cloisite® 15A Properties	81
Table 4.3: Fusabond® P M613-05 Properties	82
Table 4.4: Injection moulding process parameters	96
Table 4.5: Injection moulding processing temperatures	96
Table 4.6: Drawn samples dimensions ($\lambda=2$)	101
Table 4.7: Drawn samples dimensions ($\lambda=3$)	101
Table 4.8: Drawn samples dimensions ($\lambda=4$)	101
Table 4.9: Strain Rates Used in Video Extensometer Experiment	112
Table 4.10: Different Sample Geometries of Tensile Video Extensometer Test of Undrawn and Drawn PPNCs	113
Table 4.11: Different Sample geometries of Fracture Test of Isotropic and Oriented PPNCs	117
Table 5.1: In-line viscosity index values of different PPNCs	141
Table 5.2: Spherulitic Morphology of PPNC Samples	149
Table 5.3: Wide Angle X-Ray Diffraction Analysis of PPNCs	163
Table 5.4: Transmission Electron Microscopy Analysis of drawn and undrawn PPNC Samples	169
Table 5.5: Tensile Modulus of undrawn Compression Moulded Sheets of PPNCs	175
Table 5.6: Tensile Modulus of undrawn Injection Moulded Sheets of PPNCs	175
Table 5.7: Tensile Modulus of drawn PPNC Samples, $\lambda= 2$	190
Table 5.8: Tensile Modulus of drawn PPNC Samples, $\lambda= 3$	191
Table 5.9: Tensile Modulus of drawn PPNC Samples, $\lambda= 4$	191

بسم الله الرحمن الرحيم
الحمد لله والصلاة والسلام على رسول الله

This thesis is dedicated to my wonderful parents. Without their guidance, I would not accomplish my goals in education and life.

Acknowledgements

I would like to thank the following people for their contributions:

My supervisor: Dr John Sweeney for his encouragement, guidance and support in the different stages of my thesis. I am also heartily grateful for his reading and commenting on my report.

I would like to show my appreciation to my supervisors: Professor Phil Coates for his support and Dr Fin Caton-Rose for his valuable suggestions, and assistance in the die-drawing process and mechanical testing.

I am also grateful to my colleague Mr Omar Alkoles for his valuable discussions and assistance during the experimental work.

Many thanks to Mr Glen Thompson for his assistance during video-extensometer tensile experiment, die-drawing process, and fracture testing. I also convey my thanks to Dr. Adrian Kelly, Dr. Emma Burton, and Mr John Wyborn for their assistance in the compounding stage.

I also appreciate the assistance of Dr Leigh Johnson, Mr Mohammed Umar and Mr Salah Elsheikhi, for their support in the injection moulding process.

I wish to extend my heartfelt gratitude to Dr Ahmed Toseef for his excellent job in the POM study. My special thanks to Ms Pallavi Mb who provided us with the TEM images and first part of WAXD results. Many thanks to Dr Abdulhamid Mokdad, Mr Soliman Almohimeed and Mr Ashok Menon for their arrangements for characterization testing.

I owe a lot of thanks to my wife, Huda, and children (Rand, Wajd, Jana, and Omar) for their love and patience.

My sincere thanks are due to my brothers (Mohammed, Abdullah, Abdulaziz and Abdulilah) and sisters (Mona, Manal, Manar, and Mariam) for their encouragement and continuing support.

Finally, I appreciate the financial support from SABIC.

1 Introduction

1.1 General

Since the Toyota group developed a nylon 6/montmorillonite nanocomposite with good mechanical properties, polymer-clay nanocomposites represent a new class of materials with potential utility in many areas (automotive, tyres and rubber, packaging, etc.) [1].

Because of the geometry and structure of nanoparticles, they can provide high surface-to-volume ratio. This massive internal interfacial area with nanoscale dimensions between the clay particles differentiates polymer-clay nanocomposites from traditional composites and filled plastics. Polymer coils are 40 nm in diameter, and the nanometer clay particles are on the same order of magnitude; as a result, molecular interaction between the polymer and the nanoparticles will give polymer nanocomposites unusual material properties that polymer alone does not possess [2].

This structure results in an essential property modification in polymer-nanoparticles at small filler contents as compared to neat polymers. For example, polypropylene nanocomposites (PPNCs) achieve better stiffness than the pure polymer by adding 2 to 5% clay. It is also shown that addition of clay could improve other properties such as thermal stability, flame retardancy, and gas permeability [3]. The improved performance and unique properties of these nanocomposites are established by the particle sizes, interparticle interactions, and their surface structure.

The organic polymer and nonorganic nanoparticles are nanoscale materials that contain dimensions smaller than 100 nm. The nanoparticle surface may be treated to provide hydrophobic characteristics and thus enhanced in its capability to be introduced to the hydrophobic polymer matrix. The layered silicate material used in this work is frequently utilized for the preparation of PPNCs. The montmorillonite (MMT) nanoparticles material was selected from the smectite group mineral to be introduced to the PP.

Uniform dispersion of these nanoparticles produces large interfacial area per volume between the nanoparticle and the host polymer. However, the overall performance of PPNCs cannot be understood on the simple basis that serves for traditional polymer composites. Development of PPNCs involves several key steps. First is synthesis of size and shape of nanoparticles and their surface treatment. Second is selection of the proper processing and fabrication techniques to achieve uniform dispersibility of the nanoparticles in PP matrix. Third, characterization of nanoparticles is indispensable to understand the structure behaviour and its relation to the property. Finally, to determine the performance of these polymer-nanostructured materials, a range of different test methods is needed.

Understanding property improvement related to PPNCs is a very complex matter. Despite their initial successes (e.g., Toyota used PPNCs to make parts for automobiles [4]), nanocomposites have not yet found wide-range of application in industry. For polyolefin in particular, preparation of polymer nanocomposites is challenging. Quite often, adding clay does not increase modulus very much, but instead, dramatically decreases toughness or elongation at break, as compared to the original polymer. Most often, this is due to the poor dispersion

(distribution on a large scale) and/or poor exfoliation (distribution on a microscale) of clay platelets in the polymer matrix. Because of the strong hydrophilic structure of the clay surfaces and the strong hydrophobic structure of the PP chains, there is a significant enthalpic driving force to drive clay platelets to stick together. As a result, unmodified clay tends to remain in stacks when melt mixed with PP. Even if those stacks are broken up by shear forces in a mixer or extruder, it is still thermodynamically favourable for the platelets to reaggregate when shear removed. Thus, it is necessary to involve organic modification of the clay platelets, putting small hydrocarbon chains on their surfaces. Even then, thermodynamics of clay platelet mixing with polymer remains often unfavourable and stacks act as stress concentrators, and the material is likely to become more brittle than pure polymer (although this statement is certainly not universal).

1.2 Objective

This work contributes to the recently efforts in the nanocomposite field by investigating the property and structure behaviour of die drawn PPNCs. Performance of tensile modulus and fracture toughness of different loading die-drawn PPNCs at various speeds and draw ratios are the main objective of this work; taking into account the importance of compounding, processing and characterization. The different requirements to achieve the main objective are summarized as follows:

- Compounding and processing: ensuring that clay platelet intercalation/exfoliation and alignment is helped (imposed shear, way of mixing, orientation, etc.).

- Tensile modulus of undrawn PPNCs as compared to pure undrawn PP.
- Tensile modulus of drawn PPNCs as compared to pure drawn PP with different draw ratios.
- Fracture behaviour of undrawn PPNCs as compared to pure undrawn PP.
- Fracture behaviour of drawn PPNCs as compared to pure drawn PP. The samples are going to be prepared with three different draw ratios.
- Linking the morphology of the nanocomposite (clay loading level, degree of exfoliation, and alignment) to the desired property enhancement.

1.3 Scope and Content

After reviewing the PPNCs synthesis, characterization, rheological and mechanical properties, a new area of research was identified to be investigated to go further in understanding the PPNCs structure/property relationship. These are the tensile and fracture behaviour of the oriented PPNCs by means of die drawing as compared to unfilled PP and unfilled drawn PP.

It is well known that a considerable enhancement of some PP properties such as stiffness and strength can be produced by solid-state molecular orientation [5, 6]. This important area was not investigated for PPNCs. Orientation can also have a dawn side in strength of the directions other than the draw direction. For this reason, a combined of fracture behaviour is particular interest in studying tensile properties of drawn PPNCs. The work on fracture behaviour of PPNCs is going to be covered by means of total work of fracture. Understanding the fracture behaviour of the solid phase oriented PPNCs is particularly important because it is directly related to the service life of materials under dynamic deformation. As a reliable indicator of the impact toughness of

PPNCs, applying the total work of fracture is suggested to be the second main objective for this project.

The report is divided into six chapters: an introduction (chapter 1), literature review (chapter 2), tensile and fracture behaviour (chapter 3), experimental work (chapter 4), results and discussions (Chapter 5), conclusion, recommendation and suggestion for future work (chapter 6).

Chapter 2 summarizes the research activities in the areas of: (a) developing processes to disperse nanoparticles uniformly in the polymer; (b) using wide angle x-ray diffraction (WAXD), transmission electron microscopy (TEM), and other methods to characterize polymer nanocomposite structures; and (c) studying the structure-property relationship of polypropylene nanocomposites. The processing method that was considered to disperse nanoparticles in the polymer material is the melt compounding method. Finally, conclusions and recommendations of the literature review are presented at the end of the chapter.

Chapter 3 explains principle and theory behind the tensile and fracture behaviour of polymer materials with definitions of most used expressions in the different chapters. Attention is given to the drawing process and its effect on both molecular orientation and changes in morphology.

Chapter 4 gives the details of the raw materials, the pieces of equipment used and the procedure for samples preparation (compounding and processing). The testing methods used for material characterization are illustrated in details with schematic diagrams.

Chapter 5 presents and discusses the results of the mechanical and characterization of the sheets received from Queen's University Belfast and the characterization for different compounding samples prepared in our laboratory. Tensile modulus and fracture are then discussed with link to the results obtained in polarizing optical microscopy (POM), WAXD and TEM micrographs.

Chapter 6 presents the conclusion and recommendation for the work done in different chapters of this project. This chapter also illustrates the suggested future work toward achieving high performance PPNCs.

2 Literature Review

2.1 Introduction

One important step before working on the main thesis objective is to review recent progress in the preparation, characterization, and properties of PPNCs. This was done, in order to avoid any possible causes of confounding in the main props. A special attention is given to clay dispersion and intercalation into the polymeric system.

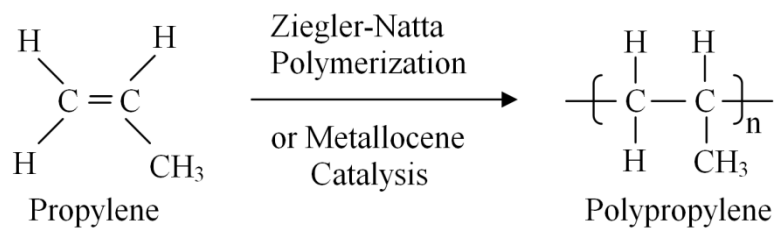
2.2 Polypropylene

2.2.1 Polypropylene general features

The mass commercial exploitation of PP has been very rapid, with the material becoming widely used in various industrial areas for fibres, films and injection moulded articles. In comparison to other polymers, this fast growth of PP production has been encouraged by excellent combination of features such as low density, high heat deflection temperature (HDT) above 100 °C, good chemical and water resistance, recyclability, low cost, range of applications and good price/property ratio [7]. Further modification of PP is possible by adding fillers or creating blends. Special monomers or elastomers can render PP structure more flexible with a variety of other properties.

2.2.2 Polypropylene structure

Homopolymer PP is a vinyl polymer that can be produced by using of organo-metallic catalysts that link the polymer together, resulting in chains that are crystallisable [8], through the following reaction:



The three configurations that can be recognized for the PP chains differ based on CH₃ groups organization along the polymer backbone. In addition to isotactic structure, which is commonly used, there are syndiotactic and atactic structures. In isotactic PP, the CH₃ groups locate on one side of the chain. This regularity in arrangement causes ease of packing, thus higher degree of crystallinity due to the higher amount of isotactic phases. When CH₃ groups exist alternately on top or bottom side of the polymer chain, syndiotactic structure is dominant and leads to have more flexible PP structure. This flexible structure is favourable for higher impact resistance and adhesion to the organic surfaces. In atactic PP, there is no order at all and methyl groups exist randomly on either side of the polymer chain and thus very low degree of crystallinity is resulted.

PP is a semi-crystalline material, where its molecular chains can arrange themselves in lamellar fibrils at low cooling temperatures. These structures expand from the crystal nucleus causing an organization that produces the whole assembly (spherulite) shown in Figure 2.1 [8]. Thus the final structure can be recognized by crystal structure on the smallest scale, lamellar structure in the mediate scale and spherulites on the largest scale.

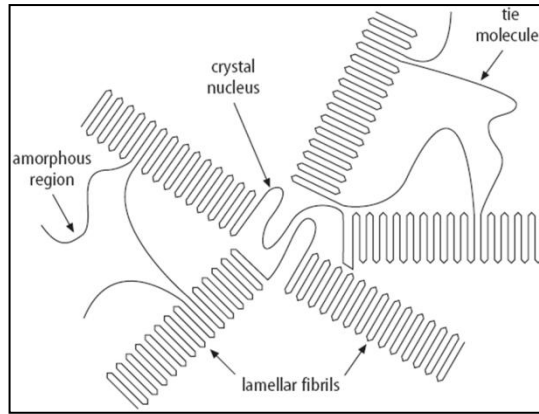


Figure 2.1: Schematic illustration of chains organization in PP spherulites

2.2.3 Polypropylene properties

The property of PP material is well investigated in many different fields and thus the properties that could directly support the thesis are going to be covered and briefly outlined.

The PP mechanical properties are strongly influenced by the arrangement of the polymer molecules in crystalline or amorphous structure that obviously affect the stiffness and ductility of PP. As the ductility is influenced by the chain regularity (tacticity), it is also affected by the thermal history. Like in injection moulding process, quenching to a low mould temperature causes the PP molecules to be frozen in an amorphous state with less arrangement of crystalline areas. This material is expected to be less stiff than slowly cooled ones.

Due to the problems of the low brittle temperature and high oxidation with light, PP material is usually mixed with fillers and commercialised in many applications as a copolymer. This incorporation of fillers such as glass fiber or nanoclay can solve the problems that come from the low stiffness and/ high mould shrinkage

2.3 Surface-Modified Montmorillonite Clay

The most commonly used surface-modified clay that incorporates to the PP material to prepare the nanocomposites is the smectite-type montmorillonite layered silicates. A brief summary of the MMT structure and its surface treatment are given in the next two sections.

2.3.1 Structure of montmorillonite clay

The montmorillonite structure is related to the general family of two silica tetrahedral to one octahedral silicate layers [3]. These two-silica tetrahedral are linked to an edge of aluminium hydroxide octahedral sheet. Figure 2.2 [1] shows the structure of MMT silicate layers. As the silicate layers stacked, gaps between them are generated, producing what it usually calls interlayer or gallery, where van der Waals forces are active. Isomorphic substitution is made by replacing of Mg^{2+} or Fe^{2+} by Al^{3+} within the layers, which generates negative charges. The amount of these charges measures by the cationic exchange capacity (CEC). These charges are balanced by the existing cations in the space of the interlayer. The CEC value is typically between 0.9-1.2 milli-equivalent per gram.

In naturally occurring montmorillonite clay, the cations are commonly hydrated Na^+ , K^+ , or Ca^{2+} . This structure is highly hydrophilic, and it is not miscible with hydrophilic polymers [9]. However, ion exchange reactions of interlayer cations with an organic cations such as alkylammonium can render the clay surface organophilic [10]. The alkylammonium reduce the energy of the clay surface and thus can be introduced to the polymer by expanding the layer or basal spacing. In addition, this cation may contain different kind of functional

groups that could interact partially with PP to introduce the inorganic clay into the organic polymer.

MMT is found naturally with a high surface area ($750 \text{ m}^2/\text{g}$). The nanoclay particles exist in aggregated tactoids structure that contains 20-25 layers with aspect ratio of 10. The desired exfoliated clay creates single clay platelets with thickness of 1 nm and aspect ratio of about 100. It is very common in these systems to be made up of partially exfoliated clay in a combination or a hybrid structure, where only part of the nanoclay exists in the exfoliated state and the other parts exist in the intercalated state [11].

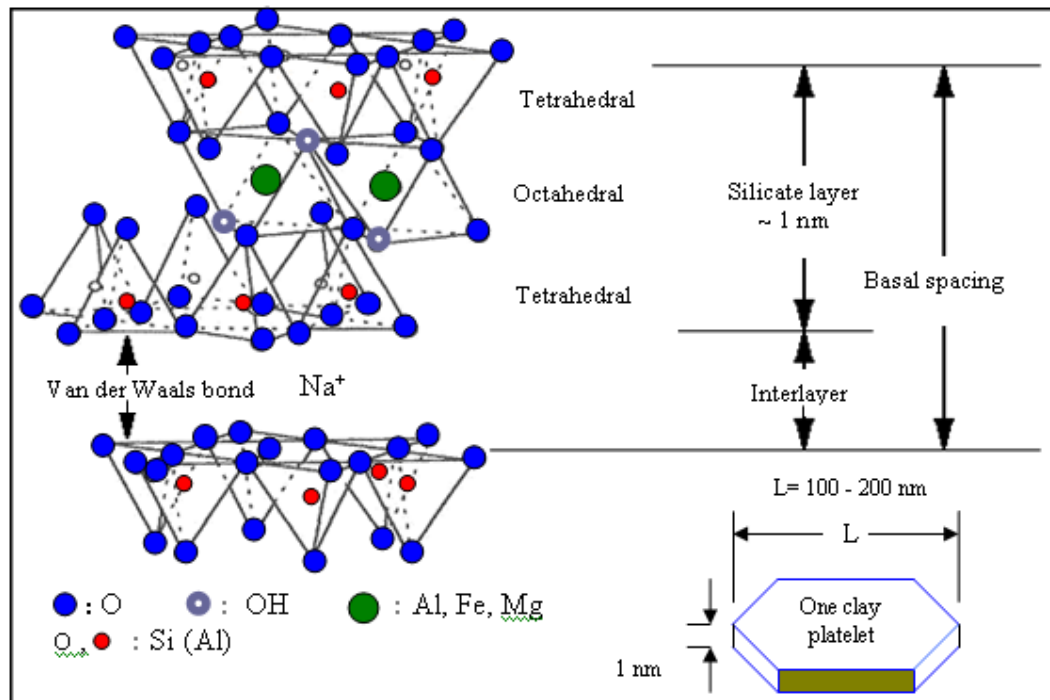


Figure 2.2: Schematic representation of the MMT chemical structure of 2:1 layered silicates (left) and the shape and dimensions of a clay platelet (right).

2.3.2 Surface treatment

The laboratory route commonly used an ion exchange reaction in solution to introduce alkylammonium ions in the interlayer, which promotes the formation of the required ion to dissolve the used amine with an acid [12] or a

salt that contains an alkyl, which is linked to counter ions such as bromide or chloride [13] into hot water (about 80°C) (schematically illustrated in Figure 2.3). This solution is introduced to another solution of dispersed MMT. A stirring is required to get precipitates that should be washed and dried before use.

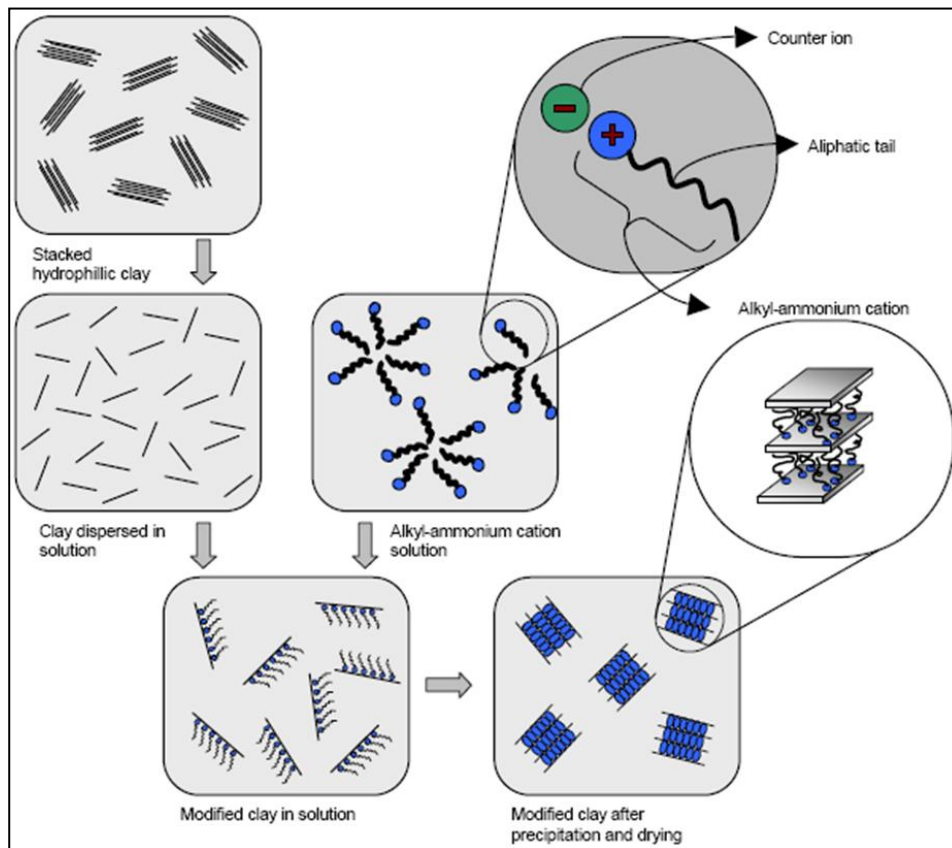


Figure 2.3: Schematic representation of clay surface treatment

The molecular chain length of alkyammonium has a clear effect on clay surface polarity, and thus affects the interaction between the polymer and organoclay particles. Reichert et al. [14] modified inorganic clay using protonated C4 to C18 alkylamine. PPNCs were then compounded using different organoclay with (or without) a polypropylene maleic anhydride (PPMA) modified as compatibilizer. In the absence of compatibilizer, modulus of polypropylene composites was very similar to that of neat PP. However, with the addition of PPMA, there was significant improvement in modulus when the

chain length was 12 carbon atoms or higher. The structure then was detected by a broadened peak from wide-angle X-ray scattering (WAXS) and TEM [14] and showed great improvement in exfoliation degree as PPMA is involved.

Theoretically, an increase in carbon chain length would give a more hydrophilic organoclay. However, in the case of making PPNCs, longer chain length doesn't necessarily translate into better properties [8]. This lack of property improvement was explained by higher organic loading in an organoclay when the alkyl chain length is longer. At the same organoclay loading level, the inorganic part of organoclay is smaller, and the reinforcement effect of organoclay will be decreased. Consequently, there is an optimal organic loading level that is determined by both alkyl chain length and clay cation exchange capacity (CEC). Typically, an increase in chain length of alkylammonium corresponds to an increase in interlayer spacing [8]. So ammonium ions such as hexadecyl tri-methyl [13] or di-octadecyl di-methyl [15] are employed. At a certain chain length, the CEC of particular clay determines the number of molecular chains per unit area.

The effect of two kinds of treatments of MMT on morphology and dynamic mechanical properties were reported by Pravin et al. [16], one was organically modified with a tallow compound and the second MMT was treated with octadecylamine. The cation-exchange capacity values for the two clay samples were reported to be 140 and 135 meq/100 g, respectively. The results showed an advantage for octadecylamine treatment in storage modulus and tensile modulus by 2.5%, But lower yield strength by 3 %.

Many attempts have been done to solve the issue of polarity because the fact that clay still polar even after the surface modification by nonpolar alkyl

groups. Liu et al. [13] introduced a co-intercalating monomer that leads to have larger interlayer spacing in clay stacks and possibility coupled on the PP backbone by a grafting reaction.

2.4 Compatibilizer

The effect of reinforcement in PPNCs is determined by two important factors: clay dispersion and interaction between clay and polymer. Organoclay can be well dispersed in the PP matrix by using appropriate compounding techniques, when the clay surface is covered by a sufficient amount of organic surfactant (such as alkylammonium). However, in many cases, the mechanical properties remain quite poor due to inadequate stress transfer from the polymer matrix under applied stress to load-bearing clay reinforcement. The cause for this weakness is attributed to poor compatibility in the interphase region that exists between non-polar PP molecules and polar clay layers. To overcome this problem, the most effective approach is to add bifunctional compatibilizer to PPNCs to enhance adhesion at the polymer-clay interface.

The introduction of PPMA as compatibilizer made it feasible to compound PPNCs without using solvent [17, 18]. Wang et al. [19] showed the importance of chemical modification with PPMA on the dispersion of the PPNCs though the change in property. Commercially available PPMA products have a wide variety of grades, including different molecular weight and maleic anhydride (MA) content. Optimization of the type and amount of compatibilizer is crucial to make successful PPNC hybrids. The content of MA is very critical, as the small functionalized PP would be not enough to have the required diffusion into the polymer matrix. Conversely, high quantities of MA would

increase the polarity to a level where the polymer molecules can not diffuse in them [20].

The maleic anhydride groups are grafted or block copolymerized in polymer chains. It is made with peroxide as an initiator in reactive extrusion that produces a free radical by a scission process for the chain of the polymer. MA is then attached to the reactive free radical. Two or three groups, where polar heads are attached to aliphatic tails, can be produced to react with the PP broken chains. MA ring with the oxygen atoms are then introduced to the hydroxyl group of the polar clay. Such structure can generate strong hydrogen bonding, which help in exfoliation process. In contrast, hydrocarbon part is introduced to the nonpolar PP.[12]. Figure 2.4 shows a schematic diagram of the clay dispersion into the polymer matrix, sketched from reference [12].

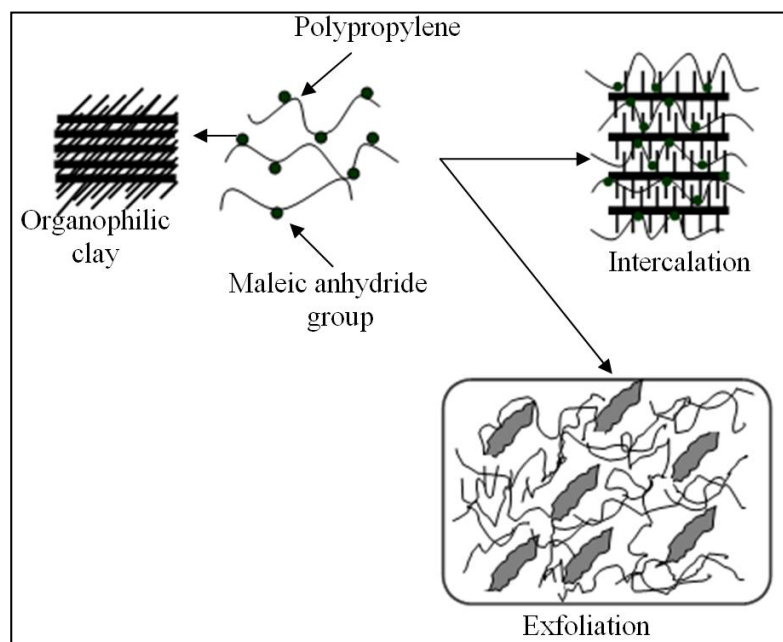


Figure 2.4: Schematic representation of the clay dispersion process

The efficiency of the PPMA in compatibilization of PPNC systems is mainly influenced by two factors. They are molecular weight (MW) and MA

content. The following two sections review the importance of these factors and how they affect the degree of exfoliation and property of PPNCs.

2.4.1 Molecular weight effect

In most publications, low MW of PPMA is involved to get best resulting interaction into clay galleries and thus enhance the mechanical properties. Svoboda et al. [7] reported that the best impact and tensile strength are obtained by the higher PPMA MW (MW = 330,000), but the best degree of exfoliation and dispersion are given by low PPMA MW (MW = 9100). Koo et al. [21] reported that Maleated PP with high molecular weight intercalates slowly and the other with low molecular weight exfoliates fast into clay layers.

Kim et al. [22] used four PP compatibilizers with varying degree of MA grafting and three PP matrix of low, medium and high viscosities. It was found that low viscosity PP with the compatibilizer of the lowest MA content (0.55%) resulted in the greatest improvement of dynamic storage modulus. Wang et al. [11] and Perrin et al. [23] found that PPMA with lower MW and higher MA content could lead to good clay dispersion, but it caused the deterioration in both mechanical and thermal properties. Perrin et al. [23] found that higher MW-PPMA produces an intercalation structure with signs of exfoliation (disordered and more distanced layers structure, small particles of 2 – 3 layers). While lower MW-PPMA did not show any further enhancement of the degree of exfoliation, but good and uniform intercalation were obtained. Such PPMA can interact largely with clay particles and intercalate easily clay platelets. They explained this shortage by the lack of miscibility with the PP matrix.

2.4.2 Maleic Anhydride content effect

The effect of MA content on the clay dispersion has been studied extensively, but the reported results are somewhat inconsistent. In most cases, high content of MA improves the PP melt intercalation into clay galleries. However, it was found to decrease the miscibility with the PP matrix [12] and thus reduce the mechanical properties of PPNCs. But some authors still found that high MA content (at 4%) improved the mechanical strength better than the low MA content (3%) under the same composition [14].

Another study [24], showed that addition of compatibilizer agent improves the mechanical properties and the best results were obtained when 5% PPMA (MA content is 0.2 %) was used and when the amount is increased, the exfoliated morphology becomes more evident. Lertwimolnun et al. [25] reported an improvement in the degree of dispersion for PPMA loading (MA content is 1 %) higher than 10 % and no further improvement above 25%. Perrin et al. [23] also found that, regardless of the type of PPMA, the weight ratio of PPMA to organoclay was roughly 3 in order to achieve maximum improvement in mechanical properties.

2.5 Polymer Nanocomposites

2.5.1 Polymer nanocomposites general features

The interest in polymer nanocomposites comes from the great enhanced performance in property that can not be obtained from the other reinforcing materials. These enhancements include mechanical, thermal and gas barrier properties, at slightly low level of loading (2-5%). This enhancement is a

consequence of the much greater surface to volume ratio of these high aspect ratio fillers.

2.5.2 Types of polymer nanocomposites

The interactions between the polymer and nanoclay depend mainly whether both interfaces of polymer and clay are modified with the compatibilizer or remain as they are. Three different morphologies types of PPNCs are attainable (see Figure 2.5).

Practically, it is difficult to define nanocomposite structures by a single measurement. The most common method to obtain structural information is X-ray diffraction (XRD), which can be utilized to measure the interlayer spacing distance (d_{001}) between clay layers.

2.5.2.1 Immiscible nanocomposites

Immiscible morphologies are those where large stacks (aggregates) of nanoclay platelets are dispersed in the polymer matrix (d spacing is similar to that of the starting layered silicate), so the polymer nanocomposite becomes almost with micron-size fillers similar to the conventional composite.

2.5.2.2 Intercalated nanocomposites

Intercalated nanocomposites are well-ordered multilayered structures where a few of polymer molecules are inserted into the spacing between the layered silicates structure (d spacing is greater than that of the initial layered silicate). However, when the layers are flocculated by matching the hydroxylated edge-edge interaction, it conceptually considers as intercalated type and call it flocculated nanocomposites.

2.5.2.3 Exfoliated nanocomposites

Exfoliated nanocomposites are well separated silicate layers with an average particle distance that may decrease or increase based on the clay loading in the polymer matrix. Then, d-spacing can not be detected by XRD. Most exfoliation systems contain much lower content of clay as compared to the intercalated systems.

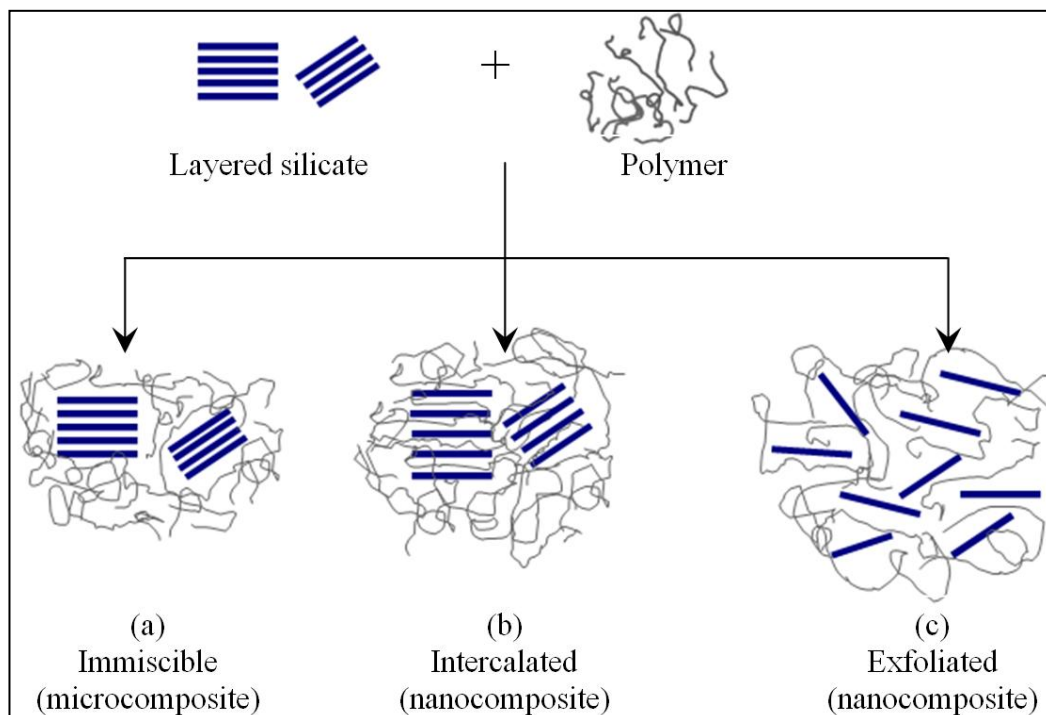


Figure 2.5: Immiscible, intercalated and exfoliated PPNCs

2.5.3 Thermodynamics and dispersion of PPNCs

In general, layered silicates have a very high aspect ratio that may reach to 1000. High surface area can be created as a few percent of dispersed layered silicates are well distributed in the polymer matrix and produce much higher PPNCs interaction as compared to other composites. Nam et al. [26] found that lamella diameter and length for PPNCs showed almost the same values as PP pure material and are independent of the clay content.

The first major piece in our understanding of the processing of PPNCs concerns the compatibility of the mixture. Whether or not the system forms a uniform dispersion depends not only on processing but also on the thermodynamic considerations. Even if well-separated, isolated clay sheets are mixed with polymers, these high-aspect ratio platelets can form ordered or crystalline structures, or can phase separate from the matrix material.

Understanding the driving forces for polymer nanocomposites could be obtained by analyzing thermodynamics of polymers confined in the gallery between two parallel clay platelets. As the matrix polymer penetrates into the gallery, its entropy decreases due to confinement of the polymer chains during the intercalation; this decrease in entropy needs to be balanced by some gain in enthalpy if exfoliation or intercalation was to occur between the polymer matrix and the silicates [3]. Vaia et al. [27, 28] developed a mean-field statistical lattice model to calculate free energy of polymers in the galleries and use this model to suggest the ways of improving the probability of exfoliation or intercalation. Balazs et al. [29] calculate such free energy profiles for a variety of model systems. As shown in Figure 2.6, increasing the free energy corresponds to immiscible morphology. In contrast, decreasing the free energy corresponds to exfoliated morphology. The free energy with a minimum at some finite gallery width represents intercalated morphology [3].

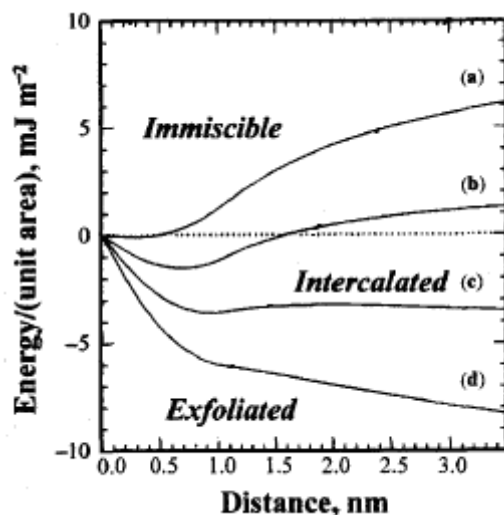


Figure 2.6: Modelling of clay intercalation and exfoliation of polymers in the galleries between adjacent clay platelets in a stack.

2.5.4 Formation of Polypropylene nanocomposites

In general, there are three ways to make PPNCs. They are: in situ polymerization, solution intercalation, and melt compounding [8]. Solution intercalation usually requires dissolving the polymer resin in an organic solvent and then intercalating into clay layers. This method is not feasible for large-scale production of PPNCs. In situ polymerization and melt compounding, on the other hand, have been used successfully to form PPNCs. The preparative method used in this work depends on the melt compounding. Thus, more attention in the review was given to this method of formation.

2.5.4.1 In situ polymerization

The successful synthesis of nylon-clay nanocomposite by in situ polymerization has drawn tremendous interest in making high-performance nanocomposite with montmorillonite clay. This success has not been extended to making polypropylene nanocomposites at commercial scale. The major impediment is the chemical sensitivity of current polymerization catalysts for polypropylene resin. However, by carefully controlling the reaction conditions,

PPNCs can be synthesized by in situ polymerization [30]. Recently, Yang et al. [31] reported a preparation of PPNCs by in situ polymerization with the combined use of a functional surfactant for MMT organic modification. XRD analysis showed a change in microstructure. TEM images revealed that some of particles were exfoliated to a few layers. However, there were still showed some microsized organoclay particles that were not dispersed.

2.5.4.2 Melt compounding

Most of the research activities have focused on preparation of PPNCs by melt compounding which was first reported by Vaia et al. in 1993 [3]. This preference is due to its cost effectiveness, ease of using conventional polymer mixing and processing equipment such as different types of mixers, extrusions or injection mouldings. This combines with its environmentally benign absence of organic solvents. Because polypropylene is a low-polarity polymer, it is extremely challenging to make well dispersed polypropylene nanocomposite.

Melt compounding or intercalation method is mainly used with introducing shear to the polymer and clay mixture above the melting temperature of the polymer. The MMT needs to be previously surface treated as discussed in 2.3, a compatibilizer (PPMA) has to be added to the PPNCs system as discussed in section 2.4, and an optimization of compounding conditions are one of the most important factors to disperse the clay layers into polymer matrix.

The most common compounding method is direct compounding using the extrusion process. By using this method, the clay is blended into base PP using a mixing tool such as twin-screw extruder (TSE) to form the PPNCs. A masterbatch compounding method is developed and has some advantages over

the direct compounding. These advantages are discussed in the following section (2.6).

Masterbatch can be prepared by using high-shear compounding devices, such as TSE or internal mixer. In order to disperse masterbatch effectively by single-screw extruder (SSE), there is a need to have high-shear mixing elements. New Castle Industrial, a SSE manufacturer, has developed a patented technology called NanoMixer. The NanoMixer is reported to product comparable dispersion and property as compared to twin-screw extrusion [8].

The masterbatch technique advantage is that the PP/PPMA compound pre-treated before introducing MMT and thus the introduced shear will promote the incorporation of clay into the polymer matrix. Conversely, in direct compounding, the introduced shear in the screw forces the clay layers to an unfavourable energy situation [9].

2.6 Processing of Polypropylene Nanocomposite

Most rheological studies show that the PPNCs melt flow is very comparable to the pure PP material. This fact is confirmed for the clay content that does not exceed 6% [32]. Thus there will be no extra cost in using PPNCs with existing processing machines. However, the dispersion problems have limited their applications.

During melt process the layered silicate and polymer matrix are mixed together in a molten condition. The polymer molecules, then crawl into the interlayer spacing of the clay particles and forms either an intercalation or an exfoliation systems. Figure 2.7 represents a schematic illustration of PPNCs formation by direct melt intercalation in MMT [28].

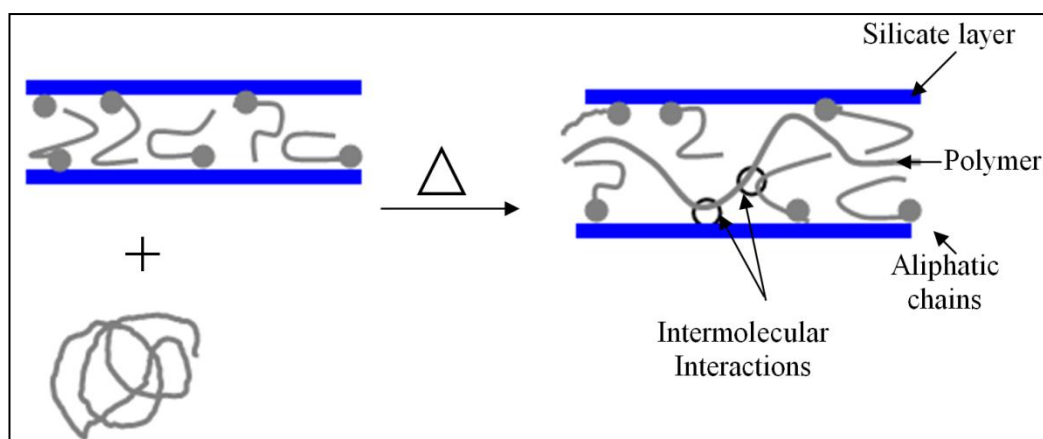


Figure 2.7: The intercalation process between a polymer melt and silicate layer

A range of PPNCs with structures from intercalated to semi-exfoliated can be obtained, depending on the degree of penetration of the polymer chains into the silicate galleries. The polymer melt flow and the compounding conditions play an important role to have a successful PPNCs processing.

2.6.1 Effect of the base polymer on PPNCs processing

The characteristic properties of PP raw material (mainly MW and molecular weight distribution (MWD)) play an important role in making PPNCs. During twin-screw extrusion, the length of the polymer molecular backbone not only affects intercalation of the clay but also affects the melt viscosity. Melt viscosity directly affects shear stress applied to the polymer melt. Various PP materials have different melt flow rates. For example, the mechanical properties of PP with different melt flow rates produced by masterbatch TSE were examined [8]. At the low melt flow range, good improvement in mechanical properties was reported. However, for high melt flow polypropylene, the improvement in mechanical properties was relatively small. The enhanced properties for low melt flow PP are attributed to the corresponding higher melt viscosity with increased shear deformation of ingredients during the extrusion process. Also, the melt viscosity of low melt flow PP has a better match with the

melt viscosity of masterbatch to enhance clay dispersion. However it has been reported by Kim et al. [20] that in case of using the compatibilizer, high or low viscosity of PP can produce a uniform dispersion. This indicates that PPMA can overcome problems that could be generated from insufficient produced shear in processing stage of the PP material that has low viscosity.

2.6.2 Effect of compounding conditions on PPNCs formation

Melt extrusion processing conditions are some of the most important factors to disperse layered silicate. It clearly appears that introducing sufficient shear stress is an essential to PPNCs formation. Wang et al. [19] studied the shear effect on the dispersion of the PP. They found that a partially intercalated morphology of PPNCs can be achieved without the help of shear. Combination with shear, a much better dispersion is obtained. Furlan et al. [33] prepared PP/MMT without compatibilizer, by using a co-rotating TSE, and showed that the shear intensity is determinant for morphology type, thermal and mechanical properties of PPNCs. They showed that the low and medium shear introduce higher crystallinity than PP (6 and 14 %), but lower crystallization temperature. On the other, the more semi-exfoliated sample as shown by TEM (high shear) increased the crystallization temperature and doesn't present a notable change in the crystallinity. However, this study did not show the MMT loading level in PPNCs.

Peltola et al. [34] studied the effect of screw speed on the degree of exfoliation of clay particles by using co-rotating TSE. It was showed through the TEM images that screw speeds can influence the PPNCs structure to be either intercalated or semi-exfoliated. However a result similar to the one presented by

Svoboda, suggests that even a highly exfoliated system is obtained, there was no notable change on the mechanical properties of PPNCs.

Another study by Cho et al. [32] compared three routes of mixing of PPNCs. The first route includes preparing of a masterbatch in TSE letdown with SSE. The second route uses a masterbatch in TSE letdown with TSE. The third route includes a direct compounding by using TSE. The results showed that a masterbatch letdown with SSE was better dispersion and mechanical properties than the direct compounding in TSE. Very comparable results between the masterbatch process with SSE and TSE are obtained. The two stage master batch processing is used by Treece et al. [35], in which MMT is first melt blended with PPMA before subsequent dilution with polymer matrix. The result shows an improvement in degree of exfoliation and dispersion relative to single stage processing at 3 and 5% loadings.

Recently, Lertwimolnun et al. [36, 37] studied the effect of three screw profiles and processing parameters (feed rate, screw speed and barrel temperatures) on the PPNCs structure by using XRD. The results showed that the level of exfoliation was dependent of the processing parameters. Conversely, intercalation system was quite independent of the processing parameters. It was also found that a partial control of the exfoliation can be obtained by the screw profile with different imposed shear rates and residence time. Quintanilla et al. [38] prepared PPNCs using compatibilizer and twin screw extruder in two-step mixing and one-step mixing. The better dispersion and exfoliation were obtained for the two-step mixing conditions.

Modesti et al. [39, 40] showed that the processing barrel temperature is a very important parameter: using lower temperature produces higher viscosity and

consequently higher shear stress and therefore, the exfoliation of the clay is promoted. They presented that the processing conditions was not strongly influenced the TGA result; instead, it greatly affect the dynamic-mechanical properties. Bettini et al. [41] reported that the processing conditions (screw speed and feed rate) has a minor effect on the PPNCs interaction as compared to the compatibilizer addition. Gopakumar et al. [42] did a batch mixing with a shaft speed of 2000 rpm until the material reached 190°C (90 seconds) and compared the results with extrusion masterbatch method using co-rotating twin screw extruder. Better dispersion was obtained when a batch mixing is used (measured by XRD), resulting in better tensile strength (3-6%), and lower strain at yield (30%) as compared to Extrusion sample. XRD patterns showed no peak indicating very exfoliation system. However, careful should be taken when only XRD results are examined, because it offers little scope for such quantifications.

2.7 Characterization and Morphology of Nanocomposite Structure

A very challenge area in PPNCs is how one can quantify the dispersion of such nanoparticles for both exfoliation and intercalation systems and use that quantifications in describing the final obtained properties.

Many studies tried to combine at least one of these analyses (WAXD and TEM) with other typical used ones for the neat polymer material. These are scanning electron microscopy (SEM), optical microscopy (OM), small angle X-ray scattering (SAXS), wide angle x-ray scattering (WAXS) and nuclear magnetic resonance (NMR). However, WAXD is very powerful in monitors the intensity of the basal reflections, and thus the PPNCs structure of the silicate layers can be identified.

SAXS and WAXS are essentially conducted to characterize the crystalline morphology and to some extent the degree of orientation of PPNC matrix, while OM is used to investigate the spherulitic texture. The following paragraphs highlight the combination used between different methods that help in PPNCs characterization.

2.7.1 Wide angle x-ray diffraction and transmission electron microscopy

XRD is the most straightforward way to evaluate the spacing between the silicate layers reflecting the relationship of the clay layers with themselves [43-45] and occasionally to investigate the melt intercalation kinetics of polymer materials [46]. However, one should be careful with the interpretation of the XRD results, because it can only detect the periodically stacked silicate layers, not sort out how well clay dispersion is throughout the polymer matrix.

On the basis of WAXD patterns and TEM images, they proposed a possible measuring mechanism for dispersion of PPNCs. Kawasumi et al. [12] believe that the driving force of the intercalation originates from the MA group and the oxygen groups of the silicate through hydrogen bonding.

Nam et al. [26] prepared PPNCs with three different amounts of clay content (2, 4 and 7.5%). WAXD patterns clearly established the formation of nearly exfoliated structures in 2 % clay system and disordered intercalated nanocomposites in 4 and 7.5%.

Liu et al. [13] reported the preparation of PPCN via grafting-melt compounding using a new type of co-intercalated organophilic MMT which has a larger interlayer spacing than the ordinarily organophilic clay that was modified with alkylammonium cations. WAXD patterns and TEM observations

established that the larger interlayer spacing and strong interaction caused by grafting can improve the dispersion effect of silicate layers in the PP-matrix.

Hasegawa et al. [18] found that PPMA was able to intercalate into the intergalleries of organic montmorillonite intercalated with octadecylammonium (C18-MMT), similar to the functional oligomer. WAXD patterns and TEM images illustrated that were exfoliated and uniformly dispersed of the silicate layers in the PPMA matrix. Similar results were obtained by Park et al. [47] where they show not only good dispersion but also clay heterogeneous intercalation. WAXD analysis of PPNC showed no peak representing dispersed C18-MMT in the PP-MA matrix. According to the authors, that means that the driving force of the PPMA originates from the strong hydrogen bonding between the MA groups and the polar clay surface. Ray et al. [48] mentioned that some layered silicates do not show well defined basal reflection. Therefore, it is very difficult to study the peak broadening and intensity obtained from the WAXD.

Ton et al. [49] found the gallery distance of the PP/Cloisite 15A to be decreased to 2.4 nm as compared to the 2.8 nm for the Cloisite 15A. They suggested that a collapse in the clay gallery is dominant. Cui et al. [50, 51] reported that the purification level and surfactant loadings of organoclay significantly affect their thermal stability; however, the results from WAXD characterization showed that these differences in thermal stability that lead to lower d-spacing do not appear to have much effect on the morphology and properties of the nanocomposites formed from them.

Although WAXD exhibits an approached method to determine the interlayer spacing of nanoclay, little information can be given for the distribution per unit area of the PPNCs. This can be considered for the layer spacing between

1 and 4 nm. But, when the layer spacing is more than 6 nm in the intercalation systems or for a disordered exfoliation system, WAXD become very weak to explain the interpretation of data [48]. TEM is therefore a necessary complement for evaluating nanocomposite structure, since it allows a qualitative method to explore of the structure, distribution per unit area, and monitoring of any deficiency in the polymer/clay structure by direct visualization. However, care must be taken in preparation of the sample and its representation of the PPNC matrix.

2.7.2 Scanning electron microscopy and wide angle x-ray diffraction

Wang et al. [19] used the SEM, TEM and WXRd to study the PPNCs dispersion., while Cho et al. [32] used OM for the same purpose. Recently Paiva et al. [52] tried to characterize the PPNCs, with different clay loading levels, by WXRd and SEM. The authors were looking to any unsatisfactory dispersion that may present as large clay aggregates in PP matrix. Even there is a slight change in micrographs of PP and PPNCs, but it was difficult to distinguish between PPNCs with different clay contents and thus the TEM images demonstrate superior sub-micro level in resolution that presents beneficial details as compared to the SEM and OM ones.

2.7.3 Small angle X-ray scattering and wide angle x-ray scattering

In addition to the possible obtaining information about the degree of exfoliated PPNCs from XRD, The orientation and crystalline morphology of PPNCs might be investigated by two-dimensional (2D) SAXS and 2D WAXS.

Bafina et al. [53] studied the orientation and structure for polyethylene film using 2D SAXS and 2D WAXS in three sample/camera orientations. Data

was fitted using a platelet approximation, and the mean size and plate-like structure of the tactoids were verified using TEM. The authors considered the measurement data on periodicity as a measure for the polymer clay dispersion. Figure 2.8 is sketched to summarize different orientations and crystallization structure that were reported and measured by SAXS and WAXS.

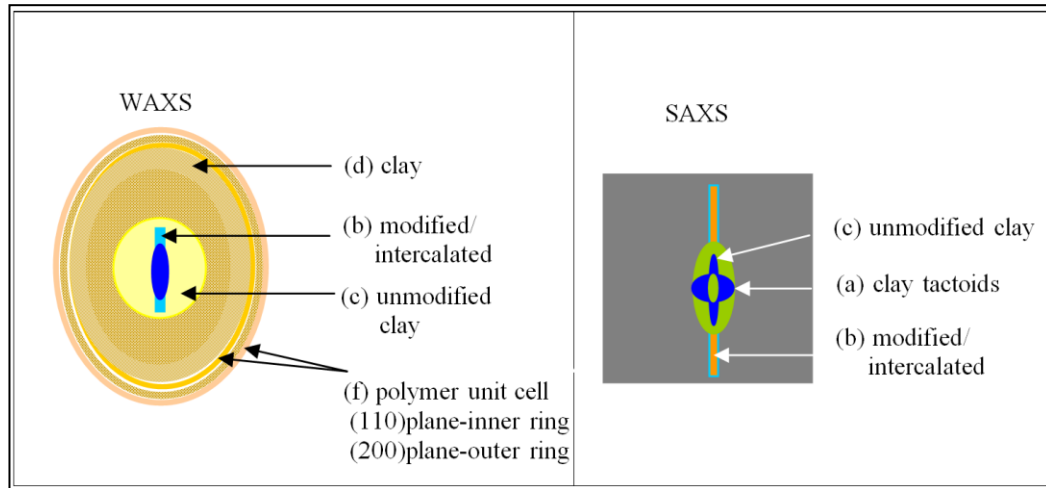


Figure 2.8: Different orientations and crystallization structure measured by SAXS and WAXS

Wang et al. [54] investigated the orientations in core, skin and oriented zone of injection moulded bars for PPNCs. MMT was found to orient parallel to the shear direction throughout the whole thickness of the moulded bar. However, for PPMA/MMT sample, a very weak reflection of orientation is detected in the skin and oriented zone.

Although SAXS and WAXS provide very useful information in orientation and crystallization structure, their results are very critical to be directly related to the dispersion and exfoliation degree, and thus the final property prediction. TEM is a recommended tool that can help researchers to have a complete picture to characterize the PPNCs.

2.7.4 Nuclear magnetic resonance

Attempts have been done to use solid-state NMR to study the different dynamics of exfoliated systems of PPNCs. Morphology and surface chemistry were also investigated. VanderHart et al. [55] first used solid-state NMR for nylon6/clay to evaluate to quantify the level of clay exfoliation. Nogueira et al. [56] tried to evaluate the changes in the polymer morphology of PPNCs. The nucleus ^{13}C , ^{29}Si and ^{27}Al were used to observe the changes in the clay structure. It was found that clay interferes in the polypropylene crystallization process due to the interaction between both components. VanderHart et al. [55] tried to correlate the differences in proton spin-lattice relaxation time (T_1^{H}), obtained from NMR and X-ray diffraction spectra and they found from XRD that there is a change observed in the polymer crystallinity due to interaction with clay layers. Homogeneity was used to measure the degree of exfoliation of the PPNCs samples. However, this result is not directly related to the structure as in WAXD and a little information can be given about the distribution of the silicate layers in polymer matrix as in TEM.

2.8 Nanocomposite Properties

Many improvements in PPNC system were reported. These improvements include modulus, strength and heat resistance, flammability and gas permeability.

Even though it was shown that the dispersion level is not necessarily for some properties such as flame retardancy and heat resistance [57]. Hasegawa et al. [18] emphasised that the silicate layers dispersion is an obligatory for a remarkable enhancements in mechanical properties of PPNCs. In this part, a brief

outlook on the main aspect and the apparently secondary improvement aspects will be discussed. However some non-related aspects by any mean to compounding, processing or dynamic and static mechanical behaviour such as permeability and transparency are not going to be covered in this review, which were reported to be improved [52] and not changed [58], respectively.

2.8.1 Crystallization Behaviour and Structure of PPNCs

Since PP is a type of semicrystalline polymers, the MMT/PPMA matrix may have remarkable effects on its terminal properties, it is meaningful to study the influence of MMT on the crystallization process of the PPNCs matrix.

Liu et al. [13] showed that addition of clay caused accelerated crystallisation by nucleation effect, but did not change the PP crystal structure. Svoboda et al. [7] reported a little decrease in the crystallinity and crystallite size increasing clay content. Okamoto et al. [59, 60] reported that the nanoparticles work as a nucleating agent of the PPMA/clay matrix, but the degree of crystallization rate is not affected by the clay particles. WAXD analyses showed that the intergallery spacing increases with crystallization temperature (T_c) for different clay contents. Furthermore, at constant T_c the extent of intercalation increases with decreasing clay content. The microstructure of the nanocomposites, observed directly by TEM, revealed that the clay particles are well dispersed at low T_c ; and that segregation of silicate layers occurs at high T_c . With the increase of T_c , there is a corresponding increase in storage modulus (G'). This enhancement was 30% for PPNC with 4% clay content decreasing to 13% with further clay addition.

However, the difference findings in publications are noticed and may be attributed to the difference in dispersion and exfoliation of PPNCs. A decrease of

crystallinity was reported by Ma et al. [61] and explained by effecting of MMT layer in confining the PP chains and hindered the crystallization. Perrin et al. [23] was studied the crystallization behaviour of PPNCs and found that the nucleating effect of clay was limited as an exfoliation system was dominant. It was also reported that and lower crystallization temperature and rate were remarked as such exfoliation system was present.

Li et al. [62] reported the nonisothermal crystallization behaviour of PPNCs at different cooling rates. It indicates that the nucleation of PPNC system is activated by the existence of the nanoclay, which increases the crystallization rate and decreases the degree of supercooling required for crystallizing nucleation (Figure 2.9). Medellin et al. [63] showed that MMT acts as nucleating agents. Nevertheless, the crystallinity remains rather constant. In another study, Lei et al. [64] studied PP with different clay types of MMT modified by alkyl ammonium (such as Cloisite 15A, 20A and 30B) and alkyl amine (such as Nanomer 130E and I31PS). The results showed that alkyl onium ion have higher crystallization and melting temperatures than alkyle amin. They found that all PPNCs had lower crystallinity than PP except the one with Cloisite 15A which achieved 4 % increment in crystallinity.

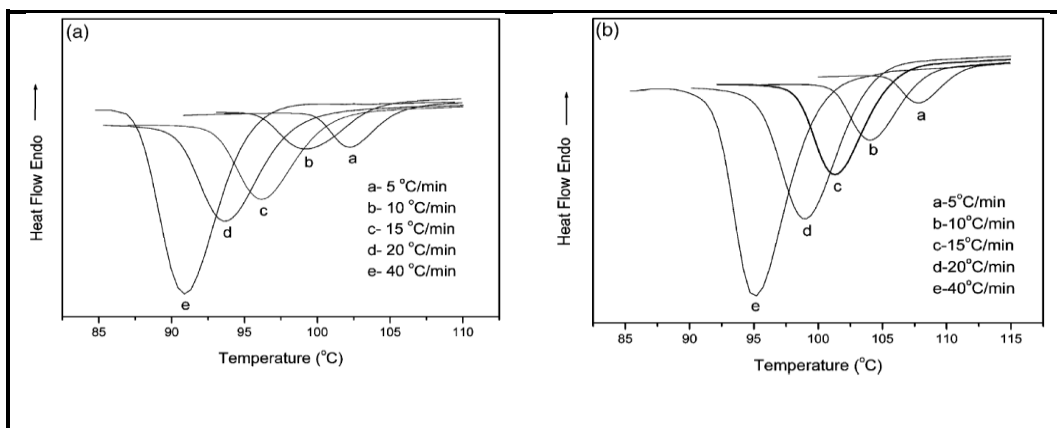


Figure 2.9: DSC curves of nonisothermal crystallization at different cooling rates: (a) PPMA and (b) PPNC.

Deshmane et al. [65] used polarizing optical microscopy (OPM) and differential scanning calorimetry (DSC) to study the crystallization and spherulitic structure of PPNCs. They explain the improvements in yield strength, modulus and impact strength at elevated temperatures, even though crystallinity remained unaffected, by increased in crystallization temperature by 14 °C, decrease the glass transition temperature by 5 °C and the reduction in spherulite size from 210 µm in neat PP to 14 µm in clay reinforced, a behaviour that is favourable for toughness. The fibrous crystalline morphology has been remarked in PPNCs. This occurs when crystallized at high shear rates, where an oriented structure was observed in well dispersed silicate layers [16]. Nowacki et al. [66] showed that the nucleation activity is greatly enhanced in shear-induced crystallization and resulted in a drastic decrease of spherulite sizes.

Other studies reported that PPNCs can either increase or decrease crystallization times for PP [7, 16, 67, 68]. These conflicting results are due to the complex relation between different variables such as contents of the MMT nucleating agent, present of the compatibilizer, and the degree of exfoliation. Another study suggested that the crystallization is controlled by the existence of PPMA and clay content does not significantly influence the crystallization time [67].

A previous study [69], on pure PP, has provided a strong evidence that when the spherulite size is say less than 1 µm, the yield stress is most likely to increase with increase in spherulite size. But when the spherulite size is greater than 10 µm, the possible presence of voids at the spherulite boundaries caused by contraction of the spherulite on cooling will weaken the boundaries, leading to reduction in yield stress. Some publications showed that the crystalline unit cell

may change as well. They confirmed the three crystalline lattices of PP, which are known previously for the isotactic system, and reported the formation of the γ -phase in PPNCs [26, 60, 70].

2.8.2 Mechanical properties

PPNCs represent a new class of plastics that are superior in enhancing of mechanical and physical properties. Modulus, yield stress, ultimate elongation and impact toughness are important measurements that relate directly to the end-use performance of PPNCs.

A general idea says that when the much better dispersion is obtained, the higher mechanical properties are achieved. However, Svoboda et al. [7] stated that “a better dispersion does not mean necessarily improved mechanical properties”. They found that the large well dispersed clay tactoids could produce better mechanical properties and these tactoids act more as nucleating agents in PP matrix than other structures. A decrease in size and an increase in the number of spherulites were also reported with enhancement in mechanical properties and impact strength of PPNCs. This may explain to some extent the conflicting data obtained from different sources.

2.8.2.1 Tensile properties

The partial immobilization of the polymer phase of PPNCs is probably responsible for the improvements in tensile properties, which include high modulus [71] and increased strength [16], but reduced ultimate elongation [7]. While there is general agreement on improvement of modulus and strength, conflicting results are still reported.

Significant increases in tensile strength and modulus have been reported at different MMT levels. Significant improvements in both strength and stiffness were reported to happen at 1 to 2% of clay [72]. More clay addition will enhance only the modulus and thereby harming the ultimate elongation. The yielding behaviour was found to disappear as clay loading reaches 7% [7]. Since few grams of an exfoliated nanoparticle may have over a million individual elements, the high concentrated unit will be achieved anyway, even at very low clay content. However, care should be taken for other important parameters such as presented shear, dispersion level, and PPMA MW. The effects of the shear and dispersion on mechanical properties are discussed in details in processing part. Using high MW of PPMA as a compatibilizer does increase the interlayer gallery as the clay decreases [26]. Reichert et al. [14] found the tensile property enhancement could be achieved only when appropriate PPMA compatibilizers and modified MMT are used. They illustrated that for the same material; very small improvement can be obtained by using different processing conditions in the practical material properties.

The tensile properties of various PPNCs prepared with a new type of co-intercalated MMT which had a larger interlayer spacing than the ordinarily organophilic clay, are reported by Liu et al. [13], showing improvements in tensile modulus of about 30%, 45% and 55% for 3%, 5% and 7% clay systems, respectively. They also found that the tensile modulus of the PPNCs increases rapidly with increasing MMT content from 0 to 5%, but the trend is less pronounced when the clay content increases beyond 5%. A similar trend is observed for the tensile strength which was reported to be increased to 12%, 25% and 30% for 3%, 5% and 7% clay systems, respectively. Pravin et al. [16]

reported about a 35% increase in the tensile modulus and about a 10% increase in the tensile strength.

Deshmane et al. [65] reported that yield strength and modulus in 4% clay system PPNCs in absence of compatibilizer are higher than pure PP (15 and 50 %, respectively), as an indication of significant interaction between them. However, ultimate elongation is decreased by 25 %. Elongation at break, which is an indicator of toughness, were reported to significantly decrease in PPNCs as compared to PP [14, 18].

Kim et al. [73] investigated PPNCs with the main focus on the ratio of PPMA to MMT. In spite of the rheological properties suggested that the interaction between polymer and clay particles could be enhanced as the ratio of PPMA to MMT increases, mechanical and thermal properties did not improve correspondingly in all cases because of the reduction of matrix properties by PPMA.

Wong et al. [74] performed an instrumented indentation on the polished samples of PPMA/MMT composites. Indentations were chosen on (1) the clay aggregated region; (2) the clay matrix boundary; (3) the unreinforced PPMA matrix. They found that the indentation stiffness for the clay congregated region to be twice as high as the unreinforced PPMA. A special care must be taken to guarantee that the sample is representative and such a potent stiffening effect can be attributed to the increase in local filler content rather whole PPNCs matrix.

2.8.2.2 Tensile properties of die-drawn polypropylene

The drawing process through a conical die was firstly described by Coates and Ward [5]. This process was used by Taraiya et al. [75] to produce

oriented polypropylene rods with draw ratio up to 23 and at room temperature. They reported elastic modulus of up to 20 GPa over the isotropic value of 1.5 GPa. The orientation process also increases the ductile–brittle temperature up to at least 40 °C. The results clearly demonstrated that die drawing is a very successful method for the manufacture of high stiffness PP rods. Taraiya et al. [76] reported that die drawing process improves the properties of the most thermoplastics. PP with draw ratio, $\lambda=6.2$ exhibited 3.5 times modulus higher than the isotropic material.

The application of die drawing to produce highly oriented polymers was also considered by Gibson and Ward [77]. It was shown that a variety of products e.g. rods, wires, tubes and sheets of relatively high stiffness could be obtained, with elastic modulus values of up to 50 GPa for linear polyethylene and 20 GPa for polypropylene. The degree of deformation attainable was found to depend strongly on the draw velocity. Highly oriented thermoplastic polymers produced by die drawing were tested under uniaxial loading [78, 79]. The results demonstrated that both longitudinal modulus and yield strength of drawn polypropylene and polyethylene strips are significantly improved by increasing the drawing ratio. Drawn polyethylene strips possess higher moduli than those of the polypropylene strips at higher drawing ratio.

Many aspects related to the application of die drawing to produce highly oriented polymers have featured in the literature. Mourad et al. [80] studied the influence of drawing process parameters of die drawn PP on mechanical properties. The results show that draw load increases with draw ratio and draw speed, but increasing draw temperature up to 150 °C diminishes both the draw load and the degree of orientation. A three-fold increase in draw speed results in

up to 80% increase in the steady state draw load. Also, a 69% increase in draw load is produced by increasing the draw ratio from 1.9 to 4. The tensile strength and modulus of drawn PP was reported to improve significantly with increase of draw velocity and draw ratio while they reduce with increasing draw temperature. Tensile strength and modulus were enhanced by 250% relative to the undrawn material.

Many attempts have been made to improve the mechanical properties of polymers by die drawing. However, there is a need for further studies that might widen the scope of knowledge on the influence of introducing clay particles in polymer matrix on the mechanical behaviour of die drawn PP, which are going to be covered in this thesis.

2.8.2.3 Impact strength

The study of impact strength is fundamentally important because majority of semi-crystalline polymers such as PP are ductile at low strain rates, but at high strain rates experienced in izod impact test, they are characterized by a brittle behaviour. Thus, the study of impact strength at high strain rates is of significant interest. Also, the observation of high tensile may not necessarily imply high impact strength.

The notched izod impact strength of the PPNCs was studied by Liu et al. [13]. It was found that the impact strength of PPNCs remains constant, within experimental error, in the MMT content range between 0 and 7% clay loading. In a recent study, Deshmane et al. [65] reported that the reinforcement of PP with 4 wt.% nanoclay exhibits an increase in notched izod impact strength in the temperature range of -40 to $+70$ °C under identical processing conditions, which

suggest the possibility of a strong PP/clay interaction without using the compatibilizer and consequent stronger nucleating effect of the clay.

Different sources of impact strength results for notched and un-notched PPNCs at different clay loading shows that notched impact strength 160% over the PP, but unnotched samples leads to 30 % decrement in impact strength [81, 82]. Wenyi et al. [83] showed an improvement of impact strength for PPNCs with loading of clay up to 2%.

The impact strength of PPNCs has been covered in several studies. However, the outputs of these studies are not similar. Different factors such as the exfoliation degree, clay distribution, orientation, compatibilizer and clay loading effects might cause this disagreement.

2.8.2.4 Fracture Toughness

Recently, researchers have focused on the fracture behaviour of PPNCs, Chen et al. [84] characterized the toughness of PPNCs and showed that J-integral fracture toughness is decreased with increasing the clay content. Bureau et al. [85] studied the fracture toughness of PPNCs based on EWF and reported a slight improvement in fracture toughness as compared to pure PP and uncompatibilized ones. These reported improvements in toughness were confirmed and explained by the microvoid process [85-87].

Recently, Saminathan et al. [88] reported the fracture behaviour of PPNCs with 5 % MMT and 1 to 20 mm/min cross-head speed. A 25 % improvement in EWF was observed. As the loading rate increases, the specific EWF for yielding increases, but the specific EWF for necking decreases. Bureau et al. [89] also showed that the toughness improvements in PPNCs were

attributed to higher voiding stresses and improved matrix resistance attributed to finer, more oriented (in melt) clay nanoparticles.

Mohanraj et al. [90] studied the fracture behaviour of die-drawn toughened PP and PP-based elastomer by drawing to different draw ratios using EWF. They reported that the fracture toughness decreases as the draw ratio increases and up to draw ratio of 4 the PP-based elastomer exhibited higher fracture toughness than PP material. Sweeney et al. [91] studied the fracture behaviour of di-drawn biaxially oriented polyethylene at high pressure and showing that the resistance to brittle failure, which presented as an assistance in inducing brittle failure at high pressure [92], can be improved by introducing of molecular orientation.

Although the fracture behaviour of solid-state molecular orientation of PP/clay has not been studied yet, such improvement of oriented melt gives a hope to the further enhancement that could be obtained if solid-state orientations are used. Section 2.8.5.2 reviewed the produced orientation in melt-state of PPNCs and its effect on the properties.

2.8.3 Dynamic mechanical analysis

Dynamic mechanical analysis (DMA) measures the material response to an oscillatory deformation over changing in temperatures. It also gives information about the glass transition temperature (T_g), where the molecular mobility starts. The DMA reported results are mainly: the storage modulus G' , the loss modulus G'' and $\tan\delta$ (G''/G').

Most studies [11, 26, 65, 93] show the temperature dependence of G' , G'' , and $\tan\delta$ for the various PPNCs and corresponding PPMA matrix. For all PPNCs,

there is a strong enhancement of the modulus over the investigated temperature range, which indicates the plastic and elastic responses of PP towards deformation are strongly influenced in the presence of clay. Below T_g , an improvement in G' is reported for intercalated PPNCs. Velasco et al [94] used DMA to relate the high storage modulus to the better clay dispersion and the presence of the compatibilizer.

The dynamic mechanical properties of neat PP and PPNCs prepared with a new kind of co-interaction MMT, in Liu study [13], showed that the incorporation of MMT into PPNCs results in a remarkable increase in stiffness (G') and a decrease in $\tan\delta$. The G' curves show an enhanced rubbery plateau, indicating that the addition of MMT induces a reinforcement effect; at very high temperatures this reinforcement effect strengthens. This behaviour further indicates enhancement of the thermal mechanical stability of these materials at high temperature. Another interesting phenomenon is that the T_g values of PPNCs do not further decrease above a MMT content of 3 wt%. However, the mechanism for this behaviour is not yet understood.

2.8.4 Thermal properties

Heat deflection temperature (HDT) measures the polymer heat resistance towards an applied load. In numerous studies, an agreement presents that the PPNCs with good dispersion promotes a higher HDT [43]. Li et al. [82] reported a maximum value of HDT at 4% MMT loading in PP without compatibilizer (2.5%). This improvement in HDT for neat PP after nanocomposite preparation is originated from the greater thermal stability of nonorganic nanoclay particles, which act as transport barrier of the volatile materials that generate during decomposition [11, 16, 93, 95, 96]. These agreements in thermal stability results

take in consideration the whole PPNCs matrix. However, the thermal stability of PPMA and clay that were measured by d-spacing in WAXD is another angle, which was reviewed previously in section 2.7.1.

The role of clay in the nanocomposite structure is the main reason for the difference in thermogravimetric analysis (TGA) results as compared to pure PP [82]. The clay acts as a heat barrier that improves the whole composite thermal stability. In the early phases of thermal decomposition, nanoclay would shift the temperature decomposition to higher level. In other words, the stacking structure of silicate layers could hold the heat that is accumulated in the system. In pure PP, this heat is a source of acceleration of the decomposition process, in conjunction with the heat flow supplied by the outside heat source.

2.8.5 Melt Rheology and Structure–Property Relationship

PPNCs show improved material properties as compared to pure PP. In order to achieve an understanding of the processability of PPNCs, the rheological behaviour in the molten state should be studied. Dynamic oscillatory shear and elongation flow measurements of polymeric materials are generally used to study PPNCs rheology and its structure–property relationships. The melt state linear viscoelasticity is considered as a useful indirect method in characterization of PPNCs structure. The rheological characterization is used in evaluating of clay treatment by alkyl amine and PPMA acid content [97, 98]. Koo et al. [99] found that the linear viscoelastic modulus (G') can detect the morphological changes by evaluating the effect of MW on the degree of PPNCs exfoliation.

2.8.5.1 Dynamic oscillatory shear

Dynamic oscillatory shear is done by employing the time dependent strain and measure the resulted shear stress. Most studies report the storage modulus G' ; loss modulus G'' and complex viscosity η^* with temperatures and frequencies. It is well known that temperature has great effect on the rheology of polymer.

Galgali et al. [100] used PPNCs with and without PPMA to show the time dependent evolution of the storage and loss modulus, subjected to small strain oscillatory shear tests every 10 min during their total annealing time of 3 h at 200 °C. At high frequencies the elastic modulus of PP/MMT and PP/MMT/PPMA are comparable at similar annealing times, and both decrease with annealing due to possible degradation of the PP-matrix. At low frequencies the elastic modulus of PP/MMT/PPMA is qualitatively always higher than that of PP/MMT, indicating that most of the microstructural development in PP/MMT/PPMA has already occurred during the extrusion process, while only subtle microstructural changes occurred during annealing. Furthermore, the elastic modulus of PP/MMT at low frequency decreases with annealing time, but that of PP/MMT/PPMA remains unchanged. Thus at high frequency, the response of the PP/MMT/PPMA hybrid is dominated by the matrix, while at lower frequencies its solid-like response is strongly affected by the existence of clay. On the other hand, the low frequency response of PP/MMT is not dominated by the presence of clay, which highlights the important role played by PPMA in the formation of the hybrids.

Ying et al. [101] reported that different PPNCs melts, which show a greater shear thinning than pure PP, have higher moduli and better processability

compared to PP. The strong shear thinning behaviour may come from such isometric nanoparticles that may lead to an oriented structure in the flow direction and/or a cluster structure causes a rupture in the melt and thus shear thinning is remarked [97].

Other studies by Li et al. and Rohlamann et al. [102, 103] reported that the viscoelastic properties are still dominated by PP matrix when the clay loading is below 3% (Figure 2.10). As the amount of clay increases, the linear viscoelastic behaviour of PPNCs changes with time and solid-like behaviour appears as they exceed 5 or 6 % of clay.

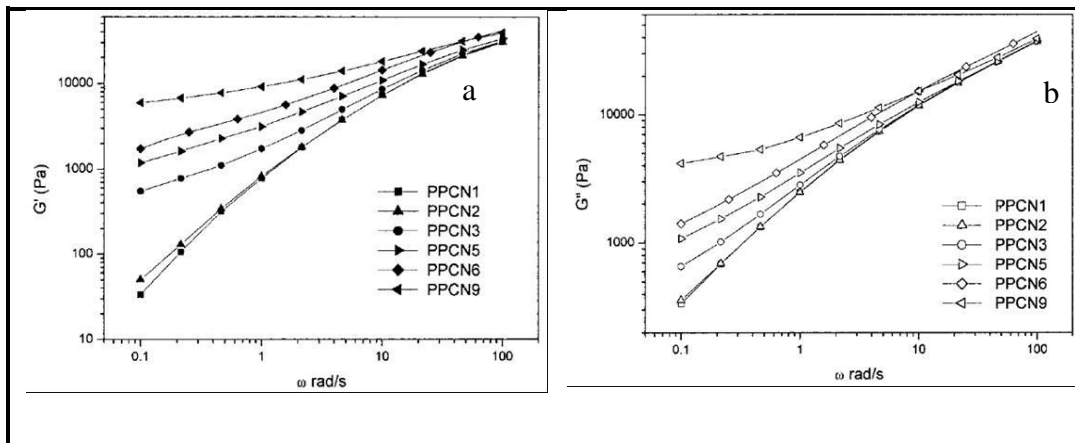


Figure 2.10: Dynamic shear modulus of PPNCs (a) storage modulus and, (b) loss modulus.

2.8.5.2 Elongation flow rheology (orientation in melt state)

Contrariwise of dynamic oscillatory shear studies that have been used as a routine rheology measurement, few studies deal with the elongational flow rheology. Okamoto et al. [104] first conducted the orientation in PP (melting temperature, $T_m=141$ °C) based nanocomposites in the melt state at 150 °C subjected to extensional flow using optorheometry, and suggest that at least some fraction of the silicate layers in PPNCs (4 % MMT) exhibit perpendicular orientation (layer normals along the neutral direction). The perpendicular orientation was observed by solid-state TEM measurements (Figure 2.11-a) and

has been attributed to a very strong strain hardening in these hybrids. As seen in Figure 2.11-b, elongational viscosity (η_E) increases gradually with time; this is generally called the linear region. After certain time $t_{\eta E}$ called the uprising time, there is a rapid increase in the linear region curves. The solid line shows that the shear viscosity increases continuously with time at constant low shear rate of 0.001 s^{-1} on a cone plate and never showing a tendency of reaching a steady state within the time (5 min or longer). This time-dependent thickening behaviour is generally called rheopexy. The same experiment conducted with a PPMA without MMT did not exhibit any strain hardening or rheopexy behaviour.

Recently, Park et al. [105] and Lee et al. [106] confirmed the strain hardening behaviour for only exfoliated systems, but they reported a parallel orientation of the silicate layers to the flow direction for both intercalated and exfoliated systems.

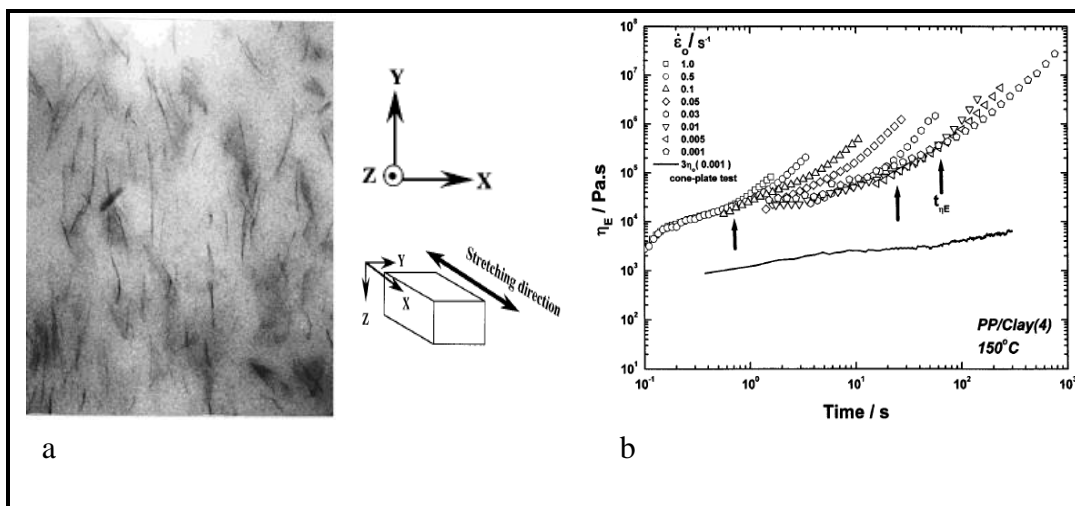


Figure 2.11: TEM micrographs (a) and elongational viscosity with time variation (b) for elongated PPNCs at 150 °C

Galgali et al. [107] studied the effect of the orientation, produced from extrusion process, on tensile modulus for the extruded tapes along the flow direction. It was found that tensile modulus is correlated well with the average orientation of the clay tactoids increased with shear rate only with PPMA

presence. In contrast, Zhang et al. [108] reported that the increment of the exfoliated structure was accompanied by the scarifying of the clay orientation along the shear direction and the PP chains intercalated between MMT layers was highly confined.

2.9 Conclusions and Recommendations

Although the significant amount of research done on different aspects of PPNCs, new topics would contribute to better understanding of the structure–property relationships of PPNCs. Many studies have investigated the enhancement of undrawn PPNCs in tensile properties. However, it is well known that additional considerable enhancement of some PP properties such as stiffness and strength can be produced by solid-state molecular orientation [6]. This important area was not investigated for PPNCs. Hence, the present study focuses on the tensile and fracture behaviours of different loading die-drawn PPNCs at various speeds. Orientation can also have a dawn side in strength of the directions other than the draw direction. For this reason, a combined of fracture behaviour is particular interest in studying tensile properties of drawn PPNCs.

From the several studies that have been presented in different areas of PPNCs, the following points are concluded and employed to direct this research:

1. Although the great progress in enhancement of PPNCs tensile modulus that has been reported, this enhancement is offset by reduction of elongation at break and, in some publications, the impact strength. In most studies, too high fraction of PPMA would be detrimental to the mechanical properties and too low fraction of PPMA could not reach the desirable degree of clay

dispersion. There would be an optimum composition for individual PPMA to be incorporated into the PPNCs.

2. Dispersion of the nanoclay particles can influence the mechanical properties of PP as a result of the high modulus clay inclusions of anisotropic and thus becomes important to mechanical property enhancement; however (as it was suggested in the review), the nanometric scale of clay may play no direct role. On the other hand, non-homogeneous dispersion that produces from the clay aggregation can cause a serious problem for the mechanical properties of PPNCs. Thus homogeneous dispersion is suggested to be desirable to get the benefit of the addition of organoclay to the polymer matrix.
3. For the effect of PPMA-MW and PPMA content, it can be said that PPMA can interact to a lower extent with clay due to non-sufficient grafting content leading to some limited intercalation. However, its higher MW and better miscibility with PP may allow some larger level of intercalation to partial exfoliation to be achieved.
4. There are several techniques that are used to characterize the nanostructure of PPNCs, including SEM, NMR, and neutron-scattering methods (SAXS and WAXS); however, WXR and TEM analyses should be more regularly employed to afford better assessment in evaluation of different compounding and processing routes. Care should be taken when XRD data alone is used, which only describe the relationship between clay layers in the polymer, not the relationship of the clay to the polymer. Therefore, TEM should be combined as a very powerful tool for the analysis of PPNCs.

5. Most publications have been reported that the PPNCs degree of crystallinity is kept constant or decreases modestly with increasing of clay loading. The average characteristic size of spherulitic structure in crystalline morphology of PPNCs has been found to decrease significantly with increase of clay loading because of a role of nanoparticles in nucleation which leads to a difference in the number of point nuclei in PPNCs. Thus, nucleation of PP crystals on nano-particles represents a phenomenon to be further investigated for the solid phase PPNCs. If this conducting to a crystallinity improvement can be found, it will be possible to better understand the link between nano-dispersion and enhanced tensile properties.
6. PPNCs consently exhibit a remarkable increase in thermal stability. However, an attention should be considered in future work whenever heat and shear are involved.
7. It was shown that the rheological behaviour of PPNCs at lower frequencies is completely independent on the fine structure of the nanocomposites, i.e. whether it is end-tethered or stacked intercalated, but it is depends primarily upon the amount of clay loading in the nanocomposites. However, the viscosity of the PPNCs even at low loading level (less than 5%) can be increased at low shear rates. But at high shear rates, which is similar to what is usually used in practical application, the viscosity is reduced to be in the normal range of PP. It was also shown that the typical rheological response in PPNCs arises from frictional interactions of the silicate layers and not due to the confined polymer molecules in the clay galleries.
8. In melt state, Layered silicate based nanocomposites, like other anisotropic materials, exhibit the ability to orient the silicate layers in response to

externally applied flow. This orientation can lead to improve some properties of PPNCs systems in presence of the compatibilizer. The orientation, which may direct the clay particles and lamellae of the crystal structure in the direction of the applied shear, are suggested to depend on the clay content, crystallinity, the interaction with PP, as well as PP molecular weight, in addition to the introduced shear or rate of deformation.

3 Tensile and Fracture Behaviour of Polymer

3.1 Introduction

Tensile experiments have been to be the most regularly used form of mechanical test. However, the non-homogeneity of different regions within the sample can make the interpretation very difficult. This non-homogeneity results in necking or cold drawing and also in crazing. Thermal history of different regions within the sample could be another source of this non-uniformity as in the injection moulding process, where orientation, size of spherulites and crystalline phases may differ from one region to another. This inconsistency seems to be more severe when fillers such as non compatible clay particles are involved in the polymer system.

The shapes of the tensile curves are dependent on the temperature and crosshead speeds used. Figure 3.1 illustrates the variations that usually can be seen in stress-strain curves of polymers at the same strain rate. When low temperature is involved, load increases linearly with the stain until a brittle failure occurs (graph A). Conversely, the higher temperature could exhibit a ductile yielding with neck before failure or in some cases the neck stabilizes and causes a strain hardening as in cold drawing (graph B). Higher temperature leads to higher uniform deformation above T_g with rubber-like behaviour (graph C).

Figure 3.2 illustrates different features of the stress-strain curve. The slope of the linear region that is indicated in equation 3.1 is the Young's modulus. The maximum point is the stress at yield (σ_y) and strain at yield (ϵ_y). The failure point is the tensile strength at break (σ_B) and elongation at break (ϵ_B). The raw data from the tensile test generate the load-displacement curves.

$$E = \frac{d\sigma}{d\varepsilon} \quad (3.1)$$

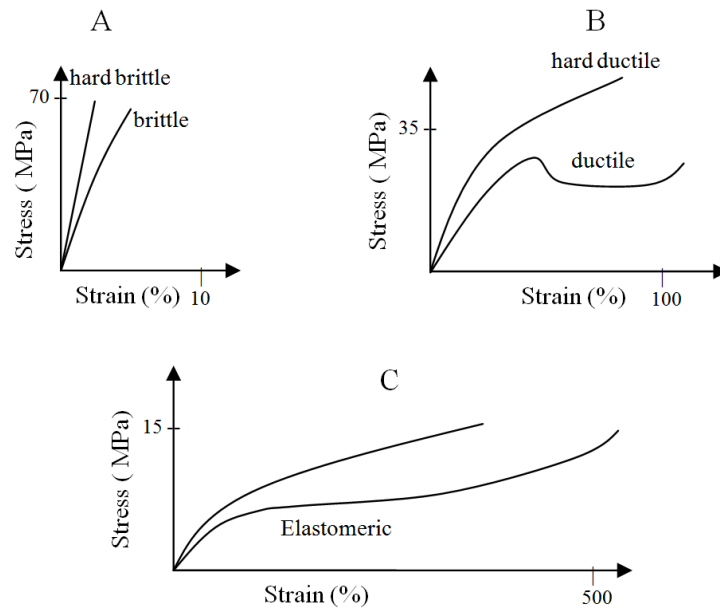


Figure 3.1: General types of stress-strain curves[109]

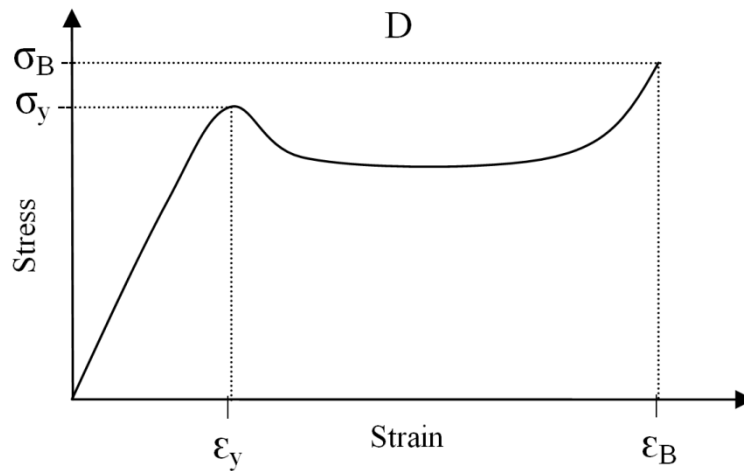


Figure 3.2: Typical stress-strain curve

3.2 The Definition of Stress

The components of the stress are showed in Figure 3.3, where the forces (F1, F2 and F3) act on the faces areas of the cubic object and is divided to the following nine components: (F1: σ_{xx} , σ_{xy} , σ_{xz} / F2: σ_{yx} , σ_{yy} , σ_{yz} / F3: σ_{zx} , σ_{zy} , σ_{zz}). The first subscript indicates the normal to the plane direction, while the second indicates the force direction. At equilibrium condition, the applied torque is zero and thus:

$$\sigma_{xy} = \sigma_{yx}, \sigma_{zx} = \sigma_{xz}, \sigma_{yz} = \sigma_{zy}$$

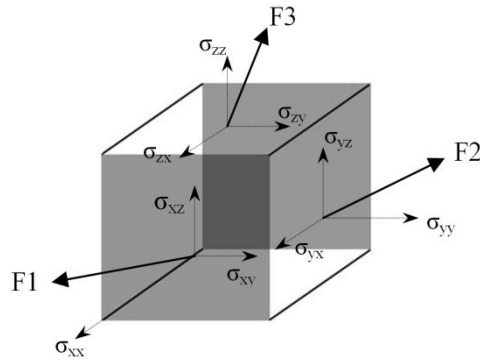


Figure 3.3: The components of stress

Stress can be then defined by the normal stresses (σ_{xx} , σ_{yy} , and σ_{zz}) and the shear stresses (σ_{xy} , σ_{yz} , and σ_{zx}) and calculated by knowing these six normal and shear stress components, which are shown in the following matrix:

$$\sigma_{ij} = \begin{pmatrix} \sigma_{xx} & \sigma_{xy} & \sigma_{xz} \\ \sigma_{xy} & \sigma_{yy} & \sigma_{yz} \\ \sigma_{xz} & \sigma_{yz} & \sigma_{zz} \end{pmatrix}$$

At small strain, the areas of the cube faces are not influenced by the strain. Thus, it is not necessary to specify whether these stress components refer to the deformed or the undeformed body. This is not true when finite strain is used. In practice, the true stress tensor refers to the stress on the basis of strained cross-section area, and the nominal stress to the force per unstrained cross-sectional area, $\sigma = F/A$.

3.3 The Definition of Strain

In practical definition of strain of the elastic region of an isotropic material, the increase in length over the original length in the same direction of the stretched material is the extensional strain as shown in Figure 3.4(a).

$$e = \frac{l - l_0}{l_0} = \frac{\Delta l}{l_0}$$

where ℓ_0 is the original length and ℓ is the length after stretching. The draw ratio, λ_e , or the nominal strain is the length after stretching over initial length [$\lambda_e = \ell/\ell_0$ ($\lambda_e \geq 1$)]. Thus the nominal strain can be related to engineering strain by $e = \lambda_e - 1$. The above two definitions of strain should be distinguished from the true strain that called Hencky strain and given by $e_t = \ln(\ell/\ell_0) = \ln \lambda_e$.

In the small strain region, there is another definition of strain derived from simple shear, where a parallel displacement occurs as shown in Figure 3.4(b). The engineering shear strain is defined by the angle in the figure, which is the displacement (d) over the perpendicular distance (ℓ).

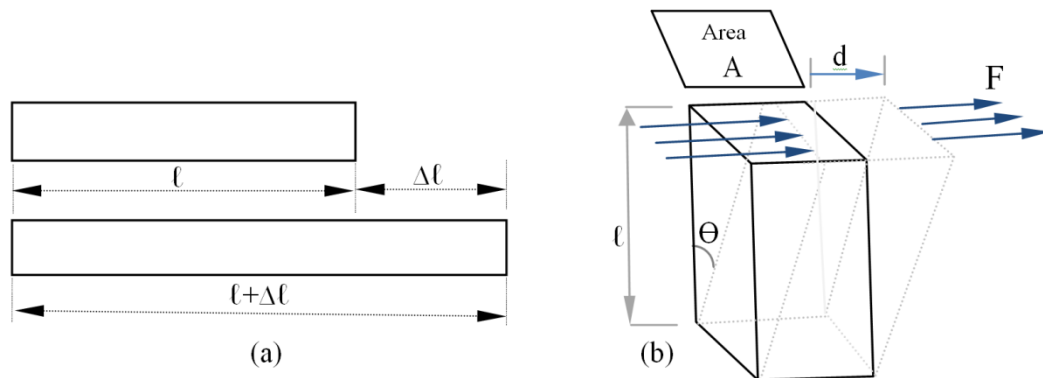


Figure 3.4: Illustration of (a) extensional strain and (b) simple shear strain

The six components of engineering strains were derived by Ward and Sweeney [110] where the deformation is given by the quantities e_{xx} , e_{yy} , e_{zz} , e_{yz} , e_{zx} and e_{xy} . These components have been defined below.

3.4 The Definition of Modulus

Based on the linear relationship between stress and strain, it was assumed that each of the six stress components has a linear relation to a strain component for both isotropic and anisotropic solids. If the shear stresses are ignored, an isotropic stress-strain relationship can be written as follows:

$$\sigma_{xx} = a e_{xx} + b e_{yy} + c e_{zz} \quad \sigma_{xz} = f e_{xz} \quad \text{where } a, b, \text{ and } c \text{ are constants.}$$

and $e_{xx} = a' \sigma_{xx} + b' \sigma_{yy} + c' \sigma_{zz}$ $e_{xz} = f' \sigma_{xz}$ where $a', b',$ and c' are constants.

Hooke's law of isotropic solid, for the strains e_{xx} and e_{yy} under applied stresses σ_{xx} and σ_{yy} , defines Young's modulus (E) and Poisson's ratio (ν):

$$e_{xx} = \frac{1}{E} \sigma_{xx}$$

in the x direction and strain.

$$e_{yy} = \frac{-\nu}{E} \sigma_{xx} \quad \text{and} \quad e_{zz} = \frac{-\nu}{E} \sigma_{xx} \quad \text{in the y and z directions, respectively.}$$

where Poisson's ratio (ν) is the contraction strain (e_{yy}) over the extensional strain.

The same concept can be used to relate the strain shear strain e_{xz} to the shear stress σ_{xz} :

$$e_{xz} = \frac{\sigma_{xz}}{G} \quad \text{where G is the shear modulus.}$$

Thus the stress-strain relationships can be given as follows:

$$e_{xx} = \frac{1}{E} \sigma_{xx} - \frac{\nu}{E} (\sigma_{yy} + \sigma_{zz})$$

$$e_{yy} = \frac{1}{E} \sigma_{yy} - \frac{\nu}{E} (\sigma_{xx} + \sigma_{zz})$$

$$e_{zz} = \frac{1}{E} \sigma_{zz} - \frac{\nu}{E} (\sigma_{xx} + \sigma_{yy})$$

$$e_{xz} = \frac{1}{G} \sigma_{xz} \quad e_{yz} = \frac{1}{G} \sigma_{yz} \quad e_{xy} = \frac{1}{G} \sigma_{xy}$$

The shear modulus (G) and the bulk modulus (K) are related to Young's modulus in the following way:

$$G = \frac{E}{2(1+\nu)} \quad \text{and} \quad K = \frac{E}{3(1-2\nu)}$$

3.5 Anisotropic Materials

Polymer molecular orientation, which can be produced by either conventional processing equipments or by the hot drawing process, mainly improves the stiffness and strength of the polymeric matrix [111]. The relationship of the stress component with the strain components, as given in the previous section, is:

$$\sigma_1 = c_{11} e_1 + c_{12} e_2 + c_{13} e_3 + c_{14} e_4 + c_{15} e_5 + c_{16} e_6$$

where $e_1 = e_{xx}$, $e_2 = e_{yy}$, $e_3 = e_{zz}$, $e_4 = e_{yz}$, $e_5 = e_{xz}$ and $e_6 = e_{xy}$ are the six components of the engineering strain. Applying the same for the stress components: $\sigma_1 = \sigma_{xx}$, $\sigma_2 = \sigma_{yy}$, $\sigma_3 = \sigma_{zz}$, $\sigma_4 = \sigma_{yz}$, $\sigma_5 = \sigma_{xz}$ and $\sigma_6 = \sigma_{xy}$ will produce the general notation for stress components:

$$\sigma_i = c_{ij} e_j$$

similarly, strain components can be written as follows:

$$e_i = s_{ij} \sigma_j$$

where c_{ij} are the stiffness constants and produce the following elements:

$$C_{ij} = \begin{vmatrix} c_{11} & c_{12} & c_{13} & c_{14} & c_{15} & c_{16} \\ c_{12} & c_{22} & c_{23} & c_{24} & c_{25} & c_{26} \\ c_{13} & c_{23} & c_{33} & c_{34} & c_{35} & c_{36} \\ c_{14} & c_{24} & c_{34} & c_{44} & c_{45} & c_{46} \\ c_{15} & c_{25} & c_{35} & c_{45} & c_{55} & c_{56} \\ c_{16} & c_{26} & c_{36} & c_{46} & c_{56} & c_{66} \end{vmatrix}$$

and s_{ij} are the compliance constants and produce the following elements:

$$S_{ij} = \begin{vmatrix} s_{11} & s_{12} & s_{13} & s_{14} & s_{15} & s_{16} \\ s_{12} & s_{22} & s_{23} & s_{24} & s_{25} & s_{26} \\ s_{13} & s_{23} & s_{33} & s_{34} & s_{35} & s_{36} \\ s_{14} & s_{24} & s_{34} & s_{44} & s_{45} & s_{46} \\ s_{15} & s_{25} & s_{35} & s_{45} & s_{55} & s_{56} \\ s_{16} & s_{26} & s_{36} & s_{46} & s_{56} & s_{66} \end{vmatrix}$$

Young's modulus, shear modulus and Poisson's ratio can be directly related to these constants of oriented polymers, which are usually reduced to nine or six independent constants in practical applications.

3.5.1 Triaxial Symmetry Specimens

When there are triaxial planes of symmetry as in drawing of the polymer film (Figure 3.5), we have three axes: x (1), y (2), and z (3).

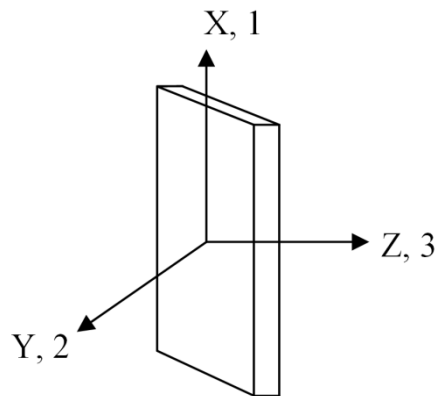


Figure 3.5: Triaxial symmetry of polymer sheet

For this system there are nine compliance constants which relate to nine independent elastic constants. The denominators in the following expressions refer to the direction x,y,z or 1,2,3; where the stress is applied.

$$S_{ij} = \begin{vmatrix} s_{11} & s_{12} & s_{13} & 0 & 0 & 0 \\ s_{12} & s_{22} & s_{23} & 0 & 0 & 0 \\ s_{13} & s_{23} & s_{33} & 0 & 0 & 0 \\ 0 & 0 & 0 & s_{44} & 0 & 0 \\ 0 & 0 & 0 & 0 & s_{55} & 0 \\ 0 & 0 & 0 & 0 & 0 & s_{66} \end{vmatrix}$$

There are three Young's moduli:

$$E_1 = \frac{1}{s_{11}}, \quad E_2 = \frac{1}{s_{22}}, \quad E_3 = \frac{1}{s_{33}}$$

six Poisson's ratios:

$$\nu_{21} = -\frac{s_{21}}{s_{11}}, \quad \nu_{31} = -\frac{s_{31}}{s_{11}}, \quad \nu_{32} = -\frac{s_{32}}{s_{22}}$$

$$\nu_{12} = -\frac{s_{12}}{s_{22}}, \quad \nu_{13} = -\frac{s_{13}}{s_{33}}, \quad \nu_{23} = -\frac{s_{23}}{s_{33}}$$

and three shear moduli:

$$G_1 = \frac{1}{s_{44}}, \quad G_2 = \frac{1}{s_{55}}, \quad G_3 = \frac{1}{s_{66}}$$

3.5.2 Uniaxial Symmetry Specimens

In a uniaxially drawn specimen, there will be no orientation in direction perpendicular to the draw direction (Figure 3.6), thus the compliance constants involve only five independent elastic constants.

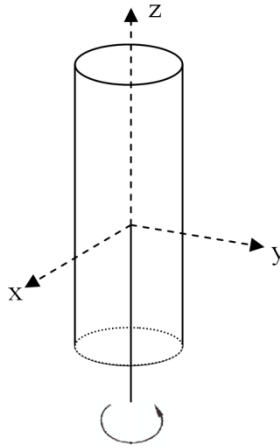


Figure 3.6: Uniaxial symmetry in drawn polymer film

$$\begin{vmatrix}
 s_{11} & s_{12} & s_{13} & 0 & 0 & 0 \\
 s_{12} & s_{11} & s_{13} & 0 & 0 & 0 \\
 s_{13} & s_{13} & s_{33} & 0 & 0 & 0 \\
 0 & 0 & 0 & s_{44} & 0 & 0 \\
 0 & 0 & 0 & 0 & s_{44} & 0 \\
 0 & 0 & 0 & 0 & 0 & 2(s_{11} - s_{12})
 \end{vmatrix}$$

There are two Young's moduli:

$$E_1 = \frac{1}{s_{11}}, \quad E_3 = \frac{1}{s_{33}}$$

two Poisson's ratios:

$$\nu_{12} = -\frac{s_{12}}{s_{11}}, \quad \nu_{13} = -\frac{s_{13}}{s_{33}}$$

and one shear modulus:

$$G_1 = \frac{1}{s_{44}}$$

3.6 Tensile Testing Graphs

As the shape of deformation in stress-strain curves of different polymer materials and/or different test conditions are discussed in section 3.1, the nature of deformation in a polymer specimen is affected by the applied stress form and the sample geometry. In this section, more attention is given to some definitions or behaviours that may be seen in the stress-strain graphs. Necking in the nominal stress curve and in cold drawing, nominal and true stresses, yield stress definition, the yield criterion and the nature of the load drop are discussed in this section.

3.6.1 Nominal and true stresses

The nominal stress (σ_a) is defined as the load at any point on the load-displacement graph over the initial cross-sectional area (A_0). Same load at any time on the graph can defined the true stress (σ), but should be divided by the actual area (A) at the same point where the load is measured. The nominal and true stresses are compared in Figure 3.7.

$$\sigma_a = \frac{F}{A_0}$$

As load increases in the nominal stress, the nominal strain increases from point (a) to point (b) in Figure 3.7, where a neck is developed. The neck is accompanied by smaller cross-sectional area. As the material is subjected to more nominal strain, a drop in the load occurs. In contrast, as the displacement increases the actual cross-sectional area decreases, which may cause the true stress to increase when the load decreases or remains at the same level. Failure then occurs at smallest cross-sectional area point in the neck.

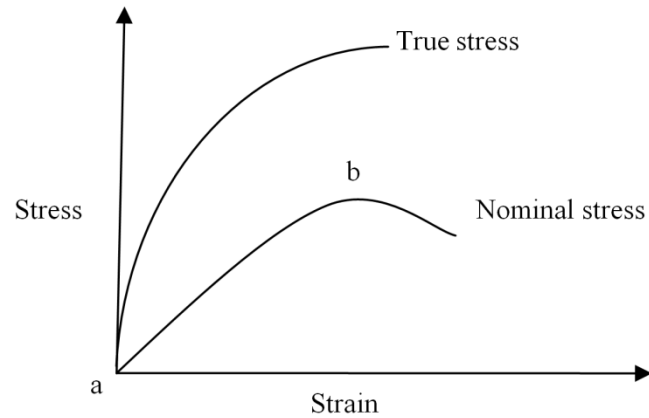


Figure 3.7: Nominal stress and true stress in tensile testing graphs

If it is assumed that the deformation is developed at the same volume.

Then $A\ell = A_0\ell_0$, and if $\ell/\ell_0 = \lambda_e$, where λ_e is the extension ratio,

$$A = \frac{A_0\ell_0}{\ell} = \frac{A_0}{\lambda_e}$$

The true stress is given by

$$\sigma = \frac{F}{A} = \frac{\lambda F}{A_0} = \lambda_e \sigma_a \quad (3.2)$$

Thus the true stress can be calculated by knowing the nominal stress and the extension ratio.

3.6.2 Cold drawing phenomenon

The change in the tensile graph that is associated with cold drawing is a remarkable phenomenon where different regions behaviours are recognized as shown in Figure 3.8.

In typical cold drawing graph, as the load is applied, the nominal stress increases linearly with the nominal strain (1) to a maximum point (2). A neck then develops and causes a drop in the stress to a minimum point or the center of

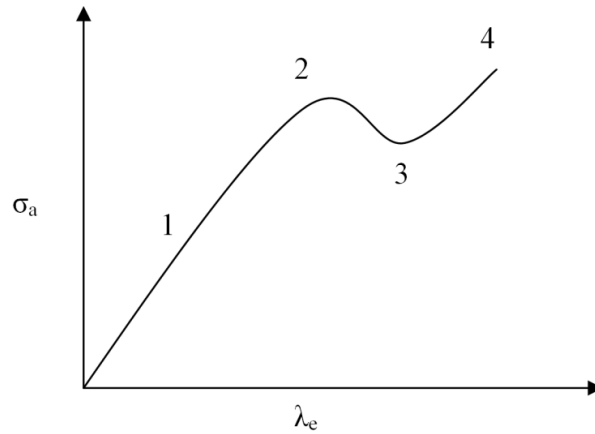


Figure 3.8: Necking behaviour of nominal stress-strain graph

the neck (3) where it comes to term of the natural draw ratio (λ_e). Now, the polymer nature and its response to the deformation and/or sample geometry between the two grips will control the length of the stable necking. The semicrystalline polymers use to have a distinct stable necking region (Figure 3.9). Finally, the necking reaches the grip and further applied load will cause an increase in the strain that is accompanied by an increase the nominal stress where it comes to term of strain hardening in region(4) in Figure 3.8. This hardening structure in such drawing process may occur due to the molecular alignment or the strain induced crystallization that happens under the stretching effect [112]. The morphological changes are considered below in some detail.

Polymer nature and/or test conditions are the keys in distinguishing of different regions. For example, some polymer do not exhibit the stable necking area where nominal stress continues in fall with a corresponding extension till the specimen becomes very thinner and breaks. Another example, the region 2 in the true stress graph may not be recognized as explained in the previous section.

The non-homogeneity of different areas within the sample due to a non-uniform cross-section in the sample can lead to a fluctuation in result [113]. This fluctuation becomes more when the nanoparticles are involved and will be more

severe if PP/clay system is not well dispersed through the cross-section area of the sample. For example, thinner cross-section area causes higher true stress and that particular area leads to reach to the yield point faster, but at lower yield stress and lower applied load as well.

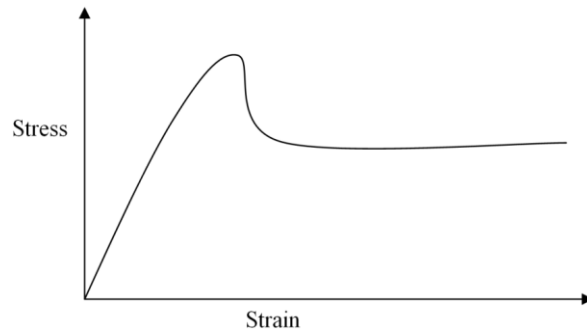


Figure 3.9: Schematic stress-strain curves for a semicrystalline polymer

Another example in PPNCs, when the stable necking area starts and reaches an area with agglomerated dispersed clay particles in PP matrix, the strain hardening starts and disappears as the other areas start necking. This can be seen in Figure 3.10 for two stress-strain graphs for the same PP with 3% clay loading (this was done in our laboratory in earlier stage of the project).

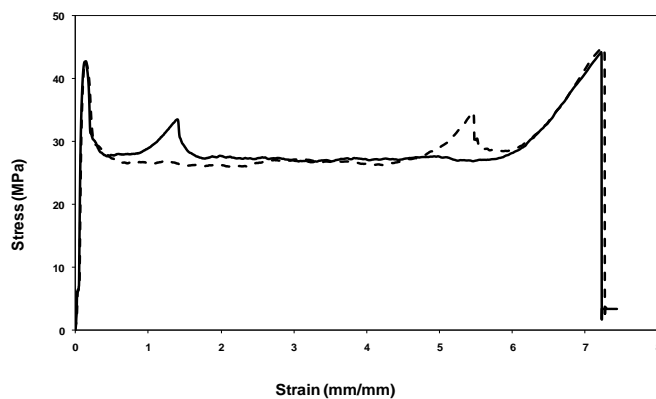


Figure 3.10 Stress-strain curves for cold drawing polymer/clay system

As it was shown above, the necking is accompanied by an initial maximum point in the load-strain curve. Whitney and Andrews[114]; and Brown and Ward [115] showed that this point of maximum load is due to not only the sample geometry, but also the load drop because the yielding initiation needs

more stress than the propagation. However this is still not clearly explained, especially for the true stress-strain curve.

The morphological changes during the drawing process are more complex than the physical changes. The morphological changes were reported by Schultz [116] to differ with the stretching process. A schematic diagram for these changes is shown in Figure 3.11, where the lamellar starts to slip past each other as the nominal stress increases and therefore spherulites turn into anisotropic structure (1). When the neck starts, the extension is introduced to the interlamellar amorphous regions. After the tie of the interlamellar amorphous regions are totally stretched, slipping in the lamellar begin (2) and cause breaking up of lamellar by pulling and unfolding of the polymer chain (3). Finally, further slipping of fragments of the lamellae in the draw direction occurs and molecular alignment is produced with crystal blocks and stretching amorphous regions (4). These fragments are connected by the ties in the drawing direction, which introduce the strength to the micro-fibrils in the fibre.

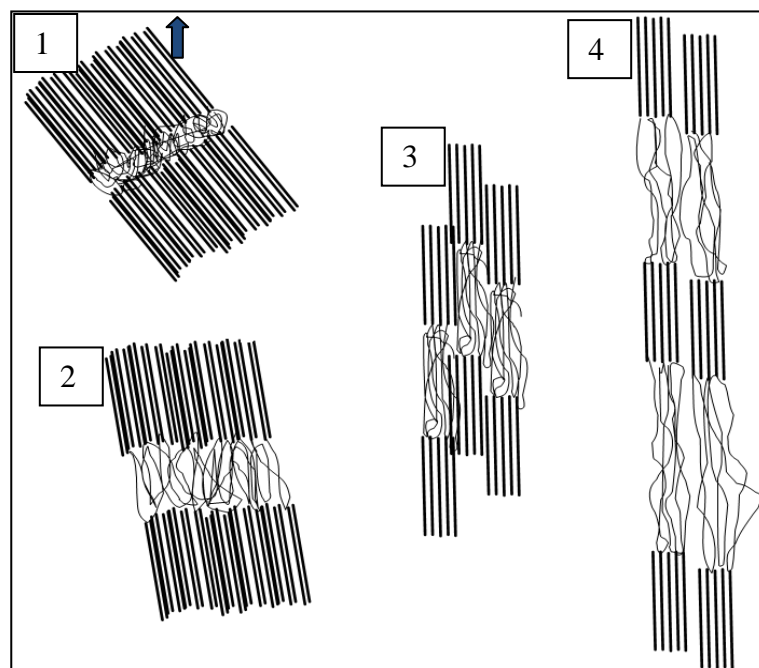


Figure 3.11: Steps in the deformation of semicrystalline polymers

3.6.3 Definition of yield stress

The more simple definition of yield stress is the stress where a permanent strain just begins to develop. However, in many cases, the distinction of that point is not so straightforward. When the yield stress corresponds with a clear distinctive maximum load as in Figure 3.12-A, it can be defined by the true stress. In this case, it is most likely to be given by the engineering yield stress as the load at point (A) is divided by the initial cross-sectional area.

When it is not clear to recognize the maximum load as in point (A), two definitions are given by Ward and Sweeney [117]. One approach is given by intersect of the two tangents of the initial and final developed stress-strain curve as shown in Figure 3.12-B. Second approach is defined by intersect of the line parallel to the initial linear slope of stress-strain curve. This line is offset by for example 2% of a specified strain as shown Figure 3.12-C.

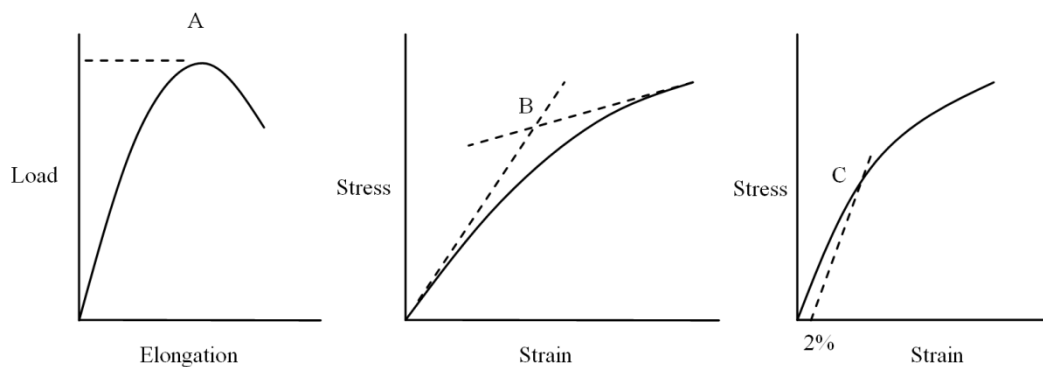


Figure 3.12: Yield stress definition

3.7 The Yield Criterion

Before the yield point, there is only elastic deformation. So the plasticity theories ignore any behaviour occurring before that point except the variability of time. Ward and Sweeney [118] consider the yield criterion as a function of six

stress components. The values of these components depend on the orientation. If this dependency is isotropic, the general stress tensor will be

$$\begin{pmatrix} \sigma_{xx} & \sigma_{xy} & \sigma_{xz} \\ \sigma_{yx} & \sigma_{yy} & \sigma_{yz} \\ \sigma_{xz} & \sigma_{zy} & \sigma_{zz} \end{pmatrix}$$

and for principal stresses (σ_1, σ_2 and σ_3) in principal directions,

$$\begin{pmatrix} \sigma_1 & 0 & 0 \\ 0 & \sigma_2 & 0 \\ 0 & 0 & \sigma_3 \end{pmatrix}$$

so the yield criterion for isotropic conditions is

$$f(\sigma_1, \sigma_2 \text{ and } \sigma_3) = \text{constant}$$

The yield criterion proposed by Tresca states that yield occurs at a maximum critical value of shear stress, and thus

$$\sigma_1 - \sigma_3 = \text{constant, with } \sigma_1 > \sigma_2 > \sigma_3$$

The Coulomb yield criterion states that the critical shear stress (τ) increases linearly with the pressure (σ_N) normal to plane shearing. τ_c was termed the cohesion and μ the coefficient of the internal friction.

$$\tau = \tau_c - \mu \sigma_N \quad (3.3)$$

The von Mises criterion gives equal yield stresses in tension and compression with no dependency on hydrostatic pressure so that

$$(\sigma_1 - \sigma_2)^2 + (\sigma_2 - \sigma_3)^2 + (\sigma_3 - \sigma_1)^2 = \text{constant} \quad (3.4)$$

In uniaxial conditions where $\sigma_2 = \sigma_3 = 0$, so that the yield stress $\sigma_Y = \sigma_1$

$$2\sigma_Y^2 = \text{constant}$$

Another way in describing the von Mises criterion is to separate the hydrostatic pressure from the total stress to give the deviatoric stresses σ'_1, σ'_2 and σ'_3 :

$$\begin{pmatrix} \sigma'_1 & 0 & 0 \\ 0 & \sigma'_2 & 0 \\ 0 & 0 & \sigma'_3 \end{pmatrix} = \begin{pmatrix} \sigma_1 + p & 0 & 0 \\ 0 & \sigma_2 + p & 0 \\ 0 & 0 & \sigma_3 + p \end{pmatrix}$$

where the pressure $p = -\frac{1}{3}(\sigma_1 + \sigma_2 + \sigma_3)$. Finally, it can be written either as

$$\sigma'^2_1 + \sigma'^2_2 + \sigma'^2_3 = \text{constant} \quad (3.5)$$

or in so-called octahedral shear stress (τ_{oct}) which is expressed the yield criterion as $\tau_{\text{oct}} = \text{constant}$

$$\tau_{\text{oct}} = \frac{1}{3} [(\sigma_1 - \sigma_2)^2 + (\sigma_2 - \sigma_3)^2 + (\sigma_3 - \sigma_1)^2]^{1/2}$$

3.8 Hot-Drawing Processes

Polymer molecular orientation can be produced by the hydrostatic extrusion and die drawing processes. The hot drawing of the solid polymer is performed above the glass transition temperature (T_g). Both hydrostatic extrusion and die drawing processes include a billet which is made to pass through a die by either back pressure (hydrostatic extrusion) or a tensile force (die drawing). In both cases, the billet is heated to a temperature just below the melting point to allow flow in order to achieve a high degree of molecular orientation.

3.8.1 Hydrostatic extrusion process

Hydrostatic extrusion is a hot drawing process technique in the solid state. A sketch diagram of the hydrostatic extrusion process is given in Figure

3.13. The process typically involves a billet that is introduced to a pressure vessel filled with fluid at high pressure. A small pressure is maintained in the heated pressure vessel to help in pushing of the billet against the walls of the die. A small force then is applied on the product tag. As the desired temperature is reached, the pressure then is gradually applied. Thus the drawn product is extruded from the vessel by the piston movement.

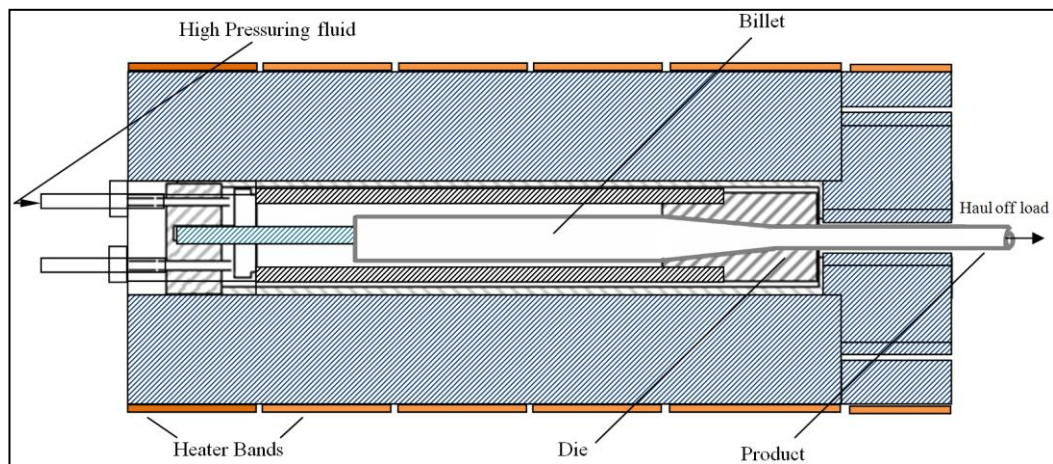


Figure 3.13: Hydrostatic extrusion process

Alexander et al [119] showed one of the earliest publications in relating to the hydrostatic extrusion of polymer materials. Parsons et al [120] used small and large scale experiments of hydrostatic extrusion on a range of polymers. A significant improvement of stiffness in axial direction has been reported for the hydrostatic extrusion of PP with Young's modulus of 15 GPa.

3.8.2 Die-Drawing Process

Die drawing process was developed by Ward et al. [5, 77]. It combines the best obtained features of free cold drawing and solid phase extrusion of polymers. It is performed at temperature above T_g and just below the T_m .

As shown in Figure 3.14, the heated billet is drawn through the heated conical die by pulling the billet with a mechanical force at the exit of the die. The

billet then is shown a neck through the die exit in the extensional direction. The flow stress is optimized by an appropriate point where the billet leaves the die walls. The three distinct deformation zones (A, B, and C) are shown in Figure 3.14. In zone A, the billet remains isothermally in contact with the conical die. The billet then passes an isothermal region (B), which is similar to the die temperature, with a neck due to the free tensile flow just before leaving of the die. Nonisothermal conditions start just outside the die (region C), where the neck is more developed. The product then cools and the deformation is brought to the end at a point after leaving the die. Thus the cross-sectional area remains constant.

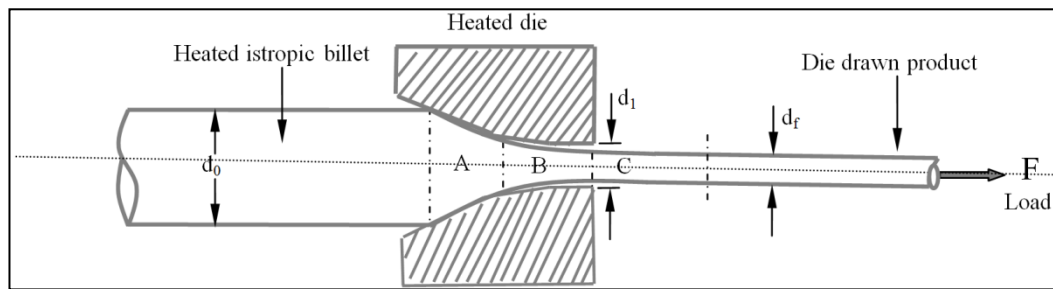


Figure 3.14: Die drawing process

In die drawing process, the degree of deformation is measured by the actual draw ratio (λ_A) and expressed by the initial and final billet cross-sectional area for circular rods:

$$\lambda_A = \frac{d_0}{d_f}$$

where d_0 and d_f are billet diameter and final product diameter, respectively. The nominal extension ratio (λ_{Nom}) characterizes the size of the initial billet and is defined by the ratio of the cross-sectional area of the billet to the die exit (d_1). Thus the actual draw ratio (λ_A) is always greater than the nominal extension ratio (λ_{Nom}).

$$\lambda_{Nom} = \frac{d_0}{d_1}$$

The true stress at any point along the drawing path is the stress of the drawn product at the same point for stable drawing process and is given by:

$$\sigma_{max} = \frac{4F\lambda}{\pi d_0^2}$$

where F is the haul-off load. The maximum draw stress (σ_{max}) is the stress where the product deformation is limited at and beyond the end of region C and is given by

$$\sigma_{max} = \frac{4F\lambda_A}{\pi d_0^2} = \frac{4F}{\pi d_f^2} \quad (3.6)$$

3.9 Fracture Toughness

Izod and Charpy impact tests determine the required energy to breaking a notched specimen with a specific geometry and fracture area. Thus the energy absorption is denoted in the notched samples, which is not considered to be a reliable measurement of the fracture toughness. So the fracture mechanics is properly involved to characterize the notched specimens of the fracture toughness of polymer and polymer composites.

Fracture toughness approach assumes that the failure in the polymer material occurs as a result of initiation and propagation of material cracks [121]. Linear elastic fracture mechanics (LEFM) is used for the characterization of materials with elastic deformation or materials with small scale yielding near the tip of the crack. It is assumed that radius of the crack (r) is much smaller than the initial length of flaw (c). The useful LEFM variables include the critical stress

intensity factor (K_c) and critical strain energy release rate (G_c). The LEFM is developed by Irwin [122] based on the previous work of Griffith [123]. The fracture toughness can be measured by K_c , which implies the stress at fracture (σ_b) and is given by

$$K_c = \sigma_b \sqrt{\pi c}$$

Failure occurs when the local energy release rate exceeds the critical value (G_c). Polymer materials have a threshold limit of this energy dissipation (G_0) about 50 J/m², where the crack can not grow below this limit. G_c can be related to K_c by knowing the Young's modulus (E)

$$G_c = \frac{K_c^2}{E}$$

For ductile materials where a large plastic zone is developed at tip of the crack as the case in most semicrystalline materials, the LFEM based on the K_c and G_c is invalid due to the large scale yielding that takes place just prior to the failure. In this case, the Griffith and Irwin theories for brittle fracture of polymer can not be used, and therefore non-linear elastic fracture mechanics variables should be adopted.

The J-integral concept and the essential work of fracture approach (EWF) can be used to characterize the fracture behaviour of ductile materials. The J-integral method is developed by Rice [124]. A critical value of J-integral (J_c) is generally determined by making a resistance curve J- Δa , where Δa is the advanced crack length. The J_c value is determined from the intersection point between the J- Δa curve and the blunting line ($J = 2\sigma_y \Delta a$, where σ_y is the yield stress or craze stress).

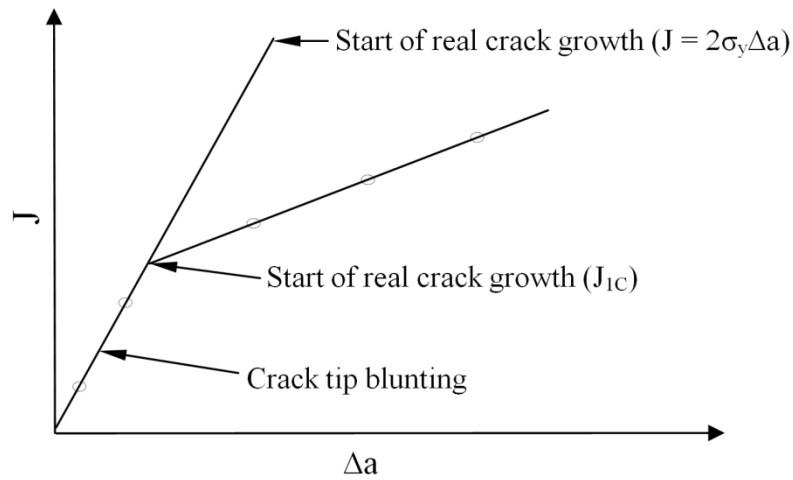


Figure 3.15: Plot of the flow energy versus the amount of crack extension [125]

The EWF method gains more acceptance for the description of polymer fracture toughness of ductile materials over the J-integral approach, due to the simplicity of the experiment and manipulation of the data. The EWF test separates the fracture work of a specimen into two parts: the first part is designated as the EWF that is defined by the work required to fracture the specimen in the inner process zone (W_e) and the second part is designated as non-EWF, which is related to the dissipation of the plastic work in the process zone (W_p). The non-EWF depends upon the specimen geometry and its process zone. This approach was originally suggested by Broberg [126] and developed by others [127-129].

The typical double-edge notched tension (DENT) geometry of specimen is commonly used for tensile measurement. Other geometries have been employed for the experimental determination of EWF parameters [130]. The DENT sample is loaded in tension till the ligament, L , is completely yielded and the propagation of the crack across the ligament causes a complete failure. Load (P) versus displacement (δ) curve is obtained (Figure 3.16), where δ is measured over the gauge length. The total dissipation work of energy is given by

$$W_f = \int_0^{\delta} P d\delta \quad (3.7)$$

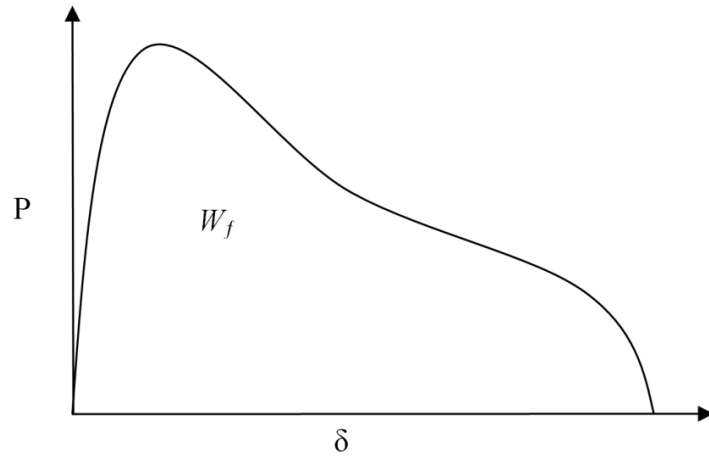


Figure 3.16: The load- displacement curve of fracture

This dissipated energy goes into the two separate processes, i.e. EWF and non-EWF. Thus the total work of fracture (W_f) can be written as:

$$W_f = W_e + W_p \quad (3.8)$$

Equation 3.8 can be introduced in the following three equations:

$$W_e = w_e tL$$

$$W_p = \beta w_p tL^2$$

$$W_f = w_e tL + \beta w_p tL^2 \quad (3.9)$$

As it is shown in Figure 3.17, w_e and w_p are the specific essential work of fracture and the specific plastic work of fracture, respectively. L is the ligament length, t is the sample thickness, and β is the shape factor of the plastic zone. In Figure 3.17, the zone is drawn as circular so $\beta = \pi/4$.

After normalizing of the total work of fracture, in Equation 3.9, by area of the ligament $A=tL$, the specific total work of fracture can be written as

$$w_f = \frac{W_f}{tL} = w_e + \beta w_p L \quad (3.10)$$

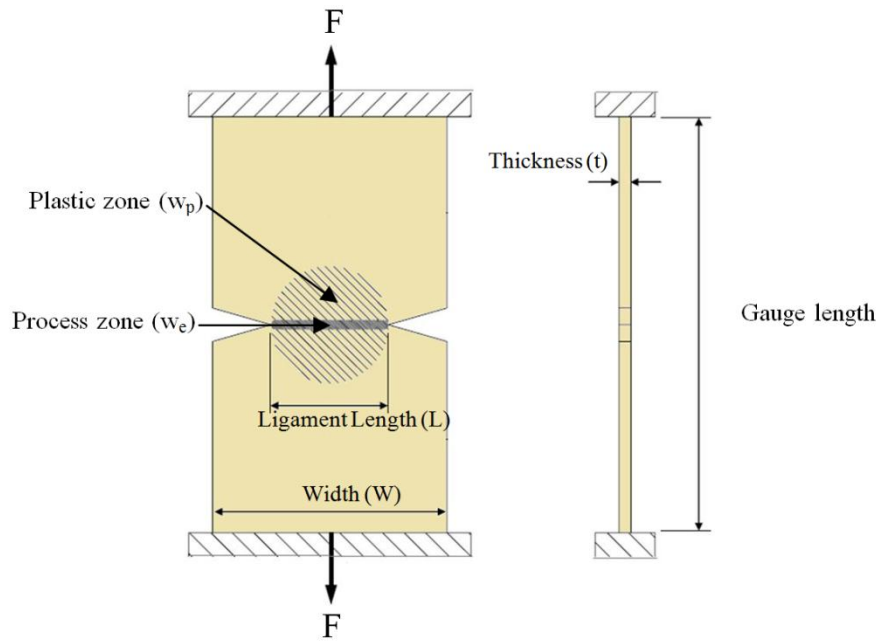


Figure 3.17: : Essential work of fracture test specimen diagram

The total specific work of fracture and the ligament length have a linear relationship. At high ligament length, the plane stress is dominant and thus the specific EWF (w_e) for plane stress is calculated by extrapolating the linear fit to zero ligament length. The non-EWF (i.e. work required for plastic deformation) is given by the slope of the line. At low ligament length, the plane strain is dominant and specific EWF for plane strain can be calculated by extrapolating to zero ligament length. The validity range of ligament under the plane stress condition is given in Figure 3.18.

It is suggested to divide the specific total work of fracture (w_f) into specific work of fracture for yielding (w_y) and specific work of fracture for necking (w_n) and apply the same for w_y and w_n as shown in Equation (3.11) and (3.12) [131].

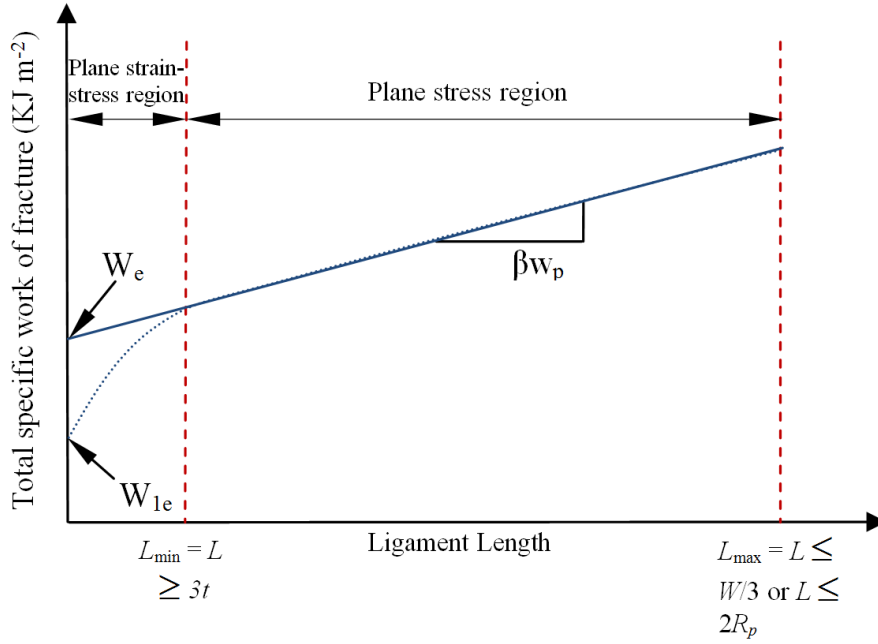


Figure 3.18: Specific total work of fracture against ligament length [132]

$$w_f = w_y + w_n \quad (3.11)$$

$$w_f = (w_{e,y} + \beta' w_{p,y} L) + (w_{e,n} + \beta'' w_{p,n} L) \quad (3.12)$$

where $w_{e,y}$, $w_{p,y}$, $w_{e,n}$ and $w_{p,n}$ are the specific essential and non-EWF for yielding and necking, respectively. β' is the shape factor for yielding and β'' is the shape factor for necking.

The assumptions that give the validity criteria of DENT test should be maintained to get the representative results of both EWF and non-EWF [133]. These include the geometrical similarity of different ligaments during crack growth and a fully yielded of the ligament prior to a complete failure. Thus the fracture occurs under plane stress conditions, so w_e and βw_p are both independent of the ligament length. It also requires that the outer plastic zone size and volume is proportional to the ligament length square.

For the above assumptions to be satisfied and also to maintain a linear correlation between w_f and L as given in Equation 3.10, it has been recommended that the length of ligament to meet some prerequisites that are shown in Figure 3.18. First is $L \leq 2R_p$, to ensure that a fully yielded of the ligament prior to crack growth, and hence maintain the proportionality of w_p and L^2 . R_p is the plastic zone radius at the tip of the crack. Second is $L \leq W/3$ to ensure that the edge does not affect the size of the plastic zone and, thus plastic deformation is limited to the ligament area. Third is $L \geq 3t-5t$ to ensure that w_e and w_p are not ligament length dependent and thus is mixed mode of stress and strain planes.

The above range validity of ligament length can be summarized by

$$3t - 5t \leq L \leq \min\left(\frac{W}{3}, 2R_p\right)$$

The plastic zone radius at the tip of the crack can be given by [134, 135]

$$2R_p = \frac{Ew_e}{\pi\sigma_y^2} \quad (3.13)$$

Where E is the Young's modulus and σ_y is the uniaxial tensile yield stress of the material.

4 Experimental Work

4.1 Introduction

A study on the same general area as this work was recently conducted in Queen's University Belfast. In order to take advantage of their analysis and to have a valid comparison, similar raw materials and clay weight percentages were used as a preliminary starting point for the present study. Materials, characterization methods, and equipments used in preparation of recently compounded samples are presented in this chapter.

In the first section of the chapter, the material grades were shown. The pieces of equipment used and the procedure for samples preparation will be depicted. Finally, in the last section, the testing methods for material characterization will be illustrated.

As a first step, some physical and mechanical features of the PP/MMT composites for the samples received from Queen's University Belfast, such as crystallinity and tensile properties, were evaluated and the assessed level of clay dispersion achieved were estimated by means of property results fluctuations. Advanced evaluation of nanoclay dispersion is going to be considered after overcoming all possible defects that might be produced in mixing and processing stages. All the test results done will be listed and commented in Chapter 5.

4.2 Raw materials

4.2.1 Polypropylene

In the previous work done by Queen's University Belfast, a PPH 5042 grade from TOTAL Petrochemical was used. The received sheets were evaluated

and based on the technical data sheet of the old grade, the new grade was selected to be polypropylene homopolymer (PPH 5060) due to the similarity with PPH5042. This similarity can be shown from both materials technical data sheets. However, tensile strength is slightly higher in case of PPH 5042 while the elongation is slightly higher in PPH 5060 grade. No information was given to know if and which additives it contains. Table 4.1 shows the information available about their properties although more details are available in Appendix B1 and B2.

Table 4.1: TOTAL PPH 5042 & PPH 5060 Properties

	Unit	PPH 5042	PPH 5060
Rheological properties			
Melt Flow Index 230°C/2.16 kg	g/10min	6	6
Mechanical properties			
Tensile Strength at Yield	MPa	35	32
Elongation at Yield	%	9	10
Tensile modulus	MPa	1600	1500
Flexural modulus	MPa	1550	1400
Izod Impact Strength (notched) at 23°C	kJ/m ²	5	4
Charpy Impact Strength (notched) at 23°C	kJ/m ²	6	5
Hardness Rockwell - R-scale		95	92
Thermal properties			
Melting Point	°C	165	164
Vicat Softening Point	°C		
50N-50°C per hour		95	85
10N-50°C per hour		153	150
Heat Deflection Temperature	°C		
1.80 MPa - 120°C per hour		57	55
0.45 MPa - 120°C per hour		105	100
Other physical properties			
Density	g/cm ³	0.905	0.905
Bulk Density	g/cm ³	0.525	0.525

4.2.2 Nano-clays (MMT)

The silicate material, which is studied in this work and in previous work at Queen's University Belfast, was supplied by Southern Clay Products® (Cloisite® 15A). Another synthetic montmorillonite SOMASIF ME100 (ME)

material was used in Queen's University Belfast and evaluated for only the received sheets in this work as well.

SOMASIF is a synthetic fluorohectorite produced by CO-OP Chemical Co., Japan. The cation exchange capacity (CEC) of ME is 70 meq/100g, and its interlayer spacing is 0.96 nm. Its formula is $\text{Na}_{2x} \text{Mg}_{3.0-x} \text{Si}_4 \text{O}_{10} (\text{F}_y \text{OH}_{1-y})_2$, ($x = 0.15 - 0.5$, $y = 0.8 - 1.0$).

Cloisite® 15A consists of organically modified layered magnesium aluminium silicate platelets. Montmorillonites have a sheet-type structure. The particles are agglomerated because the surface attraction between them, which can be reduced by the surface treatment. The formula of montmorillonite is: $\text{M}_y^+(\text{Al}_{2-y} \text{Mg}_y) (\text{Si}_4) \text{O}_{10} (\text{OH})_2 \cdot n\text{H}_2\text{O}$.

Both SOMASIF and Cloisite 15A use patented surface treatment technology. MMT particles exist in agglomerated structure with a distance of about 3.5Å. Surface treatment helps in reduction of particle-particle attraction, and thus promoting the expansion of the distance to about 20Å.

The silicate platelets of Cloisite® 15A are 1 nanometre thick and 70 – 150 nanometres across. C15A is surface modified with an organic chemistry (di-methyl, di-hydrogenated tallow, quaternary ammonium as a chloride salt) to help in dispersion issue and provide miscibility with the PP.

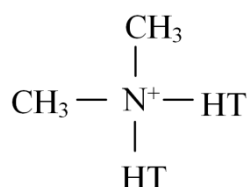


Illustration above shows the structure of the cation used in surface modification of C15A, where HT is Hydrogenated Tallow (~65% C18; ~30%

C16; ~5% C14). Table 4.2 summarizes some properties of C15A although more details are available in Appendix B3. In this work, clay loading levels were kept at 3 and 5% on a weight basis in order to evaluate the influence of PPNCs content on the mechanical and fracture behaviours of PPNCs.

Table 4.2: Southern Clay® Cloisite® 15A Properties

	Property Value		
Colour	Off-white		
D-spacing	$d_{001}=31.5 \text{ \AA}$		
Density	Loose Bulk	Packed Bulk	Specific Gravity
	10.79 lbs/ft ³	18.64 lbs/ft ³	1.66 g/cc
Modifier Concentration	125 meq/100g clay		
Moisture	Result	Min	Max
	0.9%	0.4%	2.5%
Weight Loss on Ignition	Result	Min	Max
	43%	42.5%	44.5%
Typical Dry Particle Sizes (by volume)	10% less than:	50% less than:	90% less than:
	2 μm	6 μm	13 μm

4.2.3 Compatibilizer

As mentioned before that the clay was already surface treated, the compatibilizer was in any case required to improve the interfacial adhesion between the organophilic silicate and the PP matrix, the problem being the incompatibility between the nano-clay with strongly electro-negative atoms (mainly oxygen), which are polar sites in its molecular structure, and the polymer, completely apolar.

Therefore this coupling agent promotes the dispersion of MMT in the bulk of the matrix. Among the several commercially available products, DuPont™ Fusabond® P M613–05 was chosen. Being in pellet form, it was easily dispersible into the matrix by melt blending with PP and MMT.

Fusabond® P M613–05 is a maleic anhydride modified homopolymer PP recommended for coupling of clay in PP composites. Table 4.3 summarizes some

Fusabond physical properties although more details are available in Appendix B4.

Table 4.3: Fusabond® P M613–05 Properties

	Unit	Value	Min	Max
Melt Index	g/10min	45.13	37.0	61.0
Maleic Anhydride	%	0.55	0.35	0.70
Melting Point	°C		162	

In this work, loading levels were kept at 3, 6 and 9% on a weight basis in order to evaluate the influence of compatibilizer content on the mechanical and fracture behaviours of PPNCs.

4.3 Compounding of Polypropylene Nanocomposite

4.3.1 Compounding: the prism eurolab twin-screw extruder

A Prism Eurolab KX 16 mm co-rotating twin-screw extruder (Figure 4.1) with rod die was used. It is driven by a KX-16 2.0 KW servomotor. The small, laboratory scale extruder has a length to diameter (L/D) barrel ratio of 40:1. The L/D ratio is the barrel length/barrel diameter and plays a major role in mixing and processing abilities of the extruders including the type of material that can process and the motor torque.

The extruder barrel consists of ten zones including a water-cooled feed zone. Each zone is independently heated by a control thermocouple situated in the lower section of the barrel, allowing control of the temperature profile along the barrel. A touch screen control panel allows control of the temperature profile and process parameters such as screw speed and feed rate. The screw speed is variable up to 500 rpm and the feed rate, measured as a percentage of the screw speed (Prism feeder), is also variable but the extruder will only run up to a torque maximum of 104 %, any higher may lead to torque-out and the extruder

automatically shutting down as part of its safety features. The Prism extruder houses two 16mm diameter co-rotating, intermeshing screws.

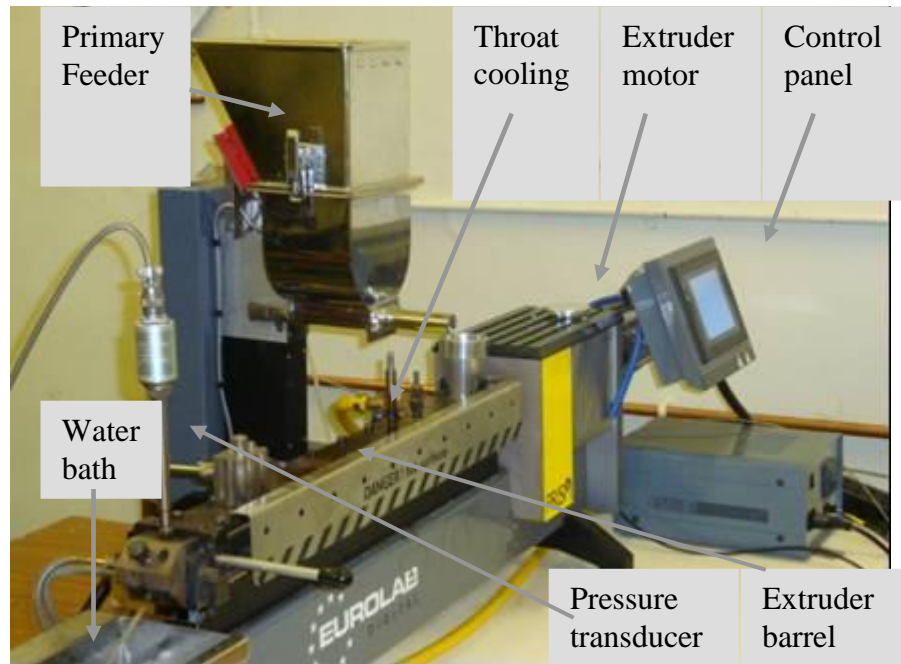


Figure 4.1: Prism Eurolab 16 mm twin-screw extruder

The ten barrel zones (zone 1 is the throat and feed zone and zone 10 is the final barrel zone before the die). Barrel zones 1 and 2 were for solids transport and for melting of PP to begin. Throat cooling, using water, was employed at zone 1. The first part of the screw (from the throat zone to the end of zone 2) comprised of 9 x 1D conveying elements and was designed to transport the polymer to the first mixing section (beginning at zone 3). The first mixing section comprised of 15 x 0.25D mixing elements. In this section the polymer is melted fully and highly mixed. Following this section of the screw, at zone 4, two 1D conveying elements were inserted to reduce potential issues with torque. The two conveying elements were then followed by a second mixing section. This zone consists of four small mixing sections, separating by one or two 1D conveying elements. Four 1D conveying elements follow the second mixing section, at zone 7. The third mixing section is located at zone 8. A reversing

element located at zone 9 was inserted to build up pressure and increase the resistance to flow resulting in an increase of the fill degree and the residence time in the third mixing section. The remainder of the screw design focussed on conveying of the polymer to the die with intermittent mixing sections to achieve excellent mixing. Figure 4.2 shows the mixing section of the twin screw used in the compounding stage in this work. Full design of the twin screw is provided in Appendix C.

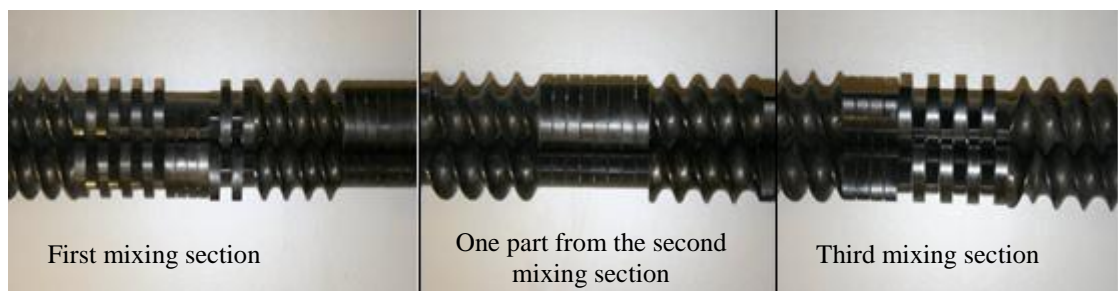


Figure 4.2: Twin screw mixing sections of Prism Eurolab 16 mm TSE

4.3.2 Primary and secondary screw feeders

A secondary screw feeder (Figure 4.3), which was designed in IRC department, was used to have the required proportions of the clay, PPMA and the master batches. PP pellets were introduced separately through the primary feeder (Figure 4.4). The secondary screw feeder has a rotated plastic sheet that attaches to a metal shaft to help conveying clay with reasonable output consistency. For all of the experiments, the primary feed rate was between 0.4 and 1.0 kg/hr and the secondary feeder between 0.15 and 0.25 kg/hr.



Figure 4.3: Secondary screw feeder

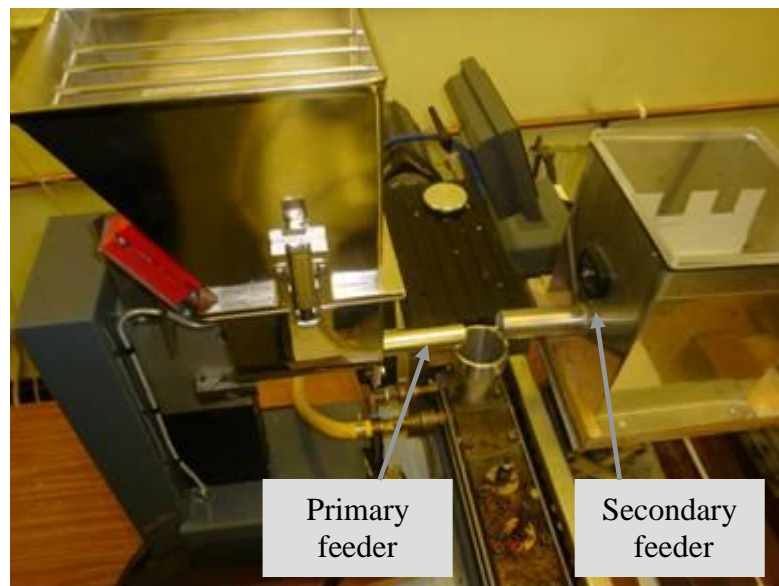


Figure 4.4: Primary and secondary feeders

4.3.3 Sample preparation and production

PP material was introduced to the extruder through the primary feeder, whereas the secondary feeder was used to introduce the clay material in powder form, compatibilizer in pellets form, and for different master batches. A calibration for both feeders was performed before starting each sample experiment. The different concentrations of clay and compatibilizer have been added to obtain the desired different weight percentages of filler and

compatibilizer in PP matrix. All the weight measurements were performed with the same balance having an accuracy of a tenth of gram. The clay and compatibilizer master batches were prepared based on 80% PP and 20% from the clay or PPMA. Before melt processing, clay was dried at 80 °C for 24 hours.

Upon exiting the die, the extrudate was drawn through the water bath; fan dried, pelletized using the Varicut pelletizer and collected. The extruder was purged with PP between runs so no cross contamination between samples occurred. Before beginning the next experiment, a stabilisation time was allowed before collection of the extrudate. This stabilisation time was to allow the extruder torque to stabilise to the set parameters and thus to ensure that the collected sample was produced at the processing conditions stated and that no residual purge material was present in the sample.

4.3.4 Extruder processing conditions

A standard processing temperature profile for PP was chosen. The barrel temperatures were set from 175 °C at the first barrel to 200 °C at the last barrel that can keep reasonable torque and melt temperatures to avoid any possible degradation and/or thermal stability effect for different compounding batches. The screw speed was set at 75 and 150 rpm for preparation of clay and PMMT master batches respectively, and increased to 200 rpm for PP/Clay/PPMA preparation. Figure 4.5 and Figure 4.6 show the processing conditions used for different compounding stages. Figure 4.7 show the processing conditions for recycle PP pellets. This was done to study any thermal degradation or stability that might be presented during different stages of the compounding processes.

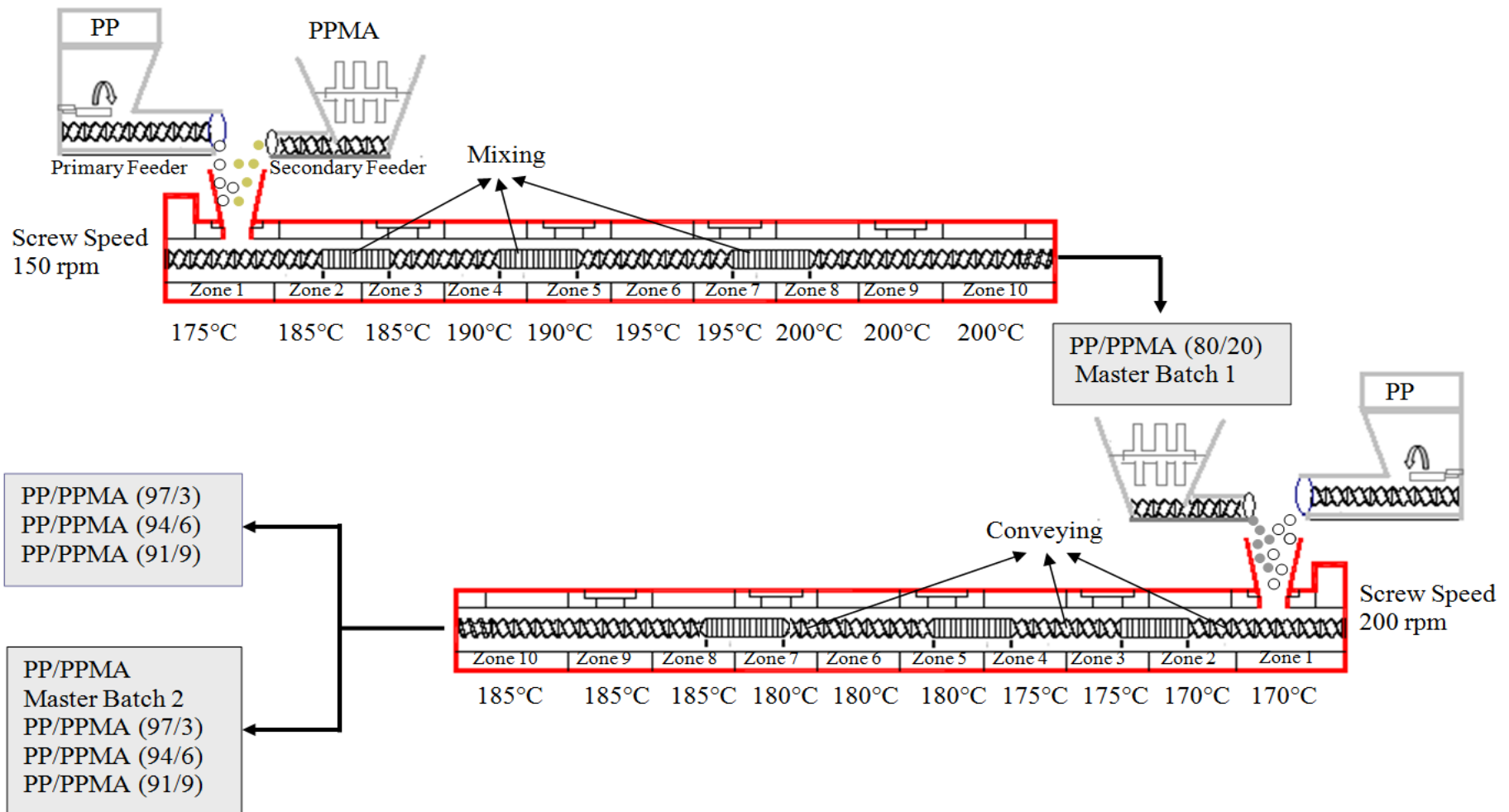


Figure 4.5: Processing conditions for different PPMA master batches compounding

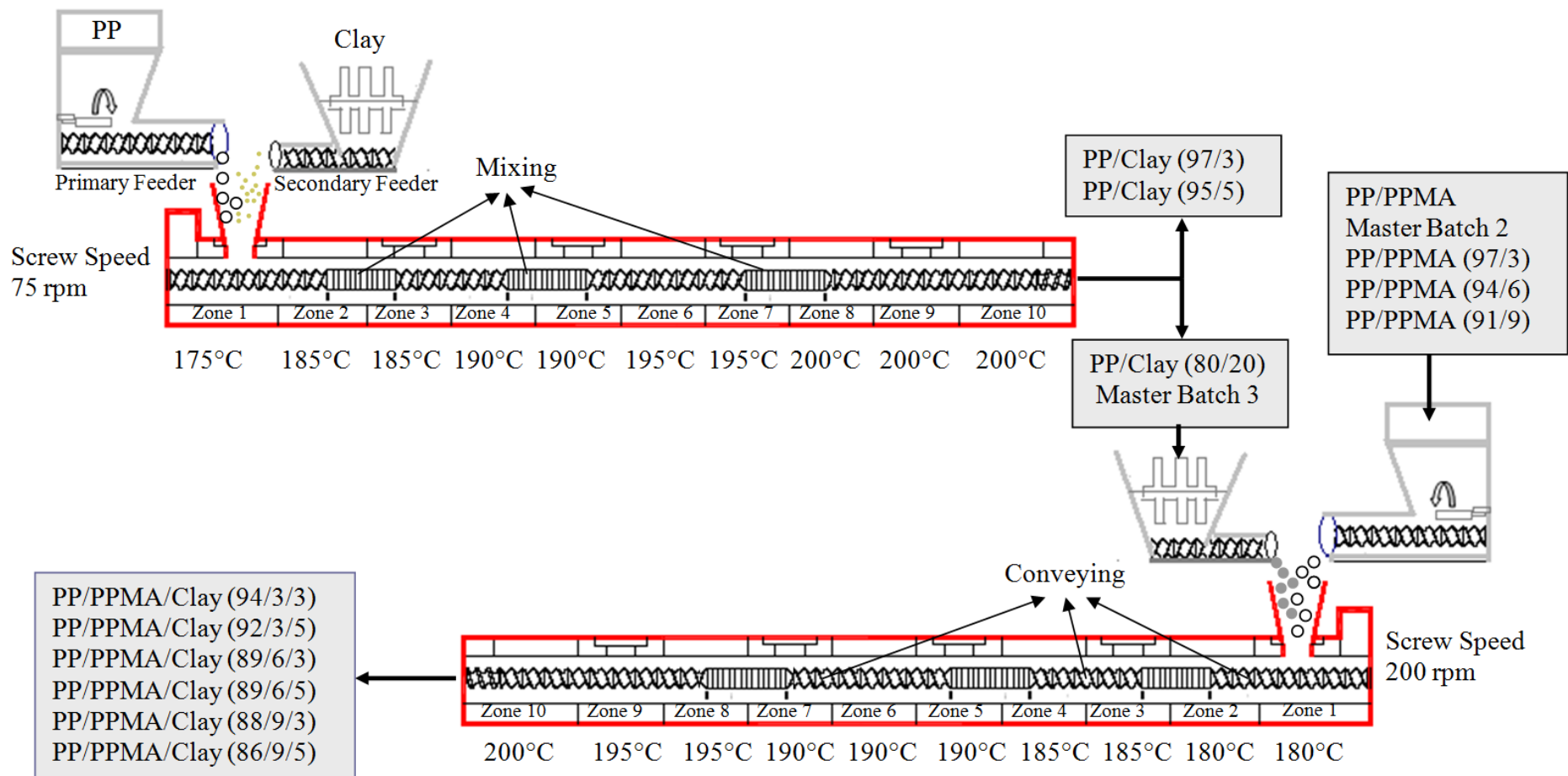


Figure 4.6: Processing conditions for clay master batch and PP/PPMA/MMT compounding

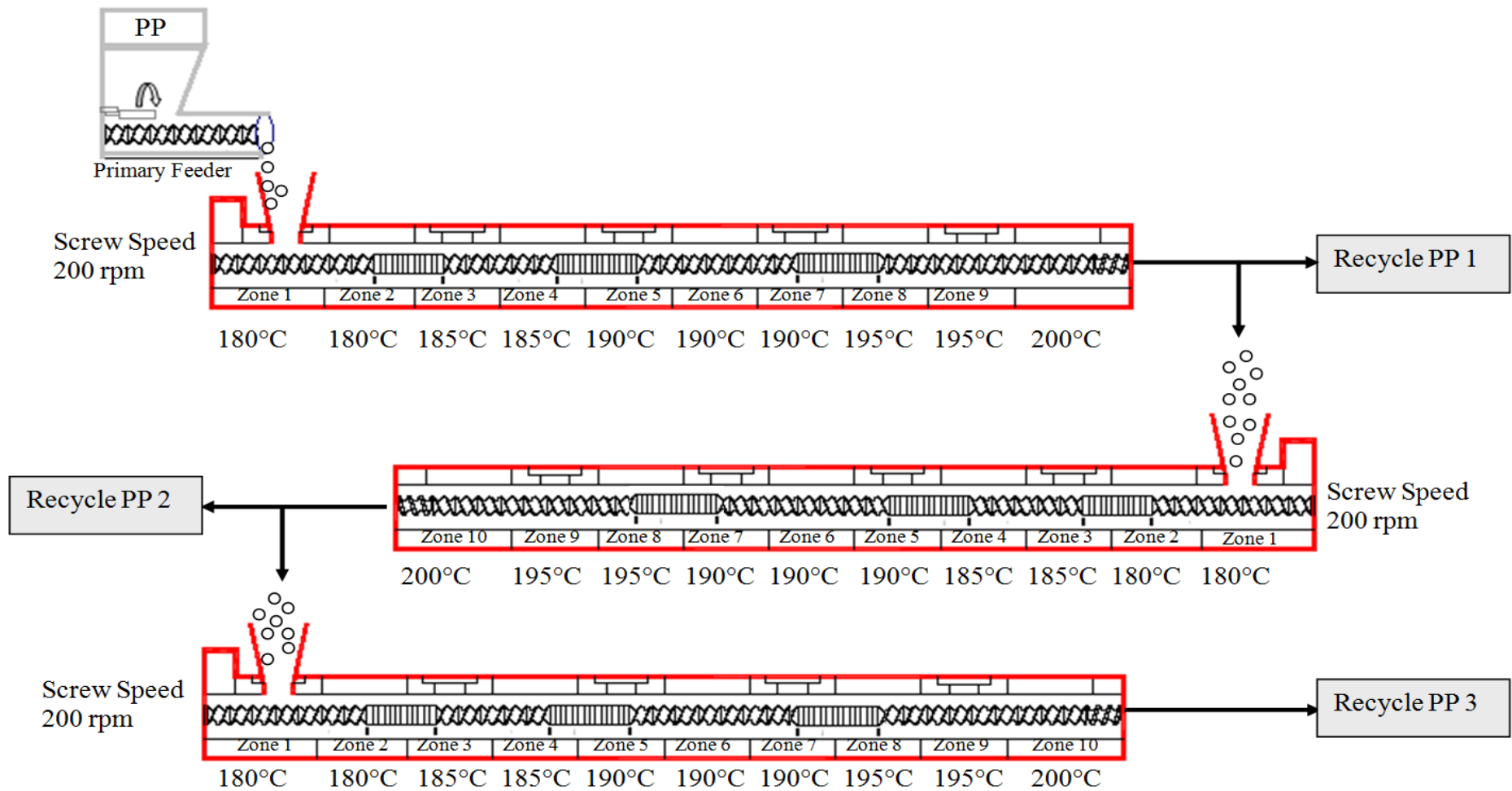


Figure 4.7: Processing conditions for recycle Polypropylene pellets

4.4 Processing and Sample Preparation of Polypropylene Nanocomposite

4.4.1 Queen's University Belfast Samples

4.4.1.1 Tensile testing

Dumbbell shaped testing specimens, using Wallace Instrument, were cut from the extruded sheet and used for tensile testing for all the samples received from Queen's University Belfast. ISO 527-2 standard was used. The dimensions are illustrated in Figure 4.8.

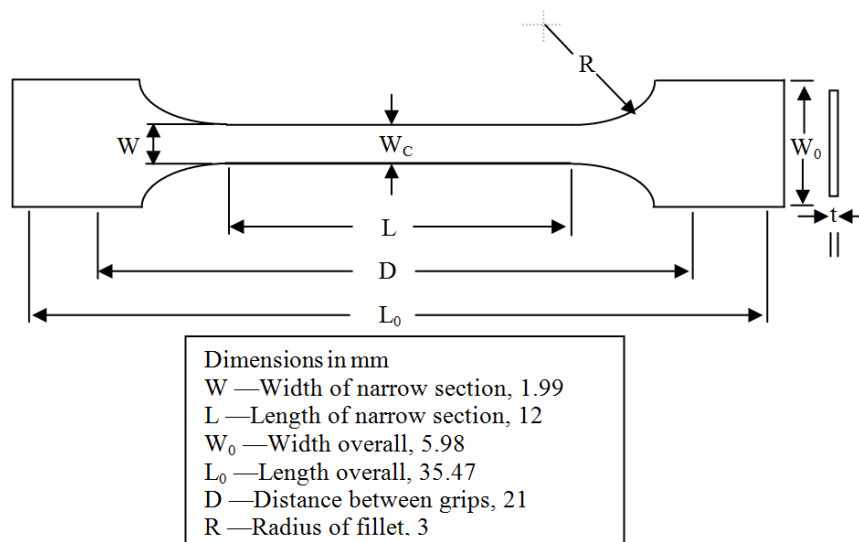


Figure 4.8: ISO 527-2 dimension for tensile test specimen

In all samples, the dumbbell specimens were cut in machine and transverse directions. All the experiments were carried out on the Instron model 5564. Tensile test was repeated for at least seven specimens per each sample at 5 mm/min crosshead speed at room temperature. The software plots a load (F , Newton) versus displacement (Δl , millimetre) curve. Three measurements were taken both for thickness and for width of each sample by means of a micrometer.

Average values were used to work out the cross section area (A), which was considered constant during the whole test. Assuming the gauge length (l) to be

the same for all the specimens, the stress (σ , Pascal) versus strain (ϵ) curve could be plotted, being: $\sigma = F/A$ and $\epsilon = \Delta l/l$. Such curve yielded values of maximum stress and of the Young's Modulus.

4.4.1.2 T M Long stretcher testing machine

The five sheets, received from Queen's University Belfast, were cut out into approximately 61 mm x 62 mm dimensions. Mechanical deformation induced experimentally using a T M Long stretcher (Figure 4.9) enabled an evaluation of true stress of unfilled sheet and compared to the two levels of filled sheets for both SOMASIF and Cloisite 15A. Samples were stretched to 5.5: 1 (constant width) extension at a given stretching temperature 160 °C and a fixed strain rate of 43.55 min⁻¹. The biaxial force-time curve is simultaneously generated during orientation.

Dumbbell specimens (ISO 527-2) were cut from the stretched sheets and used for tensile testing. Again, the dumbbell specimens were cut in machine and transverse directions and then the experiments were carried out on the Instron at 5 mm/min crosshead speed at room temperature. At least seven specimens were included for each sample. The software plots a load versus displacement. A micrometer was used to measure the thickness.

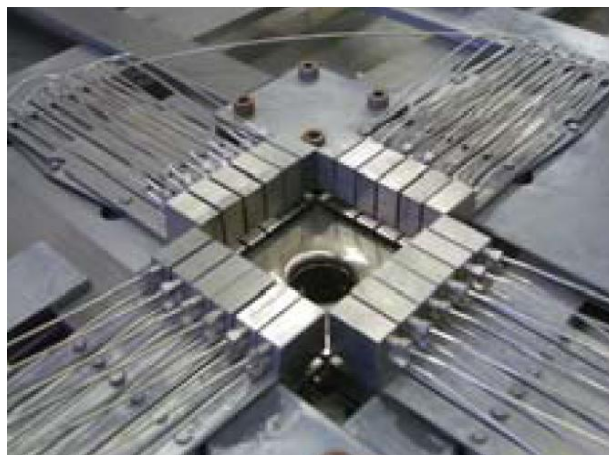


Figure 4.9: Biaxial Grips of stretching testing machine

4.4.2 Compression moulding process

The compression moulding shown in Figure 4.10 is used to produce PPNC sheets. It is a hydraulic device controlled by an electric panel, Supplied by Moore, serial number: 31757. Temperature, pressure and sample quantity were changed repeatedly to get the best condition of PPNC sheets, with uniform thickness, produced from pelletized extruded rods. An amount of 38 gm pellets, from each sample, are spread onto the middle of the frame and the bottom polished steel as shown in Figure 4.11. The set temperature was 215°C. Samples were kept under a small pressure (200 psi) for 1 minute to ensure thermal contact between the mould and hot plates of the press. Pressure was increased by 5 tons every 20 seconds till it reached to 20 tons. The press is then placed in a bath of room temperature water.



Figure 4.10: Compression moulding machine

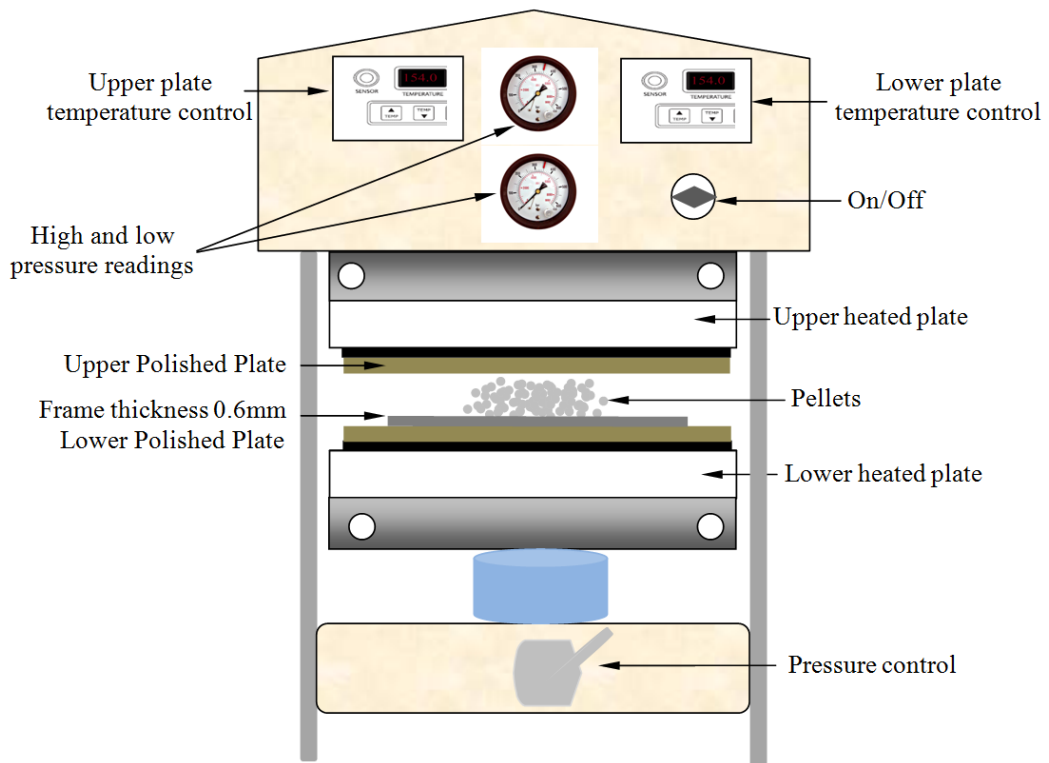


Figure 4.11: Compression moulding process

Dumbbell shaped testing specimens, using Wallace Instrument, were cut from the all produced PPNCs compression sheets and used for tensile video extensometer test. ASTM D 638 type IV standard was used. The dimensions are illustrated in Figure 4.12. The produced average thickness was 0.80 mm.

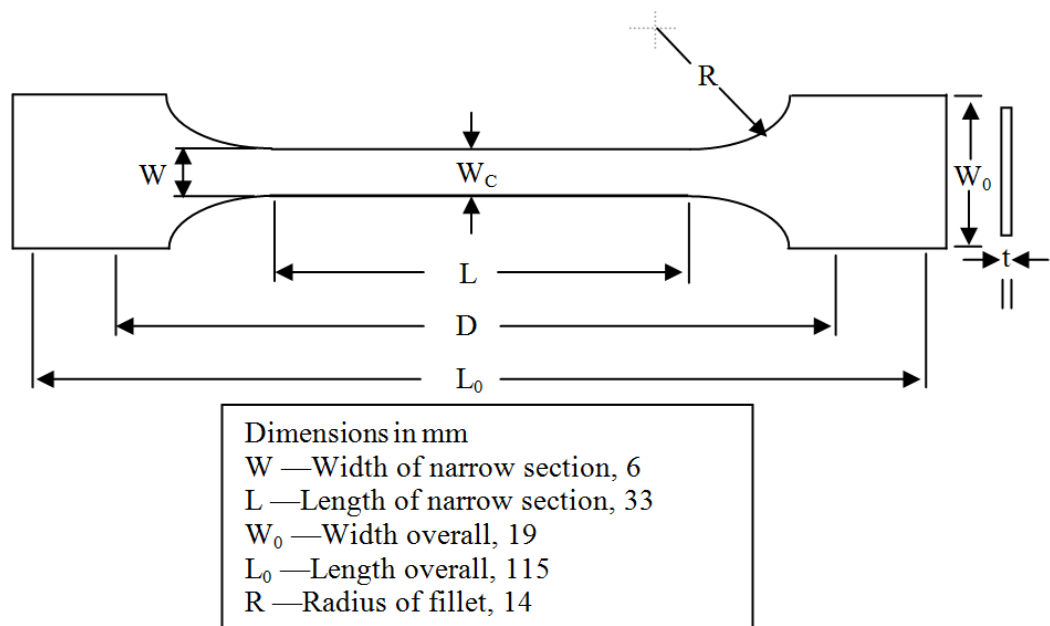


Figure 4.12: ASTM D 638 type IV dimension for tensile test specimen

4.4.3 Injection moulding process

After mixing and pelletizing of PPNCs, samples were injected into tensile test specimens by a 100 ton FANUC injection moulding machine equipped with ASTM mould, Model S-200i100A as shown in the Figure 4.13. The screw diameter is 32 mm and L/D ratio is 22:1. The pellets were introduced into the hopper. From there the material enters the plastication unit, where the screw rotates and transports melt in front of the screw into the screw chamber. The screw then moves axially backward due to the increment of melt volume in front of it. The PPNCs coming from the hopper is heated by friction and by additional heater bands around the plasticating barrel. Thus the material is melted. The screw slides back until the rear limiting switch is actuated and the screw rotation stops. Thus the melt quantity that is required for the moulding is stored in the screw chamber. The next step is closing the mould. The mould consists of two parts, which are clamped to the injection side and to the clamping side of the clamping unit, and are closed to form the cavity. The screw then is pushed forward without any rotation, forcing the melt from the screw chamber through the nozzle into the mould cavity.



Figure 4.13: Injection Moulding Machine

As the injected melt solidifies because of the cold mould walls, the screw presses additional melt into the mould under holding pressure to compensate or the volume contraction of the material as it cools. When the moulded part is cool and stiffs enough, the mould opens and the moulding is ejected from the cavity with assistance from the ejector system inside the mould. Dumbbell samples of gage length 90 mm, width 10 mm and thickness 4 mm was produced for each PPNCs. These dimensions of the produced specimen are according to ASTM D638 standards of type I (Figure 4.14 and 4.15). This completes an injection cycle and the next production cycle can start.

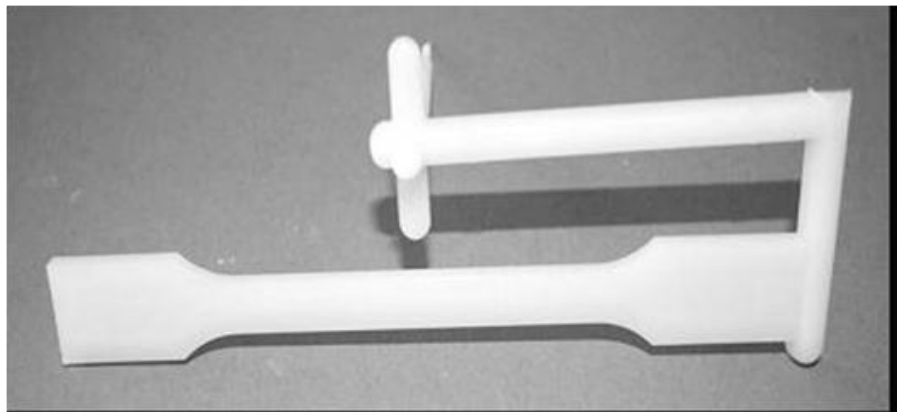
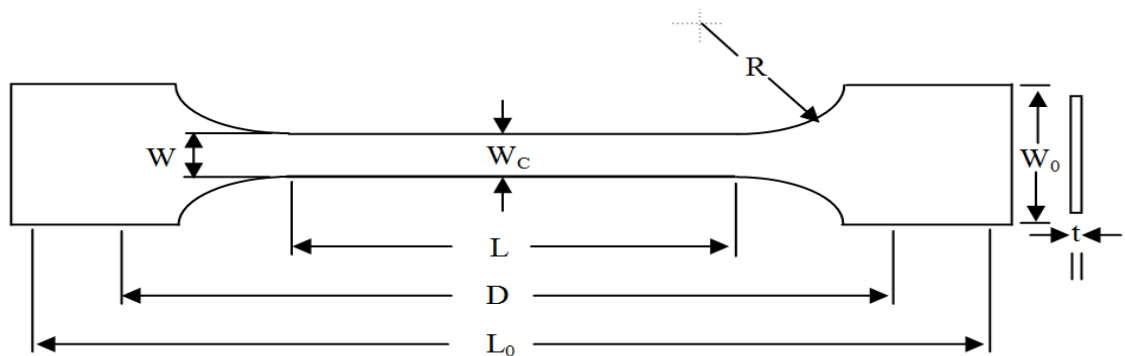


Figure 4.14: Injection Moulded Tensile Specimen



Dimensions in mm	
W	—Width of narrow section, 10
L	—Length of narrow section, 90
W ₀	—Width overall, 20
L ₀	—Length overall, 175
R	—Radius of fillet, 76
t	—Thickness, 4

Figure 4.15: ASTM D638 standard- type I specimen

The entire process as described runs fully automatically, monitored and controlled by control unit of the machine. The injection moulding processing parameters and processing temperature used are listed in Table 4.4 and 4.5.

Table 4.4: Injection moulding process parameters

Screw speed	80 rpm
Injection speed	55 mm/sec
Injection time	0.458 sec
Holding pressure	200 bar
Holding time	30 sec
Back pressure	100 bar
Shot size	30 mm
Cycle time	46.6 Sec
Mould temperature	50 °C

Table 4.5: Injection moulding processing temperatures

Feed zone °C	Zone 1 °C	Zone 2 °C	Zone 2 °C	Zone 2 °C	Nozzle zone °C
50	200	220	220	220	220

In- line viscosity index (VI) measurement is used to measure the PPNCs process variation in viscosity. This measurement was used by Speight [136]. VI was obtained from the available nozzle pressure signals recorded from FANUC machine by integrating the area under the nozzle pressure-time graph, where only the portion from 60% to 80% of the velocity controlled phase is considered. Figure 4.16 shows the selected area under the nozzle pressure graph which is integrated by Matlab program to calculate the viscosity index. Ten cycles were considered to obtain the average viscosity index. An example for the obtained graphs is given in Figure 4.17.

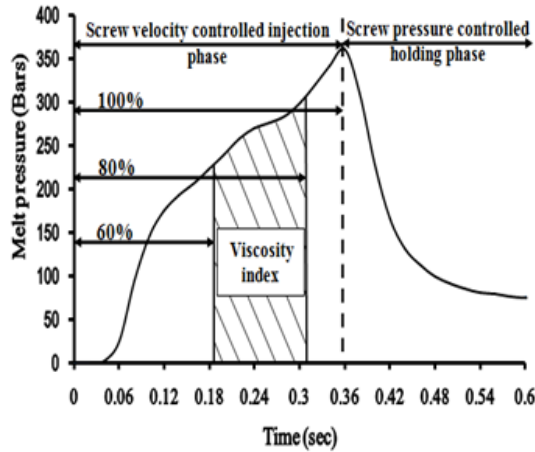


Figure 4.16: The integrating area under the nozzle pressure-time curve

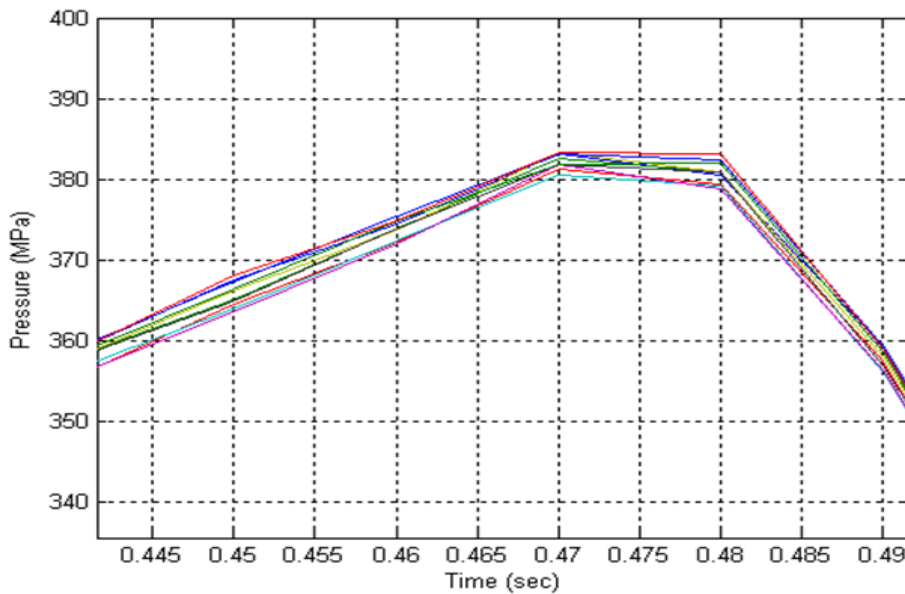


Figure 4.17: The nozzle pressure-time curve of PPNC (PP + 5% clay + 6% PPMA)

4.4.4 Die drawing apparatus

All die drawing samples were produced with equipment designed for use on Messphysik 20-10 tensile machine. A schematic diagram and a photo of the die drawn process are shown in Figure 4.18 and 4.19. The compression moulding machine edge, with a very low pressure machined each tensile bar samples with a tag thickness of 1.9 mm and a scissor was then used to allow gripping and to assist the start-up procedure for the process. The length of each sample was about

120 mm. A constant width small reg die with 15° half angle was used (Figure 4.20 and 4.21), the die thickness at the exit is 2 mm, the die width is 20 mm and the die length is 7 mm. The set die temperature was 154 °C, this is just 11 °C below the melting temperature. However the thermocouple shows 148 °C, an actual sample temperature.



Figure 4.18: Photo of the die drawing process

Three haul-off speeds were chosen (5, 120, and 950 mm/min) by use of the crosshead control. An initial draw speed of 5 mm/min was employed for PPNCs samples until the desired draw ratio was being draw ($\lambda=2$). The highly deformed material was then regripped, and the desired draw velocity set. The draw load rose to maximum, and then fell to a steady value. Drawing then continued at the set draw speed and at a steady load, until terminated.

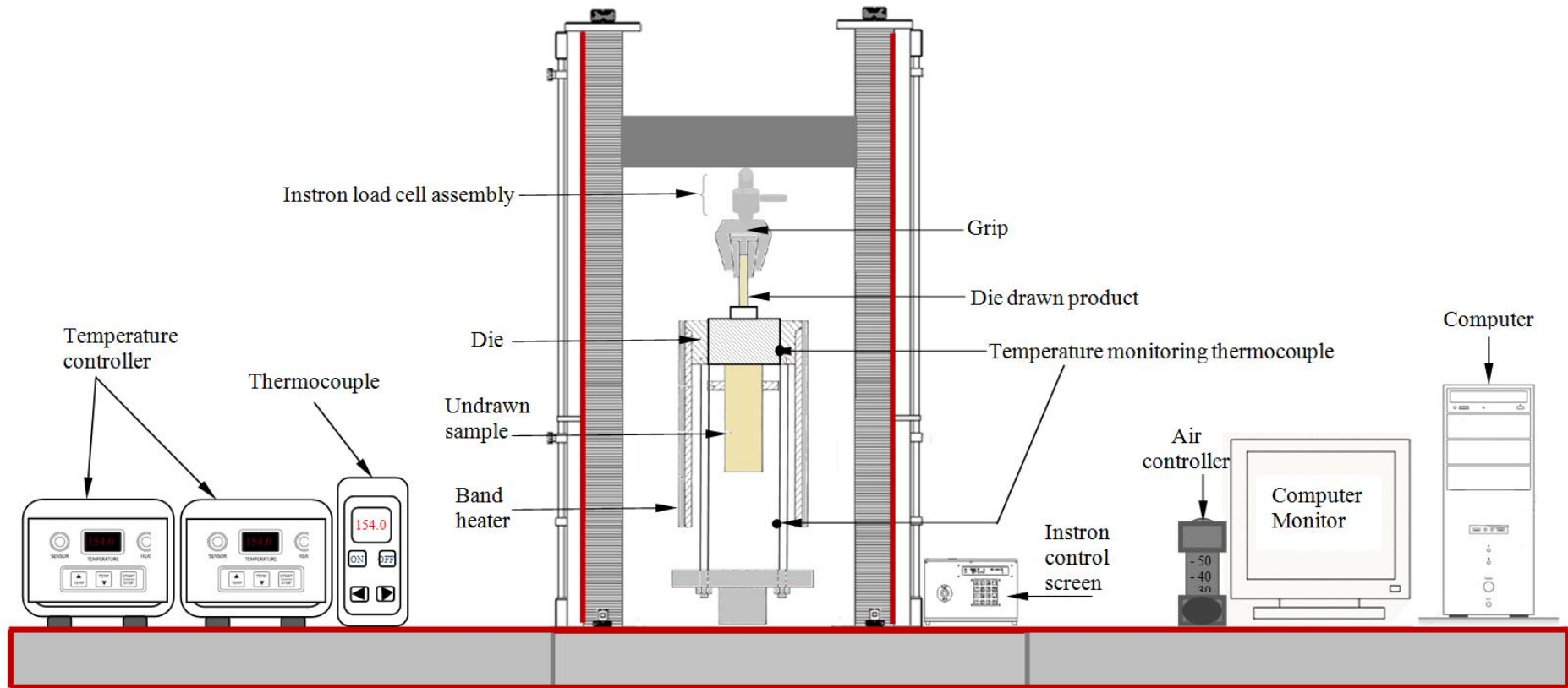


Figure 4.19: Schematic diagram of die drawing process

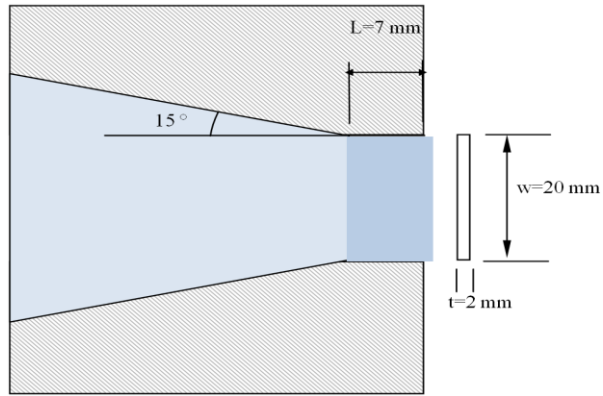


Figure 4.20: A schema diagram of constant width small reg



Figure 4.21: Constant width small reg die photos

In order to achieve the desired sample draw ratios, it was appropriate to increase the draw speed several times. Following an increase in drawing speed; a corresponding increase in draw ratios are shown in Figure 4.22. This increment slows down after 150 mm/min, where the PP molecules are slow in respond to the drawing process.

Tables 4.6, 4.7 and 4.8 show the average produced thicknesses, widths and lengths of drawn PPNCs at different draw ratios. Similarities in the obtained thickness and width between the different samples at same draw ratio are observed. As the draw ratio increases from 2 to 3 and from 3 to 4, a corresponding decrease in thickness and width of 15% are obtained. Sample photos of the three obtained draw ratios ($\lambda = 2, 3$ and 4) are shown in Figure 4.23.

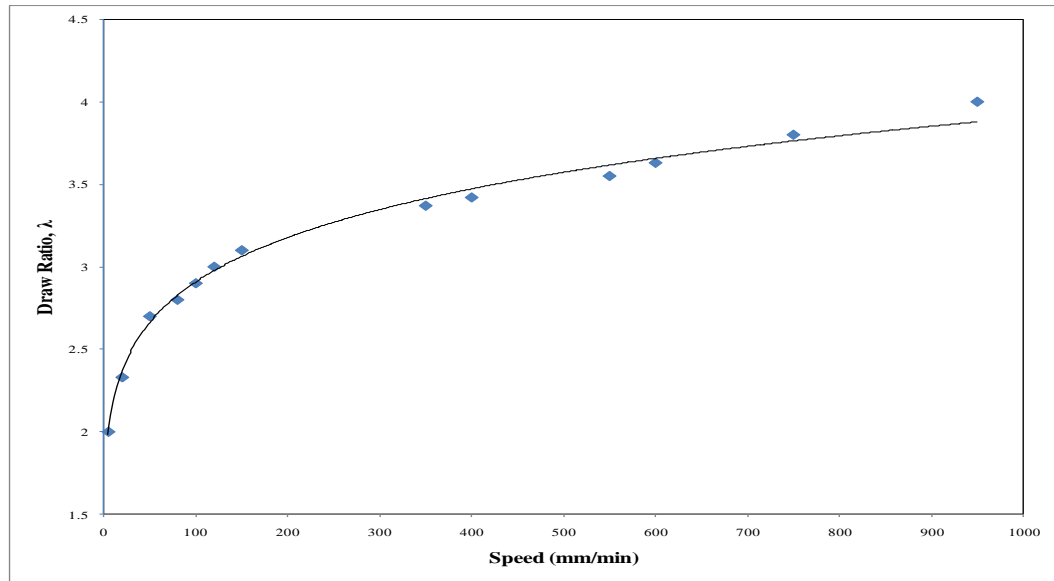


Figure 4.22: Attainable draw ratios at different haul-off speeds

Table 4.6: Drawn samples dimensions ($\lambda=2$)

Sample Identification	Thickness mm	Width mm	Length mm
Pure PP	1.90	9.83	200.8
PP + 3% Clay	1.90	10.00	200.8
PP + 5% Clay	1.89	10.03	200.3
PP + 3% Clay + 3% PPMA	1.88	10.06	204.3
PP + 3% Clay(MB) +3% PPMA(MB)	1.88	9.95	204.8
PP + 5% Clay + 3% PPMA	1.86	9.97	204.2
PP + 5% Clay + 6% PPMA	1.87	9.96	204.5

Table 4.7: Drawn samples dimensions ($\lambda=3$)

Sample Identification	Thickness mm	Width mm	Length mm
Pure PP	1.64	8.26	290.9
PP + 3% Clay	1.62	8.49	286.6
PP + 5% Clay	1.65	8.92	280.2
PP + 3% Clay + 3% PPMA	1.57	8.63	289.9
PP +3% Clay(MB) +3% PPMA(MB)	1.58	8.56	289.0
PP + 5% Clay 15A + 3% PPMA	1.53	8.58	288.6
PP + 5% Clay + 6% PPMA	1.57	8.74	289.9

Table 4.8: Drawn samples dimensions ($\lambda=4$)

Sample Identification	Thickness mm	Width mm	Length mm
Pure PP	1.39	7.22	380.9
PP + 3% Clay	1.37	7.44	374.4
PP + 5% Clay	1.36	7.51	372.6
PP + 3% Clay + 3% PPMA	1.35	7.48	387.5
PP +3% Clay(MB) +3% PPMA(MB)	1.35	7.42	381.7
PP + 5% Clay + 3% PPMA	1.34	7.36	380.5
PP + 5% Clay + 6% PPMA	1.34	7.50	378.1

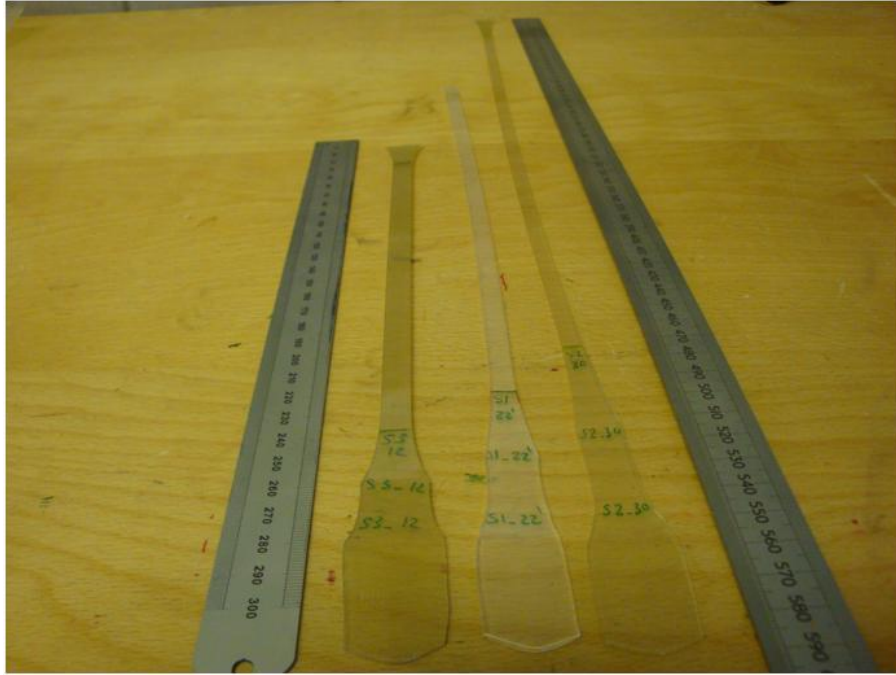


Figure 4.23: Different obtained drawn samples from the drawing process ($\lambda=2, 3$ and 4)

4.5 Characterization of Polypropylene Nanocomposite

4.5.1 Differential scanning calorimetry (DSC)

In the present work, DSC was principally used to estimate the percentage of crystalline phase, evaluated as a ratio between the latent heat of fusion of the PPNC and the theoretical heat of fusion of a 100% crystalline PP (as shown in the below equation), namely 207.1 J/g.

$$x = \frac{\Delta H_m}{f_p \Delta H_f} \times 100$$

where ΔH_m (J/g) is the enthalpy of melting of the polymer matrix, f_p is the PP weight fraction in the sample and ΔH_f is the enthalpy of melting of pure crystalline PP (207.1 J/g) [23].

DSC tests were carried out with a DSC Q2000 (Figure 4.24) from TA Instruments in order to study the crystallinity and the possible nucleating effect of PPNCs.

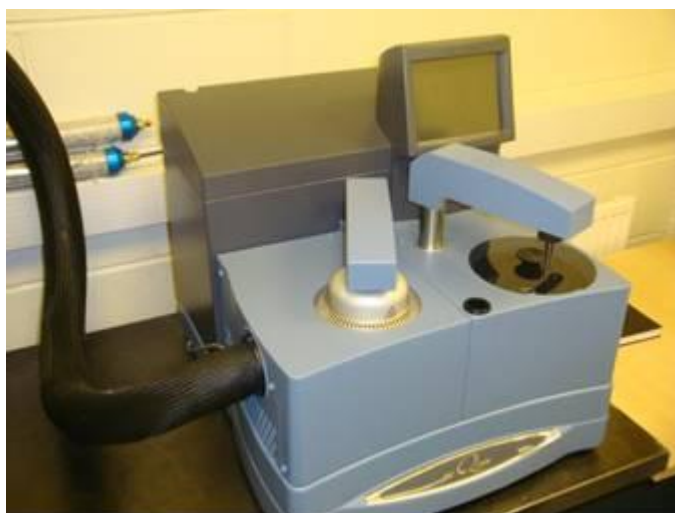


Figure 4.24: Differential scanning calorimetry equipment

The data were plotted using the thermal Advantages software in a 'heat flow/temperature' curve and a further elaboration of the curves made it possible to calculate temperatures and heats of fusion and crystallization as well as onset temperatures of changing state.

A small piece of the material to be tested was weighted with a high precision balance (one thousand of a milligram), placed in an aluminium pan and then covered with an aluminium lid. As reference an empty and plug aluminium pan was used.

The sample was placed in the heating cell under nitrogen flow (30 ml/min) to avoid unwanted oxidation. A cooler working with compressed nitrogen (150 ml/min) was used to control temperature in the cooling stage.

The software allowed choice of different testing methods by setting initial and final temperature as well as heating and cooling rate. In the analysis an equilibration was achieved at 30 °C, followed by a ramp of 10°C/min heating rate from 30°C to 220°C. Thermal stabilization for 3 minutes was used in order to erase the previous thermomechanical history and finally a cooling step from 220°C to 30 °C. A low temperature was chosen (-40°C) to evaluate the glass

transition temperature. However, after some trials, when the impossibility of estimating it by DSC was clear, the cycle was started from 30°C instead of -40°C.

4.5.2 Thermal gravimetric analysis (TGA)

Thermogravimetric analysis (TGA) is commonly used to investigate the thermal stability and possibility of degradation process of the polymer matrix. The volatile materials weigh losses are plotted as a function of temperature. The used inert gas heats the sample and causes the nonoxidative degradation, while the oxidative degradation occurs from the air or oxygen.

Figure 4.25 shows the used thermal gravimetric analyzer (TGA, TA Q5000), which evaluates the different PPNC samples. The chamber was flushed with nitrogen. The scan of temperature covers a range up to 600 °C, and the used heating rate is 10 °C/min.



Figure 4.25: Thermal gravimetric analyzer

4.5.3 Polarizing optical microscopy

The evolution of spherulitic structure of PP and PPNC pellets produced from the mixing, which was done by the twin screw extruder and then by

injection moulding, was examined by hot stage optical microscopy (Leica DMRXP research optical microscope fitted with Linkam THMS600 heating stage) with Leica DC300 digital camera. Figure 4.26 shows the microscope that was used in our analysis.

Thin slices of thickness ~ 2 mm were cut from the samples by a Reichert Jung Ultracut microtome using a stainless steel blade. The samples were immersed in liquid nitrogen prior to cut and were sliced at once after taking out of liquid nitrogen bath. The 2 mm x 2 mm sliced samples were placed on 16 mm diameter round glass slides. The samples were covered with similar cover slips and heated in a hot stage optical polarizing microscope (HS-OPM) to a temperature of 200 °C at a heating rate of 20 °C/min. The samples were annealed for 3 min. and cooled to 135 °C at 10 °C/min. The sample was again annealed for 2 min and then cooled to room temperature at 10 °C/min. The examination was performed under a dynamic flow of argon. The images were recorded at a magnification of 100x using polarizing light modes at different temperatures.

The summary of observations is shown in results and discussions chapter. The scale micrometer image at 100x is shown in Figure 4.27. All sample started to melt at temperatures of 160-165 °C. The majority of samples showed poor flow properties resulting in partial adherence of liquid polymer to the cover slips. These samples were also heated to 250 °C but similar flow behaviour was observed.



Figure 4.26: Hot-stage polarizing optical microscope (Leica DMRXP)

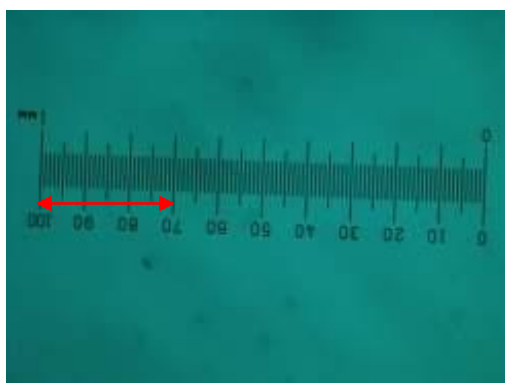


Figure 4.27: Image of calibration scale at 100x magnification used in the images

Trials were performed to collect images for oriented PPNC samples. A problem was faced when using heat to see the spherulitic structure of the oriented samples. We tried to not use heat to avoid destroying the molecular orientation of our samples. Therefore, we had to cut the samples at low temperature. But we could not observe any clear spherulitic structure for thin sample. A trial was done for relatively thick sample layers at room temperature and images are reported and discussed in chapter 5. Thin slices of thickness 20-50 μm were cut from the samples by Reichert-Jung Metacut microtome at room temperature. The obtained slices were placed on a normal glass slide. The slices were covered by 20 mm square cover slip. The slices were viewed using transmitted cross polarized light. The images were recorded at a magnification of 200 and 400x.

4.5.4 Wide-angle x-ray diffraction

Wide-angle x-ray diffraction (WAXD) was used for all our prepared PPNCs to characterize the degree of nanodispersion of MMT organoclay. WAXD measures the spacing distance in crystalline layers of such ordered clay structure. Bragg's law is used through the equation: $\sin\Theta = n\lambda_\ell/2d$ where d is the spacing between these ordered layers and λ_ℓ is the wavelength. The intensity of x-ray diffraction is given with scan of the diffracted angle (2Θ). There are no special requirements for sample preparation in WAXD.

Increase or decrease in d-spacing gives information about the formed PPNCs structure. As spacing increased, an intercalation system is obtained. Conversely, decrease of spacing is a sign of decomposition, while no changing in d-spacing indicates immiscibility between the polymer and clay particles. Absent of peak may be a sign of full exfoliation system.

An electromagnetic radiation is scattered from a regular array objects creating a diffraction pattern which produces constructive interference that can be detected at a detector as shown in Figure 4.28-a. Since the distance, travelled by the light after reflection, depends on the distance between the atoms the diffraction pattern can be used to determine the interatomic spacing as shown in Figure 4.28-b. XRD studies were done using a Panalytical X'Pert Pro X-Ray diffractometer that is shown in Figure 4.29 (C Cu $K\alpha$, $\lambda_\ell = 0.154$ nm). Instrument voltage setting was 40/40 KV/mA and beam size, on the sample, was fixed during entire scan at 3.00 mm. Data was collected by Panalytical X'celerator detector system.

As mentioned before that WAXD measures d-spacing, not overall clay dispersion in the sample. Transmission electron microscopy, described in the

following section, was combined with WAXD to provide a complete image on the distribution of clay in the PPNC samples.

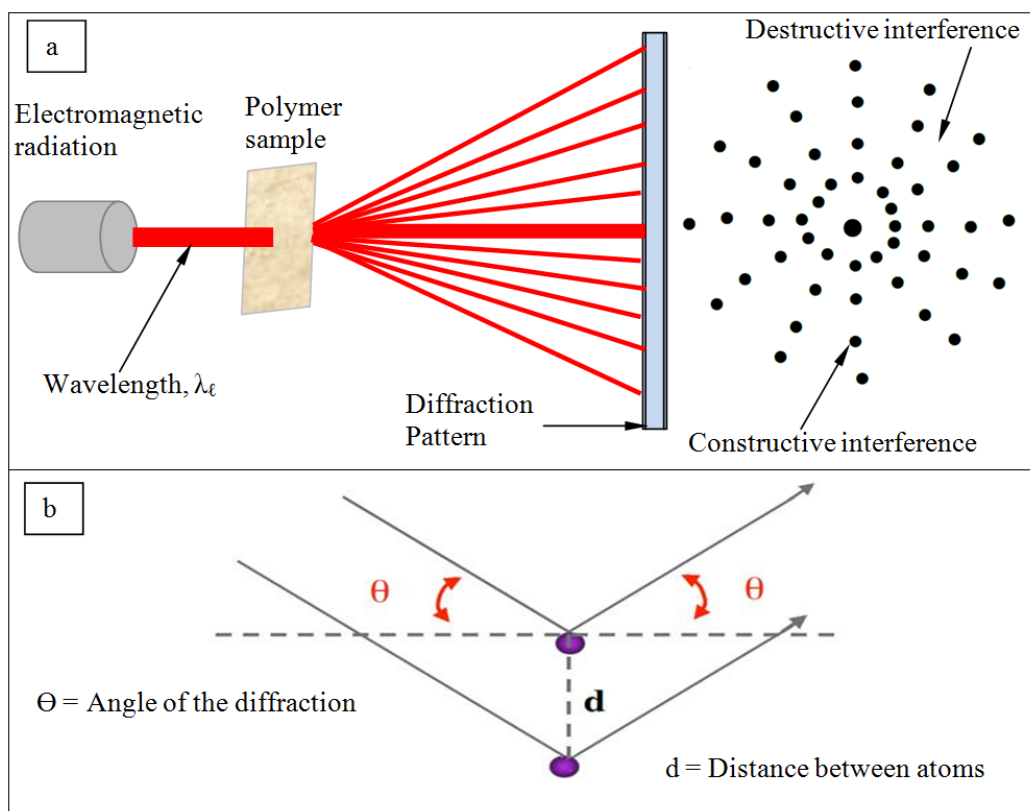


Figure 4.28: Schematic diagrams of WAXD principle

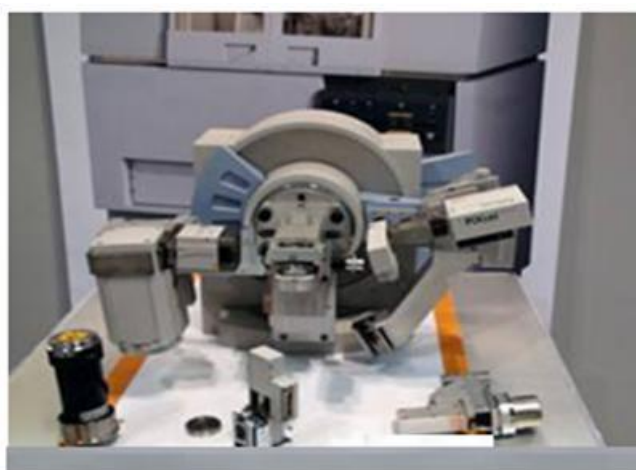


Figure 4.29: A photo of Panalytical X'Pert Pro X-Ray diffractometer

4.5.5 Transmission electron microscopy

The transmission electron microscopy consists of the following systems: illumination, lens, magnification and recording systems. A photo of the transmission electron microscopy used is shown in Figure 4.30. This FEI instrument is called Tecnai G2 model. The illumination system uses a field emission source, which gives a high microanalysis resolution. It includes a condenser lens that provides a very sensitive electron probe. The specimen is then located in its position. Objective lenses are then determining the resolution limit of the TEM images. Mediate and projected lenses are presented in the magnification system and send the data to a digital recording system. A schematic diagram of TEM is shown in Figure 4.31.

A small part of the sample was cut from the middle core and blocked using scalpel. The final microtomy was carried out on a Leica microtome (Figure 4.32) at -60°C . Leica microtome includes a disposable blade holder, X/Y orienting adapter piece, and universal quick release clamp.



Figure 4.30: Transmission electron microscopy apparatus

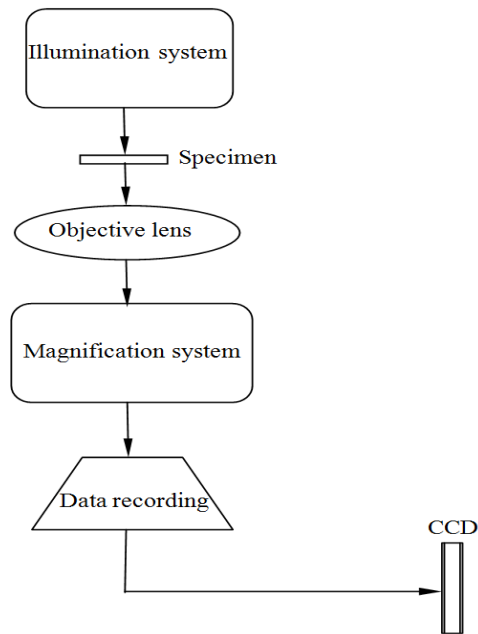


Figure 4.31: Schematic structure of transmission electron microscopy



Figure 4.32: Leica microtome

In each of the TEM images, there is a scale with the measurement value in microns ($1000\text{nm} = 1\text{micron}$). This does change with every magnification. In any measurement made on any image, the scale will be corresponding to that shown in the respective micrograph.

The parameter that was measured using the image analysis tool is the feret's diameter (FD), which was suggested by Walton [137] to measure the size of irregularly shaped particles. In non-spherical particles, this is equivalent to the longest dimension of the particle. In lamellar particles, like tactoid structure of

clay, this is more or less equivalent to the length of the clay particles. The unit of diameter is microns. The feret diameter was measured as shown in Figure 4.33. For a single layer of clay or for many layers as in tactoid structure, several measurements were taken and the maximum length is considered to be the feret diameter. The image analysis also includes an average number of particles per image. All analyses were done by using images at a magnification of 59kX; image area being $\sim 1.5 \mu\text{m} \times 1.5 \mu\text{m}$. Total of six images have been looked at for each sample with minimum of 100 particles studied. These six images were taken randomly and then one image is selected and presented in the next chapter.

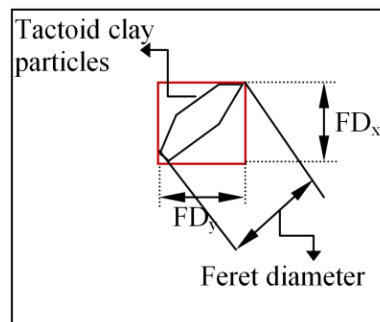


Figure 4.33: Feret diameter

4.5.6 Video extensometer test

A measurement of Young's modulus were done by using Messphysik 20-10 tensile machine and a video extensometer, where a video-camera is focussed on the specimen upon which contrasting target marks have been made and the resulting image is analysed by a PC based video program. The software continuously ensures that load and displacement between targets are measured during testing. A program was made using very small strain rate to guarantee that the modulus measurement is based on stress-strain data in elastic zone. The program was set to perform three strain rates per each sample and two measurements for each loop as shown in Figure 4.34 for one loop. The full program commands used in this measurement are given in Appendix D. Areas of

different samples were considered to obtain the linear relation of stress-strain in the elastic zone and modulus was measured based on slope measurement with a confidence interval.

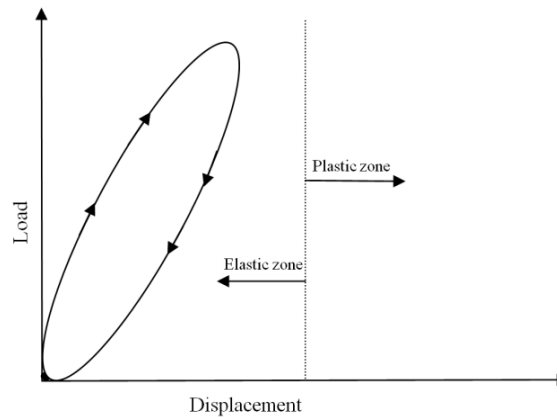


Figure 4.34: Loop of the modulus measurement program of video-extensometer experiment

This measurement were done for different PPNCs sheets produced by compression moulding, tensile bar produced by injection moulding and different drawn samples of the tensile bar (Figure 4.35). An average of at least 6 specimens for each sample was tested. One graph for each sample is presented in Appendix G. Different strain rates were calculated for different samples based on specimen gage length to validate the final result comparisons between different samples. Table 4.9 provides all used speeds to maintain same strain rates of 0.0053, 0.0105, and 0.0158 (1/min) for different samples geometry that are summarized in Table 4.10. A schematic diagram and a photo for this experiment are shown in Figure 4.36 and 4.37.

Table 4.9: Strain Rates Used in Video Extensometer Experiment

Sample Identification	Strain rate 1 (0.0053 1/min) mm/min	Strain rate 2 (0.0105 1/min) mm/min	Strain rate 3 (0.0158 1/min) mm/min
Compression moulded samples (gage length = 38 mm)	0.200	0.400	0.600
Injection moulded samples (gage length = 87 mm)	0.458	0.916	1.374
Drawn samples (gage length = 34 mm)	0.179	0.358	0.537

Table 4.10: Different Sample Geometries of Tensile Video Extensometer Test of Undrawn and Drawn PPNCs

Geometry	Compression moulded samples	Injection moulded samples	Drawn samples $\lambda=2$	Drawn samples $\lambda=3$	Drawn samples $\lambda=4$
Width	6.13	10.0	10.0	8.6	7.4
Thickness	0.80	4.0	2.0	1.60	1.36
Gage length	38.0	87.0	34.0	34.0	34.0

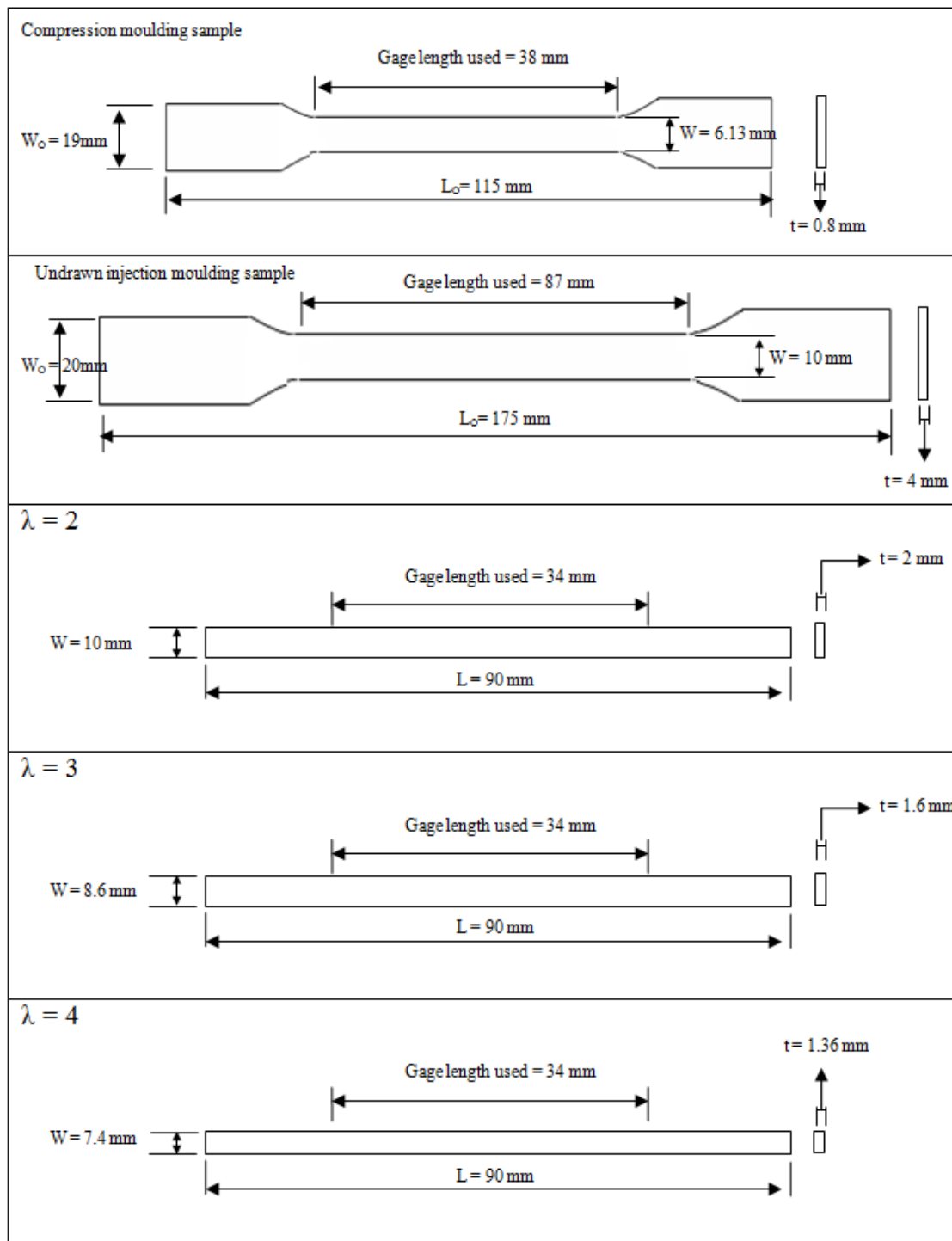


Figure 4.35: Dimensions of undrawn and drawn samples prepared for tensile video-extensometer test

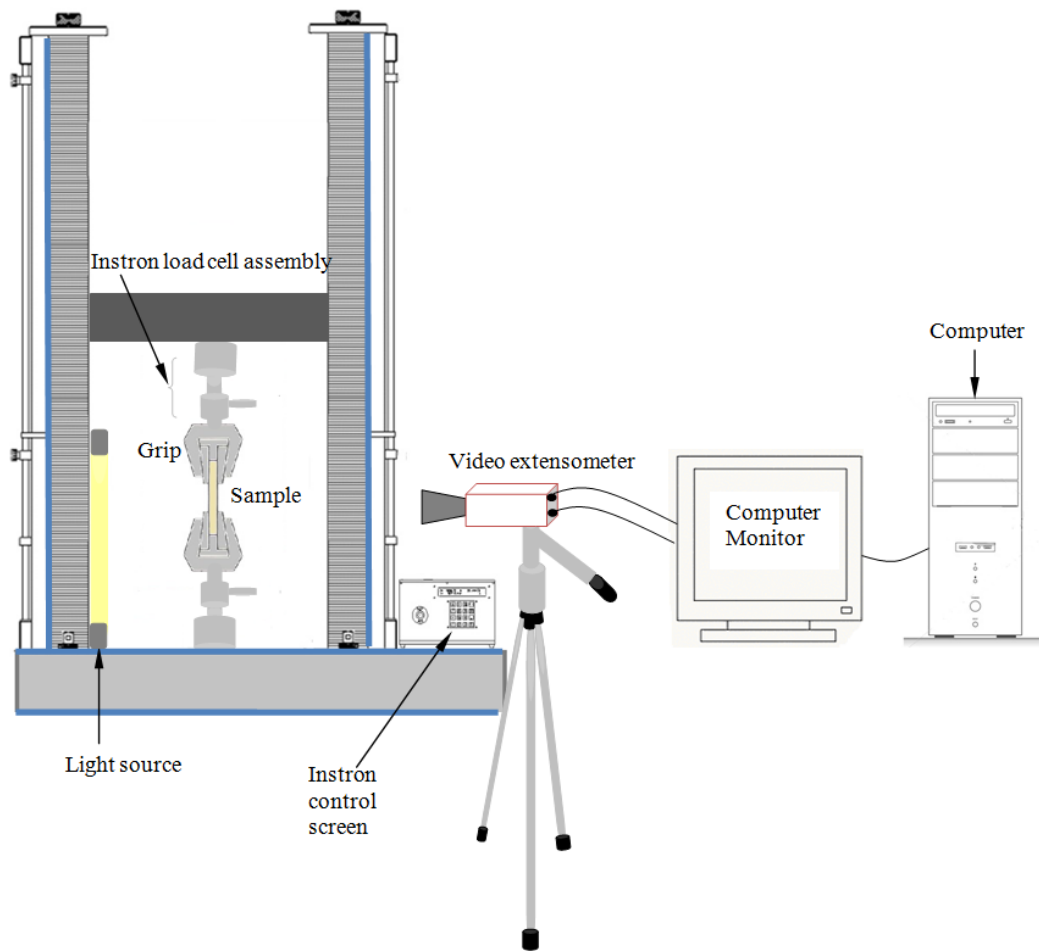


Figure 4.36: Video extensometer tensile test



Figure 4.37: Video extensometer test

4.5.7 Fracture toughness test

The fracture toughness measurement is performed by measuring load-displacement curve of double notch specimens for different PPNC samples. The required energy (total work of fracture) to develop and crack the sample is calculated from the area under the load-displacement curve. In this experiment, only the total work of fracture is considered without differentiation between the EWF and non-EWF.

All samples were tested until final fracture at crosshead speed 5 mm/min using the Instron 5564 testing machine at room temperature. An average of at least 4 specimens for each sample was tested. The load-displacement curves were recorded and the area under the curve was integrated by Matlab program to obtain the energy absorbed during the fracture process. All stress- strain graphs are given in Appendix G. A Sony digital video camera (6.1 mega pixels) works together with an Electrophysics thermal camera model PV320-L2E to study PPNCs fracture behaviour and distinguishing between crack initiation, propagation and fracture stages of drawn and undrawn samples. A schema and a photo of the fracture test are shown in Figure 4.38 and 4.39.

Double edge-notched tension (DENT) of undrawn tensile bar specimens, produced by injection moulding, with a width of 10 mm and thickness of 4 mm were subjected to Bridgeport vertical milling machine to prepare skin and core samples with width of 10 mm and thickness of 2 mm. For the purpose of comparison of the drawn samples to the isotropic samples, the notch depths were taken in relative to width of isotropic tensile bar samples.

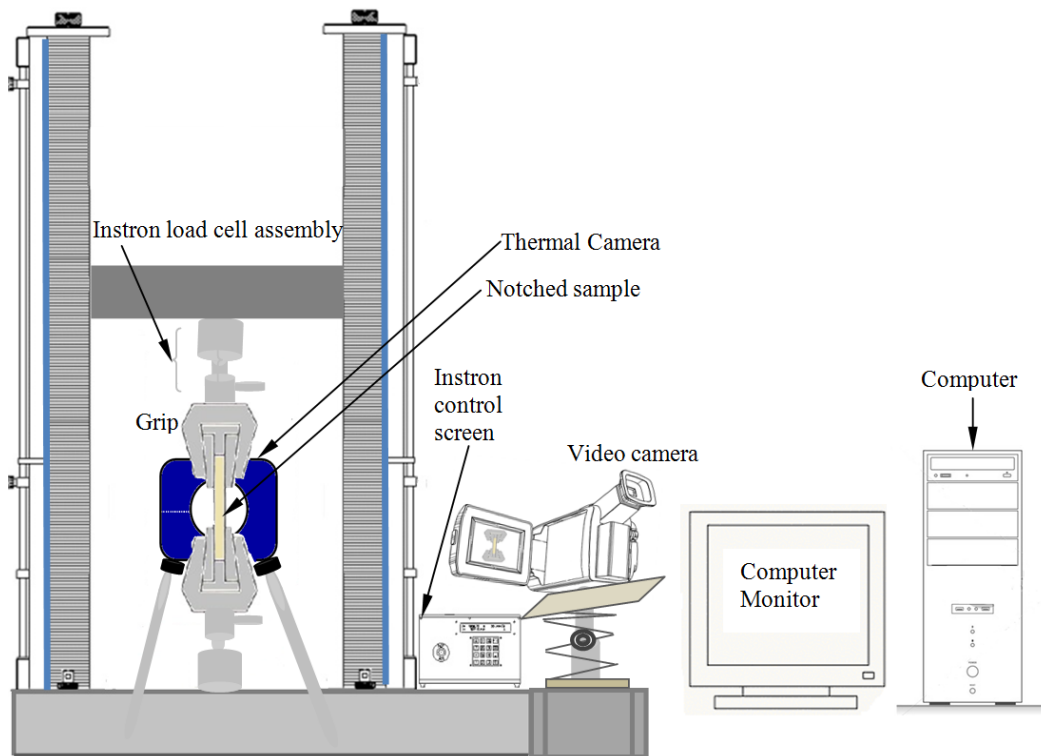


Figure 4.38: A schema of the tensile fracture test



Figure 4.39: A photo of tensile fracture test

Table 4.11 gives the different samples notch depths. Figure 4.40 illustrates the dimensions of all drawn and undrawn samples prepared to be used in tensile fracture test. The notch lengths of drawn samples, described in 4.4.4, were dimensioned by Keeton cutter shown in Figure 4.41.

Table 4.11: Different Sample geometries of Fracture Test of Isotropic and Oriented PPNCs

Geometry	Isotropic samples	Drawn samples $\lambda=2$	Drawn samples $\lambda=3$	Drawn samples $\lambda=4$
Width, mm	10.0	10.0	8.6	7.4
Thickness, mm	4.0	2.0	1.60	1.36
Gage length, mm	70.0	40.0	40.0	40.0
Notch depth, mm	1.5/2.0/2.5	1.5/2.0/2.5	1.29/1.72/2.15	1.11/1.48/1.85

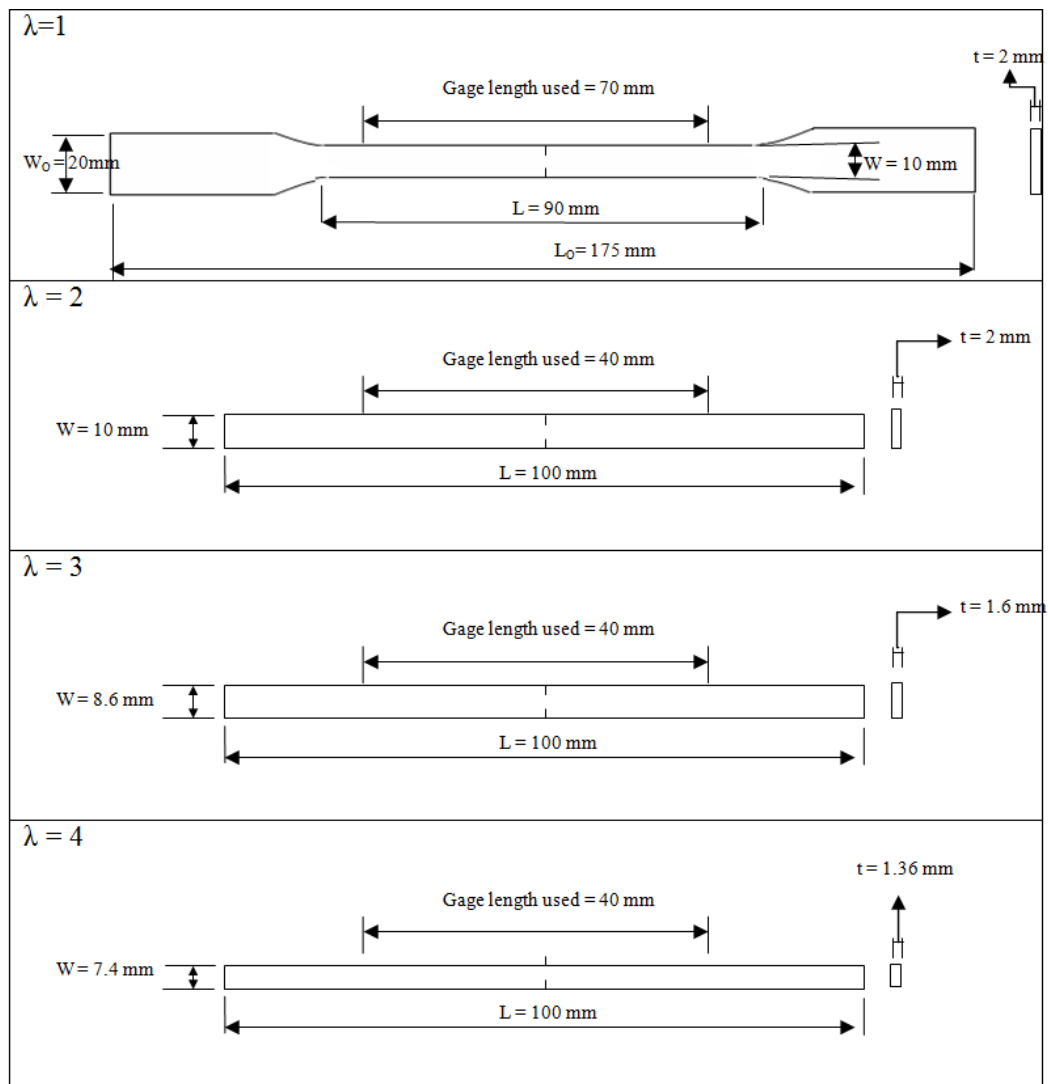


Figure 4.40: Dimensions of undrawn and drawn samples prepared for tensile fracture test



Figure 4.41: Keeton cutter machine used to dimension the length of the drawn samples

All double-notch of undrawn and drawn specimens were carefully machined by Perfecto sharper- cut machine number 1476/4 (Figure 4.42) to ensure parallelism and symmetry. This type of Perfecto sharper moves up/down, forward/backward and right/left, adjusting the knife holder. A sharp knife then is controlled precisely by an indicator to make the notches exactly in the middle of the samples.

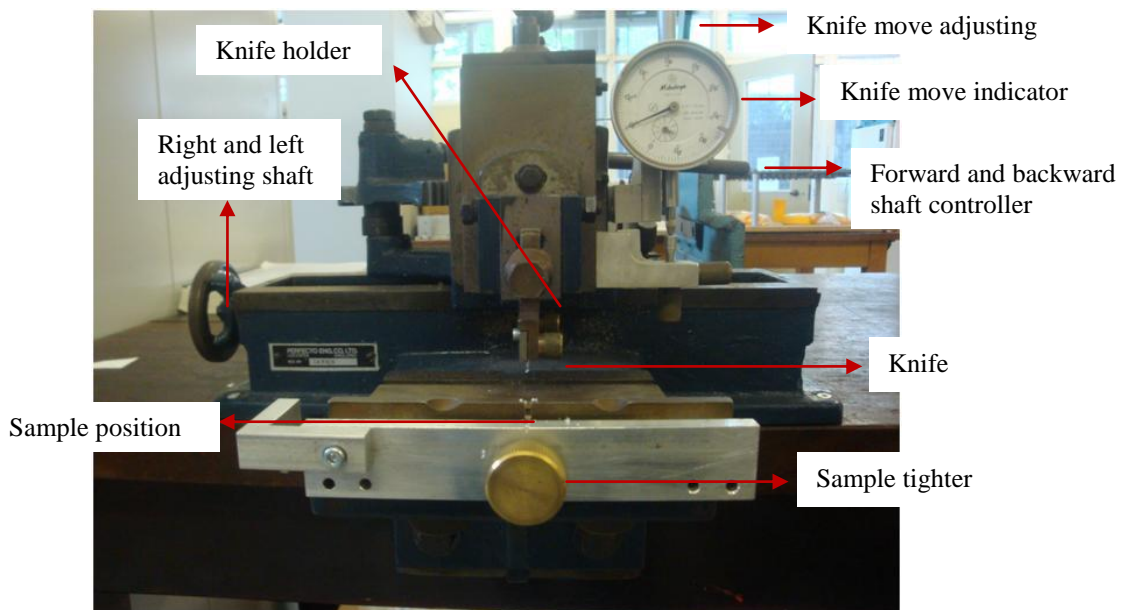


Figure 4.42: Perfecto sharper- cut machine

5 Results and Discussion

5.1 Introduction

In this chapter, the results of mechanical and characterization of the sheets received from Queen's University Belfast and different characterization results for our own compounded samples are presented and discussed.

The characterization results for the produced compounding in our laboratory include (a) the crystallization morphology obtained by POM and analyses of the result images (b) the dispersion of clay in the nanocomposites by WAXD, (c) the TEM micrographs of different PPNCs with full analyses of the obtained images, (d) the modulus measurement by video extensometer, and (e) tensile fracture results by mean of total work of fracture obtained from load-displacement graphs. It was attempted to explain the mechanical properties on the basis of the clay dispersion and morphology of the nanocomposites.

The samples extruded in Queen's University Belfast include:

Sample 1 = Pure Polypropylene, PPH 5042

Sample 2 = Polypropylene + 3% Cloisite 15A

Sample 3 = Polypropylene + 5% Cloisite 15A

Sample 4 = Polypropylene + 3% Somasif MTE

Sample 5 = Polypropylene + 3% Somasif MTE

The different samples produced by compounding at Bradford using the twin screw extruder are summarized below. These samples include:

Sample 6 = Pure Polypropylene (PPH 5060)

Sample 7 = Polypropylene + 3% Cloisite 15A

Sample 8 = Polypropylene + 5% Cloisite 15A

Sample 9 = Polypropylene + 3% maleic anhydride modified PP

Sample 10 = Polypropylene + 6% maleic anhydride modified PP

Sample 11 = Polypropylene + 9% maleic anhydride modified PP

Sample 12 = Polypropylene + 3% PPMA + 3% Cloisite 15A

Sample 13 = Polypropylene + 3% PPMA + 5% Cloisite 15A

Sample 14 = Polypropylene + 6% PPMA + 3% Cloisite 15A

Sample 15 = Polypropylene + 6% PPMA + 5% Cloisite 15A

Sample 16 = Polypropylene + 9% PPMA + 3% Cloisite 15A

Sample 17 = Polypropylene + 9% PPMA + 5% Cloisite 15A

Sample 18 = Polypropylene first recycle, PP R1

Sample 19 = Polypropylene second recycle, PP R2

Sample 20 = Polypropylene third recycle, PP R3

The following samples were prepared and evaluated by simple mixing process, i.e. mixing the PP material/ PPMA and clay manually in bags using the raw materials and the master batches as well. This way of pre-mixing is suggested because many previous works use this type of pre-mixing preparation to produce polymer nanocomposites; even it was introduced later to extrusion or injection moulding. The results will be compared to the samples that were prepared by twin screw extruder. These samples include:

Sample 21 = Polypropylene + 3% pure PPMA + 3% pure Cloisite 15A

Sample 22 = Polypropylene + 3% PPMA (PP/PPMA (80/20) master batch) + 3% Cloisite 15A (PP/Clay (80/20) master batch)

5.2 Twin Screw Extruder Compounding Samples

5.2.1 Crystallization results

In order to have a qualitative outlook of the PPNCs thermal behaviour, DSC analysis was performed on specimens of different prepared compounding samples in our laboratory. The first measurements were carried out on specimens prepared with PP and PPMA without clay. The result showed in Figure 5.1 demonstrates that PPMA does not significantly affect the crystallinity of PP for loading percentage less than 6%. However, a 6 % decrement of crystallinity is noticeable for 9% PPMA sample. On the contrary, when the clay is added to PP without PPMA, a similarity in crystallinity is detectable (precisely 5 % of clay in pure PP causes a loss in crystalline phase of only 1 %). This loss is reduced to nothing when loading decreases to 3%. This behaviour is shown in Figure 5.2.

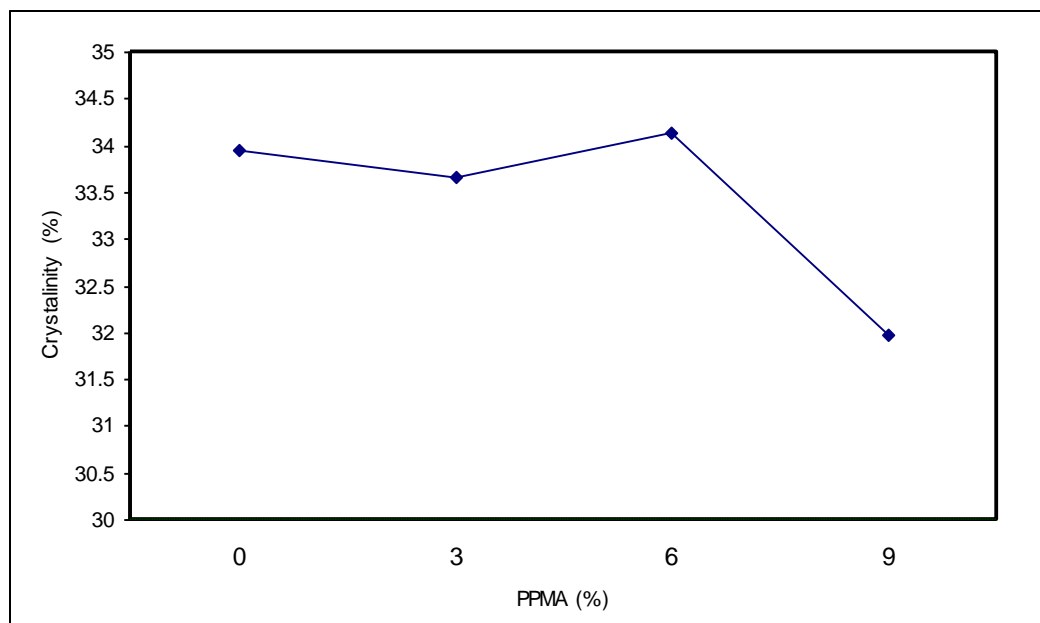


Figure 5.1: PPMA content effect on crystallization of PPNCs without clay

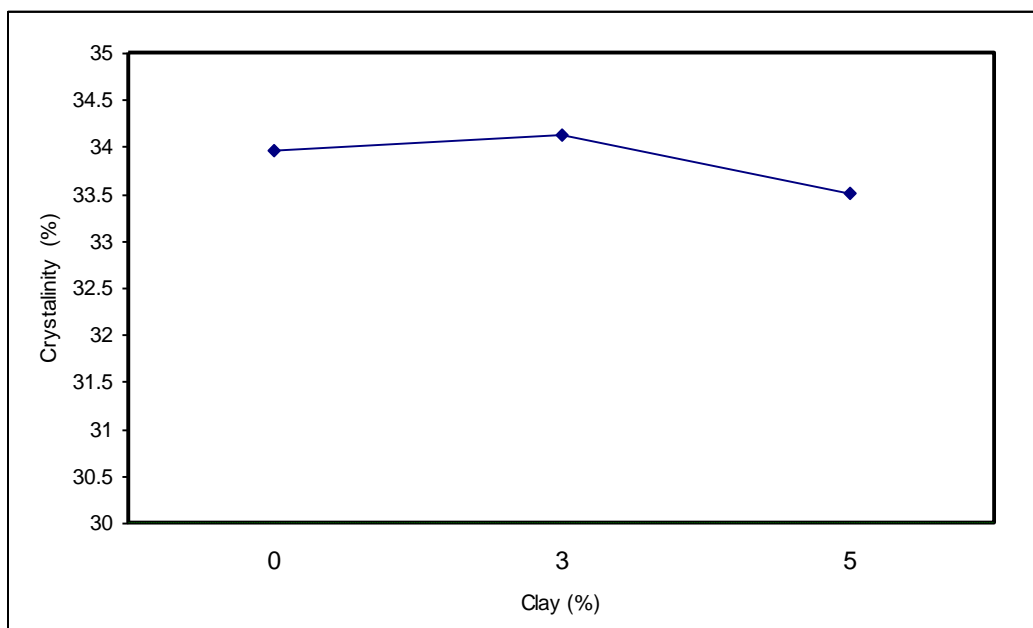


Figure 5.2: Clay content effect on crystallization of PPNCs without PPMA

When the clay effect on the crystallinity of PPNCs is evaluated in presence of PPMA, it is possible to identify a trend according to which the crystallinity increases as the clay content increases in case of 3% PPMA loading. This trend is not clear when 6 and 9 % of PPMA are involved. Figures 5.3 depict the results of DSC analysis on specimens in which the PP/PPMA loading level was kept constant at 3, 6 and 9%, and the clay content increased. In contrast, Figure 5.4 shows specimens in which the clay loading level was kept constant at 3 and 5% loading, and the PPMA content increased. At 3 % clay, higher crystallinity is reported for all samples within 6% PPMA or less. However, the same results could not be concluded at 5 % clay loading.

The study of crystallization temperature of the PPNCs showed another angle of crystallinity. PP/PPMA, PP/clay, and the hybrid PPNCs final material do increase the crystallization temperature with a percentage between 3.5 and 6 % (Figure 5.5 and 5.6). This behaviour can be explained by the nucleating effect

of dispersed platelets of clay. PPMA promotes the separation of layers increasing the number of potential crystallization nuclei.

This idea is supported by the observed variation in T_c onset. This is the starting temperature of the crystallization process for a melted material and a higher T_c onset indicates an easiest crystallization, namely a faster nucleation process.

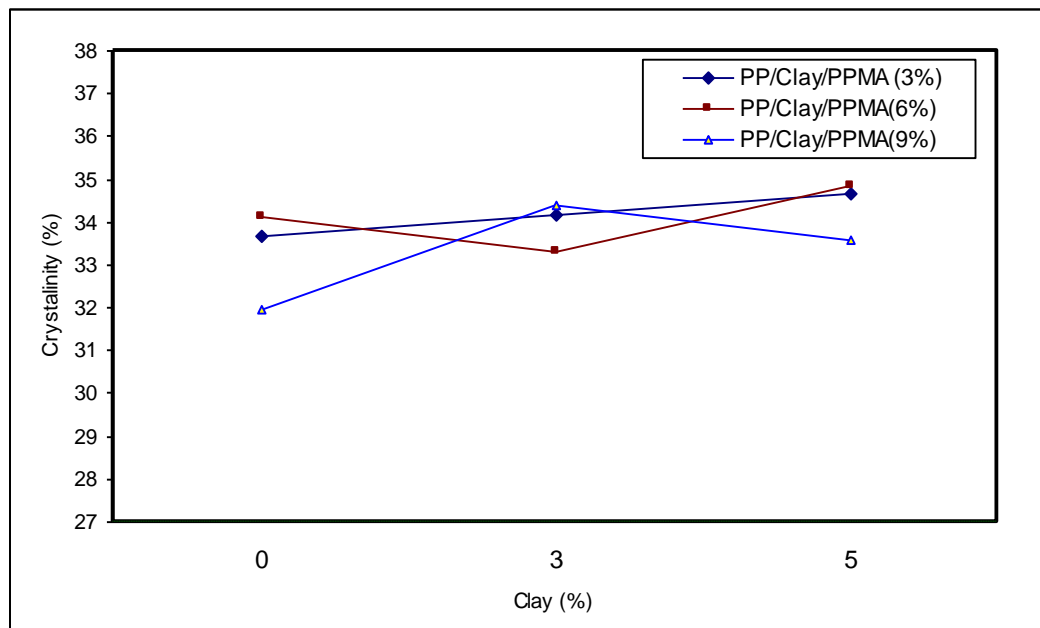


Figure 5.3: Clay content effect on crystallization of PPNCs at constant PPMA loading level

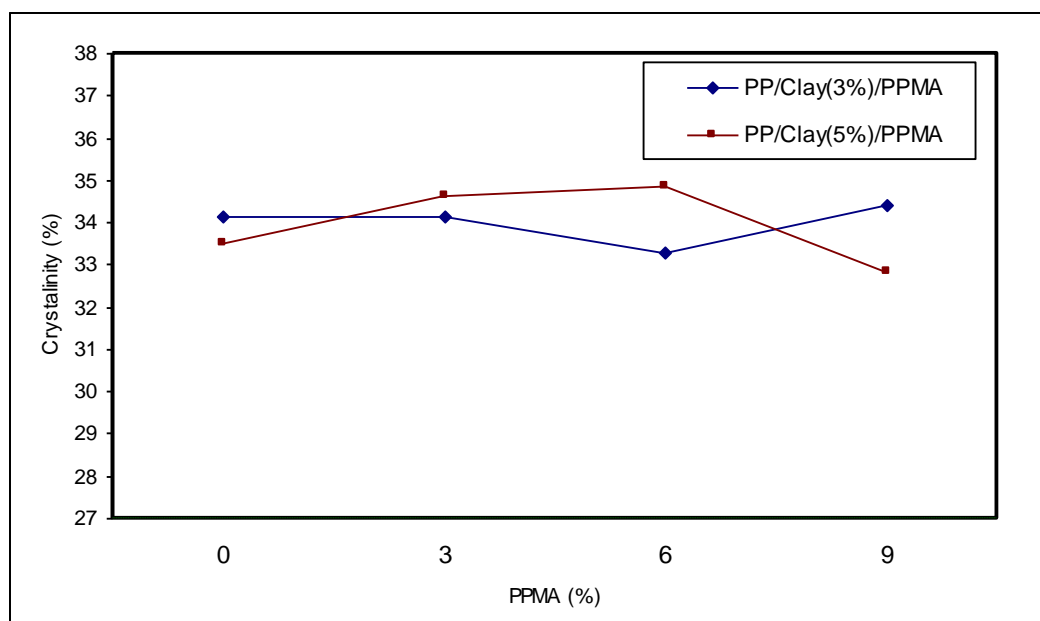


Figure 5.4: PPMA content effect on crystallization of PPNCs at constant clay loading level

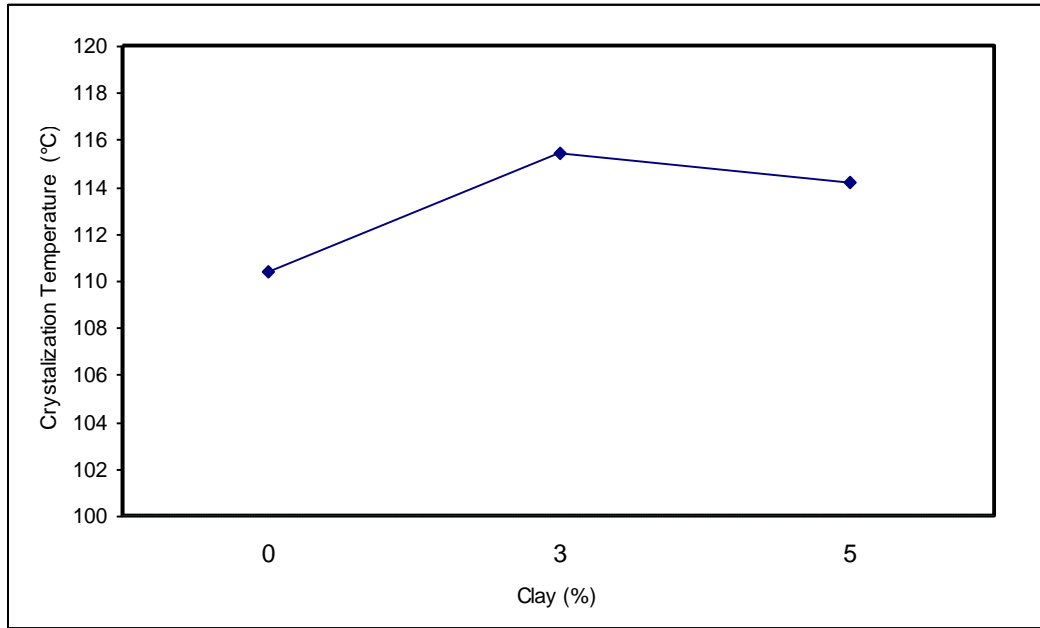


Figure 5.5: Clay content effect on nucleation of PPNCs without PPMA

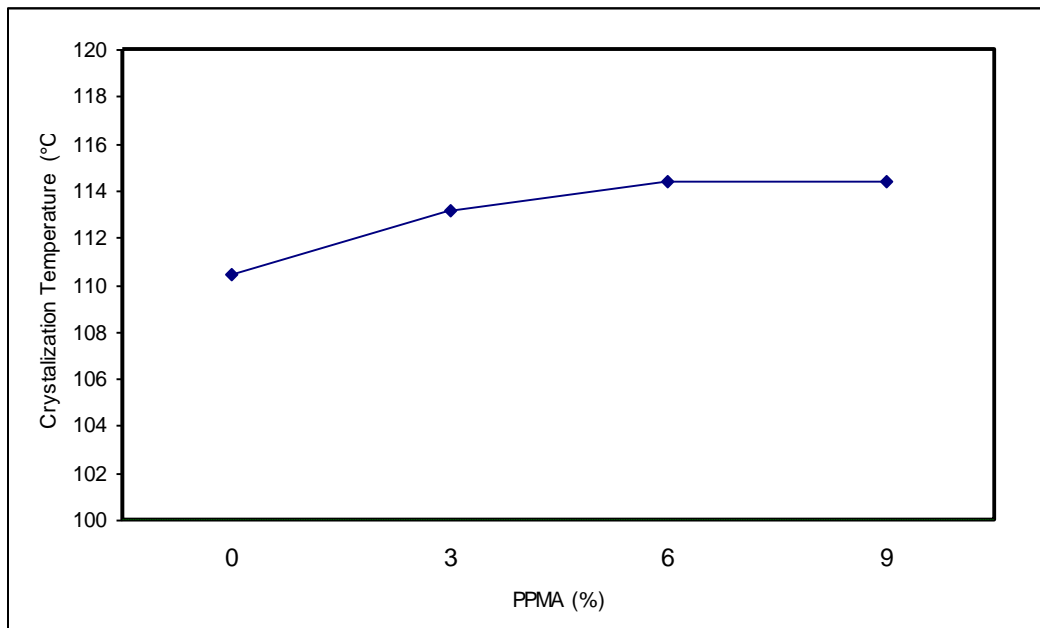


Figure 5.6: PPMA content effect on nucleation of PPNCs without clay

With the same criteria as crystallinity results, the magnification effect on T_c onset variation can be observed when the PP/PPMA loading level is kept constant at 3, 6 and 9 % and the clay content increased as in Figure 5.7 illustrates, or when PP/Clay loading level is kept constant for both 3 and 5% and PPMA content increased as in Figure 5.8 illustrates.

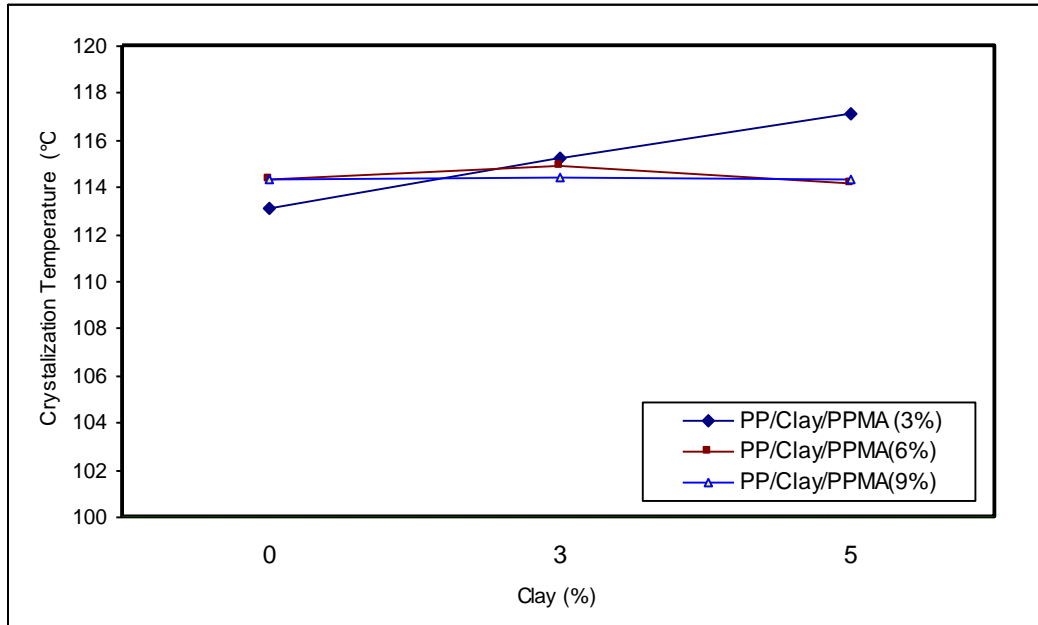


Figure 5.7: Clay content effect on nucleation of PPNCs at constant PPMA loading level

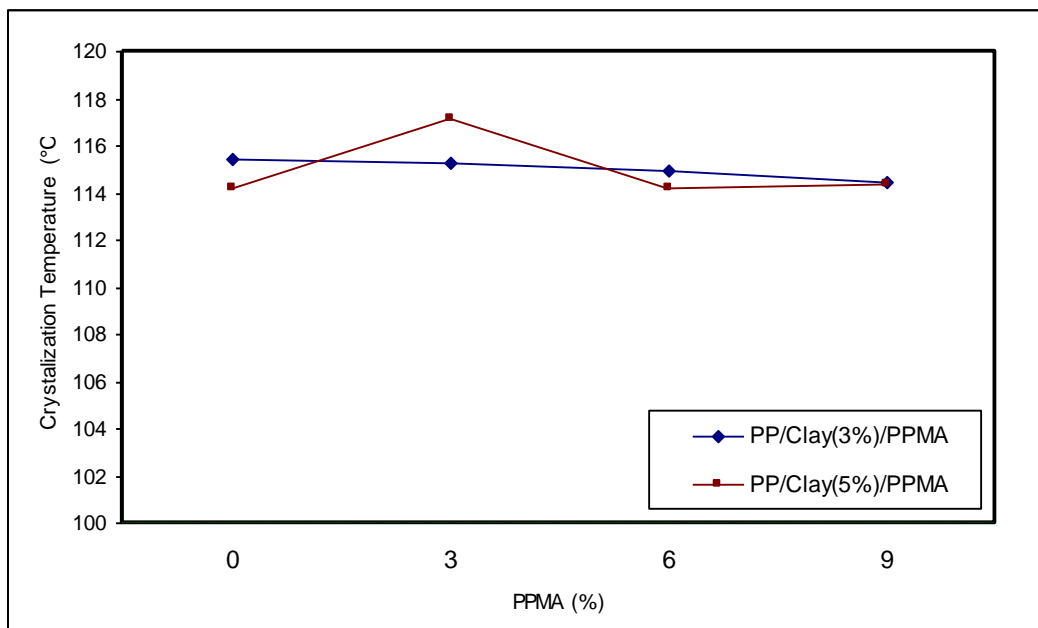


Figure 5.8: PPMA content effect on nucleation of PPNCs at constant clay loading level

Between the crystallinity, which is decreased up to 2 J/g maximum, and crystallization temperature, which is increased up to 7 °C maximum, for the PPNCs with 6 % PPMA or less and clay with 3 %; it is difficult to predict the mechanical properties of our samples and/or to consider these changes are appreciable to enhance or suffer the final PPNCs properties. In addition to this,

the melting point for all samples does not change from PP material, PP with clay, PP with PPMA, and for the hybrid PPNCs. This can be seen in Figures 5.9, 5.10, 5.11, and 5.12. For more understanding for this behaviour, an investigation on DSC for samples received from Queen's University Belfast could help to explain the results.

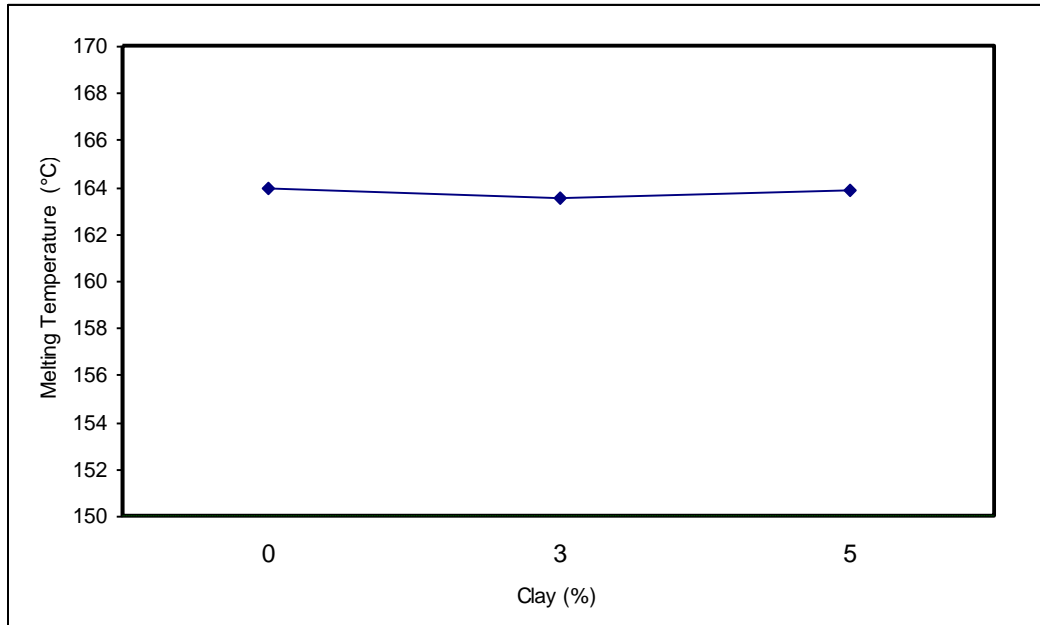


Figure 5.9: Clay content effect on melting temperature of PPNCs without PPMA

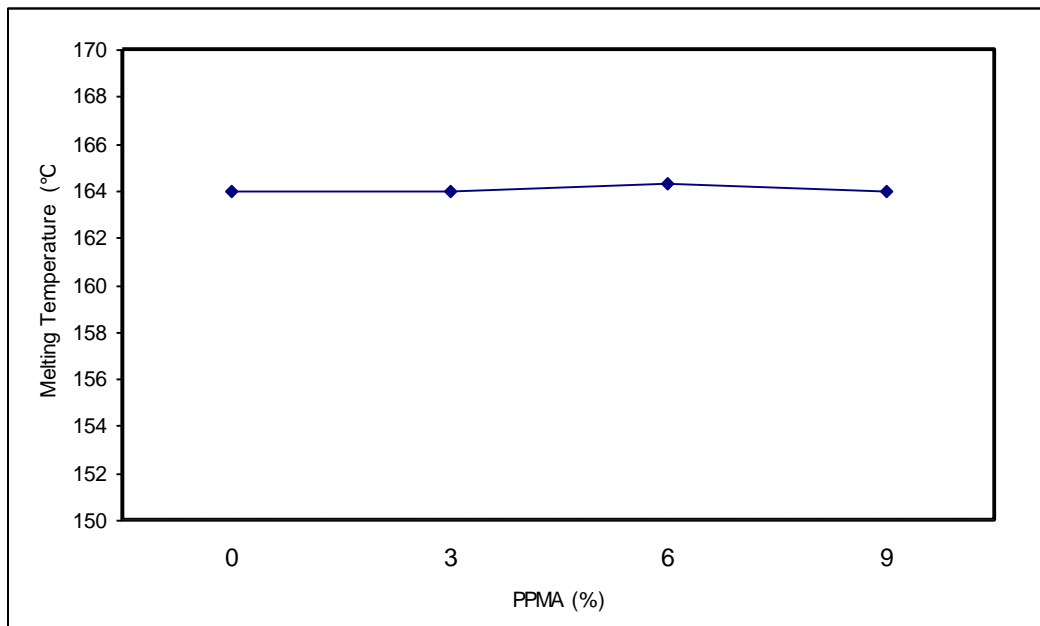


Figure 5.10: PPMA content effect on melting temperature of PPNCs without clay

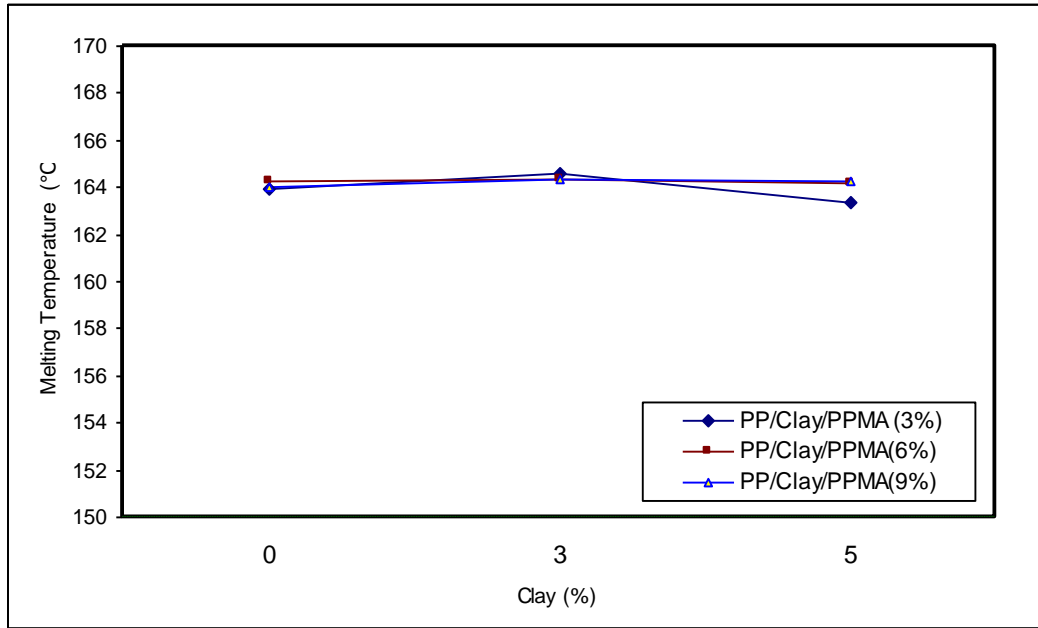


Figure 5.11: Clay content effect on melting temperature of PPNCs at constant PPMA loading level

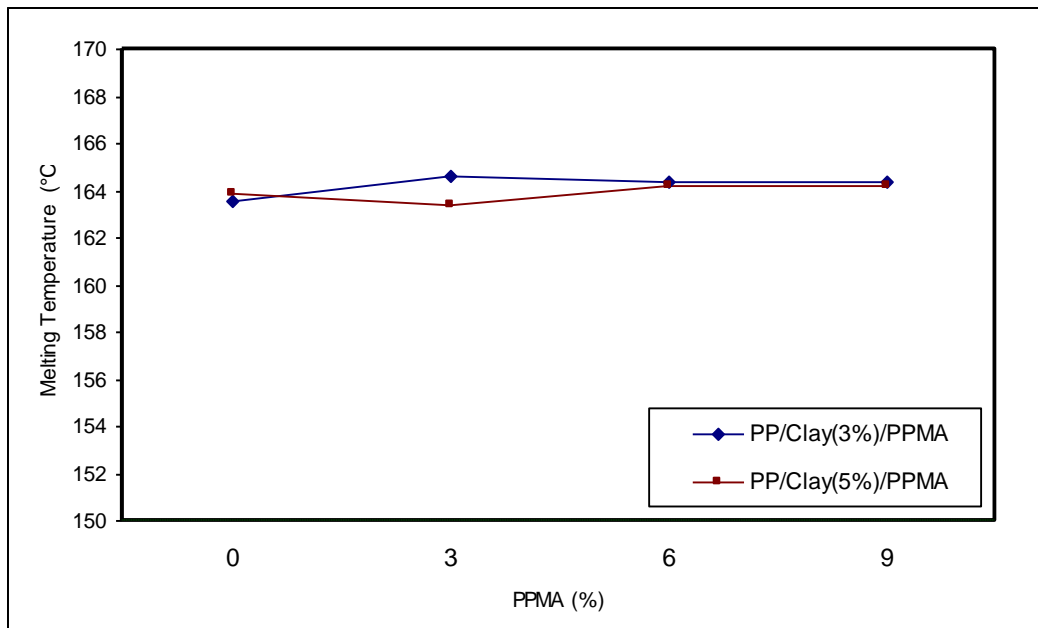


Figure 5.12: PPMA content effect on melting temperature of PPNCs at constant clay loading level

5.2.2 Sample Thermal History

Since the thermal history of each specimen has a considerable effect on crystallization, most studies use the DSC analysis at different heating and cooling rates to control the sample thermal history. In this study, this matter was

investigated on the real thermal history of the PP recycled material, produced by the twin screw extruder. A three times recycling process for our PP material are shown in the compounding section. The DSC analysis at the same heating and cooling rate (10 °C/min.) was performed for all the three PP recycled samples. Figure 5.13 shows that there is about 3 % decreases in crystallinity for all three recycling steps. This 3 % lower crystallinity may explain to some extend that this level of the decrement obtained in most PPNCs formulations could arise from the recycling process, rather than from the clay and PPMA addition.

Figure 5.14 presents the thermal decomposition graph of the PP and recycling PP samples, from TGA analysis. A slight shift for the first pure PP recycle sample was noticed as compared to pure PP received from the manufacturer. This shift was increased by a small degree for the second recycle sample. The second and third samples have the same thermal decomposition behaviour, which might indicate that this difference between the PP and recycling samples is related to additives incorporated in PP production and not originated from a degradation process.

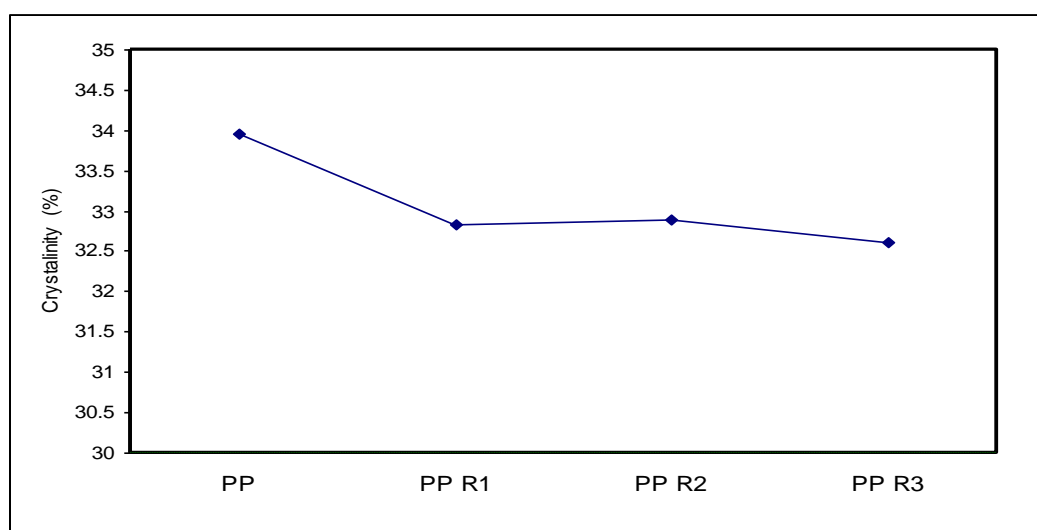


Figure 5.13: Thermal history effect on crystallization of PP, first PP recycle (R1), second PP recycle (R2) and third PP recycle (R3)

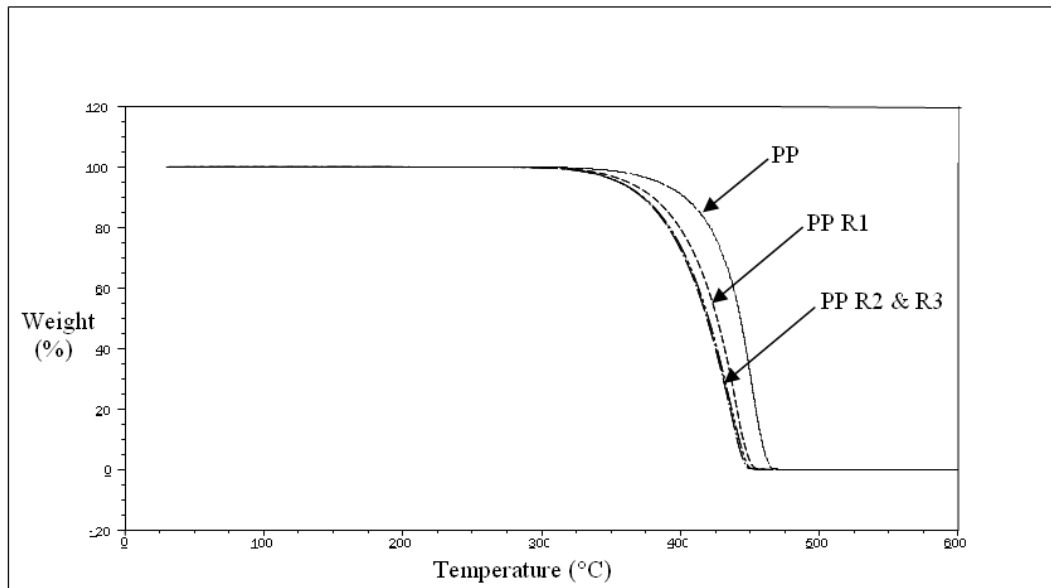


Figure 5.14: Thermal decomposition of the recycling PP, first PP recycle (R1), second PP recycle (R2) and third PP recycle (R3)

Tensile modulus results by video extensometer of the PP control sample and the three recycling PP samples are shown in Figure 5.15. It was found that no difference at all in tensile modulus of the first PP recycle sample. An increment of 1% and 2% in tensile modulus are noticed for the second and third recycle samples, respectively. This small increment confirmed the obtained results from the thermal decomposition graph and explained to some extent that this small increment might come from the additives incorporated in PP production, but not from any degradation process.

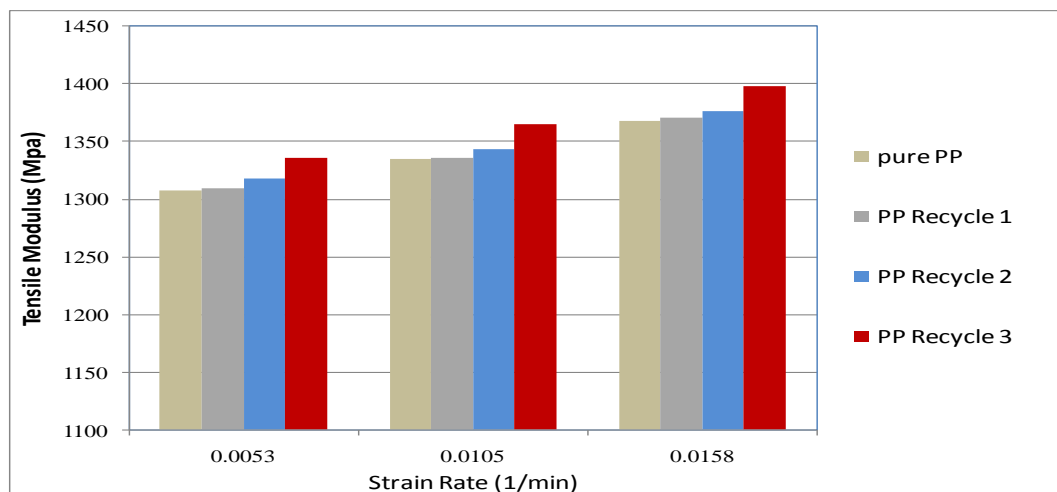


Figure 5.15: Tensile modulus of the recycling PP samples

Another TGA analysis graph (Figure 5.16) represents all PPNCs samples. They have the same decomposition behaviour except for the part of curve which represents the residual material when clay is presented. This remaining material differs from 1.5 to 3 % for any sample with 3 and 5 % clay content, respectively. On the other hand, an improvement in thermal stability of PPNCs was observed over the PP material. However, this improvement is doubled for PPNCs if the recycling PP materials are considered. This may be resulted from the interaction between organic and inorganic phases.

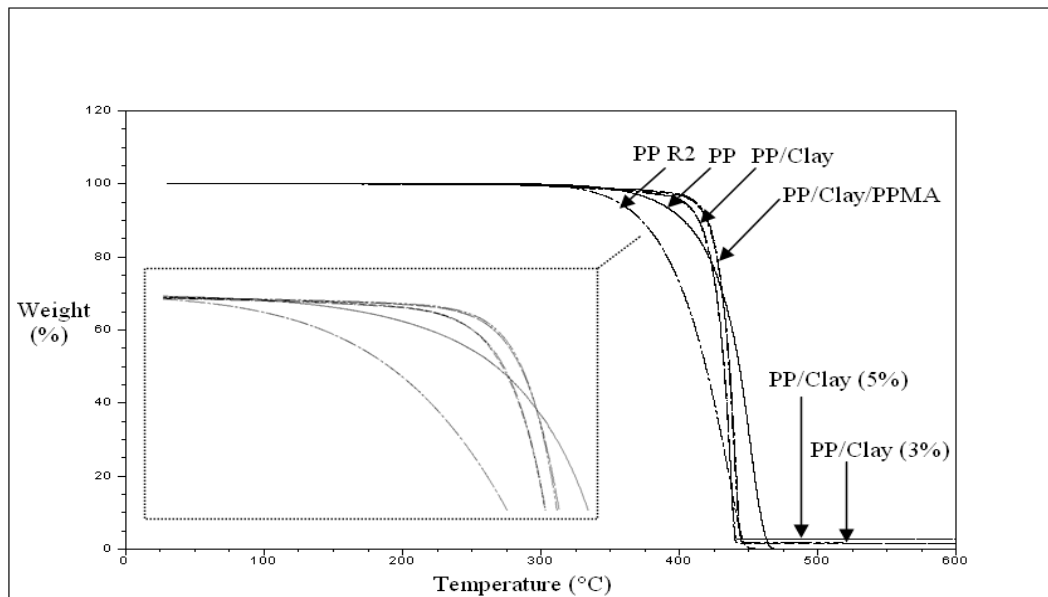


Figure 5.16: Thermal decomposition of the PP and PPNCs samples

5.3 Queen’s University Belfast Samples

5.3.1 Crystallization results

As stated in the material preparation section, Queen’s University Belfast samples do not contain any compatibilizer, which means that all comparative results are done for PP with different loading levels of clay. Also the effect of the stretched sheets with constant width (DR 5.5) on the crystallinity, crystallization temperature and melting point are illustrated below.

Results in Figure 5.17, show that the crystallinity was not enhanced remarkably by addition of both clay types (Cloisite 15A and MTE), their values were reduced to only 1 % in samples with 5 % clay loading which is very similar to our results. However, 3% clay loading exhibits 4 % loss in crystallinity for MTE as compared to 1 % increase for C15A sample. The melting temperature was the same for all samples as it has seen in Figure 5.18, with different clay type and content.

The crystallisation temperature on the other hand was reduced by about 4 % for all the samples, which indicates that clay particles are slowing down the crystallisation process (Figure 5.19). In comparison to our samples, which show an increase in T_c to 3.5 and reached to 6 % for some samples, these results match the tensile test results that show better yielding behaviour for Queen's University Belfast sample of pure PP where the crystallization temperature is increased. The way of mixing could be a major factor in these different obtained results. However, this is not enough to say that we could get better enhancement in tensile properties.

Much improvement is showed in Figure 5.17 and 5.18 for both crystallinity and melting points for all the constant width stretched samples (DR 5.5:1). Crystallinity was increased by 10 % for the drawn pure PP as compared to undrawn pure PP and about 15 % for the drawn PP/clay as compared to pure PP. The melting points are increased by 3.3 % for all drawn samples. In contrast, crystallization temperatures for the drawn sheets remain within the same range as undrawn ones. However, there is a decrement in melting point of pure drawn PP sample by 3 %.

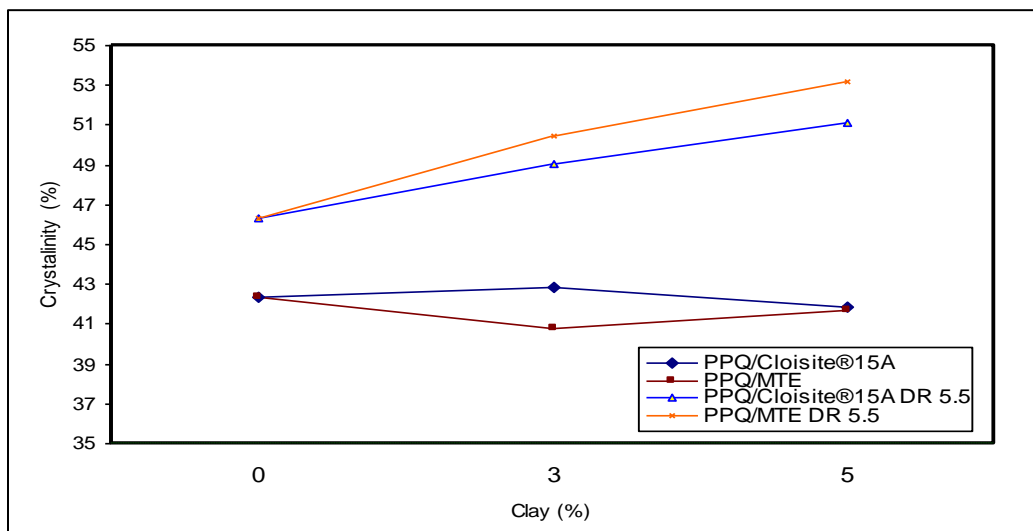


Figure 5.17: Clay content effect on crystallinity of PPQNCs without compatibilizer

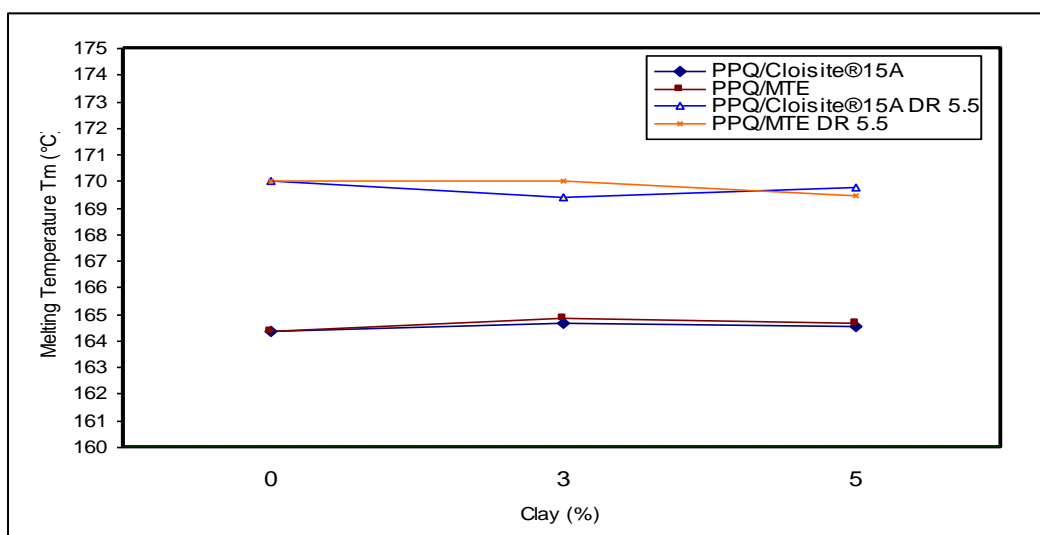


Figure 5.18: Clay content effect on melting temperature of PPQNCs without compatibilizer

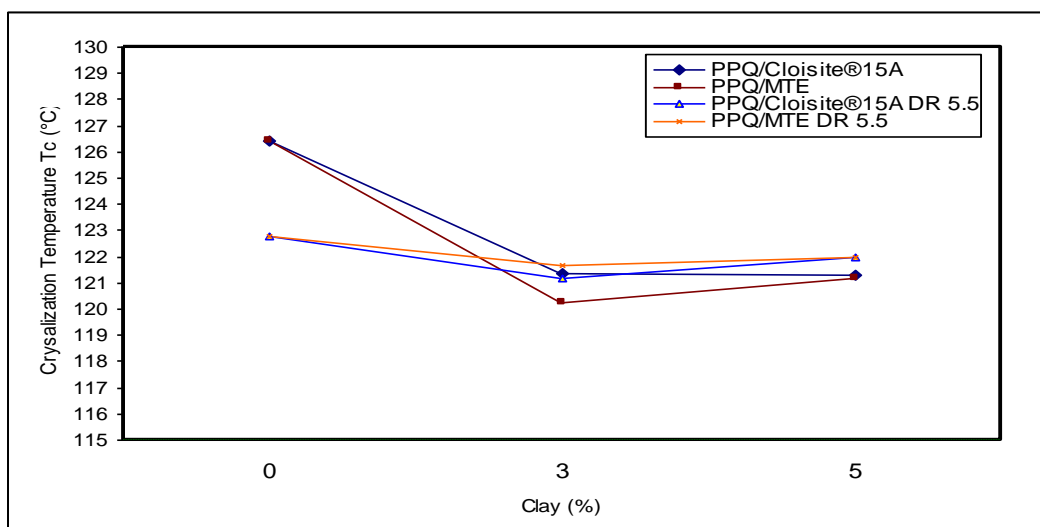


Figure 5.19: Clay content effect on crystallization temperature of PPQNCs without compatibilizer

Another interesting observation relates to the crystallinity results of drawn PP/clay as compared to drawn pure PP. Clay material acts as a crystallinity property modifier. This can be seen from the 15% higher improvement of crystallinity of drawn PP/clay over undrawn systems as compared to 10% higher improvement of drawn PP over undrawn ones. With neglecting of the unknown PPMA effects during solid phase orientation, this observation needs to be highlighted and investigated in detail. Thus, solid phase orientation by means of die drawing is a very important subject that can add a valuable input to polymer nanocomposite research.

5.3.2 Tensile Testing

As a preliminary starting point for the present study, tensile experiments are performed on the received Queen's University Belfast samples. Yield strength as indication of modulus and sample toughness by mean of elongation at break is reported as an indication of fracture toughness. These samples are prepared without compatibilizer. Also, tensile results obtained from the biaxial testing machine at 160 °C and Instron tensile test for the stretched sheets were done and presented. These tests were performed in order to check the effect of clay on the PPNCs tensile behaviour. As an example, the stress strain curve for a pure PP specimen is shown in Figure 4.20. All nominal stress-strain, load-displacement or stress-time curves are presented in Appendix E1, E2 and E3 for original, stretched, and long stretcher testing sheets properties, respectively.

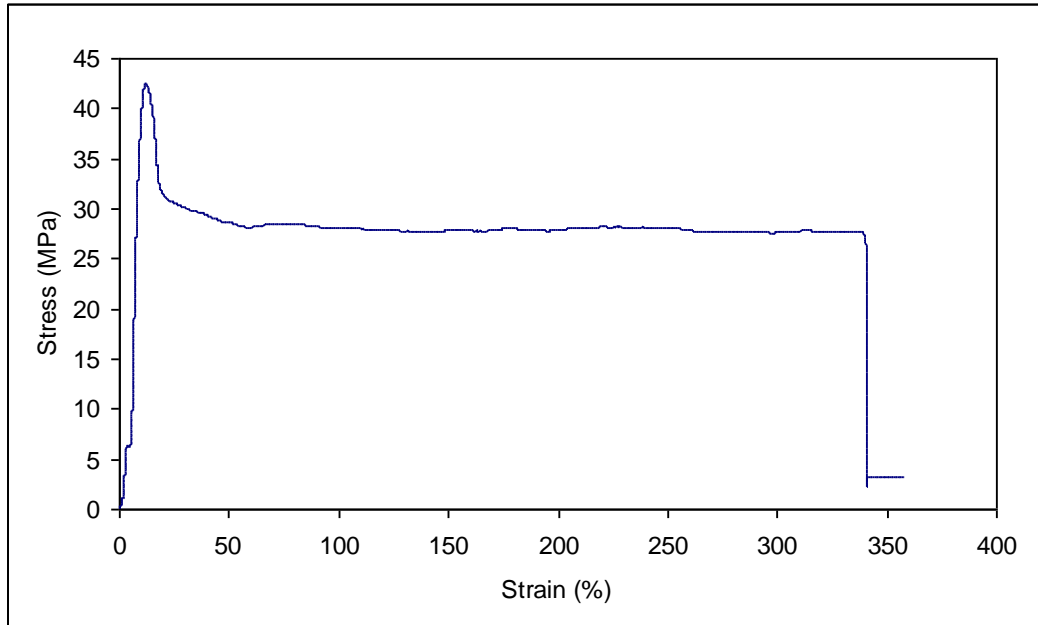


Figure 5.20: Nominal stress-strain curve for a pure PP specimen

5.3.2.1 Nano-clay loading effect on the tensile property at yield

Clay loading effect on the PP mechanical behaviour was analysed using the Instron testing machine for the original, stretched sheets and the mechanical behaviour during the stretching process.

Figure 5.21 shows the tensile test results of the samples prepared with 3% and 5 % of C15A and MTE, and compared with the pure PP sheet. In addition to machine direction results (MD), transverse direction (TD) is examined as well. These results clearly demonstrate that there is a decrement of 5% and 9% in tensile strength at yield with 3 and 5% of C15A, respectively. This effect decreases to 2 and 3.5% when 3% and 5 % of MTE are involved. These results can be explained by the compatibility or bad bonding between polymer and clay. PPMA could help to improve dispersion and thus enhance the tensile properties. As expected, greater decreases happen in specimens with higher clay content.

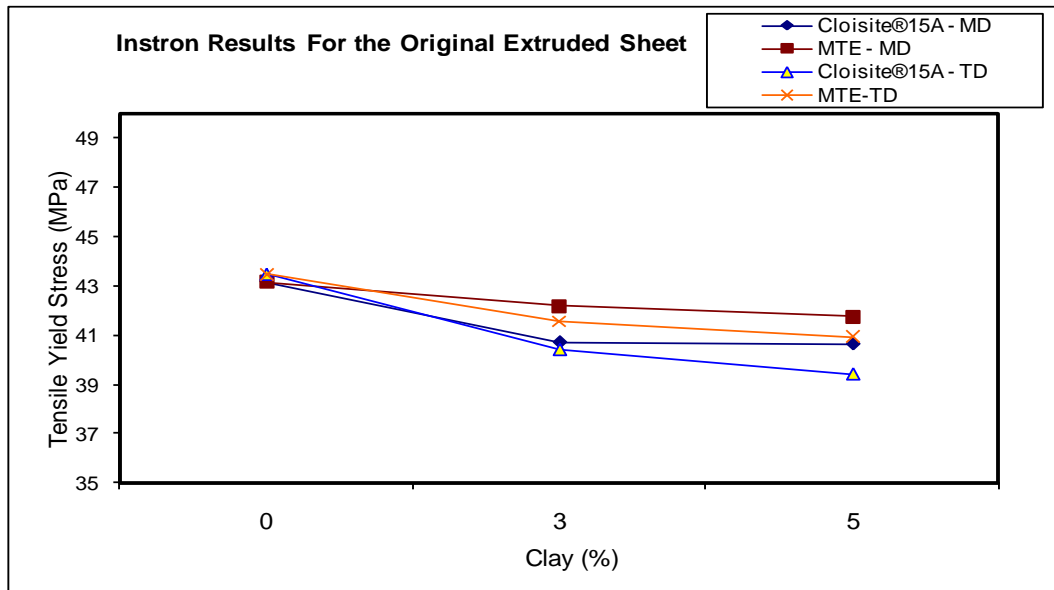


Figure 5.21: Tensile yield stress for the original extruded sheets (Instron results)

A similar decreasing trend of yield is observed for most stretched samples, as shown in Figure 5.22. An exception is seen for MD MTE with 3 % loading which shows 5 % improvement. The stretched samples show more than 200 % improvement over the un-stretched sheets due to the changing in the molecular orientation.

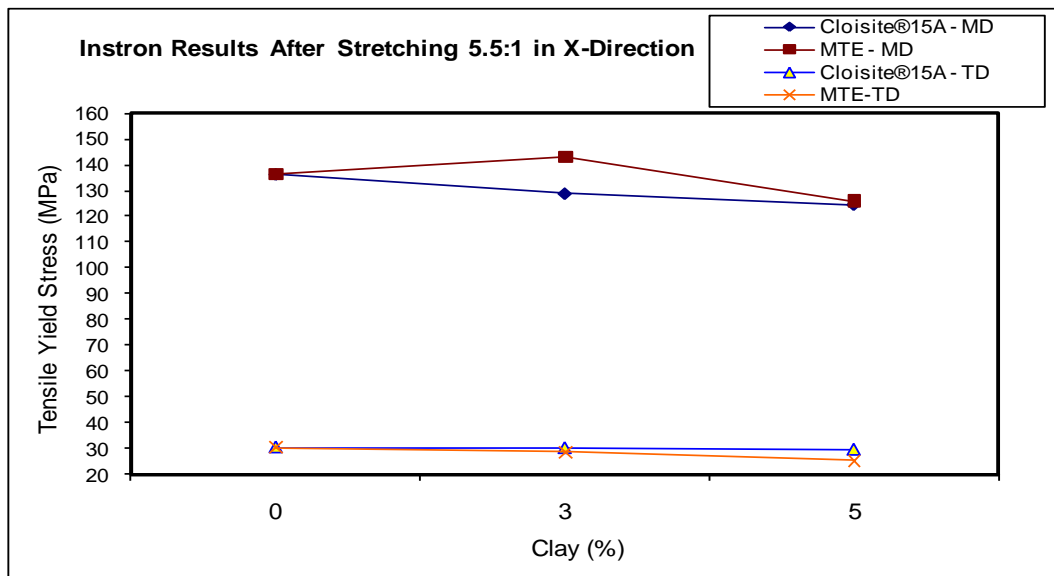


Figure 5.22: Tensile yield stress for the stretched sheets at room temperature (Instron results)

Tensile at yield of the sample stretched in x-direction at 160 °C shows an improvement of 6 % in 5 % filler loading for both PPC15A and MTE as shown

in Figure 5.23. However, the specimen with 3 % loading of C15A still loses 6 % as compared the pure PP sheet. The gain improvement just before the melting point (165 °C) give a sign of possibility to improve the interaction of PP/Clay if we introduce the compatibilizer during the melting state of PP/Clay processing stage.

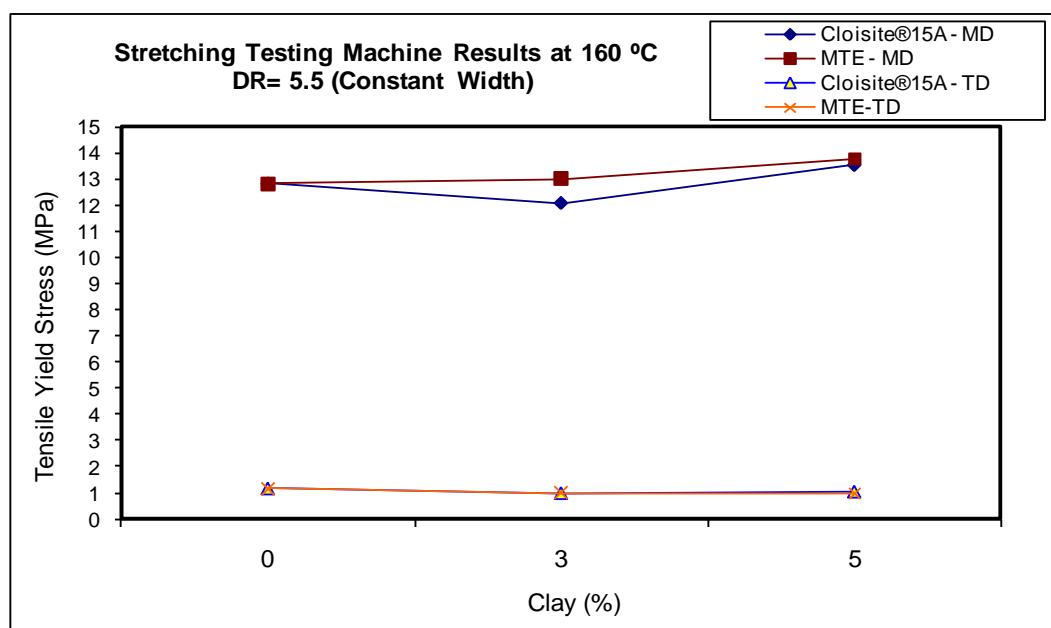


Figure 5.23: Tensile yield stress for the stretched sheets (Biaxial Testing Machine)

The result of PP/clay at 5 % loading level is an evident that incorporation of nano-clay could act as reinforcement in the polymer matrix. However, the absence of PPMA reduces this behaviour. The importance of compatibilizer was fully investigated in previous studies in the PPNCs field but uncompatibilized systems are a means of establishing baseline properties.

On other hand, the yield stress results obtained at 160 °C might be explained by the fact that the PP crystals start to melt around 125°C, the PP is partially in a molten state at a stretching temperature of 145°C and higher. As a result, the density of the sheet becomes significantly lower at the stretching

temperature of 160 °C and the yield stress exhibits lower values than the yield stress at room temperature.

5.3.2.2 Nano-clay loading effect on the tensile strength and elongation at break

It is important to note that the addition of clay alone or with the compatibilizer in most previous works does not improve the material toughness. This has not been seen for tensile and elongation at break for un-stretched 3 % loading samples, as shown in Figures 5.24 and 5.25. However, the material tends to become much more fragile than the pure PP when 5 % clay loading is used, especially when MTE type is involved. This might be due to the possible presence of voids during the Instron tensile test of 3 % clay loading. The voids may be at a level that is beneficial at 3 % loading, but detrimental at 5 %.

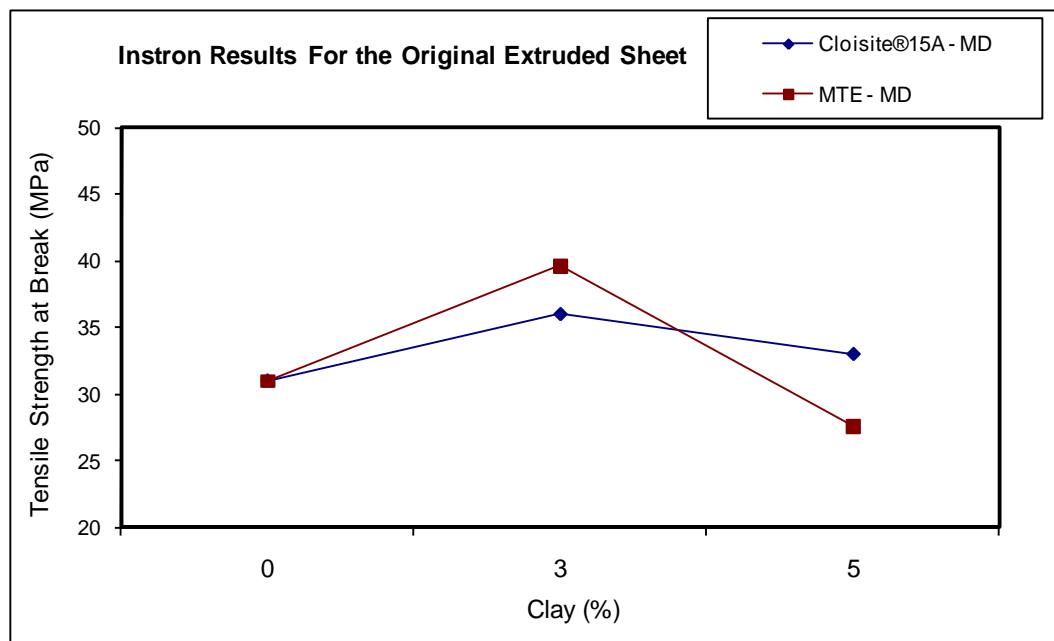


Figure 5.24: Tensile strength at break for the original extruded sheets (Instron results)

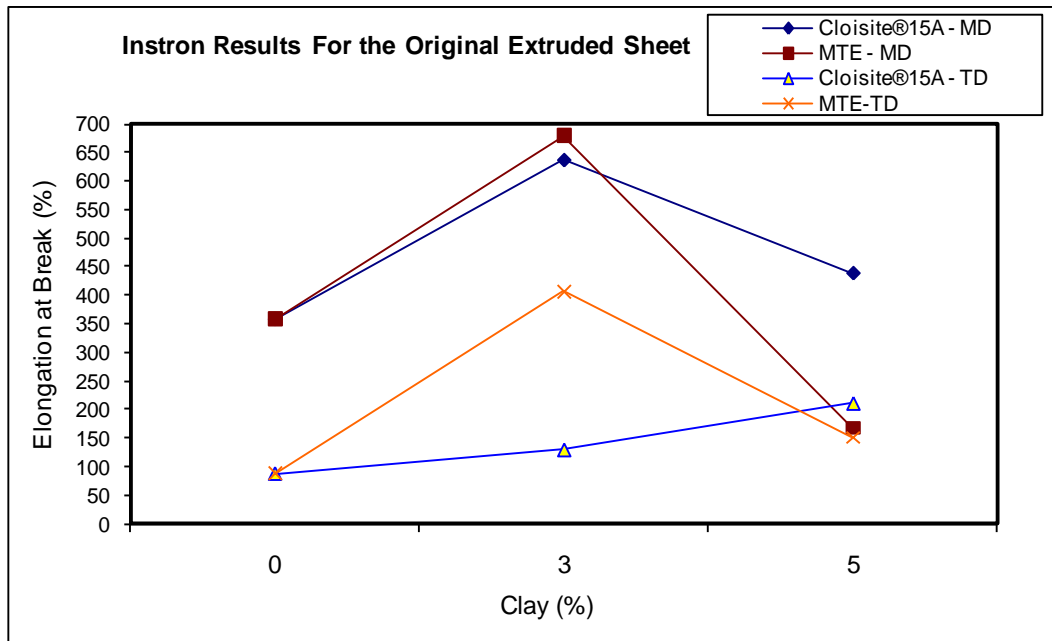


Figure 5.25: Tensile Elongation at break for the original extruded sheets (Instron results)

Tensile strength at break for the MD stretched sheets under 160 °C is shown in Figure 5.26, where a 6 to 10 % decrement of the values are observed while tensile elongation at break (Figure 5.27) still show up to 10 % improvement for different clay type and loading level. In contrast, TD samples were weakened between 10 and 20 %.

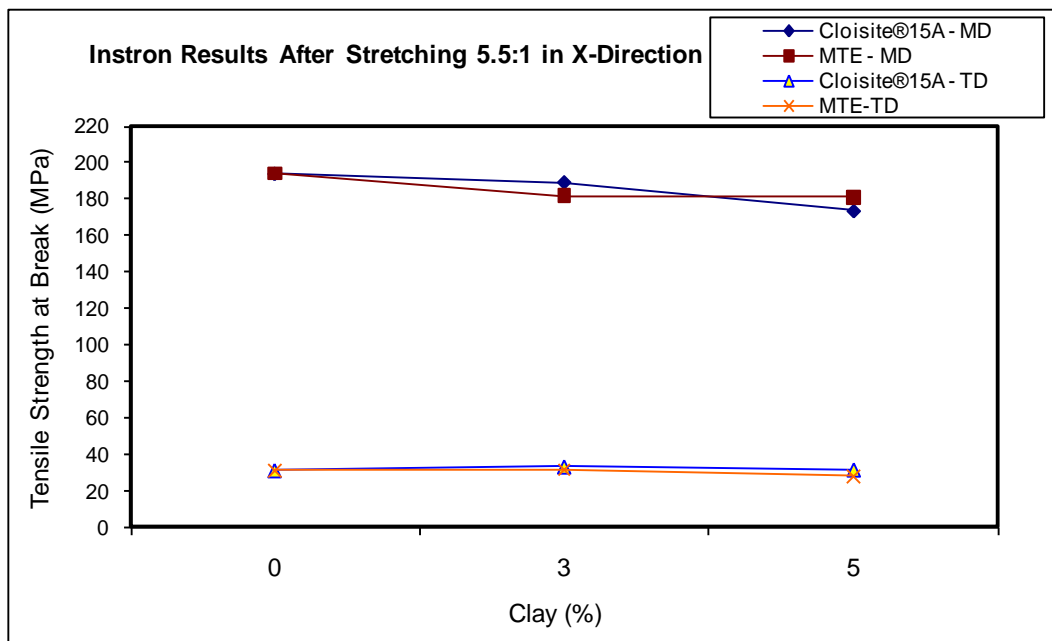


Figure 5.26: Tensile strength at break for the stretched sheets (Instron results)

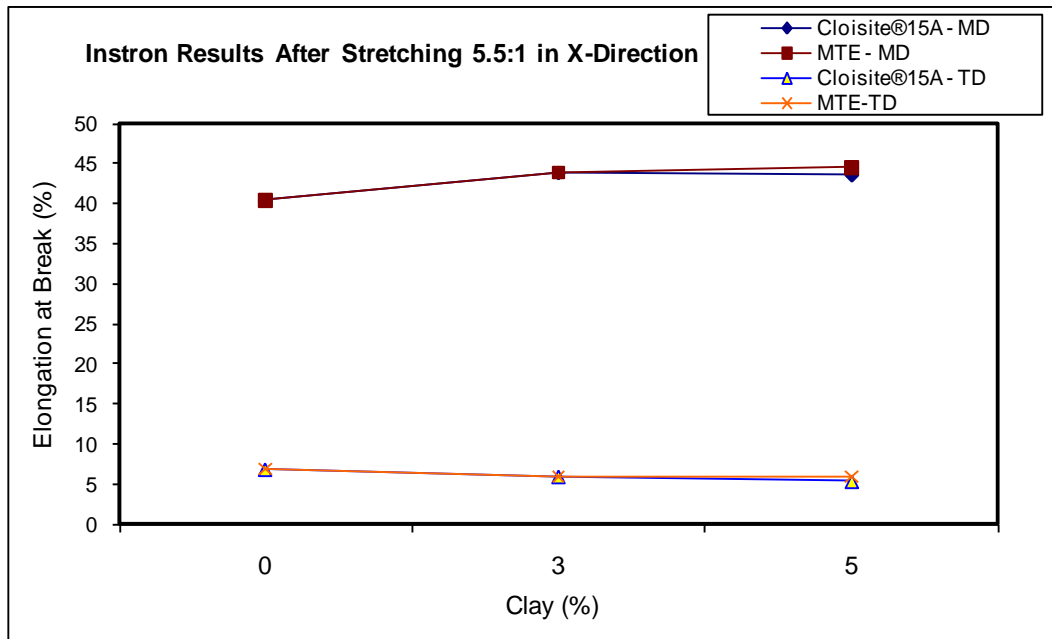


Figure 5.27: Tensile elongation at break for the stretched sheets (Instron results)

As thoroughly explained in Chapter 2, the largest part of the literature concurs that the higher the nano-particle dispersion level achieved, the higher the mechanical improvement in PPNCs. Nevertheless, when a possible connection between level of clay layer dispersion through the matrix and tensile properties was evaluated, it was found that the two aspects share only the same general trend but no direct relationship could be found.

On the other hand, as discussed in crystallization results, comparing the crystalline phase amount of the PP/clay specimens and their tensile strength at yield shows no clear correlation (Figure 5.28). However, the crystallization temperatures of PP/clay present match the tensile strength at yield, as Figure 5.29 illustrates for PP/C15A. However, this is not enough to say that we could get better enhancement in tensile properties by increasing the crystallization temperature. Spherulitic morphology investigation is highly recommended to give more input and understanding to the crystallization behaviour.

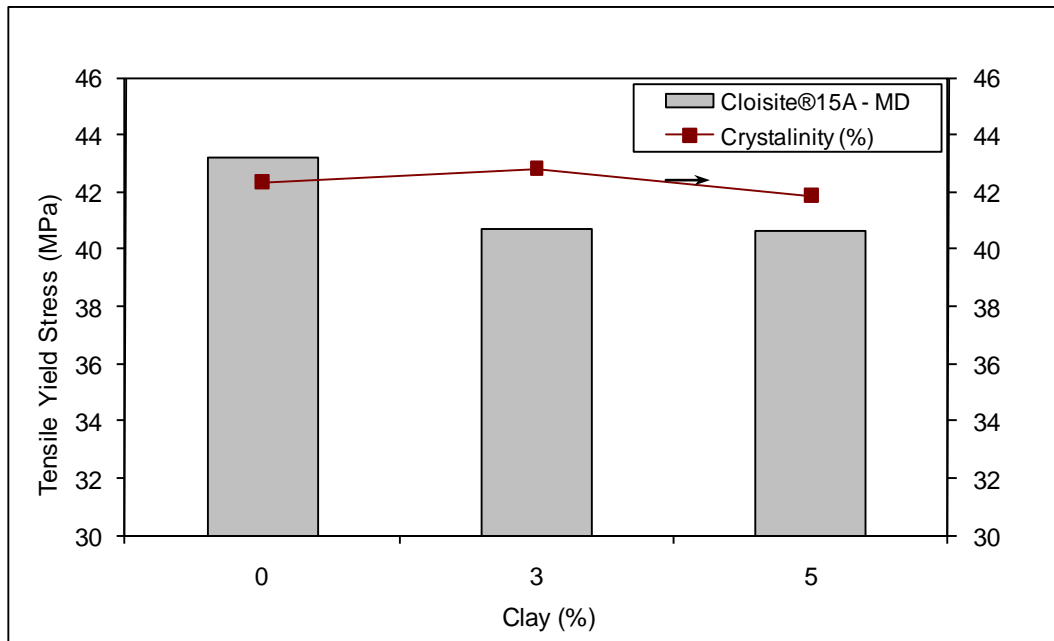


Figure 5.28: Crystallinity and tensile yield stress correlation

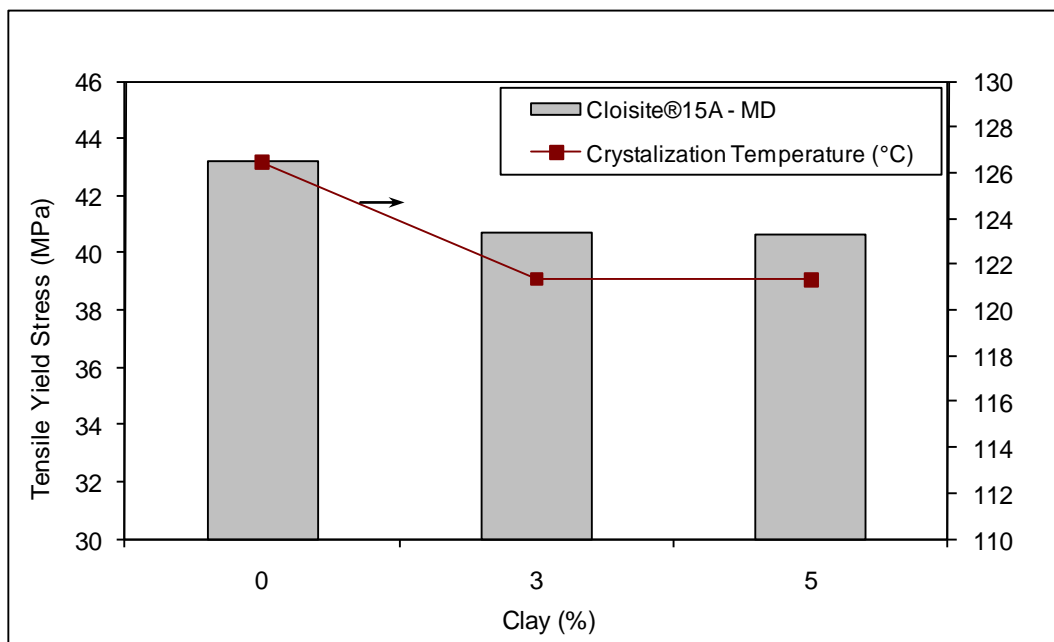


Figure 5.29: Crystallization temperature and tensile yield stress correlation

5.4 Processing behaviour of PPNCs

As described in section 4.4.3, the viscosity index used to measure the PPNCs process variation is in-line process measurement. Such measurement may give a direct indication on the real behaviour during the injection moulding process. Due to the lower viscosity of the PPMA as compared to the pure PP, the PPMA is the major player between the rheological behaviour of the pure PP and

the higher viscosity of the PP/clay composites. Table 5.1 shows the values of the viscosity index and its 10 cycle's standard deviation for each sample.

Table 5.1: In-line viscosity index values of different PPNCs

Sample Identification	Viscosity Index
PP	30.60 ±0.07
PP+3% Clay	32.60 ±0.06
PP+ 5% Clay	32.81 ±0.53
PP+3% Clay+3% PPMA	32.25 ±0.02
PP+5% Clay+3% PPMA	32.46 ±0.16
PP+3% Clay+6% PPMA	30.16 ±0.06
PP+5% Clay+6% PPMA	31.52 ±0.17
PP+3% Clay+9% PPMA	29.79 ±0.04
PP+5% Clay+9% PPMA	30.08 ±0.12

It can be seen that the viscosity Index of pure PP is 30.6, which is shown as a dot in Figure 5.30. At zero content of PPMA, the viscosity index of the 3% and 5% clay systems are about 7% higher than that of pure PP. As the PPMA level increases to 3 %, the difference in viscosity index for both systems decreases to about 5.5% higher than the pure PP. In 3% system clay with 6% and 9 % PPMA contents, the viscosity index intersects with the viscosity of pure PP and records 1.5 and 3 % lower viscosity index, respectively. In contrast, 6% PPMA content was not enough to drop the viscosity index of the 5% clay system, which remains 3% higher than pure PP system. However, the 9 % PPMA level does the decrease in viscosity index to about 2% lower than that of pure PP.

The viscosities of PPNCs were comparable with or even lower than those of pure PP system as PPMA is present because of lower molecular weight of PPMA. This equivalent range of viscosity might be considered to explain to some extent the similarities of the processing of the pure polymer and the different composites, especially when the PPMA is involved.

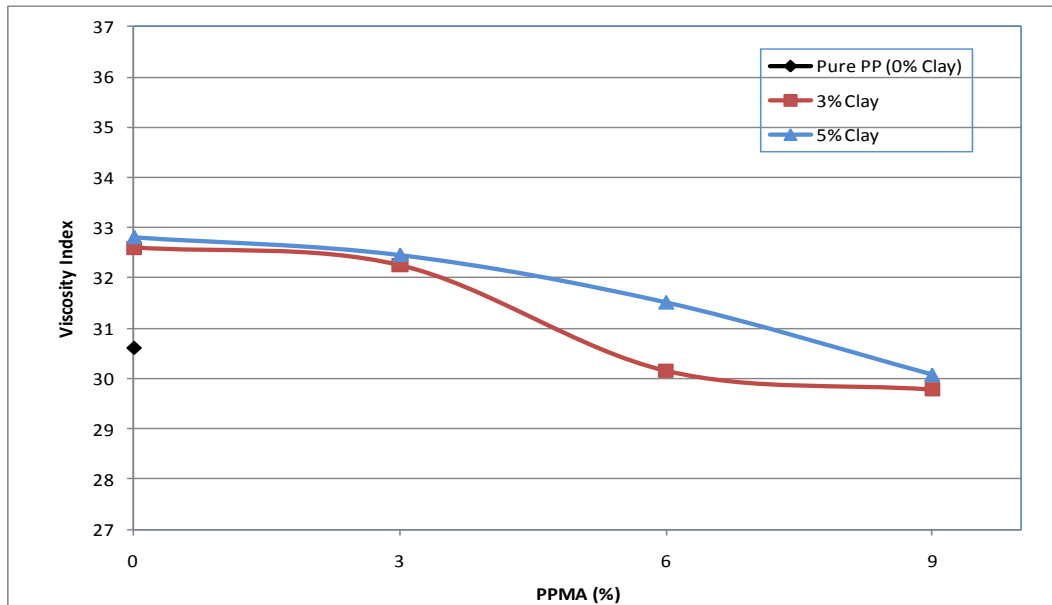


Figure 5.30: In-line viscosity index measurement vs. PPMA contents of different PPNCs

5.5 Drawing Process Curves

Chain rearrangement and alignment below the melting point of the PPNCs samples can be obtained with the die drawing process. This process is carried out at a temperature of 154 °C, just 11 °C below the T_m , which would promote melting and flow. The morphology change due to the drawing process is discussed in the following section.

Sample extension is not uniform, but it occurs through the propagation of a neck (a reduction in the cross-sectional area) occurring at some axial point of the drawn sample. Figures 5.31 to 5.36, of different draw ratios, show the necking and drawing configurations; as well as the load-displacement response. The upper yield point is associated with the neck formation and the low slope region is associated with the neck propagation process. This uniaxial orientation of the samples makes them anisotropic.

A notable observation, that can be seen in Figures 5.32, 5.34 and 5.36, is the replication of curves for the PP sample and the PP/clay samples in absence of

the compatibilizer, as an indication that the PP molecule is the elementary factor in driving the drawing process. In contrast, the difference in the steady load of the stable necking region can be seen in Figures 5.31, 5.33 and 5.35 when the compatibilizer is involved. Free moving of PP molecules and/or incompatible matrixes could be the reason of such behaviour. This might be better explained in the following sections of characterization.

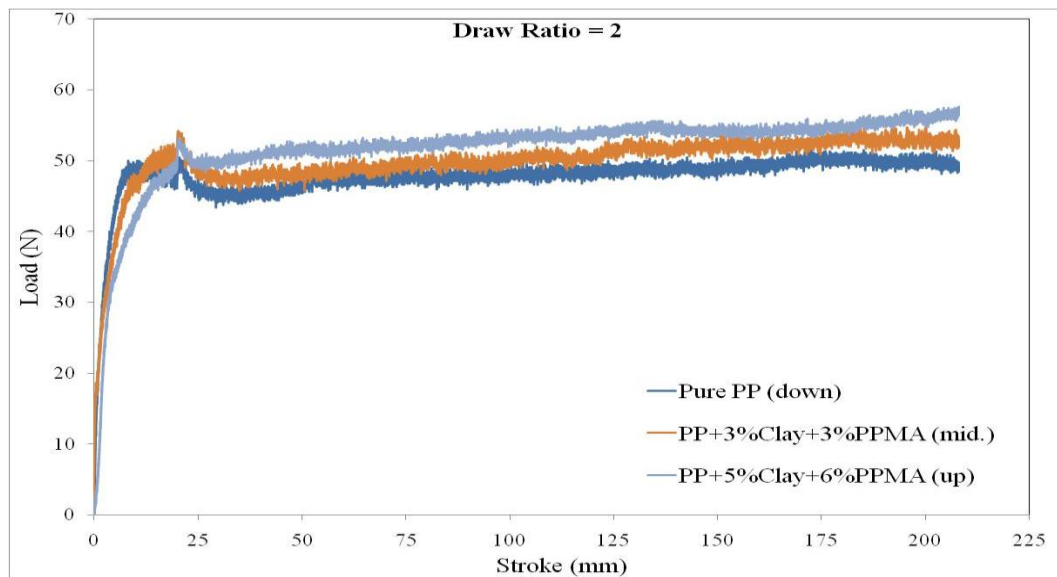


Figure 5.31: Die drawing process curves of samples with PPMA ($\lambda = 2$)

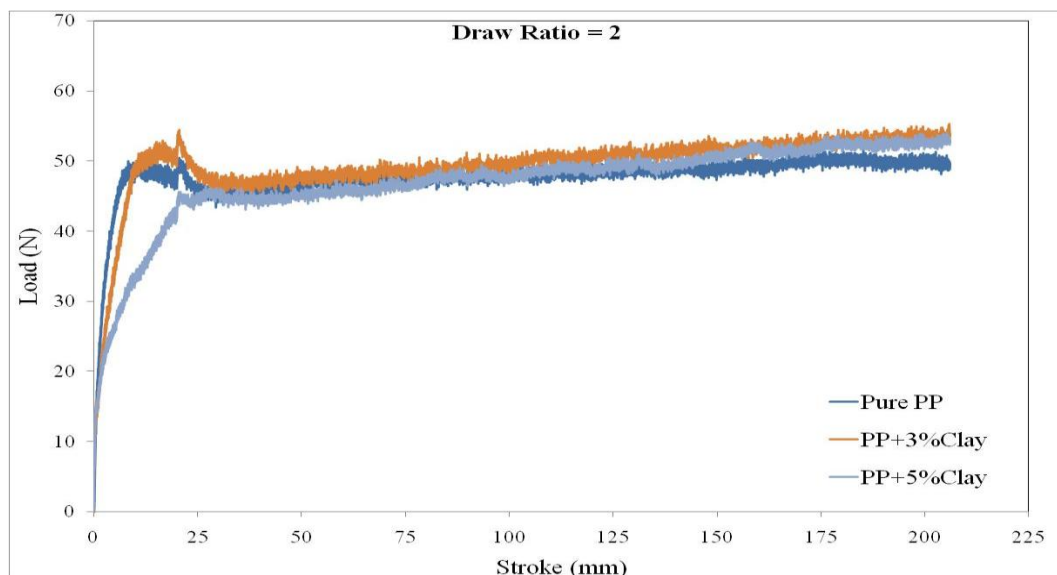


Figure 5.32: Die drawing process curves of samples without PPMA ($\lambda = 2$)

Another observation that can be seen in all die-drawing process graphs is the double peaks, which are noticed for all draw ratios. The complexity and many changing variables that associate with the die-drawing process make it very difficult to affirm which variable can produce such behaviour. However, the important stable necking area for drawing process shows perfect consistency.

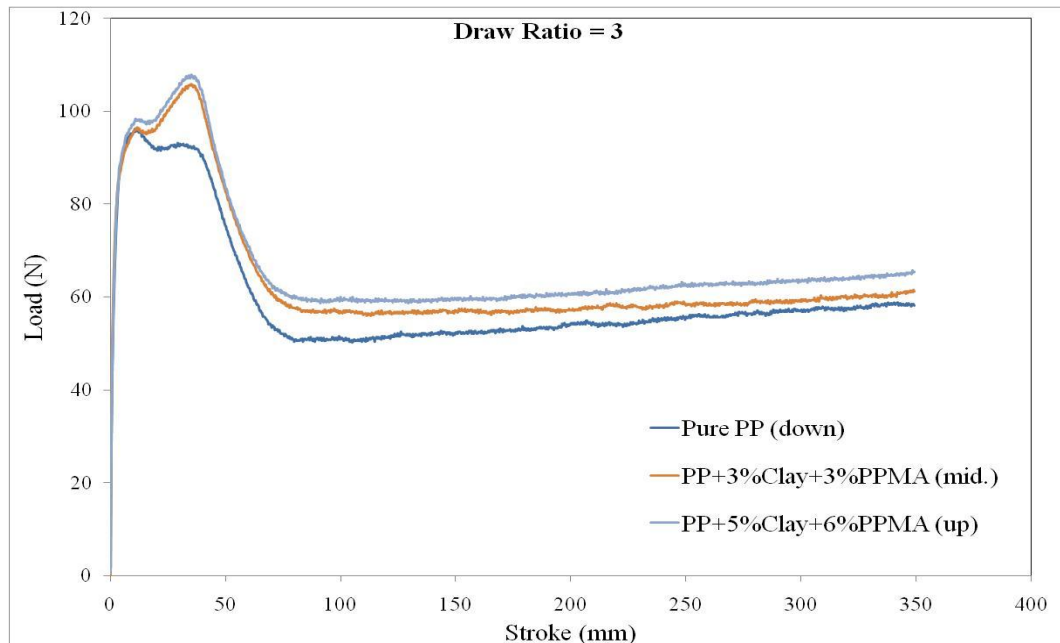


Figure 5.33: Die drawing process curves of samples with PPMA ($\lambda = 3$)

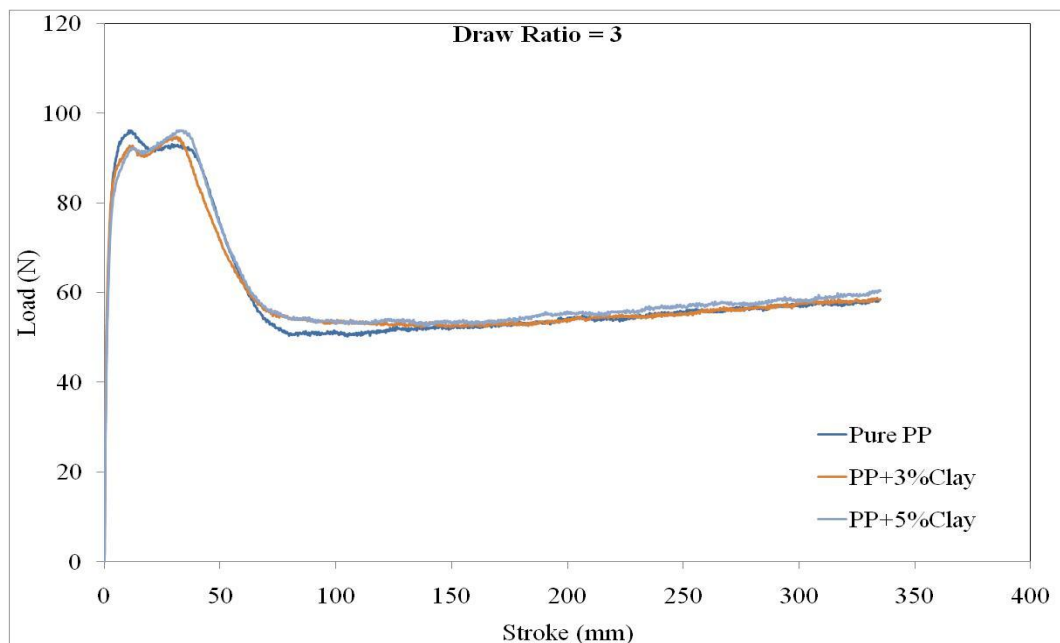


Figure 5.34: Die drawing process curves of samples without PPMA ($\lambda = 3$)

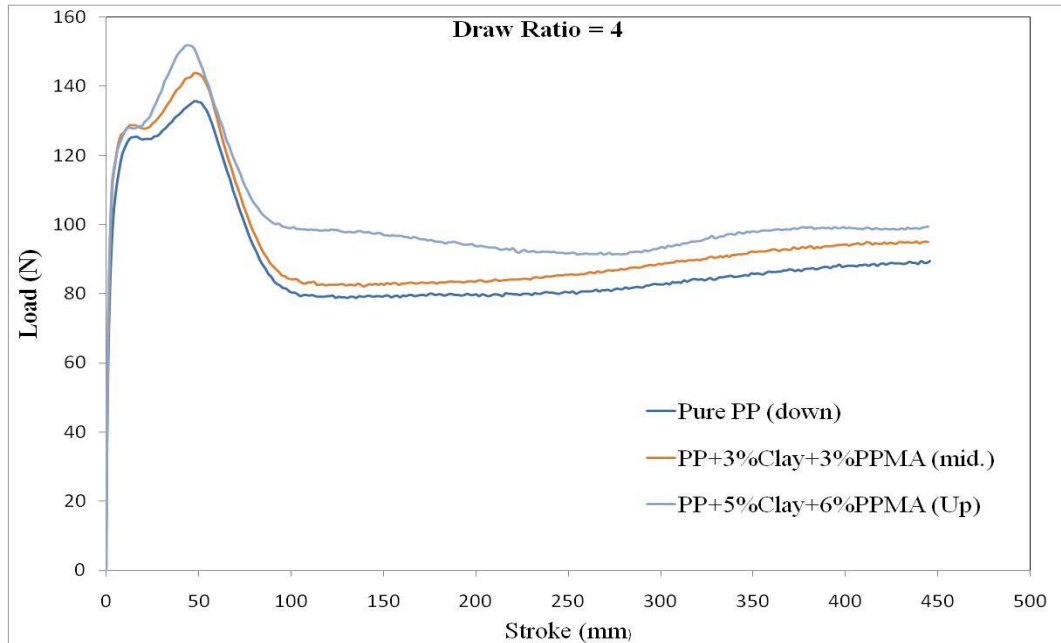


Figure 5.35: Die drawing process curves of samples with PPMA ($\lambda = 4$)

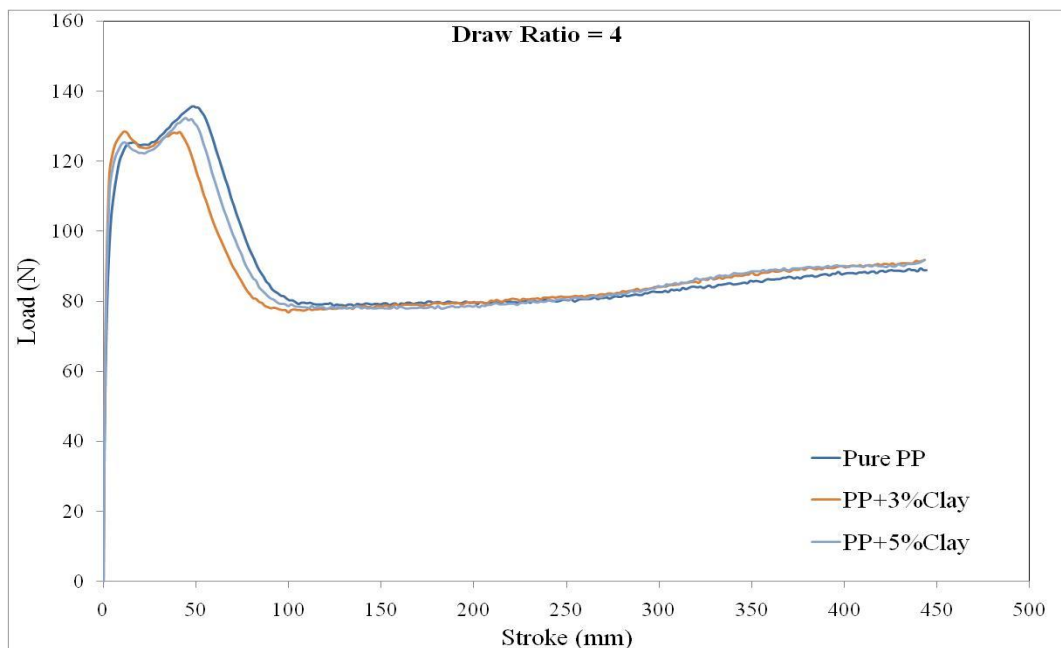


Figure 5.36: Die drawing process curves of samples without PPMA ($\lambda = 4$)

The variation of steady draw load with imposed draw ratio is shown in Figure 5.37 and 5.38 for samples of draw speeds 5, 120, and 950 mm/min. The load rises slowly with draw ratios 2 and 3. The load then rises quickly at draw ratio 4, which was subjected to high draw speed. On the other hand, as shown in Figure 5.37, a very similar load was obtained when PPMA was not involved.

in our formulation. This similarity has not dominated on the samples that contain PPMA where load increases as the clay loading increases.

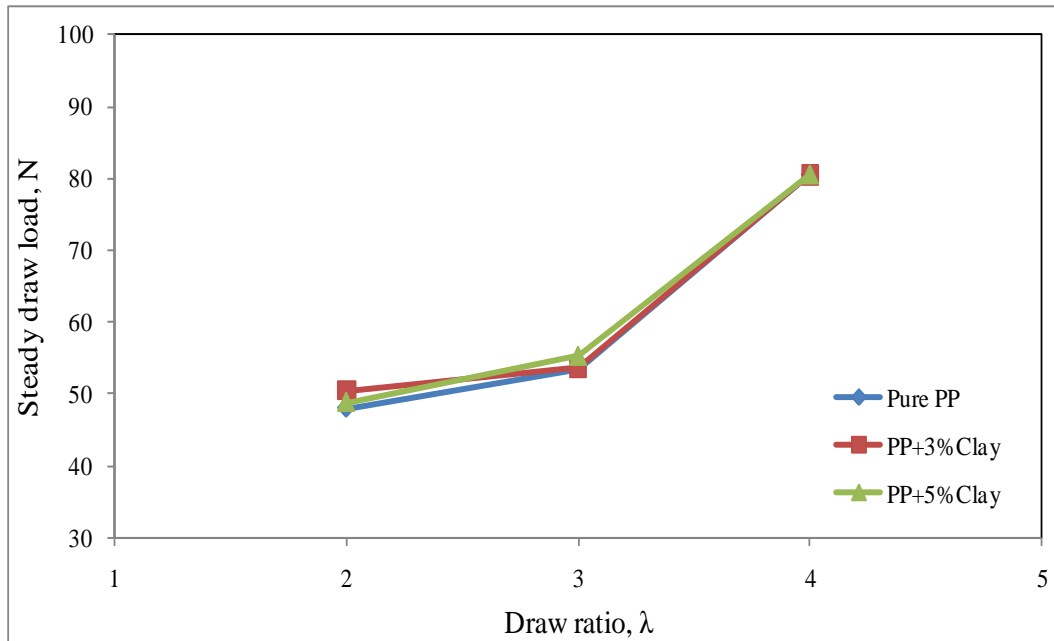


Figure 5.37: Steady draw load vs. draw ratio of the drawing process of PPNCs without PPMA

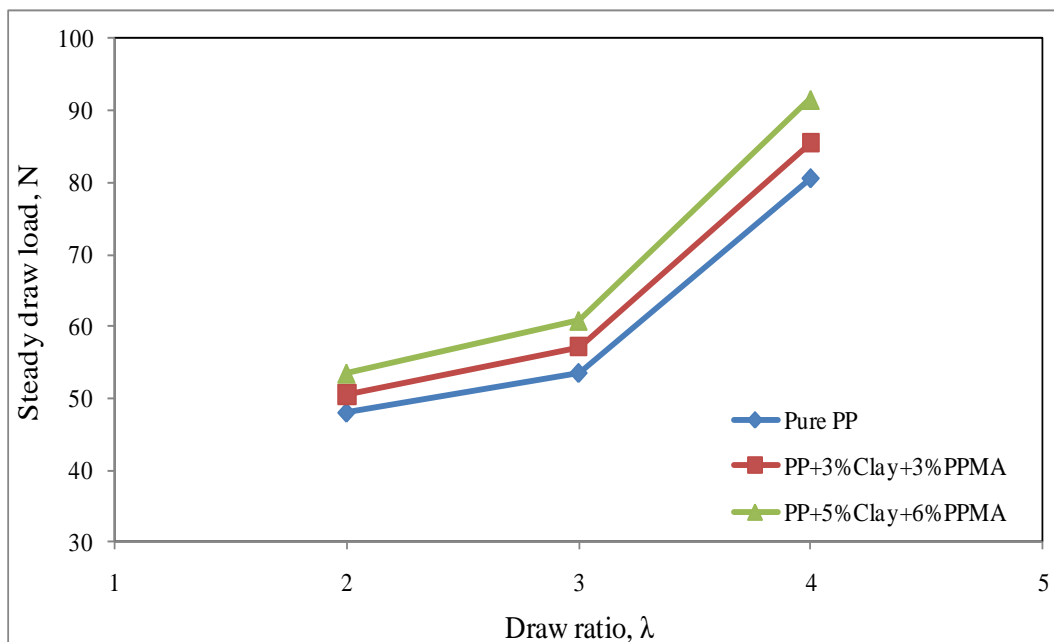


Figure 5.38: Steady draw load vs. draw ratio of the drawing process of PPNCs with PPMA

5.6 Spherulitic Morphology

5.6.1 Spherulitic morphology of undrawn PPNCs

Nucleation and crystal growth are two important parameters that affect the crystallization process. Crystallization temperature has a very pronounced effect on the spherulitic morphology. On the lamellar scale for a pure polymer, as was found, increasing the crystallization temperature increase the lamellar thickness (reported by Kavesh et al. [138, 139]). Figure 5.39 shows the spherulitic morphology of the PP used material at (a) 115 °C and (b) room temperature. Thus, as reviewed previously in chapter 2, nucleation rates are high at low crystallization temperature. On contrary, high crystallization temperature favours rapid crystal growth rates; since the chain mobility is increased. The clay particles, in finely dispersed form, act as a nucleating agent and favour the nucleation step, and should shift to a lower region temperature morphology as it can be seen in Figure 5.39 (b).

The brittleness may result from the decreased strain in the amorphous region from the crystallites, the possible existence of voids or due to the stress concentration [140].

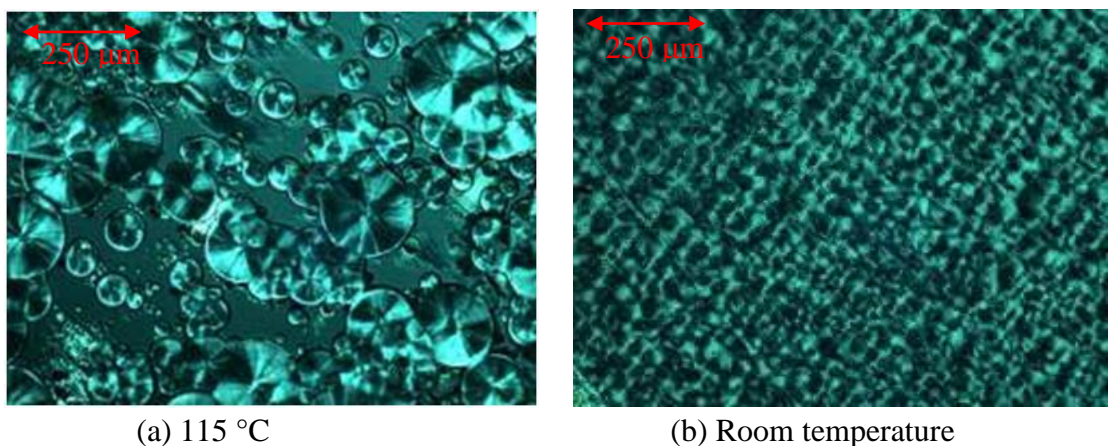


Figure 5.39: Spherulitic morphology of PP at (a) 115 °C (b) room temperature

Table 5.2 summarizes the results of different PPNC samples. The extent of variation of spherulitic size can be seen in Figures 5.40, 5.41 and 5.42. The results show that the morphology of the PPNCs differs not only by the effect of clay loading, but also it is a function of the PPMA contents and its interference with clay. The PP with 3% clay and 3% PPMA is grainy, with many very small spherulites because of the high nucleation rate (many sites). In some cases spherulite shapes are partially changed to equiaxed ones, especially when the clay loading is more than 3 %. Crystallization start temperatures for all samples are very similar and within 5 °C difference in range. However, the PP with 3% clay and 3% PPMA did crystallize at earlier stages at 130 °C, completing a full spherulite image at 120 °C over 115 °C for other composites . Therefore, compared with others, has the least of the final average spherulite size at 130 °C. A delay of 10 °C of PP and PPMA to have full spherulite images is a clear sign that clay layers acted as a nucleating agent, which promote the crystallization of PP.

Spherulite shapes for 5% clay systems are highly reduced as shown in Figure 5.42 of the full spherulite images, but the intersections of the same figure at 120 and 130 °C are still evident and clear, indicating the existence of perfect spherulite. As found in previous work by Nowacki[66], that shear could greatly enhance the nucleation of crystallization. Since, crystal growth is ultimately limited by the meeting of spherulite boundary, which leads to an irregular final structure and smaller crystalline dimension.

Table 5.2: Spherulitic Morphology of PPNC Samples

Sample Identification	Spherulite Size μm	Spherulite Shapes	Crystallization Start Temperature $^{\circ}\text{C}$
Pure PP	130 ± 70	Spherical	132
PPMA	115 ± 75	Spherical	130
PP+ 3% Clay	90 ± 40	Equiaxed	132
PP+ 5% Clay	80 ± 70	Spherical/Equiaxed	132
PP+3% Clay+3% PPMA	30 ± 20	Spherical/Fine Texture	135
PP+5% Clay+3% PPMA	75 ± 65	Spherical/Equiaxed	135
PP+3% Clay+6% PPMA	70 ± 60	Spherical/Fine Texture	135
PP+5% Clay+6% PPMA	75 ± 65	Spherical/Equiaxed	135
PP+3% Clay+9% PPMA	70 ± 30	Spherical/Fine Texture	135
PP+5% Clay+9% PPMA	70 ± 60	Spherical/Equiaxed	135

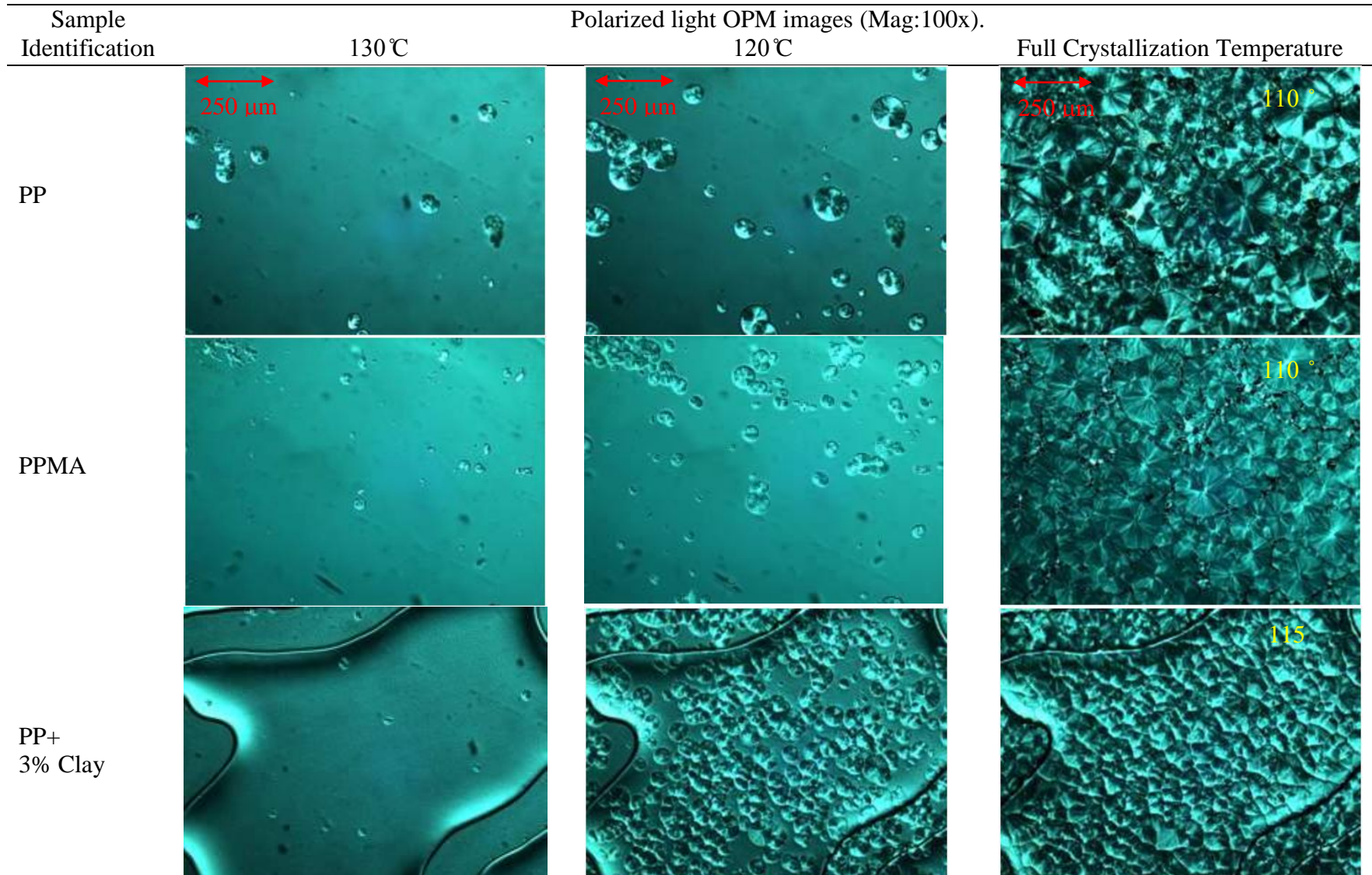


Figure 5.40: Spherulitic morphology of unoriented PPNCs at different temperatures

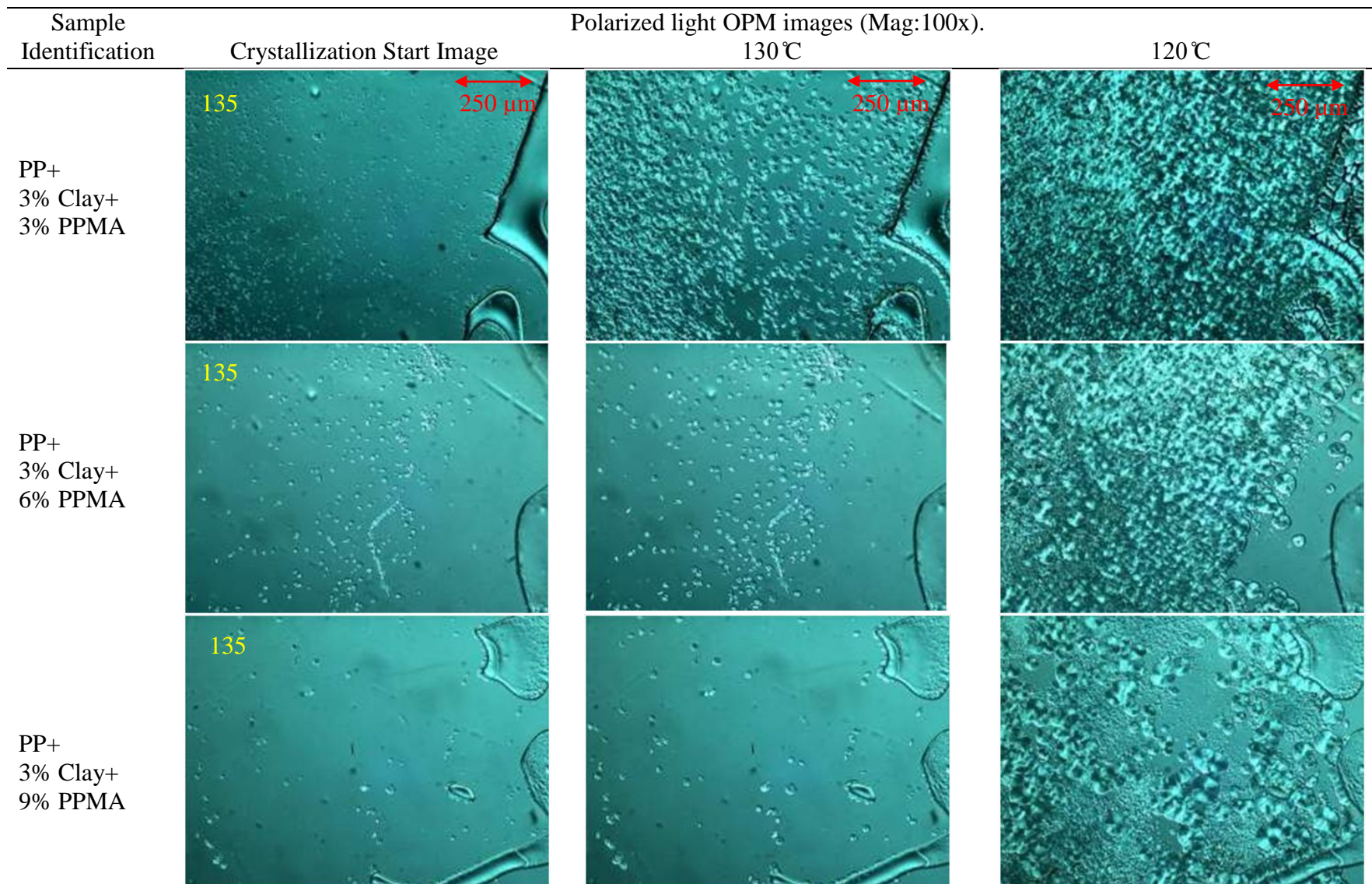


Figure 5.41: Spherulitic morphology of unoriented PPNCs with 3 % clay

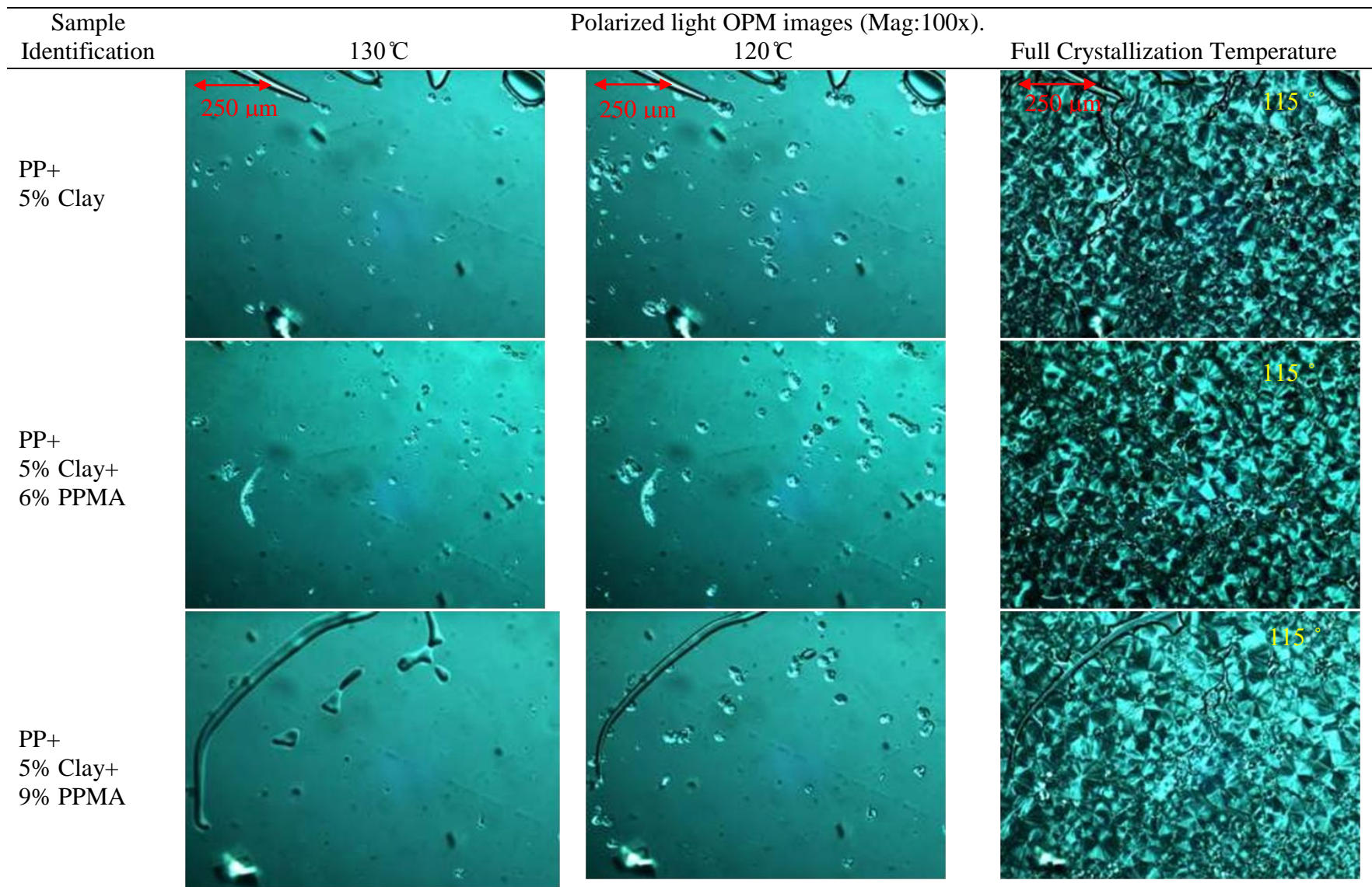


Figure 5.42: Spherulitic morphology of unoriented PPNCs with 5% clay

Spherulitic size of different PPNC samples is shown in Figure 5.43 and 5.44 for constant clay content, and Figure 5.45 and 5.46 for a constant PPMA content. At 3% clay loading, the spherulites size is reduced from 90 to 30 μm as the level of PPMA increased from 0 to 3%. Further addition of PPMA, increased the spherulites size to 70 μm at 6 and 9% of PPMA contents.

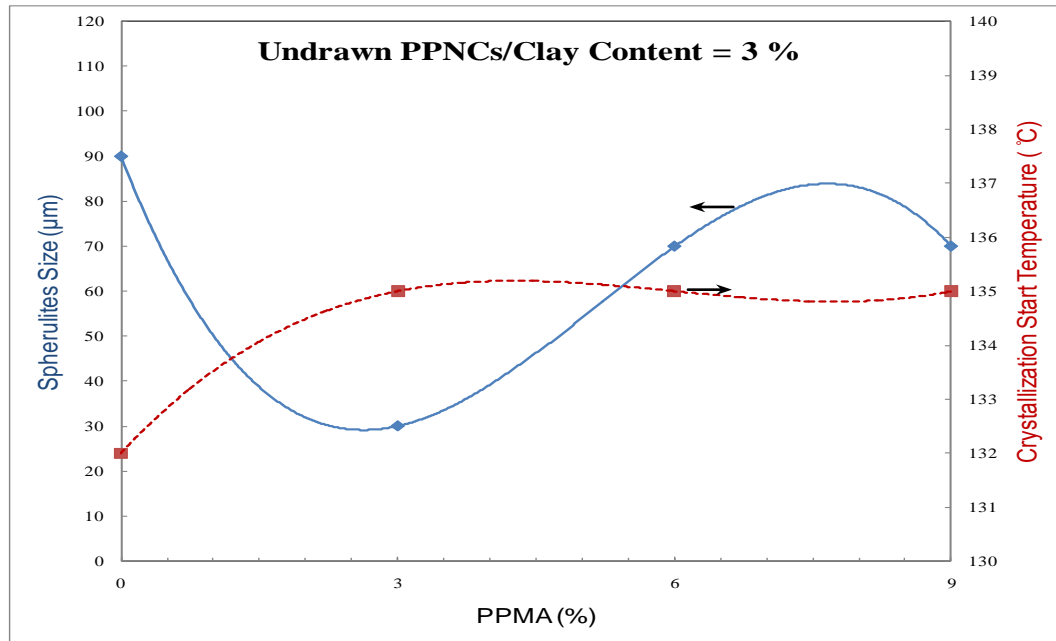


Figure 5.43: Spherulitic size and crystallization start temperature of undrawn PPNCs with 3% clay

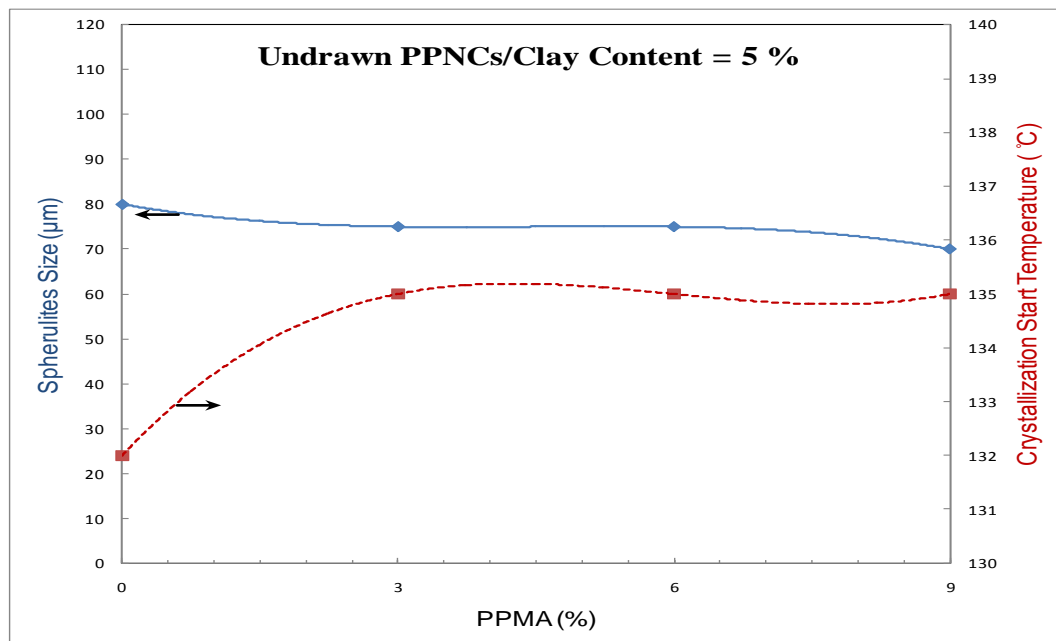


Figure 5.44: Spherulitic size and crystallization start temperature of undrawn PPNCs with 5% clay

In the absence of the compatibilizer (Figure 5.45), the spherulites size of the 3% clay loading was reduced modestly and then kept in the same region for 5% clay loading. Addition of PPMA reduces the spherulites size of the 3% clay content superiorly as shown in Figure 5.46. But return to the modest size with an equiaxed shape.

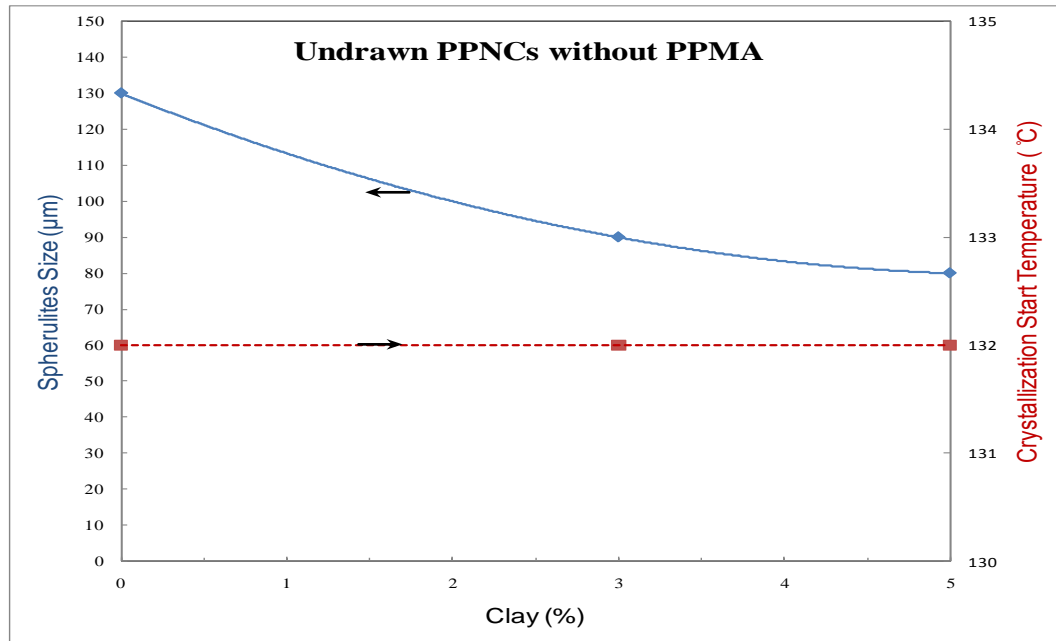


Figure 5.45: Spherulitic size and crystallization start temperature of undrawn PPNCs without PPMA

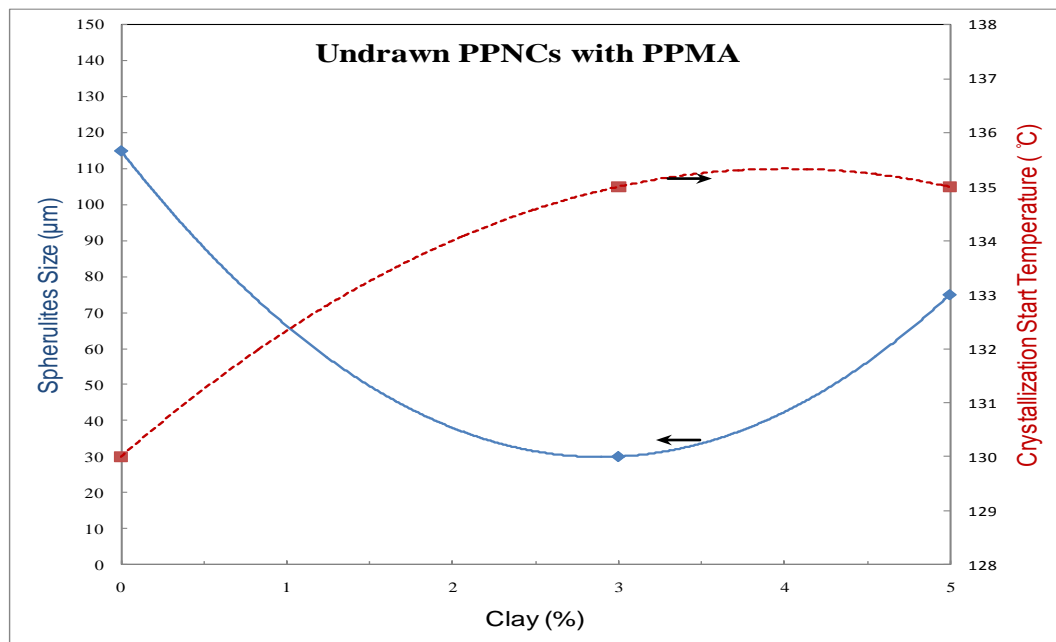


Figure 5.46: Spherulitic size and crystallization start temperature of undrawn PPNCs with PPMA

These differences in the spherulitic structure may affect the tensile modulus and fracture toughness of PPNCs. For pure polymer material, most studies agree that smaller spherulite size will lower the modulus and give higher toughness [140-144] because smaller crystals are prone to absorb crack energy; on the contrary, big spherulites tend to form local stress at the boundary, which makes the material become brittle. From the other side, chain ends and molecular imperfections tend to collect in the amorphous portion between crystallite lamellae, so very few tie molecules may exist, and a brittle material of low modulus results. On the other hand some studies suggest that small spherulites give higher modulus and lower toughness where there are few tie molecules but a high concentration of impurities that is developed between spherulites [145, 146].

In PPNCs, obtaining these smaller spherulites by the use of nucleating agent of clay particles with good bonding to the non-polar PP matrix can give a more uniform structure that can improve the modulus due to the high stiffness of inorganic particles.

5.6.2 Spherulitic morphology of drawn PPNCs

Before deformation, looking at PP morphology, we see that crystals are chain folded lamellae in a spherulitic overall arrangement. Amorphous components reside at the lamellar surfaces in the form of loose cilia or tie molecules. Tie molecules connect neighbouring spherulites. When we deform such a structure, we expect to produce changes in the crystal lattice. Additionally, we can force lamellae to slip past one another, and we can break them up by pulling and unfolding of chains that become highly aligned in the direction of the stretch, producing a fibrillar structure [147]. With small

spherulites there is an increase in ductility when T_g is below the drawing temperature and that spherulites might be destroyed, providing chain end and large ratio of tie molecules with high longitudinal elastic modulus [148].

The effect of annealing highly drawn fibres is to more or less destroy the stacked microfibrillar structure and to return the initial structure. Similarly, if the drawing process is very slow and occurs at high enough temperatures, realignment of the torn off fragments tends to reconstruct the lamellar morphology. It follows, then, that the cold drawing processing variables (rate of extension and temperature), as well as initial morphology and molecular weight and distribution, play decisive roles in fibre drawing.

Figure 5.47 and 5.48 show the optical micrographs for the oriented PPNC samples. In PP material at room temperature, the crystallites clearly deform as the draw ratio is increased with a change in the diameter and shape of the PP spherulites. Very fine structure was obtained for the sample with clay without PPMA. In contrast, the morphology of the samples with PPMA appears as a fibrous structure and seems to not show spherulites. However, there is a difficulty in taking the micrographs at higher temperatures, due to the destruction of orientation, limiting the ability to get a well defined structure of the oriented samples.

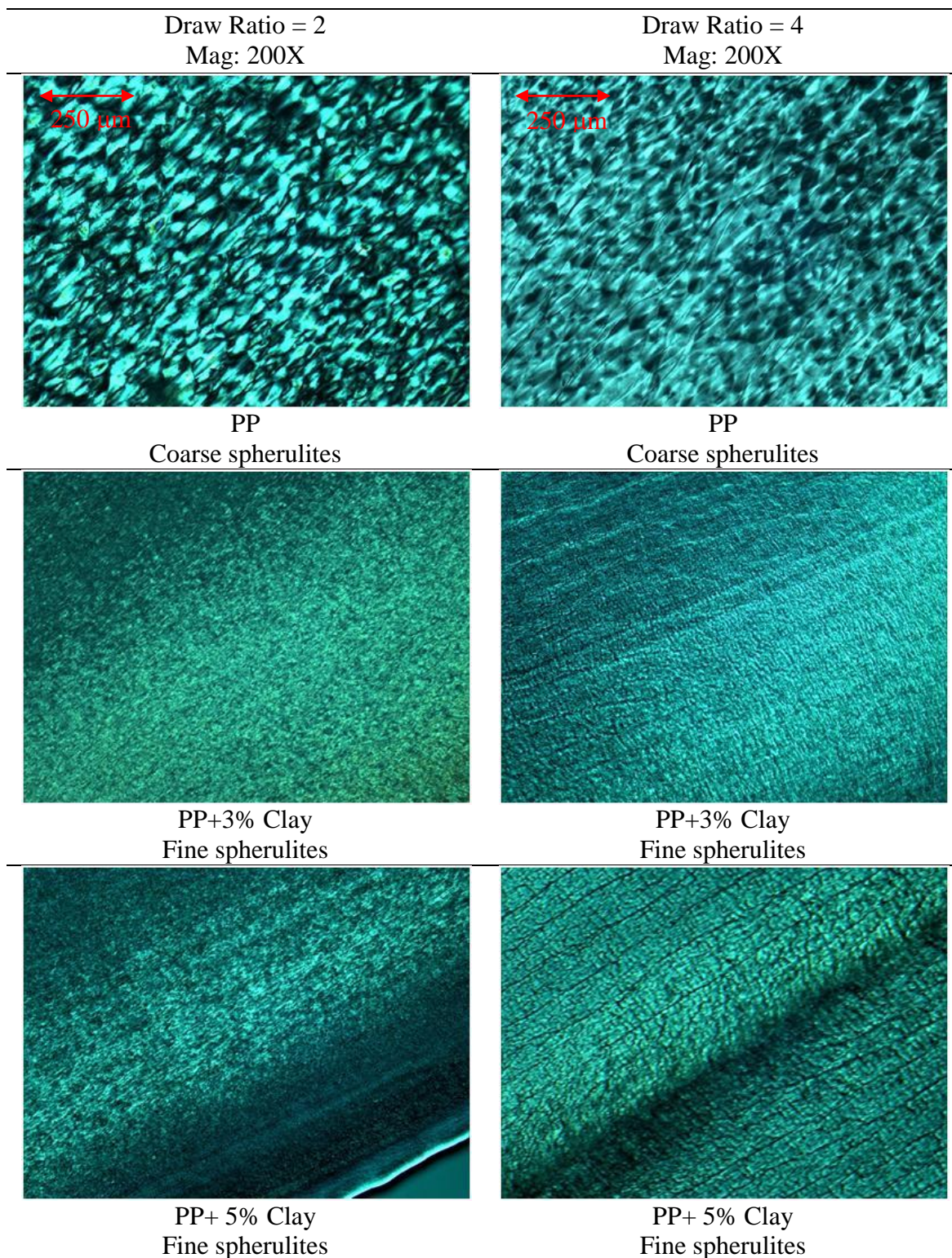


Figure 5.47: Spherulitic morphology of oriented PPNCs without PPMA at different draw ratios

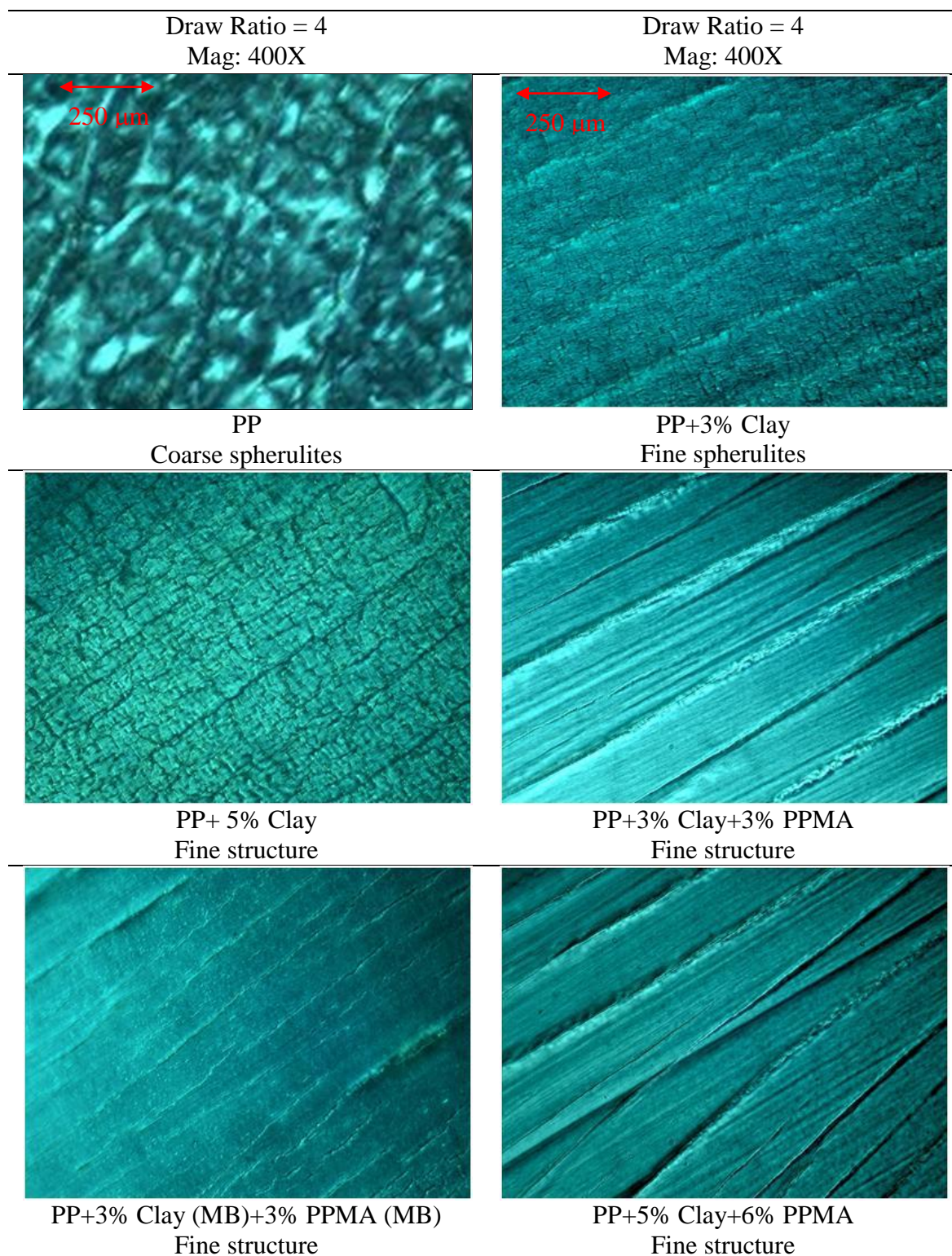


Figure 5.48: Spherulitic morphology of oriented PPNCs ($\lambda=4$)

Finally, for drawn and undrawn PPNC samples, the acceleration of crystallization and the decrease of spherulite size in nanocomposites result from the observed enhancement of spherulite nucleation by clay particles, reported

already in references [26, 61, 66, 68, 149-151]. However, it is difficult to judge whether the increase of nucleation and the acceleration of crystallization should be attributed to exfoliated or nonexfoliated PPNC matrix, as reported in reference [151]. If we consider that hundreds of MMT particles are required to nucleate one PP spherulite [66], it is worth noting that addition of the clay particles with existing of the compatibilizer contribute continually in enhancement of spherulite nucleation till all PP spherulites are fully nucleated, which might be controlled by shear.

It is difficult to relate the size of spherulites directly to the mechanical properties of the drawn and undrawn PPNCs. Many factors such as degree of crystallinity, compatibilization, clay contents, possible existence of voids and shear induced play together to govern the mechanical properties. Moreover, the drawing temperature, speed or draw ratios, and the degree of melt solid orientation should be considered for drawn samples.

5.7 Wide Angle X-ray Diffraction and Transmission Electron

Micrographs

Since the intercalation of clay layers by non-polar PP is thermodynamically unfavourable, PPMA was used to enhance the dispersion of clay in PP matrix. PPMA would enter into the silicate layers due to interactions between the maleic anhydride group and the alkyl ammonium salt thereby expanding the silicate layers that can be measured by WAXD. Results of the WAXD include even the composites without PPMA to look for possibility of the macromolecules to enter the expanded layer by the shear thus dispersing the clay into the polymer matrix. The results of WAXD accompanies with TEM

micrographs and analyses of undrawn and drawn samples to clarify the nanoscale structure of the intercalated PPNCs.

5.7.1 WAXD and TEM micrographs of undrawn PPNCs

Meanwhile all WAXD results are summarized in Table 5.3, Figures 5.49 and 5.50 show the XRD patterns and TEM images of the PPNC samples that contain 3% and 5% of clay loading with different PPMA contents. Appendix F gives TEM samples images. All WAXD graphs are compared to the peak of the pure clay, where the 001 plane peak was observed at $2\Theta = 2.88^\circ$, and to the non-existing peak of pure PP material. The intensity of the peak broadening of the PPNC samples is related to the broadening of the pure clay material, which may give a general idea about the degree of stacks aggregation in different composites.

In absent of the compatibilizer, the observations indicate very little change in the basal spacing when 3% of clay loading is involved and no change for the 5% clay loading, which is due to the incompatibility of the polar hydroxyl groups on the surface of the clay layers and the nonpolar PP. In contrast, the peak broadening is doubled for PPNCs with 3% clay loading. This might be explained by reduction of the number of stacked clay platelets in the non-crowded packed matrix by the effect of shear and/or introduction of functional groups of PP to the polar MMT. This broadening of the peak is not observed further as the clay loading is increased in the busy matrix of 5 %.

For 3% clay loading, a distinct shift to lower angle and peak broadening are observed as the PPMA is added at the 3 % level. This enhancement in the degree of exfoliation or intercalation degree reaches the maximum at 6% PPMA

and shows no further improvement at 9% PPMA contents. Similar results at a lower level were observed for 5% clay loading as 3% PPMA is added. As compared to all 5% clay loading composite, 6% PPMA content achieved the highest d-spacing and broadening of the peak. Again, high PPMA content of 9% did not enhance the intercalation degree of PPNCs with 5% clay. These results are verified by the images of TEM with magnification of 1 μm and 200 nm. The higher d-spacing PPNC samples are the better distribution image. These peaks shifting clearly indicate an intercalation structure in these composites that would enhance PP/clay affinity and polymer chain diffusion into the clay galleries.

In TEM micrographs, the clay appears as the dark areas. It can be clearly seen that clay particles without compatibilizer are poorly dispersed as aggregates in the continuous polymer phase, as shown in Figure 5.49 and 5.50 for 3 and 5% clay loading. With the WAXD results, the state of intercalation or partial exfoliation is therefore demonstrated by the TEM observations for other PPNCs that contain PPMA. TEM results and comparisons of micrographs are discussed and analyzed in section 5.7.3 below.

The sample produced from one-step master batch mixing has 3.54 nm of interspacing layers as compared to 3.14 nm for the pure clay. Thus the interspacing of silicate layers was swollen to large distance by the intercalated polymer. However, this increment is not accompanied with a good peak broadening characteristic as an indication of bad distribution of the tactoids intercalated clay particles in the PP matrix and critically of using a manual mixing even for a dispersed clay particles. Therefore, the two-stage mixing, where the master batch is distributed continuously from the second extruder feeder, is an essential to achieve a successful interaction and distribution of the

PPNCs. This result is confirmed by TEM micrograph (Figure 5.49), which shows very large tactoid structure. This kind of structure might influence the consistency of a property measurement from area to another for the same composite material.

TEM micrographs clearly show the agglomeration of clay platelets of samples without compatibilizer. Higher agglomeration with clay chunks is seen as the clay content increases to 5 %. Good distribution with possible intercalation and partial exfoliation systems are observed at 3 % clay loading with different PPMA contents. Size of the clay agglomerates in 5% clay systems are much reduced as PPMA is added and show good images for 6 and 9 % PPMA contents.

These combination results of WAXD and TEM are evidence that PPMA was able to intercalate into the galleries and caused the increase in d-spacing in both 3% and 5% clay systems that show large tactoid structure without using PPMA. However, the angle shift in WAXD was minimal in 5% clay system with PPMA as an indication of that the clay agglomeration become severe and microtactoids are shown up in TEM micrographs.

Table 5.3: Wide Angle X-Ray Diffraction Analysis of PPNCs

Sample Identification	d001 Angle (Degrees)	Basal Spacing (nm)	<u>Intensity Peak Broadening Angle</u> Intensity Peak Broadening Angle of Clay
Clay	2.88	3.14	1.0
PP+ 3% Clay	2.71	3.26	2.03
PP+ 5% Clay	2.87	3.15	0.99
PP+3% Clay+3% PPMA	2.24	3.61	2.26
PP+5% Clay+3% PPMA	2.63	3.32	1.22
PP+3% Clay+6% PPMA	2.16	3.67	2.86
PP+5% Clay+6% PPMA	2.48	3.43	1.33
PP+3% Clay+9% PPMA	2.24	3.61	2.68
PP+5% Clay+9% PPMA	2.55	3.38	1.29
PP+3% Clay (MB)+3% PPMA (MB)	2.35	3.54	1.69

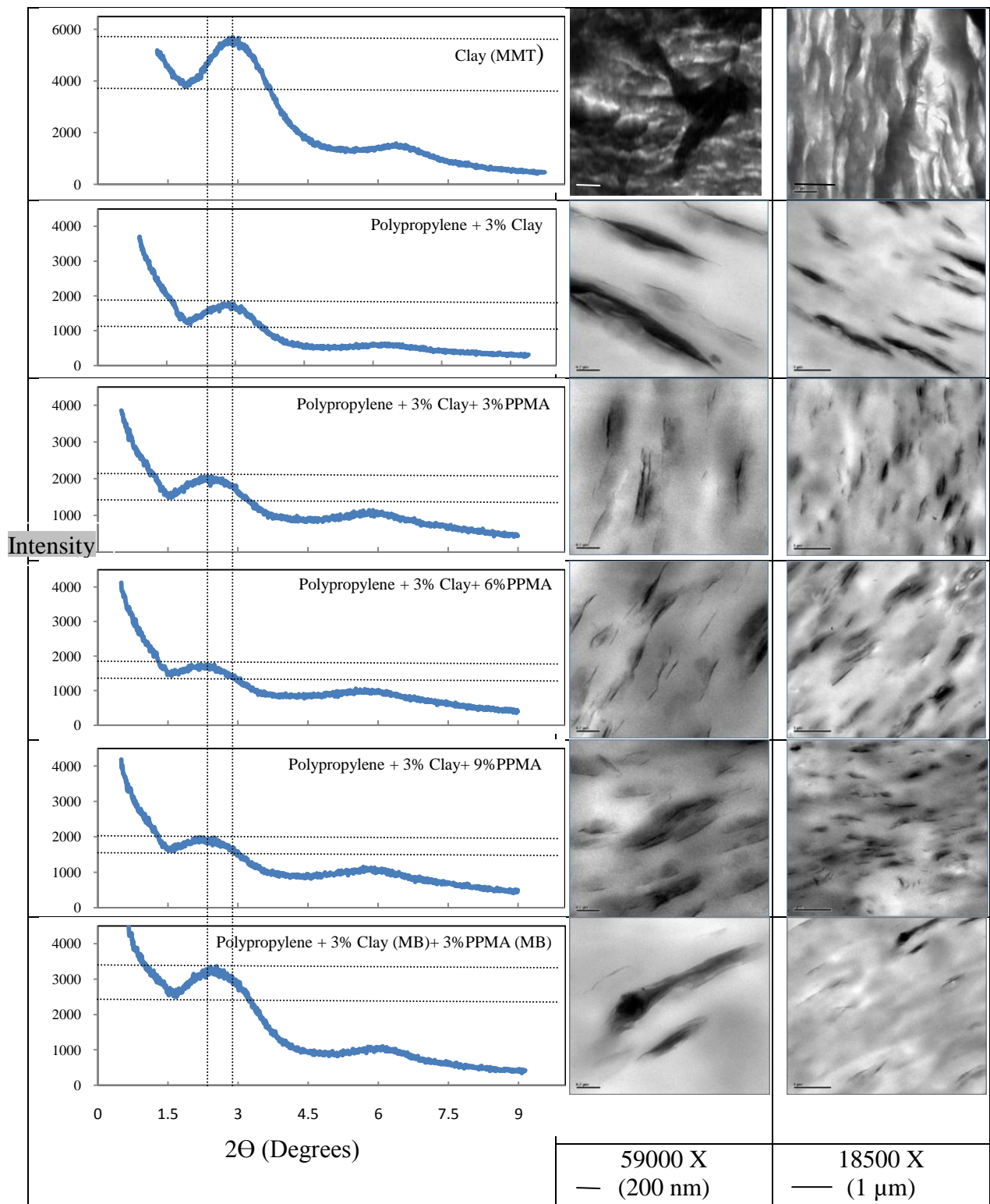


Figure 5.49: WAXD and TEM of undrawn PPNCs with 3% clay

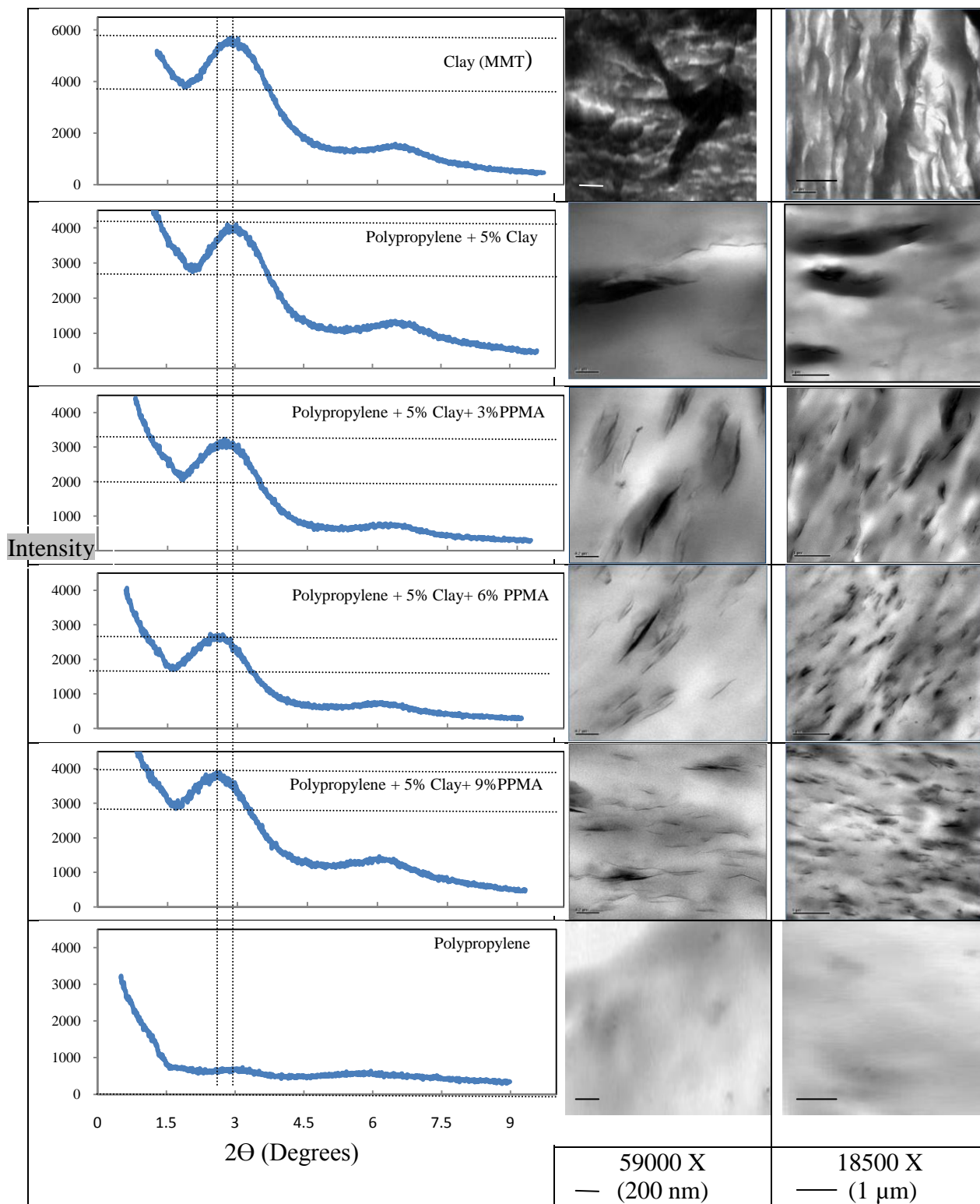


Figure 5.50: WAXD and TEM of undrawn PPNCs with 5% clay

5.7.2 TEM micrographs of drawn PPNCs

The TEM micrographs for drawn PPNC samples show the clay particles with well aligned ordered in the drawn direction and regularly spaced particles, as shown in Figure 5.51 for both 3 and 5% clay samples with compatibilizer. On the contrary, clay particles of PPNC samples without compatibilizer have similar alignment, but with large scale particles. These results are considered to be the effect of the penetration of PP, with help of the PPMA, into the interlayer spacing of the particles that eventually occurs and leads to the formation of such distribution of regularly spaced particles.

The sample produced from one-step master batch mixing is similar to the PPNC ones with compatibilizer in behaviour of intercalation or interlayer spacing gallery as shown in WAXD result, but similar to these ones without compatibilizer in distribution as presented in TEM images. Therefore, these results emphasize the importance of using a complementary technique like TEM to support the results of WXR. TEM gives a small volume characterization but with a whole representation of the materials.

The produced orientation of clay particles in the undrawn injection moulded samples are heightened after drawing process, as shown in TEM images of oriented sample (Figure 5.51). This orientation could contribute promotionally in enhancement of the mechanical properties of PPNCs.

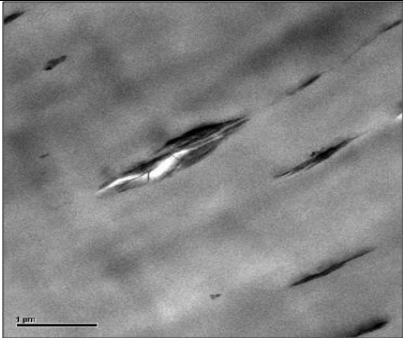
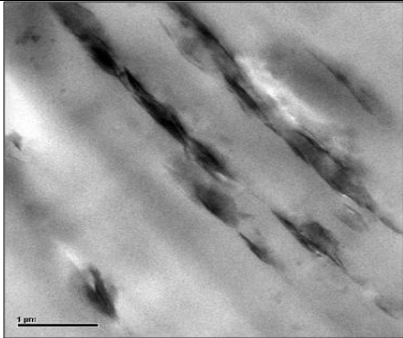
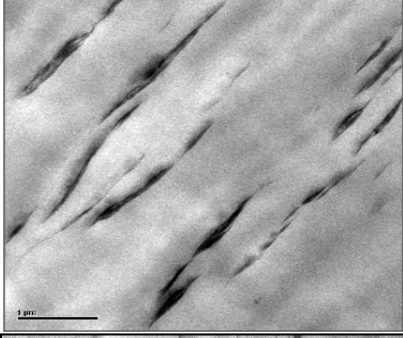
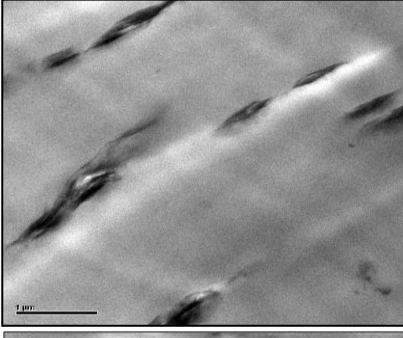
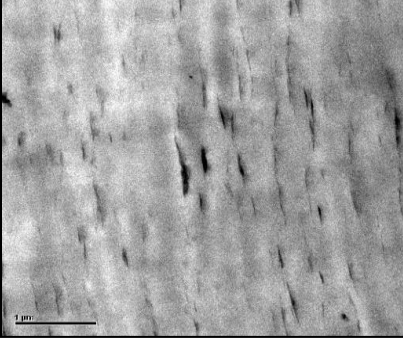
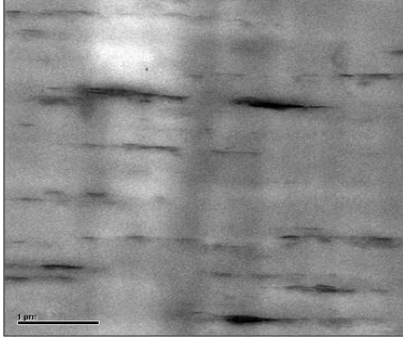
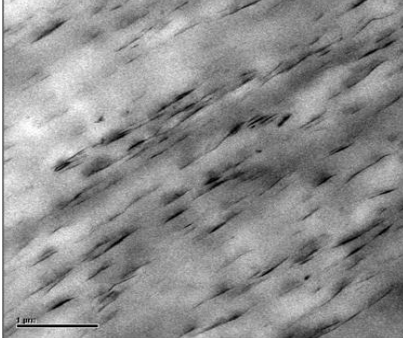
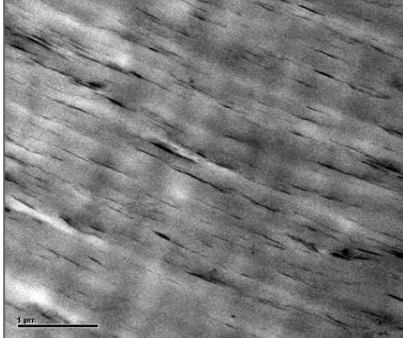
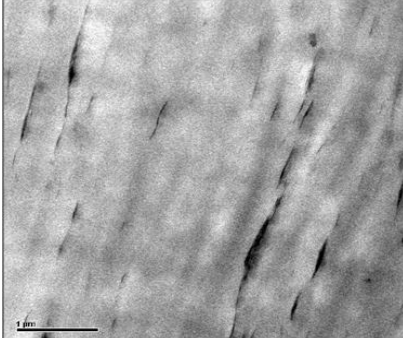
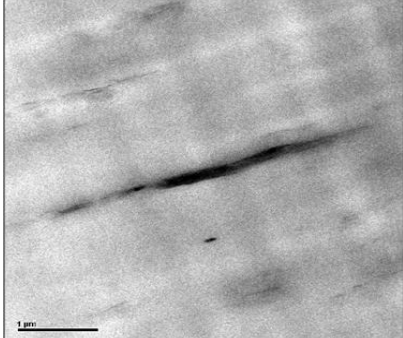
Sample Identification	Draw Ratio	Draw Ratio
	$\lambda = 2$ —— (1 μm)	$\lambda = 4$ —— (1 μm)
PP+3% Clay		
PP+ 5% Clay		
PP+3% Clay+3% PPMA		
PP+5% Clay+6% PPMA		
PP +3% Clay (MB) +3% PPMA(MB)		

Figure 5.51: TEM photos of drawn PPNCs (scale bar is 1 μm)

5.7.3 TEM micrographs analyses of undrawn and drawn PPNCs

The feret diameter and average number of clay particles are used for analyses of the TEM micrographs. The obtained tactoid structure in many prepared samples does make the use of the normal diameter non-expressive measurement in comparison between samples due to the significant fluctuation within the same diameter of the one tactoid particle. These analyses are done for the undrawn samples and drawn samples with 2 and 4 draw ratios.

Table 5.4 summaries TEM micrographs for undrawn and drawn samples. It can be seen clearly in Figures 5.52 and 5.53 that the number of particles is increased tremendously by increase the PPMA levels. This increment reaches to 4 and 13 times for the composites with 3% and 5% clay contents, respectively. For both composites, higher number of particles is accompanied with a reduction in feret diameter size. The reduction in diameter found to be stable after 3% PPMA level for the 3% clay content systems and after 6 % for the 5% clay content systems.

The 5% clay system shows more clay stacks particles at lower percentages of PPMA and reach to a very comparable number of particles as compared to the 3% clay system (with consideration of different quantity of both systems per unit area). The interesting result of feret diameter of the well compatibilized clay systems, in the range of low clay contents (1 - 5%), it can be assumed that the diameter of the tactoids is not big influenced by the clay content but rather by the PPMA content and shear introduced to the PPNCs system.

These results shows obviously the importance of the compatibilizer to reduce the aggregation areas that might be built between the non-preferable systems and confirm the dispersion state, which is reported in WAXD results.

Table 5.4: Transmission Electron Microscopy Analysis of drawn and undrawn PPNC Samples

Sample Identification	Draw Ratio, $\lambda=1$		Draw Ratio, $\lambda=2$		Draw Ratio, $\lambda=4$	
	Avg. Feret Diameter, FD μm	Avg. No. of Particles per $2.25 \mu\text{m}^2$	Avg. Feret Diameter, FD μm	Avg. No. of Particles per $2.25 \mu\text{m}^2$	Avg. Feret Diameter, FD μm	Avg. No. of Particles per $2.25 \mu\text{m}^2$
PP+3% Clay	0.57 ± 0.39	6.0	0.49 ± 0.49	6.0	0.53 ± 0.49	5.2
PP+ 5% Clay	0.61 ± 0.62	3.7	0.76 ± 0.66	5.2	0.925 ± 0.63	2.5
PP+3% Clay+3% PPMA	0.31 ± 0.16	17.6	0.26 ± 0.17	22.6	0.27 ± 0.17	19.8
PP+5% Clay+3% PPMA	0.31 ± 0.16	17.0				
PP+3% Clay+6% PPMA	0.29 ± 0.19	21.0				
PP+5% Clay+6% PPMA	0.22 ± 0.13	24.0	0.32 ± 0.19	27.0	0.27 ± 0.15	35.0
PP+3% Clay+9% PPMA	0.222 ± 0.12	26.0				
PP+5% Clay+9% PPMA	0.241 ± 0.165	50.0				
PP +3% Clay (MB) +3% PPMA(MB)	0.43 ± 0.31	7.5	0.35 ± 0.24	11.6	0.34 ± 0.22	14.8

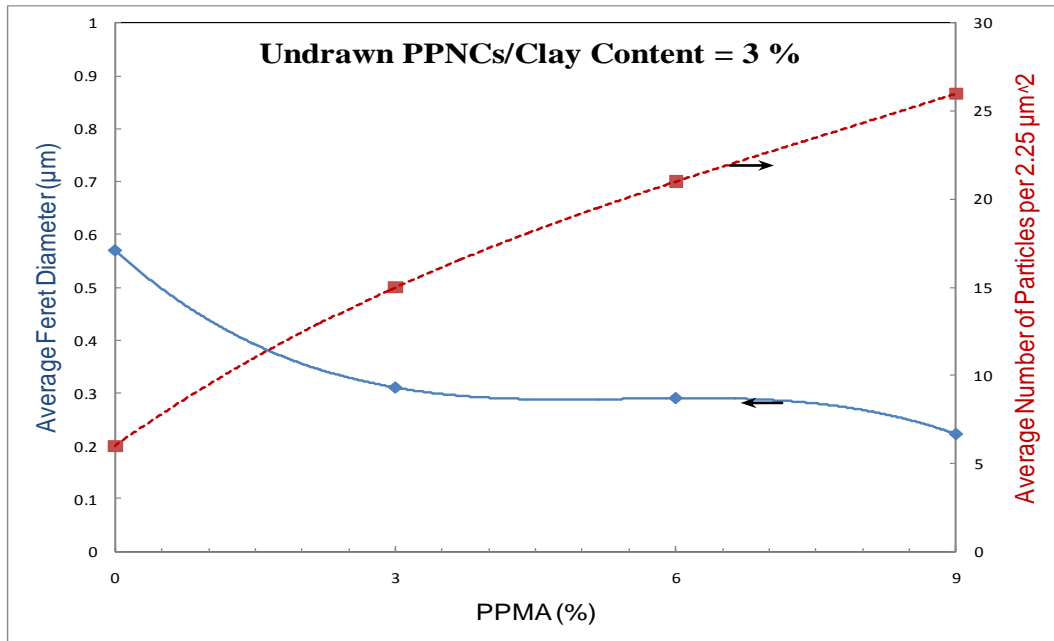


Figure 5.52: Feret diameter and number of particles per unit area at different PPMA contents of undrawn PPNCs with 3% clay

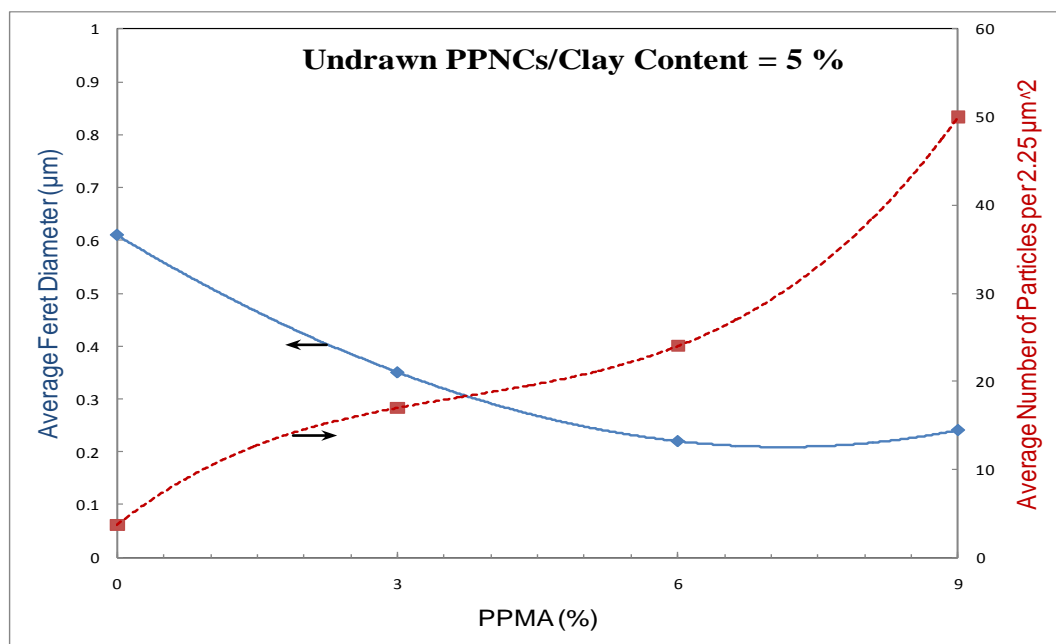


Figure 5.53: Feret diameter and number of particles per unit area at different PPMA contents of undrawn PPNCs with 5% clay

The effect of drawn process of PPNCs on the feret diameter and number of particles per unit area with and without PPMA, as analyzed in Figures 5.54 to 5.57, shows in general no or a minor effect on the diameter and number of particles. However, the notable increase after drawing in the feret diameter of the

5 % clay loading without PPMA might be attributed to the microvoids that can introduce some errors to the diameter measurement. Thus the average number of particles remains at the same magnitude.

On the other hand, the compatibilized samples are remarked to increase in the number of the particles with drawing process. If we consider that such static drawing process can not cause any reduction in the stacked clay platelets as it may happen in the dynamic ones, such as in extrusion and injection processes. This increment might be explained by the moving of linked MMT particles to the middle core of the drawn samples; where the images were taken for all undrawn and drawn samples. This annotation may be supported by the similar obtained feret diameters of undrawn and drawn samples.

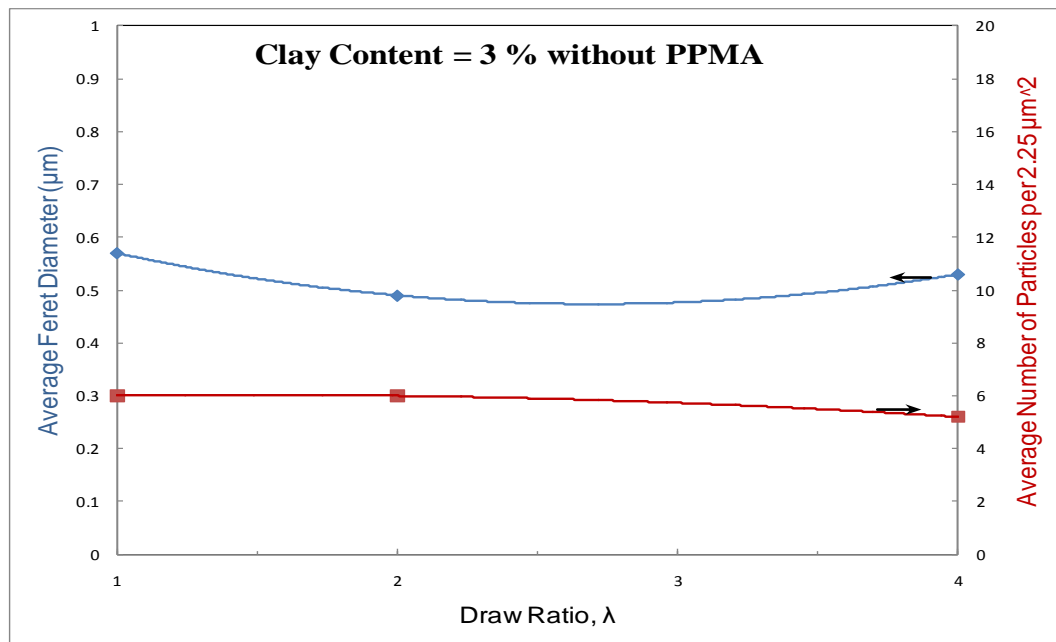


Figure 5.54: Feret diameter and number of particles per unit area vs. draw ratio of PPNCs with 3% clay

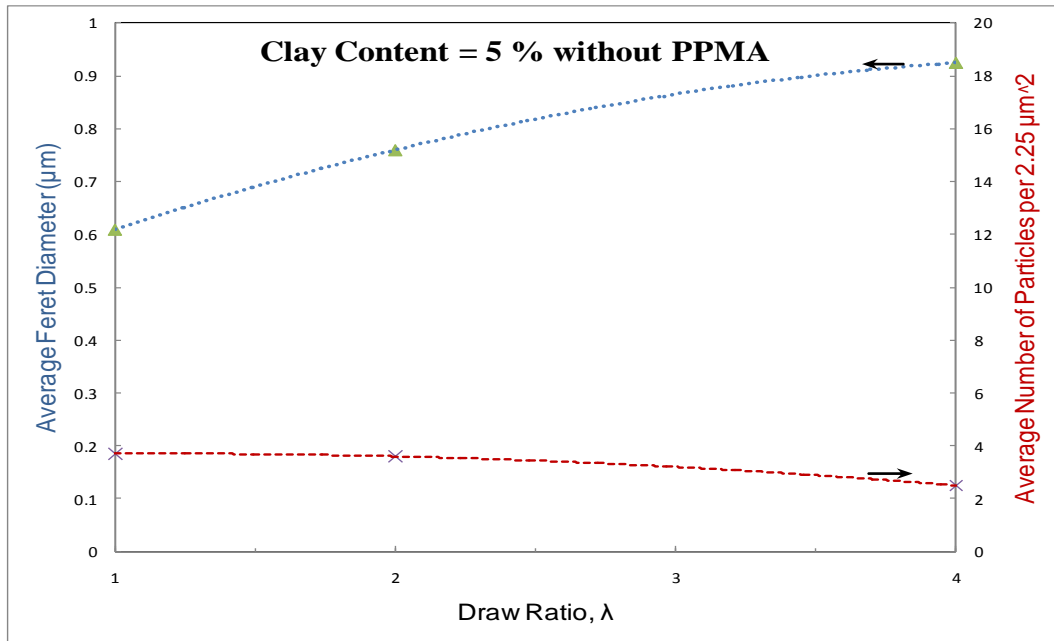


Figure 5.55: Feret diameter and number of particles per unit area vs. draw ratio of PPNCs with 5% clay

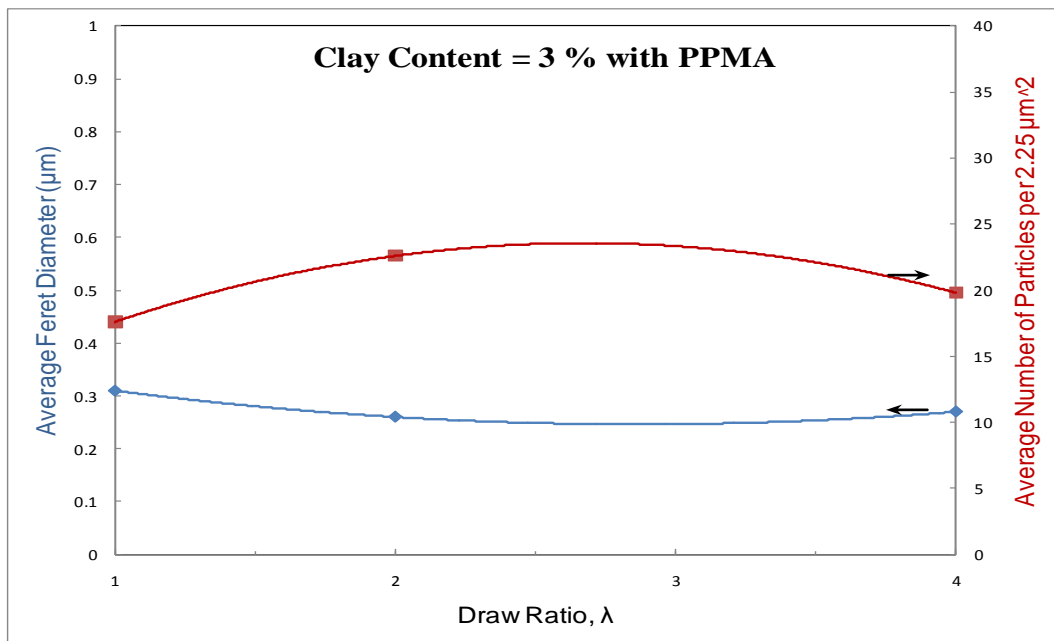


Figure 5.56: Feret diameter and number of particles per unit area vs. draw ratio of PPNCs with PPMA and 3% clay content

Comparison of the two compatibilized samples that were produced by either one or two-step master batch compounding is shown in Figure 5.58. It is clearly shown that the one produced by two-step compounding achieves more than double number of particles and lower diameter than the one-step procedure. Same tendency are observed as both samples are drawn. Both samples exhibit an

increase in the number of particles, accompanied by a slight lower diameter as draw ratio increases. The different obtained distribution and sample uniformity is a sign that more mixing, in present of compatibilizer, would help the formation of better PPNCs by breaking up clay particles.

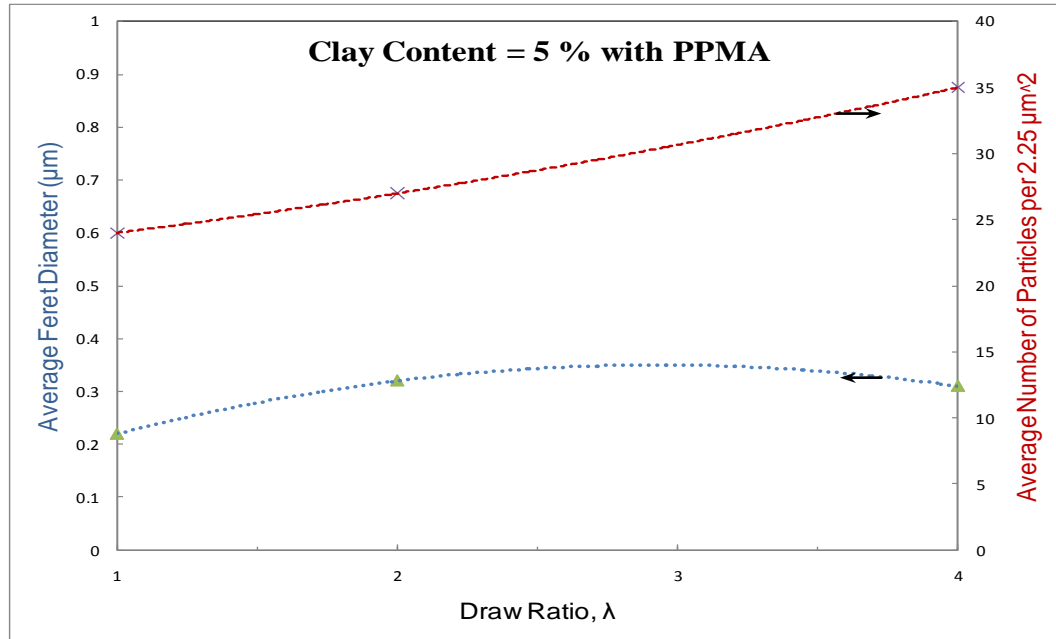


Figure 5.57: Feret diameter and number of particles per unit area vs. draw ratio of PPNCs with PPMA and 5% clay content

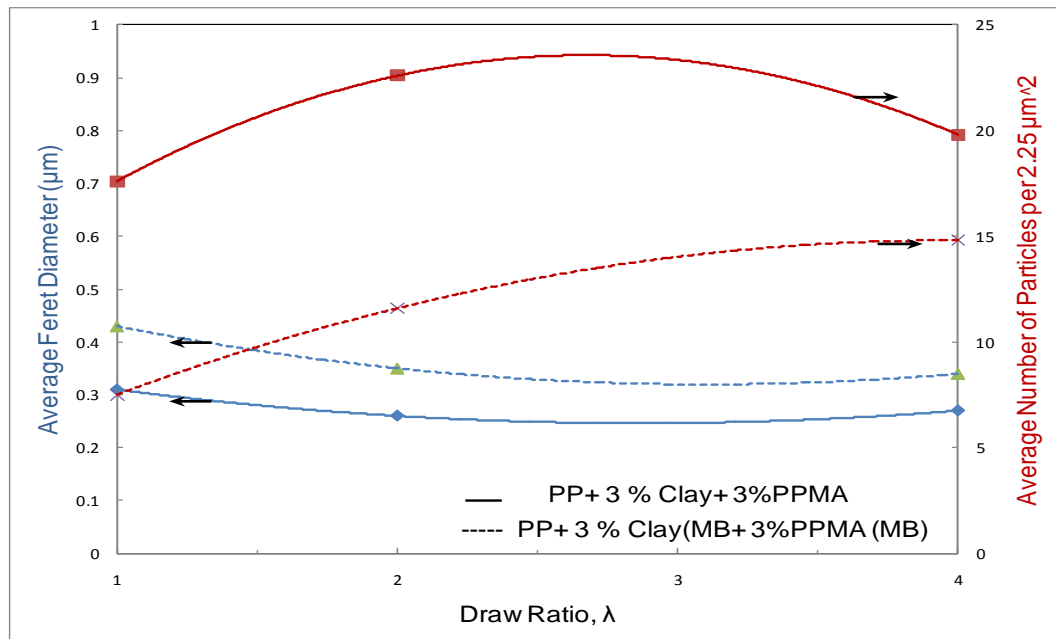


Figure 5.58: Feret diameter and number of particles per unit area vs. draw ratio of PPNCs prepared with different procedure of mixing

5.8 Tensile Video Extensometer of PPNCs

Figure 5.59 shows a room temperature stress-strain curve for sheet sample at strain rate 0.0158 1/min using a videoextensometer to obtain Young's modulus. It can be seen on the scale the small deformation at cross-head speed of 0.6 mm/min, which is the highest speed used for the compression sheet samples. All stress-strain curves are presented in Appendix H.

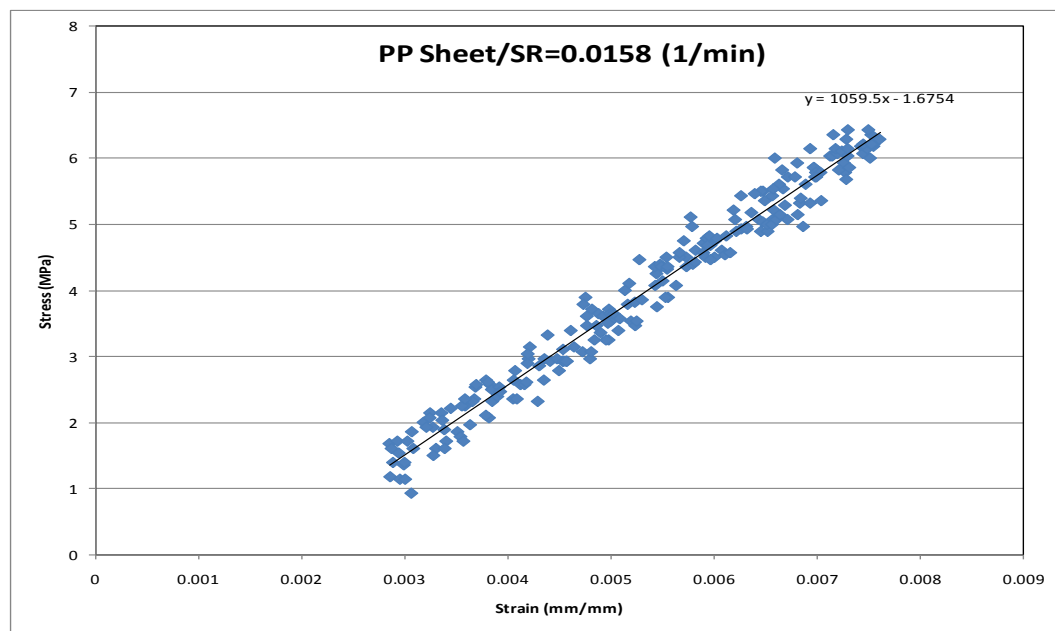


Figure 5.59: Stress-strain curve obtained using the video-extensometer at 0.0158 1/min strain rate

5.8.1 Tensile modulus of undrawn PPNCs

The modulus results of compression moulded sheets are shown in Table 5.5 at different PPMA/MMT contents and strain rates. The PP with 3% clay and 3% PPMA shows the greatest improvement among all 3% composites systems (42% more than PP, which is indicated by a dot in the graphs). In contrast, the greatest improvement in 5% systems is found to be for the one with 6% PPMA loading (50 % more than PP). These absolute increments are verified by similar tendency obtained in injection moulded bars for the mentioned 3% and 5 %

systems (40% and 50% over the pure PP system, respectively). The results of the injection moulded bars are shown in Table 5.6.

Table 5.5: Tensile Modulus of undrawn Compression Moulded Sheets of PPNCs

Sample Identification	Tensile Modulus, MPa		
	Strain Rate 1	Strain Rate 2	Strain Rate 3
PP	907 ±6	1006 ±9	1050 ±19
PP+3% Clay	1043 ±55	1197 ±42	1230 ±47
PP+ 5% Clay	1089 ±11	1215 ±44	1210 ±44
PP+3% PPMA	974 ±89	1073 ±73	1113 ±62
PP+ 6% PPMA	878 ±23	986 ±22	1020 ±90
PP+ 9% PPMA	875 ±30	997 ±21	1023 ±17
PP+3% Clay+3% PPMA	1292 ±17	1354 ±8	1379 ±16
PP+5% Clay+3% PPMA	1334 ±56	1330 ±60	1332 ±51
PP+3% Clay+6% PPMA	1257 ±40	1305 ±63	1340 ±59
PP+5% Clay+6% PPMA	1362 ±31	1402 ±43	1412 ±29
PP+3% Clay+9% PPMA	1226 ±42	1253 ±48	1271 ±33
PP+5% Clay+9% PPMA	1249 ±63	1277 ±60	1326 ±48

Table 5.6: Tensile Modulus of undrawn Injection Moulded Sheets of PPNCs

Sample Identification	Tensile Modulus, MPa		
	Strain Rate 1	Strain Rate 2	Strain Rate 3
PP	1308 ±35	1335 ±53	1368 ±49
PP+3% Clay	1526 ±46	1571 ±49	1605 ±62
PP+ 5% Clay	1543 ±50	1619 ±26	1611 ±70
PP+3% PPMA	1383 ±41	1436 ±24	1471 ±25
PP+ 6% PPMA	1279 ±53	1352 ±42	1383 ±32
PP+ 9% PPMA	1269 ±67	1337 ±94	1350 ±98
PP+3% Clay+3% PPMA	1824 ±42	1884 ±30	1928 ±34
PP+5% Clay+3% PPMA	1883 ±48	1863 ±52	1877 ±38
PP+3% Clay+6% PPMA	1799 ±60	1819 ±32	1820 ±52
PP+5% Clay+6% PPMA	1970 ±62	1979 ±41	2024 ±29
PP+3% Clay+9% PPMA	1752 ±61	1765 ±63	1791 ±45
PP+5% Clay+9% PPMA	1791 ±37	1826 ±57	1851 ±77
PP +3% Clay (Pure) +3% PPMA(Pure)	1470 ±82	1477 ±63	1520 ±72
PP +3% Clay (MB) +3% PPMA(Pure)	1285 ±92	1346 ±84	1347 ±97
PP +3% Clay (MB) +3% PPMA(MB)	1363 ±64	1397 ±79	1443 ±89
PP Recycle 1	1309 ±25	1336 ±56	1371 ±72
PP Recycle 2	1318 ±42	1343 ±40	1377 ±37
PP Recycle 3	1336 ±27	1365 ±59	1398 ±73

Similar results of improvement were reported in previous works by Liu et al [13] and Deshmane et al. [65]. The particle bonding to the polymer molecules in presence of the compatibilizer might be the main reason of such enhancement. The 5% clay system with compatibilizer enhances the modulus further more although the WAXD peak showed a small shift in the angle and TEM showed more microtactoid structure. According to Kojima et al. [152], a region where the polymer molecules are restricted in mobility contributes to the improvement of the tensile modulus in a polymer/clay composite. Increasing the clay content will greatly constrain the polymer chains mobility so that the modulus is improved. This restriction in mobility is minimized when the PPMA is not involved so that a lower increment in tensile modulus was obtained for the 3% and 5% clay systems.

5.8.1.1 Tensile modulus of undrawn PPNCs at 0.0053 (1/min) strain rate

At low strain rate, Figure 5.60 shows that the tensile modulus of PPNCs increases rapidly with increasing PPMA content from 0 to 3%. But the increasing trend is less when the PPMA content increases beyond 3% for the composite systems with 5% clay loading and gets worse at 9% PPMA content. The 3% PPMA level was enough to have the highest modulus and possible that 3 % clay system is undergone to the preferable compatibilization effect. A discontinuation in this improvement is then noticed as the PPMA increases to level of 6 and 9%. This side effect of the PPMA can be seen clearly in Figure 5.61 that shows the change of tensile modulus versus the clay loading. The cross between the 3 and 6% PPMA curves might be explained by the difference in quantity of clay particles and its surface contact with the polymer matrix between the 3 and 5%

clay systems. Thus the 5% clay system required more quantity of PPMA to continue supporting the compatibilization function.

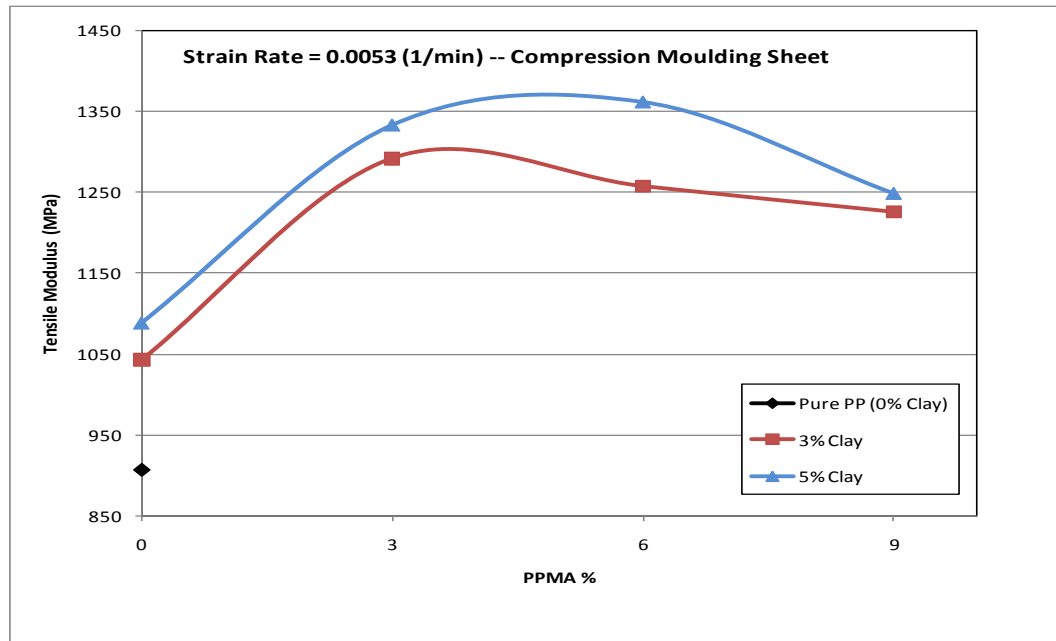


Figure 5.60: Tensile Modulus vs. PPMA contents for compression moulded sheets at 0.0053 1/min strain rate

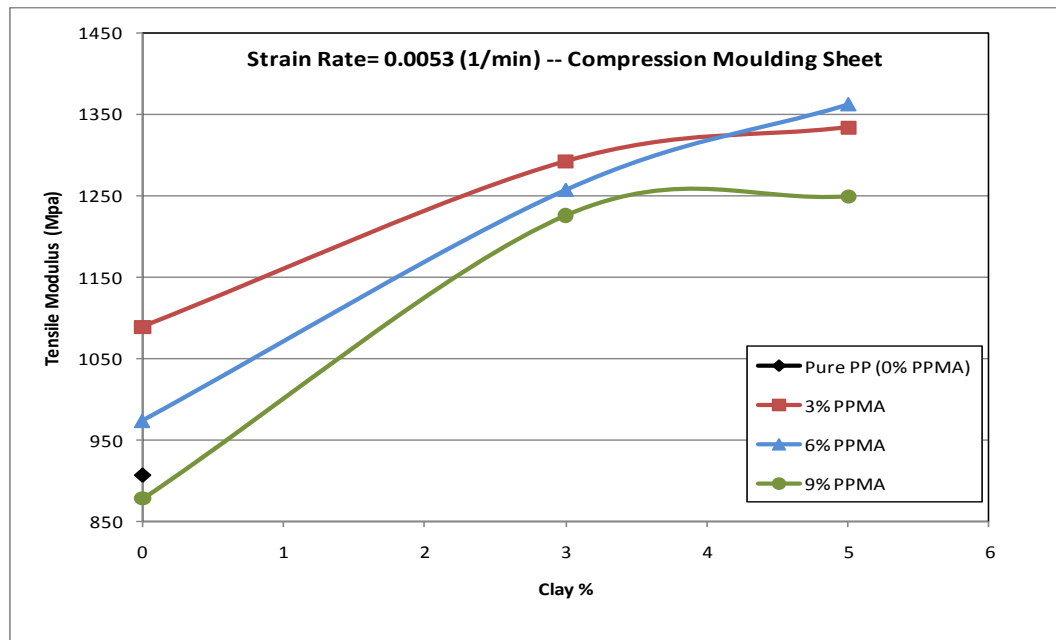


Figure 5.61: Tensile Modulus vs. clay contents of compression moulded sheets at 0.0053 1/min strain rate

Figure 5.62 and 5.63 shows similar results and observations of the tensile modulus are found for the injection moulded samples as compared to the obtained compression moulded sheets results. However, there was a shift with approximately 40-45% for all curves of PPNCs samples to higher absolute values of tensile modulus for the samples that were produced in injection moulding process.

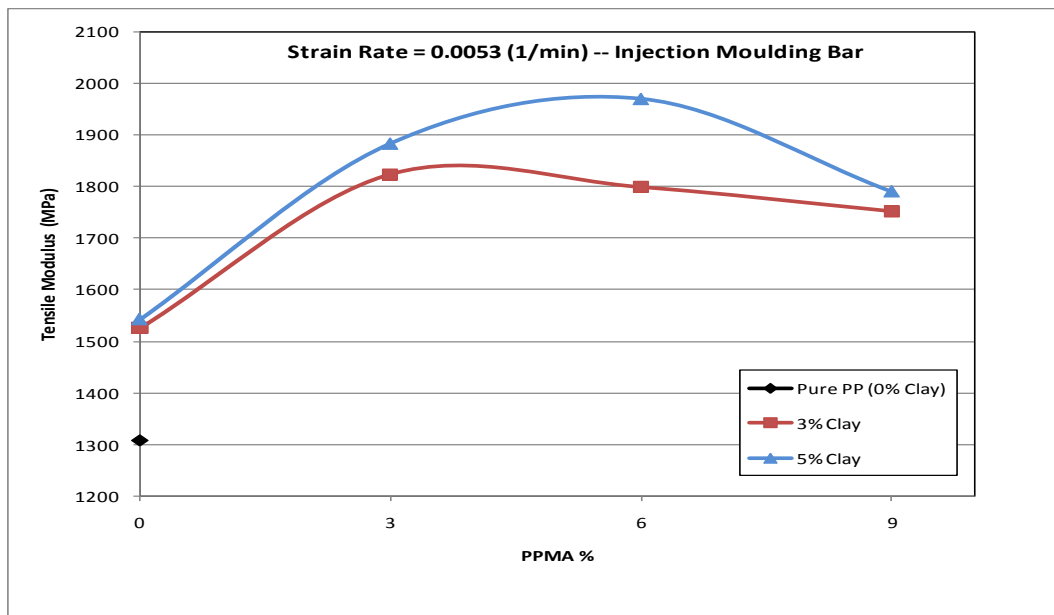


Figure 5.62: Tensile Modulus vs. PPMA contents of injection moulded bars at 0.0053 1/min strain rate

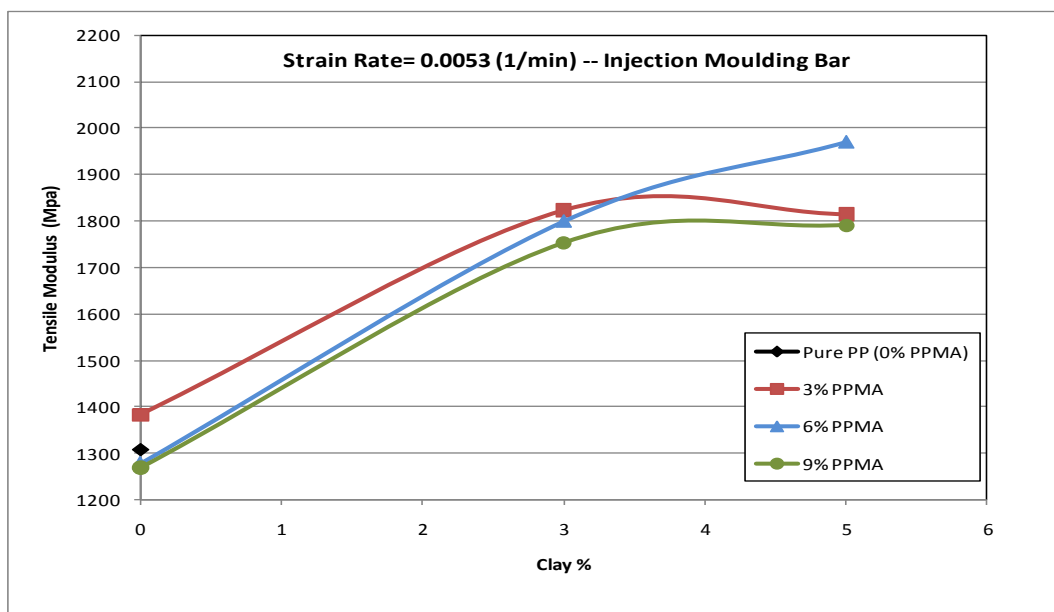


Figure 5.63: Tensile Modulus vs. clay contents of injection moulded bars at 0.0053 1/min strain rate

Although the modest level of stress in compression moulded sheets, the molecular orientation that can be involved in the injection moulding makes the difference in modulus results. The molten polymer melt undergoes high shear with stretched motion as the melt catches with unrestricted flow to the front and then moves outward to the mould cavity and freezes as soon as its temperature match the mould temperature. The orientation can be further exacerbated during the packing stage. This may impart high orientation to the producing injection moulded bars and thus enhance the absolute values of tensile modulus in all injection moulded samples over the compression moulded samples, as shown in Figure 5.64 for 0.0053 1/min strain rate.

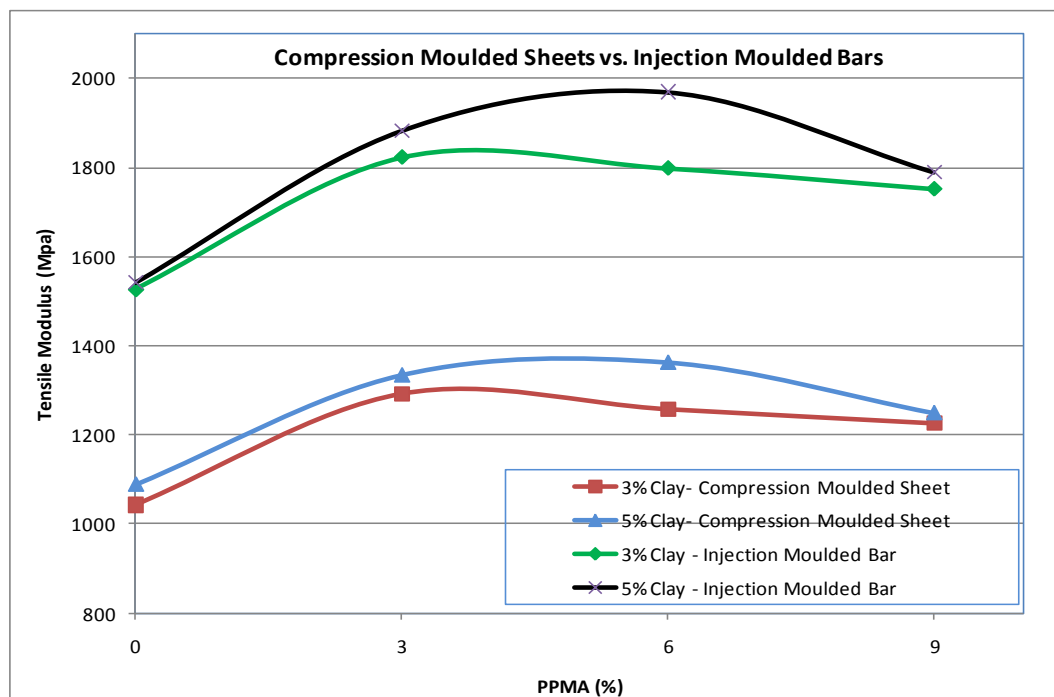


Figure 5.64: Tensile Modulus of compression moulded sheets vs. injection moulded bars at 0.0053 1/min strain rate

5.8.1.2 Tensile modulus of undrawn PPNCs at 0.0105 and 0.0158 (1/min) strain rate

As the strain rate is increased to 0.0105 and 0.0158 1/min, a corresponding increase in modulus is observed for pure PP and the PPNCs. The

percentage of increase in modulus is approximately between 3-5%. However, the same trend of tensile modulus behaviour of different PPNCs can be clearly seen in Figures 5.65 to 5.72 for both compression moulded and injection moulded samples. Slower rate of testing will permit the molecule to respond flexibly and demonstrate lower modulus, while faster rates of testing will simulate stiffer molecules and produce higher modulus.

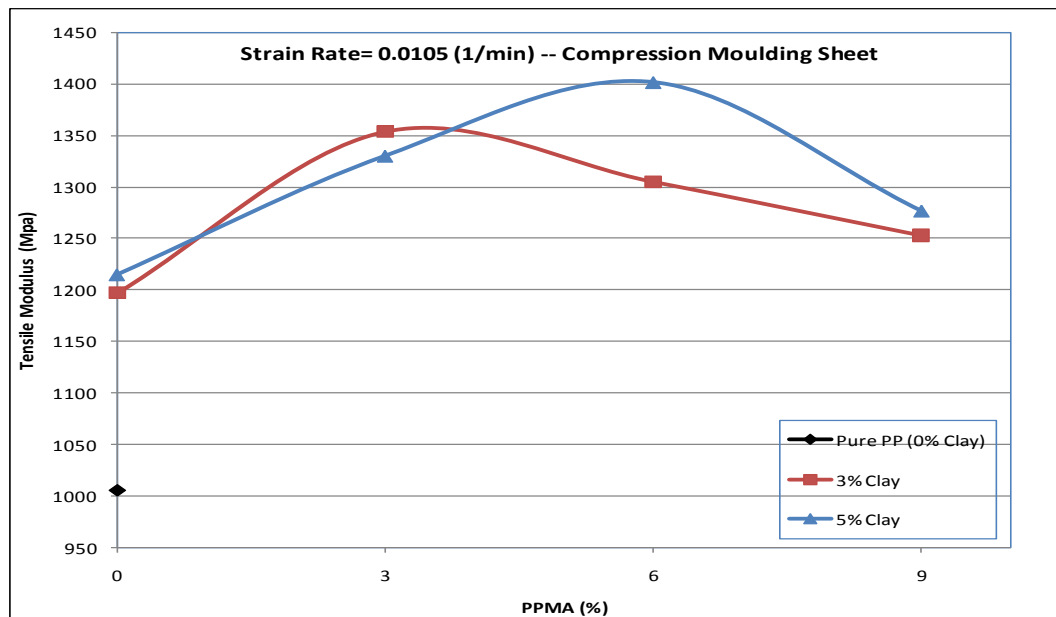


Figure 5.65: Tensile Modulus vs. PPMA contents of compression moulded sheets at 0.0105 1/min strain rate

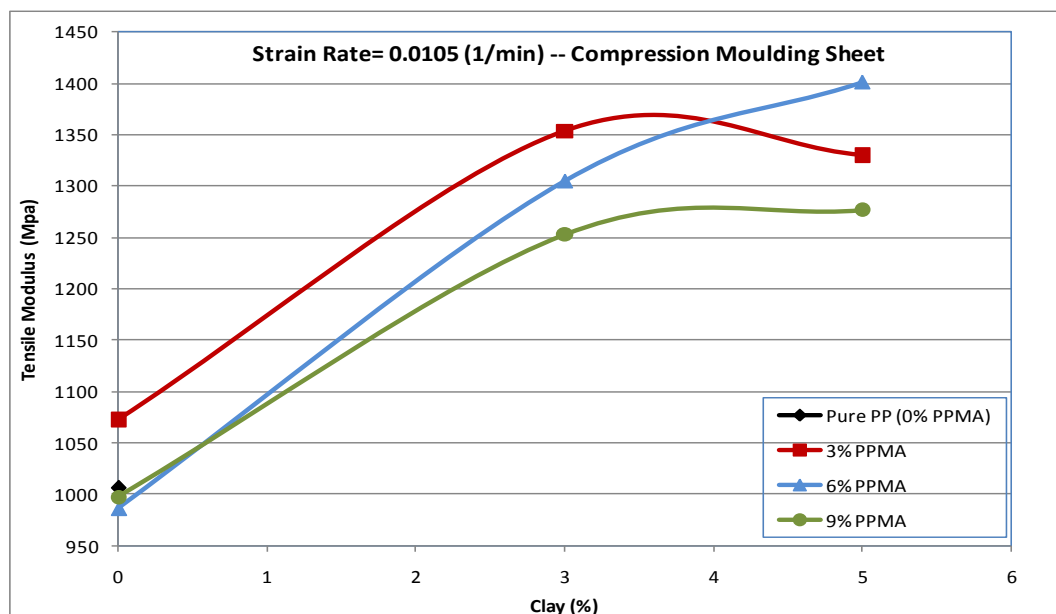


Figure 5.66: Tensile Modulus vs. clay contents of compression moulded sheets at 0.0105 1/min strain rate

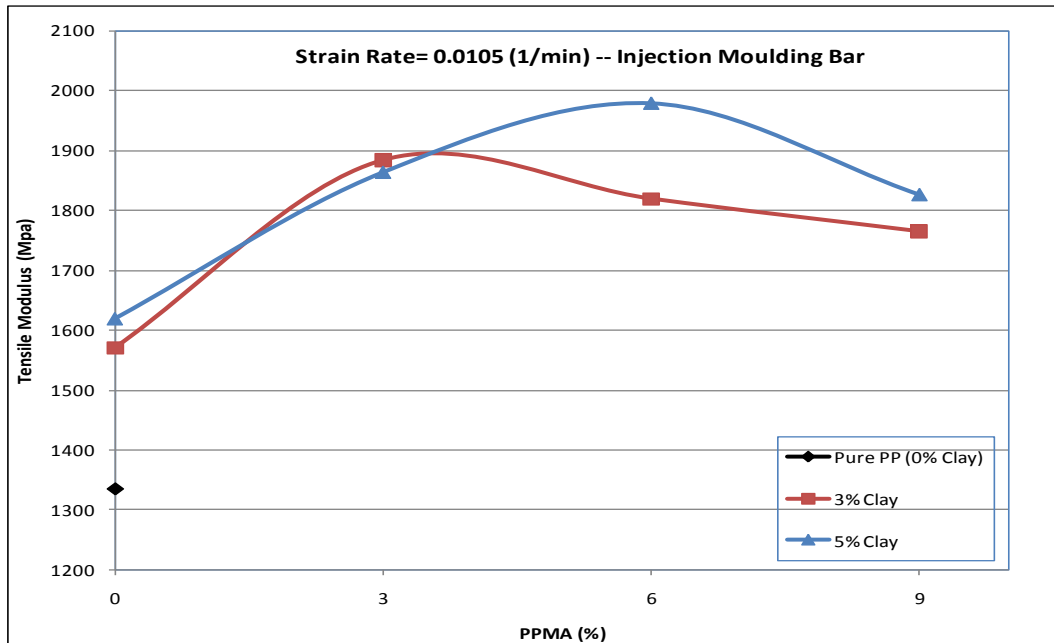


Figure 5.67: Tensile Modulus vs. PPMA contents of injection moulded bars at 0.0105 1/min strain rate

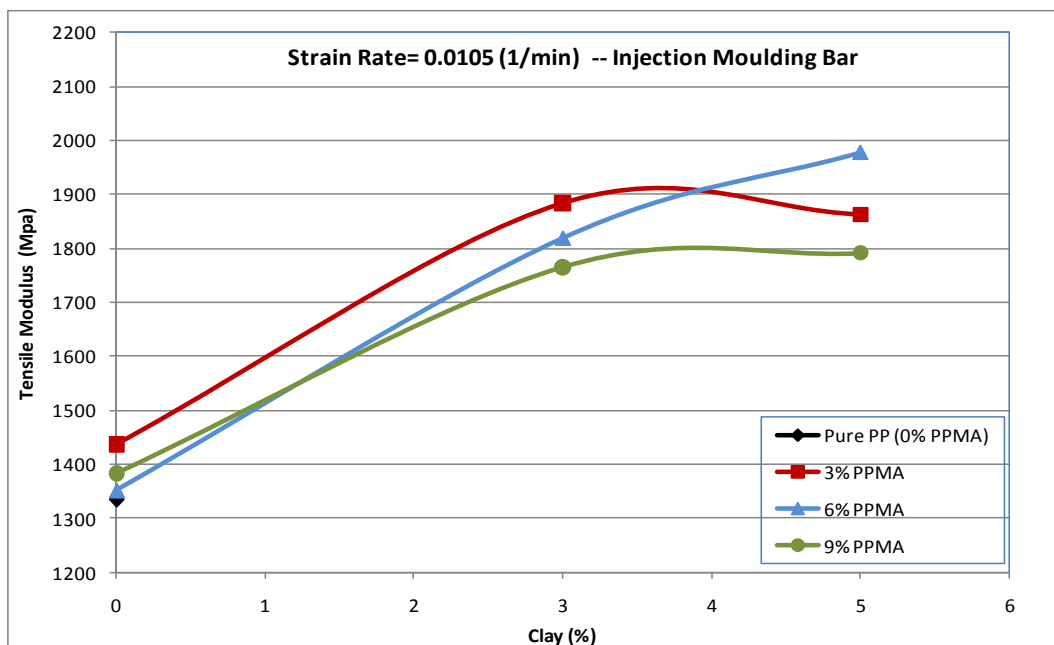


Figure 5.68: Tensile Modulus vs. clay contents of injection moulded bars at 0.0105 1/min strain rate

At 3% PPMA level, as it is seen in Figures 5.65, 5.67, 5.69 and 5.71, the 3% clay system at higher strain rates (0.0105 and 0.0158 1/min) exhibits higher values of tensile modulus than the 5% clay system. This might be explained by the existing of voids in all systems that either do not contain PPMA or contain low ratio of PPMA/clay that probably build weak contact surface between

polymer and clay. This was not seen for the low strain rate (0.0053 1/min), where the molecules are given more time to relax and lower the stress. Injection moulded samples showed the same tendency for all three strain rates.

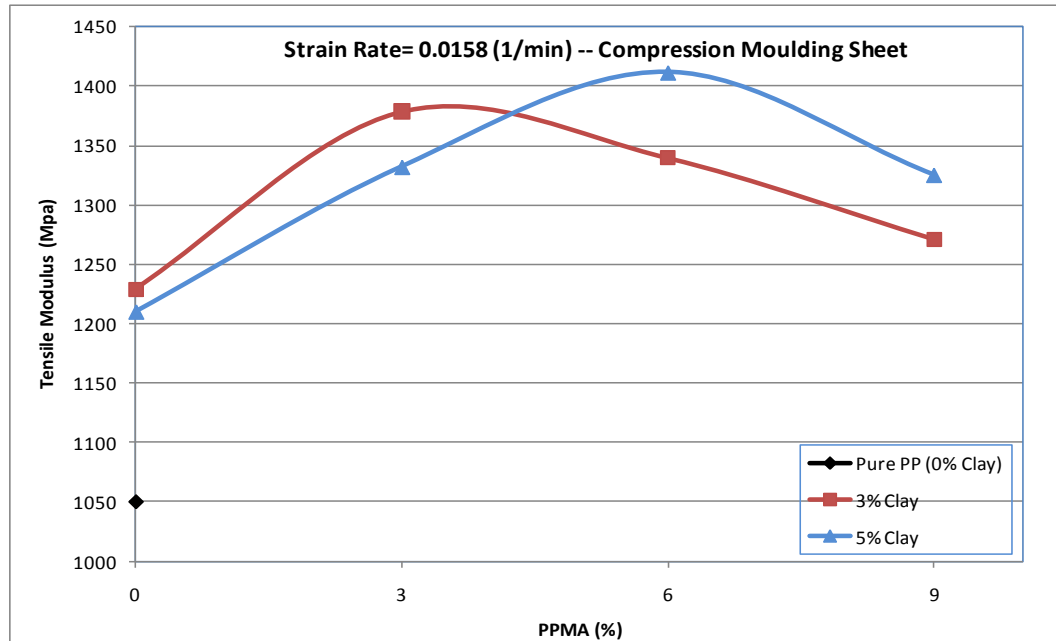


Figure 5.69: Tensile Modulus vs. PPMA contents of compression moulded sheets at 0.0158 1/min strain rate

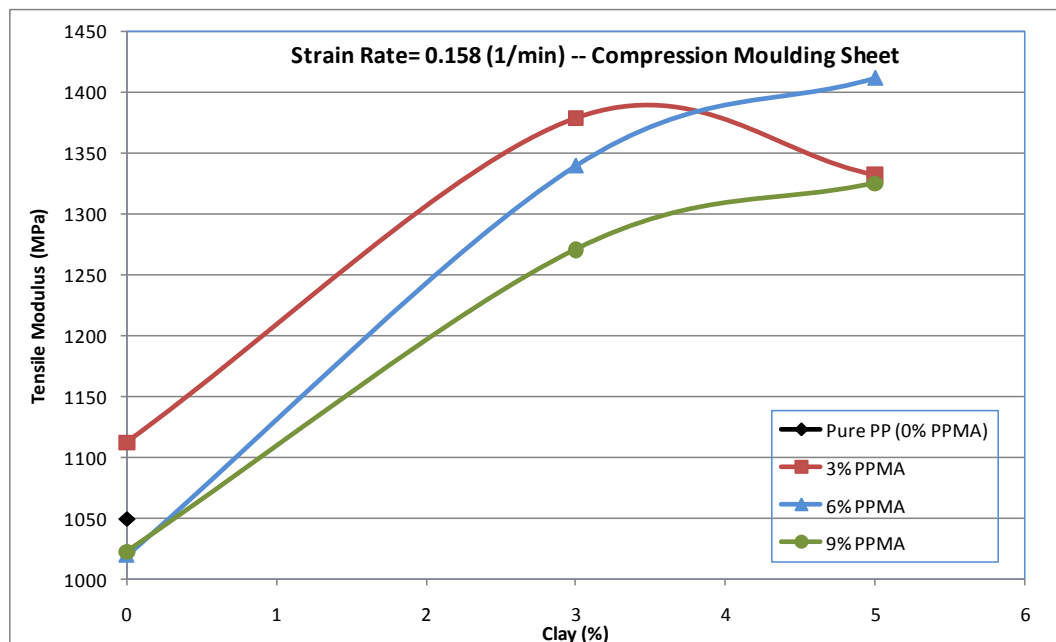


Figure 5.70: Tensile Modulus vs. clay contents of compression moulded sheets at 0.0158 1/min strain rate

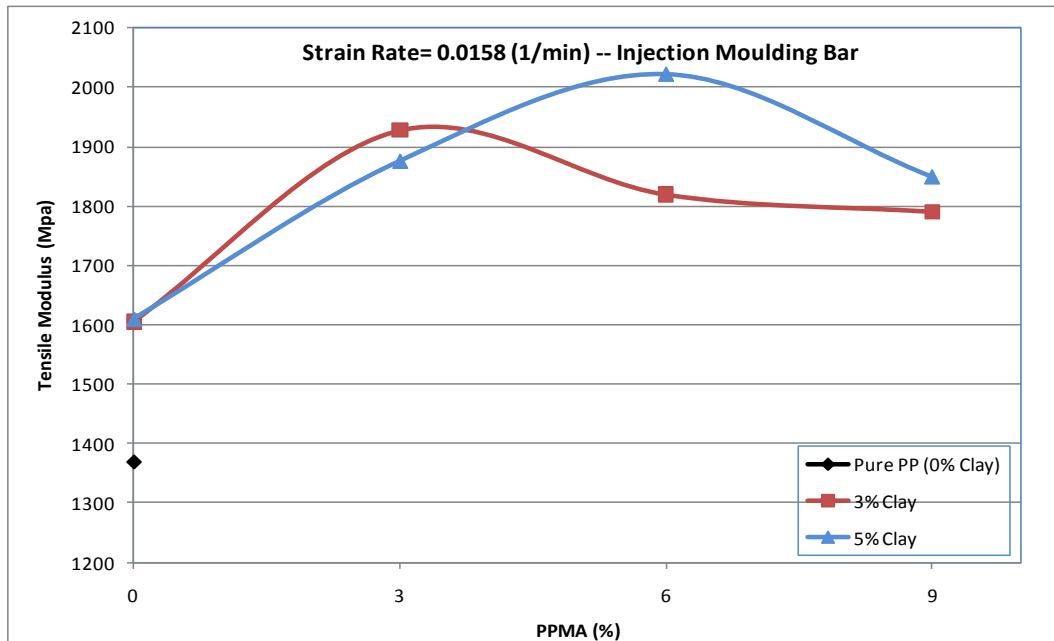


Figure 5.71: Tensile Modulus vs. PPMA contents of injection moulded bars at 0.0158 1/min strain rate

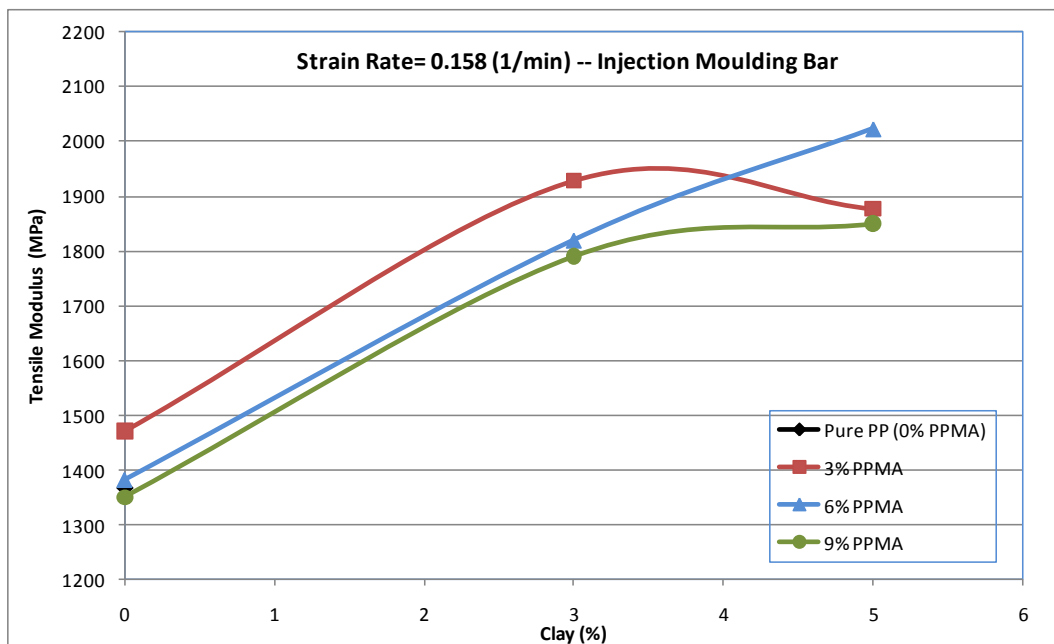


Figure 5.72: Tensile Modulus vs. clay contents of injection moulded bars at 0.0158 1/min strain rate

5.8.1.3 Effect of PPMA/clay ratio on modulus at different strain rates

Figure 5.73 of compression moulded sheets and Figure 5.74 of injection moulded bars give a clear relation for all 3% clay systems. Increase of the PPMA/clay ratio beyond 1, decreases the modulus to about 4% at 2 PPMA/clay ratio and a further 4 % decrease is observed as the ratio increases to 3. On the

other hand, at the same PPMA/clay ratio, 2-3% increment in modulus is remarked as the strain rate increases from 0.0053 to 0.0105 1/min and from 0.0105 to 0.0158 1/min.

In 3% clay systems, the ratio of 1:1 of PPMA/clay that achieves the highest modulus, higher crystallization temperature with lower spherulites size, increased d-spacing of silicate layers, and good distribution of intercalated microtactoids with possible semi-exfoliated particles might be suggested to be the optimum ratio for such used mixing route and introduced shear.

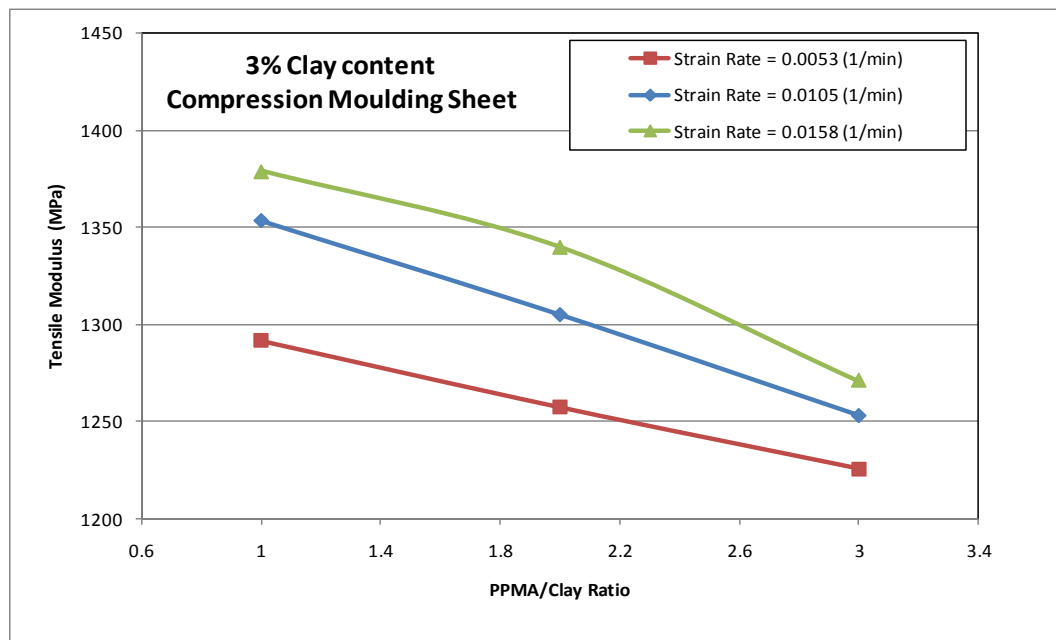


Figure 5.73: Tensile Modulus of 3% clay systems vs. PPMA/clay ratio of compression moulded sheets at different strain rates

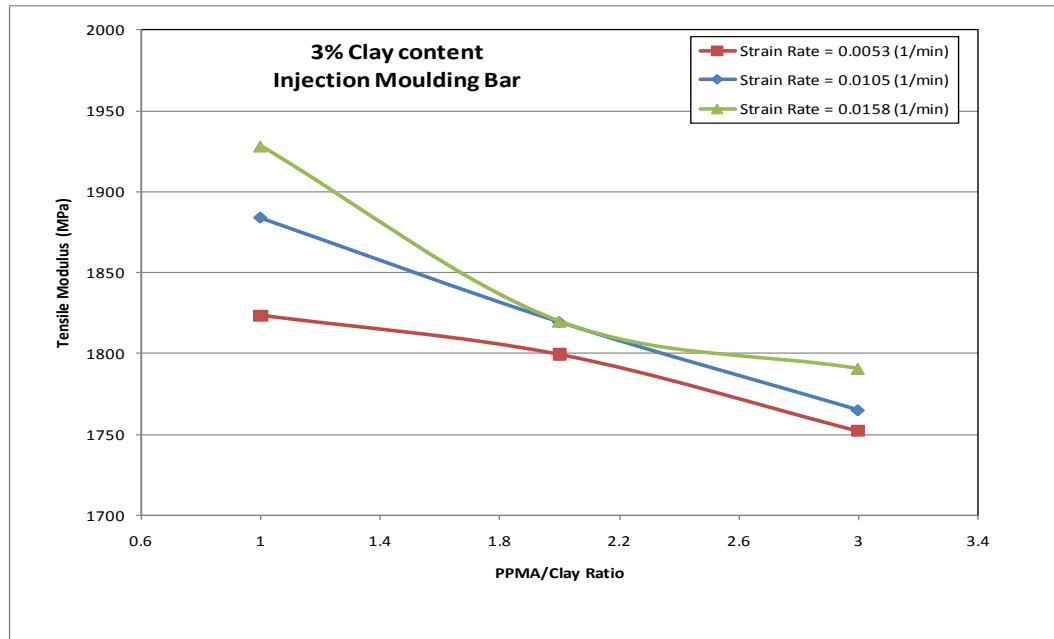


Figure 5.74: Tensile Modulus of 3% clay systems vs. PPMA/clay ratio of injection moulded bars at different strain rates

In the compatibilized 5 % system, Figure 5.75 and 5.76 show that the low PPMA/clay ratio of 3:5 was not enough to achieve the highest modulus as compared to the 3% clay system. The modulus then increases to the highest values as the ratio increases to 6:5 for all strain rates for both compression sheets and injection moulded samples. A drop in modulus is then noticed as the PPMA/clay ratio increases to 9:5.

As compared to the 3% clay system, the compatibilizer in the 5% clay system is employed in a more densely packed system so that higher PPMA/clay ratio might be used to get better properties. However, such a packed system could benefit from the very high modulus of clay (160 GPa) to enhance the property, but at the same time could influence the compatibility of PP and clay particles and thus minimizes or even harms the property.

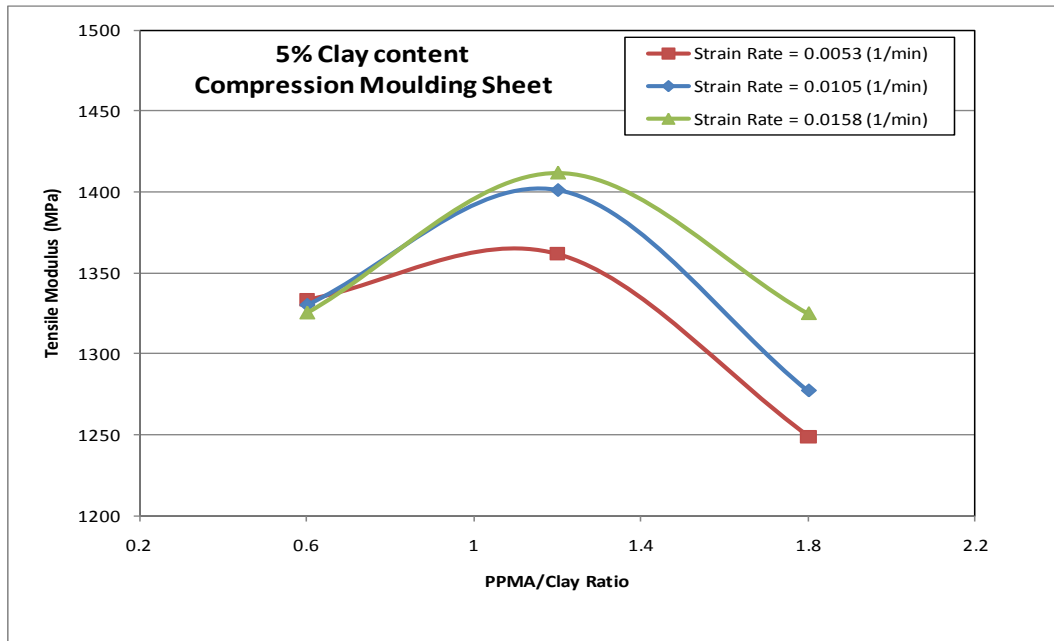


Figure 5.75: Tensile Modulus of 5% clay systems vs. PPMA/clay ratio of compression moulded sheets at different strain rates

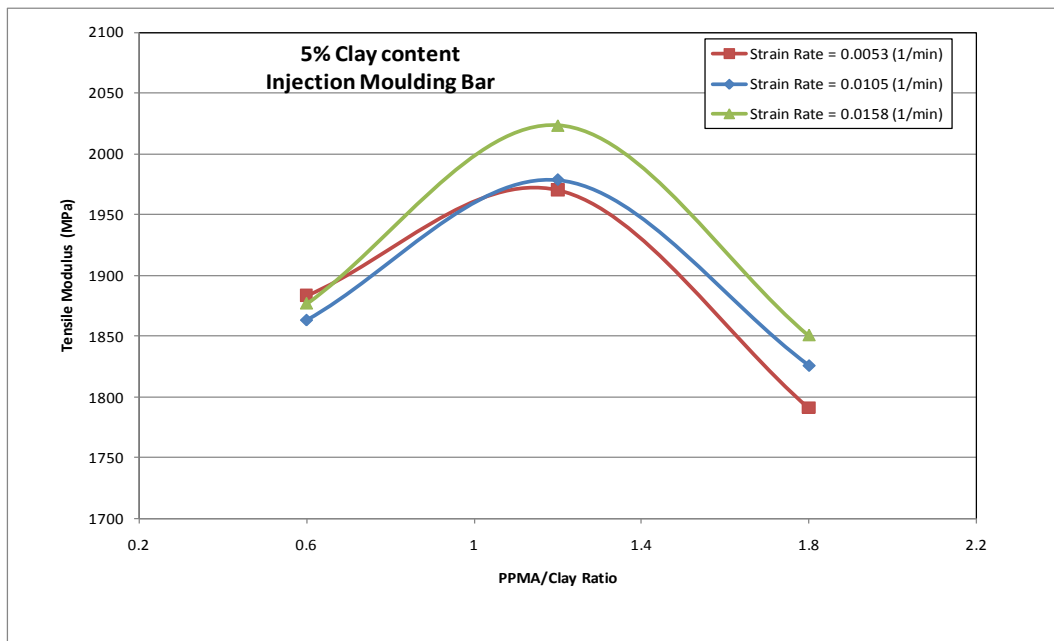


Figure 5.76: Tensile Modulus of 5% clay systems vs. PPMA/clay ratio of injection moulded bars at different strain rates

An adopting of loading of PPMA based on the processing and clay content is a mandatory step to make balance between the compatibilizer stiffness effect and its compatibilization effect to achieve maximum improvement of composite properties.

The combination of the obtained results of WAXD, TEM and tensile modulus measurement showed that even though the 5% clay systems with PPMA achieve the highest tensile modulus values, the modest trend as the clay level exceeds 3% clay content may assume that the room of such compatibilized systems of clay reinforcement in PP is reduced at 5% clay system. The percentage of clay, PPMA, introduced shear and final property should be balanced to obtain an optimum PPNCs.

5.8.1.4 Effect of mixing route on tensile modulus at different strain rates

For inorganic clay particle reinforced non-polar PP, the PPNC matrix interaction is an important factor in determining the mechanical properties of composites because a weak interface would impart lower modulus. The reported modulus of PPNC (PP+ 3% clay+ 3% PPMA) in the previous section is the one prepared by two-step master batch for both PP/PPMA and PP/clay. These master batches were mixed with polymer in a final extruder pass. The second way of mixing uses the same master batches with same contents of clay and PPMA. But instead of final extruder pass step, the PP/PPMA and PP/clay were mixed manually with polymer and introduce to the injection moulding process. A third way was mixed manually only the clay master batch, but pure PPMA and polymer. The fourth way includes mixing all three dry-materials manually without preparing any master batches.

Figure 5.77 shows the tensile modulus results for different mixing procedures. The PPNC prepared with the two-step master batch was 40% higher than pure PP, 24% higher than the second mixing procedure, 34% higher than the third, and 42% higher than the fourth way of mixing.

Compared to all mixing procedures used, the two-step master batch procedure shows a clear sign to promote the partial exfoliation or intercalation of the PP molecules into the silicate layers galleries. This might be attributed to the sufficient introduced shear and mixing during the compounding stage. It then acts to enhance the modulus of the final PPNC. These improvements in dispersion and distribution are confirmed previously in TEM and WAXD results. Conversely, although the one-step mixing achieves good compatibility with PP molecules, as reported in WAXD results, but it fails to show good distribution in the TEM micrograph. Thus lower modulus as compared to two-step master batch sample is obtained, but still 12% higher than the pure PP sample.

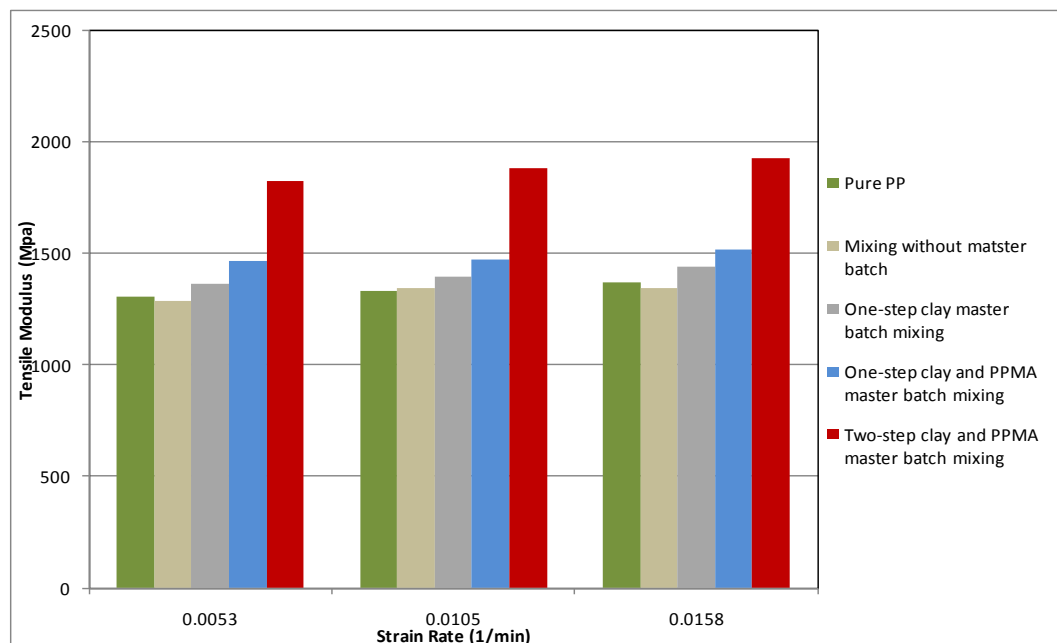


Figure 5.77: Tensile Modulus of 3% clay system with 3% PPMA for different mixing procedures at different strain rates

The result of the two-step master batch procedure may indicate of significant interaction between nanoclay particles and PP matrix as compared to other procedures. The two passages of clay material through the TSE during the preparation of the master batch and the second passage with PP/PPMA system are enough to make the dispersion and distribution to take place.

5.8.2 Tensile modulus of drawn PPNCs

The work of Ward, cited in the beginning of this thesis [5], produces very high modulus polymer drawn fibres as a result of molecular orientation. This orientation may make the PP molecules parallel enough to induce crystallization [153]. Orientation requires considerable mobility of large segments of the polymer molecules, and thus can not occur below the glass transition temperature. Mechanical properties, such as modulus and stiffness, increase in the direction of orientation [154]. The used PP enhancement reaches to about 47% as compared to the undrawn one. Conversely, modulus decreases and toughness increases in the direction perpendicular to the axis of orientation, because stress along the axis of orientation of polymer molecules is applied against the strong covalent bonds within the polymer molecules, whereas stress perpendicular to the axis of orientation is applied only against the weak secondary forces between the polymer molecules [155]. The effect of the clay particles on the orientation and thus tensile modulus is mainly discussed in this section for draw ratios 2, 3, and 4.

The modulus results of different draw ratios of PP and PPNCs are shown in Table 5.7, 5.8 and 5.9 for different draw ratios and strain rates. The results of drawn PP are comparable to that obtained by Taraiya et al. [156] for PP material with same melting point (165 °C), where the 2, 3 and 4 draw ratios at 155 °C draw temperature achieve improvement in modulus of about 17%, 33% and 47% as compared to 18%, 23% and 47% respectively of our results at 154 °C draw temperature.

The results show similar tendency between different drawn PPNCs to that presented in the undrawn PPNCs. The drawn PP with 3% clay and 3% PPMA

shows the greatest improvement among all 3% drawn composites systems (12-15% over the drawn pure PP system for all draw ratios, $\lambda = 2, 3,$ and 4). In contrast, the greatest improvement in 5% systems is found to be for the one with 6% PPMA loading (12-15% over the drawn pure PP system for all draw ratios, $\lambda = 2, 3,$ and 4).

The tendency of improvement in the drawn PPNCs is significantly minimized as compared to the obtained improvement in undrawn samples. Addition of the polar structure MMT to the non-polar PP produces weak interface boundaries, which still exist even with using of the compatibilizer. When drawing is involved, microvoids might be more dominant in the drawn PPNCs structure. Thus the improvement of PPNCs tensile modulus tendency of undrawn compatibilized 3% clay and 5% systems is reduced from 40% and 50% to 12-15% and 22-25% respectively over the pure PP system.

Table 5.7: Tensile Modulus of drawn PPNC Samples, $\lambda= 2$

Sample Identification	Tensile Modulus, MPa		
	Strain Rate 1	Strain Rate 2	Strain Rate 3
PP	1553 \pm 56	1626 \pm 22	1670 \pm 71
PP+3% Clay	1617 \pm 29	1695 \pm 33	1720 \pm 39
PP+ 5% Clay	1663 \pm 29	1801 \pm 71	1892 \pm 29
PP+3% Clay+3% PPMA	1743 \pm 28	1816 \pm 59	1857 \pm 45
PP+5% Clay+6% PPMA	1893 \pm 60	1942 \pm 54	1975 \pm 49
PP +3% Clay (MB) +3% PPMA(MB)	1697 \pm 79	1790 \pm 99	1836 \pm 92

Table 5.8: Tensile Modulus of drawn PPNC Samples, $\lambda= 3$

Sample Identification	Tensile Modulus, MPa		
	Strain Rate 1	Strain Rate 2	Strain Rate 3
PP	1606 \pm 66	1652 \pm 33	1710 \pm 59
PP+3% Clay	1666 \pm 52	1717 \pm 35	1759 \pm 50
PP+ 5% Clay	1704 \pm 72	1774 \pm 44	1830 \pm 52
PP+3% Clay+3% PPMA	1842 \pm 65	1927 \pm 56	2035 \pm 60
PP+5% Clay+6% PPMA	1985 \pm 45	2106 \pm 63	2165 \pm 60
PP +3% Clay (MB) +3% PPMA(MB)	1774 \pm 79	1873 \pm 83	1978 \pm 78

Table 5.9: Tensile Modulus of drawn PPNC Samples, $\lambda= 4$

Sample Identification	Tensile Modulus, MPa		
	Strain Rate 1	Strain Rate 2	Strain Rate 3
PP	1924 \pm 69	2006 \pm 45	2110 \pm 36
PP+3% Clay	1983 \pm 42	2072 \pm 56	2166 \pm 69
PP+ 5% Clay	2018 \pm 60	2080 \pm 54	2124 \pm 54
PP+3% Clay+3% PPMA	2181 \pm 50	2303 \pm 67	2466 \pm 35
PP+5% Clay+6% PPMA	2403 \pm 51	2528 \pm 53	2628 \pm 58
PP +3% Clay (MB) +3% PPMA(MB)	2108 \pm 81	2288 \pm 91	2387 \pm 102

5.8.2.1 Effect of clay and PPMA on tensile modulus of drawn PPNCs at different strain rates

The effect of clay and PPMA on drawn polypropylene in solid phase has not studied previously. This study may contribute affirmatively to understand the structure and its influence on the properties of the PPNCs for both undrawn and drawn polymers. In present of clay and PPMA, The first and second draw ratios (2 and 3) can give an idea about how molecules will behave when they stretched, under slightly low cross head speed of 5 and 120 mm/min, and how clay will affect the parallelism of the polymer molecules. In draw ratio 4, very high oriented polymer is produced at high speed of 950 min/min.

The PPNCs results of different draw ratios of the tensile modulus are shown in Figure 5.78, Figure 5.79 and Figure 5.80 at different strain rates. Figure 5.78 shows the results of draw ratio 3 with 120 mm/min drawing speed. When the compatibilizer is not added, modest increments of 3-4% and 6-7% in

modulus at different strain rates are observed as the clay content increased to 3% and 5%, respectively. Higher enhancement in modulus is remarked as the PPMA is present. These modulus improvements reach to 15-19% and 24-27% at different strain rate for the 3% clay and 5% clay systems, respectively. Similar results are obtained for the draw ratio 2 (5 mm/min) and shown in Figure 5.79.

Figure 5.80 shows the effect of high deformed drawn PPNCs of draw ratio 4 and drawing speed of 950 mm/min. The uncompatibilized systems show a very weak trend to enhance the modulus over the drawn PP with increasing the clay contents. These tiny enhancements get worse for the 5% clay system as the strain rate increases to 0.0158 (1/min) and shows same result of drawn PP. The high drawing speed seems to influence the interference between the entanglement of the polymer molecules and the possible existence of microvoids that most likely to be more random in such high deformed system, and thus reduce the modulus at high clay content. Conversely, the compatibilized systems show an increments of tensile modulus at all used strain rates due to possible reduction of microvoids that may result from the weak interface between polymer/clay interfaces, which be less dominant in such compatibilized systems.

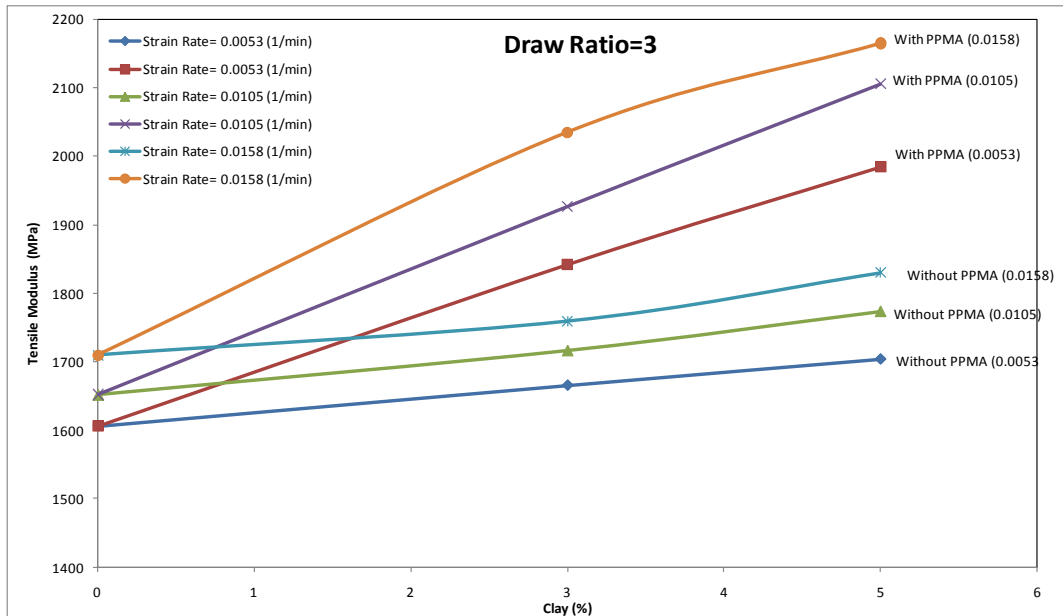


Figure 5.78: Tensile Modulus of drawn PPNCs ($\lambda=3$) vs. clay contents at different strain rates

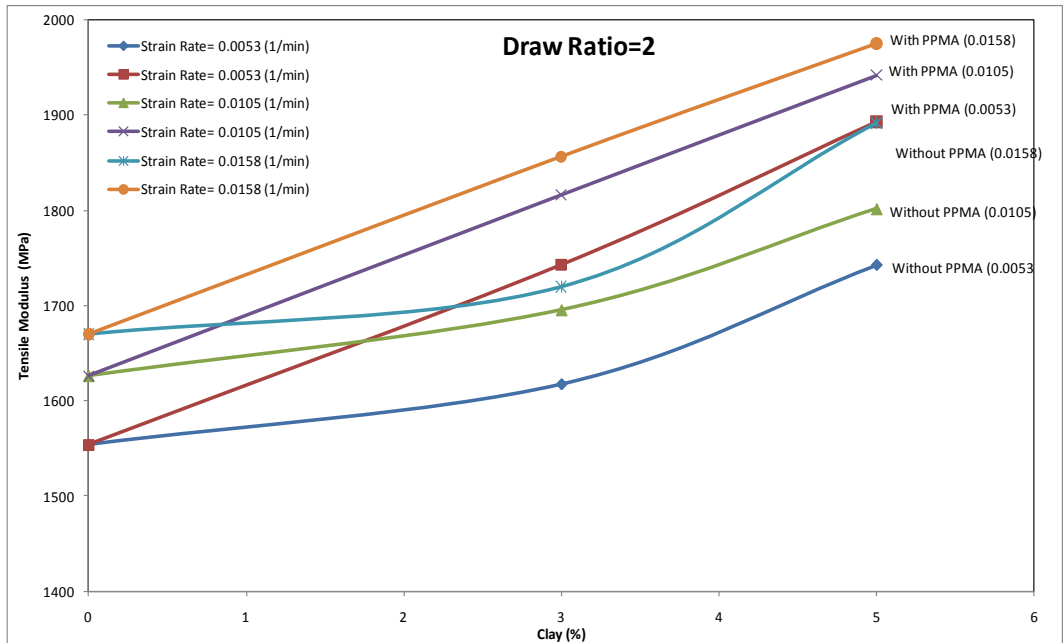


Figure 5.79: Tensile Modulus of drawn PPNCs ($\lambda=2$) vs. clay contents at different strain rates

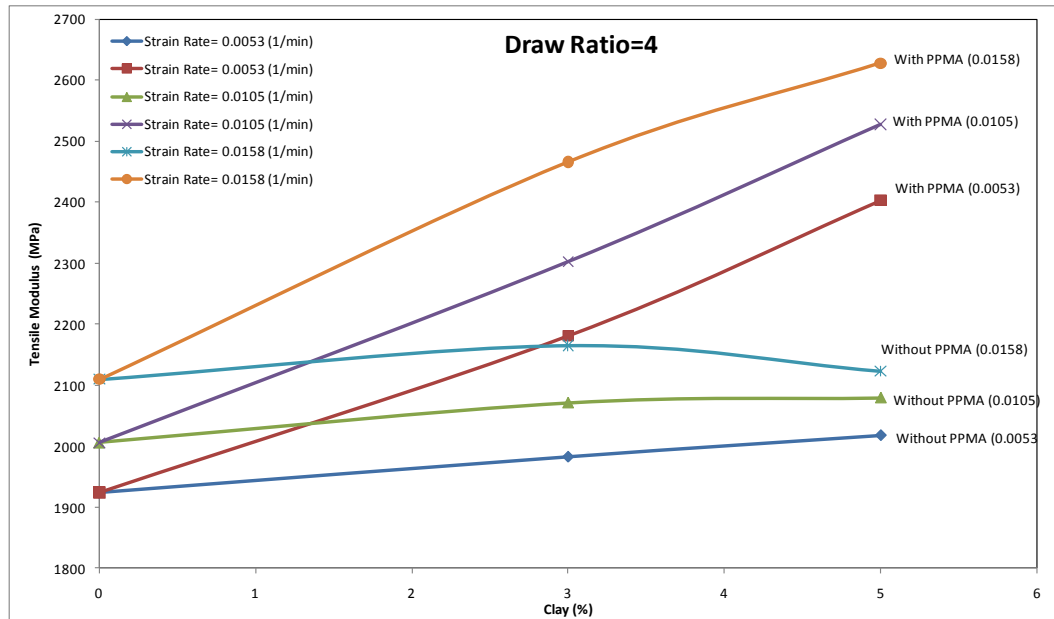


Figure 5.80: Tensile Modulus of drawn PPNCs ($\lambda=4$) vs. clay contents at different strain rates

5.8.2.2 Effect of draw ratio on tensile modulus of PPNCs at different strain rates

Effect of different draw ratios on tensile modulus is presented in Figures from 5.81 to 5.83. In spite of that the compatibilized systems achieve the highest modulus as discussed in the previous two sections, a 4 % reduction in modulus at draw ratio 2 as compared to undrawn samples is observed for all strain rates for both compatibilized 3% and 5% clay systems. This might be attributed to the applied restriction of the molecules mobility that is inhibited by the linked PP molecules to the clay galleries of the compatibilized systems at such very low drawing speed. As the speed increases ($\lambda=3$), this restriction is minimized and a slight increase in modulus is observed. This behaviour is then followed by a tremendous increase in the modulus (33% over the undrawn sample) at very high speed of 950 mm/min ($\lambda=4$).

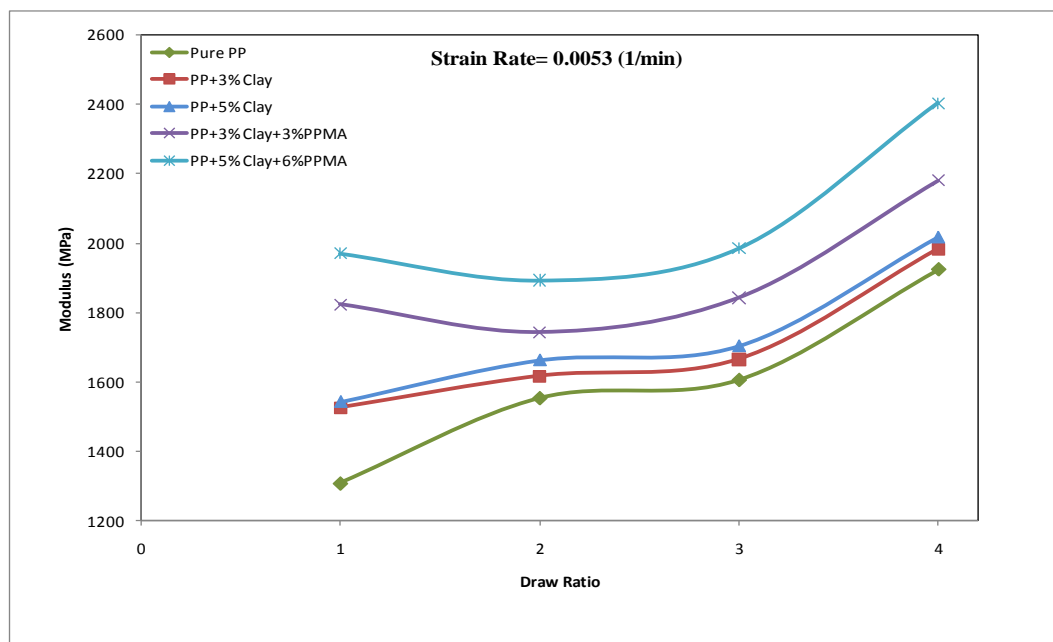


Figure 5.81: Effect of draw ratio on tensile Modulus of different drawn PPNC samples at 0.0053 (1/min)

The drawn PP and uncompatibilized 3% and 5% systems seems to have same behaviour for all strain rates in their response to the drawing process as an indication of comparable degree of orientation for unlinked polymer molecules to the clay platelet. Shifts in the curves to higher modulus of the drawn uncompatibilized systems over the PP curve are due to the high modulus of inorganic clay particles and possible interaction with the PP functional groups. Plateaus are presented for these systems between 2 and 3 draw ratios, followed by increase in modulus at high drawing speed with tendency to have equivalence in modulus between all three systems as microvoids might be more dominant in the matrix. Ability of orientation, presence of high modulus clay and the possible developed microvoids are the main factors that control the tensile modulus in such uncompatibilized systems.

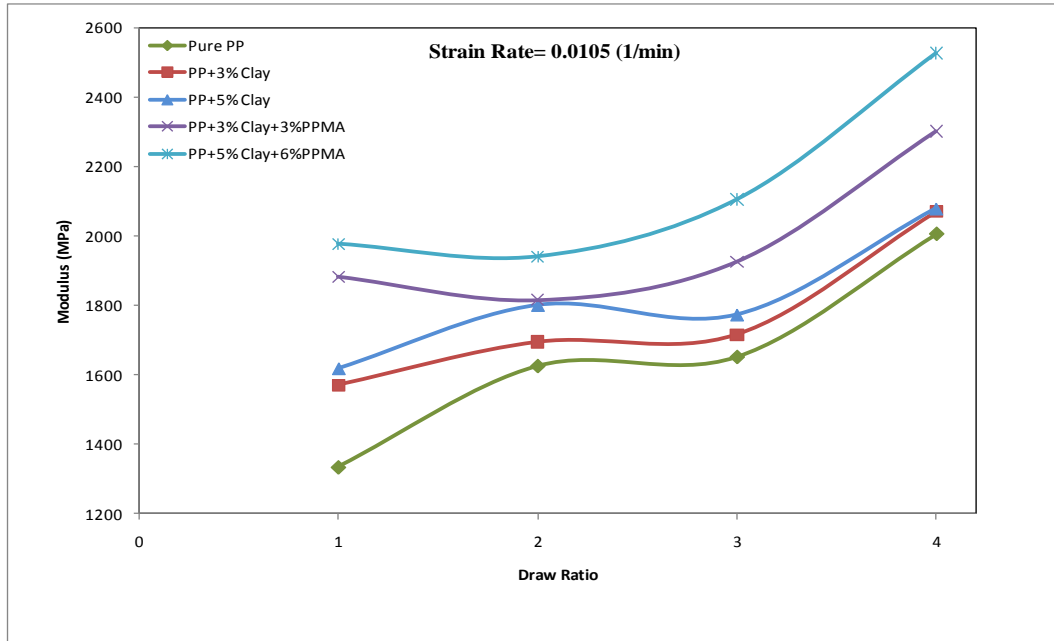


Figure 5.82: Effect of draw ratio on tensile Modulus of different drawn PPNC samples at 0.0105 (1/min)

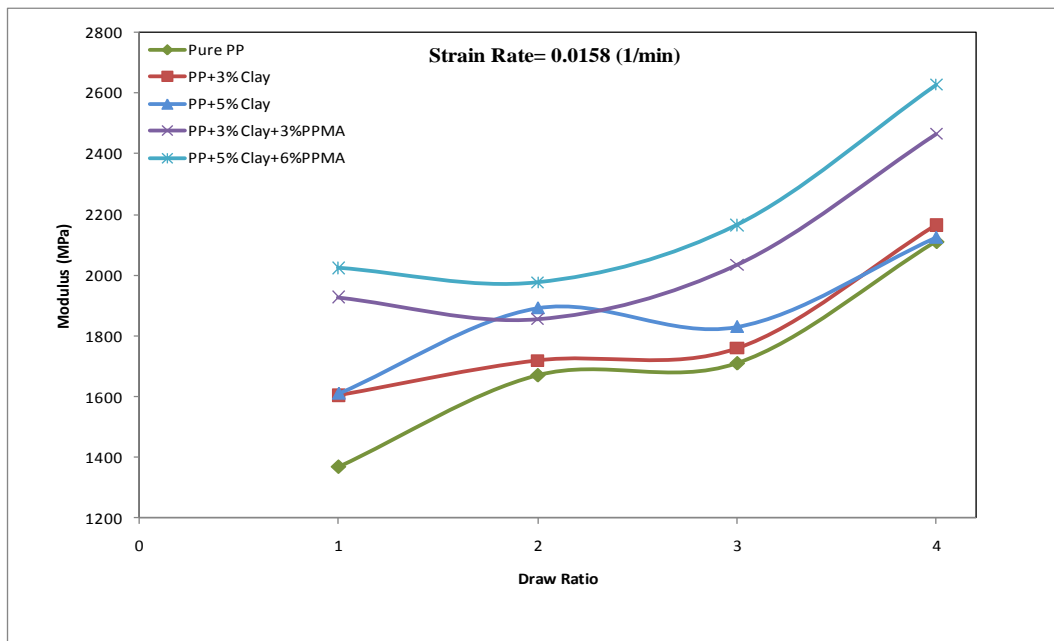


Figure 5.83: Effect of draw ratio on tensile Modulus of different drawn PPNC samples at 0.0158 (1/min)

5.8.2.3 Effect of draw ratio on tensile modulus of different mixing route of PPNCs at different strain rates

Sample with one-step master batch, which refers to the second way of mixing is drawn and compared to the similar clay and PPMA contents of the two-step master batch, as shown in Figures from 5.84 to 5.86 for different draw

ratios. As the one-step master batch sample is drawn to 2, 3 and 4 ratios, the reduction in modulus in the undrawn sample (24%) as compared to the two-master batch system is highly reduced to 3%. However, this comparable result after drawing is accompanied by a big fluctuation as shown in Tables from 5.7 to 5.9 for all strain rates. Since the sample achieves good WAXD result with bad TEM distribution image, a careful should be taken in considering such results especially if it has known that this sample denotes the highest resulted fluctuation as compared to all other samples.

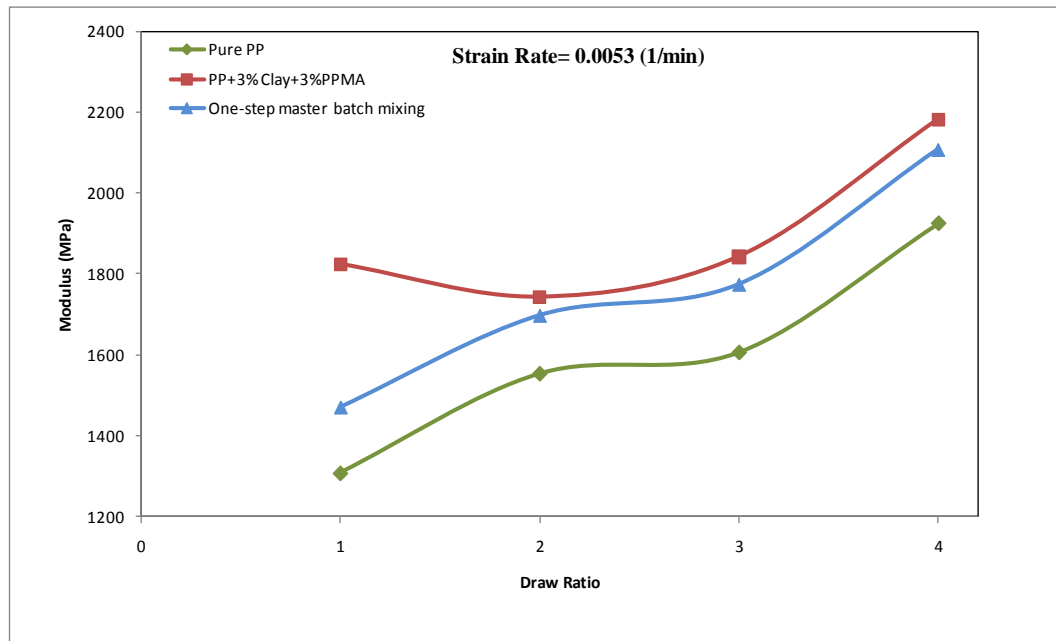


Figure 5.84: Effect of draw ratio on tensile Modulus of different mixing route of drawn PPNC samples at 0.0053 (1/min)

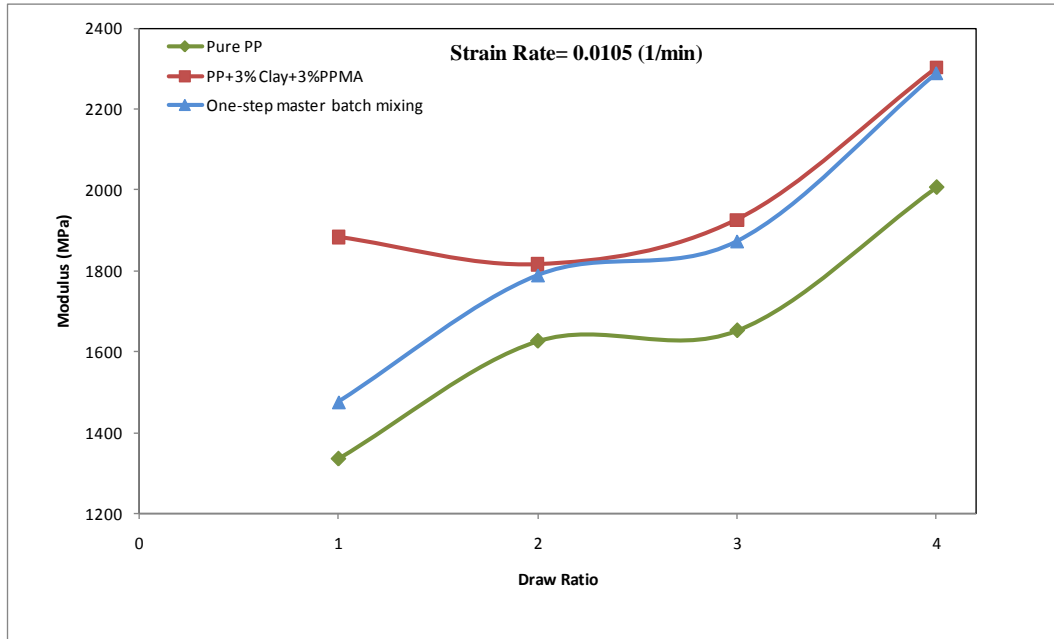


Figure 5.85: Effect of draw ratio on tensile Modulus of different mixing route of drawn PPNC samples at 0.0105 (1/min)

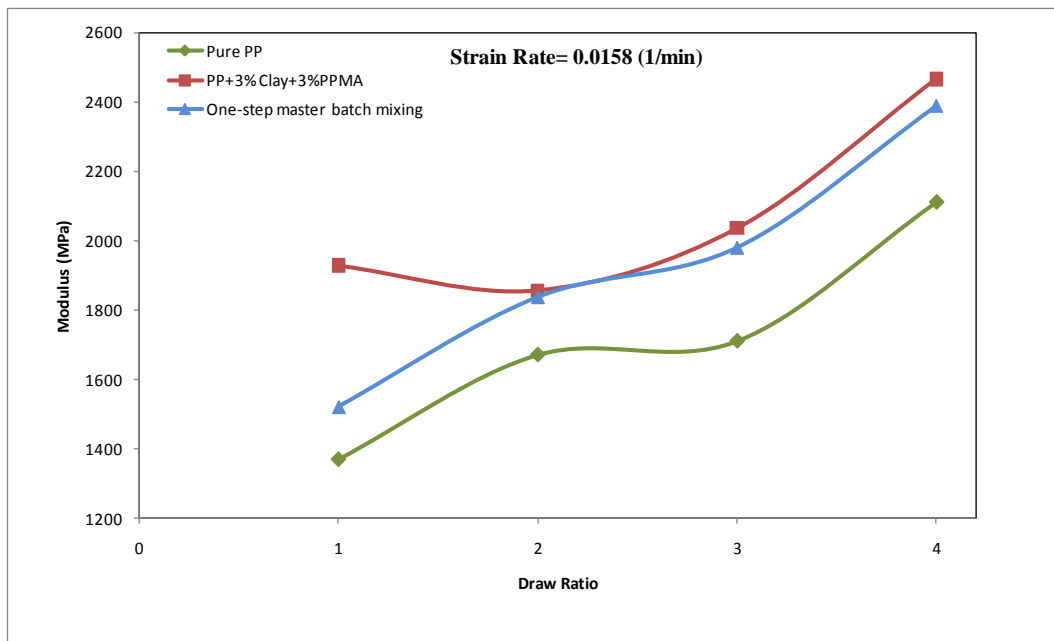


Figure 5.86: Effect of draw ratio on tensile Modulus of different mixing route of drawn PPNC samples at 0.0158 (1/min)

5.9 Fracture Toughness of PPNCs

Fracture toughness of DENT specimens for undrawn and drawn PP/PPNCs is discussed in this section. Thermal and video images were taken and compared to the tensile load-displacement graphs for better understanding of the behaviour of different composites.

When the specimen is subjected to a mechanical stress during the tensile test of the notched sample, it will either behave as a brittle material by using the concept of LEFM or as a ductile fracture. Brittle fracture behaves as in the plane strain conditions, where there is no flow in the plastic region at the crack tip. K_{IC} and G_C have been used to for this plane strain fracture. Conversely, ductile fracture is favoured by plane stress, where the energy is dissipated in the plastic region ahead of the tip of the crack. J integral and EWF have been used for this kind of crack.

Figure 5.87 shows the different fracture behaviours that were observed during the DENT tensile fracture experiments by thermal and video cameras to distinguish between the types of fracture that might be used for the fracture analyses. The three highlighted stages of crack initiation, crack growth (before failure), and failure are considered in this discussion. It was found for the different used samples that in most cases the fracture deals with one of the following behaviours:

First one deals with a semi-brittle behaviour where the thermal images show no heat dissipation before the crack stage, but there was a very tiny plastic flow at the crack tip. In video images, whitening appears as it is shown in A. This behaviour happens in some undrawn samples.

Second behaviour is shown in B images. A brittle behaviour is noticed without any heat dissipation or flow in the plastic region. This occurs in some undrawn samples as well.

Third one starts with whitening and is followed by extensive plasticity ahead of the tip of the crack until the complete failure as shown in video images (C). Thermal images confirm the observations by strong heat dissipation through the

plastic region. This ductile fracture happens in undrawn samples of uncompatibilized 5% clay systems as well as the drawn samples at ratio 2 and 3. The degree of heat and the size of the zones are different from sample to another. Fourth observed development of fracture is shown in D images. As shown in thermal images, it starts with a weak heat in the crack initiation stage, followed by concentrated heat just before failure at the crack tip. This appears in thermal images as dots. Such ductile behaviour is similar to the third fracture behaviour but with limited extension in the processing zone. This happens only for PP with draw ratio 2 and 3.

Fifth behaviour occurs for the high oriented samples (draw ratio 4). In this anisotropic sample, the crack initiation could not be developed in the direction of the notch (perpendicular to the applied load). An excessive mechanical stress will produce a complete rupture along the oriented molecules. During this resistance, sample was extended and heat was dissipated through whole the specimen and not only in the fracture working zones as shown in E images.

Comparison of different PPNC load-displacement graphs are going to be discussed in the next section with relating to their images. All stress-strain curves are presented in Appendix I.

According to the different obtained fracture behaviours of both undrawn and drawn PP and PPNCs, all samples are evaluated based on the total work of fracture as a valid comparison measurement of the material toughness for all undrawn and drawn samples with ratios 2 and 3. For draw ratio 4, the crack did not occur across the ligament. But the data was still analyzed for the purpose of comparisons.

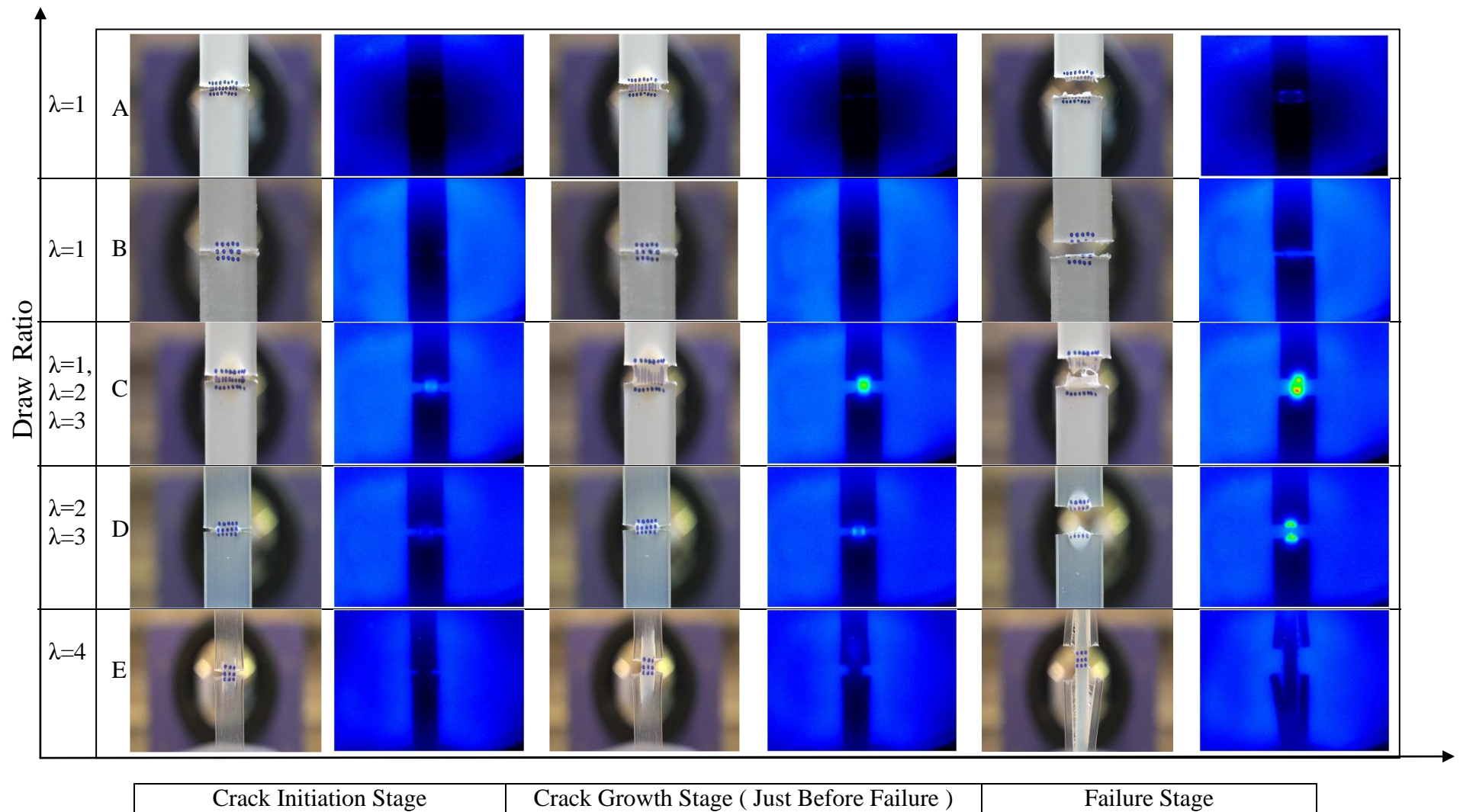


Figure 5.87: Thermal and video images taken during the fracture test showing general behaviours of undrawn and drawn PP and PPNCs

5.9.1 Load-displacement behaviour of undrawn 3% clay systems of PPNCs

The load displacement curves of different notch length during DENT tests for the undrawn core and skin of PP and PPNCs are shown in Figures from 5.88 to 5.93. For the 3% clay system at low notch length (Figures 5.88 and 5.89), there are linear elastic regions up to the point where plastic regions are generated as the displacement is developed horizontally with small increment in load at the tip of the two-crack sides, which indicates a very limited necking of the yielded ligament. On further loading, the crack starts for the PP and PPNCs. Core and skin similarly behave for PP and PPNCs. A tiny shift to lower displacement of the PP core as compared to the skin is attributed to the more relaxation of the polymer molecules in the core that lead to more brittle structure.

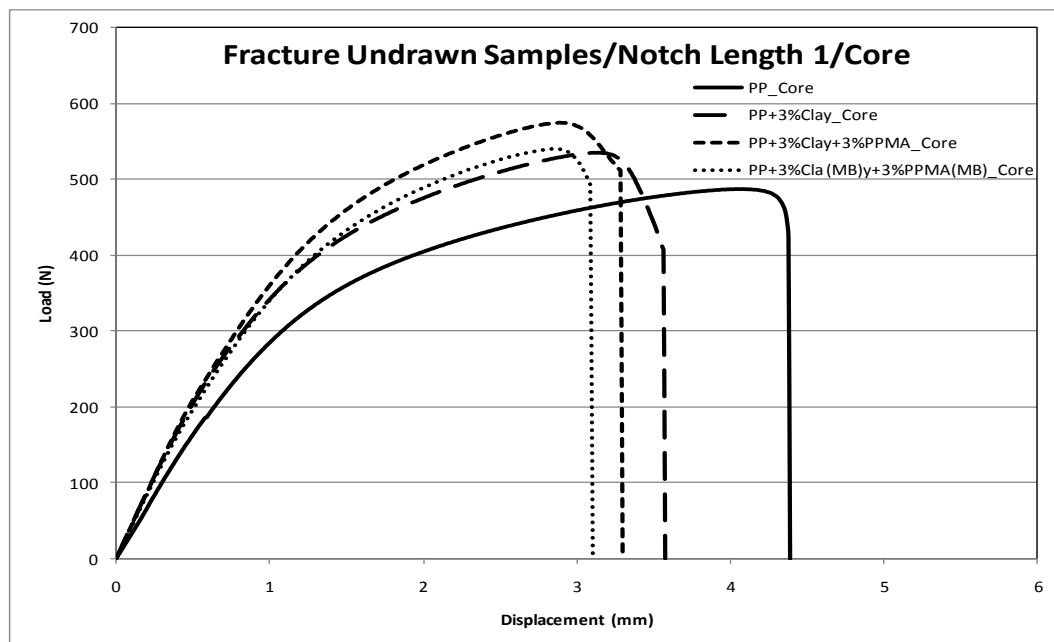


Figure 5.88: Load-displacement plot of 1.5 mm notch for the undrawn core PP and 3% clay systems of PPNCs

Thermal images in Figure 5.101 for the 3% clay systems show a minor heat that was dissipated in the plastic zone of the ligament area over the elastic zone at the tip of the two-crack sides. Similar behaviours with reduction in the displacement are noticed in load-displacement curves as the notch length

increases in Figures from 5.89 to 5.93 and in thermal images that are shown in Figure 102 and 103. The very limited necking behaviour at notch length of 1.5 mm is significantly reduced with increasing the notch length and almost disappears at notch of 2.5 mm.

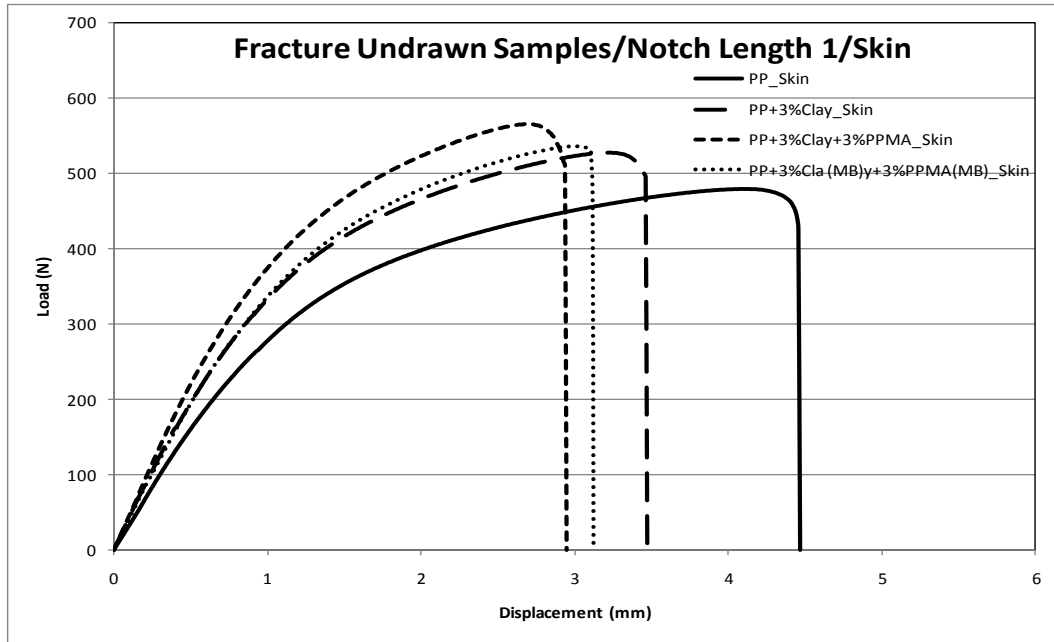


Figure 5.89: Load-displacement plot of 1.5 mm notch for the undrawn skin PP and 3% clay systems of PPNCs

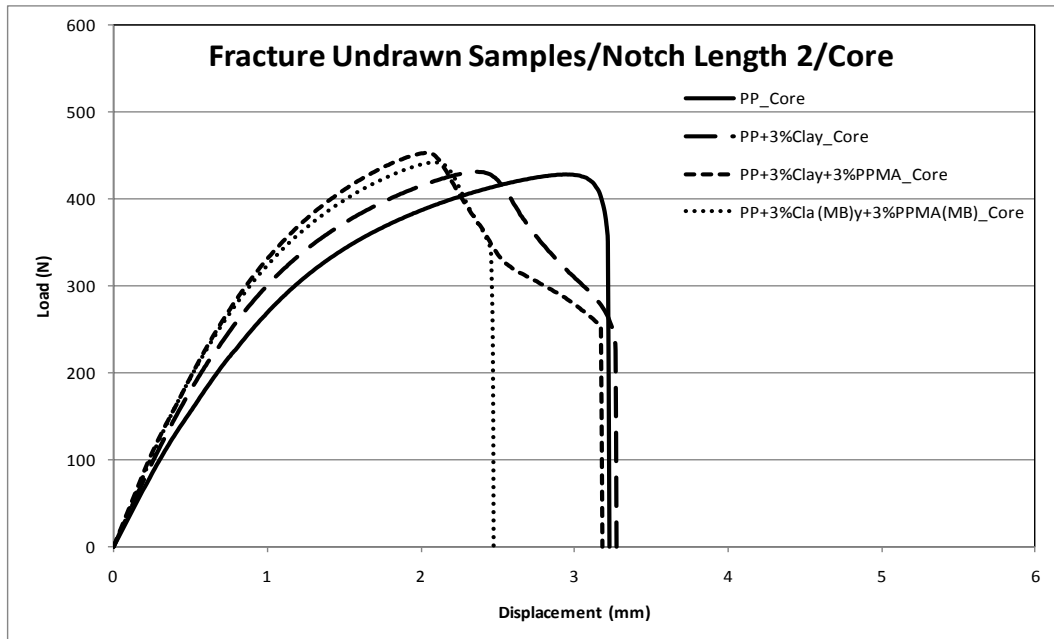


Figure 5.90: Load-displacement plot of 2.0 mm notch for the undrawn core PP and 3% clay systems of PPNCs

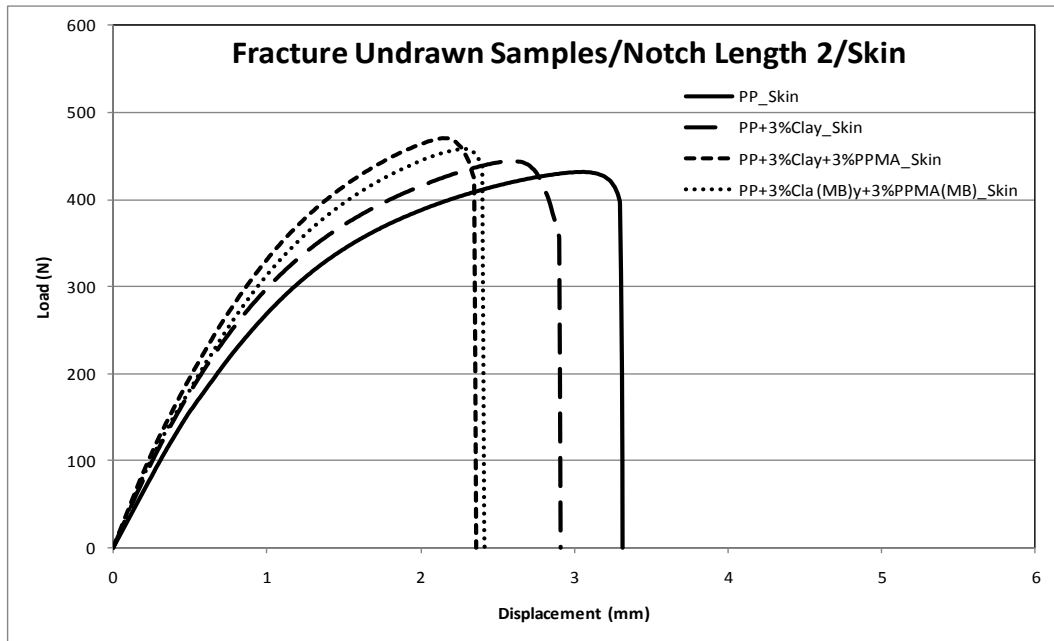


Figure 5.91: Load-displacement plot of 2.0 mm notch for the undrawn skin PP and 3% clay systems of PPNCs

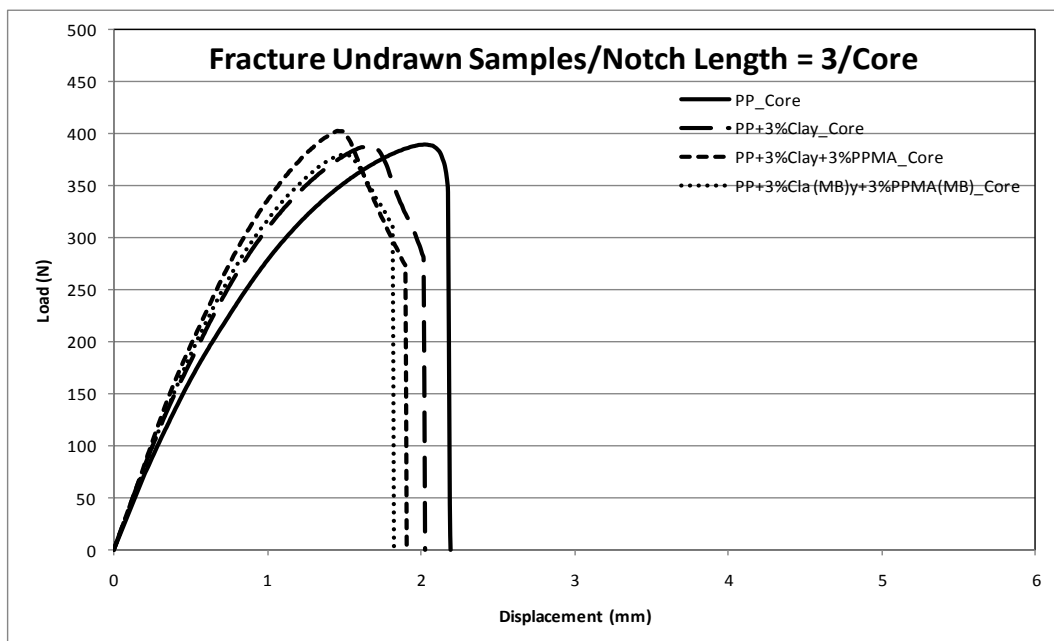


Figure 5.92: Load-displacement plot of 2.5 mm notch for the undrawn core PP and 3% clay systems of PPNCs

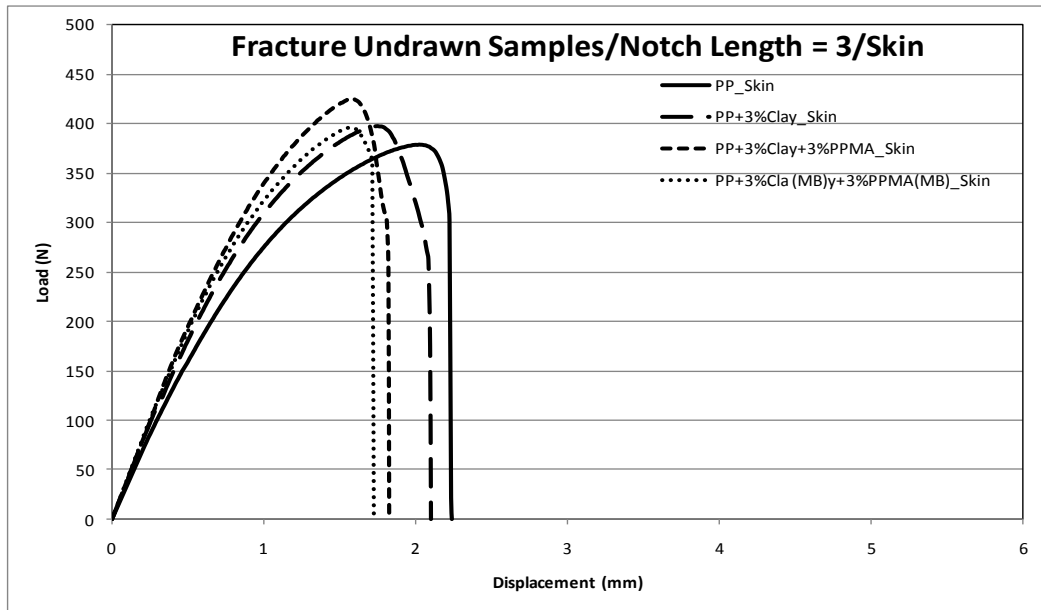


Figure 5.93: Load-displacement plot of 2.5 mm notch for the undrawn skin PP and 3% clay systems of PPNCs

5.9.2 Load-displacement behaviour of undrawn 5% clay systems of PPNCs

In 5% clay systems load-displacement plot (Figures from 5.94 to 5.99), there are two completely different shapes of curves between the core and the skin specimens. In addition to the distinct linear elastic region and the limited necking of the yielded ligament that was showed in the 3% systems, a complete necking is noticed for the core of 5% clay systems.

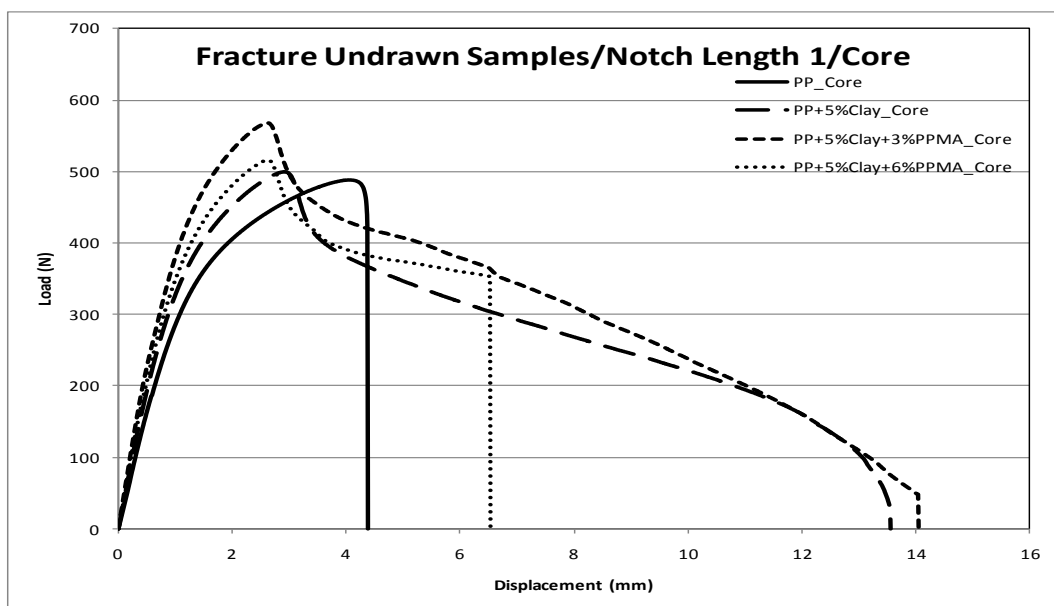


Figure 5.94: Load-displacement plot of 1.5 mm notch for the undrawn core PP and 5% clay systems of PPNCs

After complete necking, the cracks started to grow in a stable mannered slope till the final fracture. Sample with compatibilizer shows less grow with a slight horizontal slope. Skin specimen curves show either behaviour similar to the 3% clay systems or complete necking with small slope grow before the final fracture of specimen.

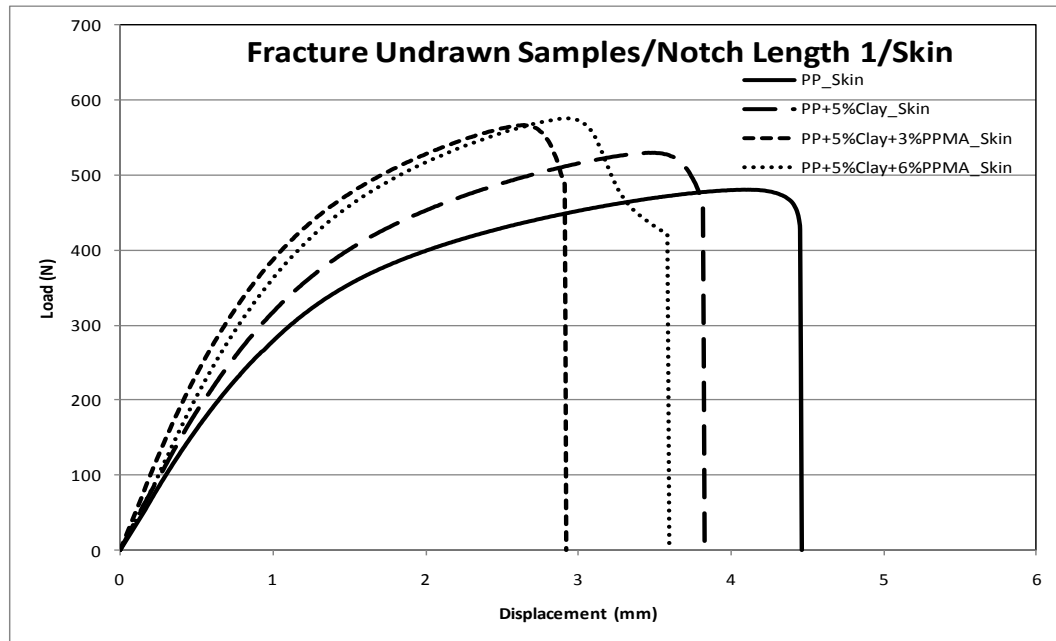


Figure 5.95: Load-displacement plot of 1.5 mm notch for the undrawn skin PP and 5% clay systems of PPNCs

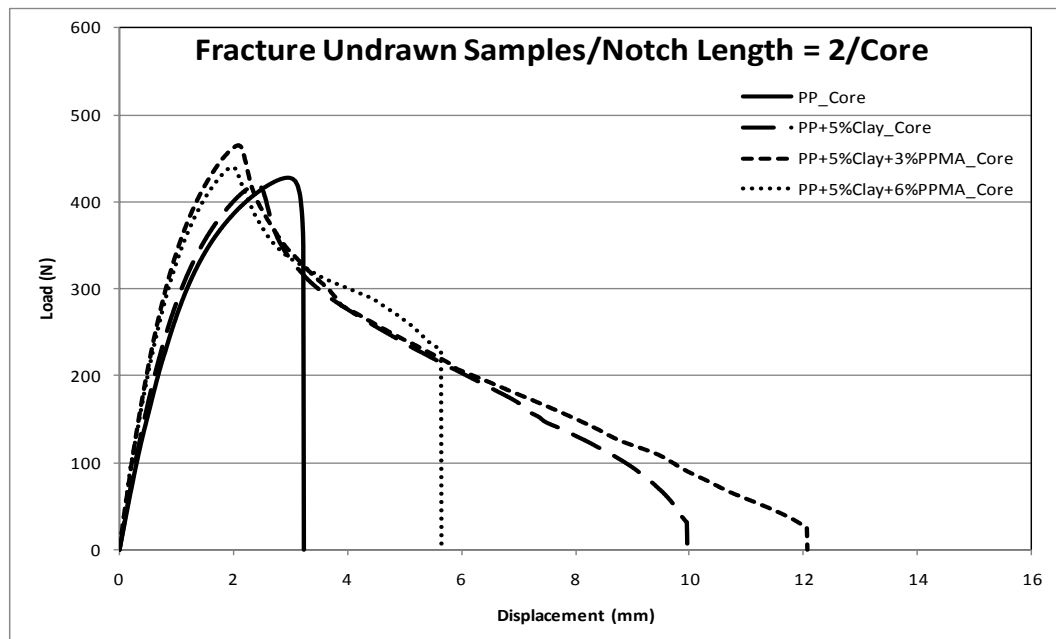


Figure 5.96: Load-displacement plot of 2.0 mm notch for the undrawn core PP and 5% clay systems of PPNCs

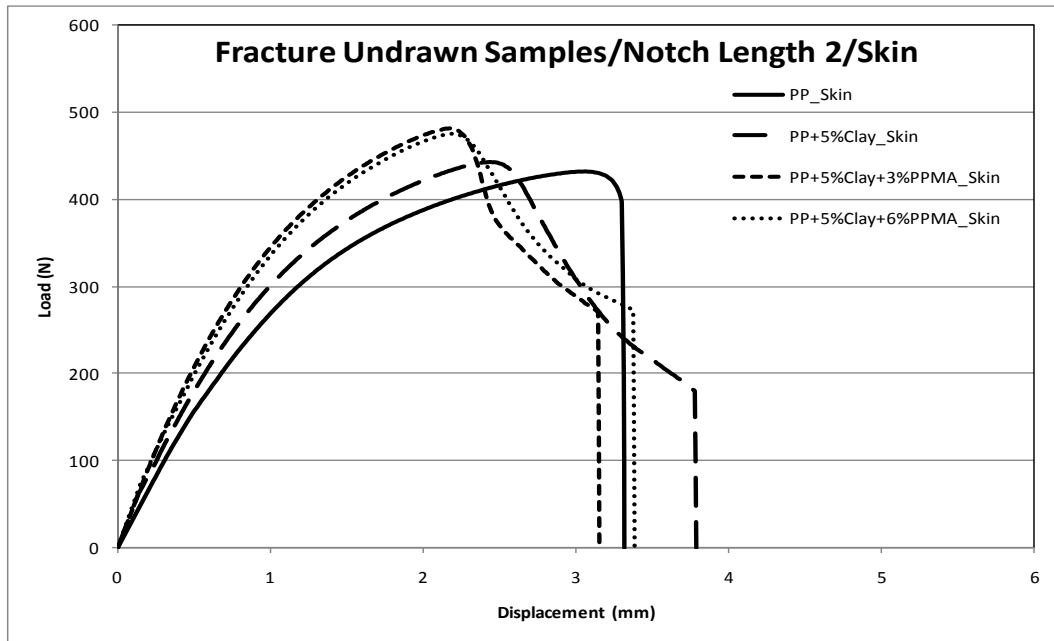


Figure 5.97: Load-displacement plot of 2.0 mm notch for the undrawn skin PP and 5% clay systems of PPNCs

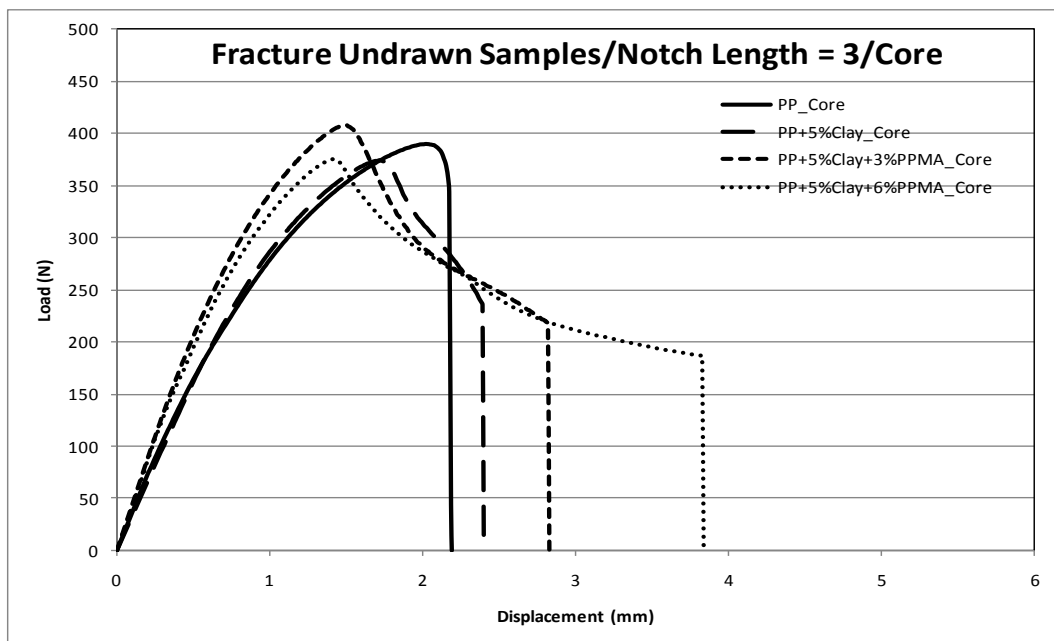


Figure 5.98: Load-displacement plot of 2.5 mm notch for the undrawn core PP and 5% clay systems of PPNCs

In attempt to understand the behaviour of fracture of different 5% clay systems, TEM micrographs were taken for the skin PPNC sample that contains 5% clay and 3% PPMA and compared to the micrograph that were taken from the core of the same sample.

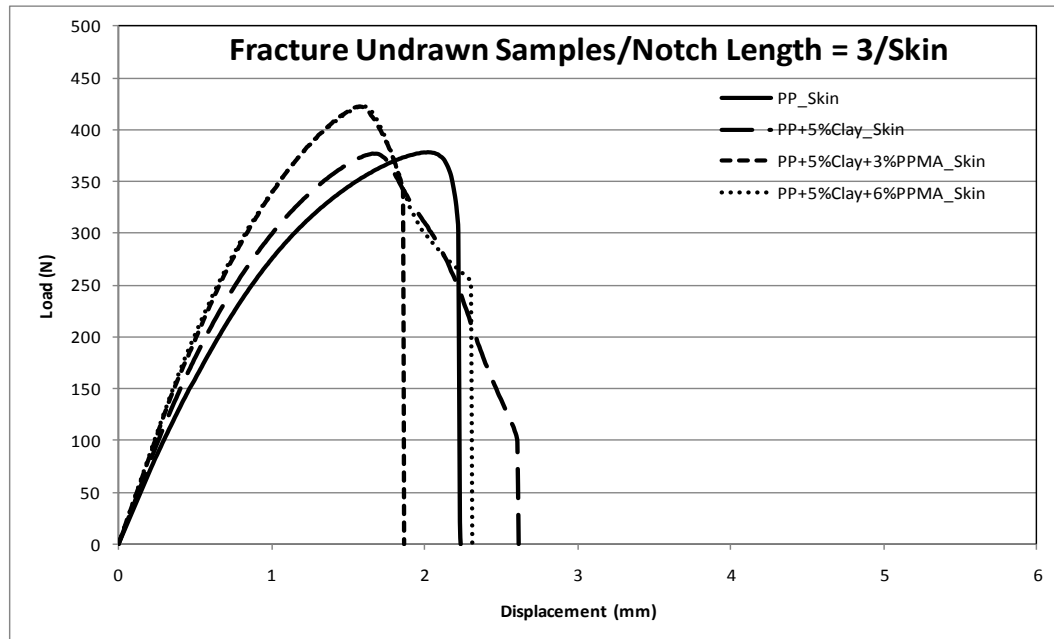


Figure 5.99: Load-displacement plot of 2.5 mm notch for the undrawn skin PP and 5% clay systems of PPNCs

Figure 5.100 shows the two micrographs with their analyses. While the feret diameters are almost the same for the skin and core, there is 20% higher average number of particles in the core micrograph. This may indicate that the clay particles tend to be more in the core during the injection of the polymer melt into the mould cavity. However, this trend may become restrained for the more compatibilized systems and thus the growth of the slope is minimized in sample with 6% PPMA. Conversely, 5% clay system without compatibilizer is expected to have higher tendency to be in the core part of the specimen due to their higher loose of molecular movement as compared to the compatibilized ones. Large size of the clay particles may act as an initiator of voids that might be grown under the imposed deformation and finally coalesce to the neighbouring voids. Such partial precipitate structure with large size clay particles in the core of the injection moulded bar might be responsible for the reported different shapes of the fracture curves and more heat generated that can be seen in thermal images of undrawn samples in Figures from 5.101 to 5.103 at different notch length.

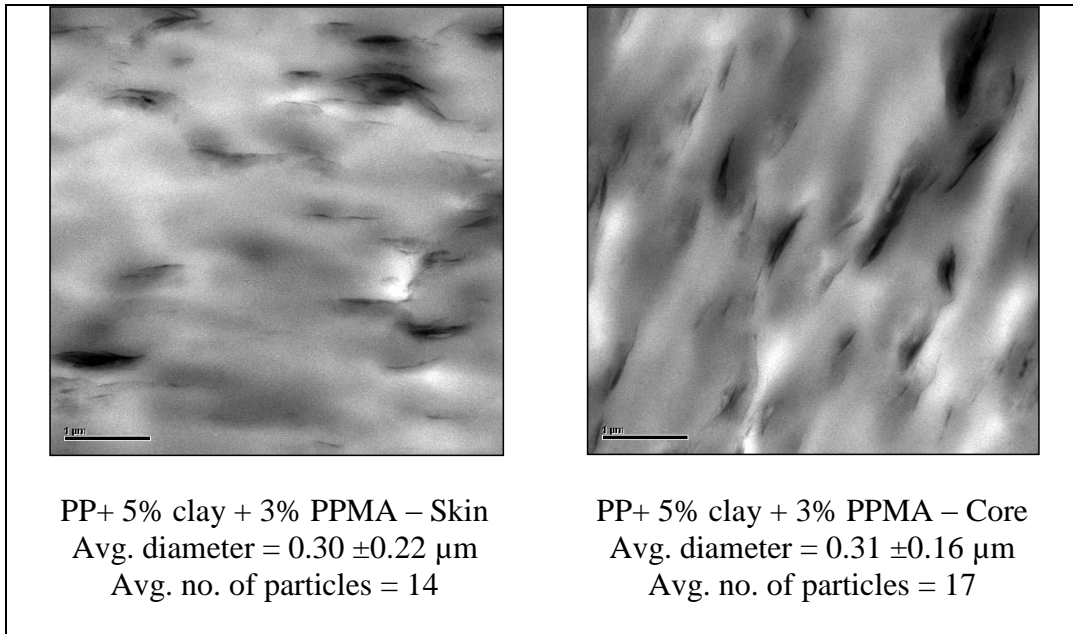


Figure 5.100: TEM micrographs for skin and core of undrawn (PP+ 5% clay+ 3% PPMA

Another important reason that may make the difference in fracture behaviour response of the PPNCs is the orientation of the PP molecules and the clay particles. If it is assumed that the clay particles have a similar degree of orientation in core and skin as it may be concluded from the two micrographs in Figure 5.100, where the clay particles seem to rotate into a position parallel to the direction of stress, the polymer molecular orientation could be the main player in such failure process. In compatibilized 5% clay system, where the PP molecules are linked to the clay gallery, a parity movement of PP and clay hinders to some extent the response of PP molecules to the orientation. This may be supported by the slanting shape of heat generated that can be seen in Figures 5.102 and 5.103 for only some of the compatibilized systems.

5.9.3 Load-displacement behaviour of drawn PPNCs tensile fracture

The load-displacement graphs of the DENT specimens of draw ratios 2, 3, and 4 are discussed in this section with relating to the thermal images that were taken for ligament yielding just before the failure stage and showed in Figures from 5.101 to 5.103 for both undrawn and drawn specimens.

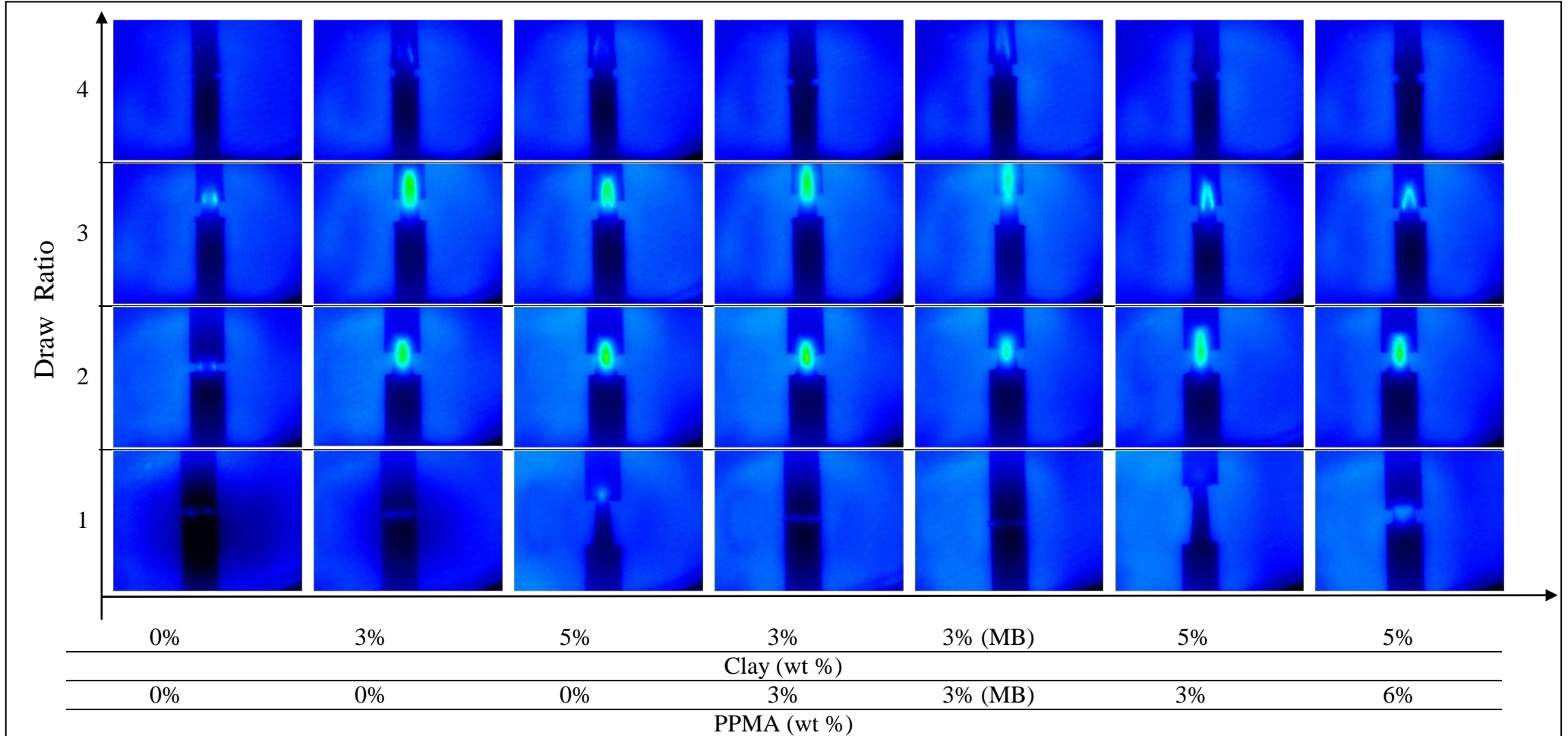


Figure 5.101: Thermal images taken during the fracture test for the first notch length just before the yielded ligament had fully ruptured

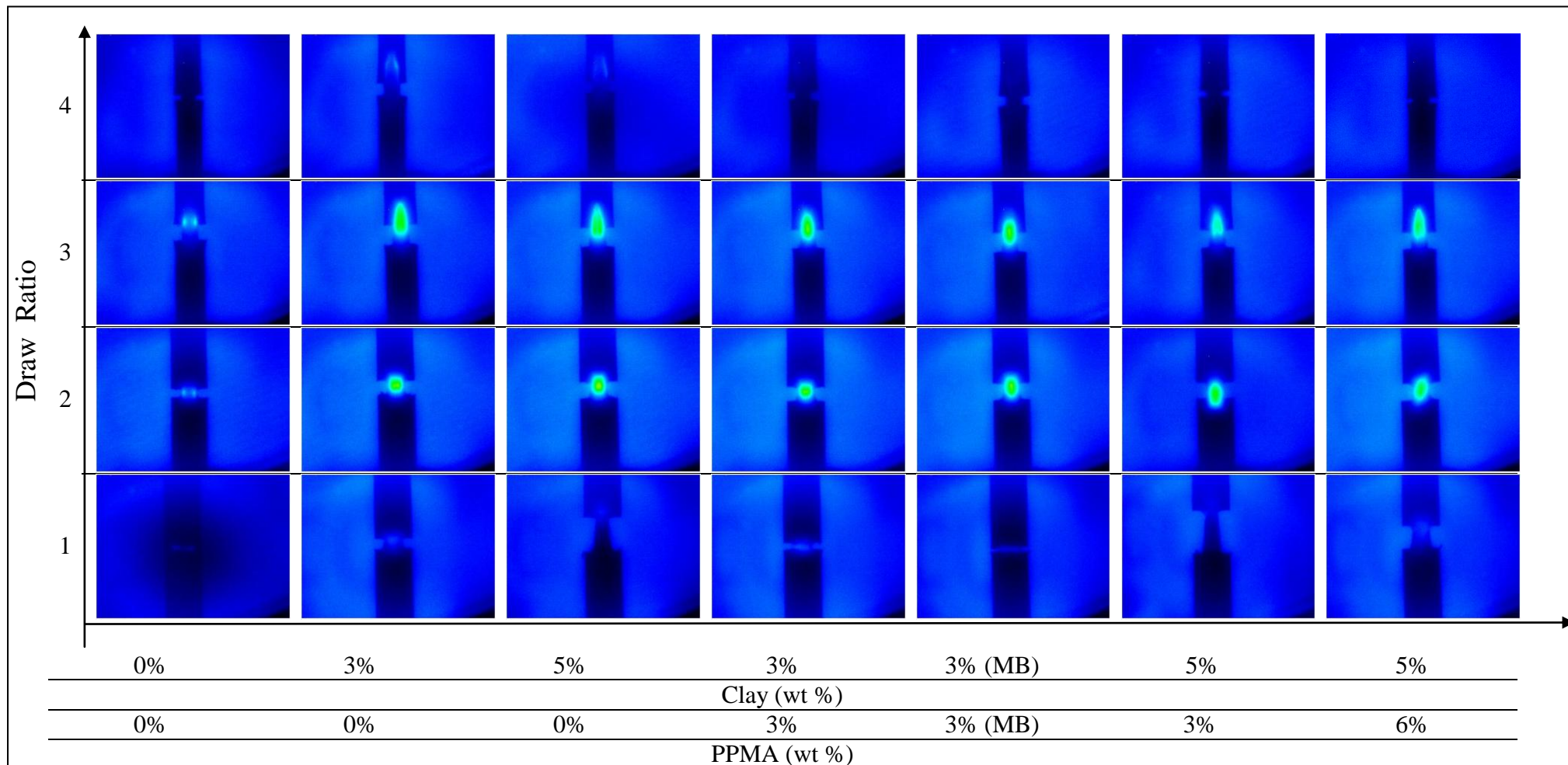


Figure 5.102: Thermal images taken during the fracture test for the second notch length just before the yielded ligament had fully ruptured

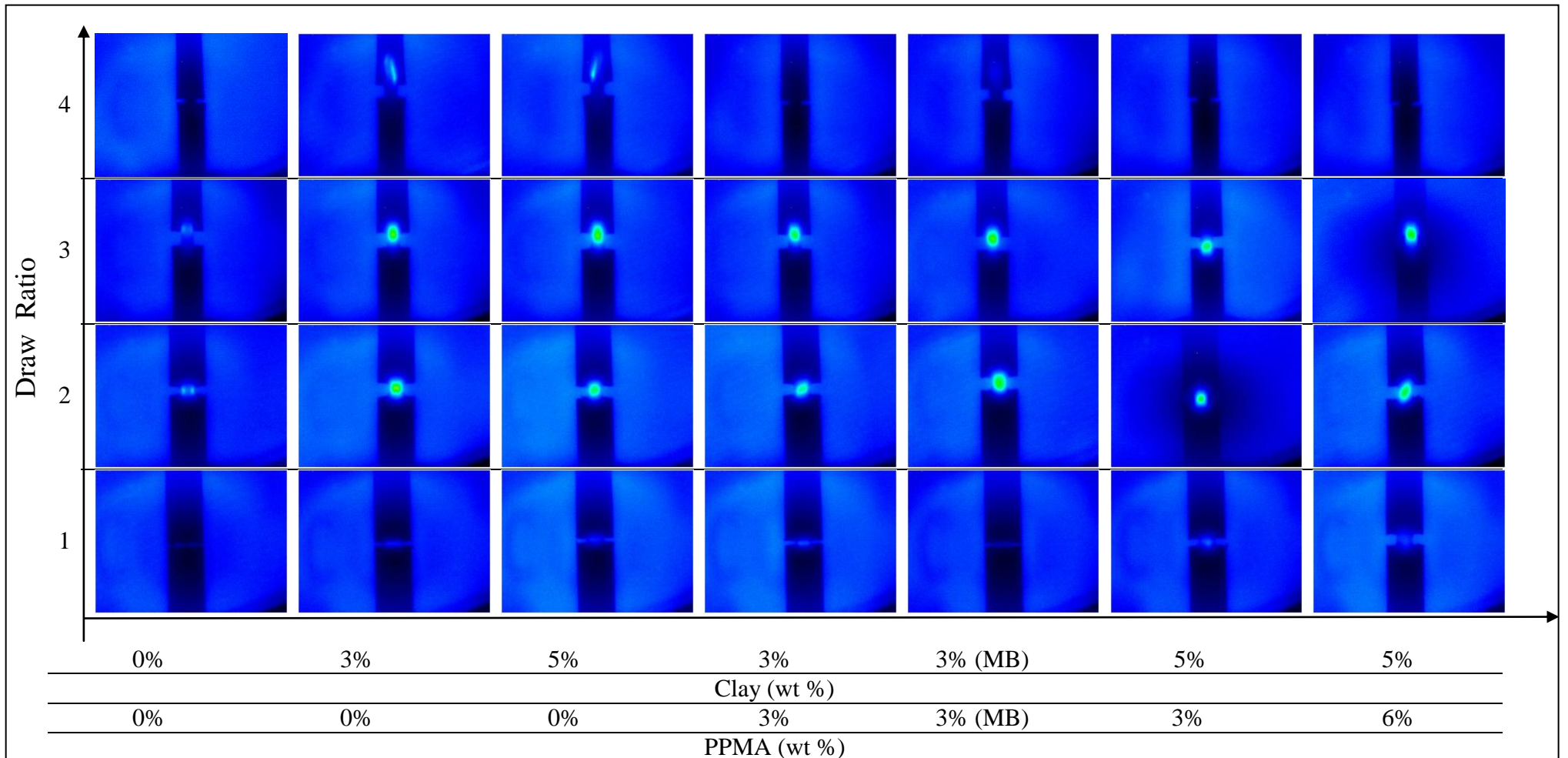


Figure 5.103: Thermal images taken during the fracture test for the third notch length just before the yielded ligament had fully ruptured

5.9.3.1 PPNCs tensile fracture of draw ratio 2

Figures from 5.104 to 5.109 show the fracture behaviour of the PP and PPNCs of draw ratio 2. All PPNCs, for both 3% and 5% clay systems, start with linear elastic regions. Plastic regions are then generated as the displacement is developed at the tip of both sides of the crack. For all PPNCs systems, the ligament completely yielded before the crack starts to propagate and causes the final fracture of the specimen.

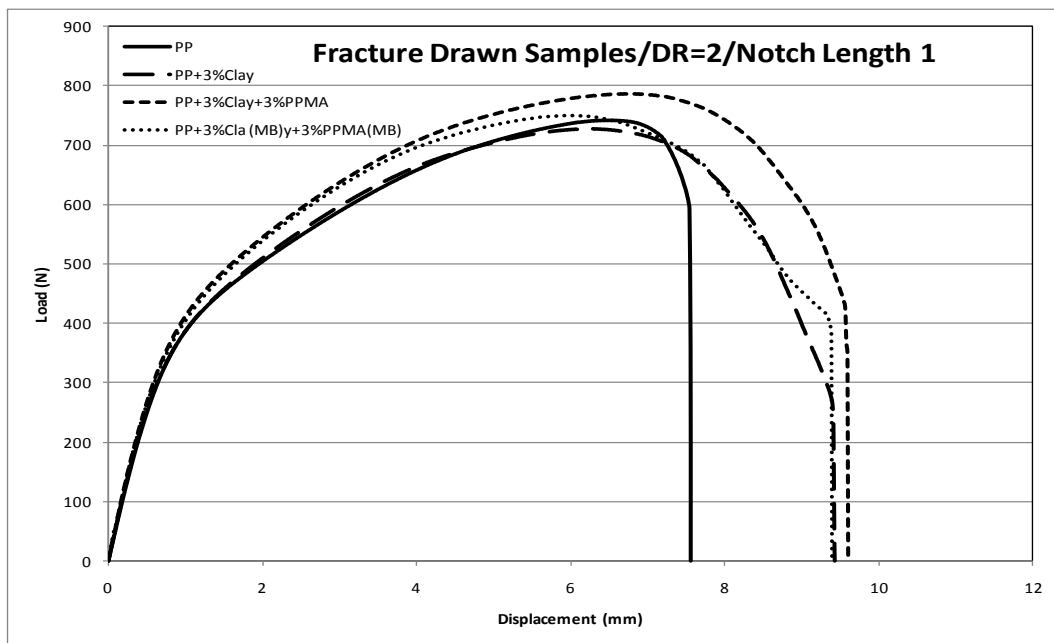


Figure 5.104: Load-displacement plot of the first notch for the drawn PP and 3% clay systems of PPNCs ($\lambda=2$)

These graphs are confirmed by the heat generated and clear yielding of the ligament in thermal and video images (Figures from 5.101 to 5.103). In PP material, the dissipated heat is concentrated on the two sides of the tip due the higher molecular orientation of the polymer than other PPNC systems and possible existing of microvoids in PPNCs. Thus the PP specimens at different notch lengths started the crack propagation in earlier stage as compared to other PPNCs. Thermal images for the draw ratio 2 of the compatibilized 3% and 5% clay systems, as shown in Figure 5.103, exhibit a non-diagonal shapes of heat.

This might be due to the imposed orientation of the linked polymer molecules to the clay galleries.

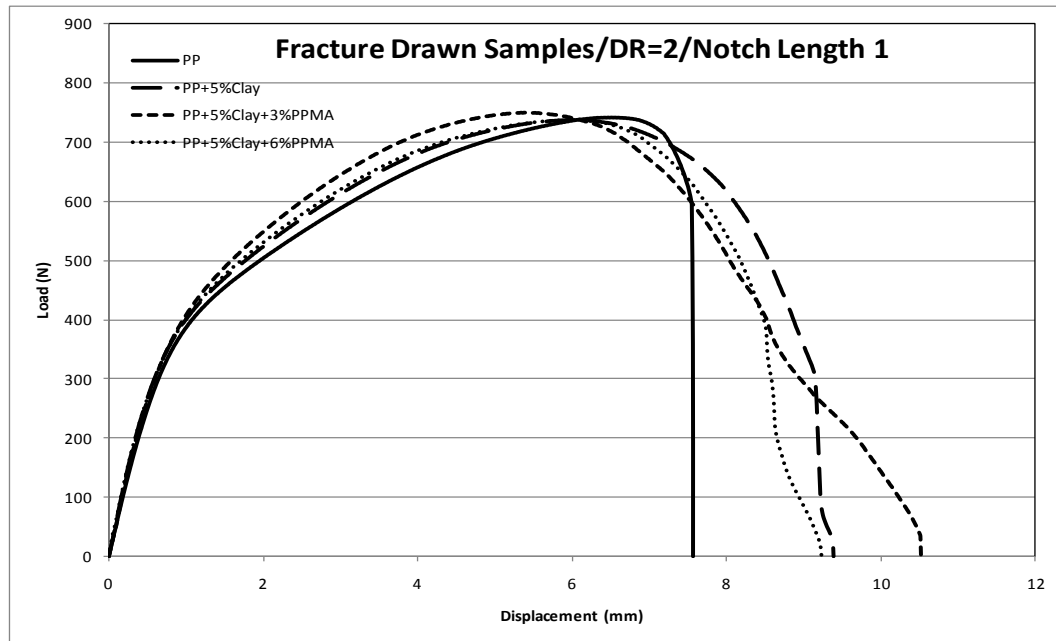


Figure 5.105: Load-displacement plot of the first notch for the drawn PP and 5% clay systems of PPNCs ($\lambda=2$)

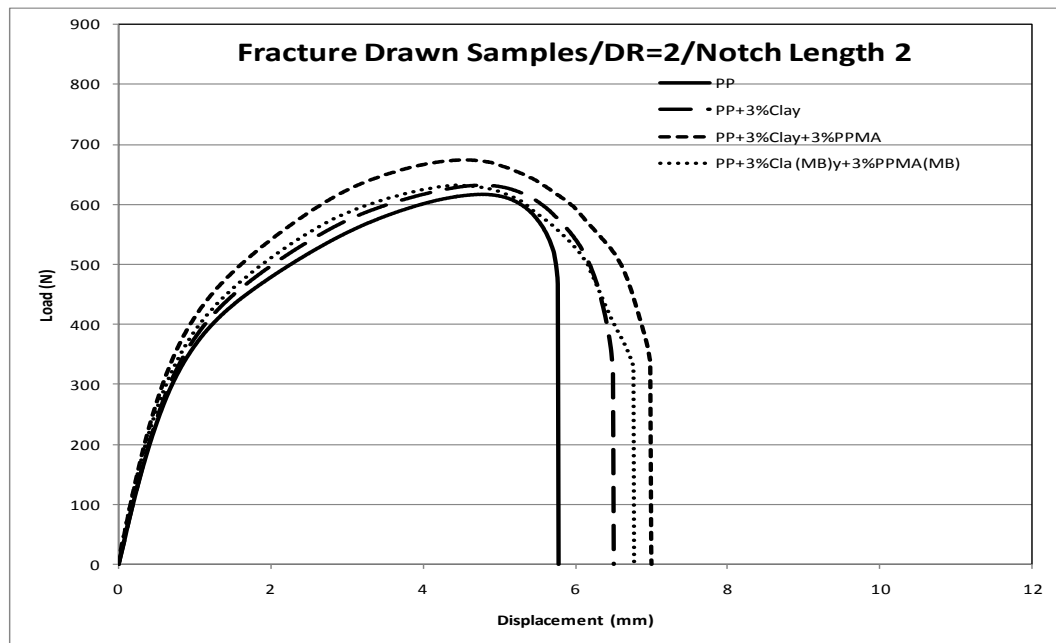


Figure 5.106: Load-displacement plot of the second notch for the drawn PP and 3% clay systems of PPNCs ($\lambda=2$)

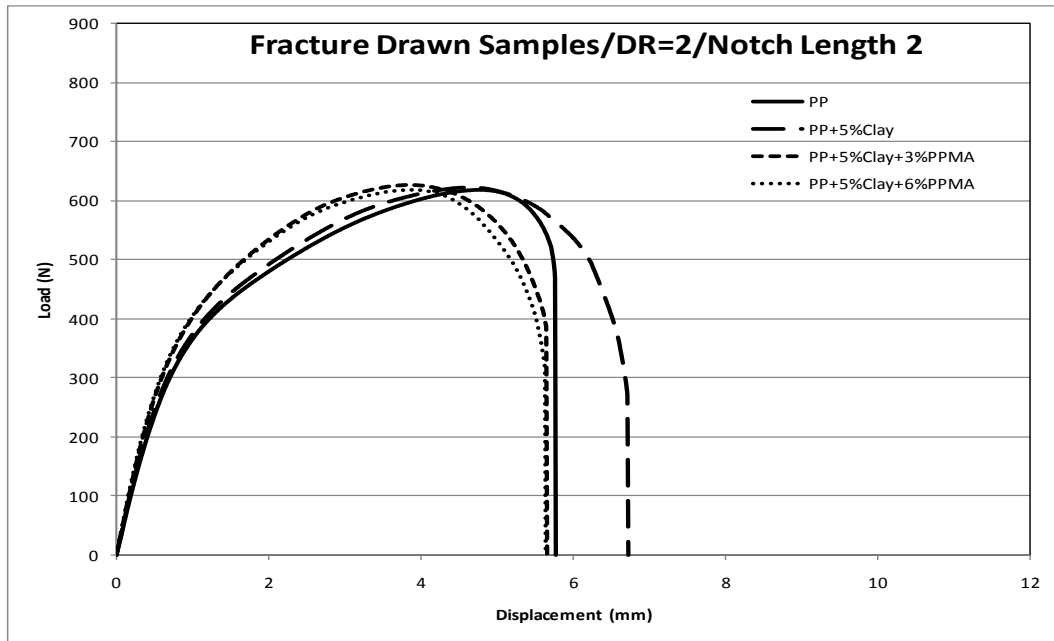


Figure 5.107: Load-displacement plot of the second notch for the drawn PP and 5% clay systems of PPNCs ($\lambda=2$)

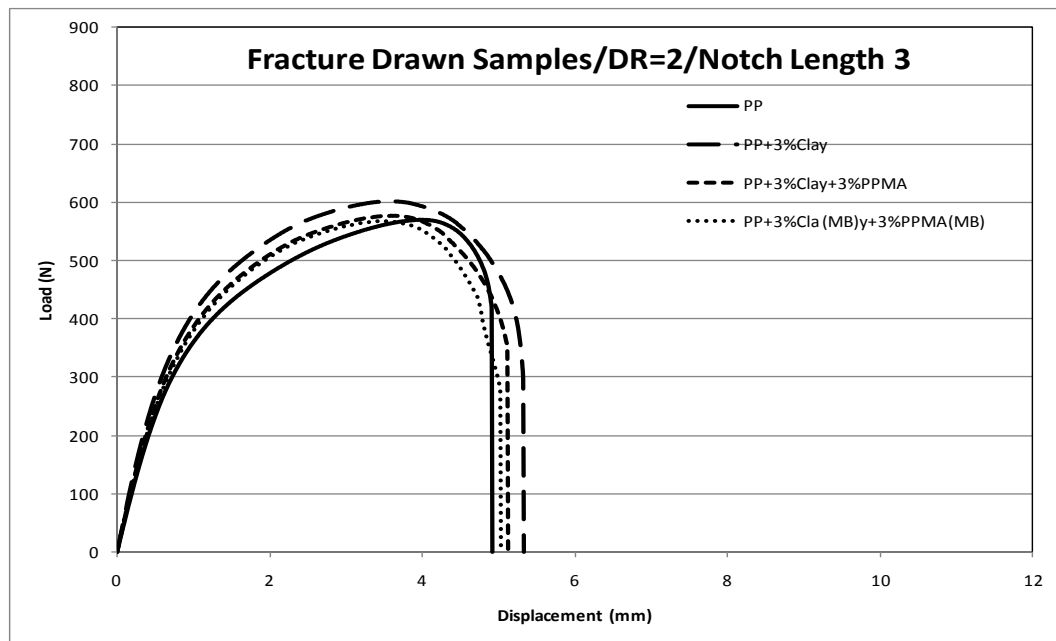


Figure 5.108: Load-displacement plot of the third notch for the drawn PP and 3% clay systems of PPNCs ($\lambda=2$)

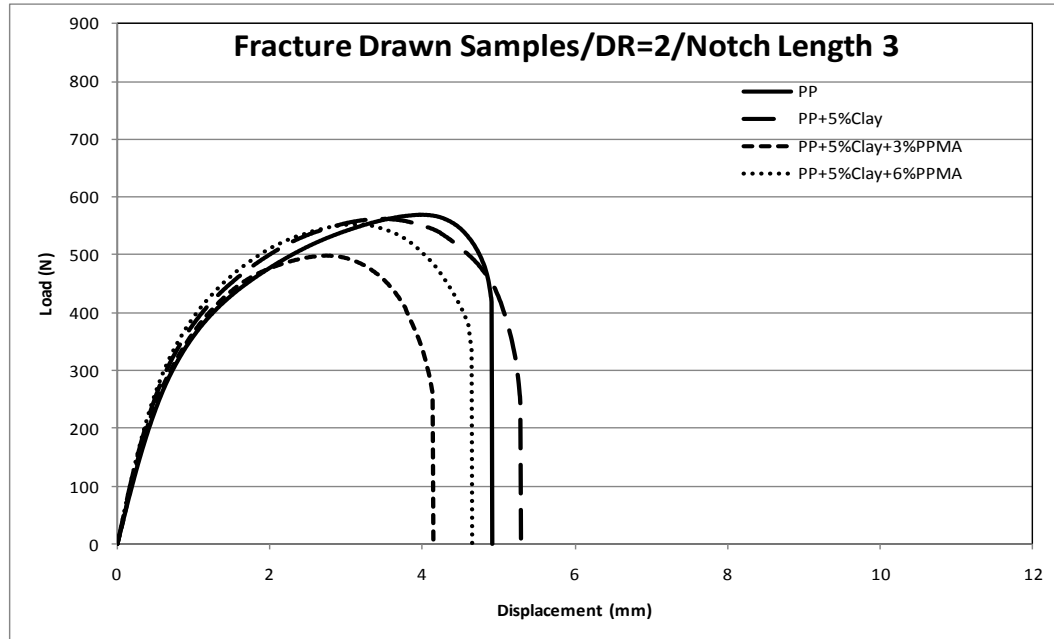


Figure 5.109: Load-displacement plot of the third notch for the drawn PP and 5% clay systems of PPNCs ($\lambda=2$)

5.9.3.2 PPNCs tensile fracture of draw ratio 3

More oriented molecules and clay particles are expected to be higher for the draw ratio 3 as compared to the orientation of the draw ratio 2. TEM micrographs confirmed the higher clay particles orientation as the draw ratio increases. This higher orientation system of PP molecules can concentrate more stresses at the two-tip sides of the ligament, as shown for the PP material in thermal images (Figure 5.101 and 5.102). The contribution of the clay particles with possible existence of microvoids resists such excessive stresses at the tip of the ligament. However, the compatibilized systems at higher ligament length, where the microvoids might be expected to be less than the uncompatibilized systems, show very two stressed lines start from the two-tip sides of the ligament in the direction of the applied load. This behaviour is not observed for the uncompatibilized systems at different notch length.

Although the effect of PP molecular alignments can change the fracture behaviour, it is confirmed by the thermal images that the produced yield for all

draw ratio 3 samples are taken place in the ligament area and not dissipated by any mean through the specimen. Figures from 5.110 to 5.115 show clearly that the degree of fully yielded ligaments of the load-displacement is reduced in the draw ratio 3 of PPNCs as compared to that can be seen in draw ratio 2.

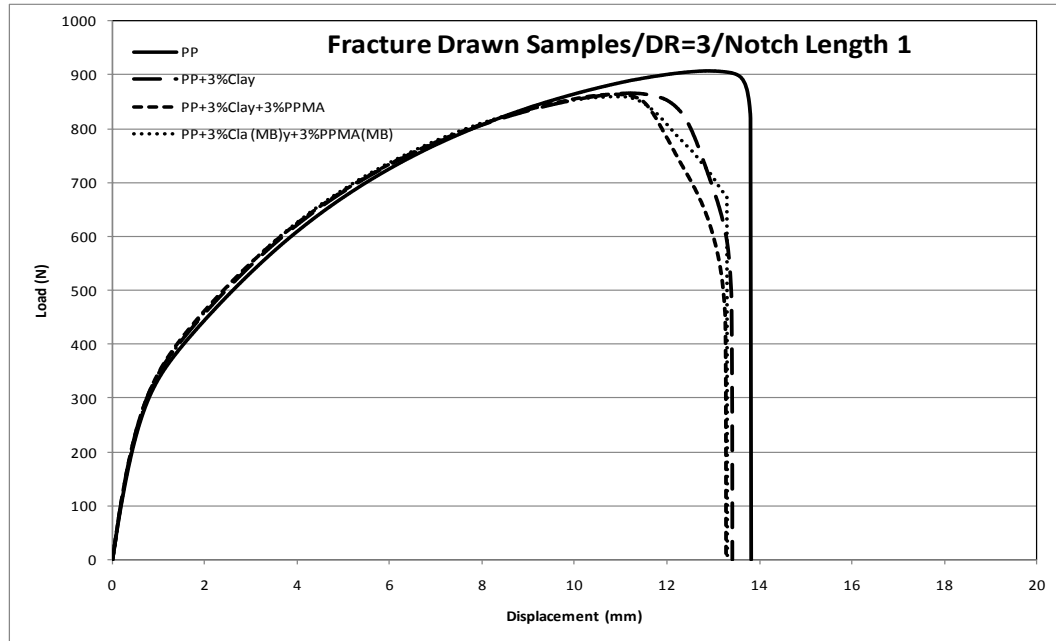


Figure 5.110: Load-displacement plot of the first notch for the drawn PP and 3% clay systems of PPNCs ($\lambda=3$)

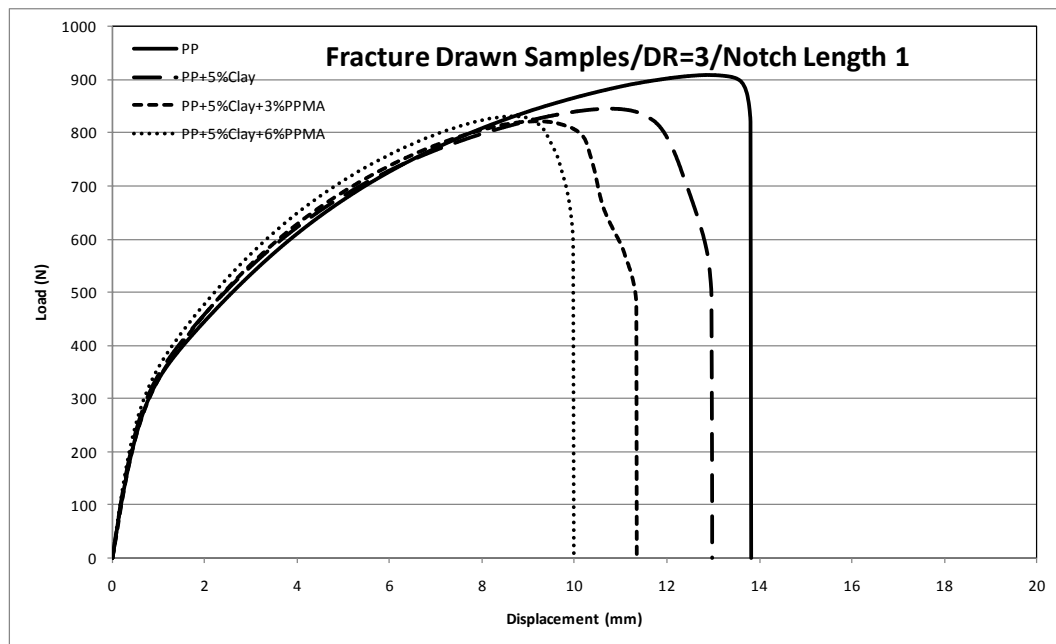


Figure 5.111: Load-displacement plot of the first notch for the drawn PP and 5% clay systems of PPNCs ($\lambda=3$)

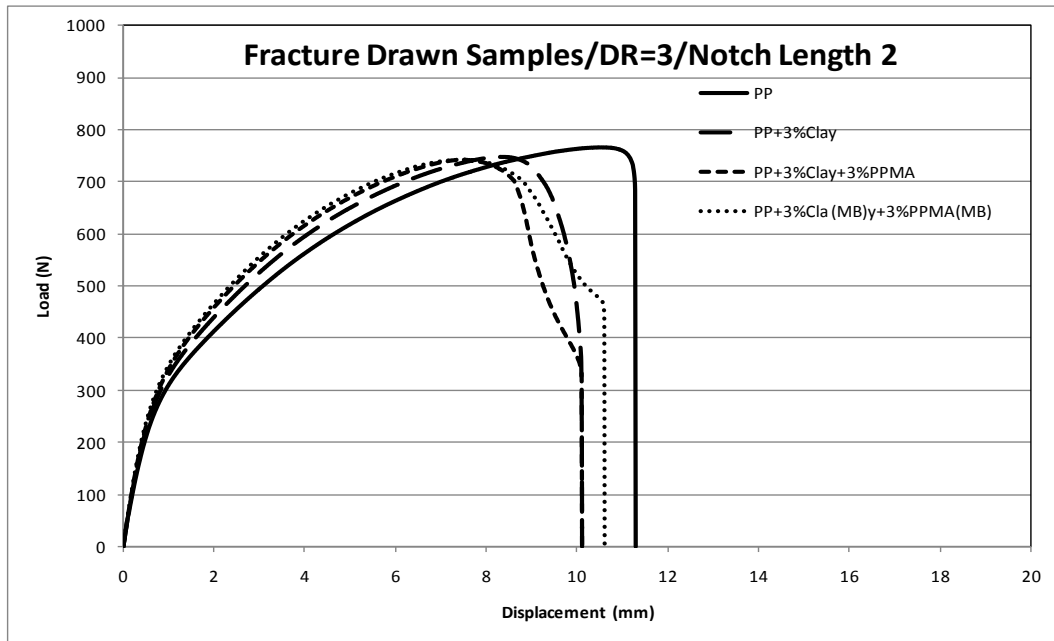


Figure 5.112: Load-displacement plot of the second notch for the drawn PP and 3% clay systems of PPNCs ($\lambda=3$)

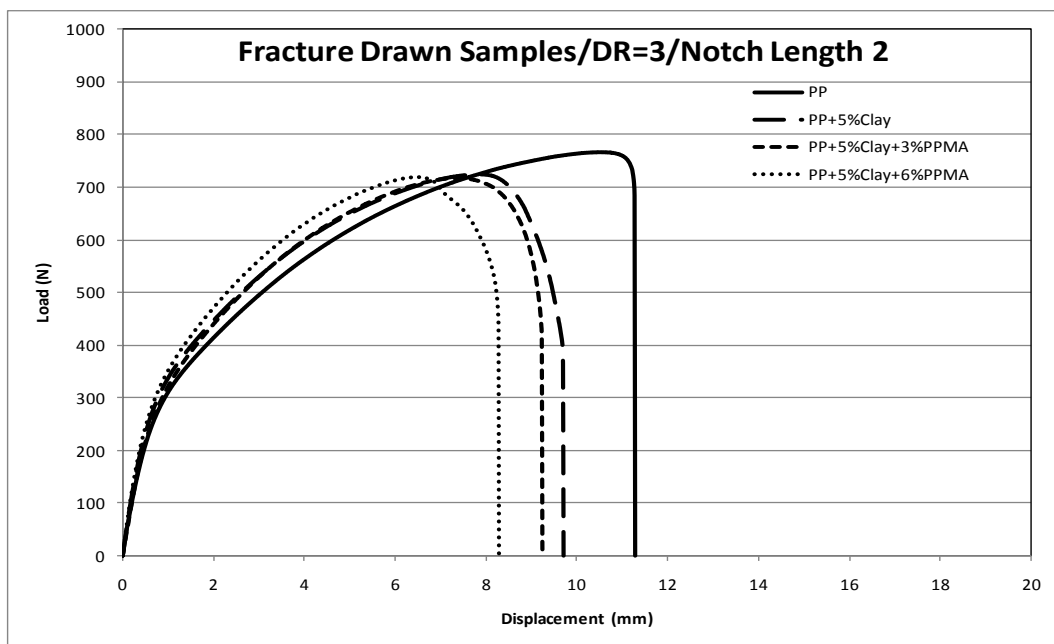


Figure 5.113: Load-displacement plot of the second notch for the drawn PP and 5% clay systems of PPNCs ($\lambda=3$)

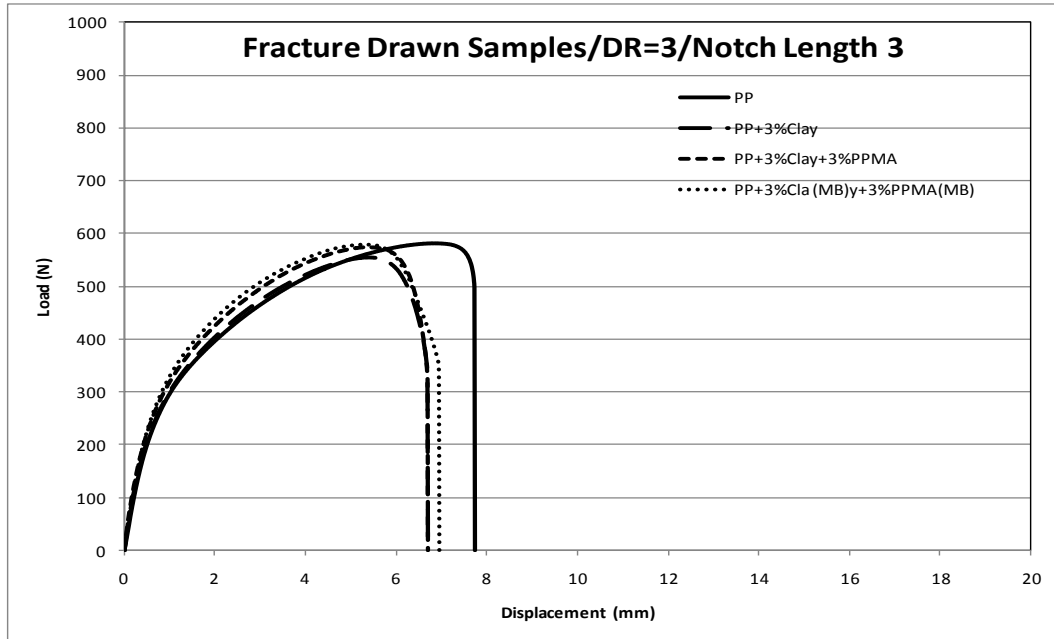


Figure 5.114: Load-displacement plot of the third notch for the drawn PP and 3% clay systems of PPNCs ($\lambda=3$)

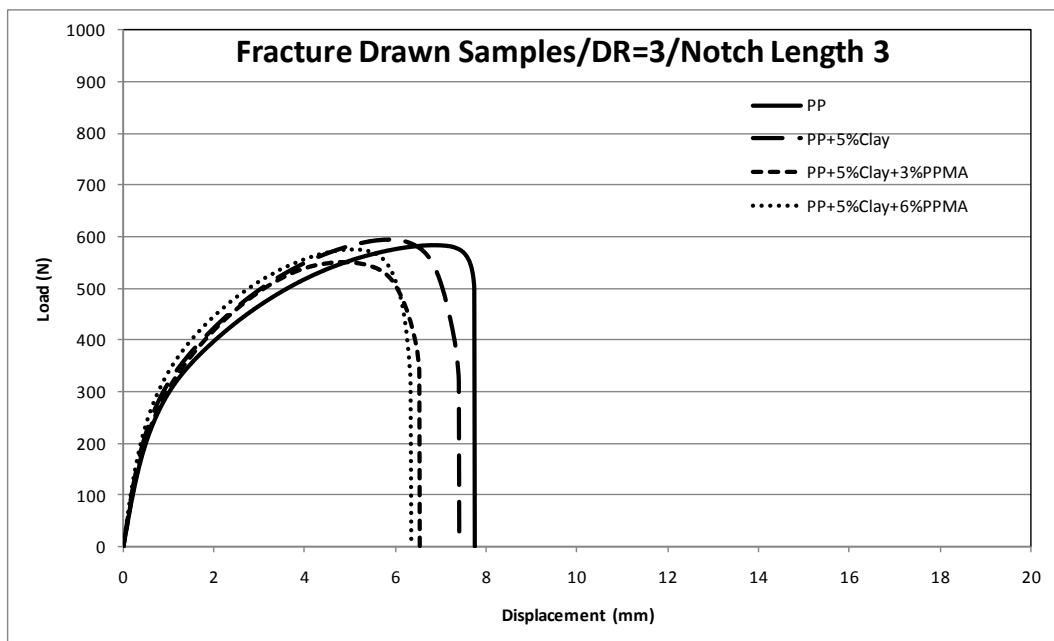


Figure 5.115: Load-displacement plot of the third notch for the drawn PP and 5% clay systems of PPNCs ($\lambda=3$)

5.9.3.3 PPNCs tensile fracture of draw ratio 4

The load-displacement graphs of PP and PPNCs, at draw ratio 4, are shown in Figures from 5.116 to 5.121. It can be seen clearly that after the linear elastic regions, the plastic regions are generated, showing that the energy is dissipated through all specimen and not only in the ligament area. However, the

PP and some compatibilized systems as shown in the thermal images do not exhibit any heat dissipation in the sample ligament, but rather go through the whole specimen. This might be attributed to the very high molecular alignment system. In contrast, the uncompatibilized systems slightly disturb this molecular alignment, but cannot reduce its effect. Thus the uncompatibilized systems are noticed to have higher fracture toughness at draw ratio 4.

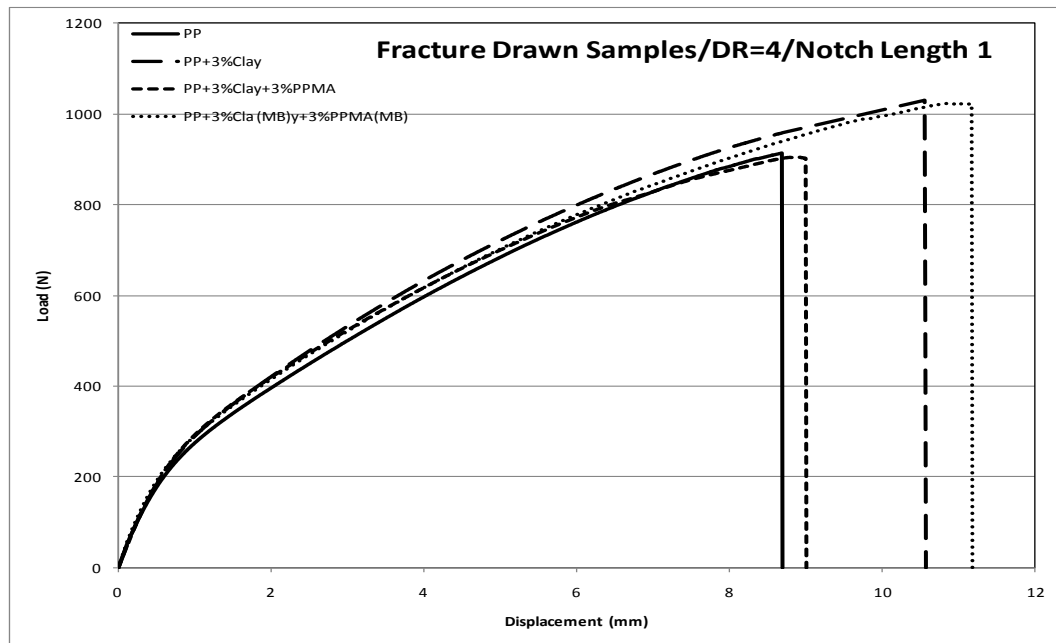


Figure 5.116: Load-displacement plot of the first notch for the drawn PP and 3% clay systems of PPNCs ($\lambda=4$)

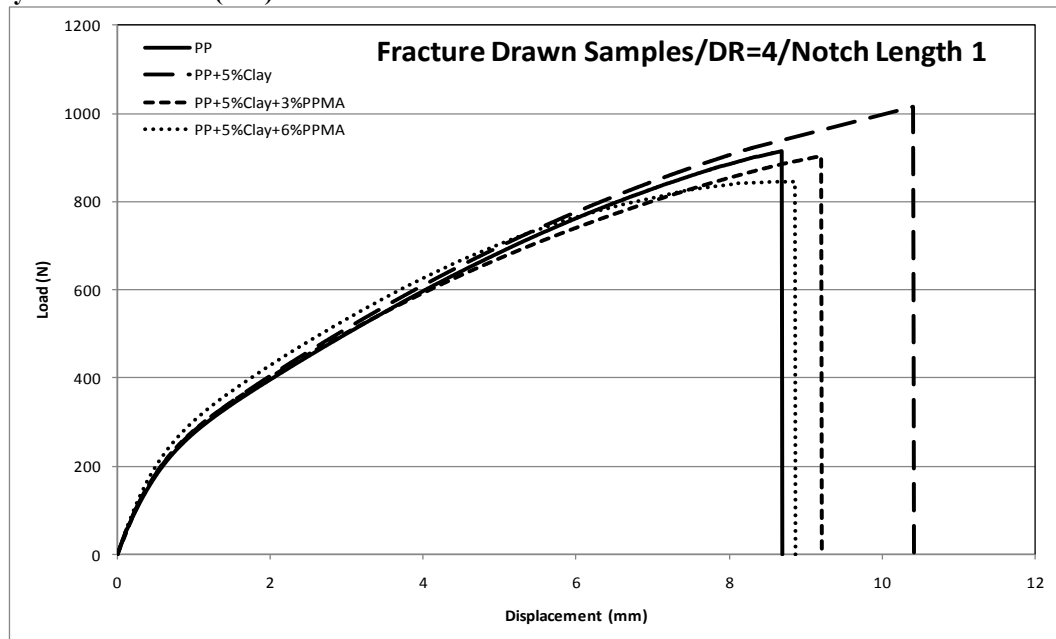


Figure 5.117: Load-displacement plot of the first notch for the drawn PP and 5% clay systems of PPNCs ($\lambda=4$)

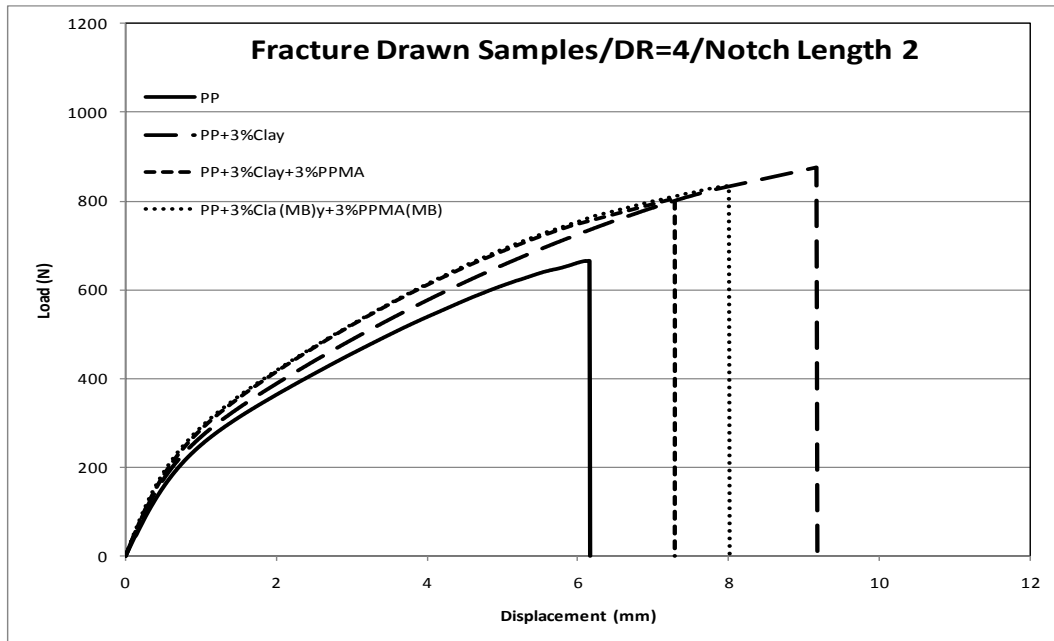


Figure 5.118: Load-displacement plot of the second notch for the drawn PP and 3% clay systems of PPNCs ($\lambda=4$)

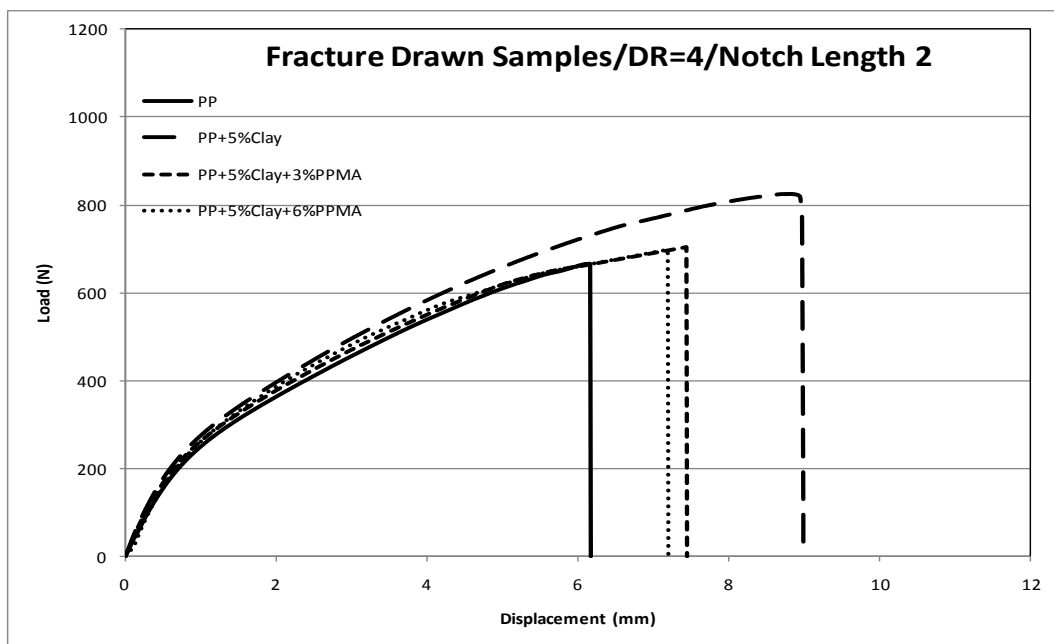


Figure 5.119: Load-displacement plot of the second notch for the drawn PP and 5% clay systems of PPNCs ($\lambda=4$)

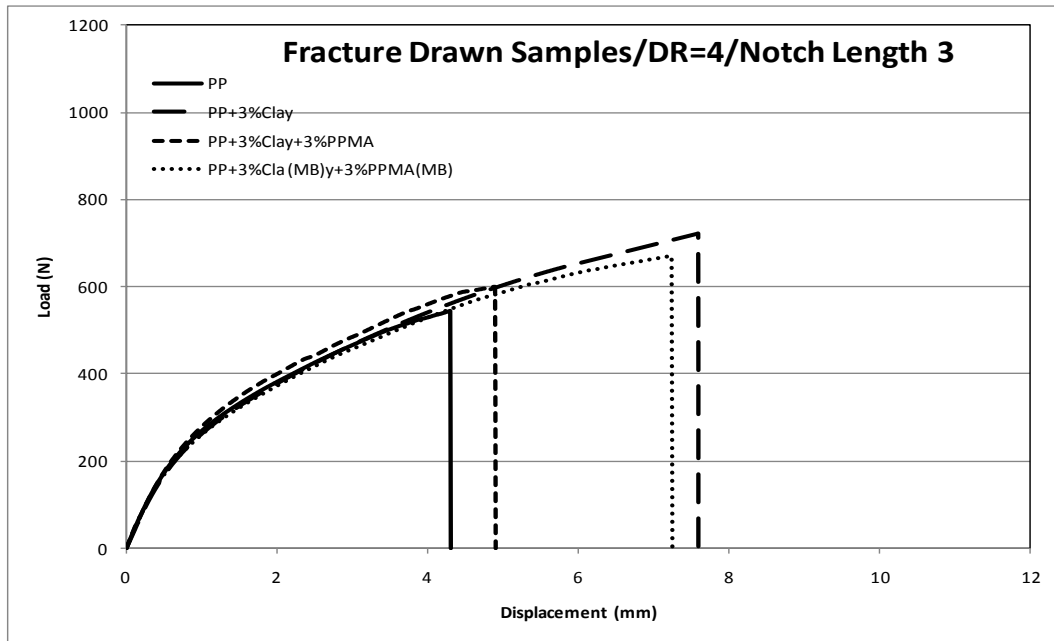


Figure 5.120: Load-displacement plot of the third notch for the drawn PP and 3% clay systems of PPNCs ($\lambda=4$)

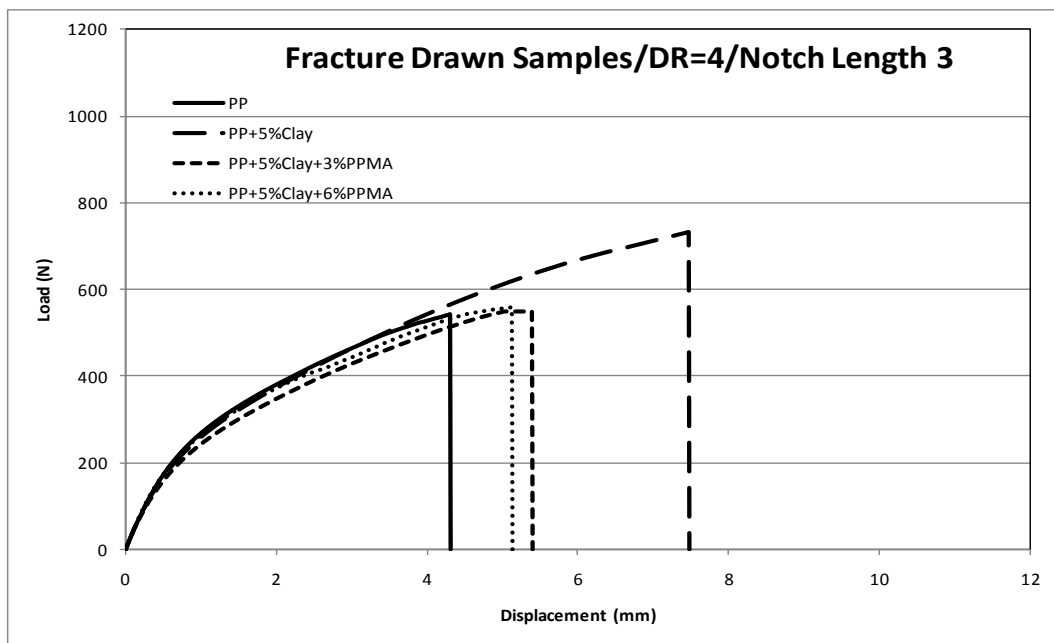


Figure 5.121: Load-displacement plot of the third notch for the drawn PP and 5% clay systems of PPNCs ($\lambda=4$)

5.9.4 Total work of fracture of PPNCs

The different behaviour of tensile fracture that are discussed in the previous two sections makes the toughness measurement by the area under the curve of load-displacement to be very expressive method to evaluate the different drawn and undrawn PP and PPNC samples. However care should be taken in the

following comparison of total work of fracture for the draw ratio 4, where it is remarked that the yielding occurs in whole specimen rather than works in the specified area between the tips of ligament. This may cause a conflicting conclusion in the obtained results between load-displacement graphs and thermal images. Total work of fracture for all draw ratio 4 samples is presented with dots in all Figures from 5.122 to 5.130, which refer to different behaviour of failures. Total work of fracture as a function in the ligament length for different draw ratios is given in Appendix J.

5.9.4.1 Effect of draw ratio on the total work of fracture at low notch length

Figure 5.122 shows the total work of fracture at low notch length of 3% clay systems as compared to the pure PP. The undrawn PP shows 12% and 15% higher toughness than the uncompatibilized and compatibilized systems respectively, but 14% lower than the 3% clay system, which was produced from one-step master batch compounding. The toughness tends to improve as enough microvoids might be introduced to the system. The TEM micrographs of the one-step master batch sample do not show good distribution of clay particles, but 30% lower in feret diameter than the 3% uncompatibilized clay system. This higher surface contact between polymer and clay of the one-step master batch system might be enough to have the microvoids structure that improves the toughness. Conversely, the large agglomeration areas reduce the surface contact of 3% clay system and do not allow the system to resist the failure. At the same time, the well distributed 3% clay system with compatibilizer makes very high surface contact but such interaction structure of the polymer into clay gallery

may reduce the generated microvoids and cause a reduction in the toughness measurement.

As the draw ratio increases to 2, the possible existence of microvoids in such well distributed compatibilized systems are grown and reached to a favourable degree that allows higher fracture toughness as compared to PP and other 3% clay systems. More sample stretching, at draw ratio 3, may increase the microvoids of all 3% clay systems to a level where materials can not stand and crack propagates at earlier stages. The more flexibility of the pure PP molecules and/or the possible microvoids at draw ratio 3, give the turn to the PP samples to take advantage over all 3% systems. More stretching to draw ratio 4 does not pursue a better property, as the PP free volume does not permit any further mobility of other segments of the polymer chains.

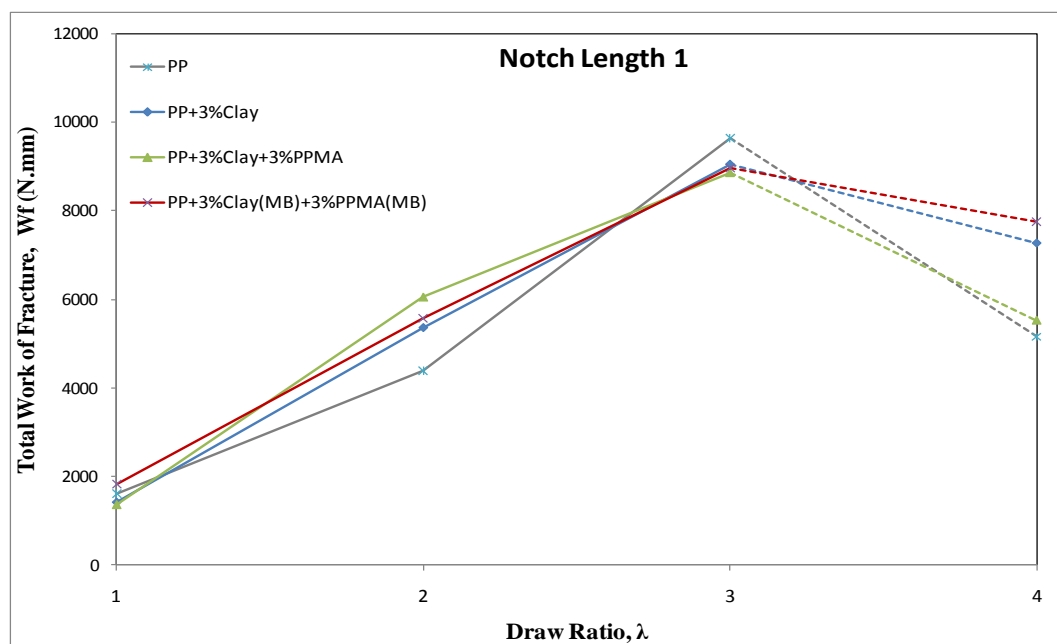


Figure 5.122: Effect of draw ratio on the total work of fracture of PP and 3% clay systems PPNCs at low notch length

5% clay systems of PPNCs are shown in Figure 5.123 and compared to the pure PP. The 5% compatibilized systems have higher total work of fracture

than pure PP for undrawn samples and that with draw ratio 2. However, they do not show any notable increase after draw ratio 2. At draw ratio 3, PP records about 34% and 11% higher toughness than the compatibilized and uncompatibilized systems, respectively.

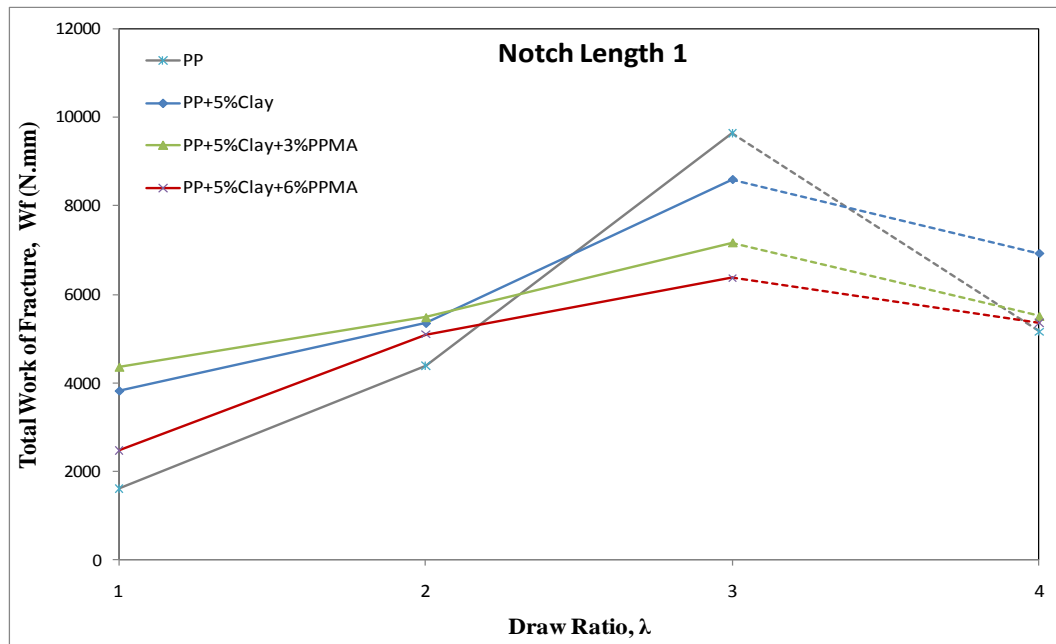


Figure 5.123: Effect of draw ratio on the total work of fracture of PP and 5% clay systems PPNCs at low notch length

This behaviour is similar to some extent the explained 3 % systems with taking in consideration that the packed 5% clay system can lead to higher toughness for undrawn and low draw ratio systems, but as the draw ratio increases the microvoids coalesce with neighbouring voids that bridged the crack in process zone and eventually may lead to an earlier failure. This behaviour may explain the difference between the uncompatibilized 3% and 5% clay systems that are shown in Figure 5.124, as the 5% clay system achieves a huge improvement over the 3% clay system for undrawn samples (170%). This increment is minimized to be exactly the same as the 3% clay system at draw

ratio 2 and a reduction of 5% at draw ratio 3 as the coalescence phenomena of the microvoids might be dominant.

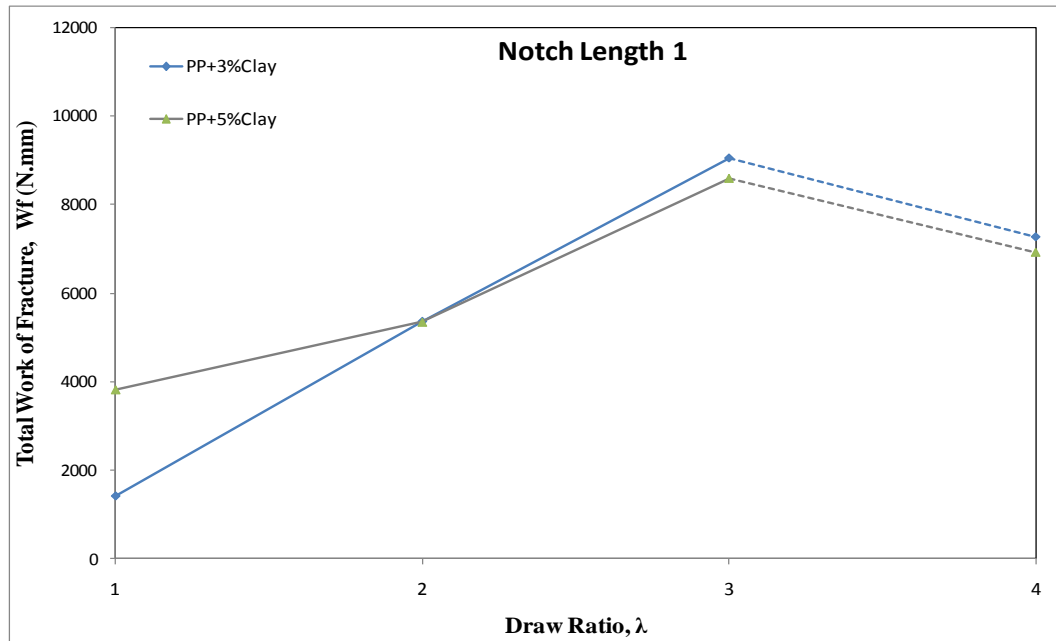


Figure 5.124: Effect of draw ratio on the total work of fracture of uncompatibilized 3% and 5% clay systems PPNCs at low notch length

5.9.4.2 Effect of draw ratio on the total work of fracture of PPNCs of medium notch length

As the ligament of the compared samples is reduced at medium notch length, very similar behaviours of undrawn and drawn PPNCs are obtained and shown in Figures from 5.125 to 5.127. All graphs are shifted to about 30% lower total work of fracture as the medium notch length is introduced. The superior improvement of the pure PP at draw ratio 3 tends to be more, especially in the 5% clay systems. This might be explained by the difference in sample uniformity of the same PP and the PP/clay matrixes. Such composite system could initiate the crack in earlier stage as it is exposed to smaller ligament length, which may reduce the ability of microvoids to spread through the ligament area without causing the failure.

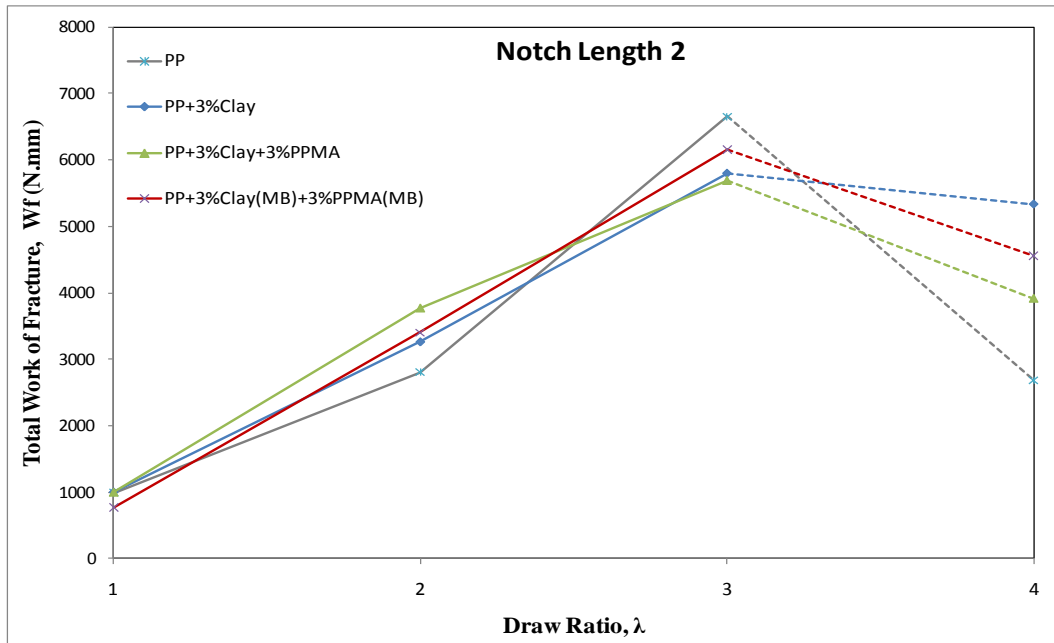


Figure 5.125: Effect of draw ratio on the total work of fracture of PP and 3% clay systems PPNCs at medium notch length

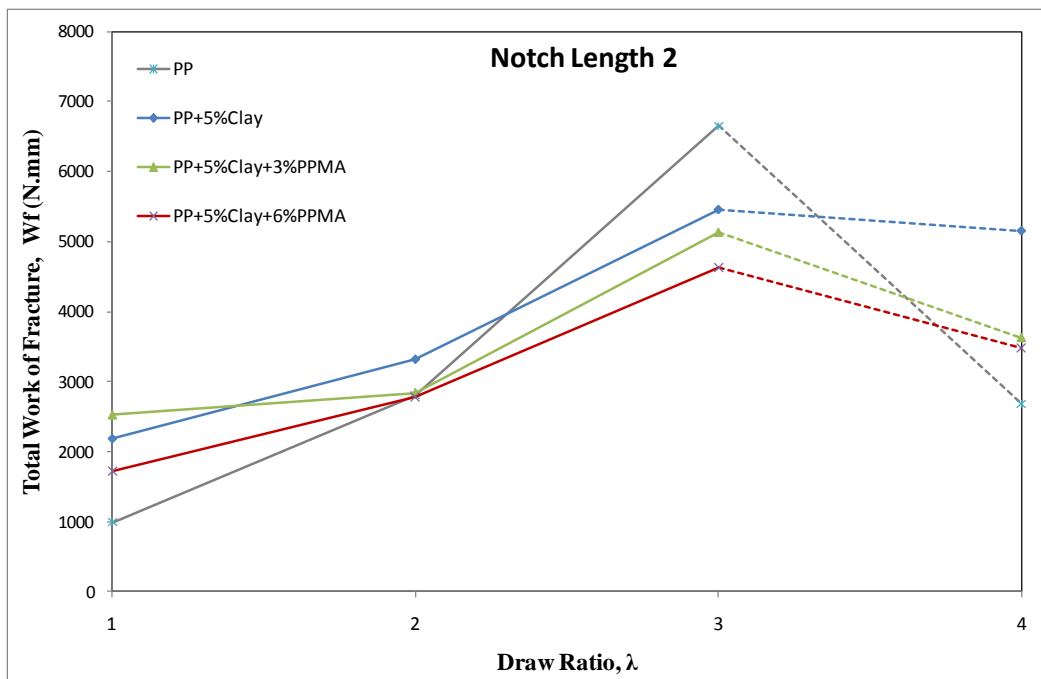


Figure 5.126: Effect of draw ratio on the total work of fracture of PP and 5% clay systems PPNCs at medium notch length

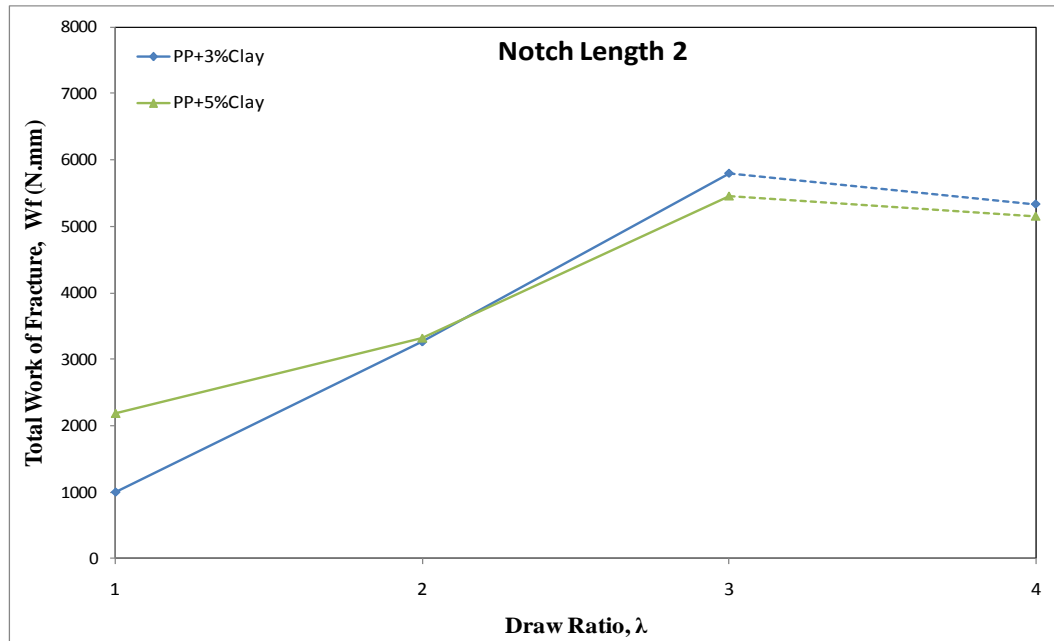


Figure 5.127: Effect of draw ratio on the total work of fracture of uncompatibilized 3% and 5% clay systems PPNCs at medium notch length

5.9.4.3 Effect of draw ratio on the total work of fracture of PPNCs of high notch length

Figures 5.128, 5.129 and 5.130 show the effect of high notch length on the total work of fracture of different PPNCs. As the notch increased to the highest used length, the total work of fracture is decreased to 63% as compared to the lowest notch length.

The results fluctuations at the smallest used ligament length and the slight different obtained results for some PPNCs might be attributed to the nonuniform microvoids structure of composites that may happen even the well clay particles distribution is involved. In these clay-microvoid systems, the used high notch length should be avoided or adjusted with higher sample width and thickness. Such higher geometry should consider a large produced part in injection moulding or compression moulding and a larger designed die of drawing to get

benefit from the reported toughness improvement of drawn PP at draw ratio of 3 and reported improvement of composite systems at draw ratio 2.

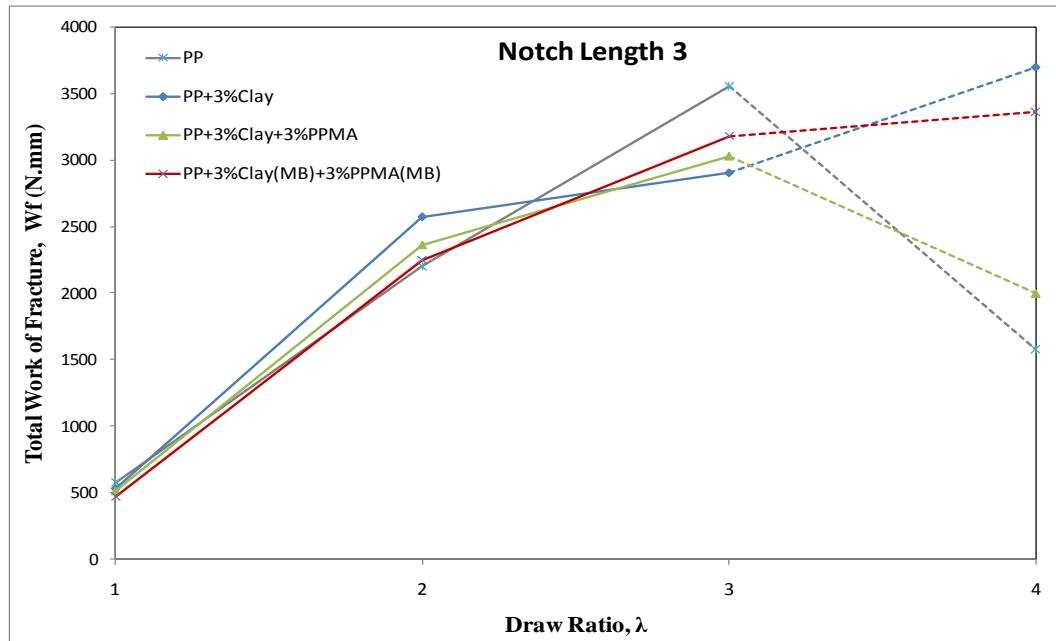


Figure 5.128: Effect of draw ratio on the total work of fracture of PP and 3% clay systems PPNCs at high notch length

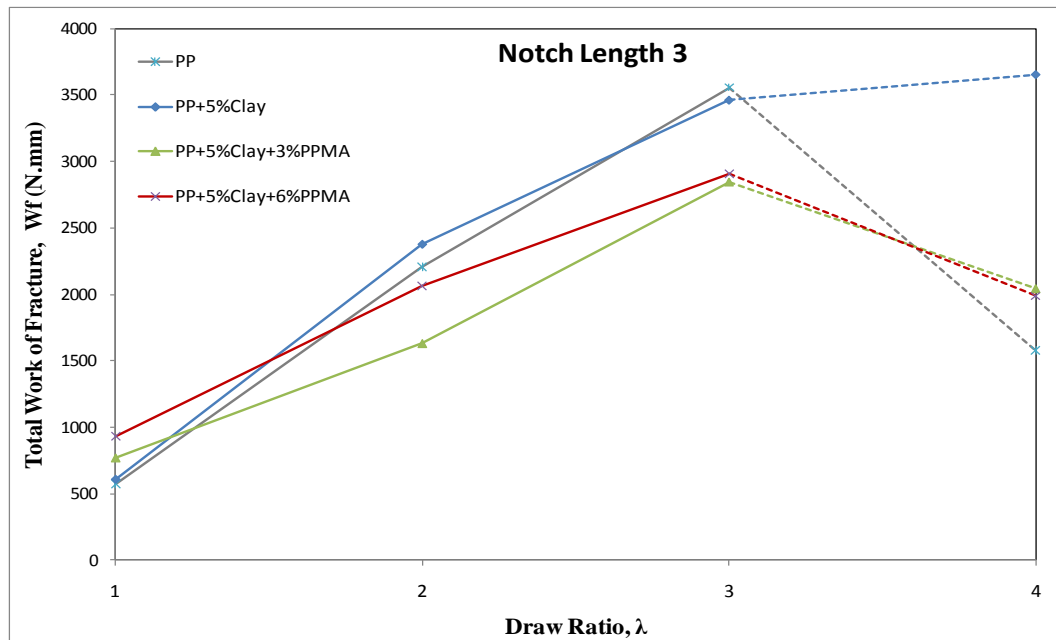


Figure 5.129: Effect of draw ratio on the total work of fracture of PP and 5% clay systems PPNCs at high notch length

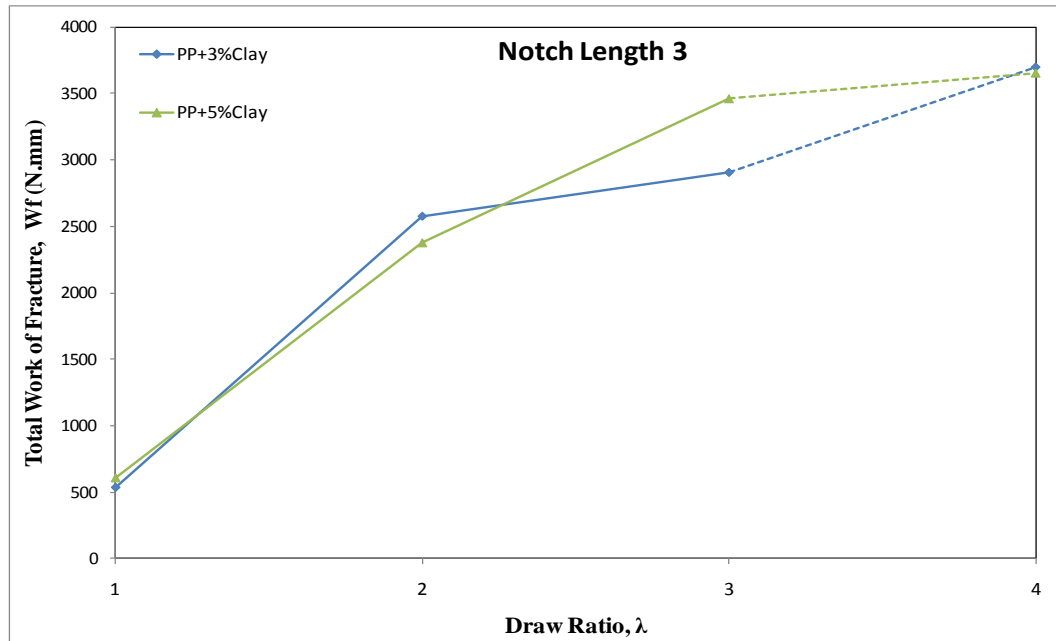


Figure 5.130: Effect of draw ratio on the total work of fracture of uncompatibilized 3% and 5% clay systems PPNCs at high notch length

In general, it is concluded that an understanding of the balance between any measured macroscopic property and the clay content can suggest new applications for undrawn PPNCs and drawn composite systems at low draw ratios, where the composites exhibit highly significant improvement over the PP. At moderate and high draw ratios, PPNCs failure might be governed by either the growth of microvoids at low clay content or the coalescence of microvoids at high clay content, when failure is at an earlier stage than for pure PP.

6 Conclusions, Recommendations and Suggestions for the Future Work

6.1 DSC and TGA Results of PPNCs Compounding Samples

6.1.1 DSC Results of PPNCs Compounding Samples

The result of crystallinity demonstrates that PPMA does not significantly affect the crystallinity of PP for loading percentage less than 6%. On the contrary, when the clay is added to PP without PPMA, a similarity in crystallinity is detectable (precisely 5 % of clay in pure PP causes a loss in crystalline phase of only 1 %). This loss is reduced to nothing when loading decreases to 3%. PP/clay/PPMA systems showed slight increments in crystallinity at 3 % clay with 3% and 6% PPMA. However, same results could not be concluded at 5 % clay loading or even for 3% clay system with 9% PPMA. The 3 % lower crystallinity of pure PP recycle samples may explain to some extent that this level of the decrement obtained in some of PP/Clay/PPMA formulations could arise from the recycling process, rather than from the clay and PPMA addition.

Between the crystallinity, which is decreased up to 2 J/g maximum, and crystallization temperature, which is increased up to 7 °C maximum, for the PPNCs that contain PPMA with 6 % or less and clay with 3 %; it is difficult to predict the mechanical properties of our samples and/or to consider these changes are appreciable to enhance or suffer the final PPNCs properties.

6.1.2 TGA Results of PPNCs Compounding Samples

An improvement in thermal stability of PPNCs over the PP material is observed. However, this improvement is doubled for PPNCs if the recycling PP materials are considered. This may be resulted from the interaction between organic and inorganic phases. Individual layers of semi-exfoliated clay platelets act as insulator, and the formation of tortuous path between layers inhibits the passage of volatile degradation products, hence enhances the thermal stability of PPNCs.

The TGA analysis of the three prepared pure PP recycling compounds shows that a slight shift for the first pure PP recycle sample was noticed as compared to pure PP received from the manufacturer. This shift was increased with a tiny bit degree for the second recycle. The second and third samples have the same thermal decomposition behaviour, which might indicate that this difference between the PP and recycling samples is related to additives incorporated in PP production and not originated from a degradation process.

6.2 Queen's University Belfast Samples

Queen's University Belfast samples exhibit low yield stresses of PPNCs as compared to pure PP. This decrement can be explained by considering the use of compatibilizer, mixing routes and processing parameters. The poor bonding might refer to poor dispersion, and thus low yield stresses were obtained. Voids that can be supported by intercalated PP/clay phases might be responsible for improvement of elongation at break. The voids may be at a level that is beneficial at 3 % loading, but detrimental at 5 %.

The crystallinity results of the drawn PPNCs that show 15 % over the undrawn ones, as compared to 10% of drawn PP over undrawn PP, with neglecting the big fluctuations in mechanical testing results can supports the idea of studying cold and hot drawing of PPNCs.

The degree of crystallinity was not enhanced remarkably by addition of both clay types (Cloisite 15A and MTE), their values were reduced to only 1 % in samples with 5 % clay loading which is very similar to our results. However, 3% clay loading exhibits 4 % loss in crystallinity for MTE as compared to 1 % increase for Cloisite 15A sample.

The crystallisation temperature on the other hand was reduced by about 4 % for all the Queen's University Belfast samples, which indicates that clay particles are slowing down the crystallisation process. In comparison to our samples, which show an increase in T_c to 3–6 %, these results match the tensile test results that show better yielding behaviour for Queen's University Belfast sample of pure PP where the crystallization temperatures is higher.

The way of mixing could be a main playing factor in these different obtained results. However, this is not enough to say that we could get better enhancement in tensile properties by increasing the crystallization temperature. Spherulitic morphology investigation is highly recommended to give more input and understanding to the crystallization behaviour.

6.3 Processing Behaviour of PPNCs

The results of the in-line viscosity index measurements showed 7% higher values when the compatibilizer content is zero. As the PPMA level increases for 3% and 5% clay systems, the differences in viscosity index

decrease until it become very similar or even less at higher PPMA levels. Therefore, the viscosities of PPNCs are very comparable with pure PP system as PPMA is present because of lower molecular weight of PPMA. Thus there will be no extra cost in using PPNCs with this clay content range with existing processing machines.

These similarities in processing behaviours of the pure polymer and the different PPNCs can lead to a conclusion that the applied shear rates in the final processing step is similar and thus reduces the possible difference in PP molecular orientation in the final product of the hybrid as compared to the pure PP. However, the compounding step of the twin screw extruder is very critical in processing of PPNCs, especially during the preparation of the PP (80%)/clay (20%) master batch. In the industrial level, where the high output is demanded, this step can annoyingly affect the build up shear rate and leads to degradation problems.

6.4 Drawing Process Curves of PPNCs

The replications of drawing process curves for the PP sample and the PP/clay samples in absent of the compatibilizer and the incongruent curves when the compatibilizer is involved may lead to a conclusion that the state of PP molecules is a critical element in prediction of the molecular orientation during the drawing process of PPNCs. Free moving of PP molecules in pure PP and in incompatible matrixes could be the reason of such replication behaviour. Conversely, the immobilization of confined polymer chains between the silicate layers might be the reason for the difference in behaviour.

The above conclusion is supported by results of the variation of steady draw load with imposed draw ratio where very similar loads were obtained when

the PPMA was not involved in our formulation for both 3% and 5% clay systems. These similarities have not dominated any more on the samples that contain PPMA, which exhibit higher steady draw load.

The same concept might be used for the produced orientation in injection moulding process when the PPNCs are forced into the mould cavity. Thus the confined PP molecules between the clay layers may affect the orientation and may help in explanation of the difference in the property.

6.5 Spherulitic Morphology of PPNCs

Crystallization start temperature for PPNCs samples was similar within 5 °C difference in range. The PP with 3% clay and 3% PPMA did crystallize at earlier stage. Therefore, compared with others, has the least of the final average spherulite size. A delay of 10 °C of PP and PPMA to have full spherulite images is a clear sign that clay layers acted as a nucleating agent, which promote the crystallization of PP. So it can be concluded that the morphology of the PPNCs differs not only by the effect of clay loading, but also it is a function of the PPMA contents and its interference with clay particles.

The addition of the clay particles with existing of the compatibilizer contributes continually in enhancement of spherulite nucleation until a certain level of loading, which might be controlled by shear, where the system is fully equipped and nucleation is not enhanced any more.

For the drawn samples, the crystalline morphology of pure PP at room temperature showed a transformation from the spherulitic structure to an oriented structure when it crystallizes at high draw speeds. Very fine structure was obtained for the clay systems without PPMA. Conversely, the morphology of the

samples with PPMA appears as a fibrous structure and seems to not show spherulites. However, the difficulty to have the micrographs at higher temperatures, due to the destroying of orientation, limits the ability to get a well defined structure of the oriented samples. Using thick samples is highly recommended for any future work on the crystalline morphology of drawn PPNCs samples.

In PPNCs, obtaining these smaller spherulites with good bonding to the non-polar PP matrix can give a more uniform structure that may improve the modulus. On the other hand, the fracture toughness could be improved due to the increase of the amorphous portions (more tie molecules) between crystallite lamellae. This might be not the case for the compatibilized systems where the confined chains are dominant.

Care should be taken in linking of the size of spherulites directly to the mechanical properties of the drawn and undrawn PPNCs. Many factors can play together to give an overall explanation of different mechanical properties such as compatibilization, clay contents, possible existence of microvoids and shear involved. Moreover, the drawing temperature, speed or draw ratios, and the degree of melt solid orientation should be considered for the drawn samples.

6.6 WAXD and TEM Micrographs of PPNCs

6.6.1 WAXD measurements of PPNCs

In absence of the compatibilizer, very little change in the basal spacing is obtained for 3% of clay loading and no change for the 5% clay loading, which is due to the incompatibility of the polar hydroxyl groups on the surface of the clay layers and the nonpolar PP. The peak broadening is doubled for PPNCs in 3%

clay system without compatibilizer. This might be explained by reduction of the number of stacked clay platelets in the non-crowded packed matrix by the effect of shear and/or introduce possible functional groups of PP to the polar MMT. This broadening of the peak is not obtained as the clay loading is increased in the busy matrix of 5 %.

In presence of the compatibilizer, a distinct shift to lower angle and peak broadening are observed for 3 % clay system. This enhancement in the degree of exfoliation or intercalation degree reaches the maximum at 6% PPMA and shows no further improvement at 9% PPMA contents. As compared to all 5% clay loading composite, 6% PPMA content achieved the highest d-spacing and broadening of the peak. These results are verified by the images of TEM. The higher d-spacing PPNC samples also show better distribution platelets according to the TEM image. These peaks shifting clearly indicate an intercalation structure in these composites that would enhance PP/clay affinity and polymer chain diffusion into the clay galleries.

6.6.2 TEM images of undrawn PPNCs

TEM micrographs clearly show the agglomeration of clay platelets of samples without compatibilizer. Higher agglomeration with clay chunks is seen as the clay content increases to 5 %. Good distribution with possible intercalation and exfoliation systems are observed at 3 % clay loading with different PPMA contents. Size of the clay agglomerates in 5% clay systems are much reduced as PPMA is added and show good images for 6 and 9 % PPMA contents.

These combination results of WAXD and TEM are evident that PPMA was able to intercalate into the galleries and caused the increase in d-spacing in

both 3% and 5% clay systems that show large tactoid structure without using PPMA. However, the angle shift in WAXD was minimal in 5% clay system with PPMA as an indication of that the clay agglomeration become severe and microtactoids are shown up in TEM micrographs.

From the TEM images analyses, it can be concluded that the number of particles is increased as PPMA levels increase. The higher number of particles is accompanied with a reduction in feret diameter size.

6.6.3 TEM images of drawn PPNCs

The TEM micrographs of drawn PPNCs show the clay particles with well aligned ordered in the drawn direction and regularly spaced particles, for both 3 and 5% clay samples with compatibilizer. Conversely, clay particles of PPNC samples without compatibilizer have similar alignment, but with large scale tactoids. These results are considered to be the effect of the penetration of PP, with help of the PPMA, into the interlayer spacing of the particles that eventually occurs and leads to the formation of such distribution of regularly spaced particles.

The produced orientation of clay particles in the undrawn injection moulded samples are heightened after drawing process. This orientation could contribute promotionally in enhancement of the mechanical properties of PPNCs.

From the TEM images analyses, the effect of drawing process shows no or minor effect on average number of particles and feret diameter size of different drawn PPNCs. The possible produced microvoids and/or clay particles tendency to the diagonal axis of the specimen might be the source of errors in some reported micrographs analyses.

6.6.4 WAXD and TEM images for different mixing routes

The sample produced from one-step master batch mixing is similar to the ones with compatibilizer in behaviour of intercalation or interlayer spacing gallery as presented in WAXD result, but similar to these ones without compatibilizer in distribution as presented in TEM images. So it become apparent of the critically of using a manual mixing even for a dispersed clay particles. Thus the two-stage mixing, where the master batch is distributed continuously from the second extruder feeder, is an essential to achieve a successful interaction and distribution of the PPNCs. Therefore, these results emphasize on the importance of using a complementary technique like TEM in any future work to support the results of WAXD. TEM gives a small volume characterization but with a whole representation of the sample.

From the TEM images analyses, comparison of the two compatibilized samples that were produced by either one or two-step master batch compounding is clearly confirmed the recommendation that is made for using the two-step master batch that achieves more than double number of particles and lower diameter than the one-step procedure. The different obtained distribution and sample uniformity is due to the better mixing, in present of compatibilizer, which works on breaking up clay tactoids to semi-exfoliated or microtactoids particles.

6.7 Tensile Modulus of Undrawn PPNCs

The tensile modulus results of the PP with 3% clay and 3% PPMA shows the greatest improvement among all 3% clay systems (40% more than PP). The greatest improvement in 5% systems is found to be for the one with 6% PPMA loading (50 % more than PP). The particle bonding to PP molecules in presence of the compatibilizer might be the main reason of such enhancement. Increasing

the clay content will greatly constrain the polymer chains mobility so that the modulus is improved. This restriction in mobility is minimized when the PPMA is not involved so that a lower increment in tensile modulus was obtained for the uncompatibilized 3% and 5% clay systems.

6.7.1 Effect of PPMA/clay ratio

The ratio of 1:1 of PPMA/clay of the 3% clay system achieves the highest modulus, higher crystallization temperature with lower spherulites size, increased d-spacing of silicate layers, and good distribution of intercalated microtactoids with possible semi-exfoliated particles. This ratio might be suggested to be the optimum ratio of such used mixing route and introduced shear. However, this conclusion can not be generalized because that the used PP (MFI= 6 g/10 mins.) plays a significant rule in this optimization process. In general, more degree of exfoliation system might be obtained as the diffusion process of lower molecular weight polymers are involved and thus might introduced more polymer molecules into the clay galleries. In that case, the higher quantity of PPMA might be used and its ratio to the clay content is increased. However, the ratio of 2:1 of the 3% clay system is confirmed the statement that indicates that the higher obtained degree of exfoliation system does not necessarily improved mechanical properties.

The combination of the obtained results of WAXD, TEM and tensile modulus measurement showed that even though the 5% clay systems with PPMA achieve the highest tensile modulus values, the modest trend as the clay level exceeds 3% may assume that the room of such compatibilized systems of clay reinforcement in PP is reduced at 5% clay system. An adopting of loading of PPMA based on the processing and clay content is a mandatory step to make

balance between the compatibilizer stiffness effect and its compatibilization effect to achieve maximum improvement of composite properties.

6.7.2 Effect of orientation produced from different processing equipments

Similar results and observations of the tensile modulus are found for the injection moulded samples as compared to the obtained compression moulded sheets results. However, there was a shift with approximately 40-45% for all PPNCs samples to higher values of tensile modulus for the samples that were produced in injection moulding process. Although the modest level of stress in compression moulded sheets, the molten polymer melt undergoes complex shear and stretching motions that produce higher orientation in all injection moulded samples and make the difference in tensile modulus results.

6.7.3 Effect of different strain rates

As the strain rate is increased, a corresponding increase in modulus is observed for pure PP and the PPNCs for both compression moulded and injection moulded samples. Slower rate of testing will permit the molecule to respond flexibly and demonstrate lower modulus, while faster rates of testing will simulate stiffer molecules and produce higher modulus.

6.7.4 Effect of different mixing routes

Compared to all mixing procedures used, the two-step master batch procedure achieves the higher values of modulus. This might be attributed to the sufficient introduced shear and mixing during the compounding stage. It then acts to enhance the modulus of the final PPNC. These improvements in dispersion and distribution are confirmed by TEM and WAXD results. Conversely, although the one-step mixing achieves good compatibility with PP

molecules, as reported in WAXD results, but it fails to show good distribution in the TEM micrograph. Thus lower modulus as compared to two-step master batch sample is obtained, but still 12% higher than the pure PP sample.

6.8 Tensile Modulus of drawn PPNCs

The samples with 2, 3 and 4 draw ratios of pure PP achieve improvement in modulus of about 18%, 23% and 47%, respectively. These enhancements occur because the high produced orientation of the PP molecules that makes the stress along the axis of orientation is applied against the strong covalent bonds within the polymer molecules.

The results show similar tendency between different drawn PPNCs to that presented in the undrawn PPNCs. The drawn PP with 3% clay and 3% PPMA shows the greatest improvement among all 3% drawn systems (12-15% more than PP for all draw ratios, $\lambda = 2, 3, \text{ and } 4$). In contrast, the greatest improvement in 5% systems is found to be for the one with 6% PPMA loading (22-25% more than PP for all draw ratios, $\lambda = 2, 3, \text{ and } 4$).

The tendency of improvement in the drawn PPNCs over the pure polymer is significantly minimized as compared to the obtained improvement in undrawn samples. Addition of the polar structure MMT to the non-polar PP produces weak interface boundaries, which still exist even with using of the compatibilizer. When drawing is involved, microvoids might be more dominant and thus the improvement of PPNCs tensile modulus tendency of undrawn compatibilized 3% clay and 5% systems is reduced from 40% and 50% to 15% and 25%, respectively.

6.8.1 Effect of low and high deformation systems

For uncompatibilized low deformed systems (draw ratios 2 and 3), modest increments of 3-4% and 6-7% in modulus over PP at different strain rates are observed as the clay content increased to 3% and 5%, respectively. Higher enhancement in modulus is remarked as the PPMA is present. These modulus improvements reach to 15-19% and 24-27% at different strain rates for the 3% and 5% clay systems, respectively.

The uncompatibilized high deformed systems (draw ratio 4) show a very weak trend to enhance the modulus over the drawn PP with increasing the clay contents. These tiny enhancements get worse for the 5% clay system as the strain rate increases and show same result obtained for drawn PP. The high drawing speed seems to influence the interference between the entanglement of the polymer molecules and the possible existence of microvoids that most likely to be more random in such high deformed system, and thus reduce the modulus at high clay content. Conversely, the compatibilized systems show increments of tensile modulus (13-17% and 25-26% for 3% and 5% clay systems, respectively) at all used strain rates due to possible reduction of microvoids that may result from the weak interface between polymer and clay particles, which are less dominant in such compatibilized systems.

6.8.2 Effect of draw speed on modulus of drawn PPNCs

In spite of that the compatibilized systems achieve the highest modulus as compared to the drawn PP, a 4 % reduction in modulus at draw ratio 2 as compared to same undrawn samples is observed for all strain rates for both compatibilized 3% and 5% clay systems. This might be attributed to the applied restriction of the molecules mobility that is inhibited by the confined PP

molecules in the clay galleries at such very low drawing speed. As the speed increases, this restriction is minimized and a slight increase in modulus is observed. This behaviour is then followed by a tremendous increase in the modulus (33% over the undrawn sample) at very high speed of 950 mm/min.

The drawn PP and uncompatibilized 3% and 5% systems seems to have same behaviour for all strain rates in their response to the drawing process as an indication of comparable degree of orientation for loose polymer molecules to the clay platelet. Shifts in the curves to higher modulus of the drawn uncompatibilized systems over the PP curve are due to the high modulus of inorganic clay particles. Plateaus are presented for these systems between 2 and 3 draw ratios, followed by increase in modulus at high drawing speed with tendency to have equivalence in modulus between all three systems as microvoids might be more dominant in the matrix. Ability of orientation, presence of high modulus clay and the possible developed microvoids are the main factors that control the tensile modulus in such uncompatibilized systems.

6.9 Fracture Toughness of PPNCs

According to the different obtained fracture behaviours of both undrawn and drawn PP and PPNCs, all samples are evaluated based on the total work of fracture as a valid comparison measurement of the material toughness.

6.9.1 Load-displacement behaviour for core and skin of undrawn samples

Different fracture behaviours between core and skin samples for uncompatibilized systems are obtained. Clay systems without compatibilizer is found to have higher tendency to be more in the core part during the injection moulding process due to their higher loose of molecular movement as compared

to the compatibilized ones. Large size of the clay particles act as an initiator of voids that might be grown under the imposed deformation and finally coalesce to the neighbouring voids. Such partial precipitate structure with large size clay particles in the core of the injection moulded bar might be responsible for the reported different shapes of the fracture curves and more heat generated that can be seen in thermal images of undrawn samples.

6.9.2 Effect of orientation of clay particles on the fracture behaviour

Another important reason that may make the difference in fracture behaviour response of the PPNCs is the orientation of the PP molecules and the clay particles. If it is assumed that the clay particles have a similar degree of orientation in core and skin as it may be concluded from the TEM micrographs, the polymer molecular orientation could be the main player in such failure process for the compatibilized systems. In compatibilized 5% clay system, where the PP molecules are linked to the clay gallery, a parity movement of PP and clay hinders to some extent the response of PP molecules to the orientation. This may be supported by the slanting shape of heat generated that can be seen in the thermal images for only some of the compatibilized systems.

6.9.3 Total work of fracture

The undrawn PP shows 12% and 15% higher toughness than the undrawn uncompatibilized and compatibilized systems that were produced by two-step master batch route, but 14% lower than the 3% clay system, which was produced by one-step master batch route. This higher surface contact between polymer and clay of the one-step master batch system as compared to the uncompatibilized 3% system was enough to produce a structure that may generate more uniform

microvoids and thus improves the toughness. At the same time, the well distributed 3% clay system with compatibilizer, which has low molecular weight than PP, makes very high surface contact but such interaction structure of the polymer into clay gallery may reduce the possible generated microvoids and cause a reduction in the toughness measurement.

As the draw ratio increases to 2, the microvoids in such well distributed compatibilized systems might be grown and reached to a favourable degree that allows higher fracture toughness as compared to PP and other 3% clay systems. More sample stretching, at draw ratio 3, may increase the microvoids of all 3% clay systems to a level where materials can not stand and crack propagates at earlier stages. The more flexibility of the pure PP molecules and/or the possible uniform microvoids at draw ratio 3, give the turn to the PP samples to take advantage over all 3% systems. More stretching to draw ratio 4 does not pursue a better property, as the PP free volume does not permit any further mobility of other segments of the polymer chains. The 5% compatibilized systems have higher total work of fracture than pure PP for undrawn and drawn samples with draw ratio 2. At draw ratio 3, PP records about 34% and 11% higher toughness than the compatibilized and uncompatibilized 5% clay systems, respectively.

As the ligament of the compared samples is reduced at medium notch length, very similar behaviours of undrawn and drawn PPNCs are obtained. All graphs are shifted to about 30% lower total work of fracture as the medium notch length is introduced. As the notch increased to the highest used length, the total work of fracture is decreased to 63% as compared to the lowest notch length.

The fluctuations in the results at the smallest ligament length and the slightly different results obtained for some PPNCs might be attributed to the non-

uniform microvoided structure of composites that may happen even when the dispersion of clay particles is good. In these clay-microvoid systems, the highest value of notch length used should be avoided or adjusted with a higher sample width and thickness. Such a geometry would correspond to a large produced part in injection moulding or compression moulding and a larger designed die for drawing to get benefit from the reported toughness improvement of drawn PP at draw ratio 3 and reported improvement of composite systems at draw ratio 2.

In general, it is concluded that an understanding of the balance between any measured macroscopic property and the clay content can suggest new applications for undrawn PPNCs and drawn composite systems at low draw ratios, where the composites exhibit highly significant improvement over the PP. At moderate and high draw ratios, PPNCs failure might be governed by either the growth of microvoids at low clay content or the coalescence of the microvoids at high clay content, when failure is at an earlier stage than for pure PP.

7 References

1. T. J. Pinnavaia , G.W.Beall, *Polymer-Clay Nanocomposites*. December 2000: Wiley. p. 98-99.
2. Koo, J.H., *Polymer Nanocomposites: Processing, Characterization, And Applications: Processing, Characterization, and Applications*. Jun 2006: McGraw-Hill. p. 3.
3. Domasius Nwabunma , T. Kyu, *Polyolefin Composites*. February 2008: Wiley. p. 417.
4. J. M. Garcés, D. J. Moll, J. Bicerano, R. Fibiger, D. G. McLeod, *Polymeric Nanocomposites for Automotive Applications*. *Advanced Materials*, 2000. **12**(23): p. 1835-1839.
5. Coates, P.D. and I.M. Ward, *Drawing of polymers through a conical die*. *Polymer*, 1979. **20**(12): p. 1553-1560.
6. Coates P D and Ward I M, *Die drawing: solid phase drawing of polymers through a converging die*. *Polymer Engineering and Science*, 1981. **21**(10): p. 612-618.
7. Petr Svoboda, C. Zeng, H. Wang, L. Lee, D. Tomasko, *Morphology and mechanical properties of polypropylene/organoclay nanocomposites*. *Journal of Applied Polymer Science*, 2002. **85**(7): p. 1562-1570.
8. Harutun G. Karian, e., *Handbook of Polypropylene and Polypropylene Composites*. 2003: Marcel Dekker. p.12.
9. Manias, E., A.T., L. Wu, K. Strawhecker, B. Lu, and T. C. Chung, *Polypropylene/Montmorillonite Nanocomposites. Review of the Synthetic Routes and Materials Properties*. *Chemistry of Materials*, 2001. **13**(10): p. 3516-3523.
10. Alexandre, M. and P. Dubois, *Polymer-layered silicate nanocomposites: preparation, properties and uses of a new class of materials*. *Materials Science and Engineering: R: Reports*, 2000. **28**(1-2): p. 1-63.
11. Wang, Y., C. Feng, L. Yann, W. Kai, *Melt processing of polypropylene/ clay nanocomposites modified with maleated polypropylene compatibilizers*. *Composites Part B: Engineering*, 2004. **35**(2): p. 111-124.
12. Kawasumi, M., et al., *Preparation and Mechanical Properties of Polypropylene-Clay Hybrids*. *Macromolecules*, 1997. **30**(20): p. 6333-6338.
13. Liu, X. and Q. Wu, *PP/clay nanocomposites prepared by grafting-melt intercalation*. *Polymer*, 2001. **42**(25): p. 10013-10019.
14. Peter Reichert, Nitz, H. Klinke, S. Brandsch, R. Thomann, R. Mülhaupt, R., *Poly(propylene)/organoclay nanocomposite formation: Influence of compatibilizer functionality and organoclay modification*. *Macromolecular Materials and Engineering*, 2000. **275**(1): p. 8-17.
15. Qin Zhang, Qiang Fu, Luxia Jiang, and Yong Lei, *Preparation and properties of polypropylene/montmorillonite layered nanocomposites*. *Polymer International*, 2000. **49**(12): p. 1561-1564.
16. Pravin Kodgire, R. Kalgaonkar, S. Hambir, N. Bulakh, J. P. Jog, *PP/clay nanocomposites: Effect of clay treatment on morphology and dynamic mechanical properties*. *Journal of Applied Polymer Science*, 2001. **81**(7): p. 1786-1792.

17. Makoto Kato, A. Usuki, A. Okada, *Synthesis of polypropylene oligomer - clay intercalation compounds*. Journal of Applied Polymer Science, 1997. **66**(9): p. 1781-1785.
18. Naoki Hasegawa, H. Okamoto, M. Kato, A. Usuki, *Preparation and mechanical properties of polypropylene-clay hybrids based on modified polypropylene and organophilic clay*. Journal of Applied Polymer Science, 2000. **78**(11): p. 1918-1922.
19. Wang, L. Si, D. Rongni, Z. Qin, F. Qiang, *The interplay of thermodynamics and shear on the dispersion of polymer nanocomposite*. Polymer, 2004. **45**(23): p. 7953-7960.
20. Kyu-Nam Kim, H. Kimm, and J.W. Lee, *Effect of interlayer structure, matrix viscosity and composition of a functionalized polymer on the phase structure of polypropylene-montmorillonite nanocomposites*. Polymer Engineering & Science, 2001. **41**(11): p. 1963-1969.
21. Chong Min Koo, M.J.K., Min Ho Choi, Sang Ouk Kim, In Jae Chung, *Mechanical and rheological properties of the maleated polypropylene-layered silicate nanocomposites with different morphology*. Journal of Applied Polymer Science, 2003. **88**: p. 1526-1535.
22. Kyu-Nam Kim, H. Kimm, and J.W. Lee, *Mixing Characteristics and Mechanical Properties of Polypropylene-Clay Composites*. 58th ANTEC Proceedings, 2000. **3**: p. 3782-6.
23. Perrin-Sarazin, M. Ton, M. Bureau, J. Denault, *Micro- and nano-structure in polypropylene/clay nanocomposites*. Polymer, 2005. **46**(25): p. 11624-11634.
24. K. S. Santos, R.S.M., I C. I. Ferreira, C. Dal Castel, S. A. Liberman, M. A. S. Oviedo, *The Effect of the Compatibilizer Agent in the Dispersion of the PP/Clay Nanocomposites*. The Polymer Processing Society 23rd Annual Meeting.
25. Lertwimolnun, W. and B. Vergnes, *Influence of compatibilizer and processing conditions on the dispersion of nanoclay in a polypropylene matrix*. Polymer, 2005. **46**(10): p. 3462-3471.
26. Nam, P.H., M. Pralay, O. Masami, K. Tadao, H. Naoki, U. Arimitsu, *A hierarchical structure and properties of intercalated polypropylene/clay nanocomposites*. Polymer, 2001. **42**(23): p. 9633-9640.
27. Vaia, R.A. and E.P. Giannelis, *Polymer Melt Intercalation in Organically-Modified Layered Silicates: Model Predictions and Experiment*. Macromolecules, 1997. **30**(25): p. 8000-8009.
28. Vaia, R.A. and E.P. Giannelis, *Lattice Model of Polymer Melt Intercalation in Organically-Modified Layered Silicates*. Macromolecules, 1997. **30**(25): p. 7990-7999.
29. Chandrlekha Singh, A.C.B., *Effect of polymer architecture on the miscibility of polymer/clay mixtures*. Polymer International, 2000. **49**(5): p. 469-471.
30. T. Sun, J.M.G., *High-Performance Polypropylene-Clay Nanocomposites by In-situ Polymerization with Metallocene/Clay Catalysts*. Advanced Materials, 2002. **14**(2): p. 128-130.
31. Yang, K., Y. Huang, and J.-Y. Dong, *Efficient preparation of isotactic polypropylene/montmorillonite nanocomposites by in situ polymerization technique via a combined use of functional surfactant and metallocene catalysis*. Polymer, 2007. **48**(21): p. 6254-6261.

32. Jae Whan Cho, J.L., Scott Omachinski, Guoqiang Qian, Tie Lan, Timothy W, Womer and Walter S. Smith, *Nanocomposites: A Single Screw Mixing Study of Nanoclay-filled Polypropylene*. ANTEC 2002, 2002.
33. L. G. Furlan, R.S.M., K. S. Santos, C. Dal Castel, C. I. Ferreira , S. A. Liberman, M. A. S. Oviedo., *Effect of Processing Conditions on the PP Nanocomposites*. The Polymer Processing Society 23rd Annual Meeting.
34. Piia Peltola, E. Välipakka, J. Vuorinen, S. Syrjälä, K. Hanhi, *Effect of rotational speed of twin screw extruder on the microstructure and rheological and mechanical properties of nanoclay-reinforced polypropylene nanocomposites*. *Polymer Engineering & Science*, 2006. **46**(8): p. 995-1000.
35. Treece, M.A., W. Zhang, R. Moffitt, J. Oberhauser, *Twin-screw extrusion of polypropylene-clay nanocomposites: Influence of masterbatch processing, screw rotation mode, and sequence*. *Polymer Engineering and Science*, 2007. **47**(6): p. 898-911.
36. W. Lertwimolnun, B. Vergnes, *Influence of screw profile and extrusion conditions on the microstructure of polypropylene/organoclay nanocomposites*. *Polymer Engineering & Science*, 2007. **47**(12): p. 2100-2109.
37. W. Lertwimolnun, B. Vergnes, *Effect of processing conditions on the formation of polypropylene/organoclay nanocomposites in a twin screw extruder*. *Polymer Engineering & Science*, 2006. **46**(3): p. 314-323.
38. Lopez-Quintanilla, Sanchez-Valdes, S., Ramos, L. F., Medellin Rodriguez, F. J., *Effect of some compatibilizing agents on clay dispersion of polypropylene-clay nanocomposites*. *Journal of Applied Polymer Science*, 2006. **100**(6): p. 4748-4756.
39. Modesti, Lorenzetti, A., Bon, D., Besco, S., *Effect of processing conditions on morphology and mechanical properties of compatibilized polypropylene nanocomposites*. *Polymer*, 2005. **46**(23): p. 10237-10245.
40. Modesti, M., Lorenzetti, A., Bon, D., Besco, S., *Thermal behaviour of compatibilised polypropylene nanocomposite: Effect of processing conditions*. *Polymer Degradation and Stability*, 2006. **91**(4): p. 672-680.
41. Bettini, S.H.P., *Effect of Processing Conditions on Thermal Behavior and Mechanical Properties of Polypropylene-Clay Nanocomposites*. The Polymer Processing Society 23rd Annual Meeting.
42. Solomon, M.J., *Intercalated Polypropylene Nanocomposites*. Dekker Encyclopedia of Nanoscience and Nanotechnology, 2004.
43. Emmanuel, P.G., *Polymer-layered silicate nanocomposites: Synthesis, properties and applications*. *Applied Organometallic Chemistry*, 1998. **12**(10-11): p. 675-680.
44. Vaia, R.A., H. Ishii, and E.P. Giannelis, *Synthesis and properties of two-dimensional nanostructures by direct intercalation of polymer melts in layered silicates*. *Chemistry of Materials*, 1993. **5**(12): p. 1694-1696.
45. Morgan, A.B. and J.W. Gilman, *Characterization of polymer-layered silicate (clay) nanocomposites by transmission electron microscopy and X-ray diffraction: A comparative study*. *Journal of Applied Polymer Science*, 2003. **87**(8): p. 1329-1338.

46. Vaia, R.A., et al., *Microstructural Evolution of Melt Intercalated Polymer&Organically Modified Layered Silicates Nanocomposites*. Chemistry of Materials, 1996. **8**(11): p. 2628-2635.
47. Park, J.H., H. Lee, I. Chin, H. Choi, H. Kim, W. Kang, *Intercalated polypropylene/clay nanocomposite and its physical characteristics*. Journal of Physics and Chemistry of Solids. **69**(5-6): p. 1375-1378.
48. Sinha Ray, S. and M. Okamoto, *Polymer/layered silicate nanocomposites: a review from preparation to processing*. Progress in Polymer Science, 2003. **28**: p. 1539-1641.
49. Ton-That, M.-T., F. Perrin-Sarazin, M. Bureau, K. Cole, J. Denault, *Development of polyolefin nanocomposites: Relationships between formulation, structure, and performance*. 2004. Chicago, IL., United States: Society of Plastics Engineers.
50. Cui, L., D. Khramov, C. Bielawski, D. Hunter, P. Yoon, D. Paul, *Effect of organoclay purity and degradation on nanocomposite performance, Part 1: Surfactant degradation*. Polymer, 2008. **49**(17): p. 3751-3761.
51. Cui, L., D. Hunter, P. Yoon, D. Paul, *Effect of organoclay purity and degradation on nanocomposite performance, Part 2: Morphology and properties of nanocomposites*. Polymer, 2008. **49**(17): p. 3762-3769.
52. Paiva, L.B.d., A.R. Morales, and T.R. Guimarães, *Structural and optical properties of polypropylene-montmorillonite nanocomposites*. Materials Science and Engineering: A, 2007. **447**(1-2): p. 261-265.
53. Bafna, A., et al., *3D Hierarchical orientation in polymer-clay nanocomposite films*. Polymer, 2003. **44**(4): p. 1103-1115.
54. Wang, K., et al., *Correlation of rheology-orientation-tensile property in isotactic polypropylene/organoclay nanocomposites*. Acta Materialia, 2007. **55**(9): p. 3143-3154.
55. Inês Bruno Tavares, M., et al., *Polypropylene-clay nanocomposite structure probed by H NMR relaxometry*. Polymer Testing, 2007. **26**(8): p. 1100-1102.
56. Nogueira, R.F., et al., *Solid state NMR investigation of polypropylene/Brazilian clay blending process*. Polymer Testing, 2005. **24**(3): p. 358-362.
57. Morgan, A.B.G., J. W.; Kashiwagi, T.; Jackson, C. L. *Flammability of Polymer-Clay Nanocomposites*. in Fire Retardant Chemicals Association. March 12-15,2000. Washington, DC.
58. E. Manias, A.T., L. Wu, K. Strawhecker, B. Lu, and T. C. Chung, *Polypropylene Montmorillonite Nanocomposites review of synthetic routes and material properties*. Chem. Mater, 2001. **13**: p. 3516-3523.
59. Maiti, P., et al., *Influence of Crystallization on Intercalation, Morphology, and Mechanical Properties of Polypropylene/Clay Nanocomposites*. Macromolecules, 2002. **35**(6): p. 2042-2049.
60. Pralay Maiti, Nam, P.H., O. Masami, K. Tadao, H. Naoki, U. Arimitsu, *The effect of crystallization on the structure and morphology of polypropylene/clay nanocomposites*. Polymer Engineering & Science, 2002. **42**(9): p. 1864-1871.
61. Ma, J., et al., *Crystallization behaviors of polypropylene/montmorillonite nanocomposites*. Journal of Applied Polymer Science, 2002. **83**(9): p. 1978-1985.

62. Li, J., C. Zhou, and W. Gang, *Study on nonisothermal crystallization of maleic anhydride grafted polypropylene/montmorillonite nanocomposite*. *Polymer Testing*, 2003. **22**(2): p. 217-223.
63. Medellin-Rodriguez, F.J., et al., *The effect of nanoclays on the nucleation, crystallization, and melting mechanisms of isotactic polypropylene*. *Polymer Engineering and Science*, 2007. **47**(11): p. 1889-1897.
64. Lei, S.G., S.V. Hoa, and M.T. Ton-That, *Effect of clay types on the processing and properties of polypropylene nanocomposites*. *Composites Science and Technology*, 2006. **66**(10): p. 1274-1279.
65. Deshmane, C., et al., *On striking variation in impact toughness of polyethylene-clay and polypropylene-clay nanocomposite systems: The effect of clay-polymer interaction*. *Materials Science and Engineering: A*, 2007. **458**(1-2): p. 150-157.
66. Nowacki, R., et al., *Spherulite nucleation in isotactic polypropylene based nanocomposites with montmorillonite under shear*. *Polymer*, 2004. **45**(14): p. 4877-4892.
67. Somwangthanoj, A., E.C. Lee, and M.J. Solomon, *Early Stage Quiescent and Flow-Induced Crystallization of Intercalated Polypropylene Nanocomposites by Time-Resolved Light Scattering*. *Macromolecules*, 2003. **36**(7): p. 2333-2342.
68. Sangeeta Hambir, N.Bulakh, *Polypropylene/Clay nanocomposites: Effect of compatibilizer on the thermal, crystallization and dynamic mechanical behavior*. *Polymer Engineering & Science*, 2002. **42**(9): p. 1800-1807.
69. Mabrouk Ouederni, P.J.P., *Influence of morphology on the fracture toughness of isotactic polypropylene*. *Journal of Polymer Science Part B: Polymer Physics*, 1995. **33**(9): p. 1313-1322.
70. Wenge Zheng, X. Lu, C. Ling, T. Tong, H. Zheng, C. He, *Effects of clay on polymorphism of polypropylene in polypropylene/clay nanocomposites*. *Journal of Polymer Science Part B: Polymer Physics*, 2004. **42**(10): p. 1810-1816.
71. Biswas, M. and S. Ray, *Recent Progress in Synthesis and Evaluation of Polymer-Montmorillonite Nanocomposites*, in *New Polymerization Techniques and Synthetic Methodologies*. 2001. p. 167-221.
72. Nguyen Thac Kim, T.H., *Study on the Structure and Properties of Polypropylene Clay Nanocomposites*. *Advances in Natural Science*, 2006. **7**(No. 1&2): p. 49-55.
73. Kim, D.H., et al., *Structure and properties of polypropylene-based nanocomposites: Effect of PP-g-MA to organoclay ratio*. *Polymer*, 2007. **48**(18): p. 5308-5323.
74. Wong, S.-C., et al., *A study of global vs. local properties for maleic anhydride modified polypropylene nanocomposites*. *Polymer*, 2006. **47**(21): p. 7477-7484.
75. Taraiya, A.K., A. Richardson, and I.M. Ward, *Production and properties of highly oriented polypropylene by die drawing*. *Journal of Applied Polymer Science*, 1987. **33**(7): p. 2559-2579.
76. A. K. Taraiya, I.M.W., *Biaxially Oriented Polymer tubes by die drawing* *Plastics, Rubber and Composites Processing and Applications*, 1996. **25**: p. 287-290.

77. Gibson, A.G. and I.M. Ward, *The manufacture of ultra-high modulus polyethylenes by drawing through a conical die*. Journal of Materials Science, 1980. **15**(4): p. 979-986.
78. Keller, A. and J.G. Rider, *On the tensile behaviour of oriented polyethylene*. Journal of Materials Science, 1966. **1**(4): p. 389-398.
79. N. Bekhet, D.C.B., G. Craggs, *The Uniaxial Behavior of Highly-Oriented Polymers*. Processing of Advanced Materials 1993. **3**: p. 199-207.
80. Mourad, A.H.I., et al., *The effects of process parameters on the mechanical properties of die drawn polypropylene*. Polymer Testing. **24**(2): p. 169-180.
81. E Deenadayalan, S.V.A.L., *Nanocomposites of polypropylene impact copolymer and organoclays: role of compatibilizers*. Polymer International, 2006. **55**(11): p. 1270-1276.
82. Peiyao Li, et al., *New toughened polypropylene/ organophilic montmorillonite nanocomposites*. Journal of Applied Polymer Science, 2008. **108**(4): p. 2116-2121.
83. Wenyi, W., et al., *Preparation and properties of polypropylene filled with organo-montmorillonite nanocomposites*. Journal of Applied Polymer Science, 2006. **100**(4): p. 2875-2880.
84. Ling Chen, S. Wong, S. Pisharath, *Fracture properties of nanoclay-filled polypropylene*. Journal of Applied Polymer Science, 2003. **88**(14): p. 3298-3305.
85. M. N. Bureau, F. Perrin-Sarazin M. T. Ton-That, *Polyolefin nanocomposites: Essential work of fracture analysis*. Polymer Engineering and Science, 2004. **44**(6): p. 1142-1151.
86. Yuan, Q. and R.D.K. Misra, *Impact fracture behavior of clay-reinforced polypropylene nanocomposites*. Polymer, 2006. **47**(12): p. 4421-4433.
87. Saminathan, K., P. Selvakumar, and N. Bhatnagar, *Fracture studies of polypropylene/nanoclay composite. Part II: Failure mechanism under fracture loads*. Polymer Testing, 2008. **27**(4): p. 453-458.
88. Saminathan, K., P. Selvakumar, and N. Bhatnagar, *Fracture studies of polypropylene/nanoclay composite. Part I: Effect of loading rates on essential work of fracture*. Polymer Testing, 2008. **27**(3): p. 296-307.
89. Bureau, M.N., M.-T. Ton-That, and F. Perrin-Sarazin, *Essential work of fracture and failure mechanisms of polypropylene-clay nanocomposites*. Engineering Fracture Mechanics, 2006. **73**(16): p. 2360-2374.
90. J. Mohanraj, N. Chapleau, A.Ajji, R.A.Duckett, I.M.Ward, *Fracture behavior of die-drawn toughened polypropylenes*. Journal of Applied Polymer Science, 2003. **88**(5): p. 1336-1345.
91. J. Sweeney, R.A. Duckett, I.M.Ward, *The Fracture Behaviour of Oriented Polyethylene at High Pressures. Series A, Mathematical and Physical Sciences*, 1988. **420**: p. 53-80.
92. J. Sweeney, R. A. Duckett, and I. M. Ward, *The fracture behaviour of uPVC at both ambient and high hydrostatic pressures* Journal of Materials Science, 1985. **20**: p. 3705-3715.
93. Jisheng Ma, Zongneng Qi, Youliang Hu, *Synthesis and characterization of polypropylene/clay nanocomposites*. Journal of Applied Polymer Science, 2001. **82**(14): p. 3611-3617.
94. Velasco, J.I., et al., *Polypropylene/clay nanocomposites: Combined effects of clay treatment and compatibilizer polymers on the structure and*

- properties*. Journal of Applied Polymer Science, 2006. **102**(2): p. 1213-1223.
95. Qin, H., et al., *Thermal stability and flammability of polypropylene/montmorillonite composites*. Polymer Degradation and Stability, 2004. **85**(2): p. 807-813.
 96. Golebiewski, J. and A. Galeski, *Thermal stability of nanoclay polypropylene composites by simultaneous DSC and TGA*. Composites Science and Technology, 2007. **67**(15-16): p. 3442-3447.
 97. Solomon, M.J., et al., *Rheology of Polypropylene/Clay Hybrid Materials*. Macromolecules, 2001. **34**(6): p. 1864-1872.
 98. Marchant, D. and K. Jayaraman, *Strategies for Optimizing Polypropylene/Clay Nanocomposite Structure*. Industrial & Engineering Chemistry Research, 2002. **41**(25): p. 6402-6408.
 99. Chong Min Koo, M.J.K.M.H.C.S.O.K.I.J.C., *Mechanical and rheological properties of the maleated polypropylene-layered silicate nanocomposites with different morphology*. Journal of Applied Polymer Science, 2003. **88**(6): p. 1526-1535.
 100. Galgali G, R.C., Lele A., *A rheological study on the kinetics of hybrid formation in propylene nanocomposites*. Macromolecules 2001. **34**: p. 852-8.
 101. Shu-Ying Gu, J. Ren, Q-F. Wang, *Rheology of poly(propylene)/clay nanocomposites*. Journal of Applied Polymer Science, 2004. **91**(4): p. 2427-2434.
 102. Jian Li, C. Zhou, G. Wang, D. Zhao, *Study on rheological behavior of polypropylene/clay nanocomposites*. Journal of Applied Polymer Science, 2003. **89**(13): p. 3609-3617.
 103. Rohlmann, C.O., M.D. Failla, and L.M. Quinzani, *Linear viscoelasticity and structure of polypropylene-montmorillonite nanocomposites*. Polymer, 2006. **47**(22): p. 7795-7804.
 104. Okamoto, M., et al., *A House of Cards Structure in Polypropylene/Clay Nanocomposites under Elongational Flow*. Nano Letters, 2001. **1**(6): p. 295-298.
 105. Jun Uk Park, J.L.K., Do Hoon Kim, Kyung Hyun Ahn, and Seung Jong Lee, *Rheological Behavior of Polymer/Layered Silicate Nanocomposites under Uniaxial Extensional Flow*. Macromolecular Research, 2006. **14**(3): p. 318-323.
 106. Seung Hwan Lee, E. Cho, J. Ryoun Youn, *Rheological behavior of polypropylene/layered silicate nanocomposites prepared by melt compounding in shear and elongational flows*. Journal of Applied Polymer Science, 2007. **103**(6): p. 3506-3515.
 107. Galgali, G., S. Agarwal, and A. Lele, *Effect of clay orientation on the tensile modulus of polypropylene-nanoclay composites*. Polymer, 2004. **45**(17): p. 6059-6069.
 108. Zhang, Q., Y. Wang, and Q. Fu, *Shear-induced change of exfoliation and orientation in polypropylene/montmorillonite nanocomposites*. Journal of Polymer Science, Part B: Polymer Physics, 2003. **41**(1): p. 1-10.
 109. L. E. Nielsen, R.F.Landel, *Mechanical Properties of Polymers and Composites*. 1994, Dekker: New York. p. 6.
 110. I. M. Ward, J.Sweeney, *An Introduction to the Mechanical Properties of Solid Polymers*. Second ed. 2004. p. 25.

111. I. M. Ward, J.Sweeney, *An Introduction to the Mechanical Properties of Solid Polymers*. Second ed. 2004. p. 121.
112. I. M. Ward, J.Sweeney, *An Introduction to the Mechanical Properties of Solid Polymers*. Second ed. 2004. p. 268-269.
113. I. M. Ward, J.Sweeney, *An Introduction to the Mechanical Properties of Solid Polymers*. Second ed. 2004. p. 246-247.
114. Whitney, W. and Andrews, R.D., *Yeilding of Glassy Polymers*. J.Polymer Sci C, 1967. **16**: p. 2981-2989.
115. Brown, N. and I.M. Ward, *Load drop at the upper yield point of a polymer*. 1968, John Wiley & Sons, Inc. p. 607-620.
116. Schultz, J.M., ed. *Polymer Materials Science* 1974 Prentice-Hall, Englewood Cliffs NJ.
117. I. M. Ward, J.Sweeney, *An Introduction to the Mechanical Properties of Solid Polymers*. Second ed. 2004. p. 250.
118. I. M. Ward, J.Sweeney, *An Introduction to the Mechanical Properties of Solid Polymers*. Second ed. 2004. p. 250-251.
119. J. M. Alexander, J. Gilman, *Hydrostatic Extrusion of Polymers*. Ann. C.I.R.P., 1971. **19**: p. 28.
120. B. Parsons, I.M.Ward, *The Production of Oriented Polymers by Hydrostatic Extrusion* Plastics, Rubber and Composites Processing and Applications, 1982. **2**: p. 215-224.
121. Domasius Nwabunma, T.K., *Polyolefin Composites*. February 2008: Wiley. 603.
122. Irwin, G.R., *Analysis of stresses and strains near the end of a crack transversing a plate*. *J Appl Mech* 1957. **24**: p. 361-364.
123. Griffith, A.A., *The phenomena of rupture and flow in solids*. *Phil Trans Series* 1920(A 221): p. 163-198.
124. Rice, J.R., *A Path Independent Integral and the Approximate Analysis of Strain Concentration by Notches and Cracks*, *Journal of Applied Mechanics*. *Journal of Applied Mechanics*, 1968. **35**.
125. I. M. Ward, J.Sweeney, *An Introduction to the Mechanical Properties of Solid Polymers*. Second ed. 2004. p. 301.
126. Broberg, K.B., *On stable crack growth*. *Journal of the Mechanics and Physics of Solids*, 1975. **23**(3): p. 215-237.
127. Mouzakis, D.E. and J. Karger-Kocsis, *Essential work of fracture: Simulating the toughness response of deeply double-edge notched specimens*. *Polymer Bulletin*, 1999. **43**(4): p. 449-456.
128. Mai, Y.W. and B. Cotterell, *The essential work of fracture for tearing of ductile metals*. *International Journal of Fracture*, 1984. **24**(3): p. 229-236.
129. Paton, C.A. and S. Hashemi, *Plane-stress essential work of ductile fracture for polycarbonate*. *Journal of Materials Science*, 1992. **27**(9): p. 2279-2290.
130. Chan, W.Y.F. and J.G. Williams, *Determination of the fracture toughness of polymeric films by the essential work method*. *Polymer*, 1994. **35**(8): p. 1666-1672.
131. Karger-Kocsis, J., T. Czigány, and E.J. Moskala, *Deformation rate dependence of the essential and non-essential work of fracture parameters in an amorphous copolyester*. *Polymer*, 1998. **39**(17): p. 3939-3944.

132. I. M. Ward, J.Sweeney, *An Introduction to the Mechanical Properties of Solid Polymers*. Second ed. 2004. p. 304.
133. Arkhireyeva, A. and S. Hashemi, *Fracture behaviour of polyethylene naphthalate (PEN)*. *Polymer*, 2002. **43**(2): p. 289-300.
134. Arkhireyeva, A. and S. Hashemi, *Effect of temperature on work of fracture parameters in poly(ether-ether ketone) (PEEK) film*. *Engineering Fracture Mechanics*. **71**(4-6): p. 789-804.
135. Ching, E.C.Y., et al., *Effect of strain rate on the fracture toughness of some ductile polymers using the essential work of fracture (EWF) approach*. *Polymer Engineering & Science*, 2000. **40**(12): p. 2558-2568.
136. Speight, R.G., *In-line process measurements for injection moulding control*, in *Mechanical and Manufacturing Engineering*. 1993, University of Bradford: Bradford.
137. Walton, W.H., *Feret's Statistical Diameter as a Measure of Particle Size*. *nature*, 1948. **162**: p. 329 - 330
138. Kavesh, S. and J.M. Schultz, *Lamellar and interlamellar structure in melt-crystallized polyethylene. I. Degree of crystallinity, atomic positions, particle size, and lattice disorder of the first and second kinds*. *Journal of Polymer Science Part A-2: Polymer Physics*, 1970. **8**(2): p. 243-276.
139. Kavesh, S. and J.M. Schultz, *Lamellar and interlamellar structure in melt-crystallized polyethylene. II. Lamellar spacing, interlamellar thickness, interlamellar density, and stacking disorder*. *Journal of Polymer Science Part A-2: Polymer Physics*, 1971. **9**(1): p. 85-114.
140. L. E. Nielsen, R.F.Landel, *Mechanical Properties of Polymers and Composites*. 1994, Dekker: New York. p. 280-281.
141. Zehev Tadmor, C.G.G., ed. *Principles of Polymer Processing*. 1979, Wiley Interscience. 61.
142. Deanin, R.D., ed. *Polymer Structure, Properties and Applications*. 1972, Plastics World: Boston. p 353-354.
143. Way, J.L., J.R. Atkinson, and J. Nutting, *The effect of spherulite size on the fracture morphology of polypropylene*. *Journal of Materials Science*, 1974. **9**(2): p. 293-299.
144. Friedrich, K., *Crazes and shear bands in semi-crystalline thermoplastics*, in *Crazing in Polymers*. 1983. p. 225-274.
145. Billmeyer, F.W., *Text book of Polymer Science*. Third Eddition ed. 1984. p222-224.
146. Miller, M.L., *The structure of Polymers*. 1966, Reinbold Publishing Corp.: New York. p 515.
147. L. E. Nielsen, R.F.Landel, *Mechanical Properties of Polymers and Composites*. 1994, Dekker: New York. p. 282.
148. Peterlin, A., *Morphology and Properties of Crystalline Polymers with Fiber Structure*. *Textile Research Journal*, 1972. **vol. 42**(1): p. pp. 20-30.
149. Zhang, Y.-Q., et al., *Polypropylene-clay nanocomposites prepared by in situ grafting-intercalating in melt*. *Composites Science and Technology*, 2004. **64**(9): p. 1383-1389.
150. Pozsgay András, T.F., Fráter Tünde, Papp László, Sajó István, Pukánszky Béla, *Nucleating effect of Montmorillonite nanoparticles in polypropylene*. *Journal of Macromolecular Science*, 2002. **41**(4-6): p. 1249-1265.

151. Svoboda, P., et al., *Morphology and mechanical properties of polypropylene/organoclay nanocomposites*. Journal of Applied Polymer Science, 2002. **85**(7): p. 1562-1570.
152. Kojima , Y.K., A. Usuki and M. Kawasumi, *Mechanical properties of nylon-6/clay hybrid*. Journal of Material Research 1993: p. pp. 1185–1189.
153. Deanin, R.D., *Polymer Structure, Properties and Applications*. 1972, Plastics World: Boston. 258-259.
154. I. M. Ward, J.Sweeney, *An Introduction to the Mechanical Properties of Solid Polymers*. Second ed. 2004. p. 137.
155. Deanin, R.D., *Polymer Structure, Properties and Applications*. 1972, Plastics World: Boston: Boston. 265.
156. Taraiya, A.K., Richardson A., I. M. Ward *Production and properties of highly oriented polpropylene by die-drawing*. Journal of Applied Polymer Science, 1987. **33**: p. 2559-2579.

Appendix A: Nomenclature

Original cross-sectional area	A_0
cross-sectional area	A
American society of testing of materials	ASTM
Stiffness constants	C_{ij}
Charge coupled device	CCD
Cationic exchange capacity	CEC
Initial circular cross-section area	d_0
Final circular cross-section area	d_f
Die exit circular cross-section area	d_1
Clay interlayer spacing	d_{001}
Double-edge notched tension	DENT
Dynamic mechanical analysis	DMA
Differential scanning calorimetry	DSC
Young's Modulus	E
Essential work of fracture	EWF
Force (load)	F
Shear Modulus	G
Storage modulus	G'
Loss modulus	G''
Critical strain energy release rate	G_c
Heat deflection temperature	HDT
Hot stage optical polarizing microscopy	HS-OPM
International organization for standardization	ISO
Flow energy	J
Bulk modulus	K
Critical stress intensity	K_c
Original length	l_0
Stretched length	l
Ligament length	L
Linear elastic fracture mechanics	LEFM
Length to diameter ratio	L/D
Maleic anhydride	MA
Montmorillonite	MMT
Molecular weight	MW
Molecular weight distribution	MWD
Nuclear magnetic resonance	NMR
Optical microscopy	OM
Polypropylene	PP
Polypropylene maleic anhydride	PPMA
Polarizing optical microscopy	POM
Polypropylene nanocomposites	PPNCs
Radius of the plastic zone at the crack tip	R_p
Shrinkage	S
Small angle X-ray scattering	SAXS
Scanning electron microscopy	SEM
Single-screw extruder	SSE
Compliance constants	S_{ij}

Thickness	t
Crystallization temperature	T_c
Transmission electron microscopy	TEM
Glass transition temperature	T_g
Thermogravimetric analysis	TGA
Melting temperature	T_m
Twin screw extruder	TSE
Strain energy	U
Total work of fracture	W_f
Specific total work of fracture	w_f
Essential work of fracture	W_e
Specific essential work of fracture	w_e
Plastic work of fracture	W_p
Specific plastic work of fracture	w_p
Specific total work of fracture for yielding	w_y
Specific total work of fracture for necking	w_n
Specific essential work of fracture for yielding	$w_{e,y}$
Specific essential work of fracture for necking	$w_{e,n}$
Specific non-essential work of fracture for yielding	$w_{p,y}$
Specific non-essential work of fracture for necking	$w_{p,n}$
Wide angle x-ray diffraction	WAXD
Wide-angle X-ray scattering	WAXS
X-ray diffraction	XRD
Complex shear viscosity	η^*
Elongational viscosity	η_E
Tensile stress	σ
Tensile stress at yield	σ_y
Maximum draw stress	σ_{max}
Tensile strain	ε
Tensile strain at yield	ε_y
Poisson's ratio	ν
Draw ratio or actual draw ratio	$\lambda = \lambda_A$
Extensional ratio or nominal strain	λ_e
Natural draw ratio	λ_N
X-ray wavelength	λ_ℓ
Shear stress	τ
Critical shear stress	τ_c
Coefficient of internal friction	μ
Advanced crack length	Δa
Enthalpy of melting	ΔH_m
Enthalpy of melting of pure polymer material	ΔH_f
Displacement	δ
Shape factor of the plastic zone	β
Shape factor for yielding	β'
Shape factor for necking	β''
Weight fraction	f_p

Appendix B: Material Technical Data Sheets

Appendix B1: Polypropylene PPH 5060

TOTAL PETROCHEMICALS

Polypropylene PPH 5060

Technical data sheet
Polypropylene – Homopolymer
Produced in Europe

Description

Polypropylene PPH 5060 is homopolymer with a Melt Flow Index of 6 g/10 min.

Polypropylene PPH 5060 is specially suitable for tape extrusion for woven applications and for extrusion thermoforming.

Polypropylene PPH 5060 is also a general purpose injection grade for moulding technical items

Characteristics

	Method	Unit	Typical Value
Rheological properties			
Melt Flow Index 230°C/2.16 kg	ISO 1133	g/10 min	6
Mechanical properties			
Tensile Strength at Yield	ISO 527-2	MPa	32
Elongation at Yield	ISO 527-2	%	10
Tensile modulus	ISO 527-2	MPa	1500
Flexural modulus	ISO 178	MPa	1400
Izod Impact Strength (notched) at 23°C	ISO 180	kJ/m ²	4
Charpy Impact Strength (notched) at 23°C	ISO 179	kJ/m ²	5
Hardness Rockwell - R-scale	ISO 2039-2		92
Thermal properties			
Melting Point	ISO 3146	°C	164
Vicat Softening Point	ISO 306	°C	
50N-50°C per hour			85
10N-50°C per hour			150
Heat Deflection Temperature	ISO 752	°C	
1.80 MPa - 120°C per hour			55
0.45 MPa - 120°C per hour			100
Other physical properties			
Density	ISO 1183	g/cm ³	0.905
Bulk Density	ISO 1183	g/cm ³	0.525

Safety and Product Stewardship

For safe use and handling, please refer to the Safety Data Sheet.

A Product Stewardship certificate giving the conformity to various regulations or statements on absence of certain chemicals is also available on our web site www.polypropylene.totalpetrochemicals.com

An Injection Moulding troubleshooting guide is available upon request.

Information contained in this publication is true and accurate at the time of publication and to the best of our knowledge. The nominal values stated herein are obtained using laboratory test specimens. Before using one of the products mentioned herein, customers and other users should take all care in determining the suitability of such product for the intended use. Unless specifically indicated, the products mentioned herein are not suitable for applications in the pharmaceutical or medical sector. The Companies within Total Petrochemicals do not accept any liability whatsoever arising from the use of this information or the use, application or processing of any product described herein. No information contained in this publication can be considered as a suggestion to infringe patents. The Companies disclaim any liability that may be claimed for infringement or alleged infringement of patents.



TOTAL PETROCHEMICALS RESEARCH FELUY
Zone Industrielle C
B-7181 Feluy
Belgium

Rev : July 07

Page 1 of 1

mailto : polypropylene@total.com

website : www.polypropylene.totalpetrochemicals.com

Polypropylene

Appendix B2: Polypropylene PPH 5042

TOTAL PETROCHEMICALS

Polypropylene PPH 5042

Technical data sheet
Polypropylene – Homopolymer
Produced in Europe

Description

Polypropylene PPH 5042 is an homopolymer with a Melt Flow Index of 6 g/10 min.

Polypropylene PPH 5042 has been specially designed for extrusion-thermoforming, where it gives improved rigidity and impact resistance combined with high clarity, reduced cycle times and good antistatic properties.

Polypropylene PPH 5042 is suitable for the injection moulding of household articles, toys, caps & closures, providing the benefits outlined above.

Characteristics

	Method	Unit	Typical Value
Rheological properties			
Melt Flow Index 230°C/2.16 kg	ISO 1133	g/10 min	6
Mechanical properties			
Tensile Strength at Yield	ISO 527-2	MPa	35
Elongation at Yield	ISO 527-2	%	9
Tensile modulus	ISO 527-2	MPa	1600
Flexural modulus	ISO 178	MPa	1550
Izod Impact Strength (notched) at 23°C	ISO 180	kJ/m ²	5
Charpy Impact Strength (notched) at 23°C	ISO 179	kJ/m ²	6
Hardness Rockwell - R-scale	ISO 2039-2		95
Thermal properties			
Melting Point	ISO 3146	°C	165
Vicat Softening Point	ISO 306	°C	
50N-50°C per hour			95
10N-50°C per hour			153
Heat Deflection Temperature	ISO 752	°C	
1.80 MPa - 120°C per hour			57
0.45 MPa - 120°C per hour			105
Other physical properties			
Density	ISO 1183	g/cm ³	0.905
Bulk Density	ISO 1183	g/cm ³	0.525

Polypropylene

Safety and Product Stewardship

For safe use and handling, please refer to the Safety Data Sheet.

A Product Stewardship certificate giving the conformity to various regulations or statements on absence of certain chemicals is also available on our web site www.polypropylene.totalpetrochemicals.com

An Injection Moulding troubleshooting guide is available upon request.

Information contained in this publication is true and accurate at the time of publication and to the best of our knowledge. The nominal values stated herein are obtained using laboratory test specimens. Before using one of the products mentioned herein, customers and other users should take all care in determining the suitability of such product for the intended use. Unless specifically indicated, the products mentioned herein are not suitable for applications in the pharmaceutical or medical sector. The Companies within Total Petrochemicals do not accept any liability whatsoever arising from the use of this information or the use, application or processing of any product described herein. No information contained in this publication can be considered as a suggestion to infringe patents. The Companies disclaim any liability that may be claimed for infringement or alleged infringement of patents.



TOTAL PETROCHEMICALS RESEARCH FELUY
Zone Industrielle C
B-7181 Feluy
Belgium

Rev : July 07

Page 1 of 1

mailto : polypropylene@total.com

website : www.polypropylene.totalpetrochemicals.com

Appendix B3: Southern Clay Cloisite® 15A

SOUTHERN CLAY PRODUCTS / A SUBSIDIARY OF ROCKWOOD SPECIALTIES, INC.

PRODUCT BULLETIN/Cloisite®



Southern Clay Products, Inc.
1212 Church Street
Gonzales, TX 78629
Phone: 800-324-2891
Fax: 830-672-1903
www.scprod.com

Cloisite® 15A

Typical Physical Properties Bulletin

Description:

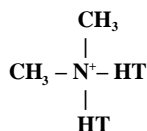
Cloisite® 15A is a natural montmorillonite modified with a quaternary ammonium salt.

Designed Used:

Cloisite® 15A is an additive for plastics to improve various plastic physical properties, such as reinforcement, HDT, CLTE and barrier.

Typical Properties:

<u>Treatment/Properties:</u>	Organic Modifier (1)	Modifier Concentration	% Moisture	% Weight Loss on Ignition
Cloisite® 15A	2M2HT	125 meq/100g clay	< 2%	43%



Where HT is Hydrogenated Tallow (~65% C18; ~30% C16; ~5% C14)

Anion: Chloride

(1) 2M2HT: dimethyl, dehydrogenated tallow, quaternary ammonium

Typical Dry Particle Sizes: (microns, by volume)

10% less than: 2µm	50% less than: 6µm	90% less than: 13µm
-----------------------	-----------------------	------------------------

Color: Off White

Density:

Loose Bulk, lbs/ft ³ 10.79	Packed Bulk, lbs/ft ³ 18.64	Density, g/cc 1.66
--	---	-----------------------

X Ray Results: $d_{001} = 31.5\text{\AA}$

For additional information or technical assistance contact Southern Clay Products, Inc. toll free at 800-324-2891.

Disclaimer of Warranty: The information presented herein is believed to be accurate but is not to be taken as a warranty, guarantee, or representation for which we assume legal responsibility. This information does not grant permission, license, or any rights or recommendations to practice any form of proprietary intellectual property without obtaining the appropriate license or grant from the property owner. The information is offered solely for your consideration, investigation and verification, but you must determine the suitability of the product for your specific application. The purchaser assumes all risk of use of handling the material, including but not limited to transferring the material within purchaser's facilities, using the material in applications specified by the purchaser and handling any product which includes the material, whether or not in accordance with any statements made herein.

Appendix B4: DuPont Fusabond® P M613 05

DuPont Packaging & Industrial Polymers



The miracles of science®

DuPont Packaging & Industrial Polymers

Fusabond® polymer modifiers

DuPont™ Fusabond® P M613?05

Description

Product Description DuPont™ Fusabond® P M613?05 is a chemically modified polypropylene.

Product Characteristics

Typical Applications Coupling agent, short glass?filled PP WPC compound containing natural fibers

Material Status * Commercial Active
Availability * Globally
Manufacturer / Supplier * DuPont Packaging & Industrial Polymers

Properties

Physical	Nominal Values	Test Method
Melt Flow Rate (190°C/1000g)	49g/10 min	ASTM D1238 ? ISO 1133
Thermal	Nominal Values	Test Method
Melting Point	162°C (324°F)	ASTM D3418 ? ISO 3146

Processing Information

FDA Status 21CFR 175.300

Read and understand the Material Safety Data Sheet (MSDS) before using this product

DuPont Worldwide

55
DuPont Singapore PTE Ltd. 1
Maritime Square #07?01 World
Trade Centre Singapore 0409
Telephone 65?27372244 Fax
65?27277494

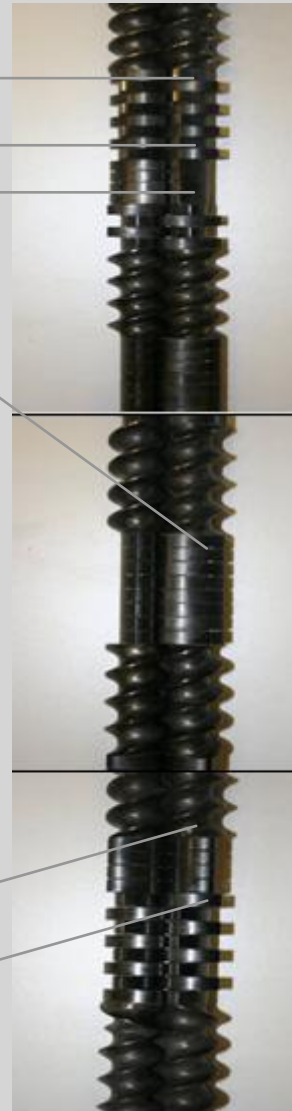
Australia
DuPont (Australia) Ltd. 254
Canterbury Road Bayswater,
Victoria 3153 Australia Telephone
37972175900 Fax 37972175650

Brazil/South America
DuPont do Brasil, S.A. Alameda
Itapecuru, 506 06454?080 Barueri,
SP Brasil Telephone
571177416678542 / 8393 Fax
55?117416678720

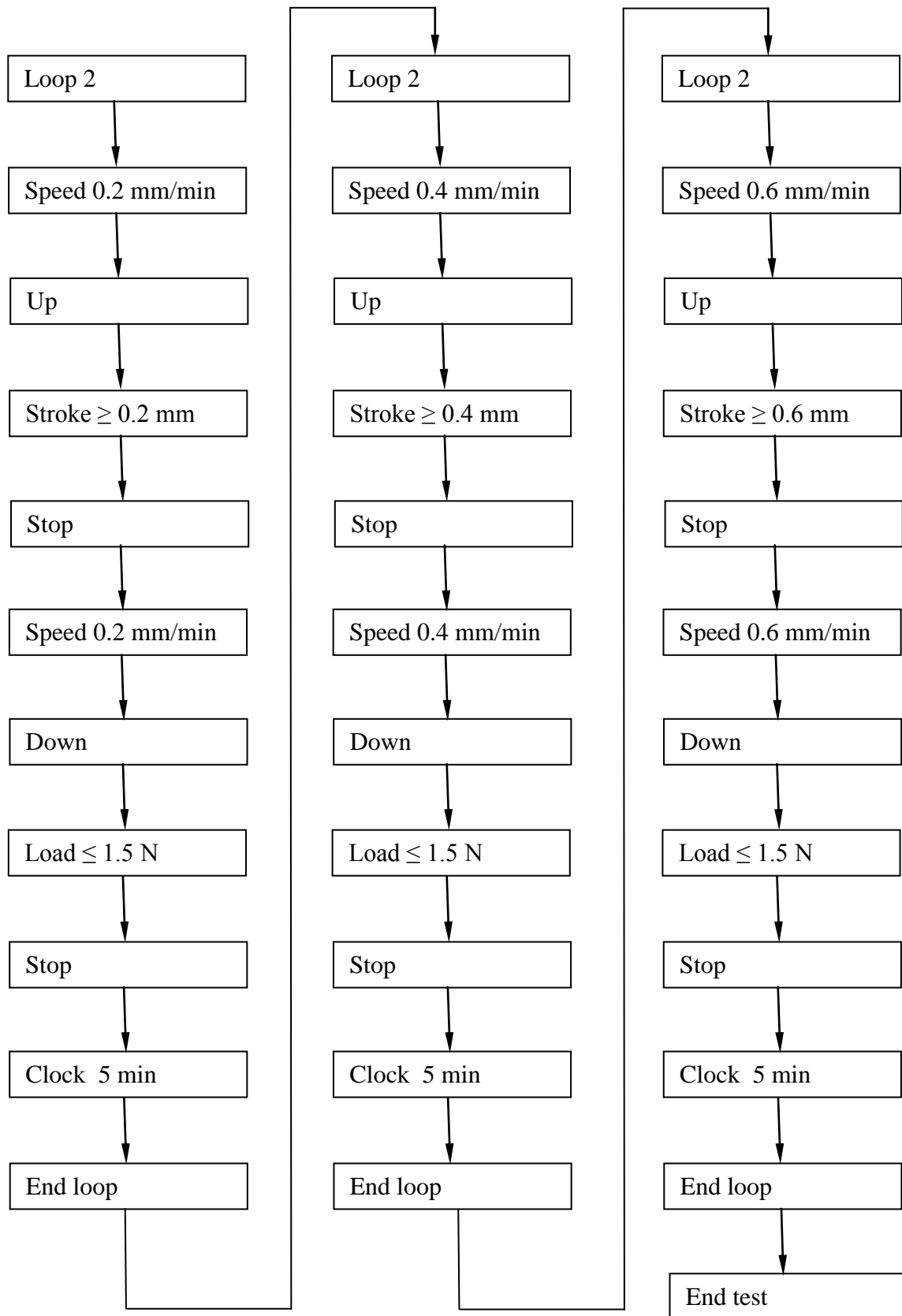
Canada
DuPont Canada Inc. P.O. Box
2200, Streetsville 7070
Mississauga, Road Mississauga,
ONT L5M 2H3 Telephone (Canada
Only): 800?268?3943 / 905?821
5953 Fax 905?821?5230

Appendix C: Twin Screw Configuration

Barrel Layout PRISM Eurolab 16mm 40:1 L/D		Screw geometry	
D		D	
1	Flange	1	1 D FS FS 1
2	Block 1	2	1 D FS FS2
3	MAIN FEED PORT	3	1 D FS FS 3
4		4	1 D FS FS 4
5		5	1 D FS FS 5
6		6	1 D FS FS 6
7	Block 2	7	1 D FS FS 7
8		8	1 D FS FS 8
9	Block 3	9	1 D FS FS 9
10		10	a90 a90 8 x 0 deg
11		11	a0 a0 4 x 60 deg
12		12	a90 a90 4 x 90 deg
13	Block 4	13	1 D FS FS10
14		14	1 D FS FS11
15	Block 5	15	a0 a0 8 x 0 deg
16		16	a0 a0 0 deg
17		17	1 D FS FS12
18		18	1 D FS FS13
19	Block 6	19	a0 a0 6 x 0 deg
20		20	a0 a0 0 deg
21		21	1 D FS FS14
22		22	a0 a0 4 x 0 deg
23	Block 7	23	1 D FS FS15
24		24	a0 a0 4 x 0 deg
25		25	1 D FS FS15
26		26	1 D FS FS16
27	Block 8	27	1 D FS FS17
28		28	1 D FS FS18
29		29	a0 a0 4 x 0 deg
30		30	a90 a90 8 x 90 deg
31	Block 9	31	a90 a90 8 x 90 deg
32		32	D/2 RFS RFS 1
33		33	D/2 RFS RFS 2
34	Block 10	34	1 D FS FS19
35		35	1 D FS FS20
36		36	1 D FS FS21
37		37	1 D FS FS22
38	Flange	38	1 D FS FS23
39		39	1 D FS FS24
40		40	1.5 D Discharge Screw discharge



Appendix D: Modulus Measurement Program by Video Extensometer

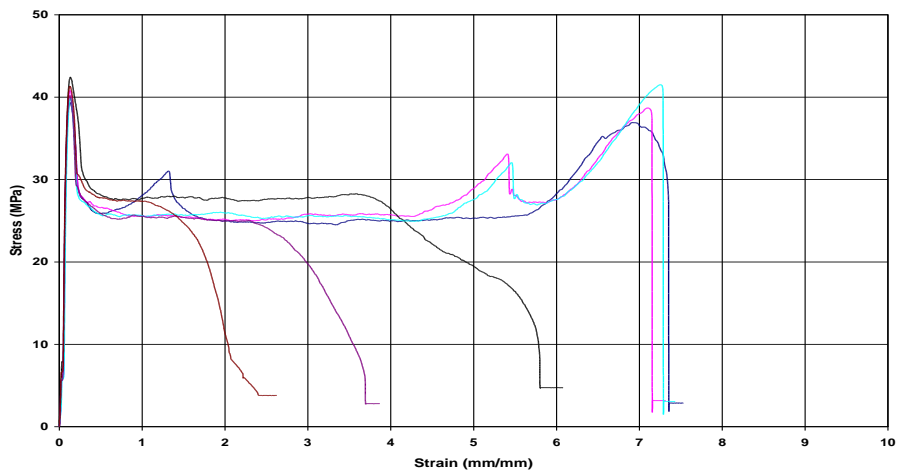
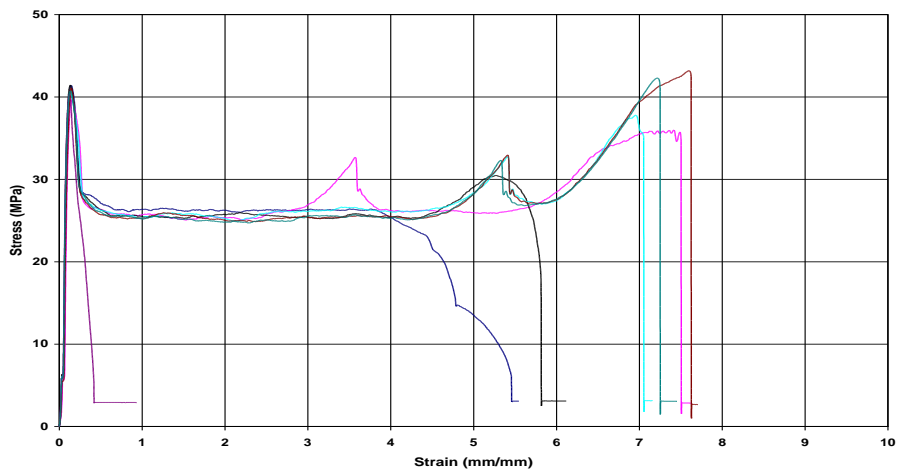
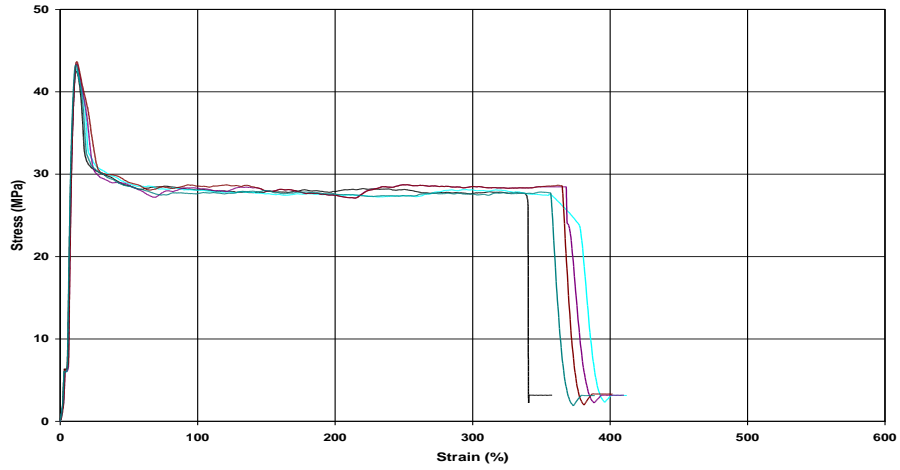


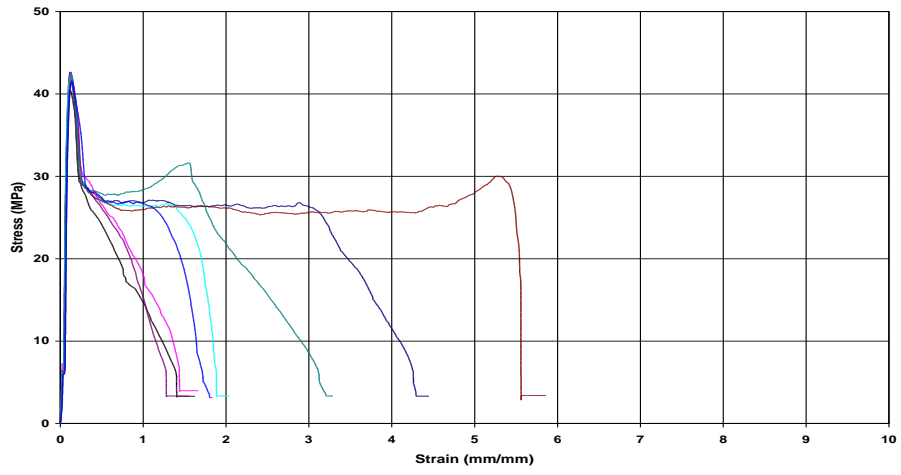
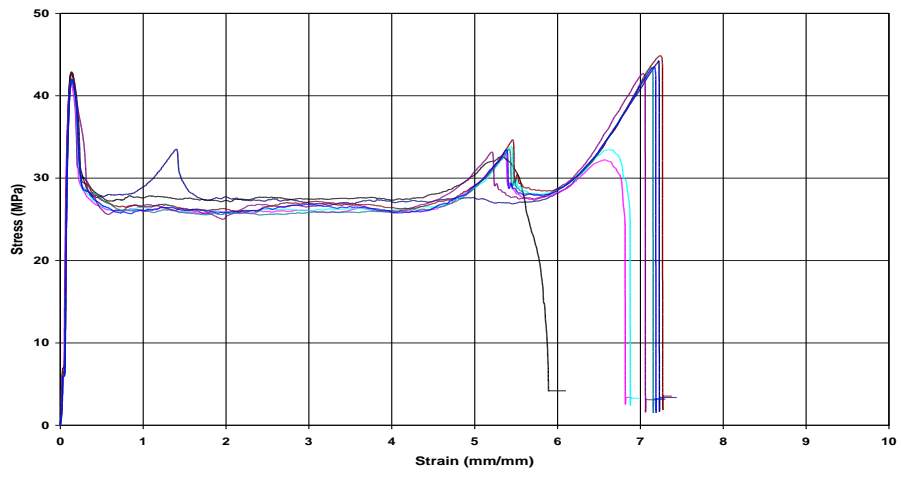
Appendix E: Tensile Graphs

PP 1 = Pure Polypropylene, PPH 5042
PP 2 = Polypropylene + 3% Cloisite 15A
PP 3 = Polypropylene + 5% Cloisite 15A
PP 4 = Polypropylene + 3% Somasif MTE
PP 5 = Polypropylene + 3% Somasif MTE

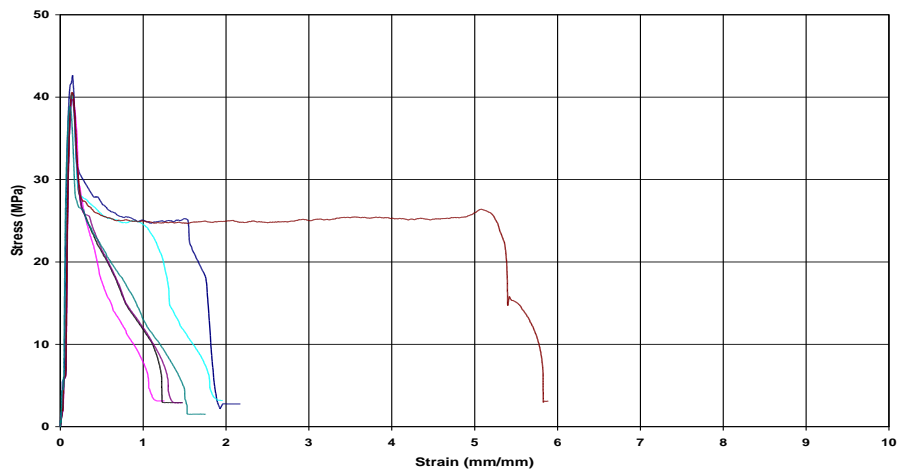
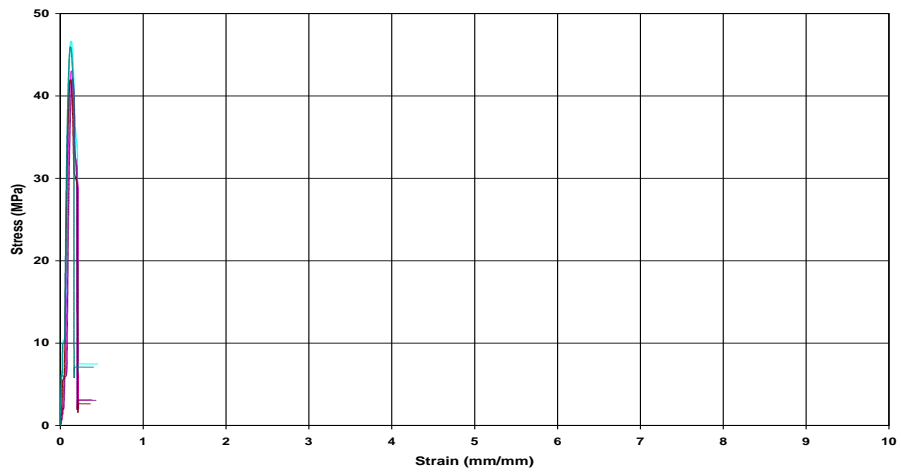
Appendix E1: Original Extruded Sheets

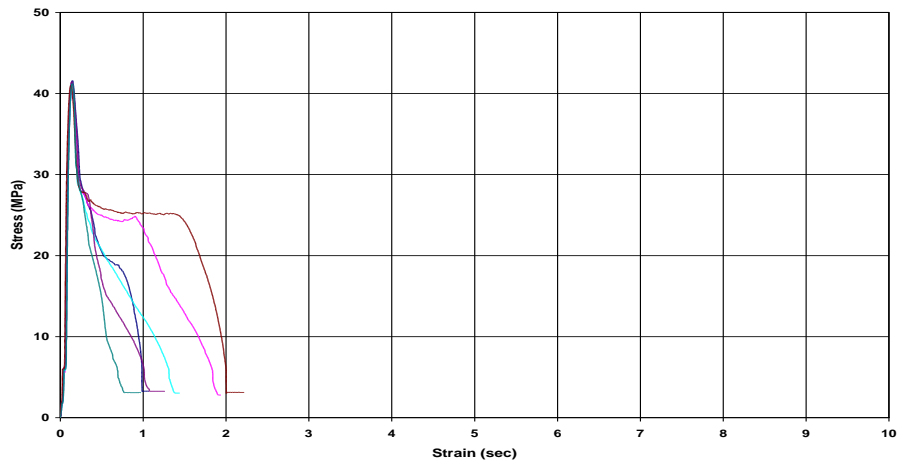
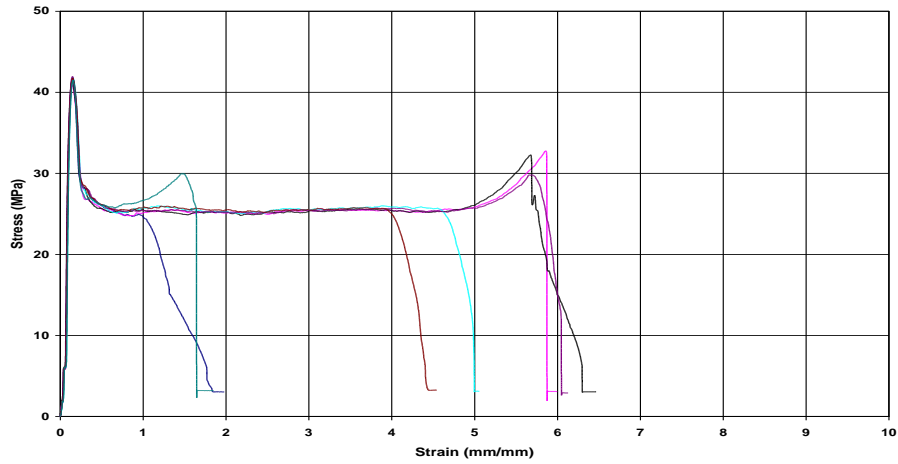
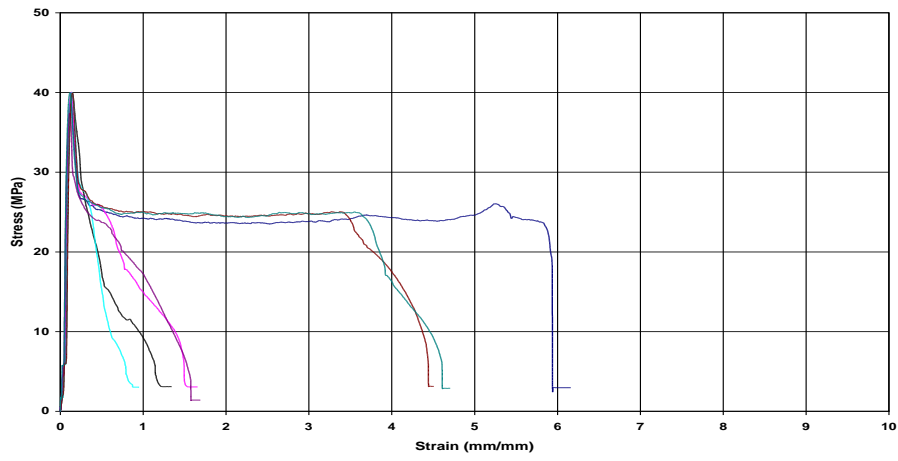
Original Extruded Sheets Machine Direction





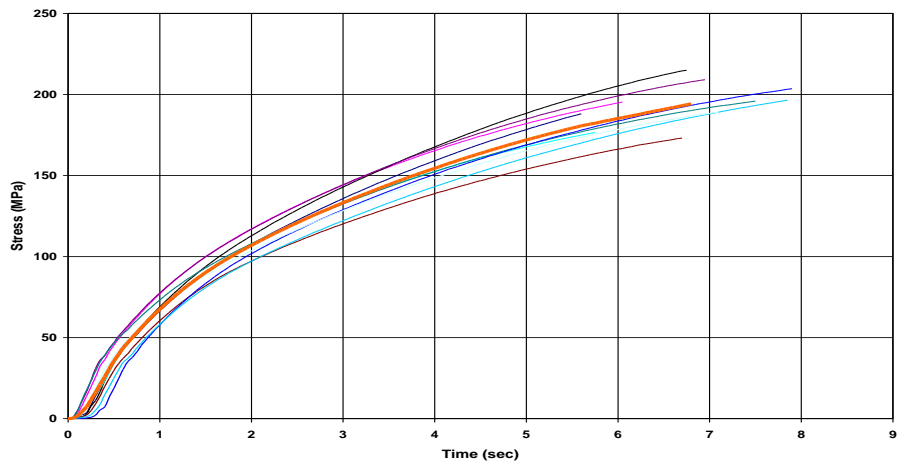
Original Extruded Sheets Transverse Direction

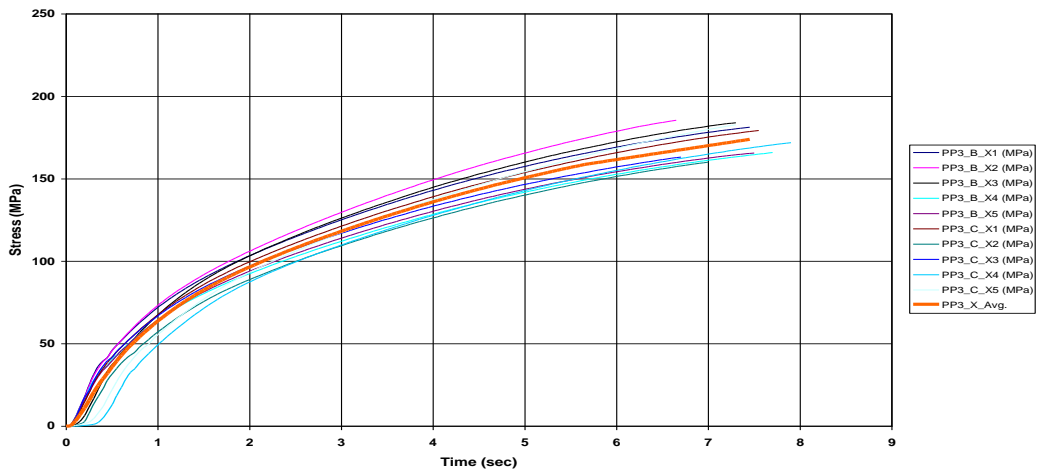
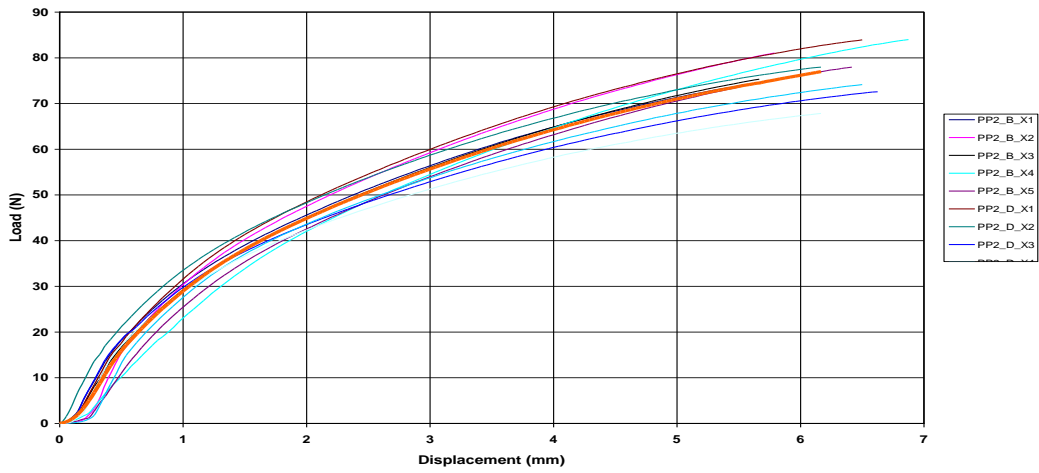
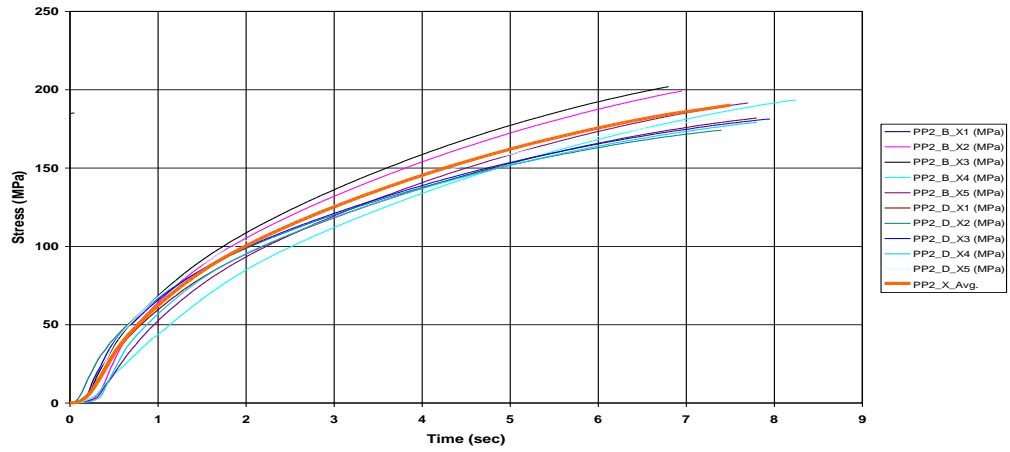
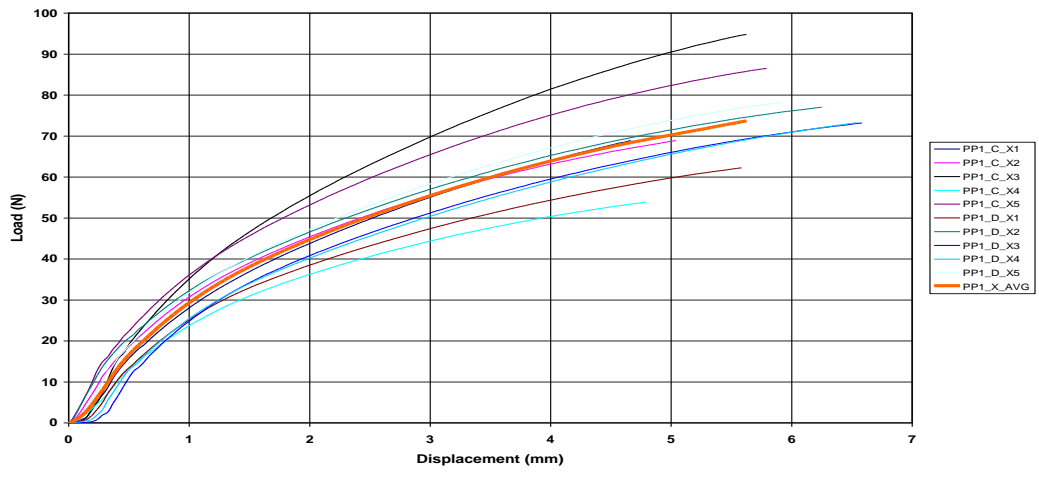


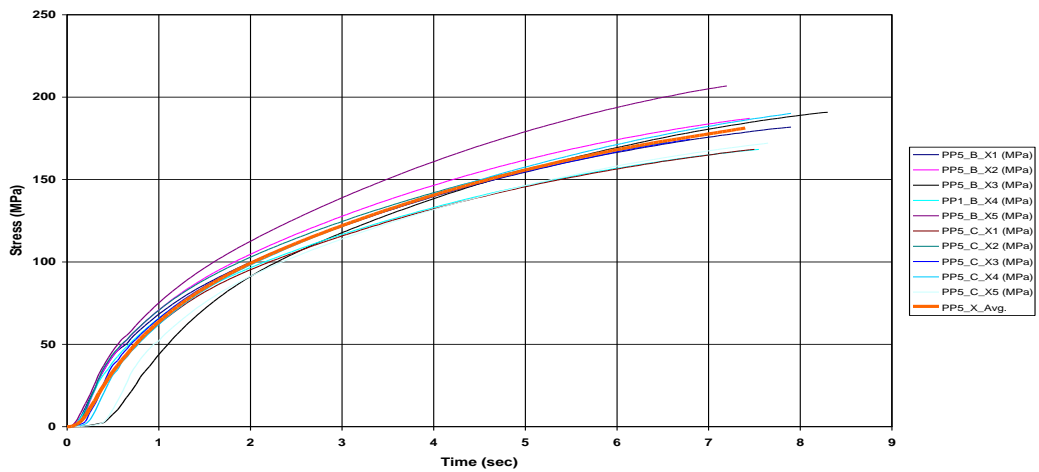
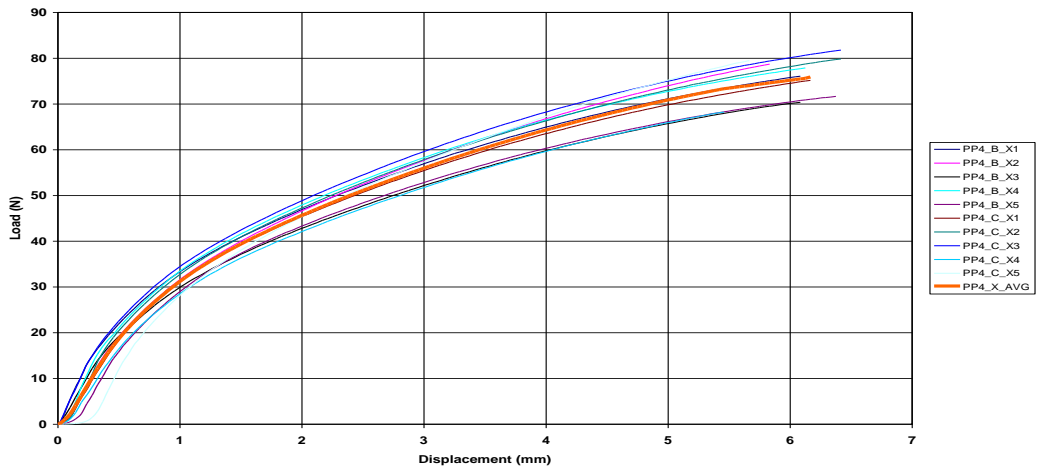
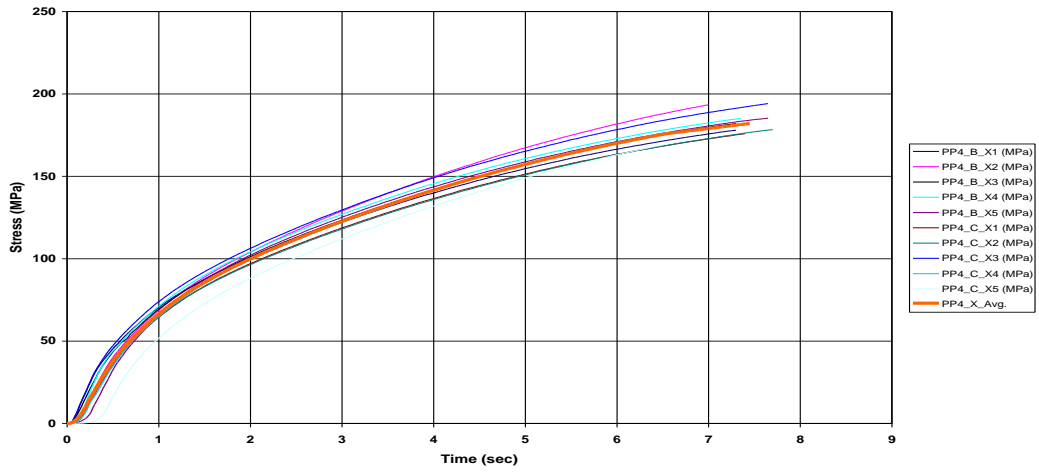
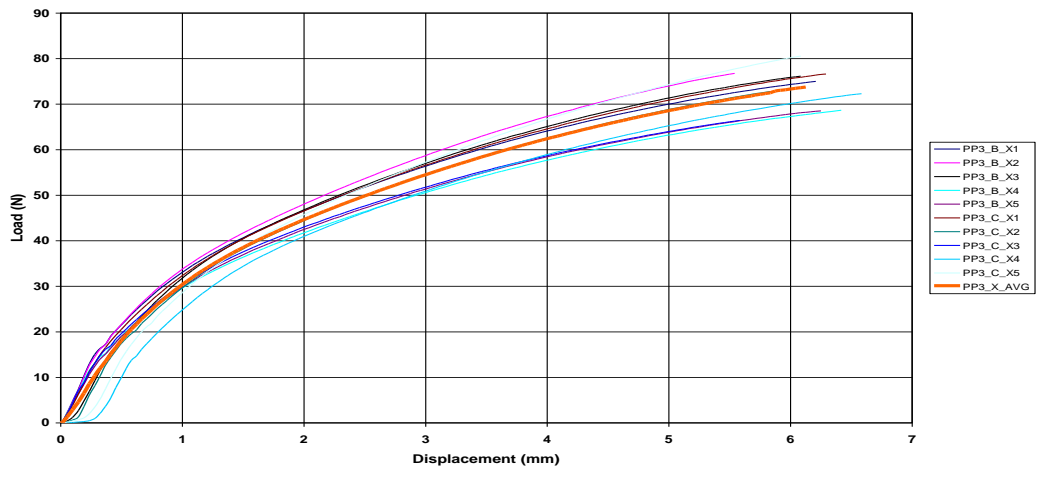


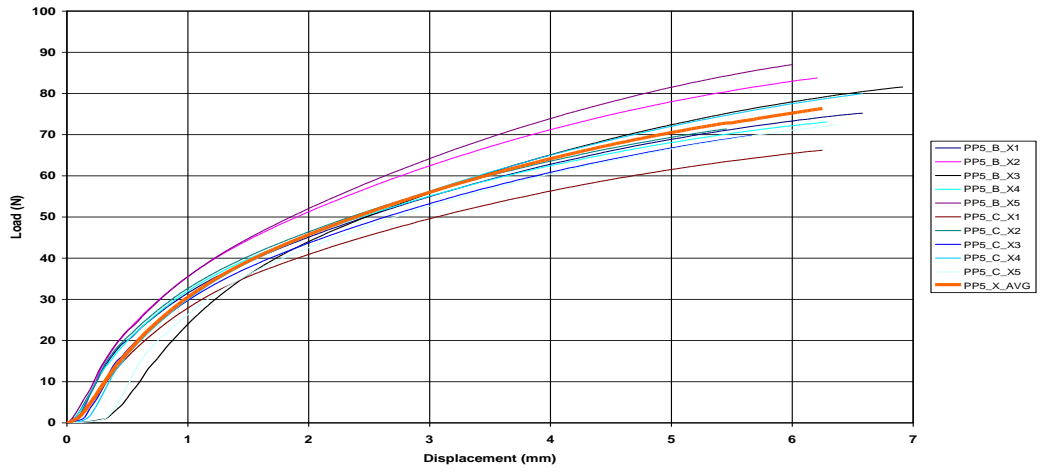
Appendix E2: PP/Clay Stretched Sheet - Instron Results

PP/Clay Stretched Sheet - Instron Results- Machine Direction



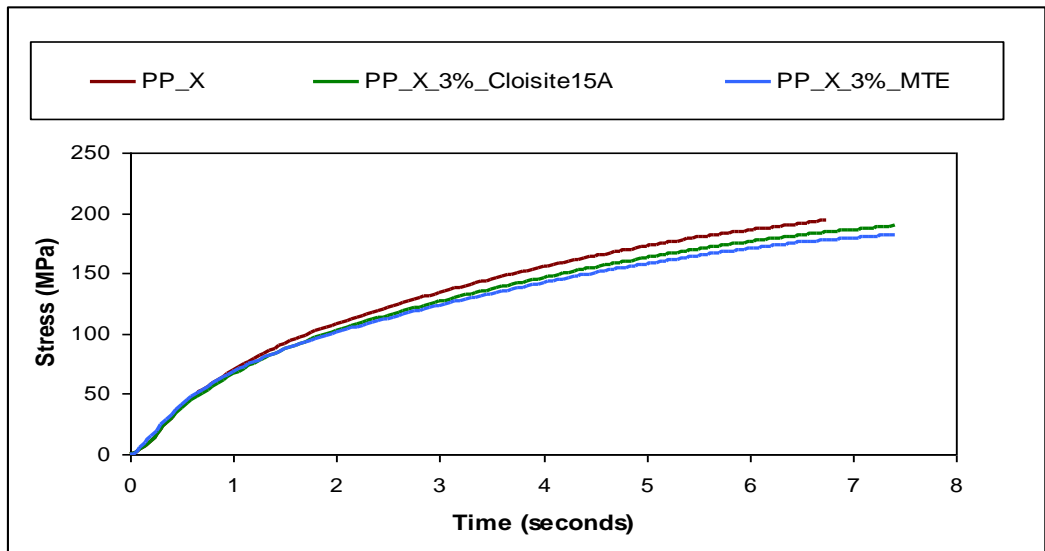
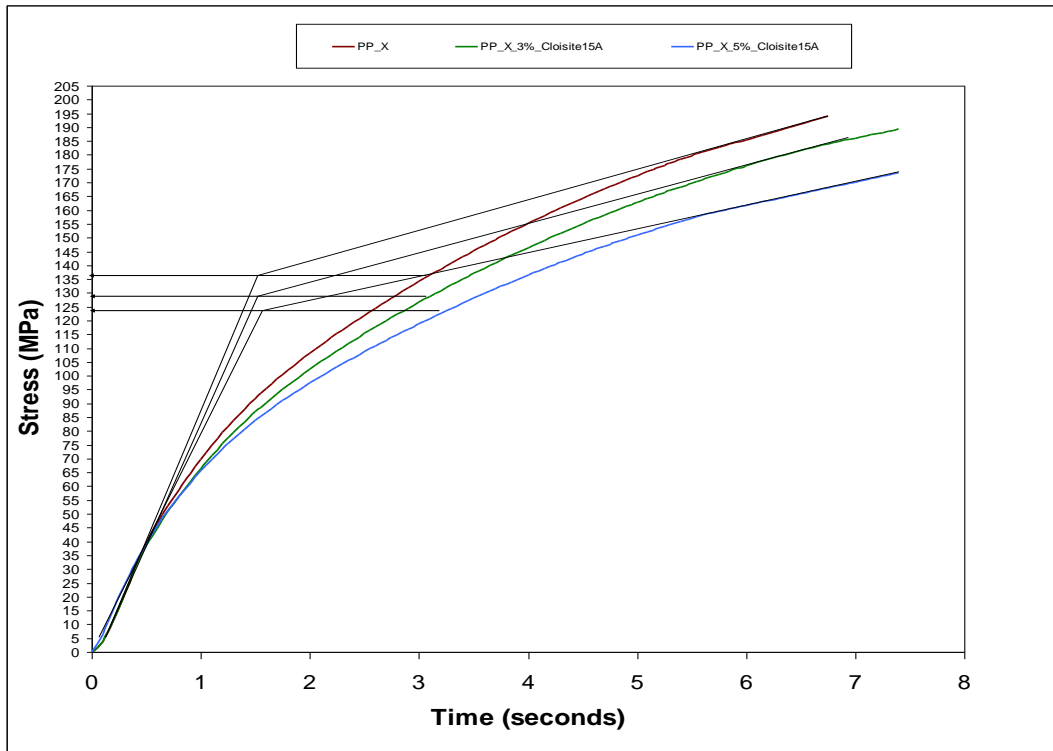


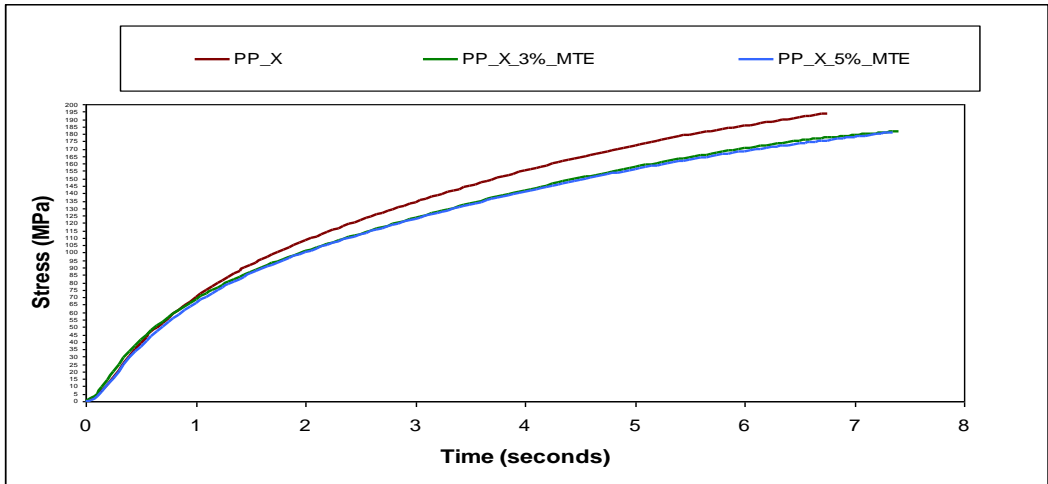
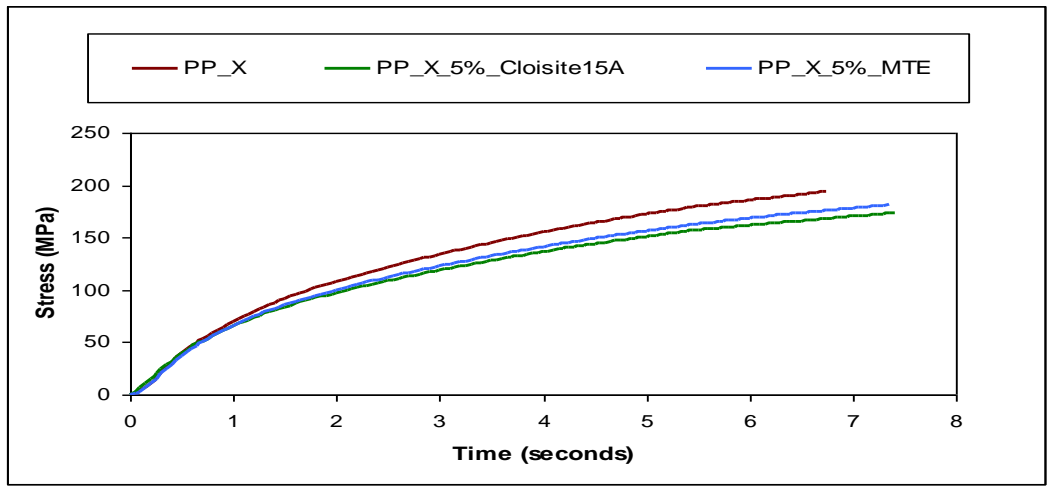




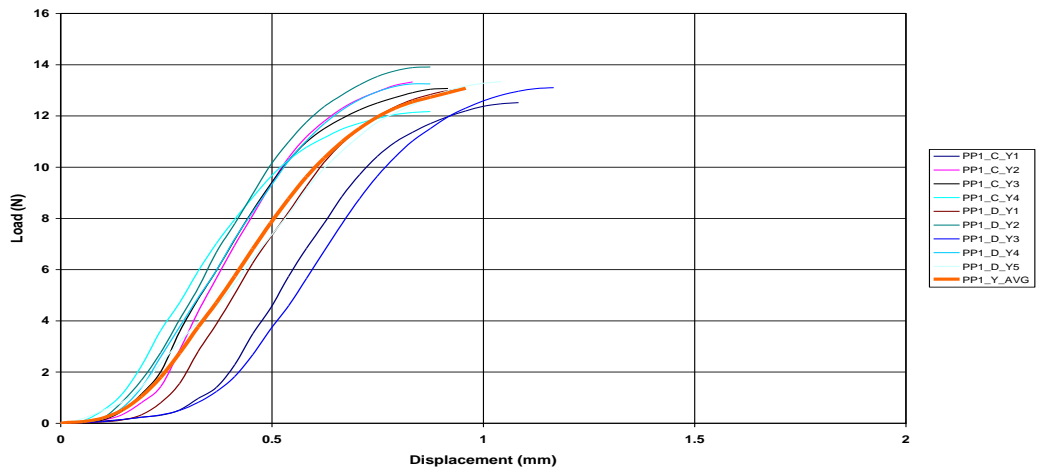
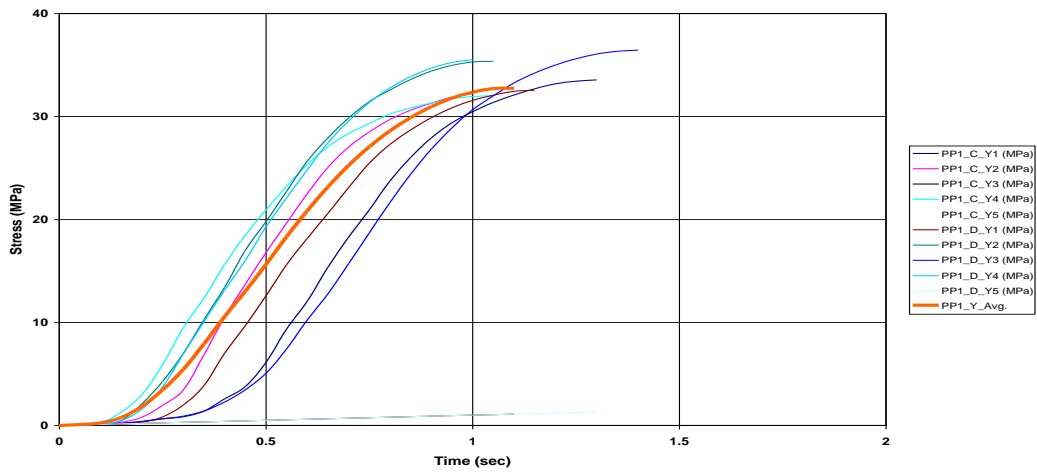
PP/Clay Stretched Sheet - Instron Comparison Results – Machine Direction

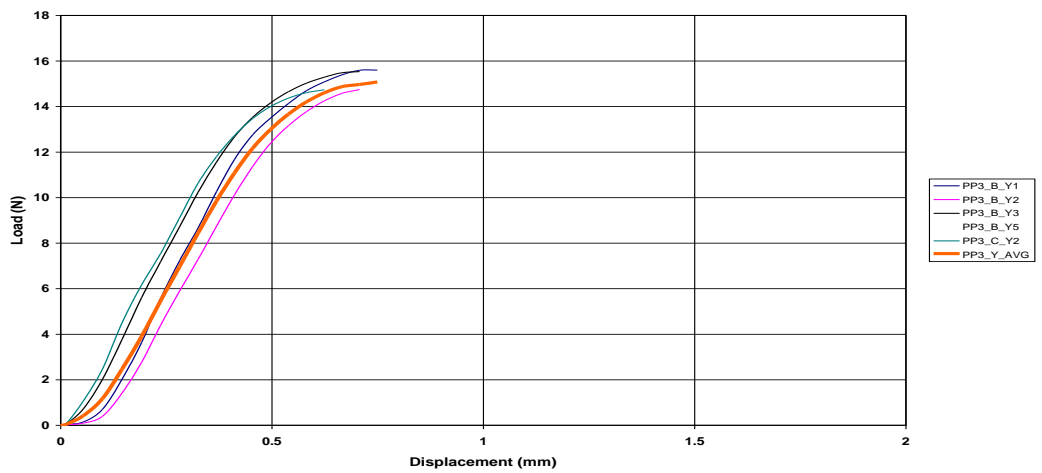
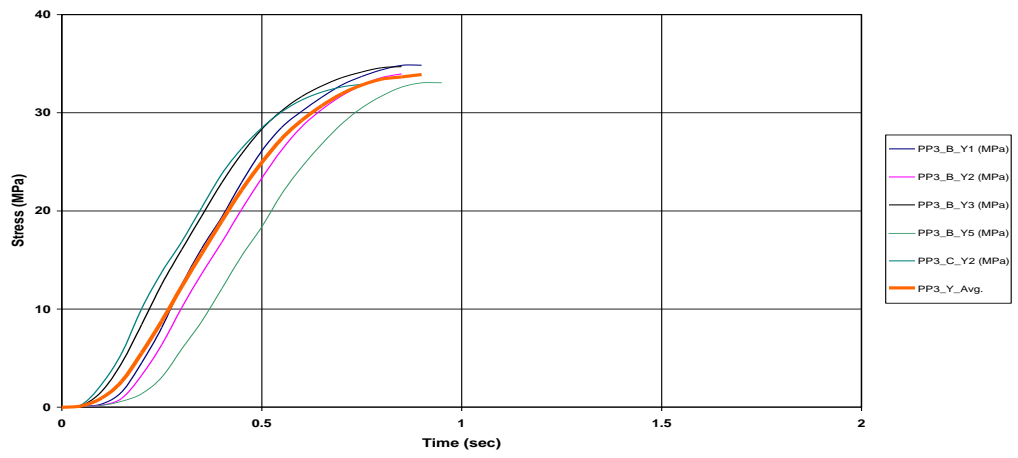
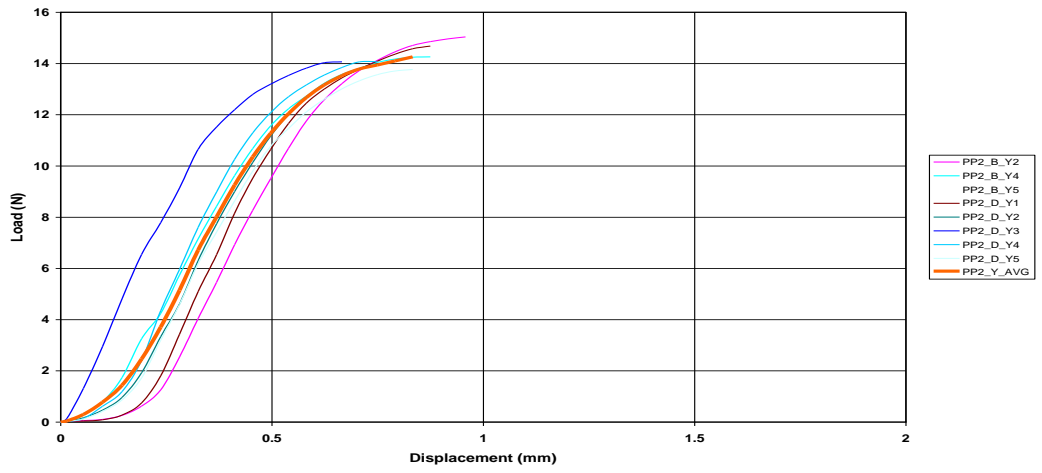
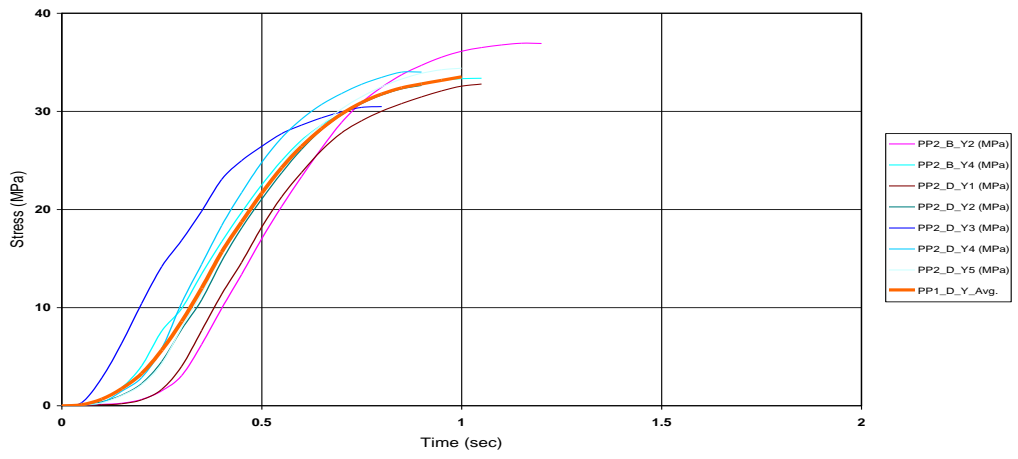
The used method to measure the yield stress is shown in the first Figure.

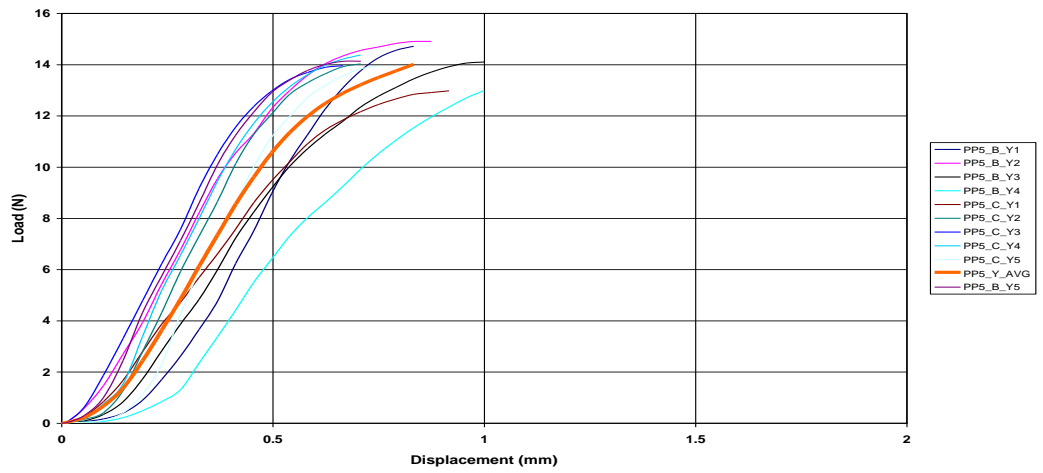
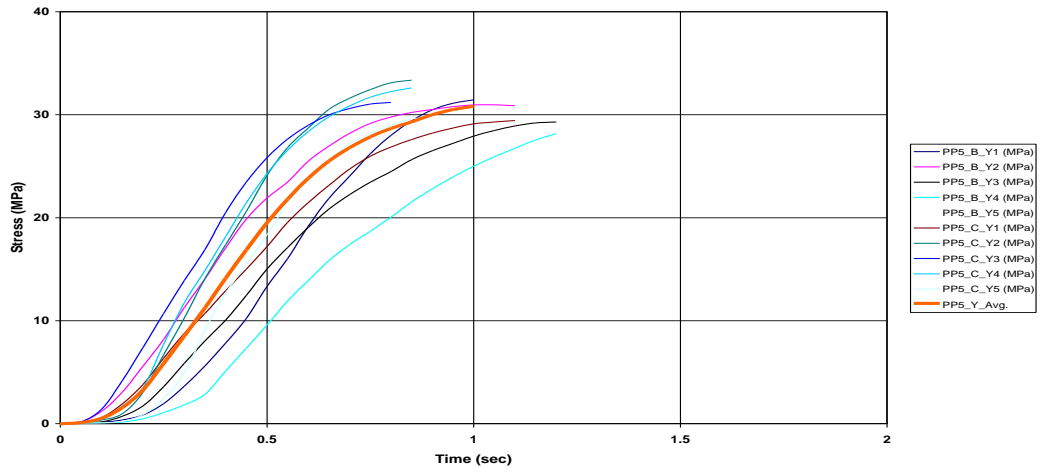
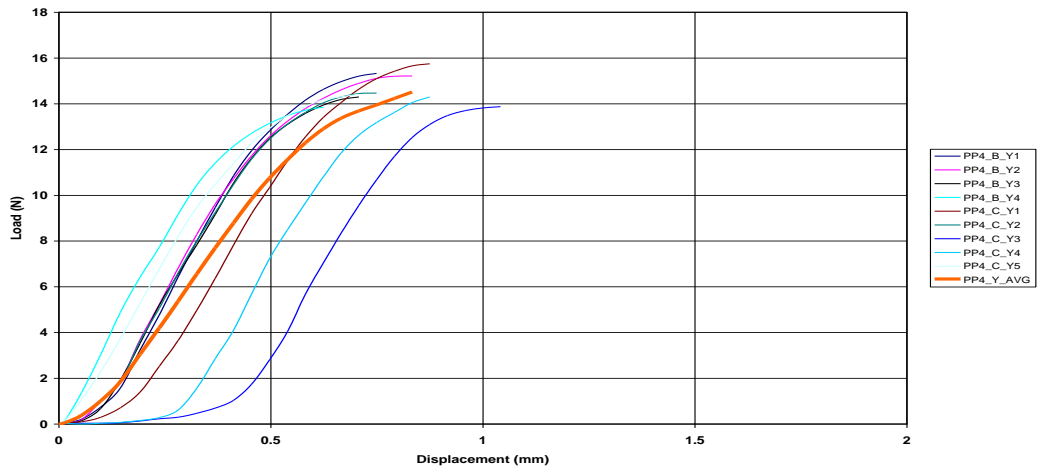
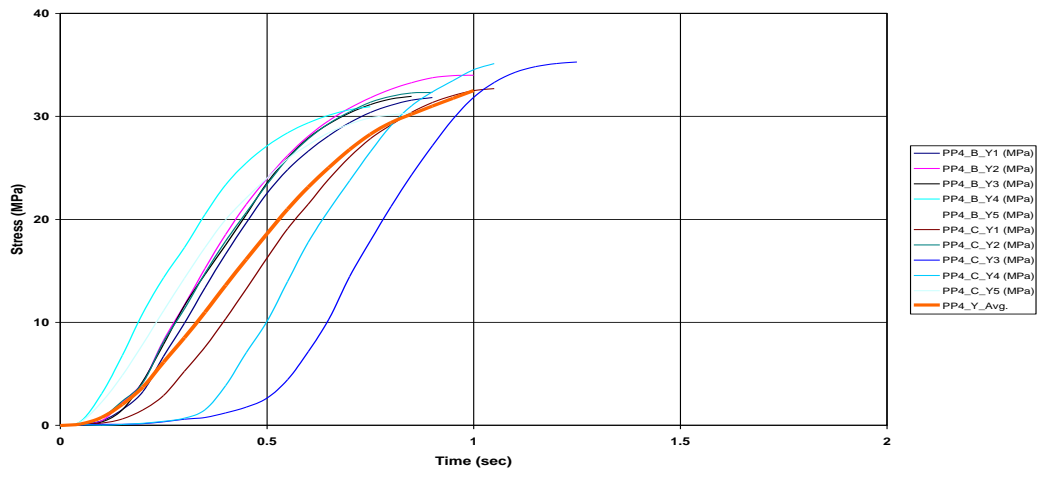




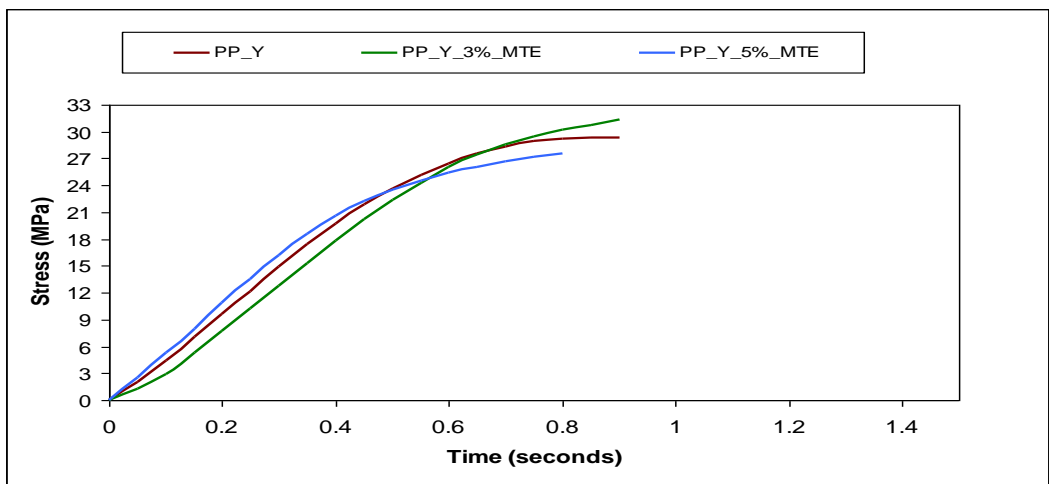
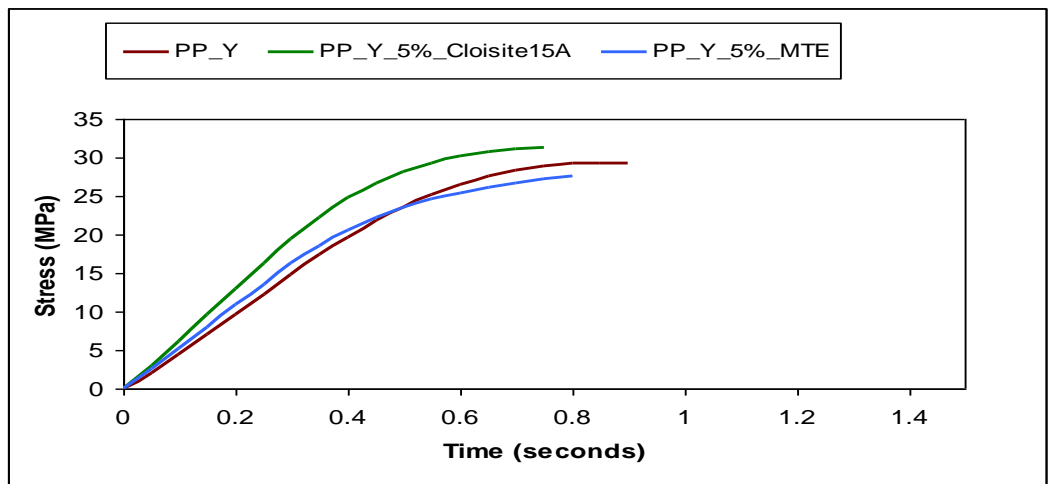
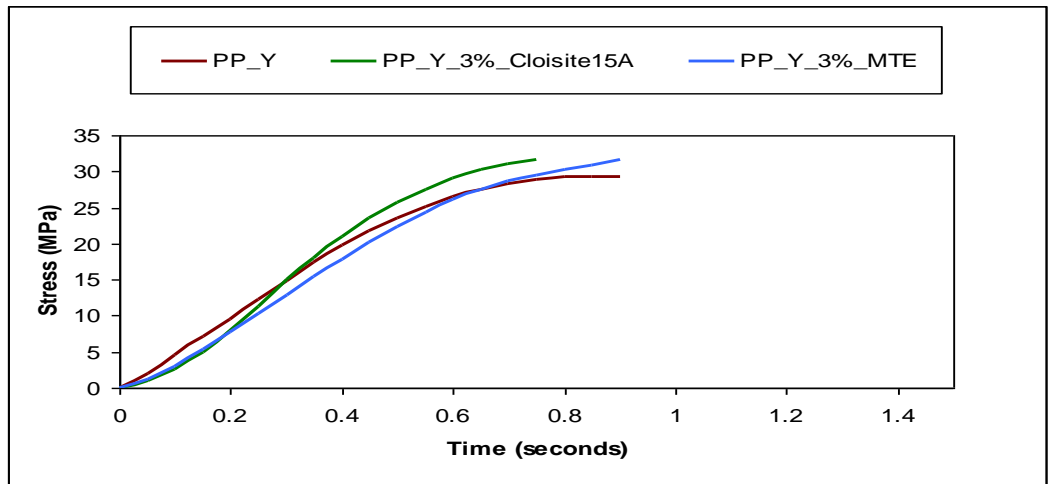
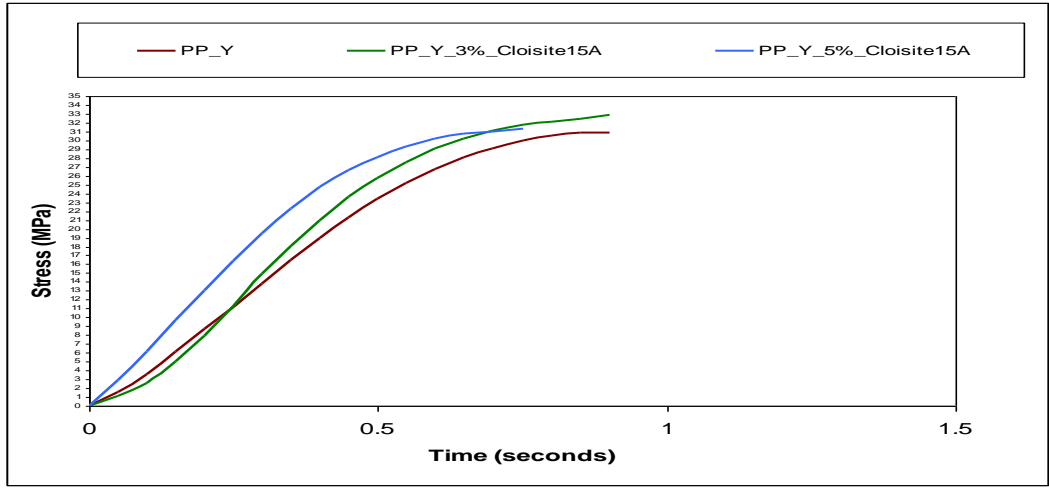
PP/Clay Stretched Sheet - Instron Results- Transverse Direction





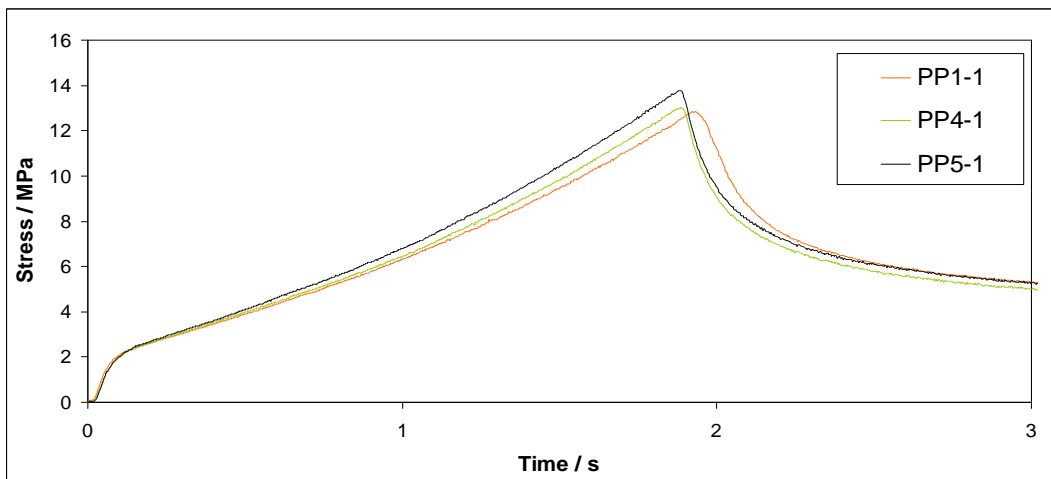
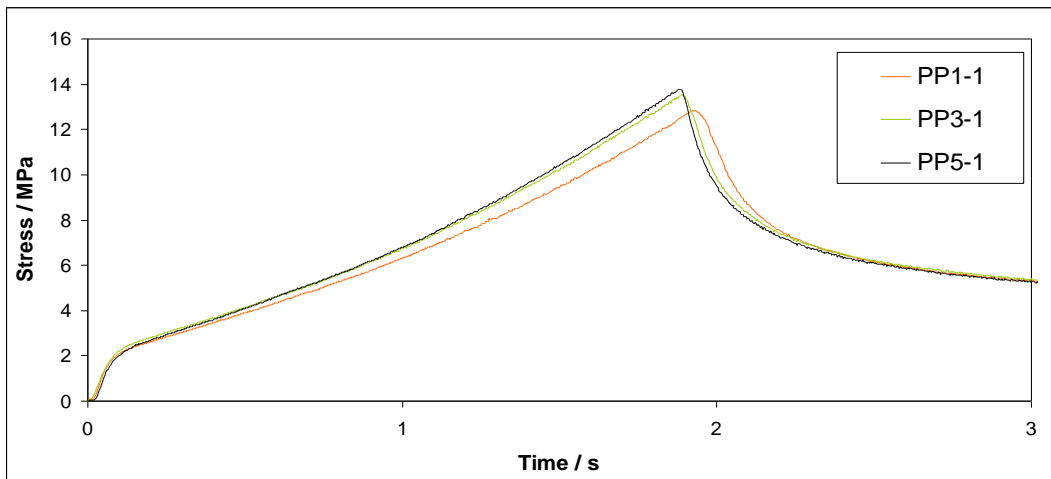
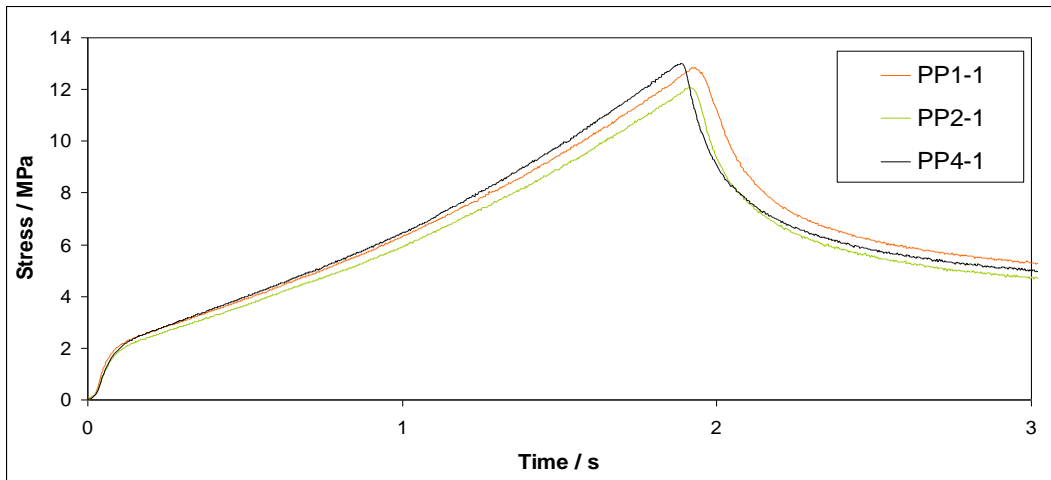
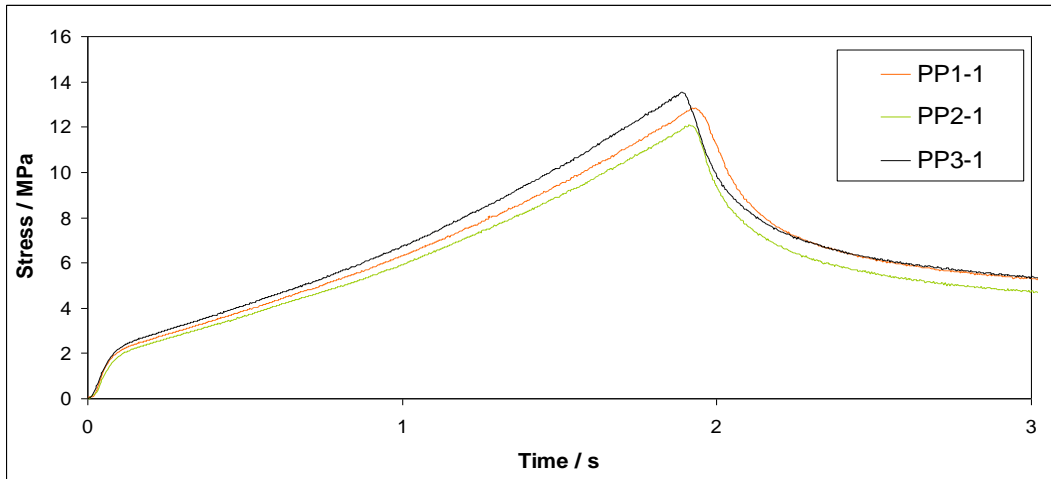


PP/Clay Stretched Sheet - Instron Comparison Results – Transverse Direction

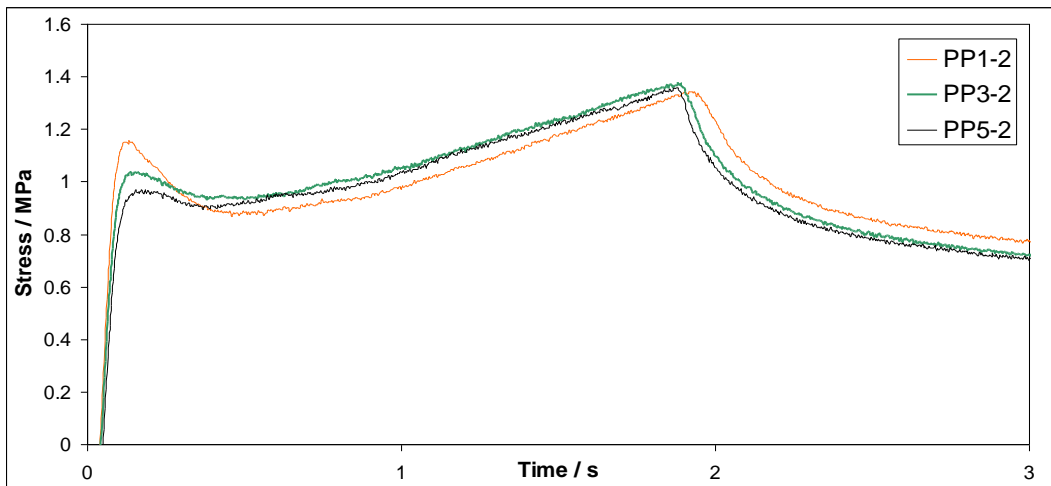
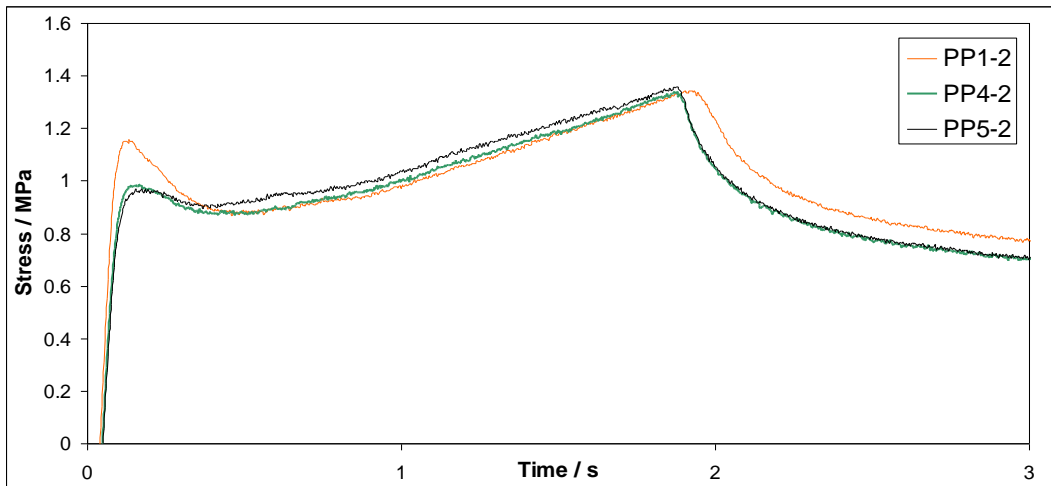
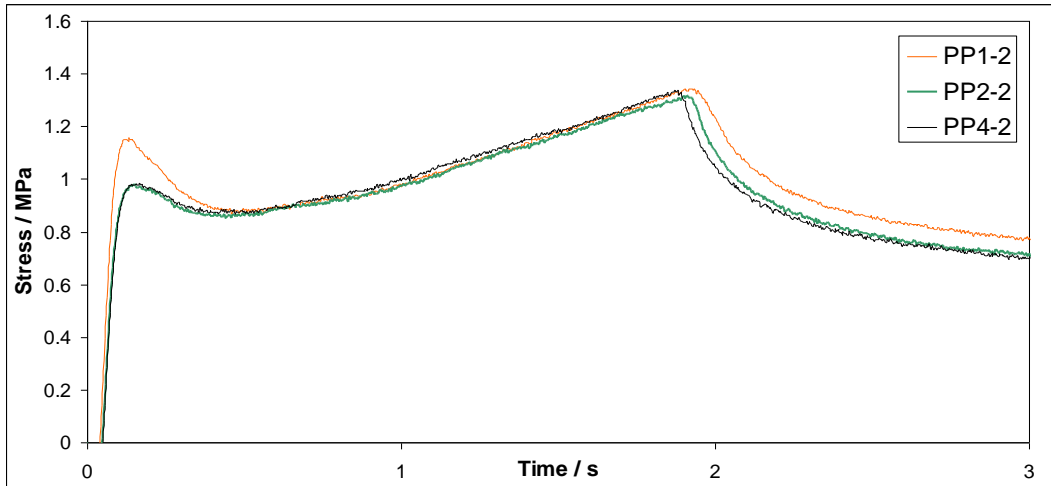
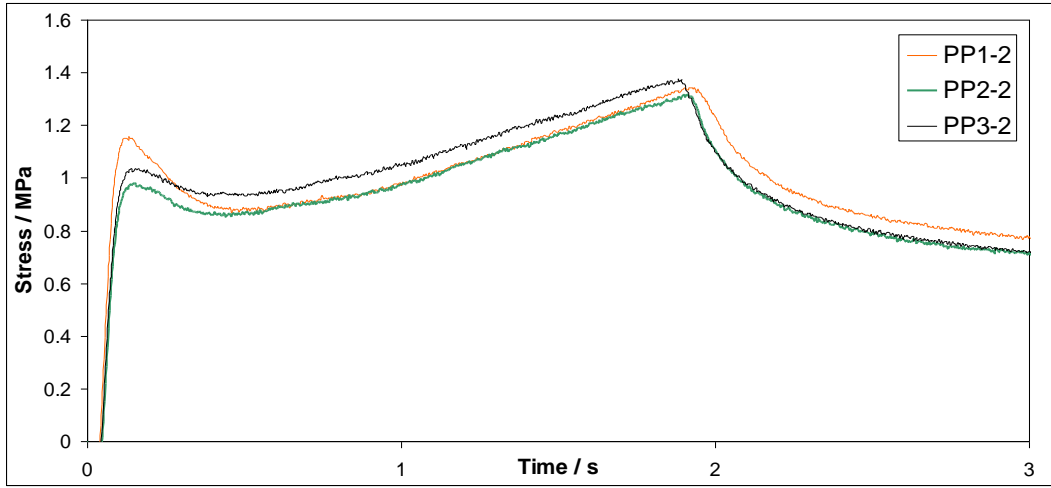


Appendix E3: PP Clay Biaxial Machine Testing Results

Biaxial Machine Testing Results - Machine Direction



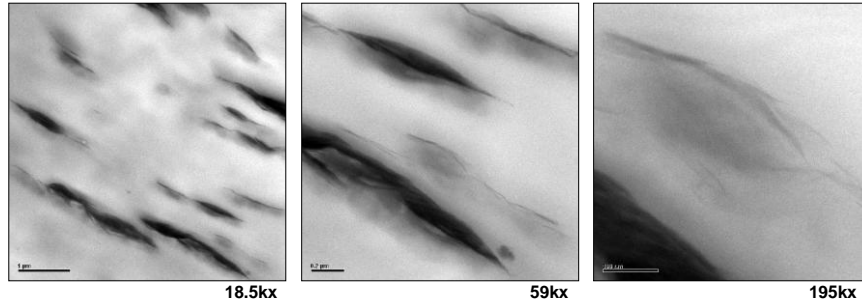
Biaxial Machine Testing Results - Transverse Direction



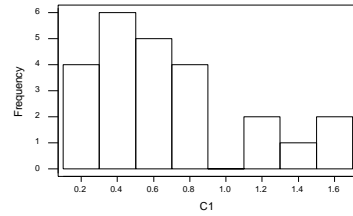
Appendix F: TEM Micrographs of PPNCs

Appendix F1: TEM Micrographs of Undrawn PPNC

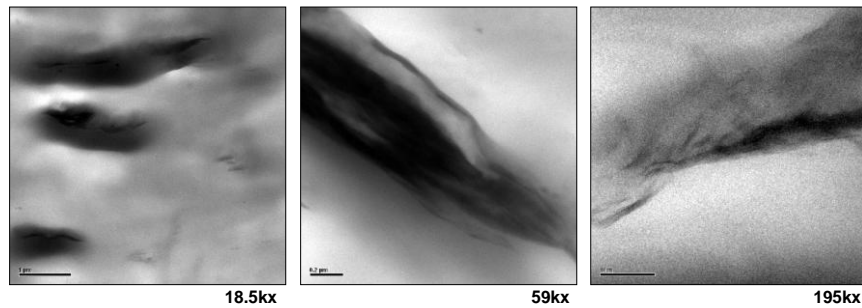
Sample ID: Undrawn PP+3%Clay



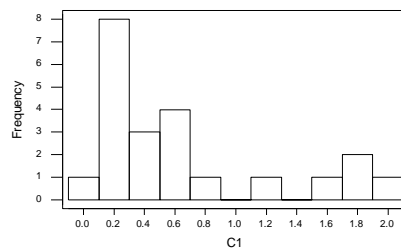
Avg diameter: 0.57
SD: 0.39
Avg no of particles per image:6



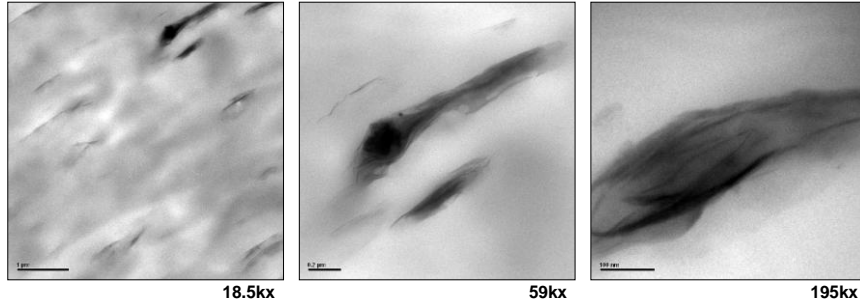
Sample ID: Undraw PP+5%Clay



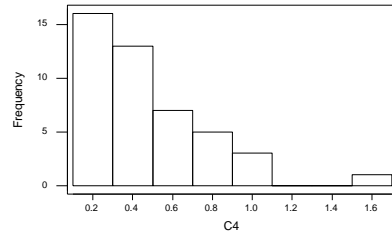
Avg diameter: 0.61
SD: 0.62
Avg no of particles per image:3.7



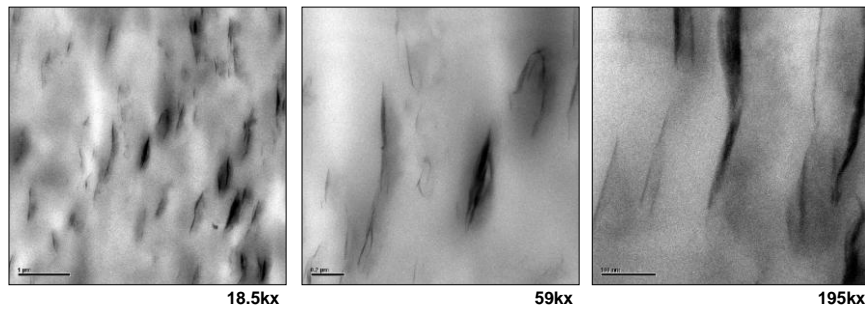
Sample ID: Undraw PP+3%Clay(MB)+3%PPMA(MB)



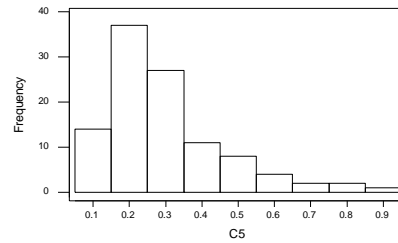
Avg diameter: 0.43
SD: 0.31
Avg no of particles per image:7.5
MB = Master Batch



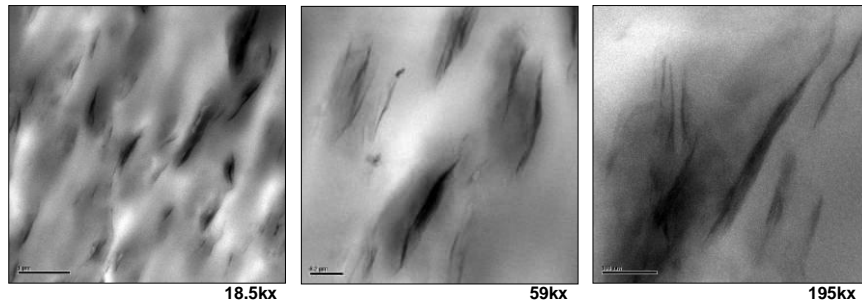
Sample ID: Undraw PP+3%Clay+3%PPMA



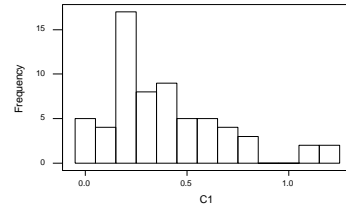
Avg diameter: 0.31
SD: 0.16
Avg no of particles per image:17.6



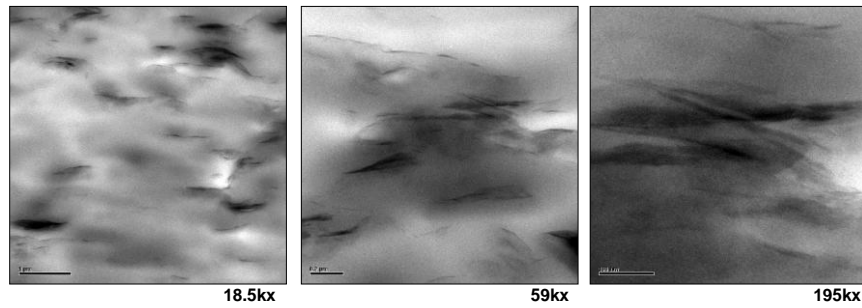
Sample ID: Undrawn PP+5%clay+3%PPMA (Core)



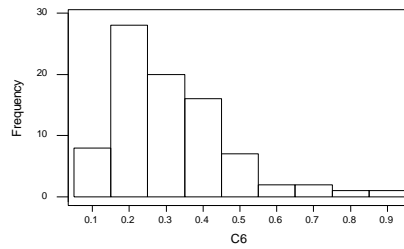
Avg diameter: 0.31
SD: 0.16
Avg no of particles per image:17



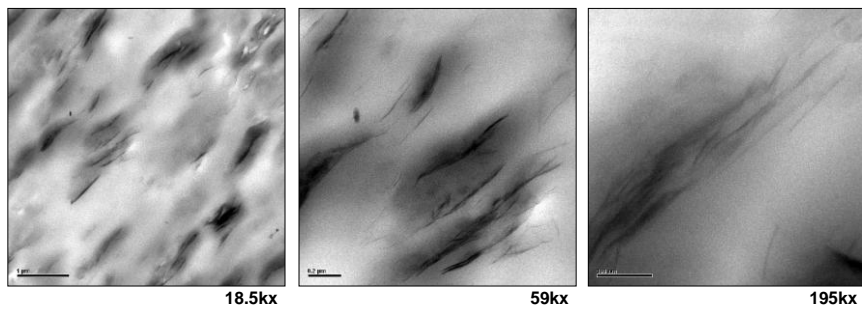
Sample ID: Undrawn PP+5%Clay+3%PPMA (Skin)



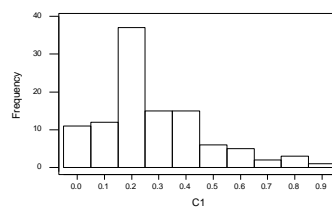
Avg diameter: 0.30
SD: 0.22
Avg no of particles per image:14



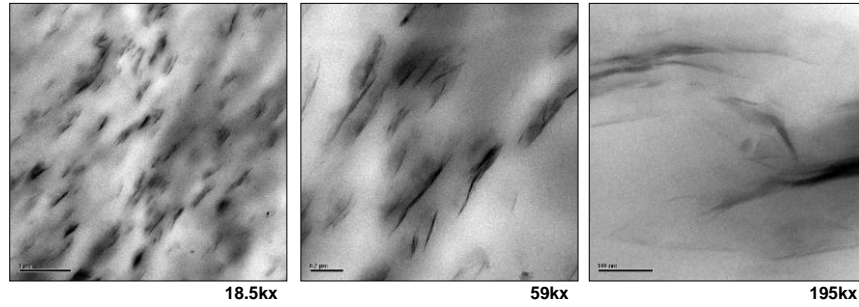
Sample ID: Undrawn PP+3%Clay+6%PPMA



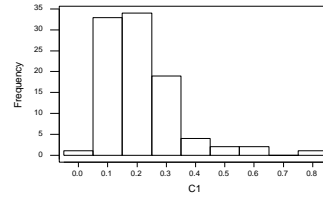
Avg diameter: 0.29
SD: 0.19
Avg no of particles per image:21



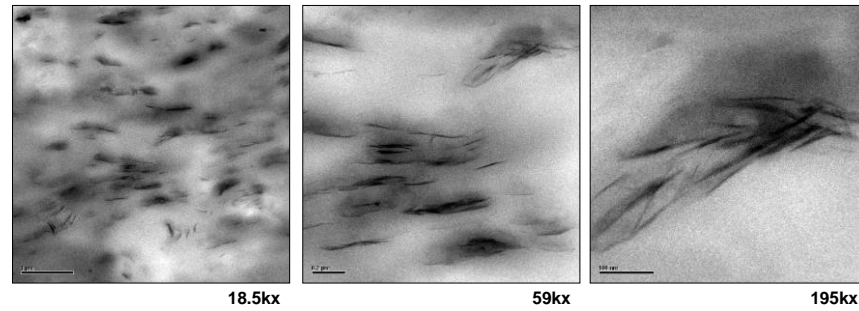
Sample ID: UndrawnPP+5%Clay+6%PPMA



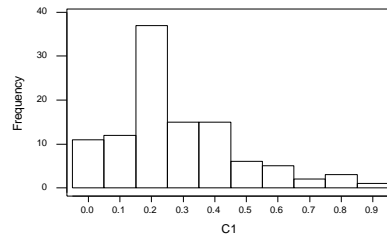
Avg diameter: 0.22
SD: 0.13
Avg no of particles per image: 24



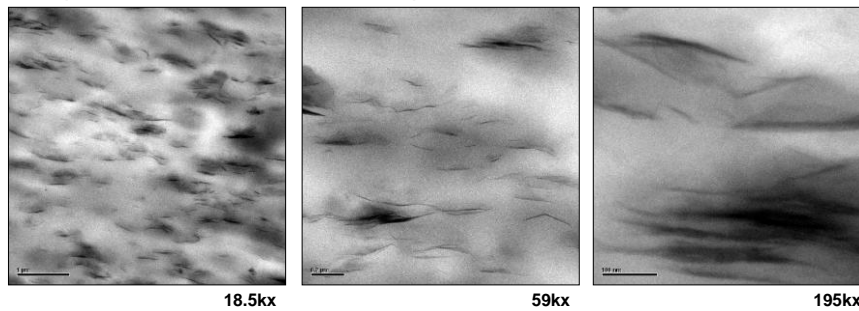
Sample ID: Undrawn PP+3%Clay+9%PPMA



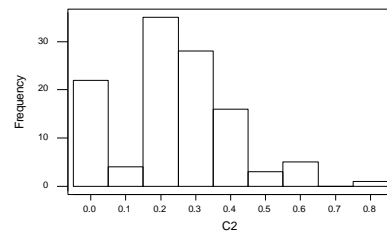
Avg diameter: 0.222
SD: 0.12
Avg no of particles per image: 26



Sample ID: Undrawn PP+5%Clay+9%PPMA

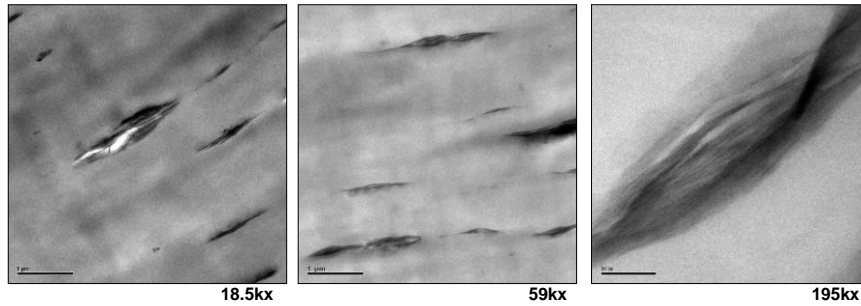


Avg diameter: 0.241
SD: 0.165
Avg no of particles per image: 50

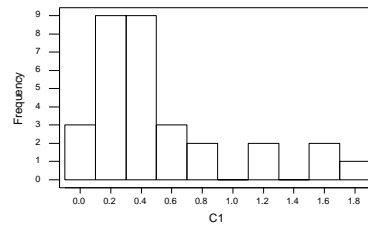


Appendix F2: TEM Micrographs of Drawn PPNCs

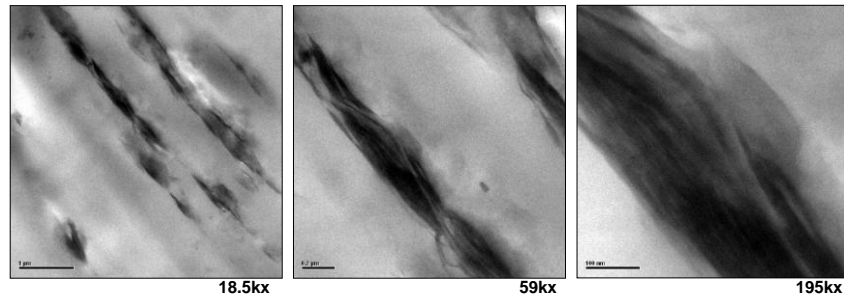
Sample ID: Draw Ratio = 2 -- PP+3%Clay



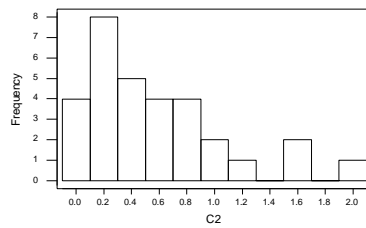
Avg diameter: 0.49
SD: 0.49
Avg no of particles per image:6



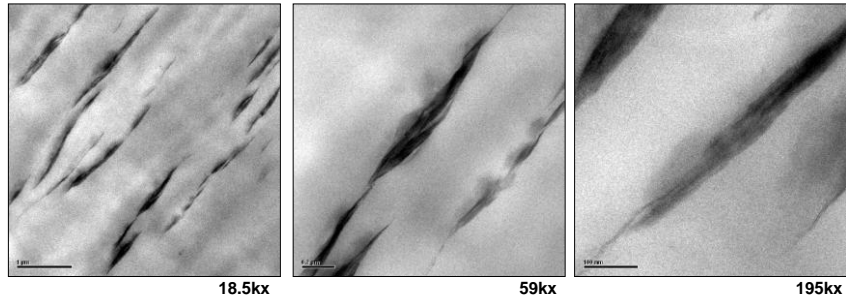
Sample ID: Draw Ratio = 4 -- PP+3%Clay



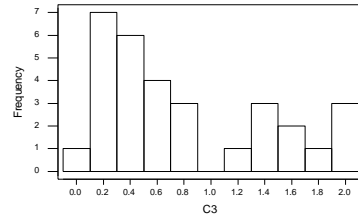
Avg diameter: 0.53
SD: 0.49
Avg no of particles per image:5.2



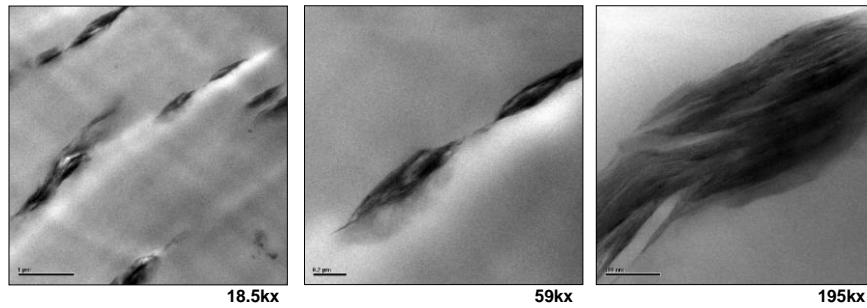
Sample ID: Draw Ratio = 2 -- PP+5%Clay



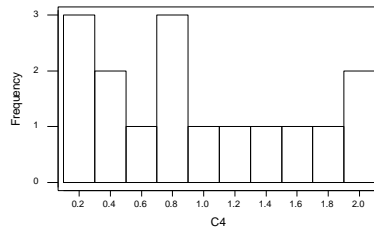
Avg diameter: 0.76
 SD: 0.66
 Avg no of particles per image: 5.2



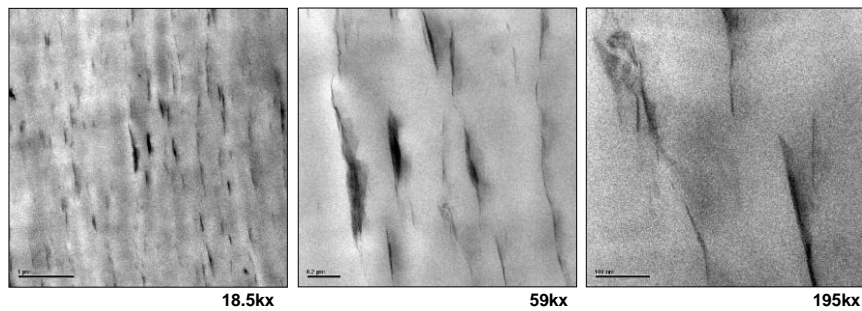
Sample ID: Draw Ratio = 4 -- PP+5%Clay



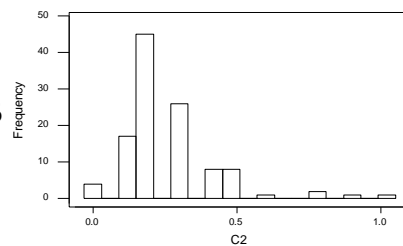
Avg diameter: 0.925
 SD: 0.63
 Avg no of particles per image: 2.5



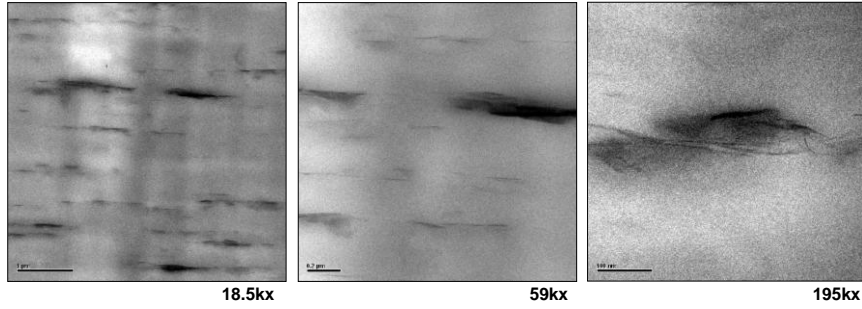
Sample ID: Draw Ratio = 2 -- PP+3%Clay+3%PPMA



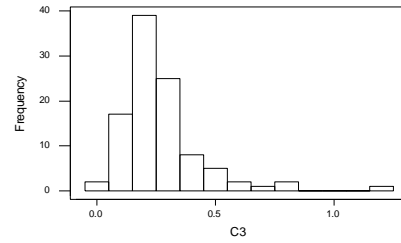
Avg diameter: 0.26
 SD: 0.17
 Avg no of particles per image: 22.6



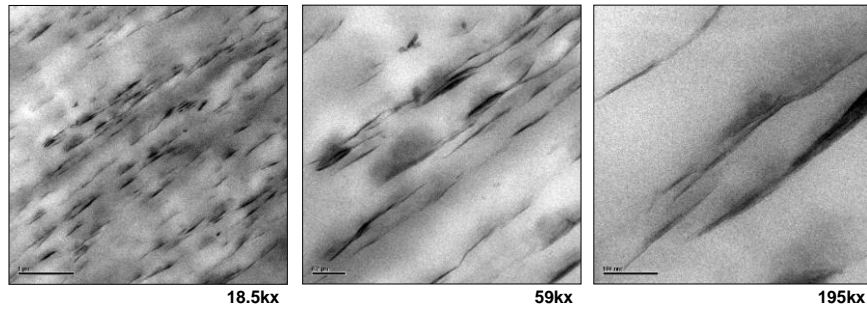
Sample ID: Draw Ratio = 4 -- PP+3%Clay+3%PPMA



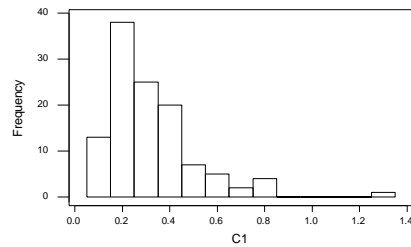
Avg diameter: 0.27
SD: 0.17
Avg no of particles per image:19.8



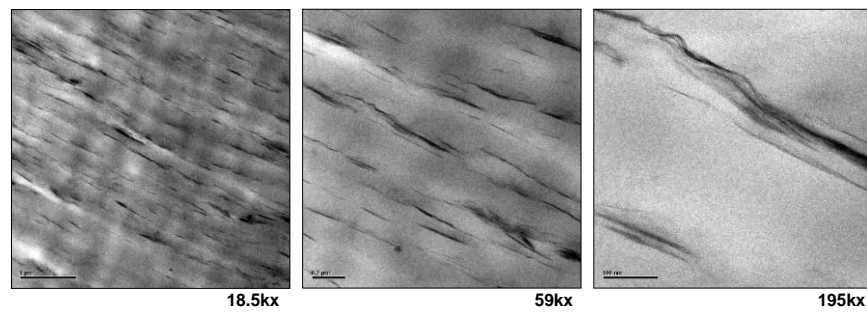
Sample ID: Draw Ratio = 2 -- PP+5%Clay+6%PPMA



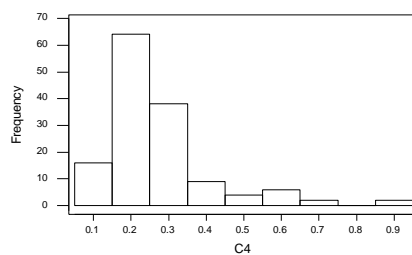
Avg diameter: 0.32
SD: 0.19
Avg no of particles per image:27



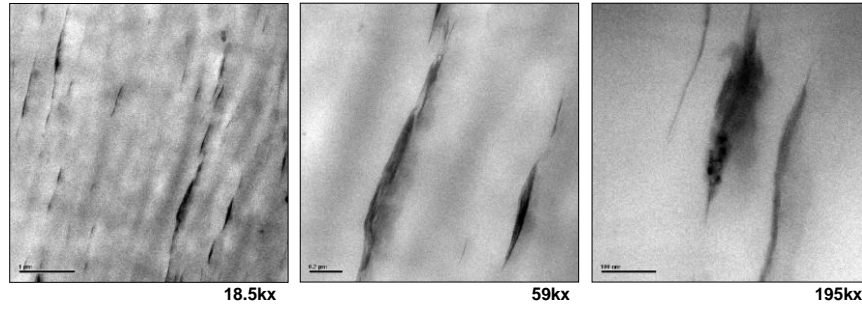
Sample ID: Draw Ratio = 4 -- PP+5%Clay+6%PPMA



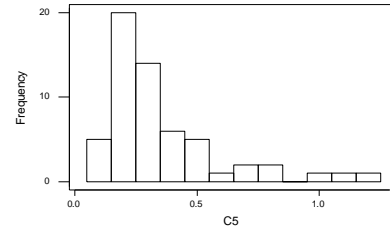
Avg diameter: 0.31
SD: 0.15
Avg no of particles per image:35



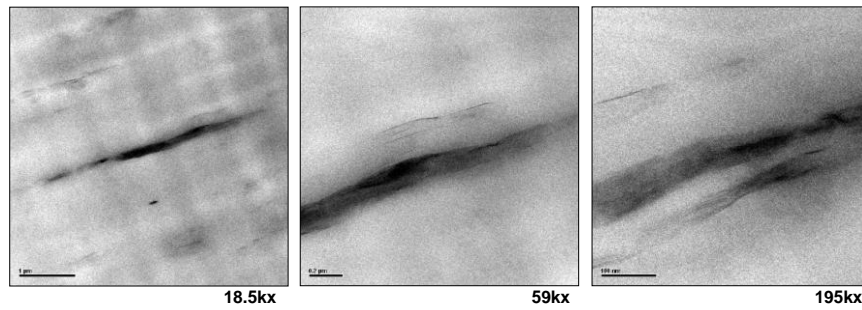
Sample ID: Draw Ratio = 2 -- PP+3%Clay(MB)+3%PPMA(MB)



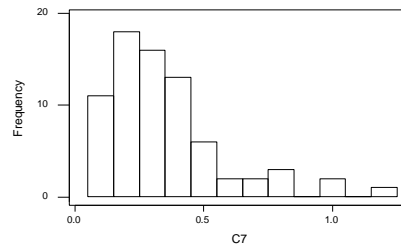
Avg diameter: 0.35
SD: 0.24
Avg no of particles per image:11.6
MB=Master Batch



Sample ID: Draw Ratio = 4 -- PP+3%Clay (MB)+3%PPMA(MB)



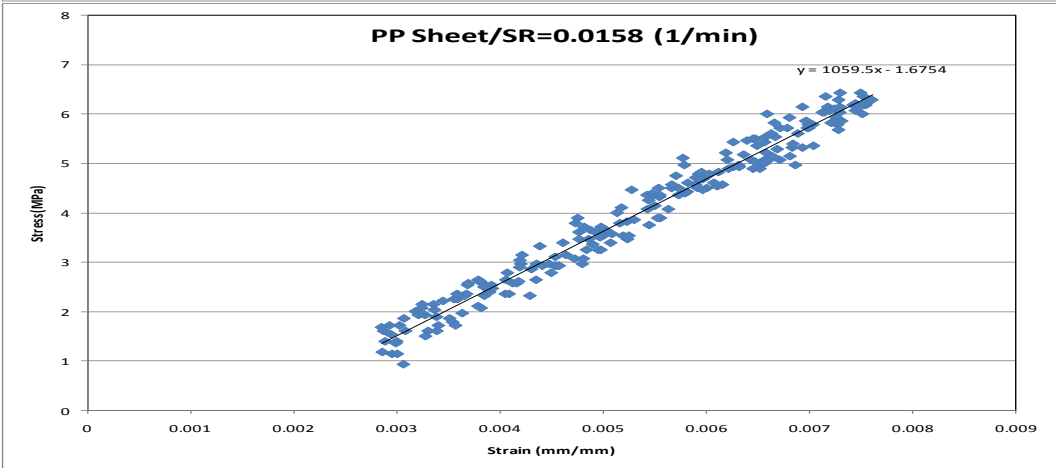
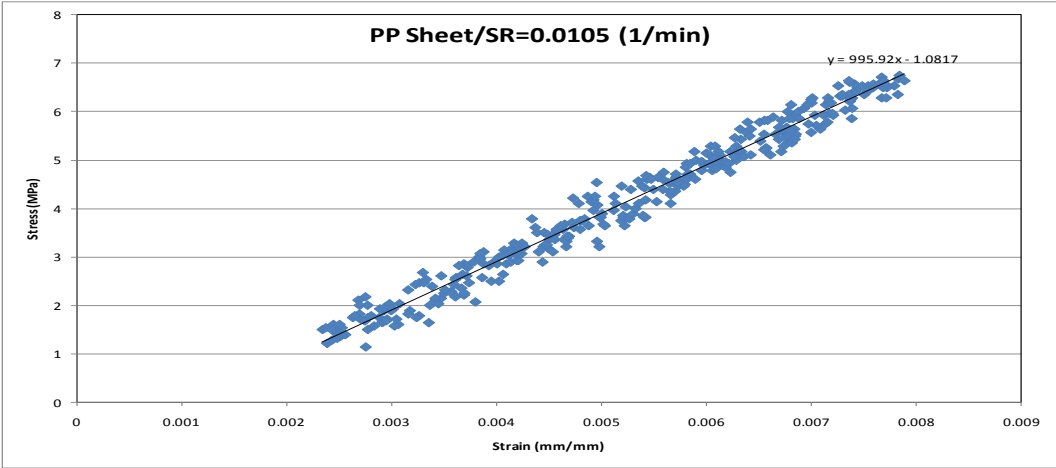
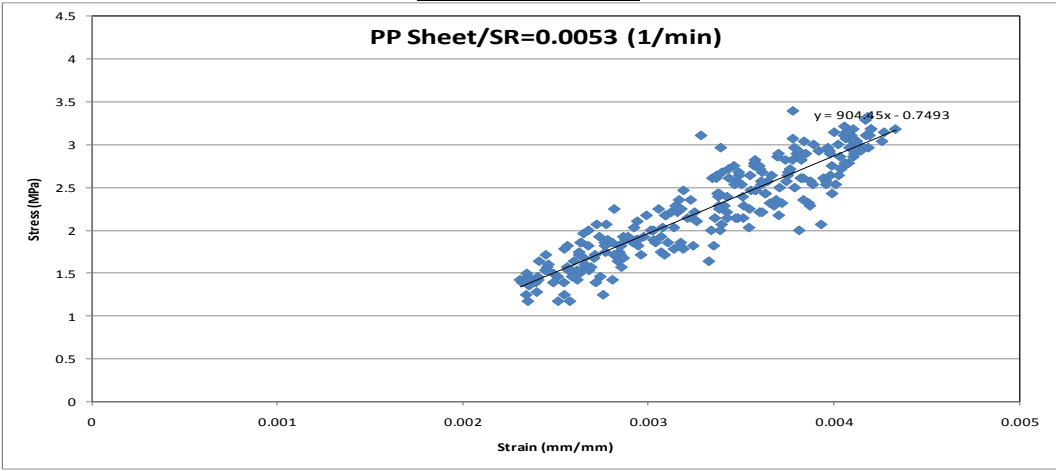
Avg diameter: 0.34
SD: 0.22
Avg no of particles per image:14.8
MB = Master Batch



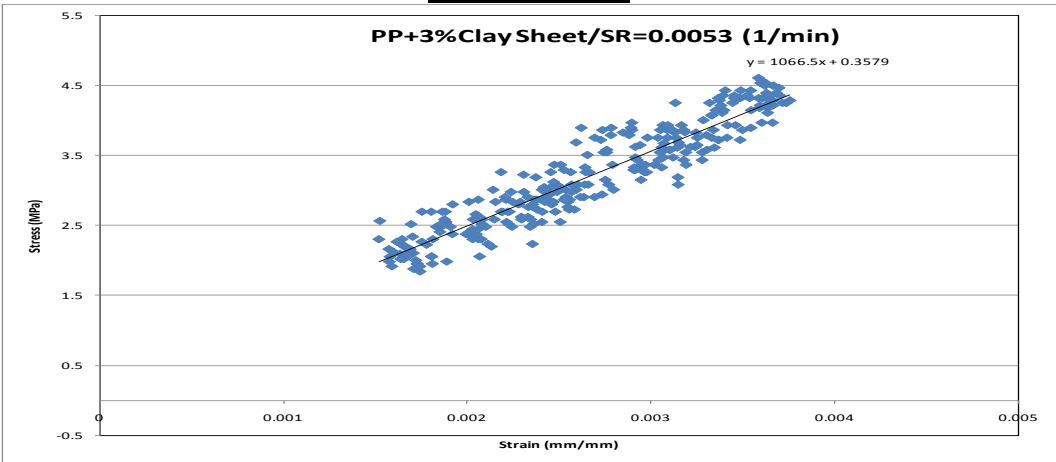
Appendix G: Tensile Video Extensometer of Undrawn PPNCs

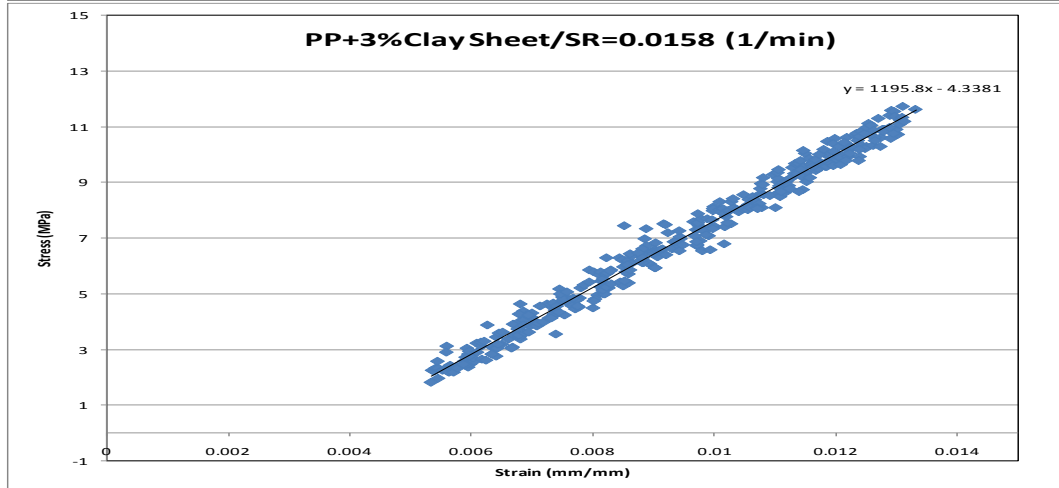
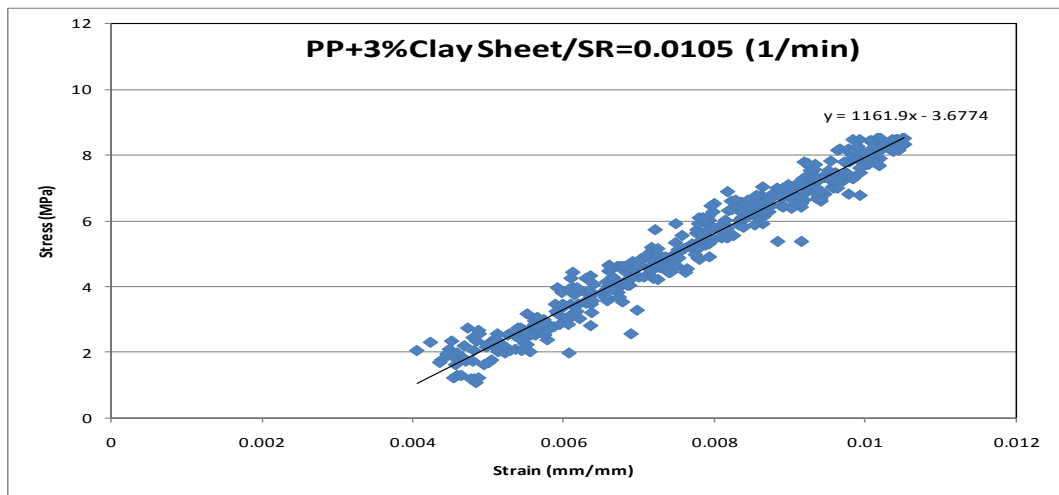
Appendix G1: Tensile Video Extensometer for Compression Sheets

Pure PP Sample

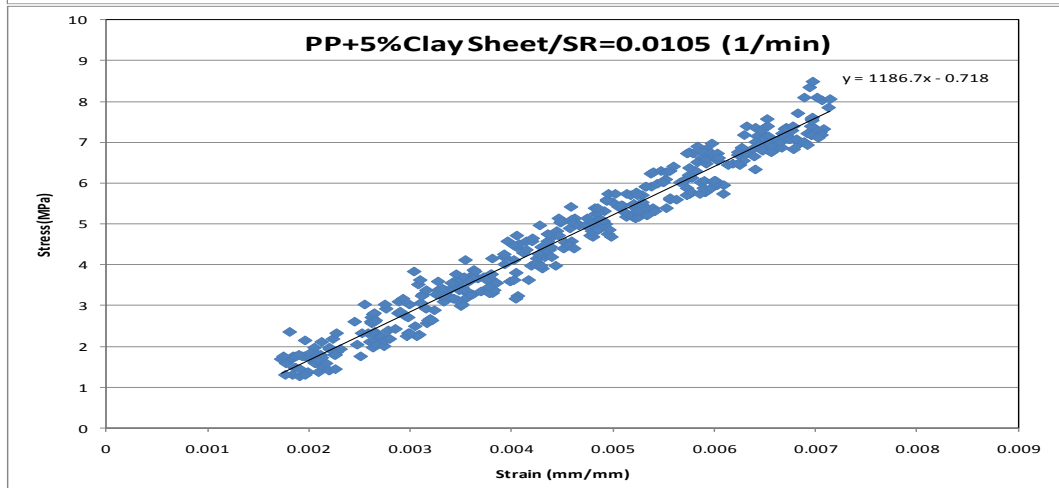
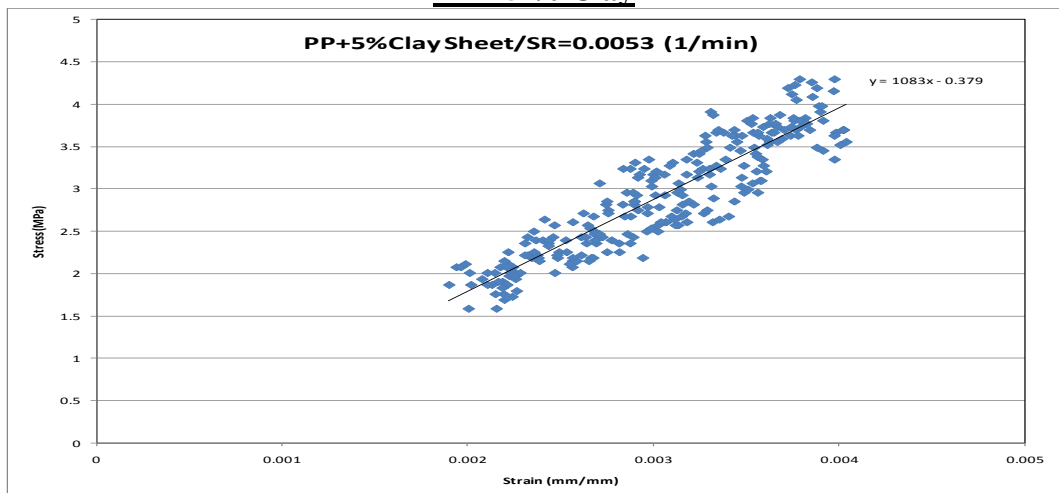


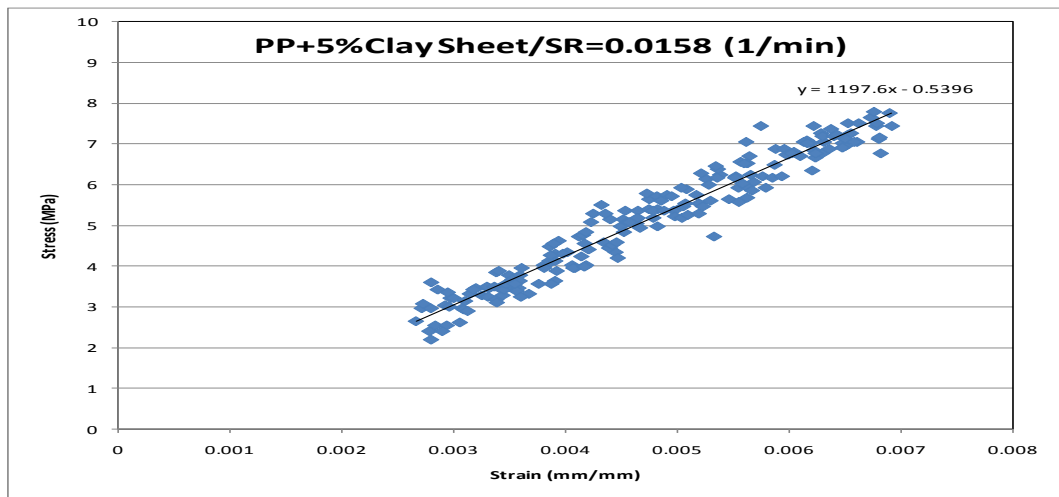
PP + 3 % Clay



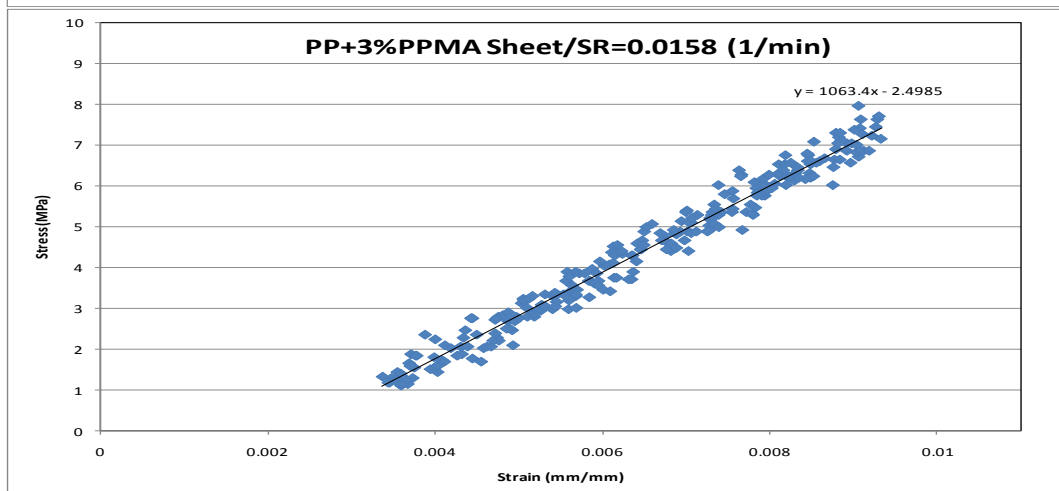
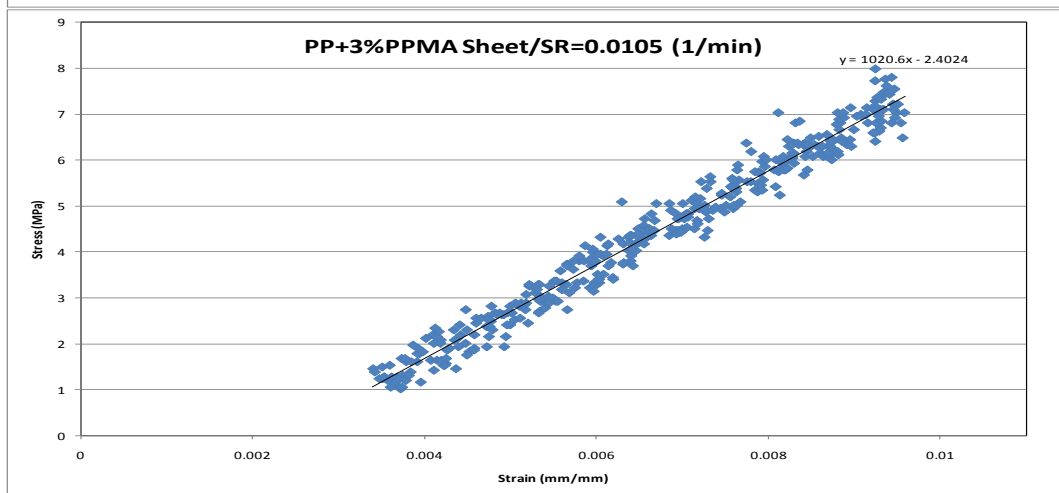
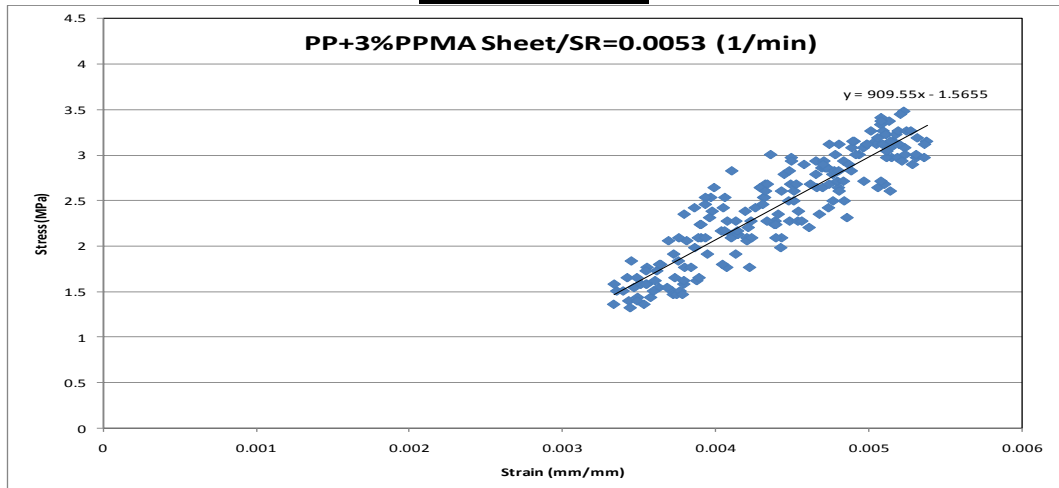


PP + 5 % Clay

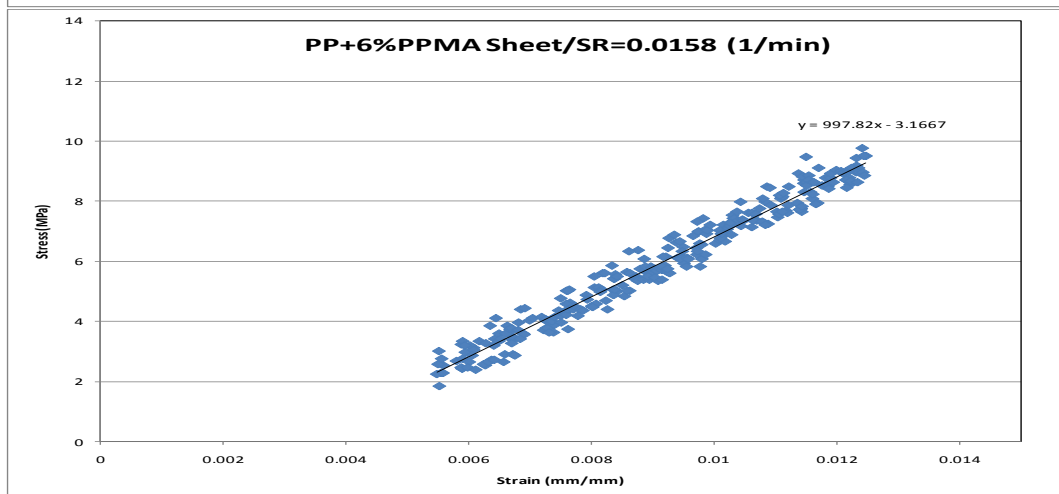
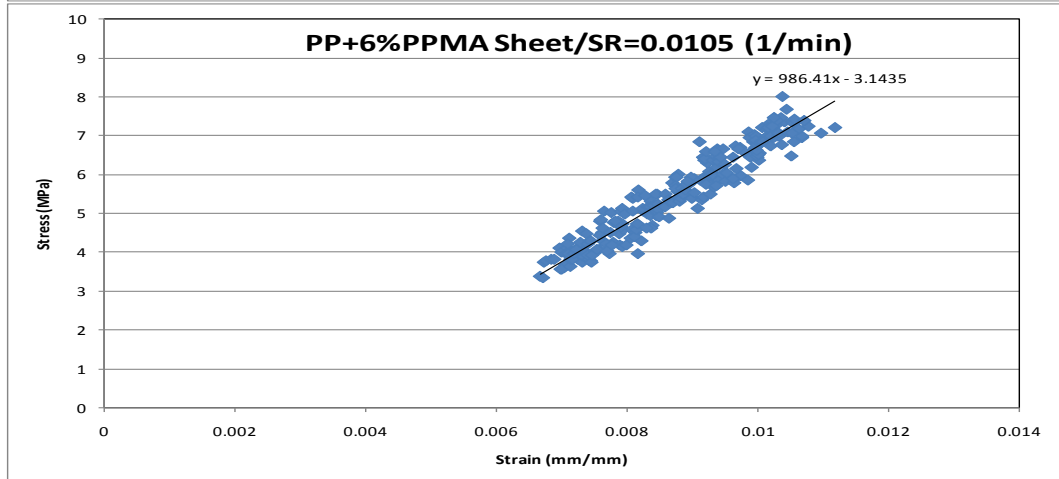
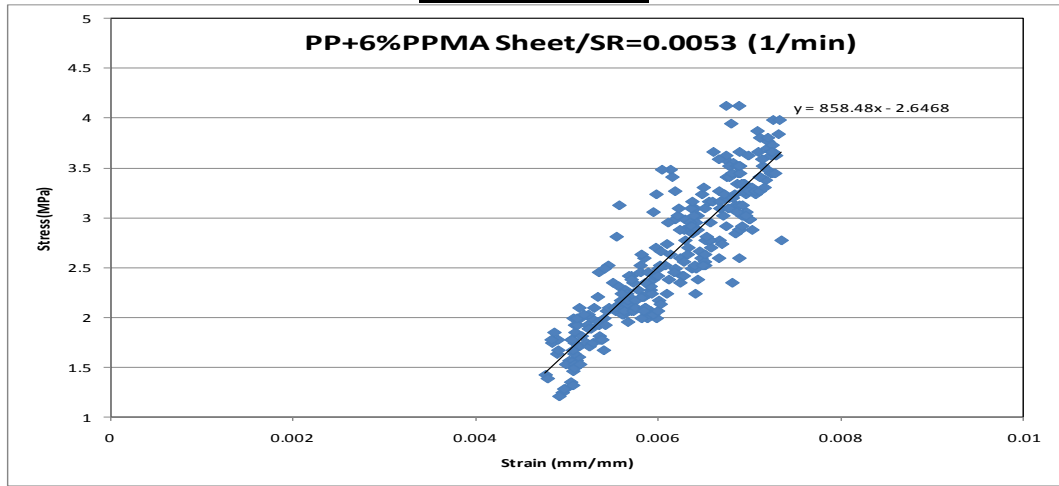




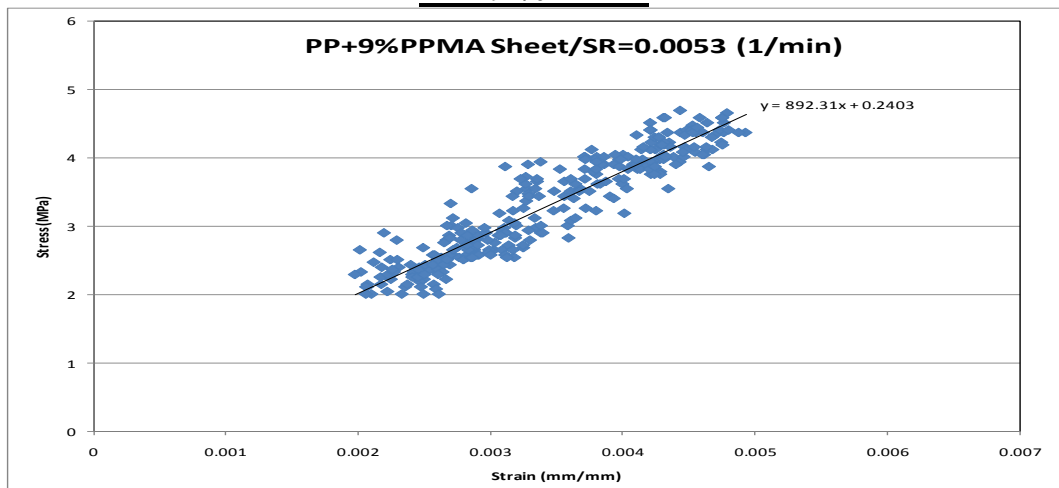
PP + 3 % PPMA

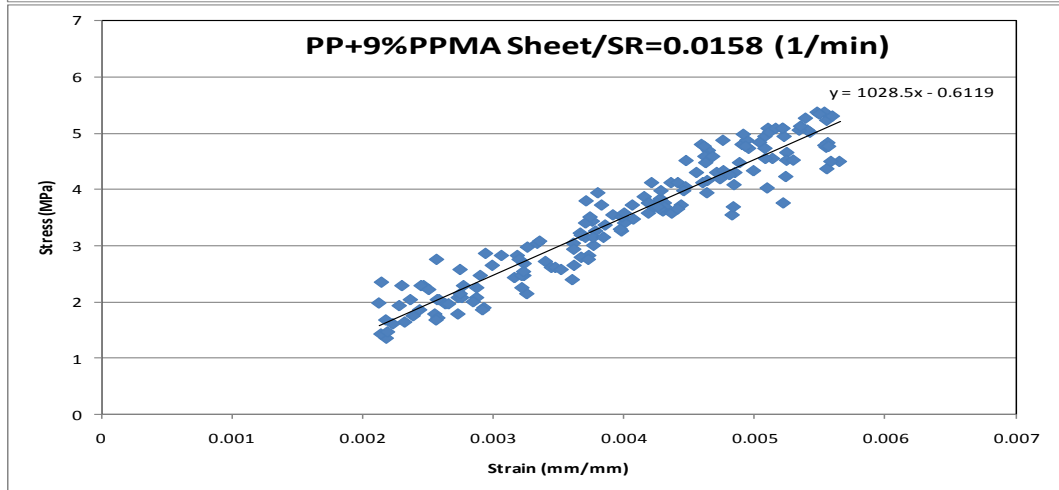
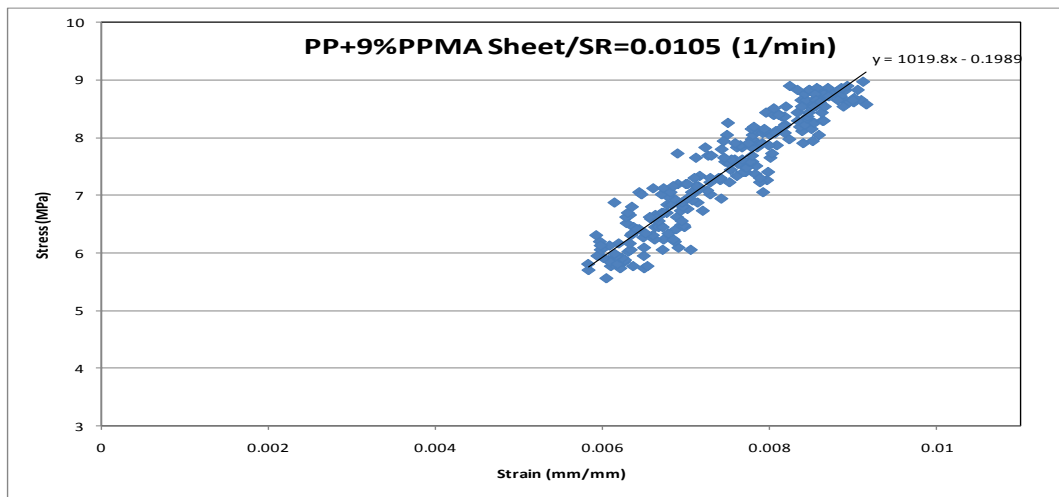


PP + 6 % PPMA

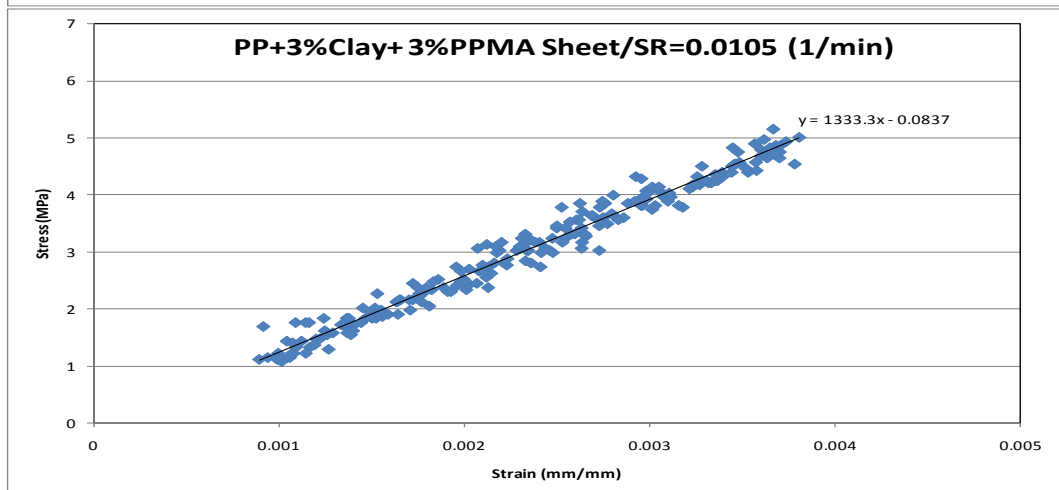
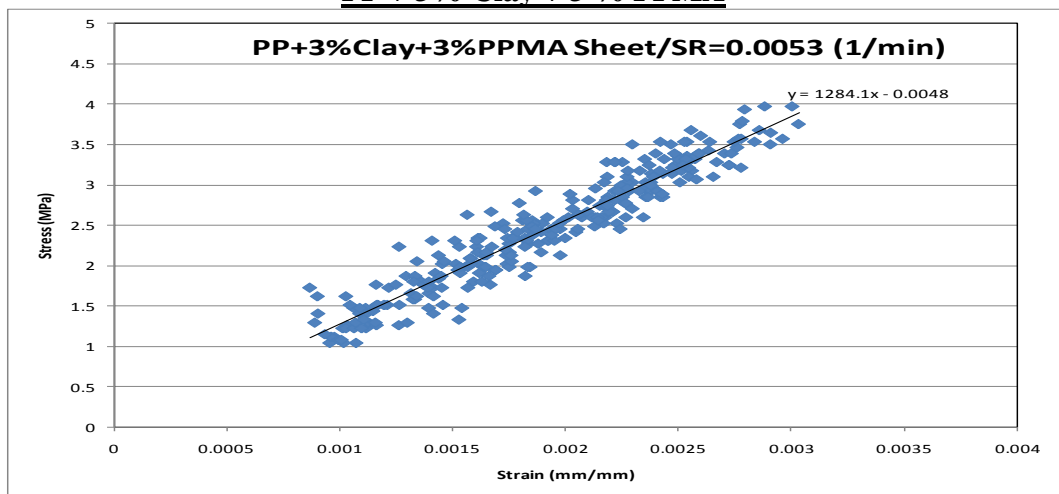


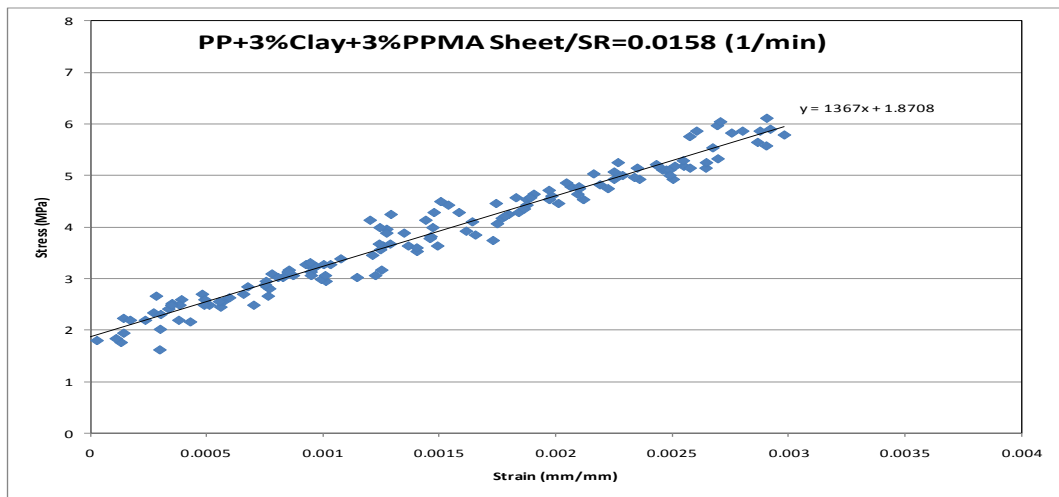
PP + 9 % PPMA



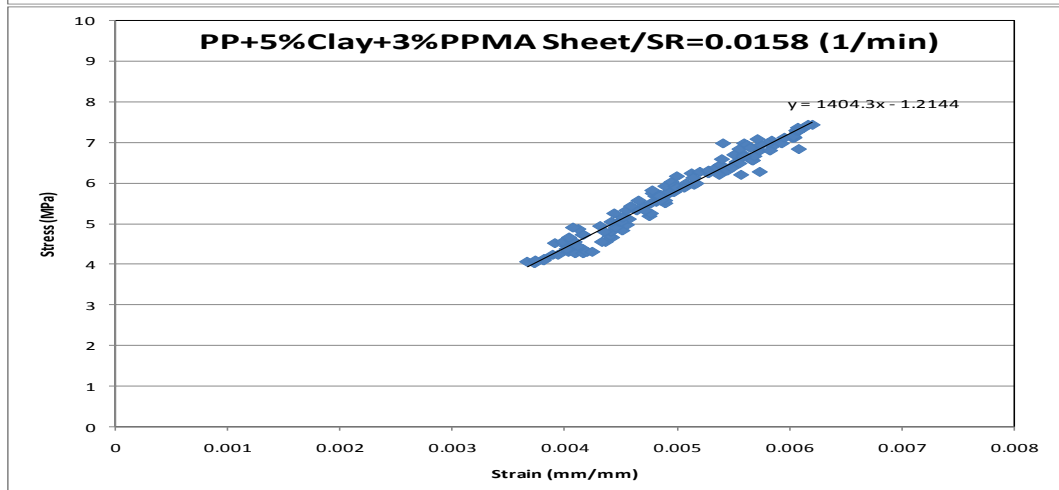
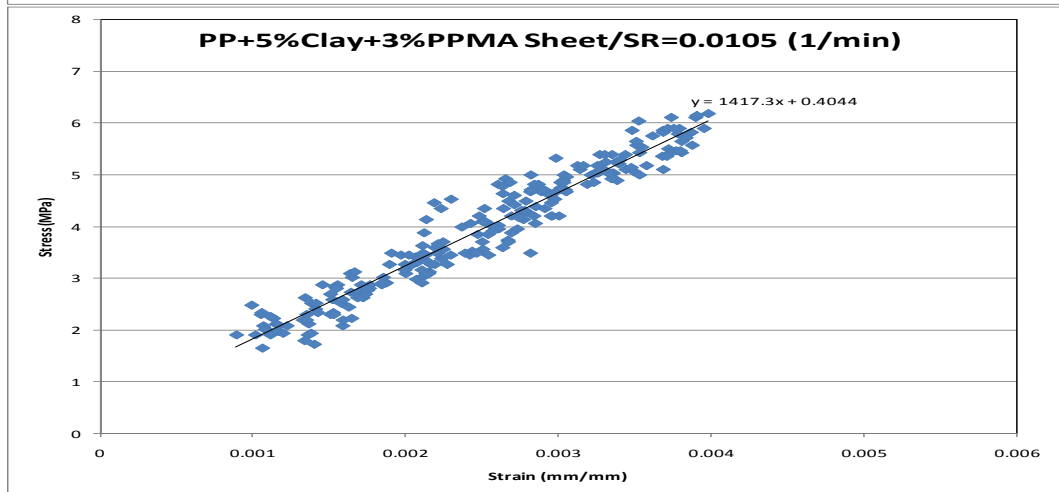
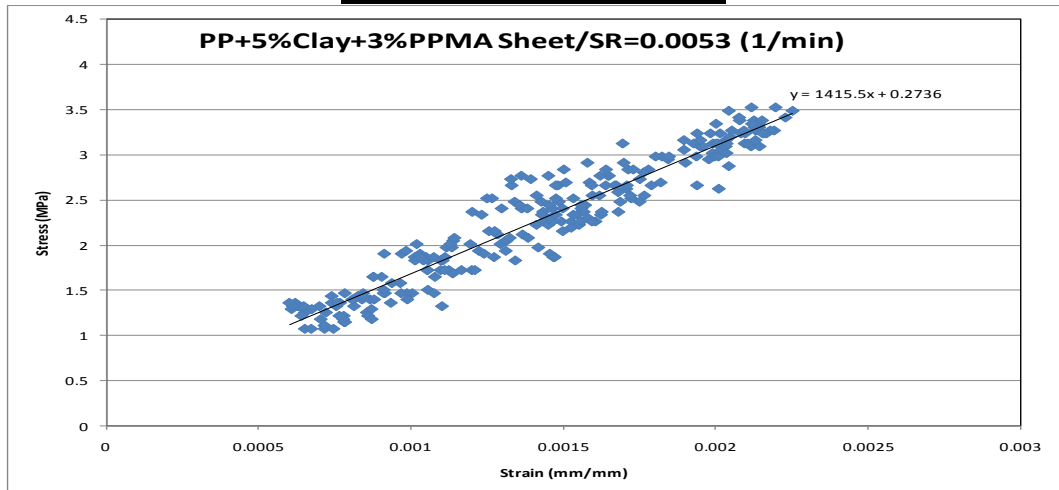


PP + 3% Clay + 3 % PPMA

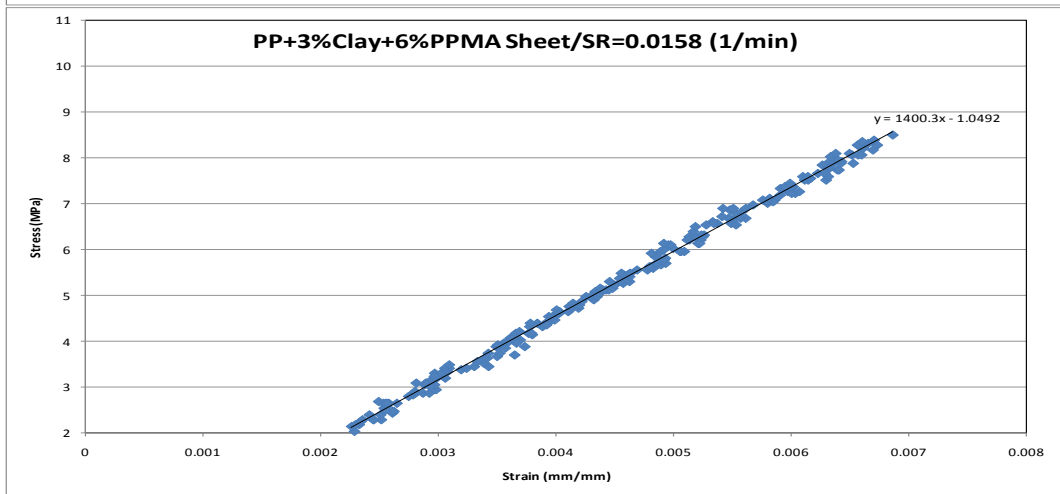
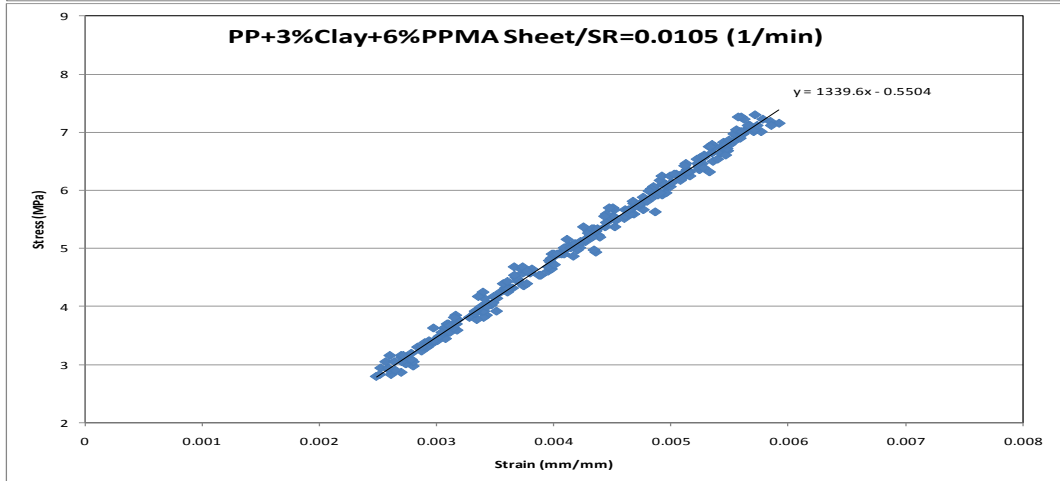
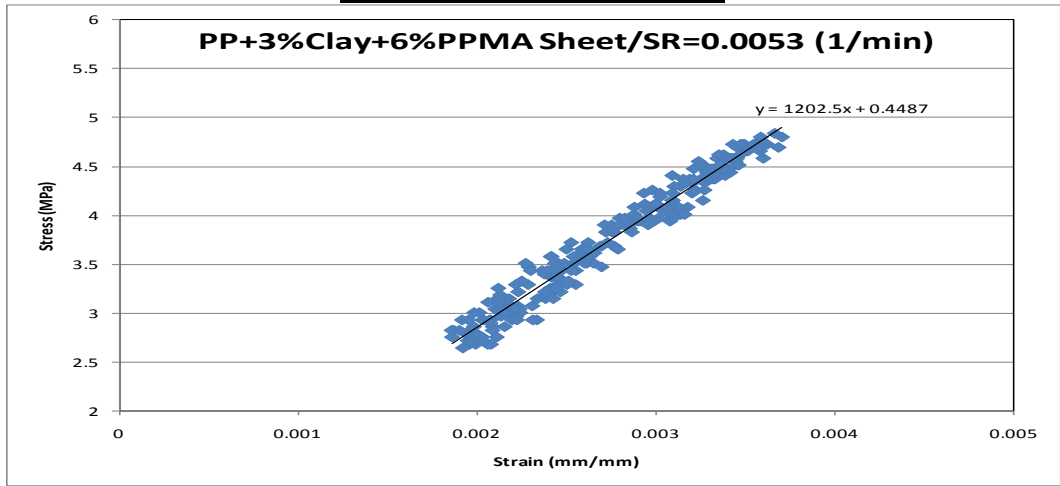




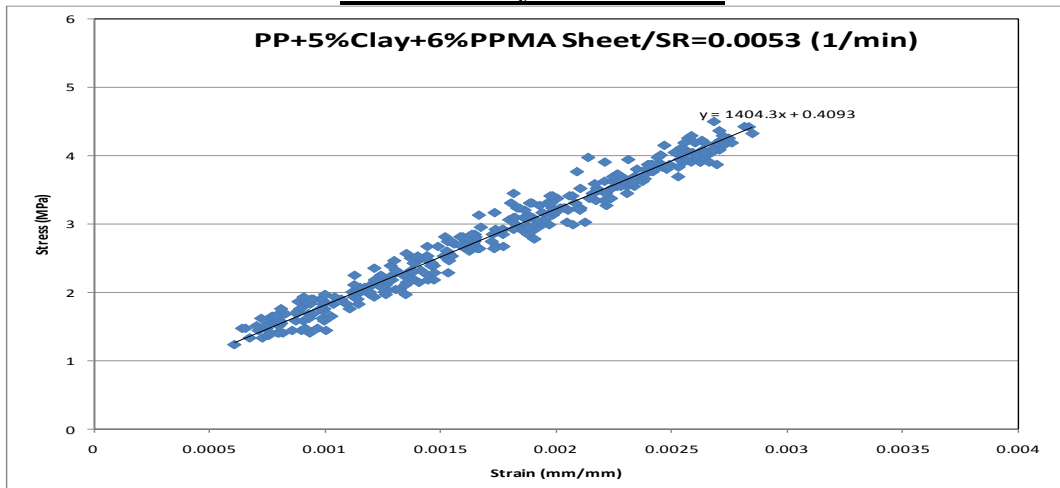
PP + 5% Clay + 3 % PPMA

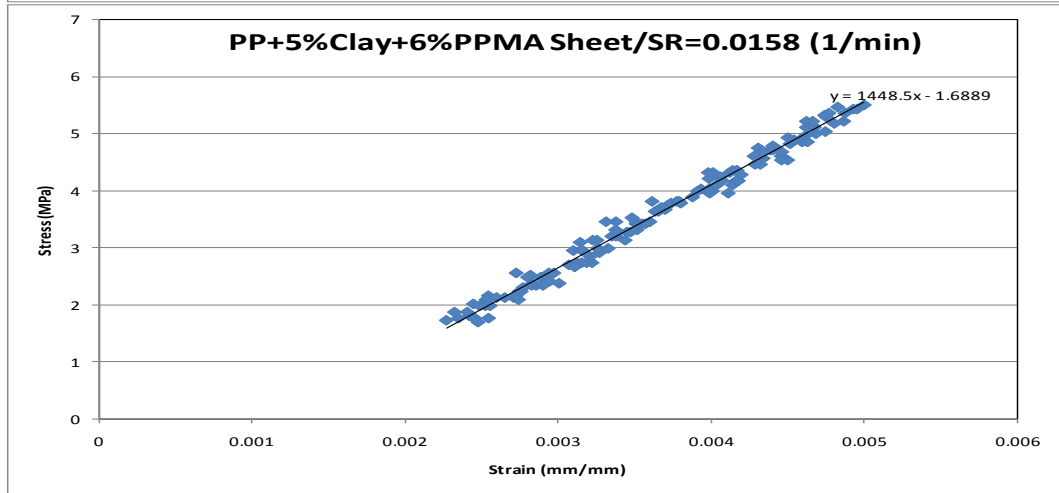
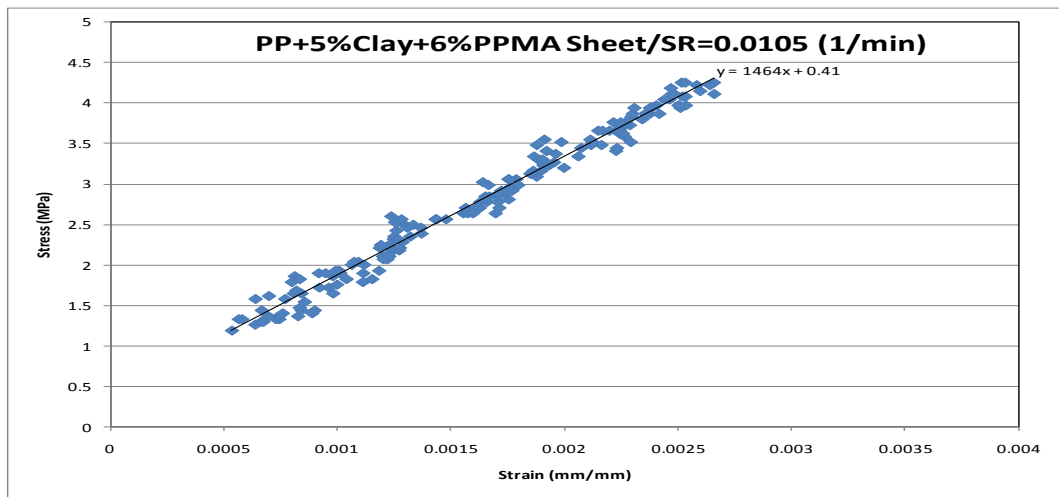


PP + 3% Clay + 6 % PPMA

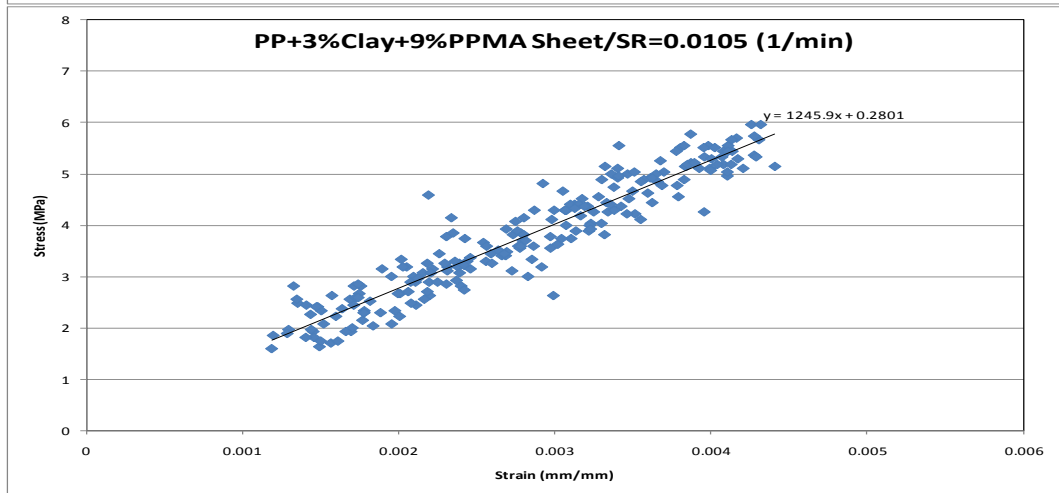
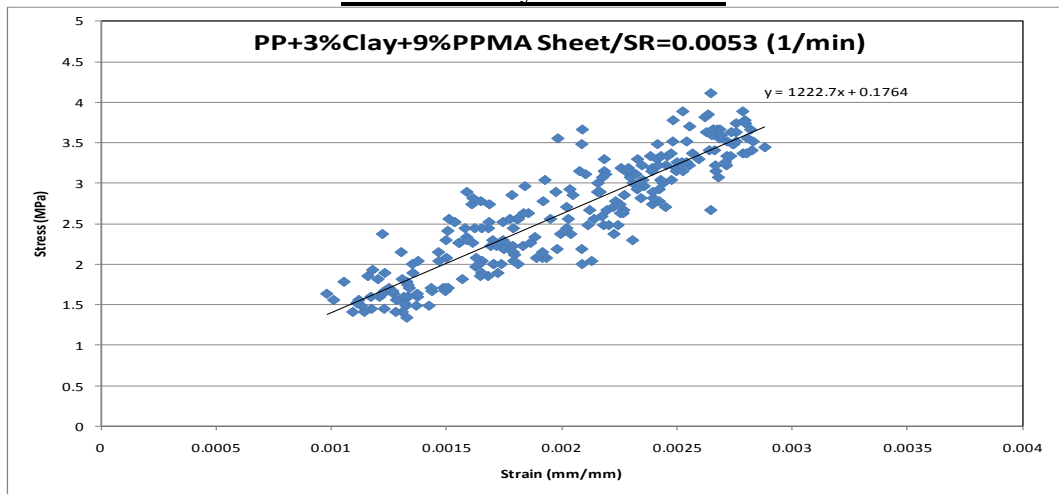


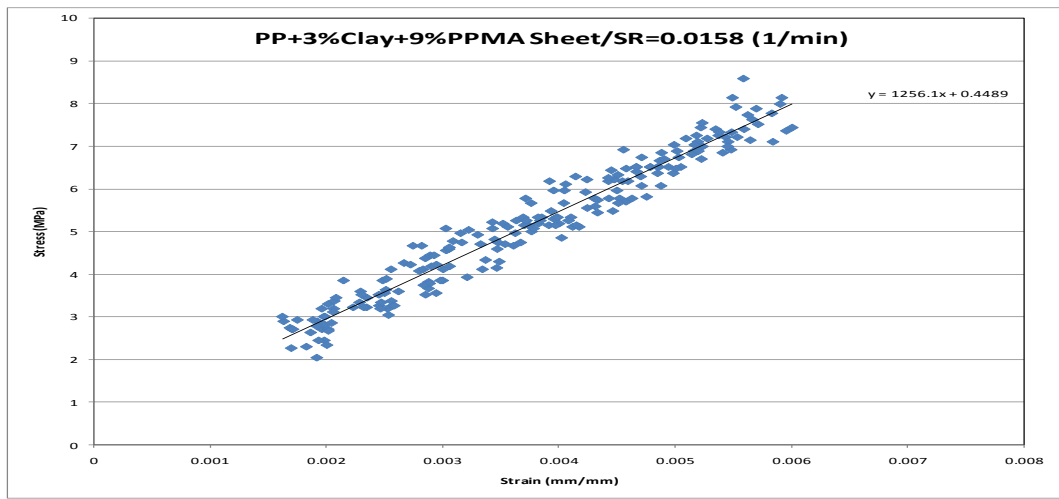
PP + 5% Clay + 6 % PPMA



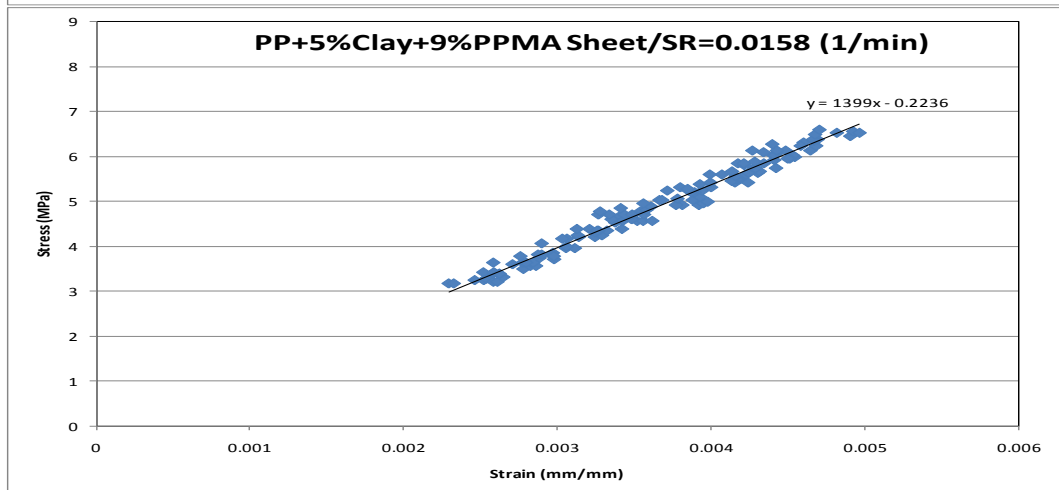
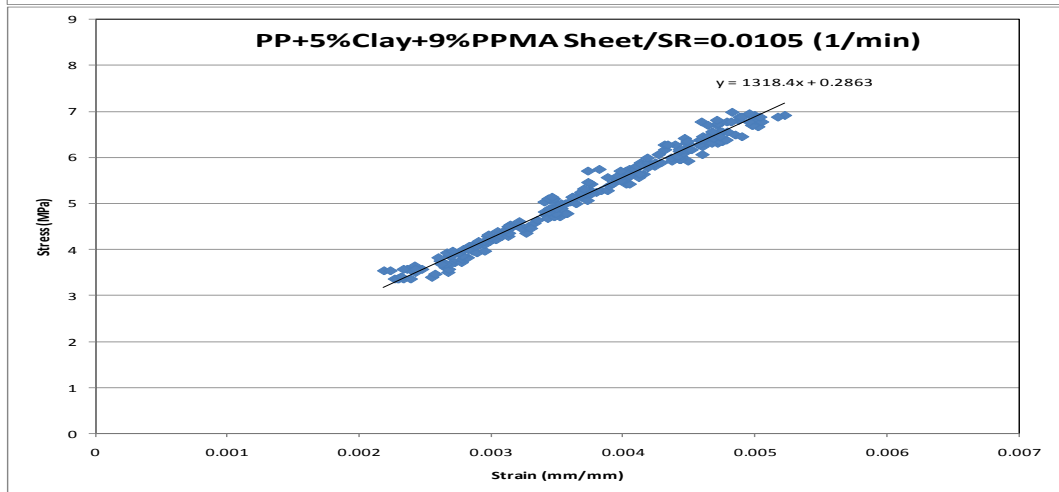
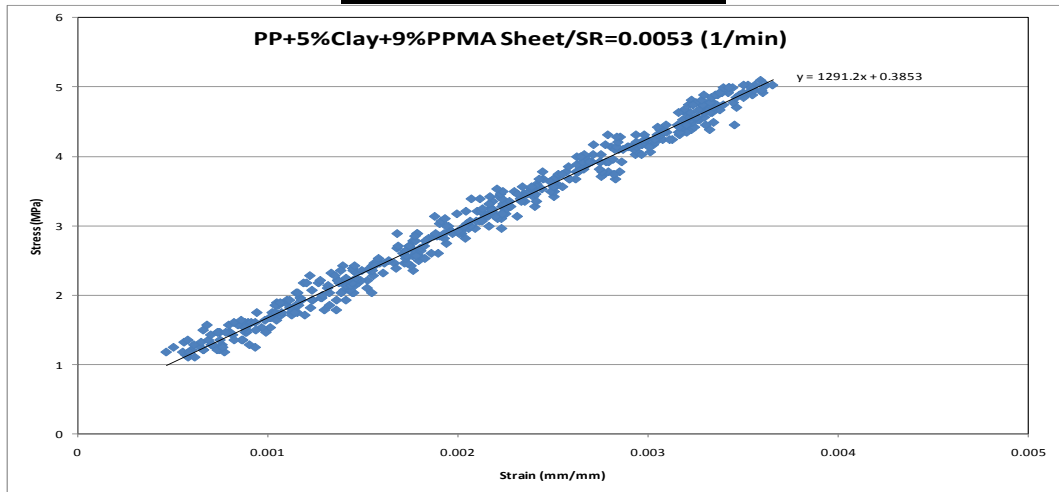


PP + 3% Clay + 9 % PPMA

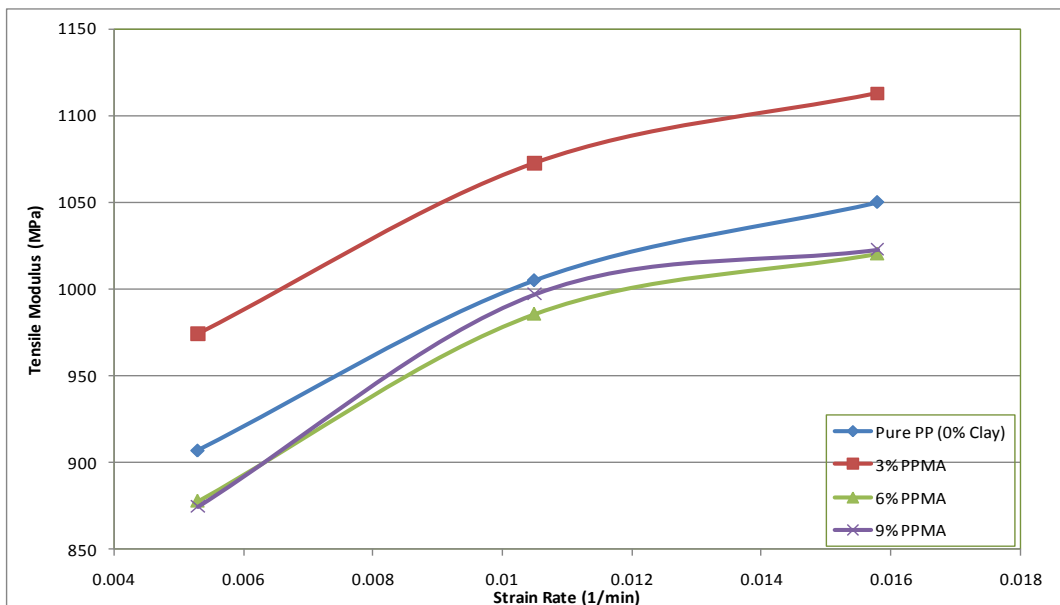
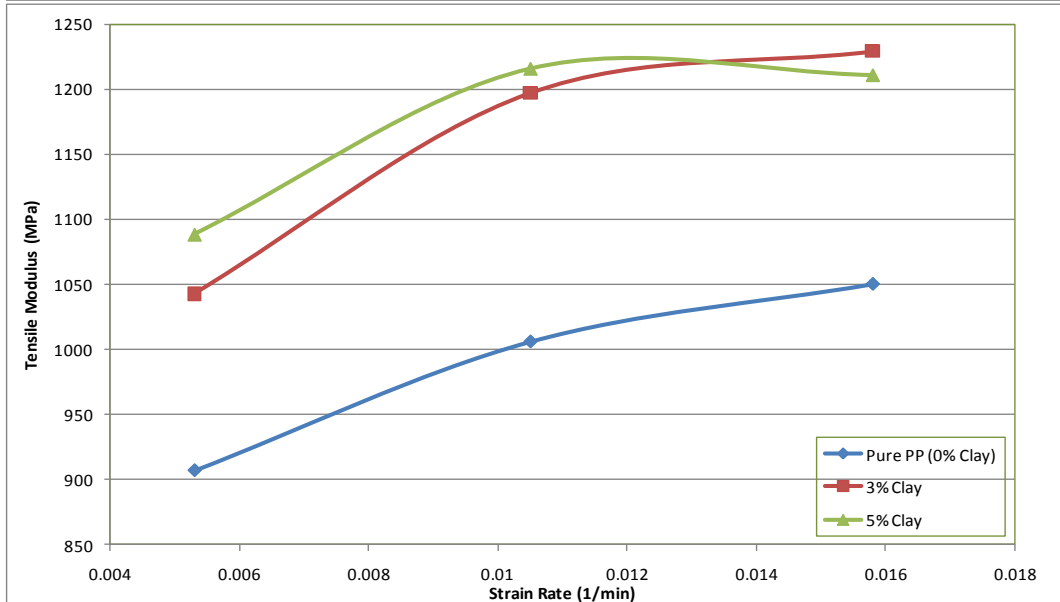
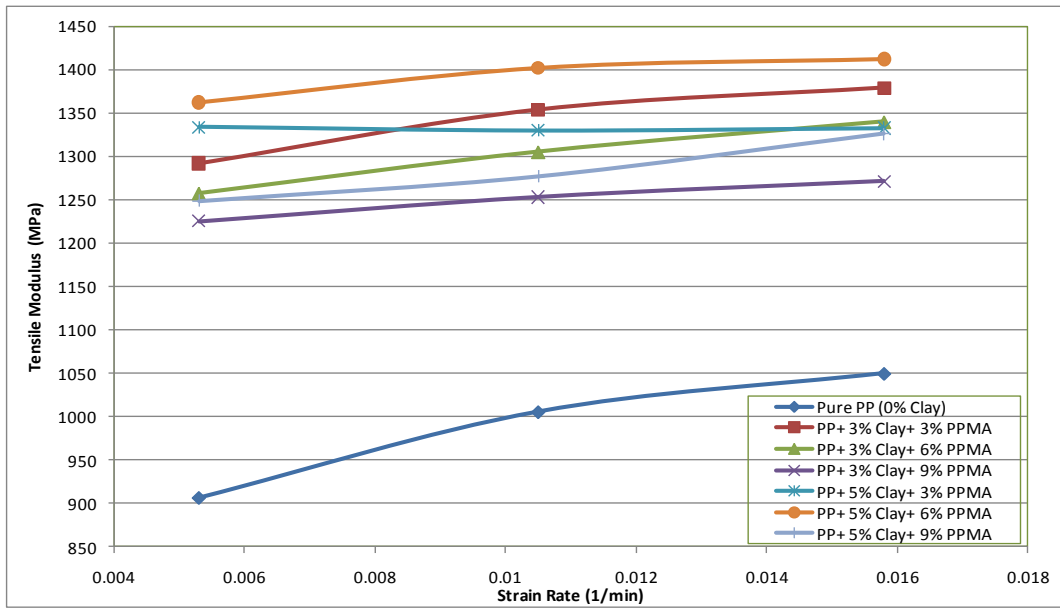




PP + 5% Clay + 9 % PPMA

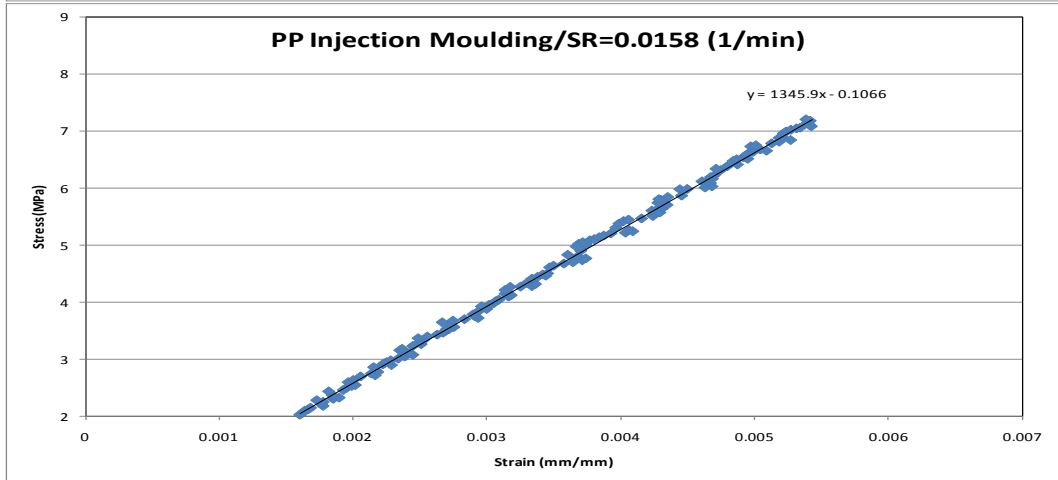
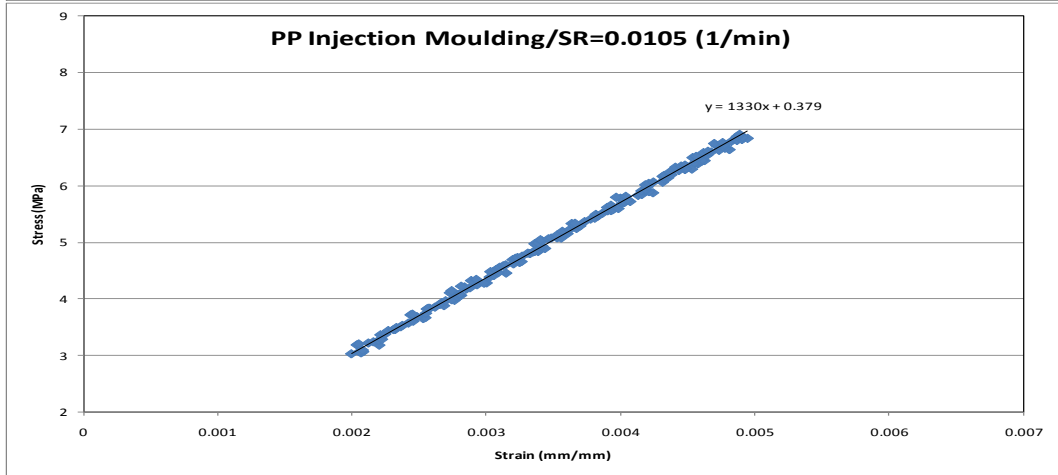
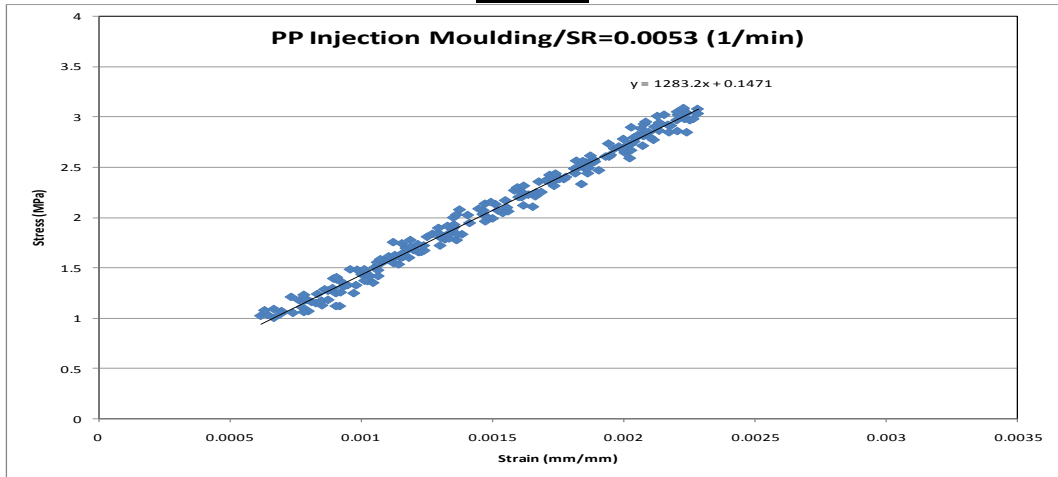


Appendix G2: Tensile Video Extensometer (Strain Rate Effect on Modulus) for Compression Sheets

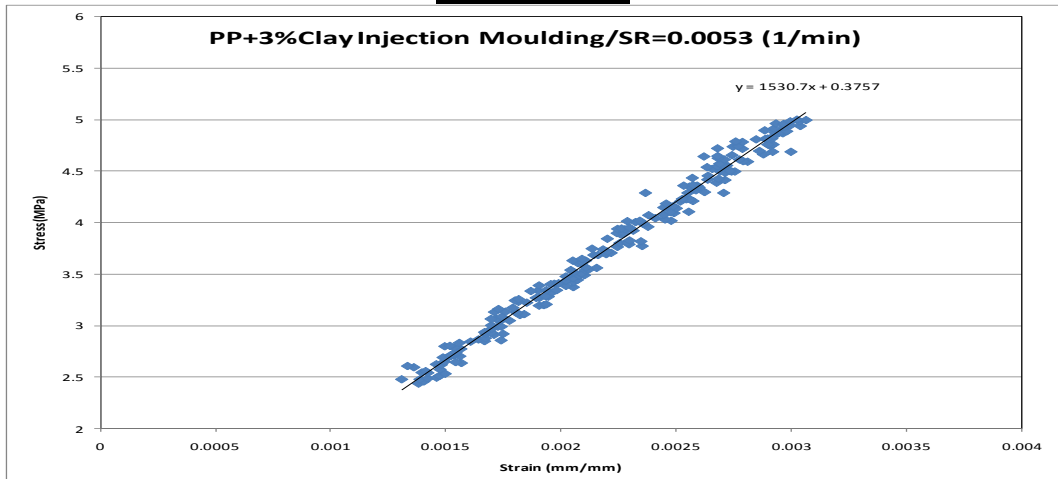


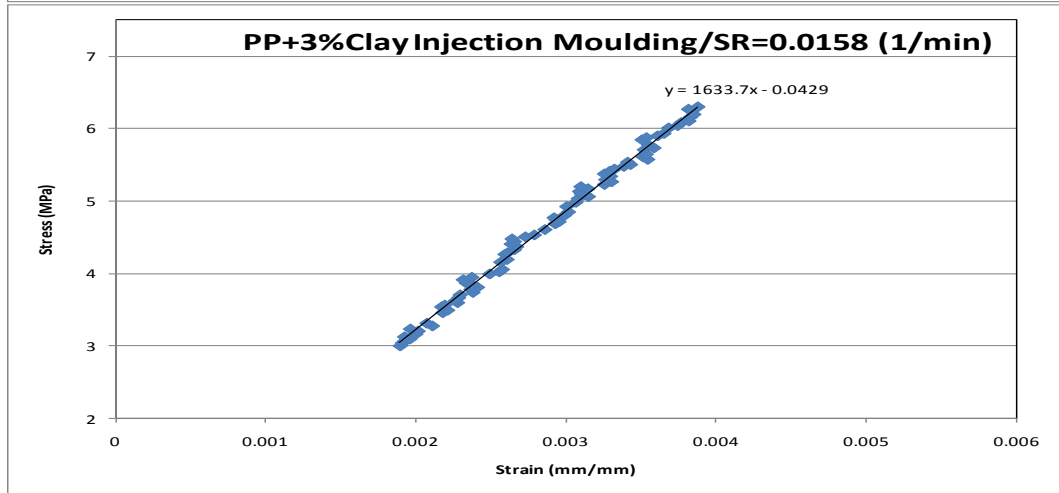
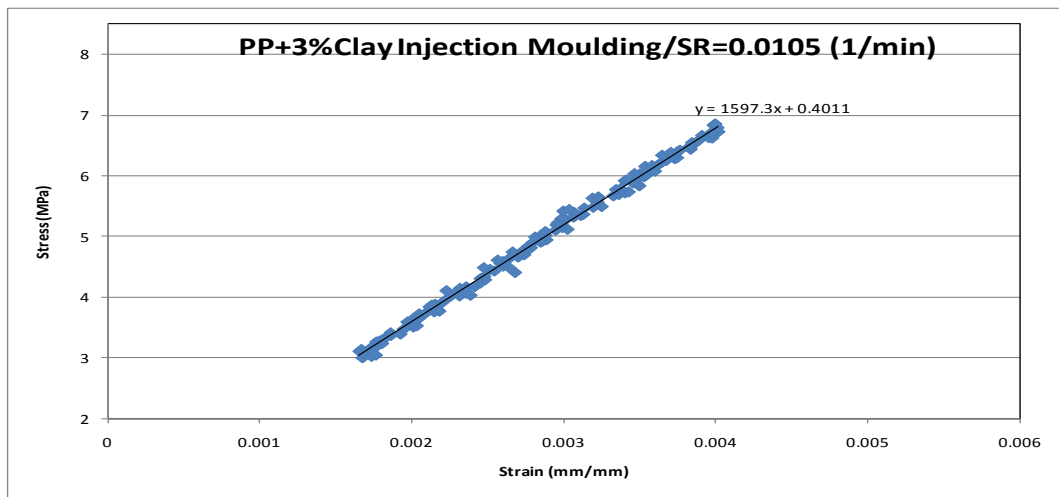
AppendixG3: Tensile Video Extensometer for Injection Moulded bars

Pure PP

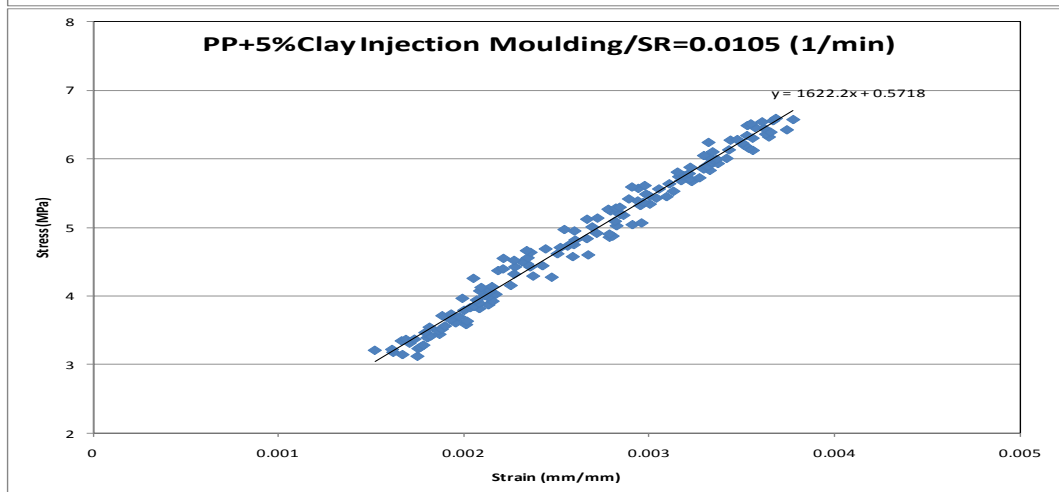
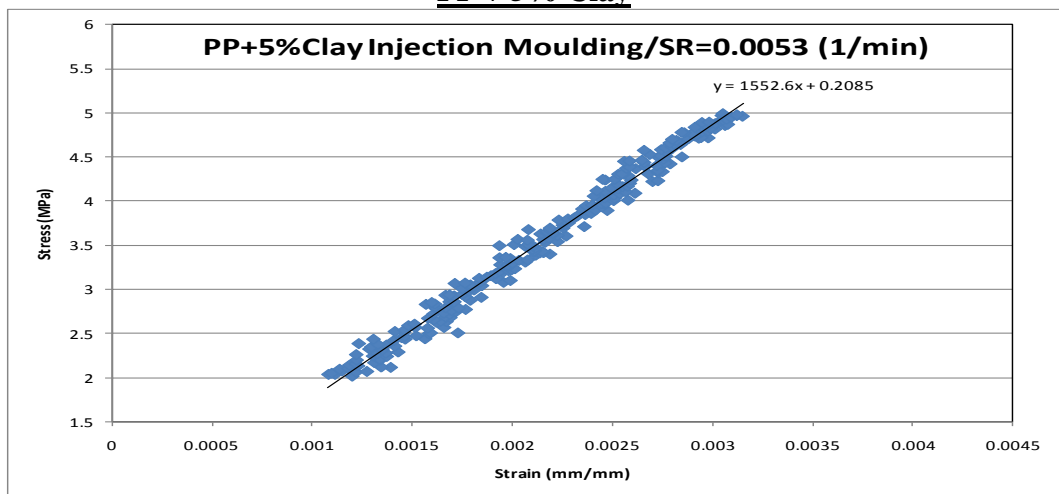


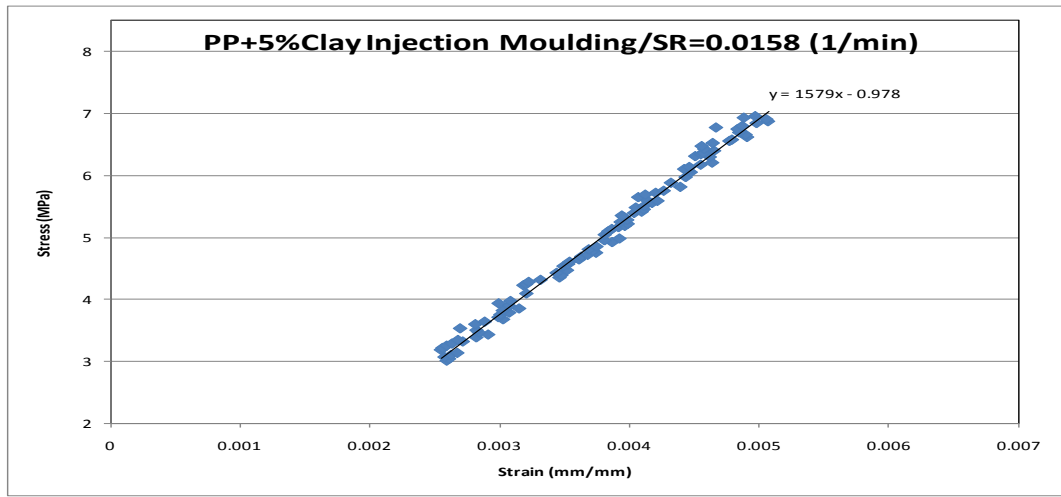
PP + 3% Clay



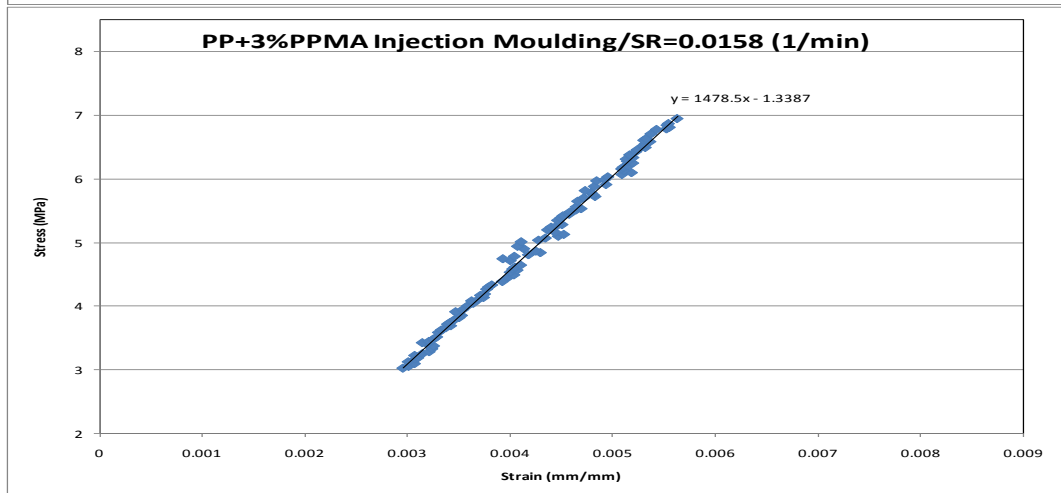
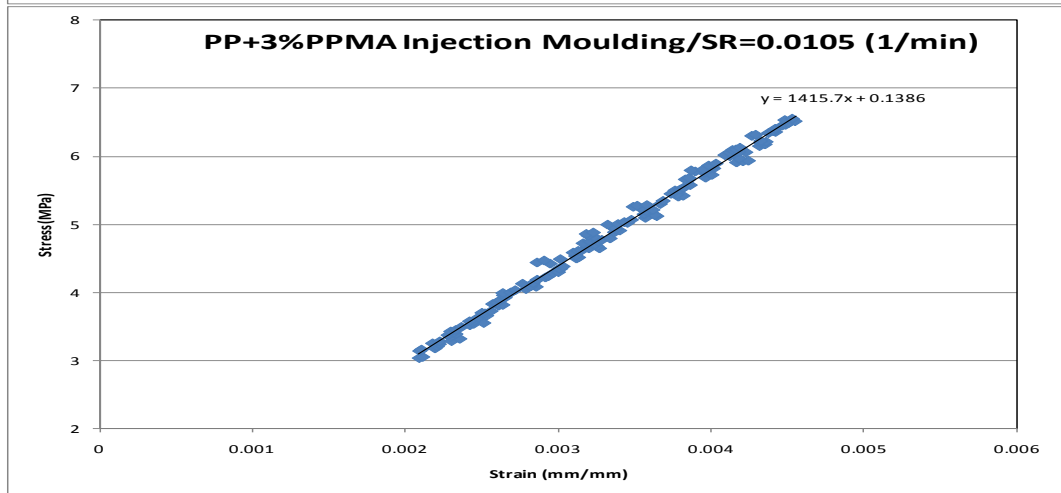
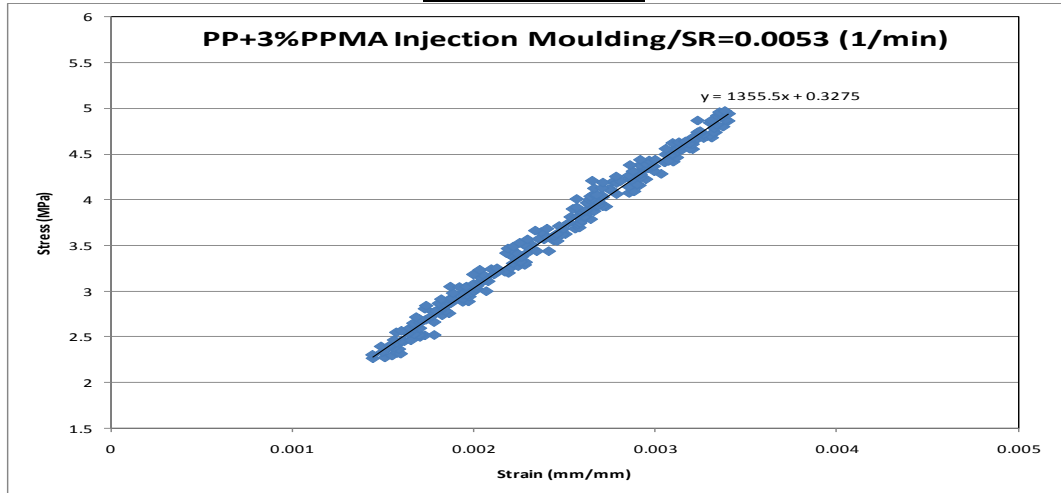


PP + 5% Clay

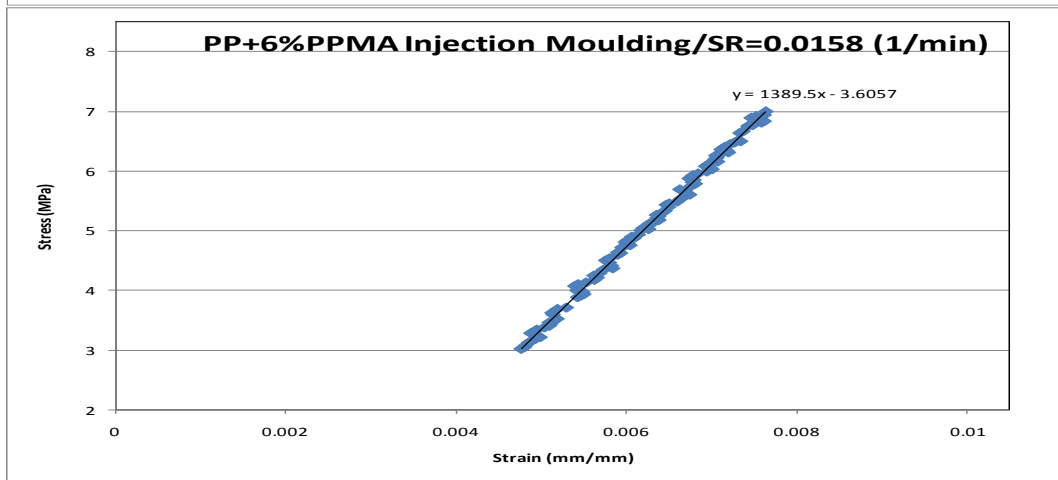
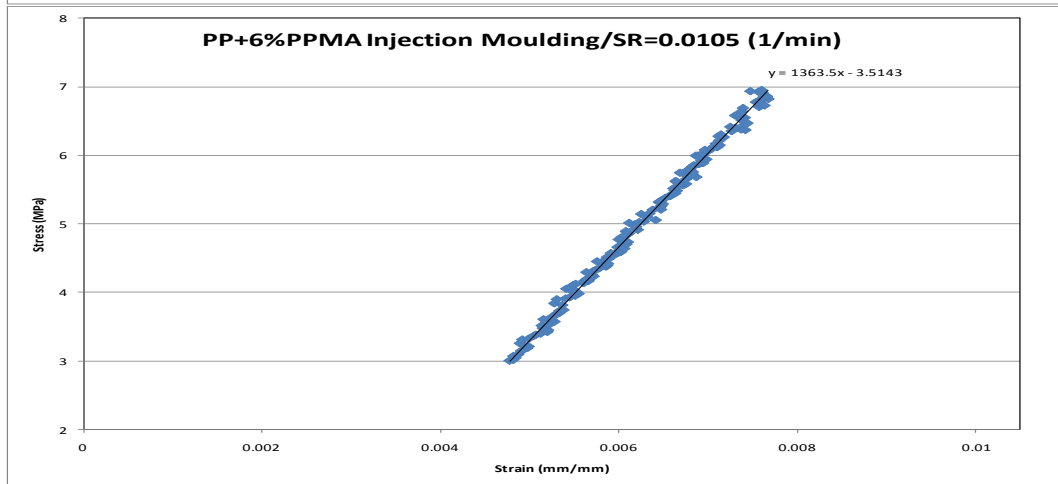
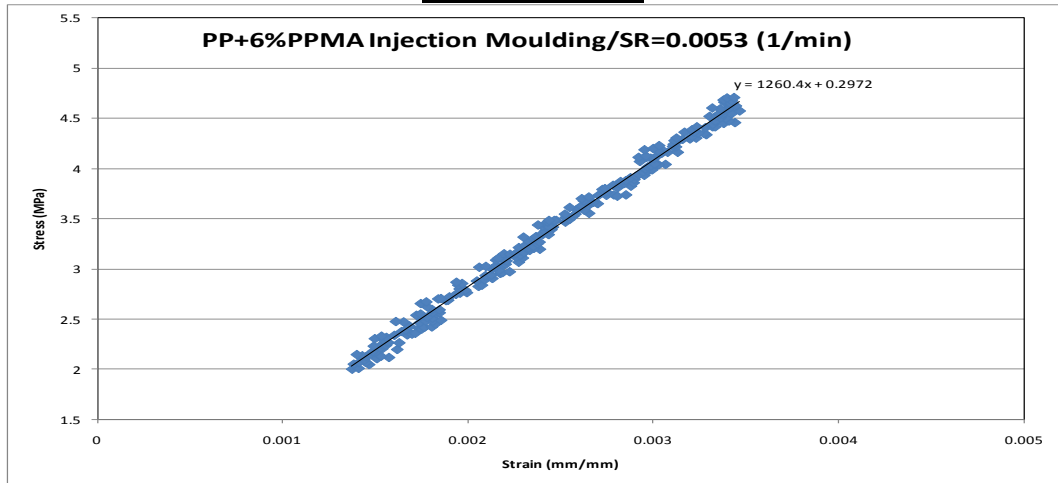




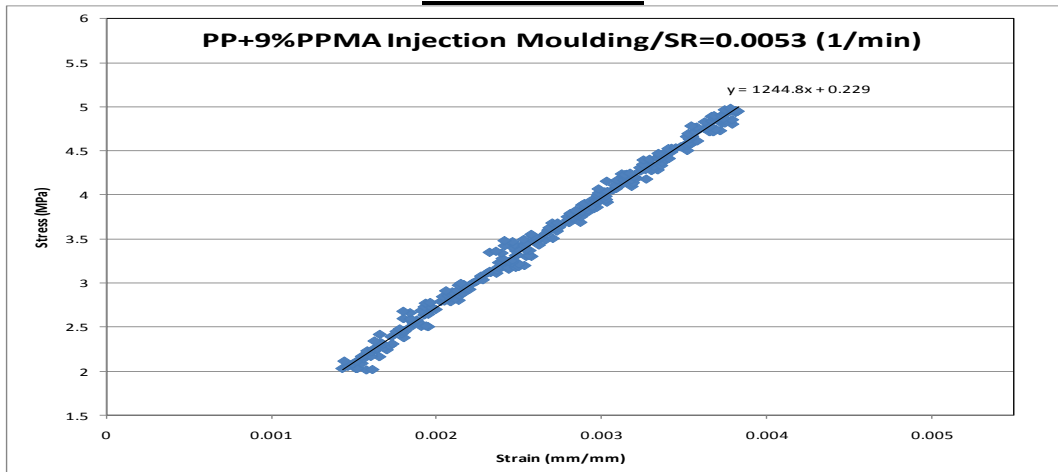
PP + 3% PPMA

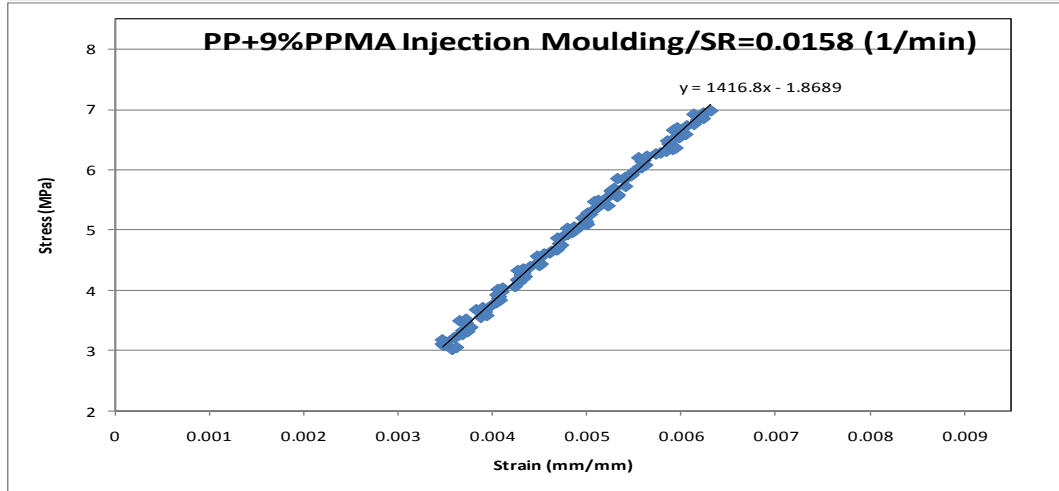
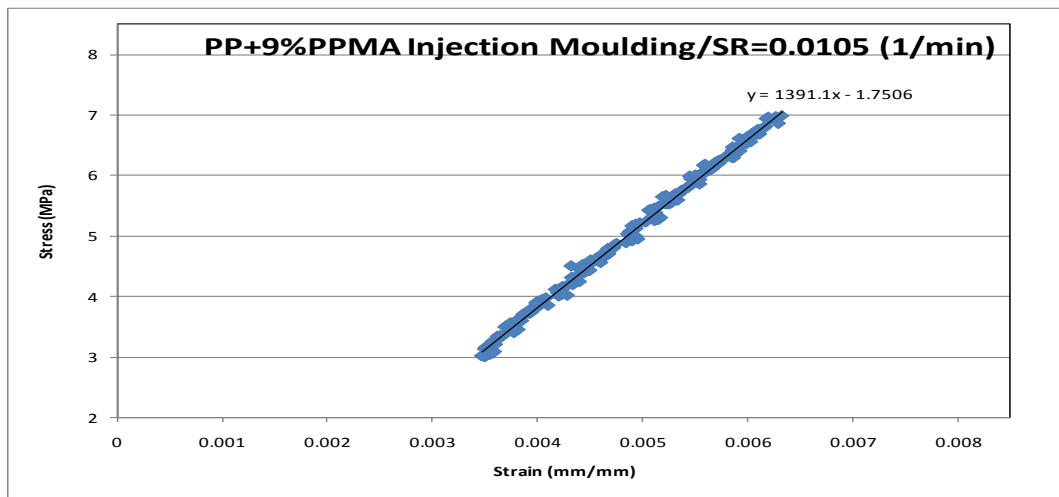


PP + 6% PPMA

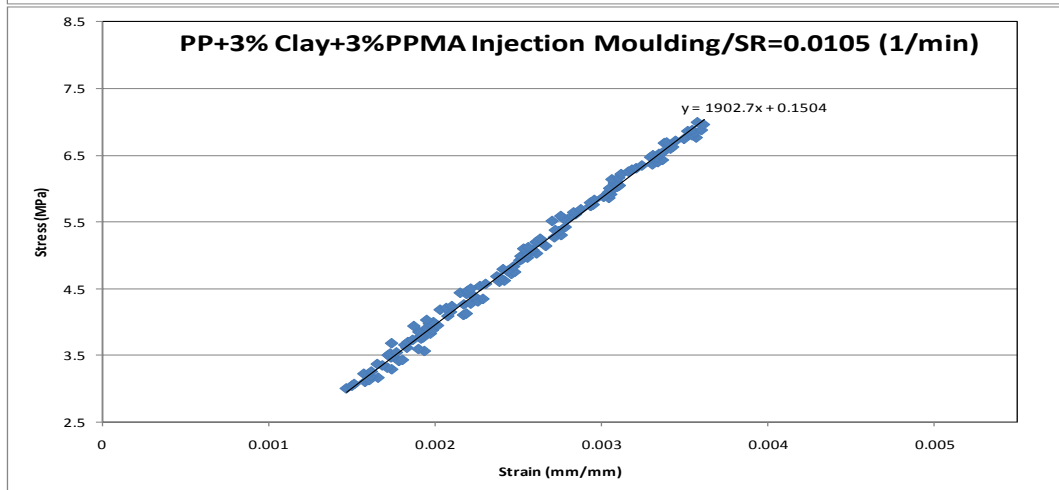
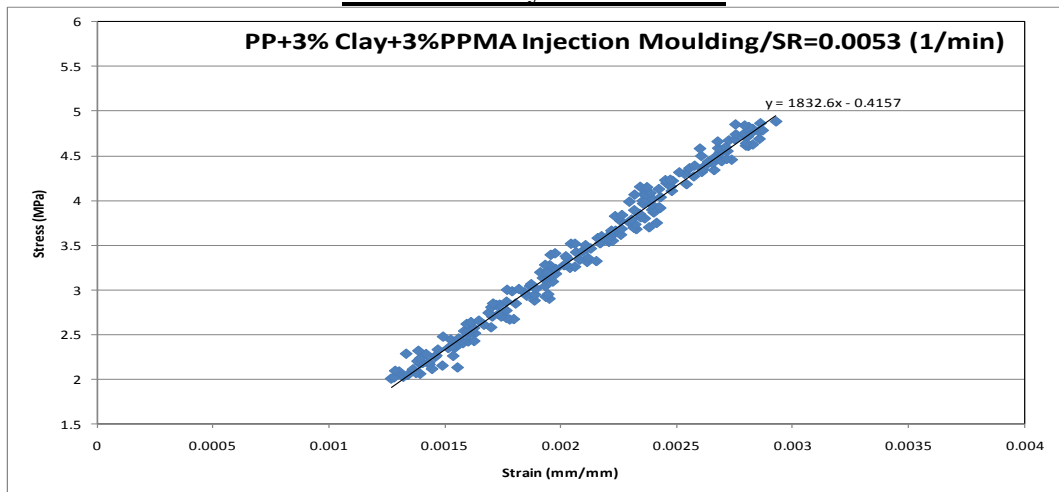


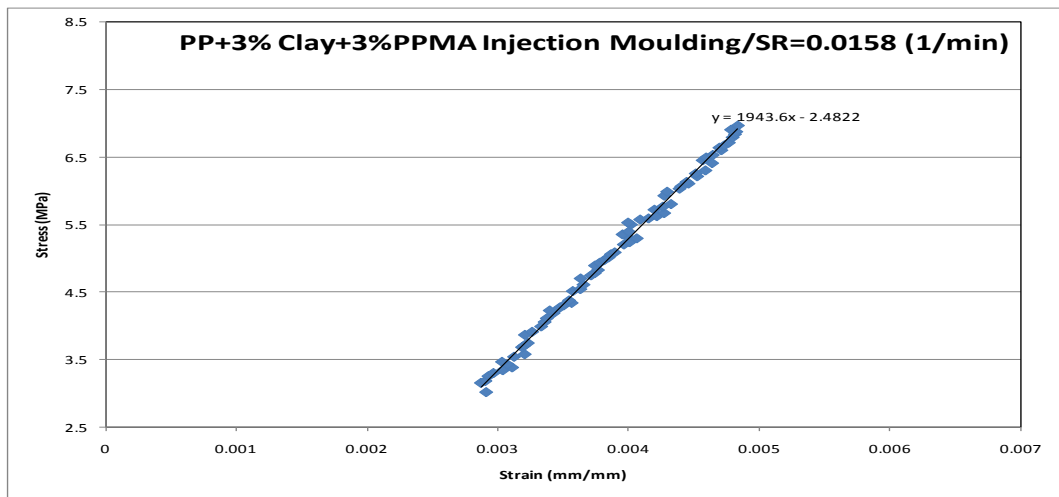
PP + 9% PPMA



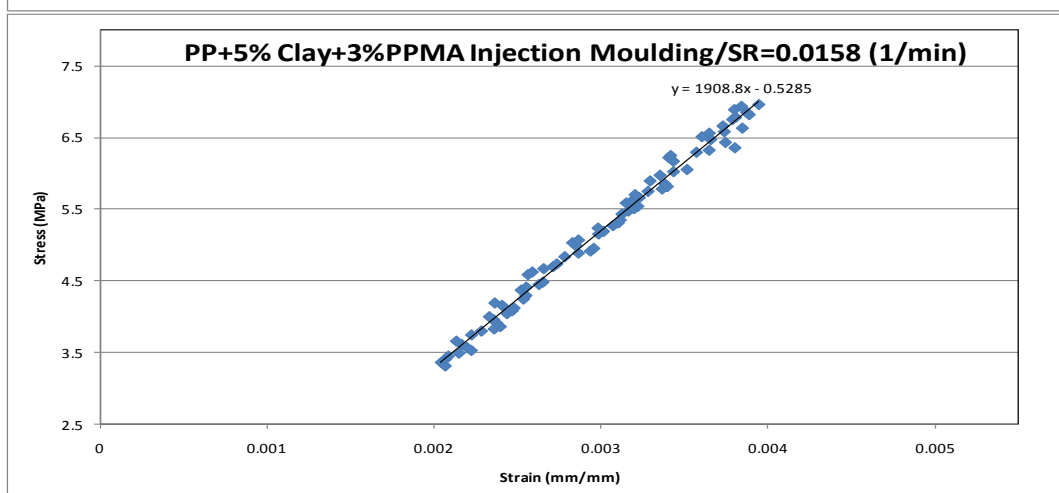
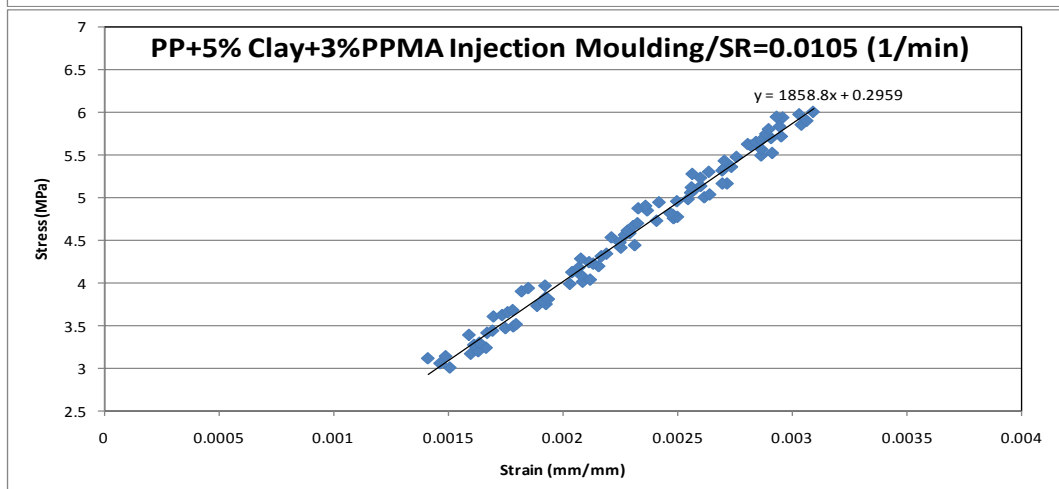
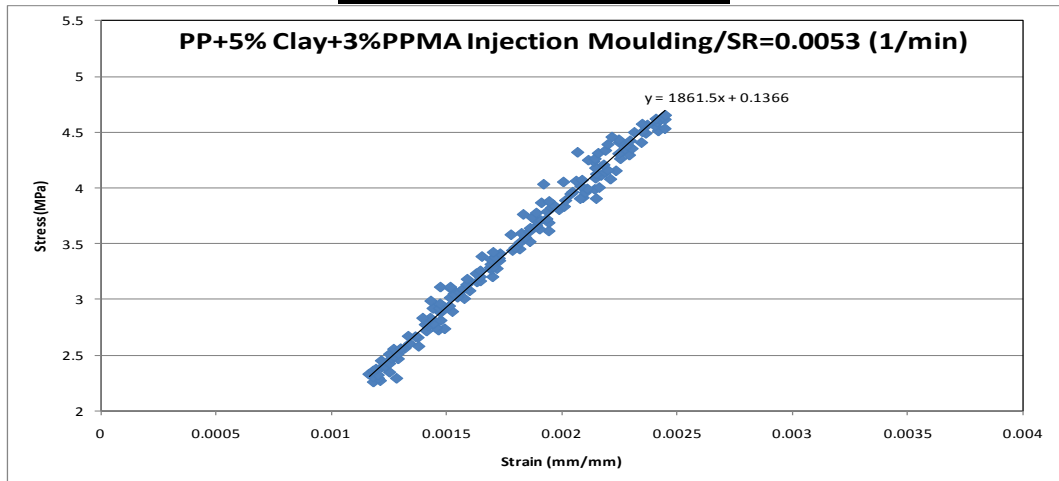


PP + 3 % Clay + 3% PPMA

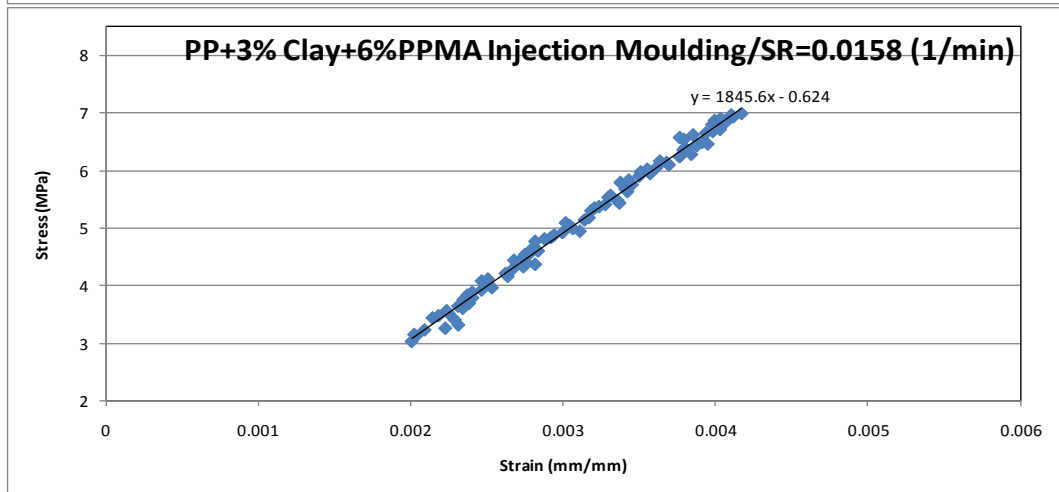
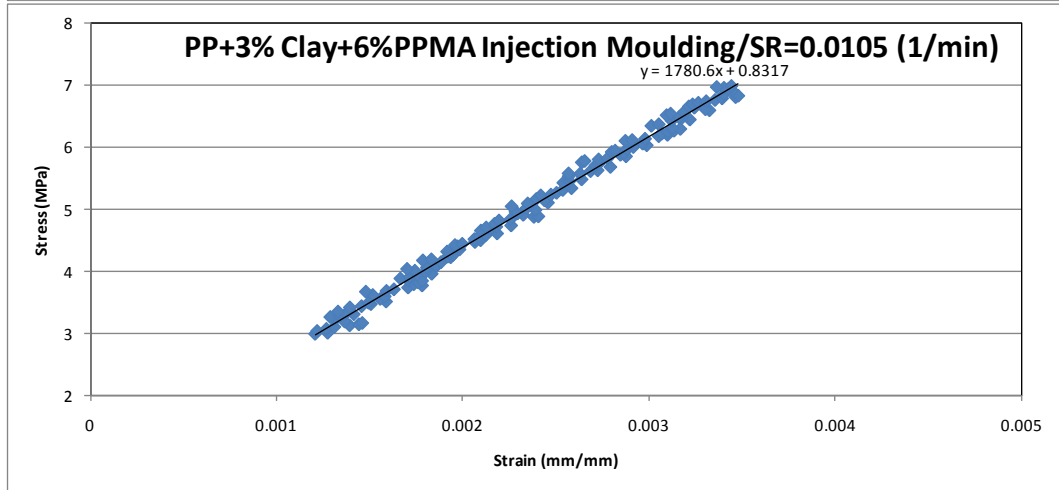
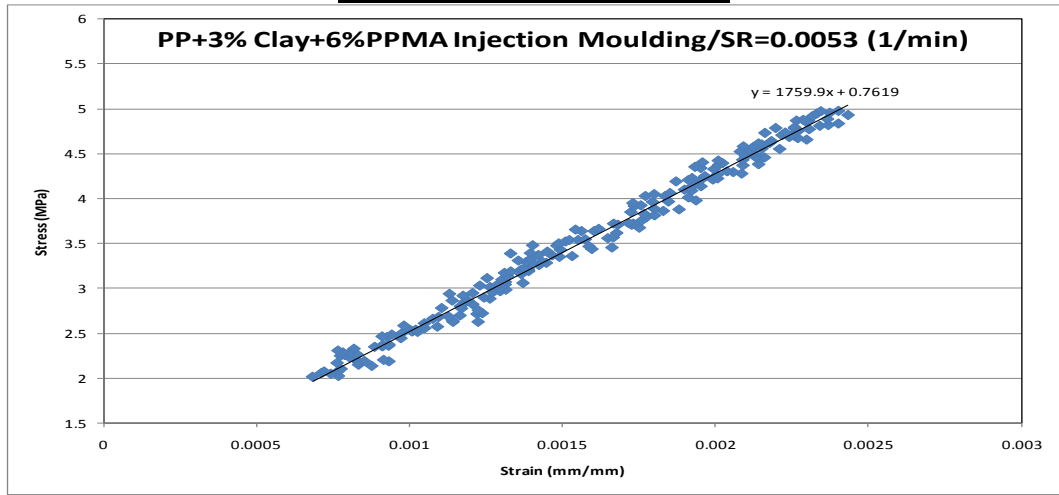




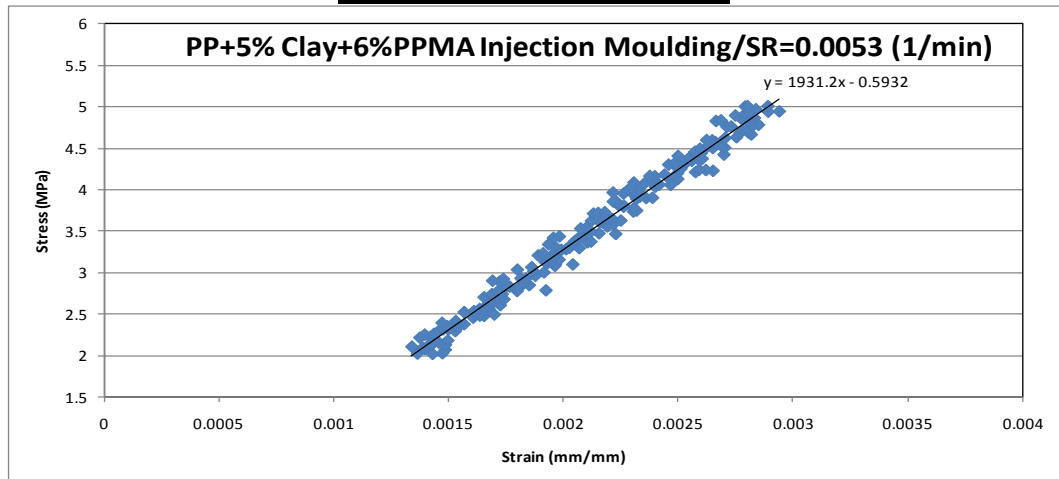
PP + 5 % Clay + 3% PPMA

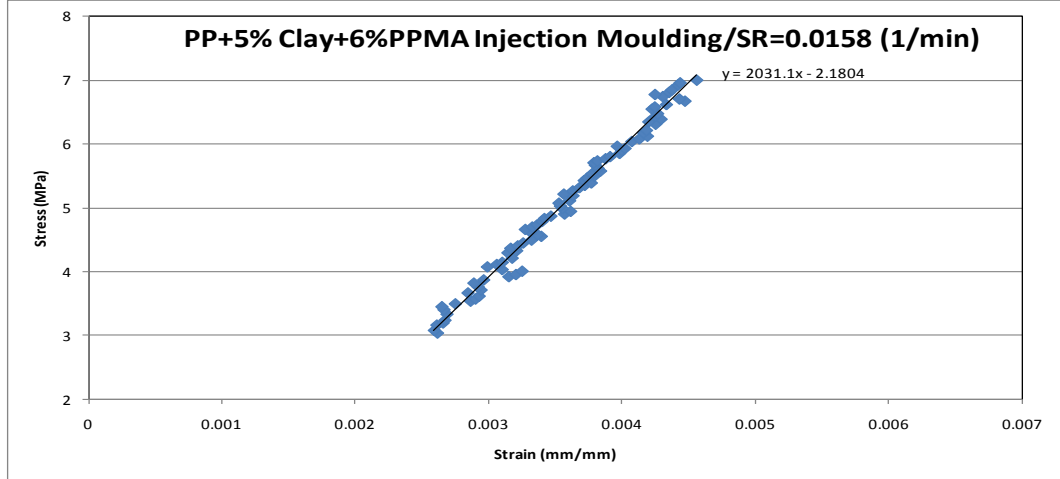
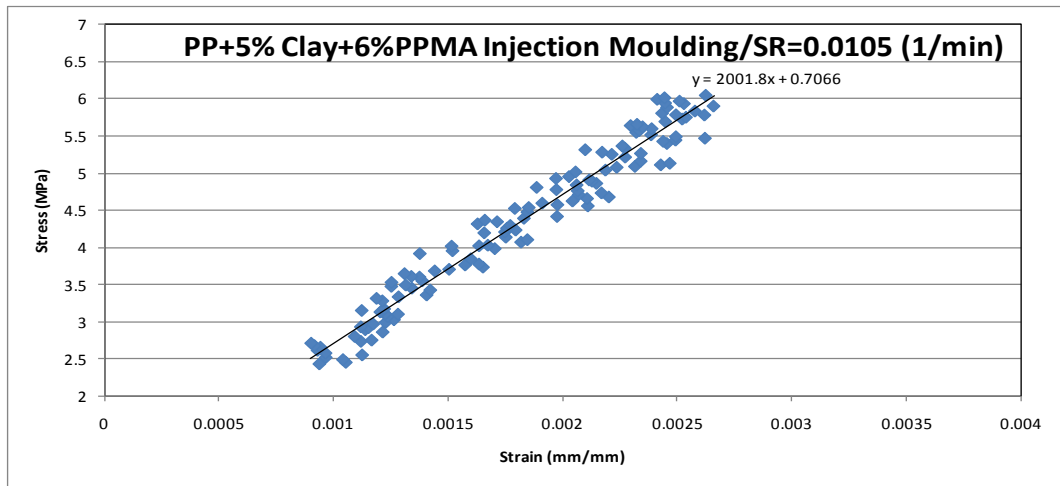


PP + 3 % Clay + 6% PPMA

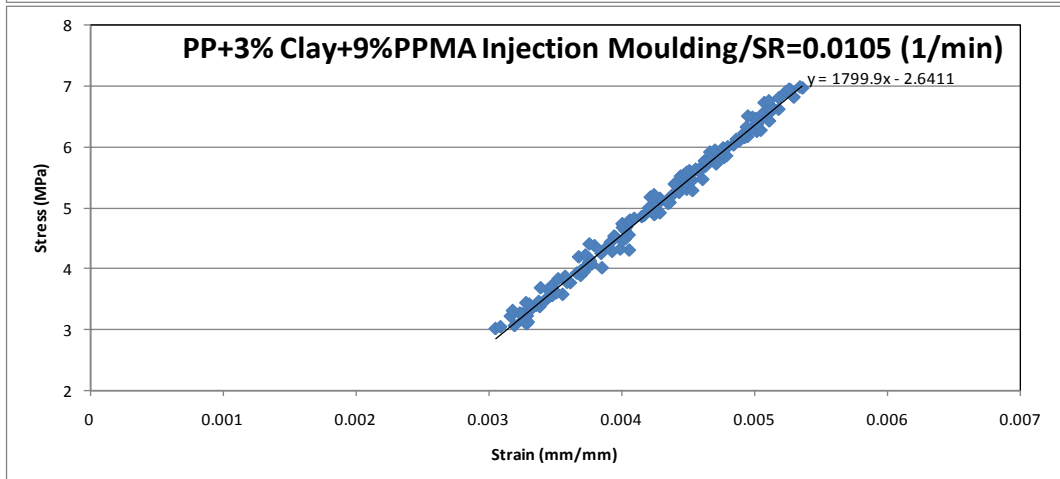
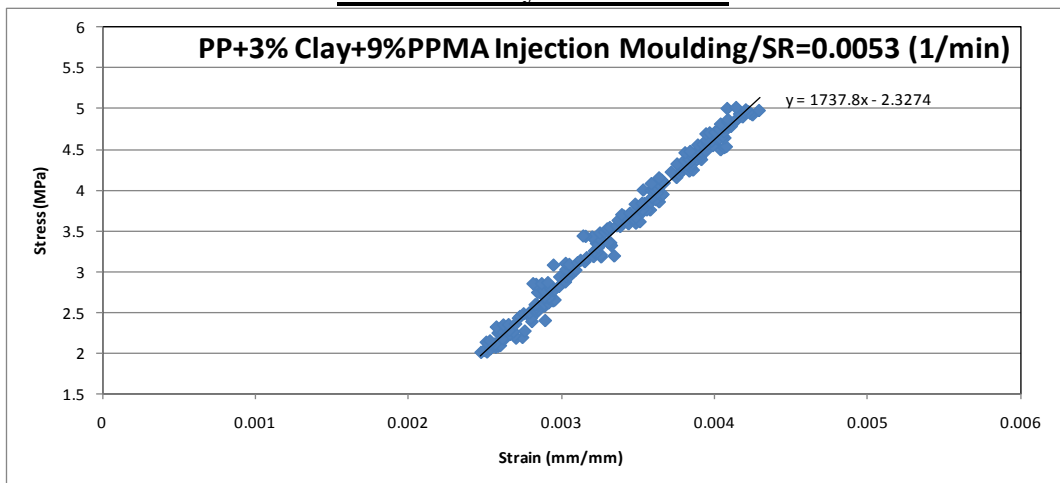


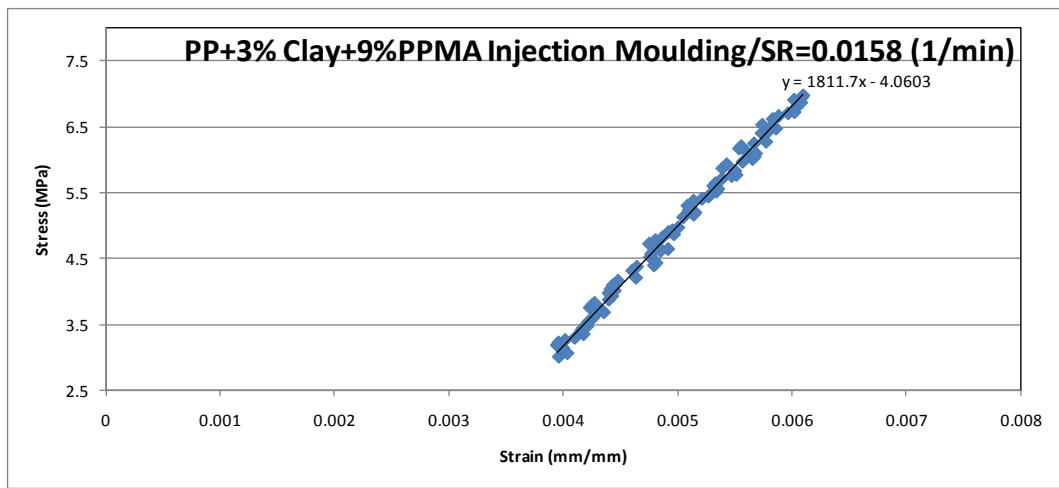
PP + 5 % Clay + 6% PPMA



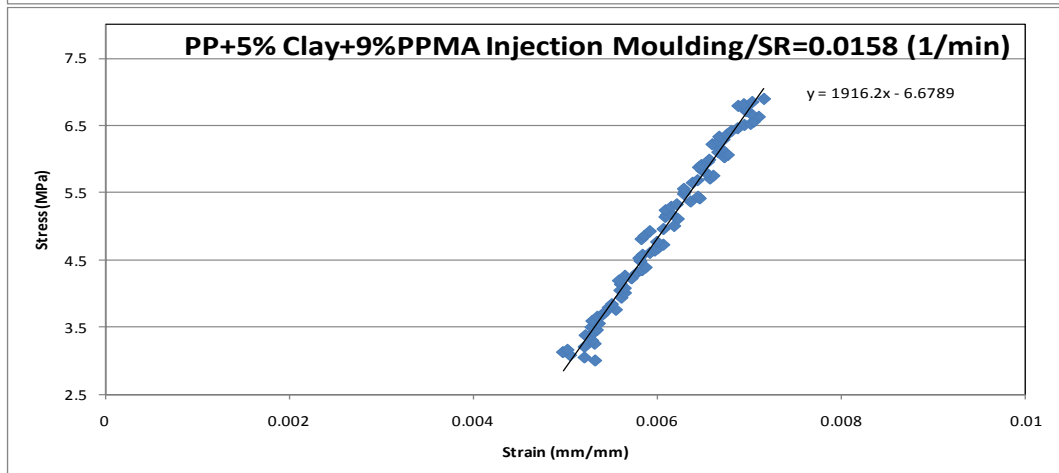
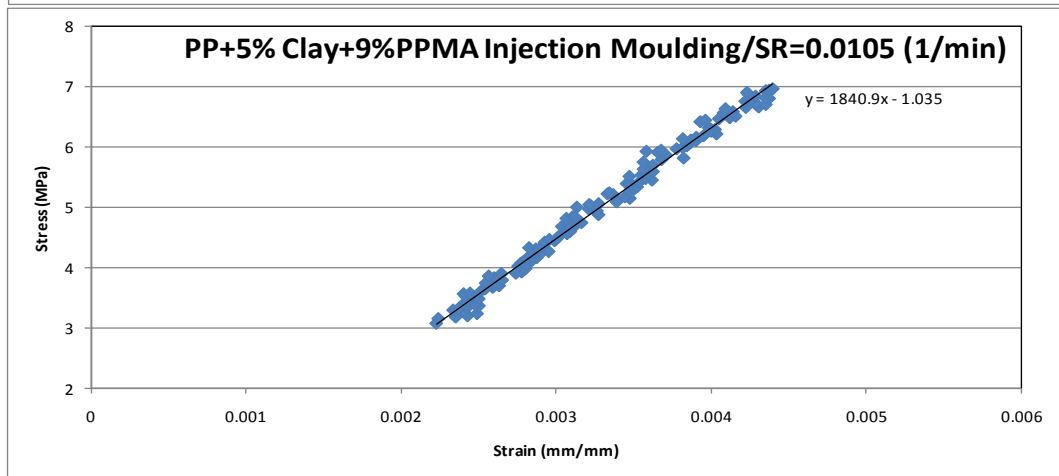
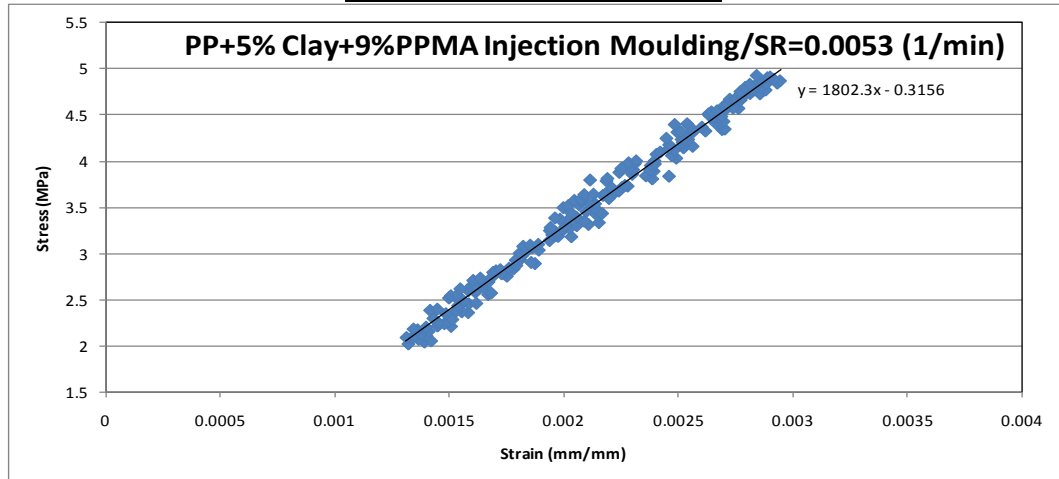


PP + 3 % Clay + 9% PPMA



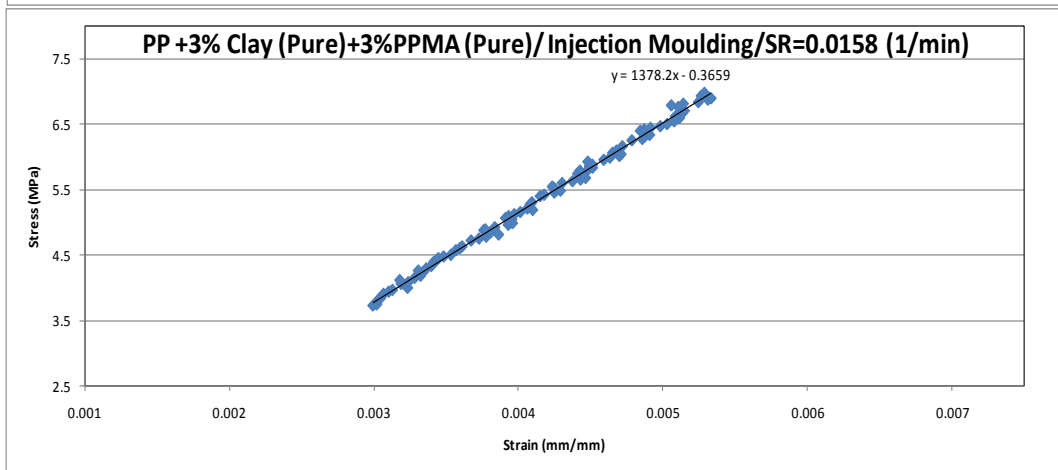
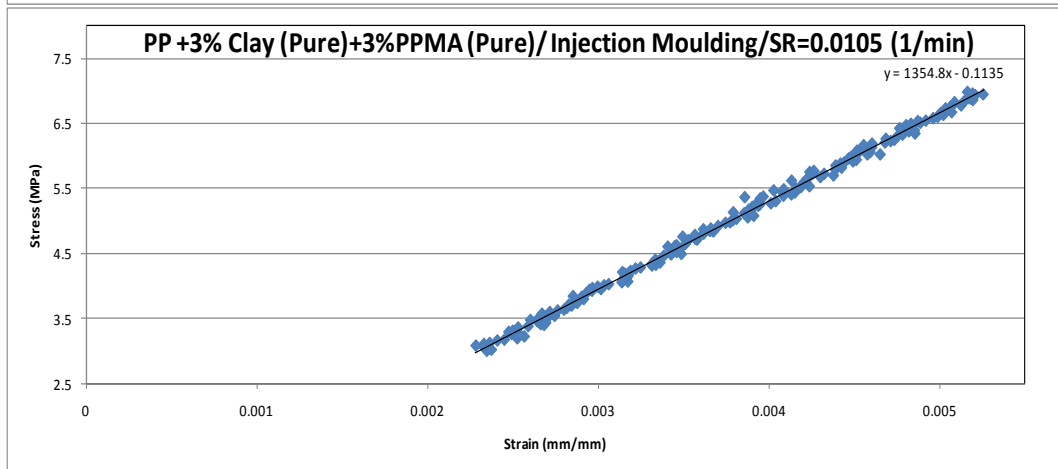
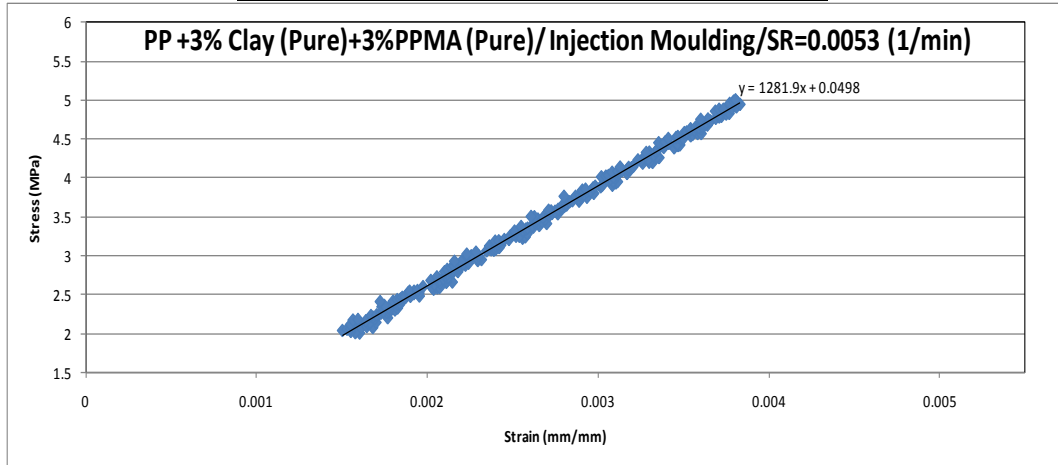


PP + 5 % Clay+ 9% PPMA

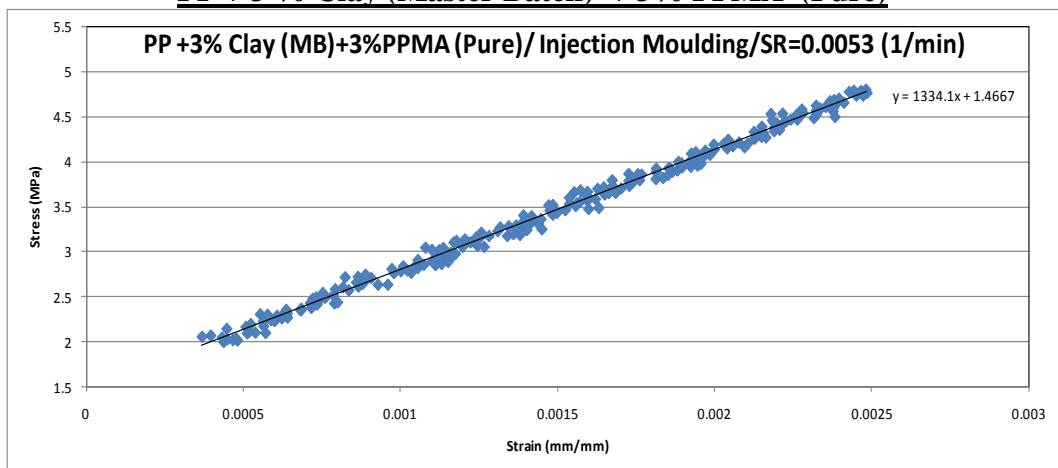


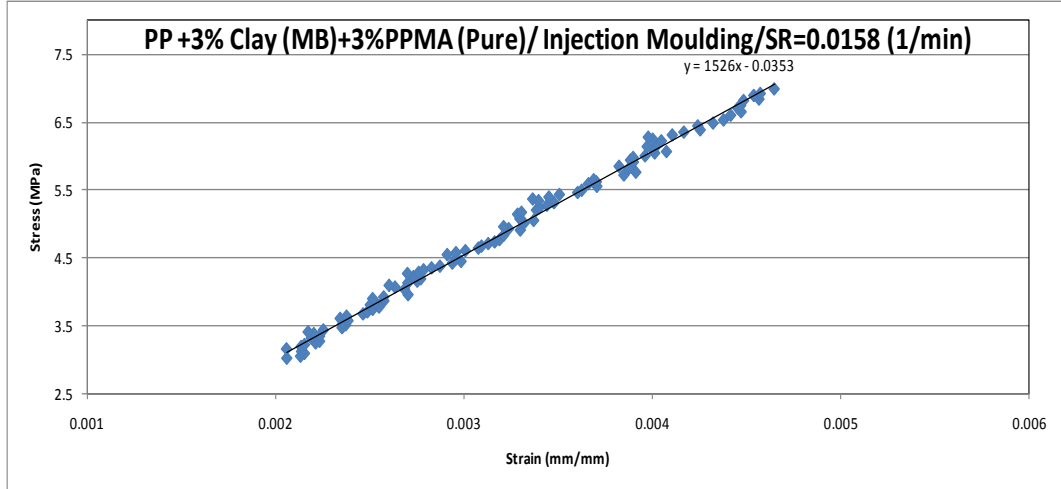
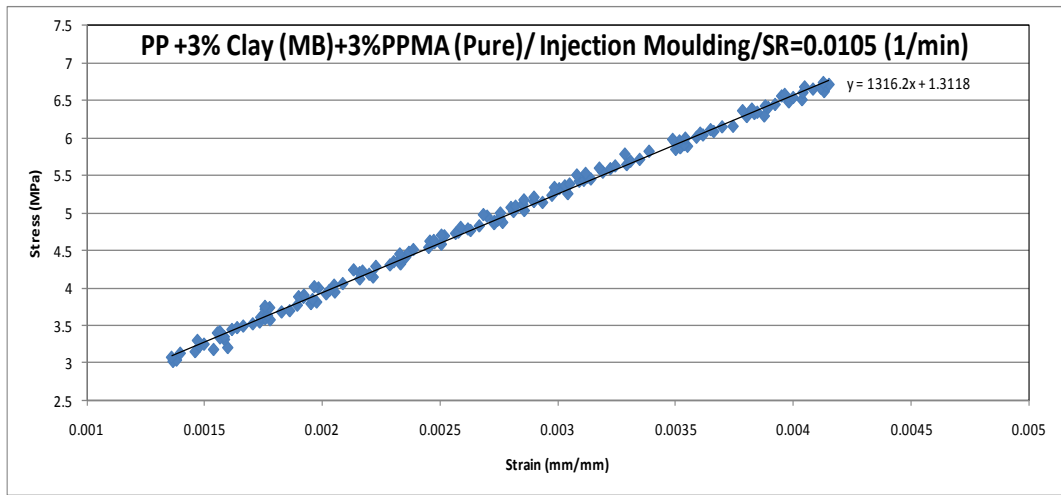
Appendix G4: Tensile Video Extensometer for Different Mixing Procedure Injection Bar Samples

PP + 3 % Clay (Pure) + 3% PPMA (Pure)

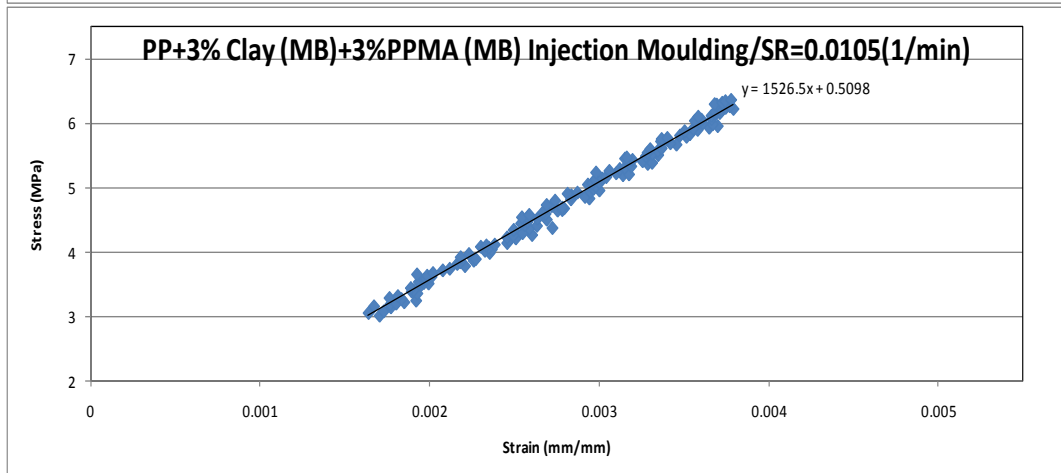
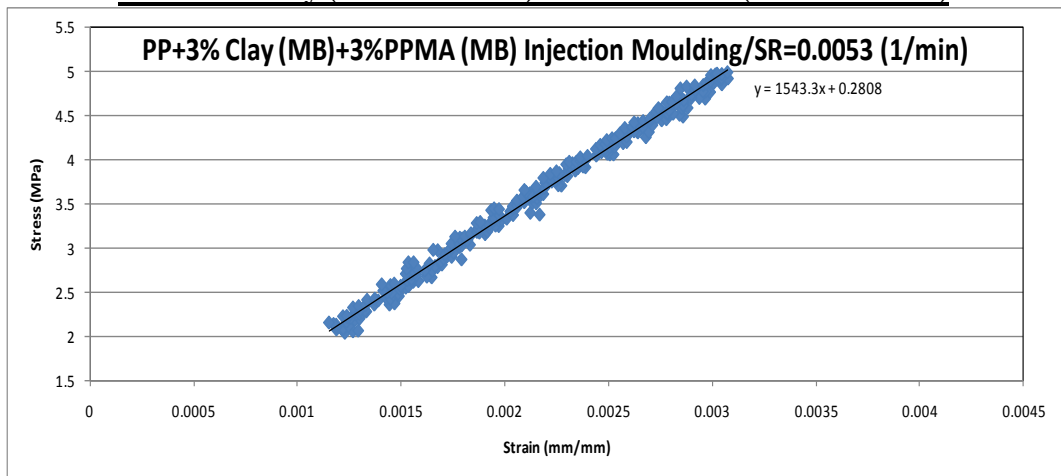


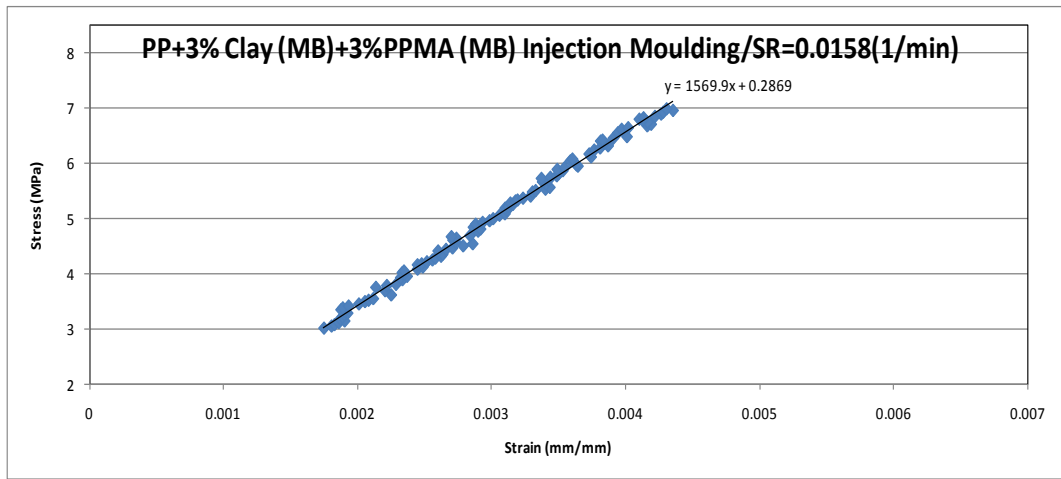
PP + 3 % Clay (Master Batch) + 3% PPMA (Pure)



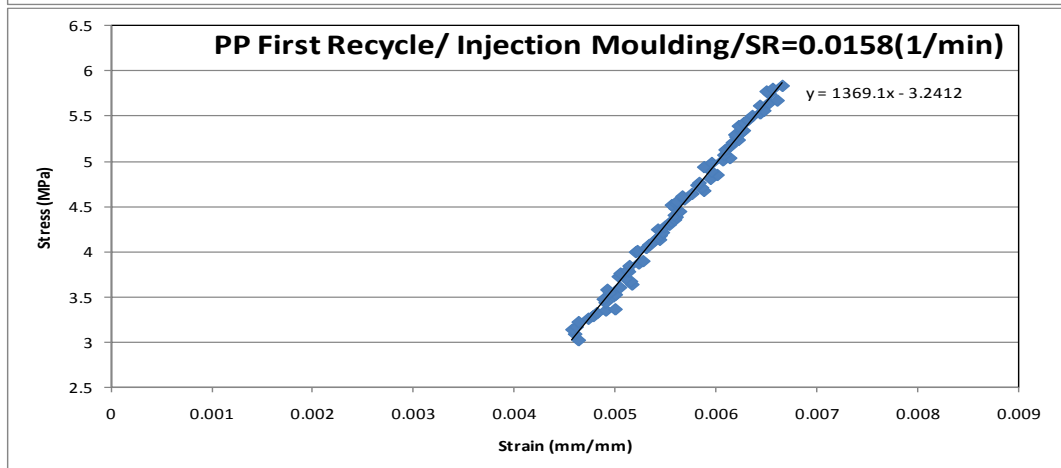
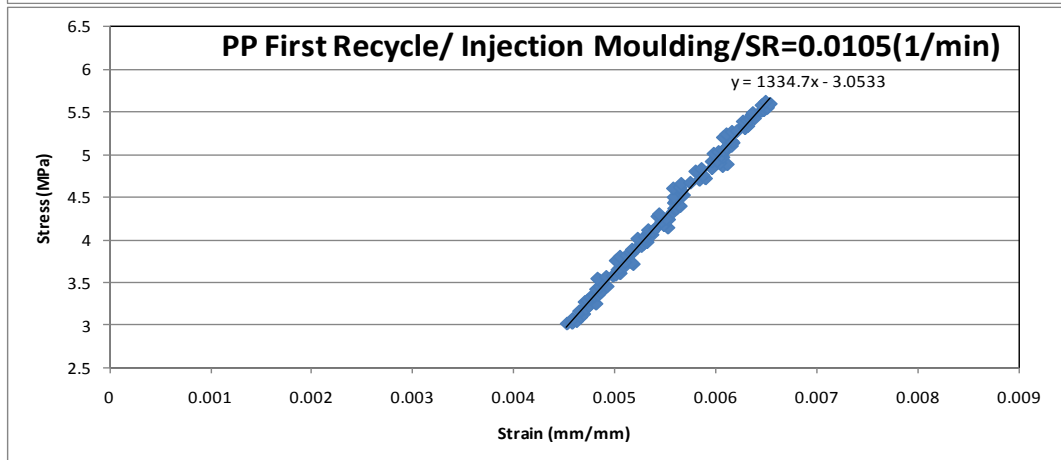
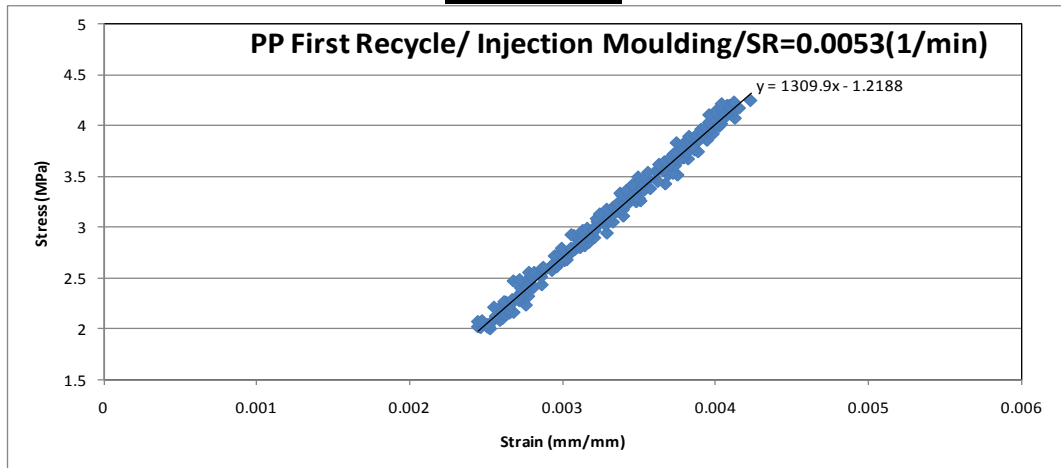


PP + 3 % Clay (Master Batch) + 3% PPMA (Master Batch)

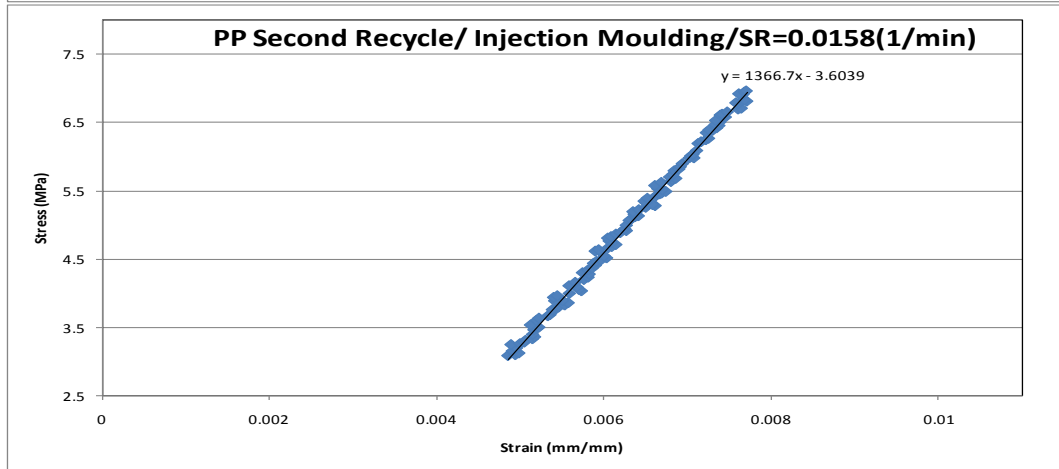
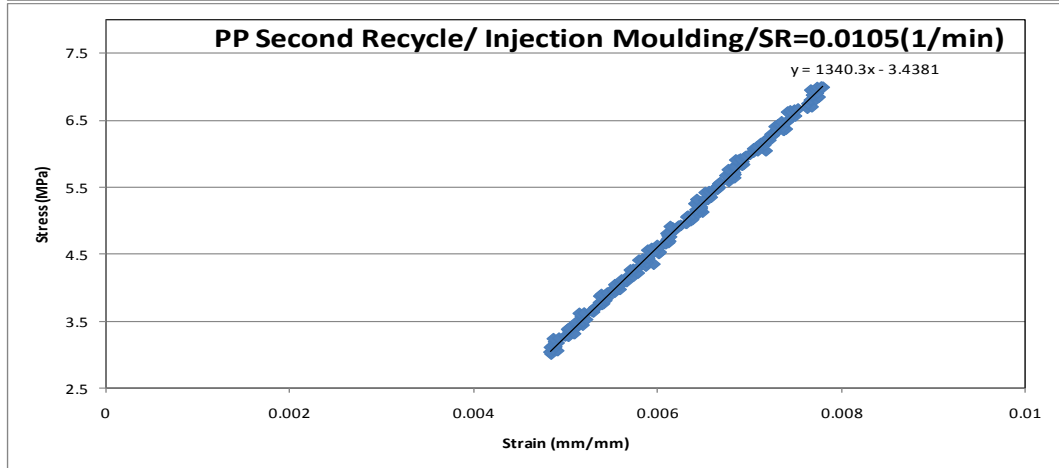
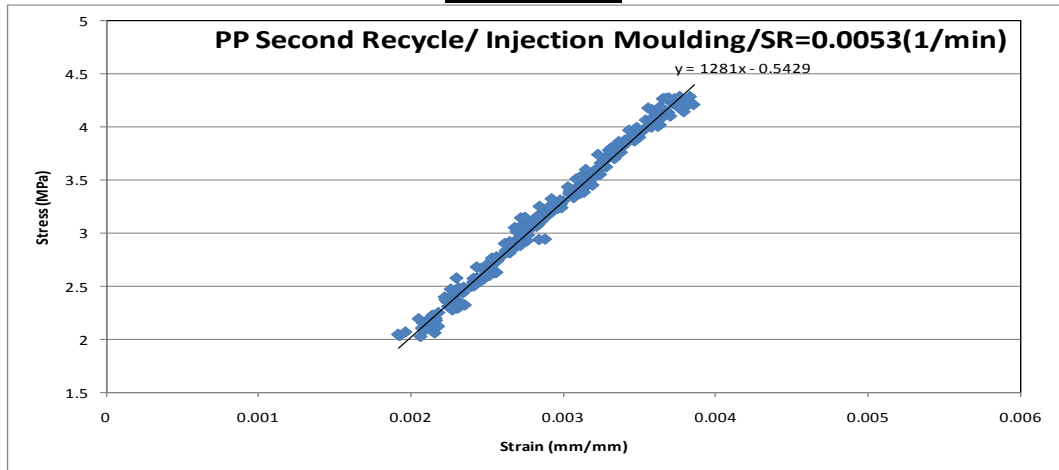




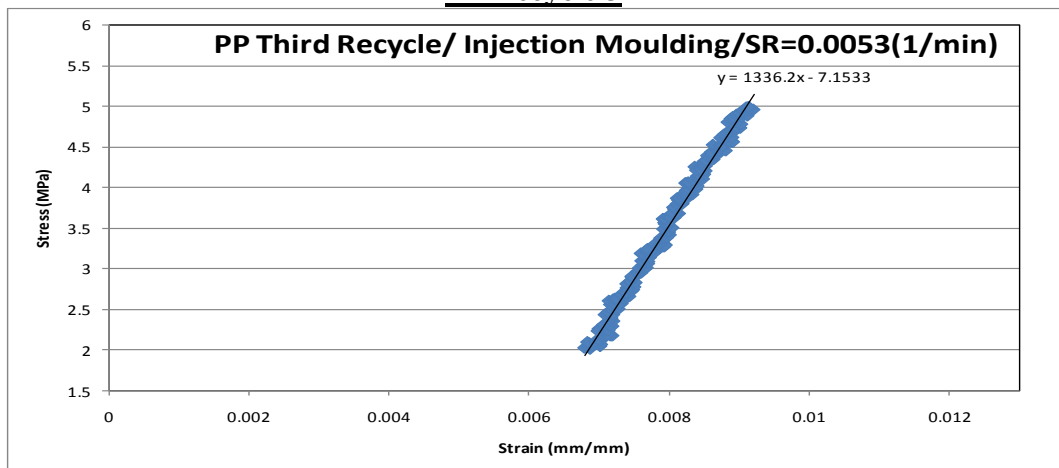
Appendix G5: Tensile Video Extensometer for Pure PP Recycle
PP Recycle 1

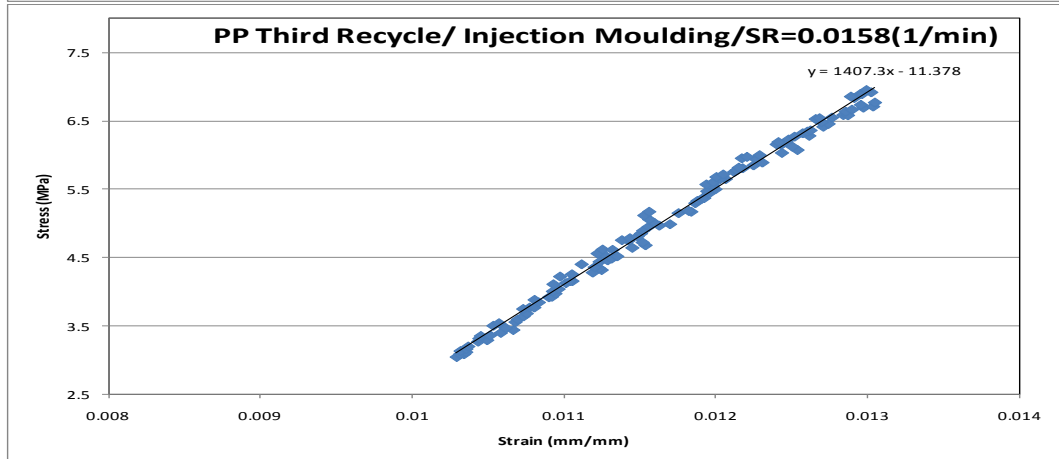
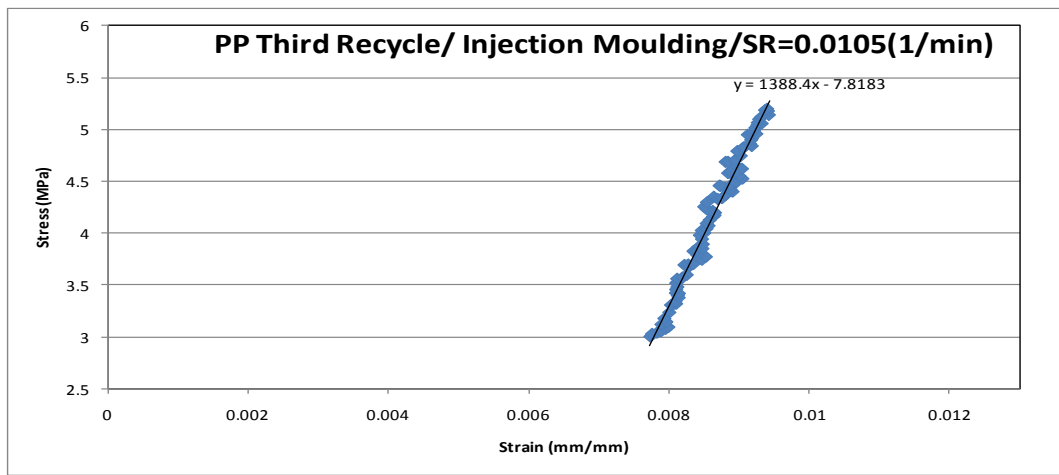


PP Recycle 2

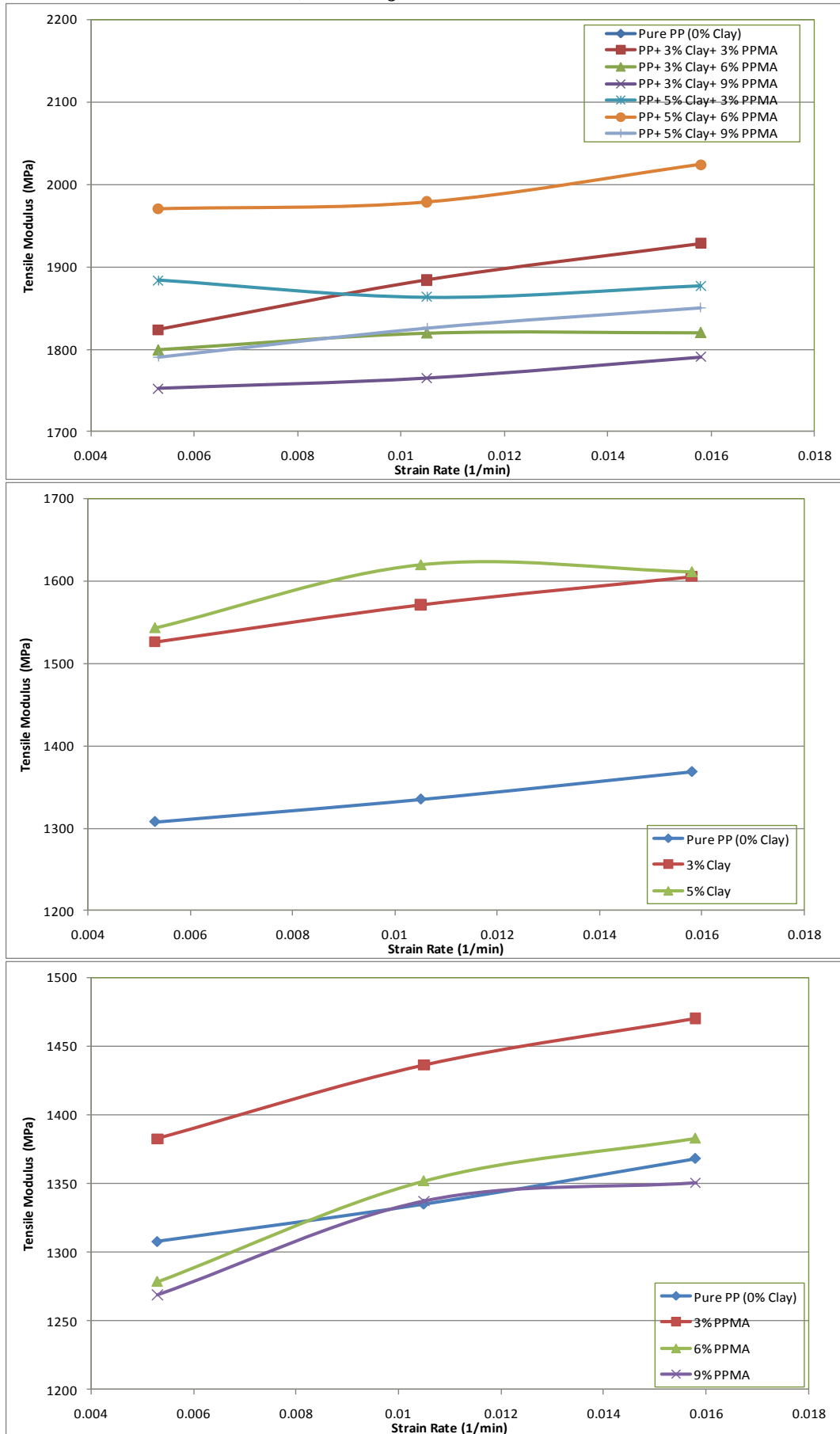


PP Recycle 3





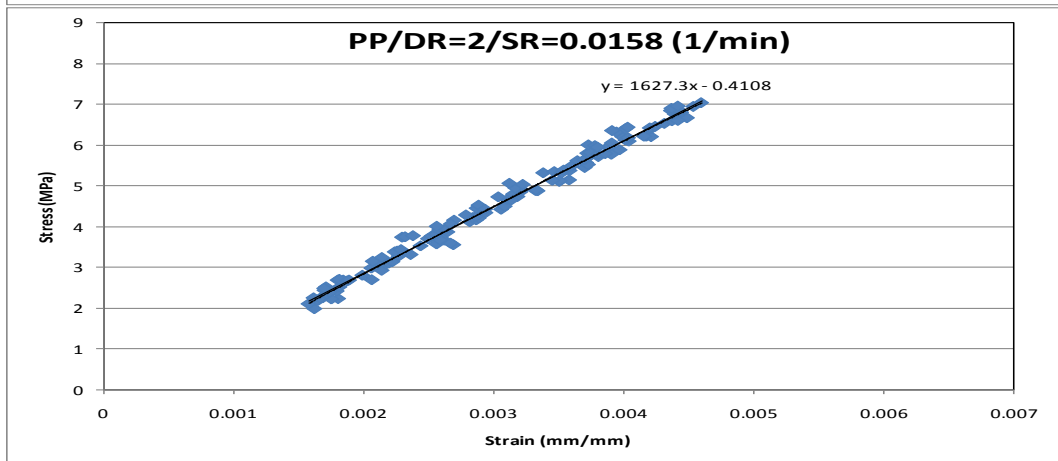
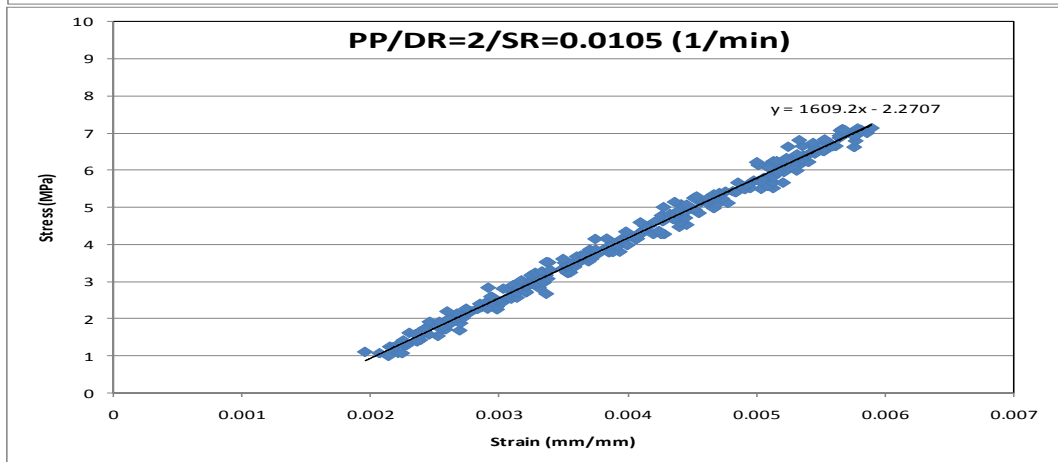
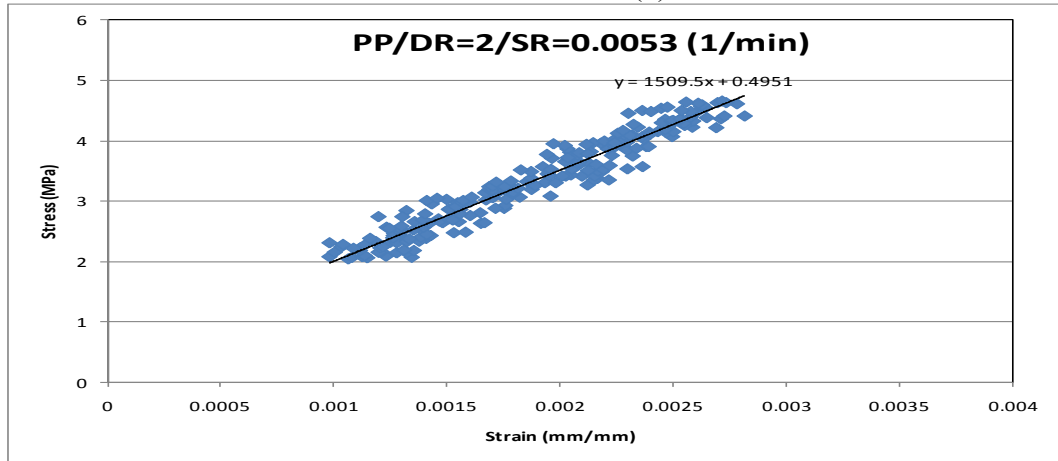
Appendix G6: Tensile Video Extensometer (Strain Rate Effect on Modulus) for Injection Moulded bars



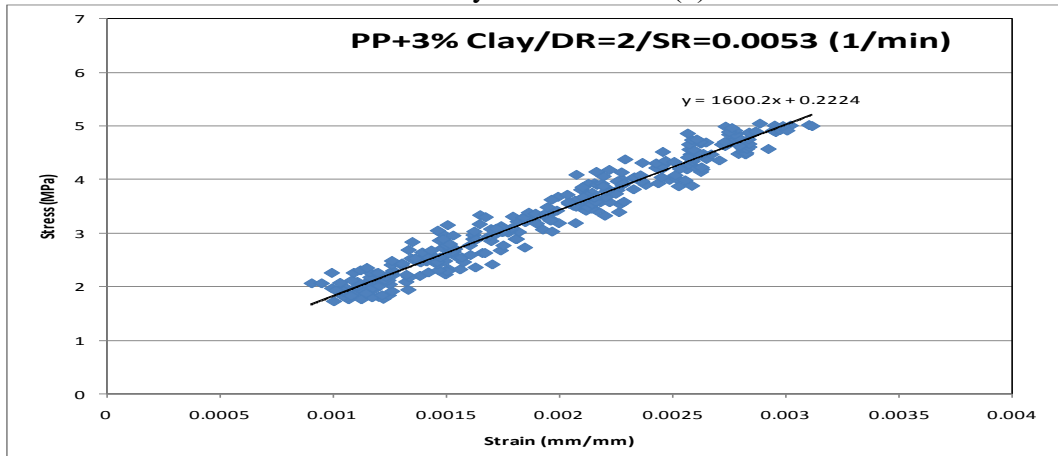
Appendix H: Tensile Video Extensometer of Drawn PPNCs

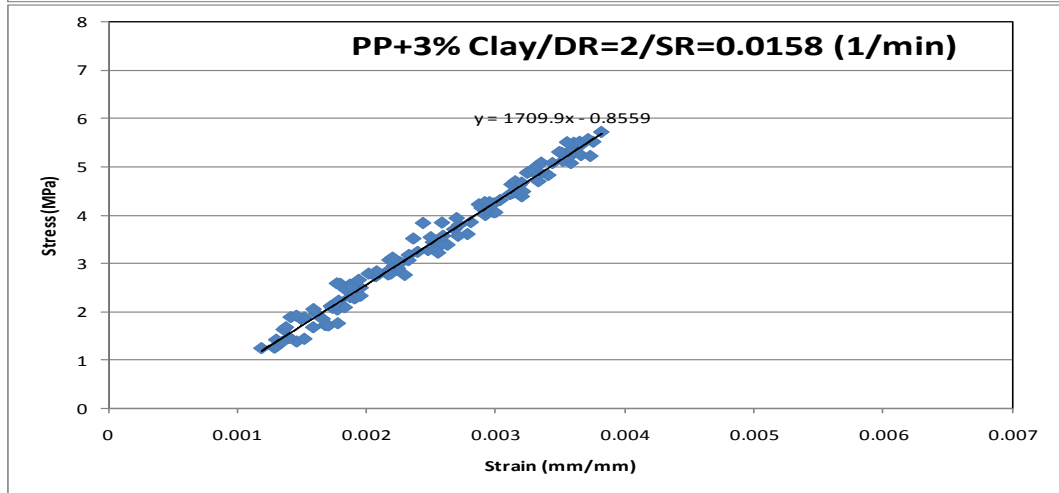
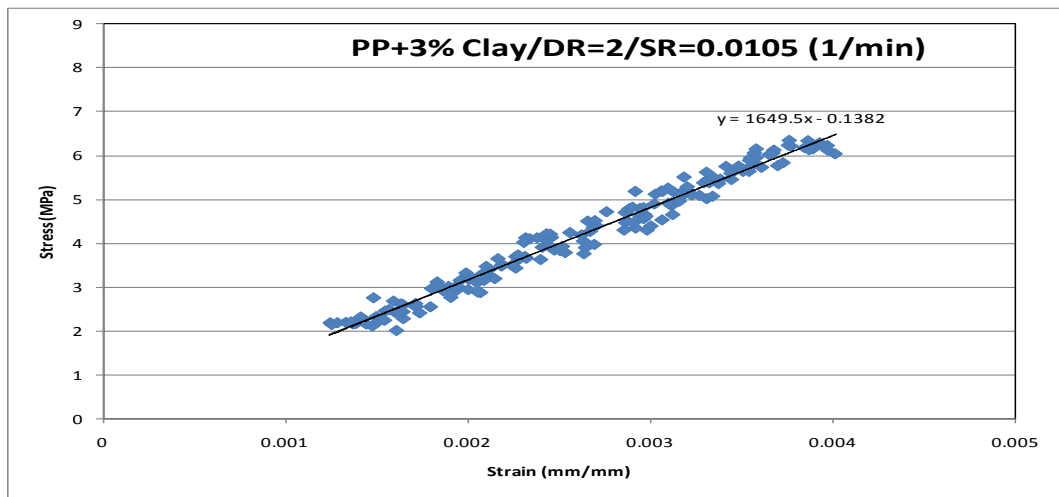
Appendix H1: Tensile Video Extensometer of Different Draw Ratios

Pure PP - Draw Ratio (λ) = 2

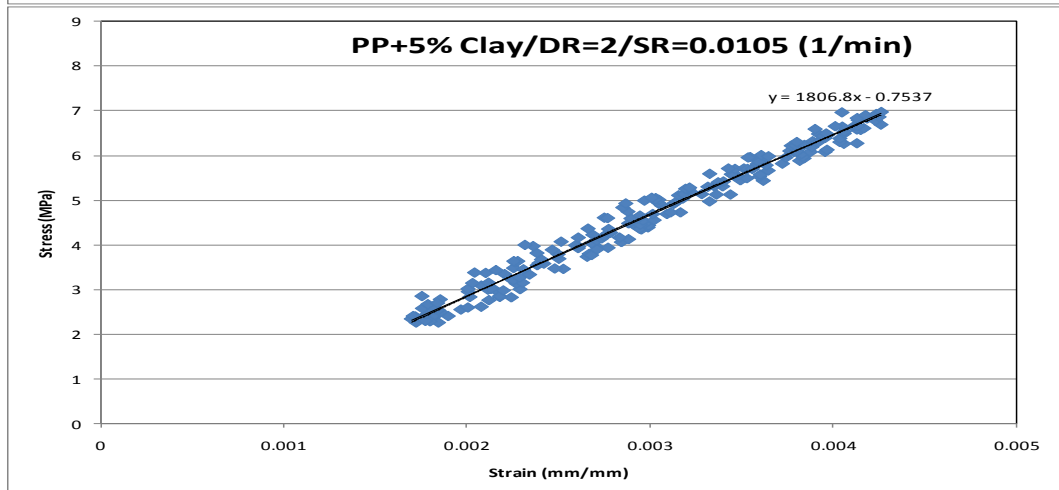
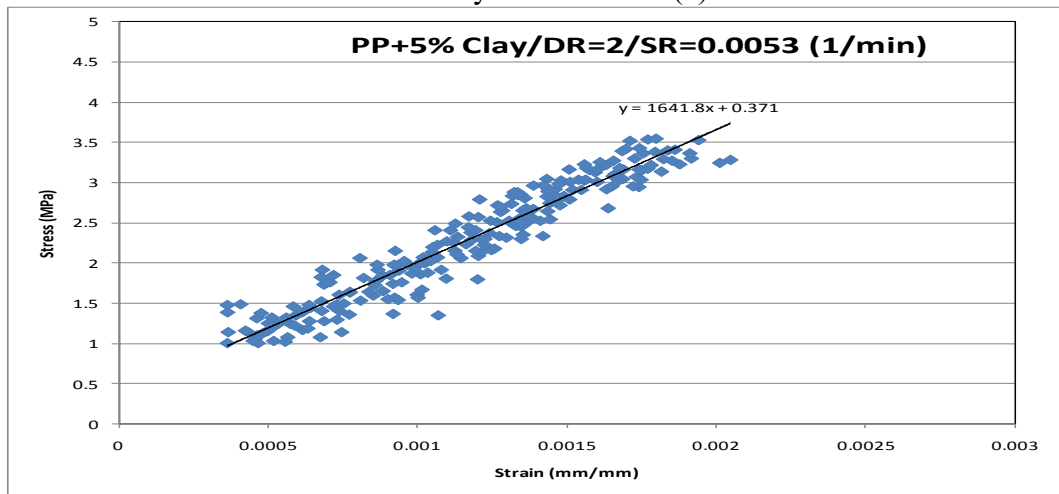


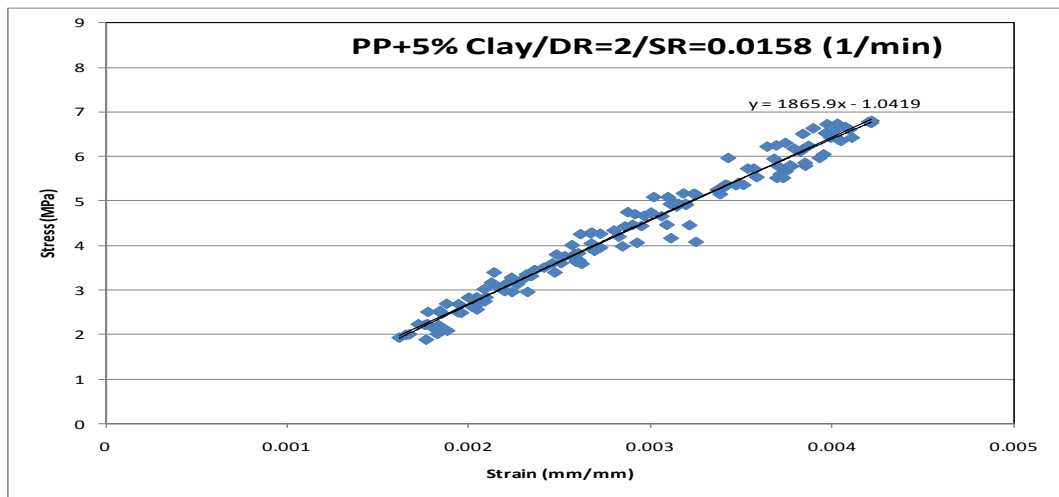
PP + 3% Clay - Draw Ratio (λ) = 2



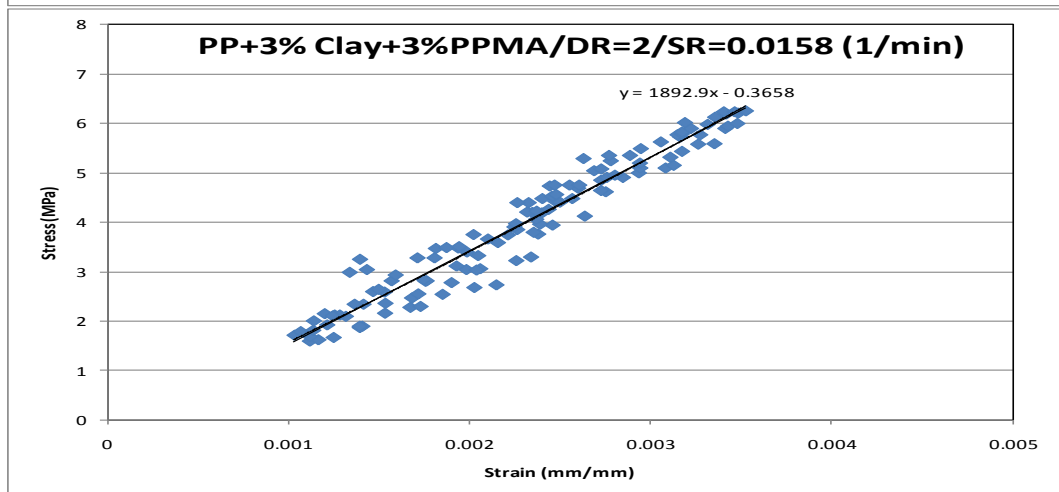
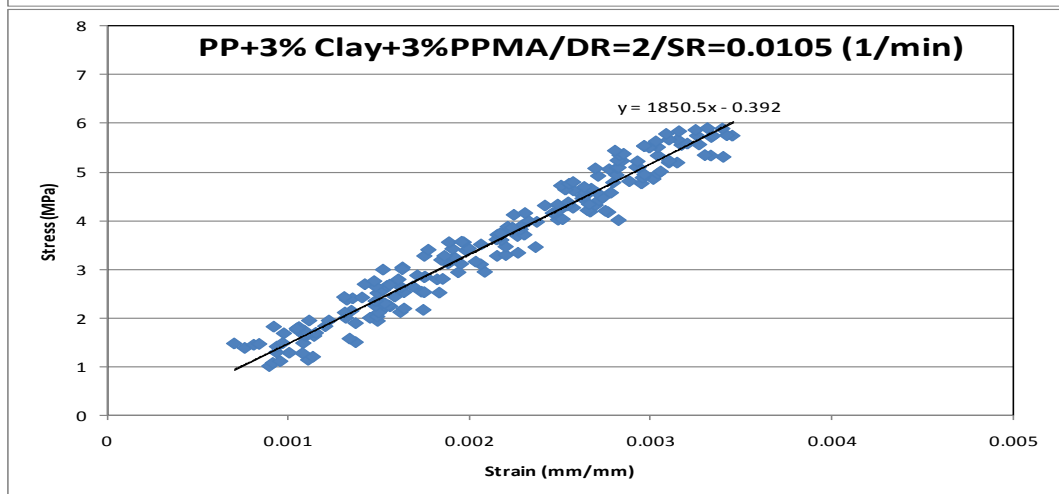
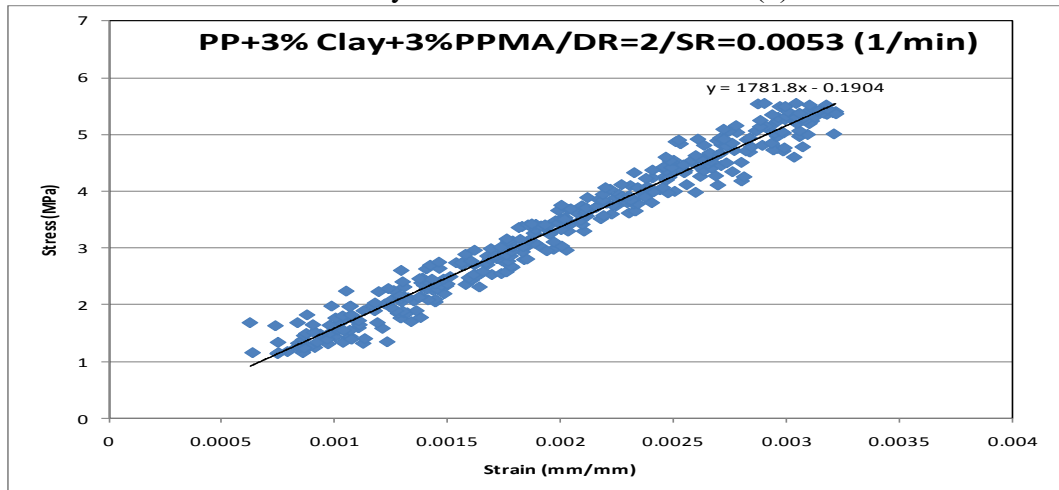


PP + 5% Clay - Draw Ratio (λ) = 2

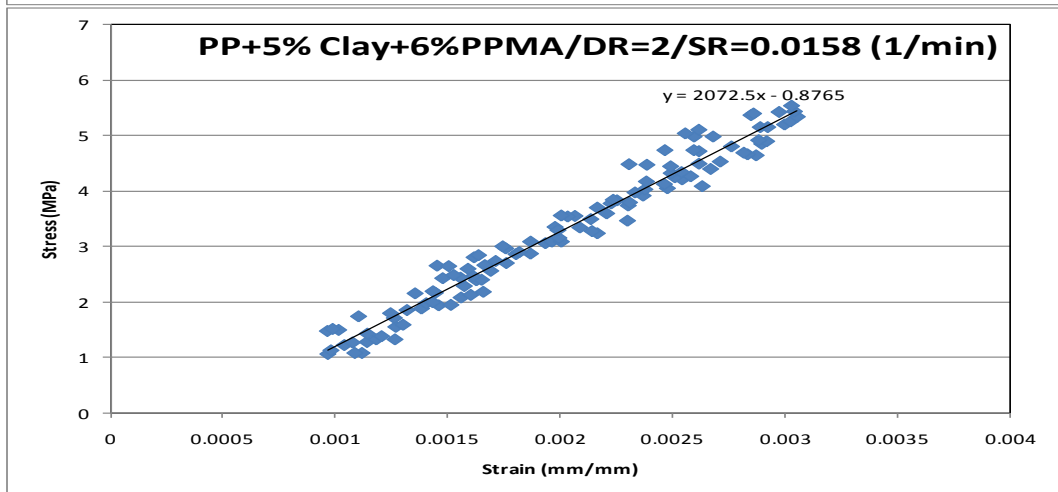
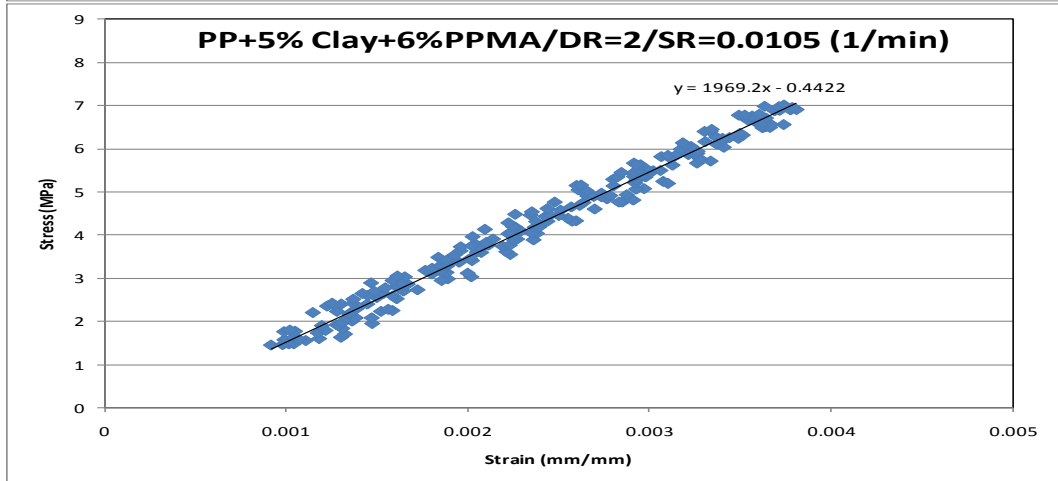
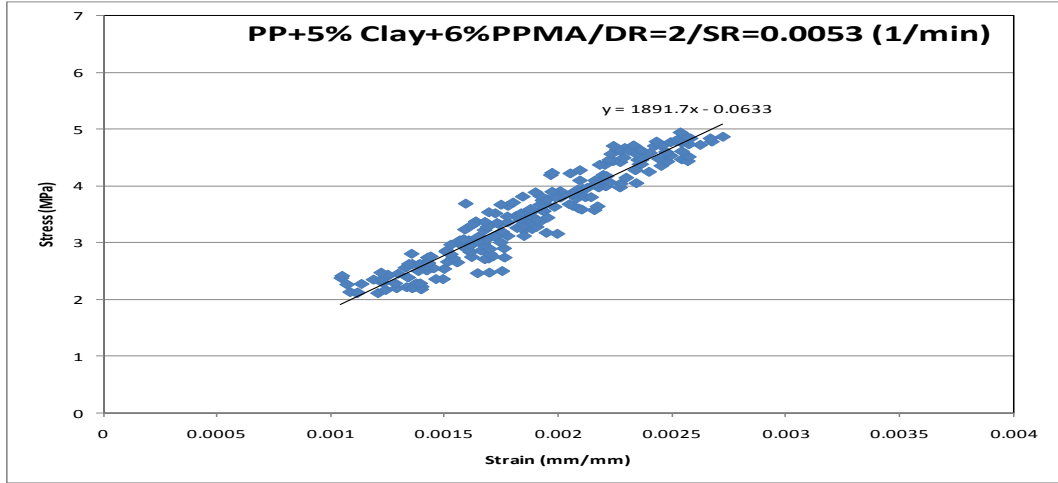




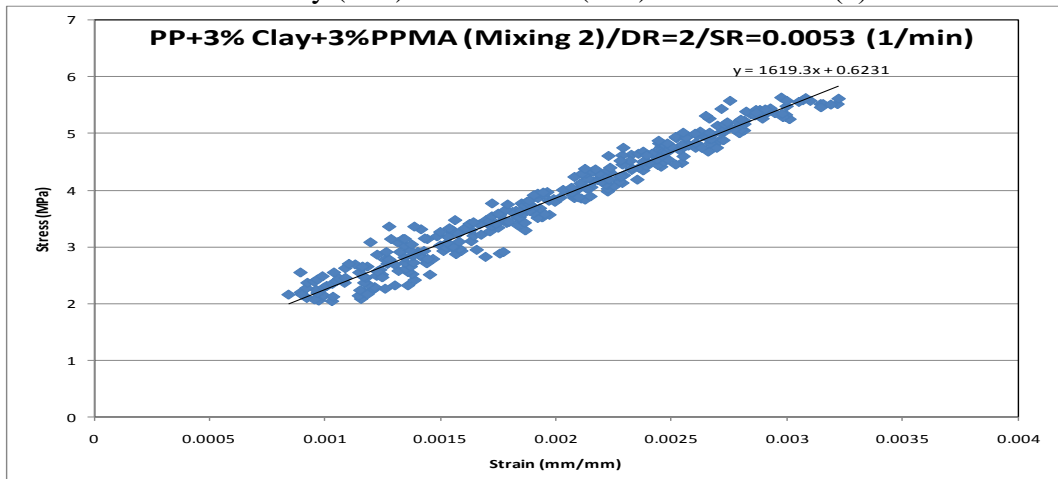
PP + 3% Clay + 3%PPMA - Draw Ratio (λ) = 2

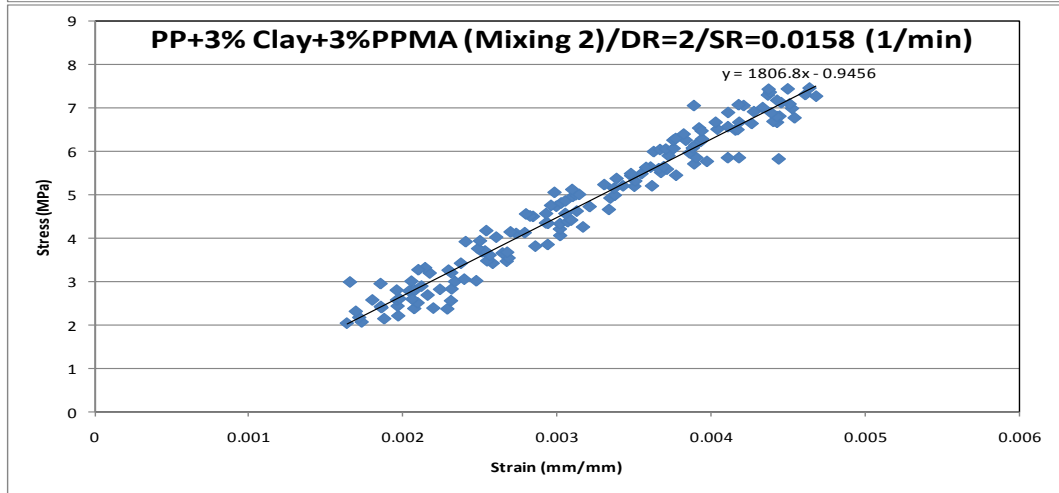
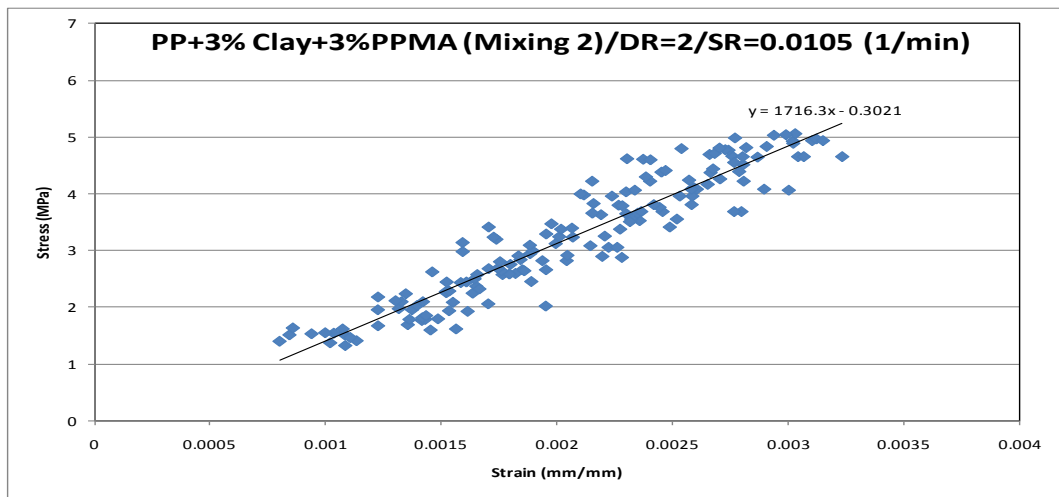


PP + 5% Clay + 6%PPMA - Draw Ratio (λ) = 2

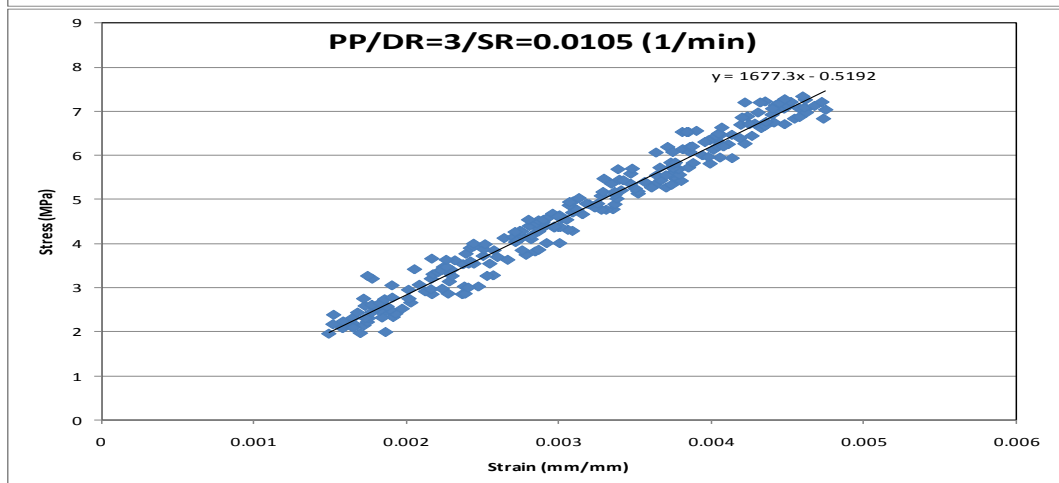
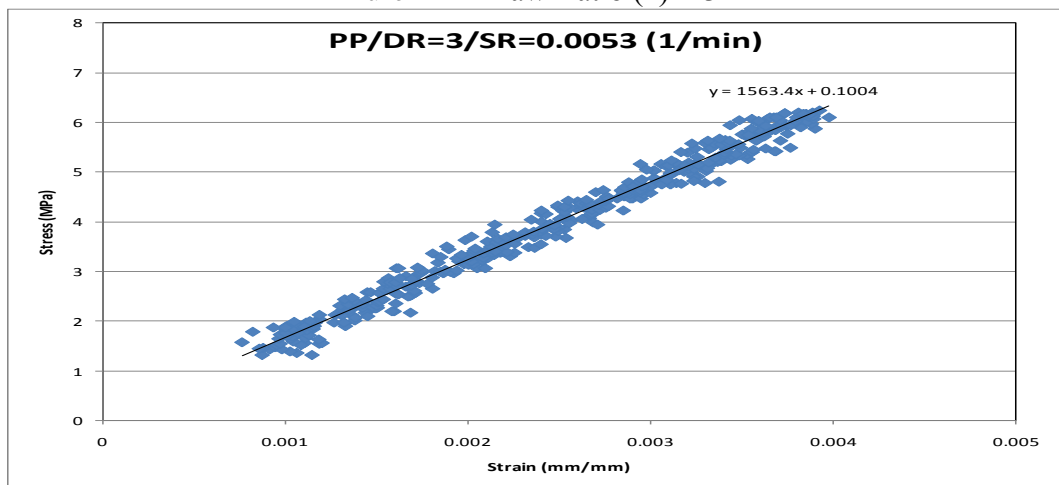


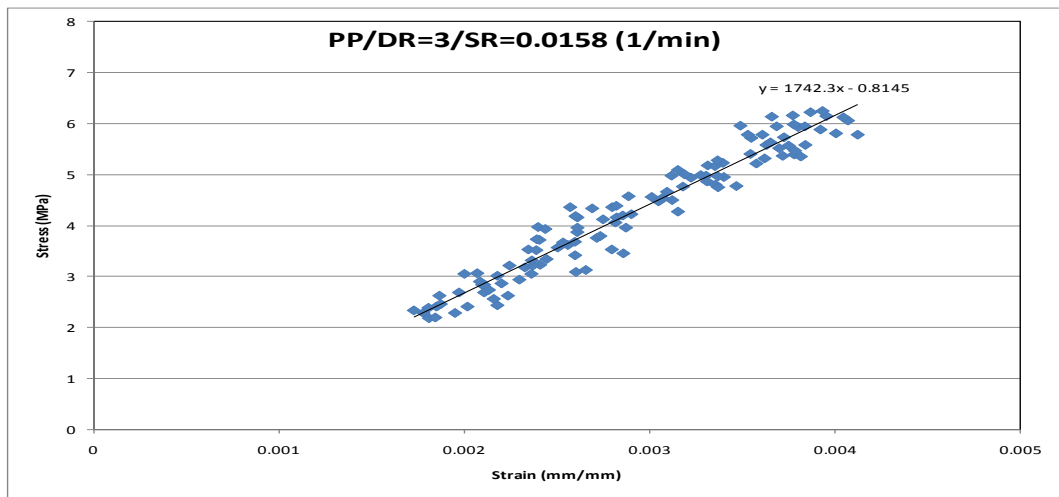
PP + 3% Clay (MB) + 3%PPMA (MB) - Draw Ratio (λ) = 2



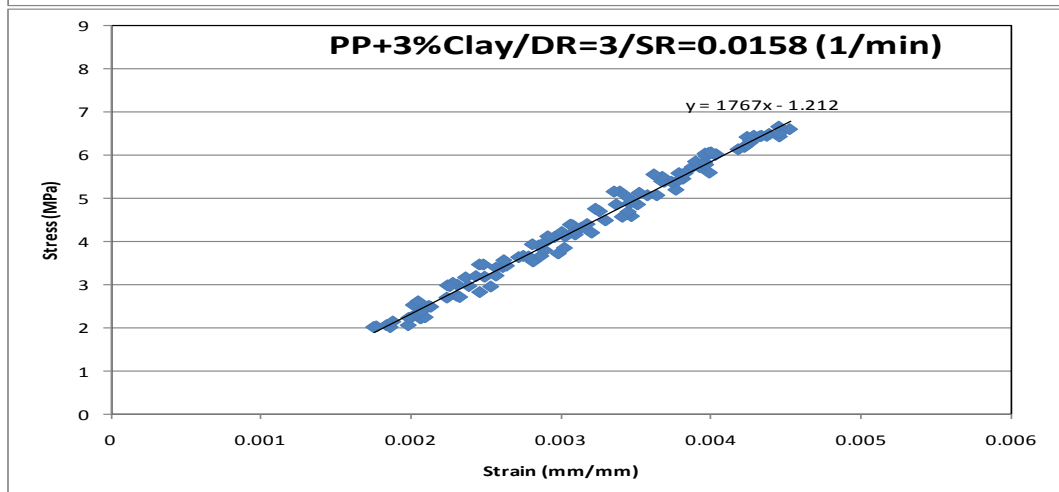
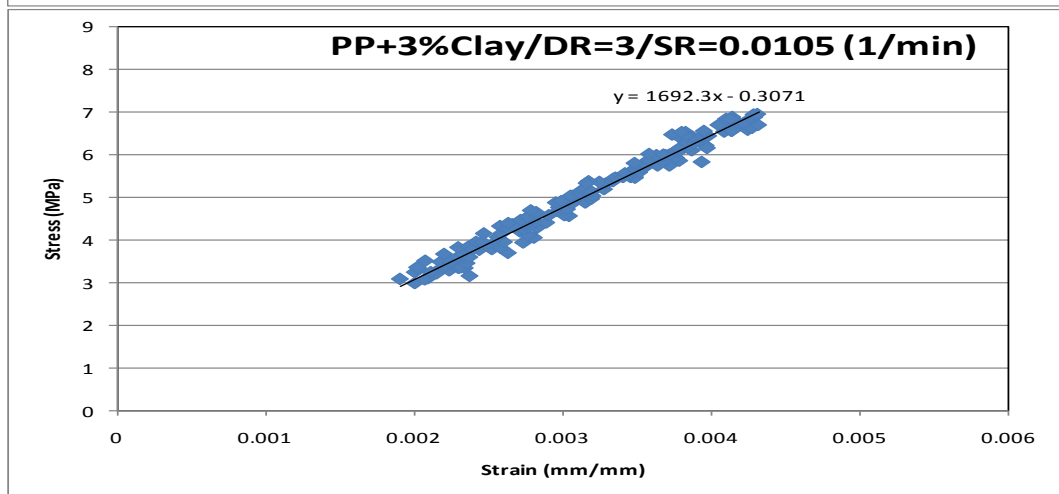
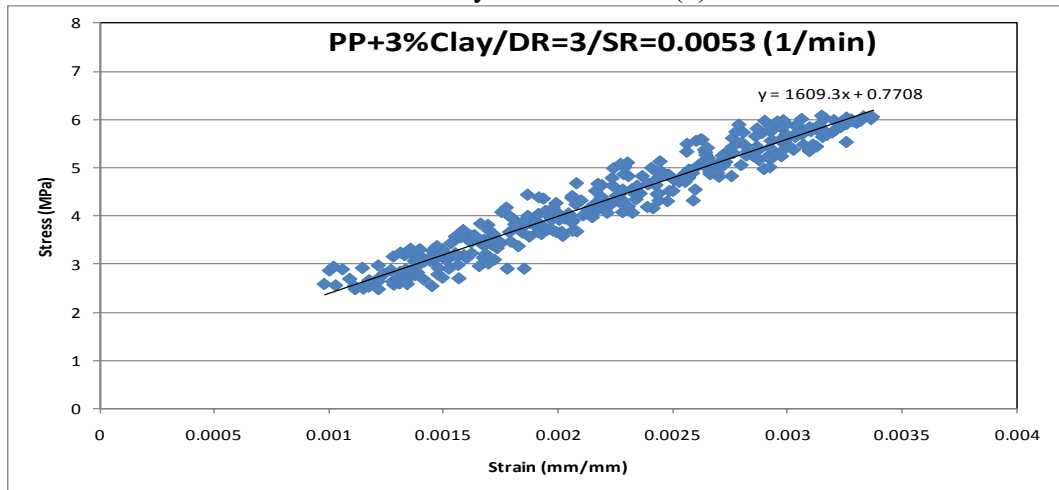


Pure PP - Draw Ratio (λ) = 3

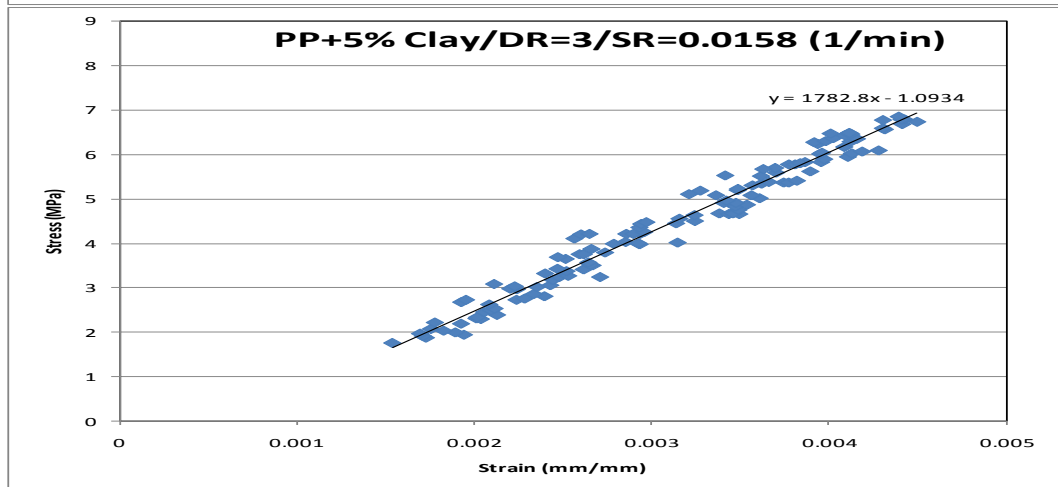
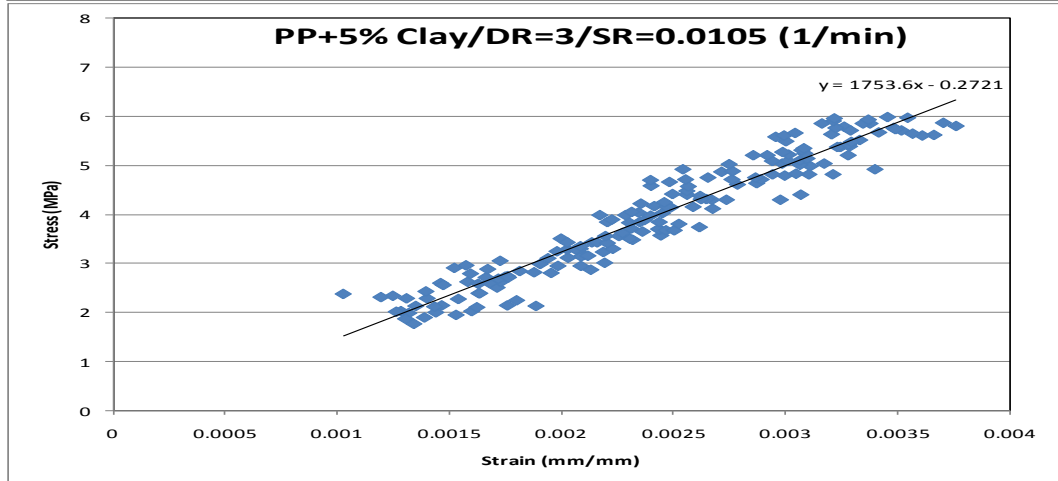
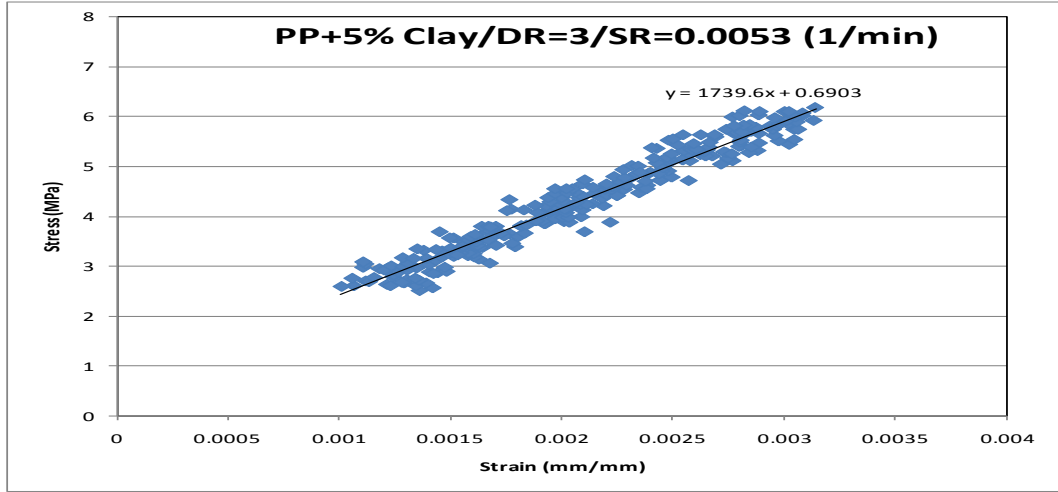




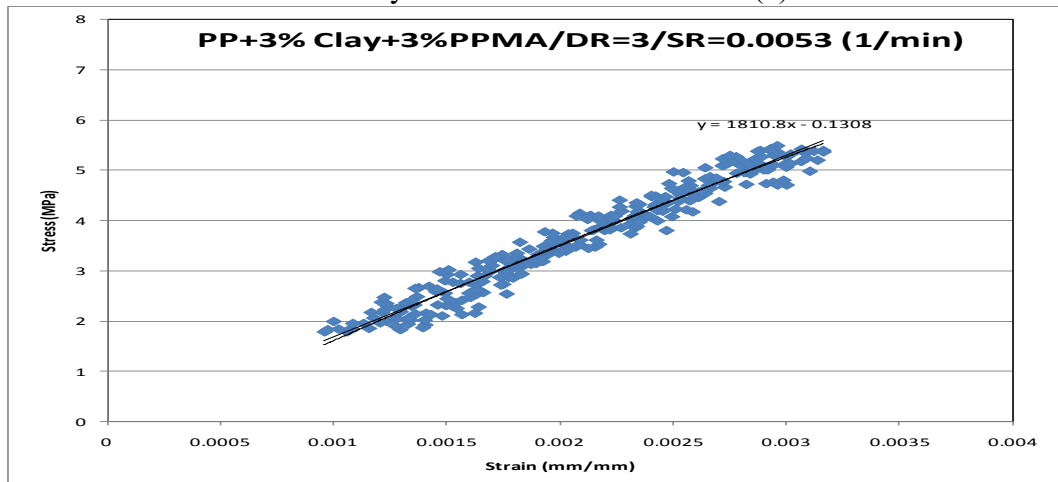
PP + 3% Clay - Draw Ratio (λ) = 3

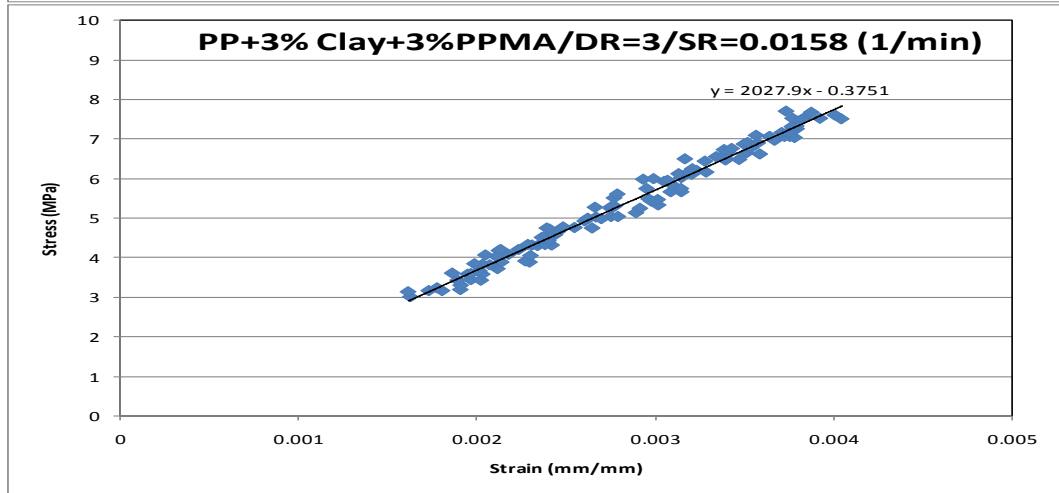
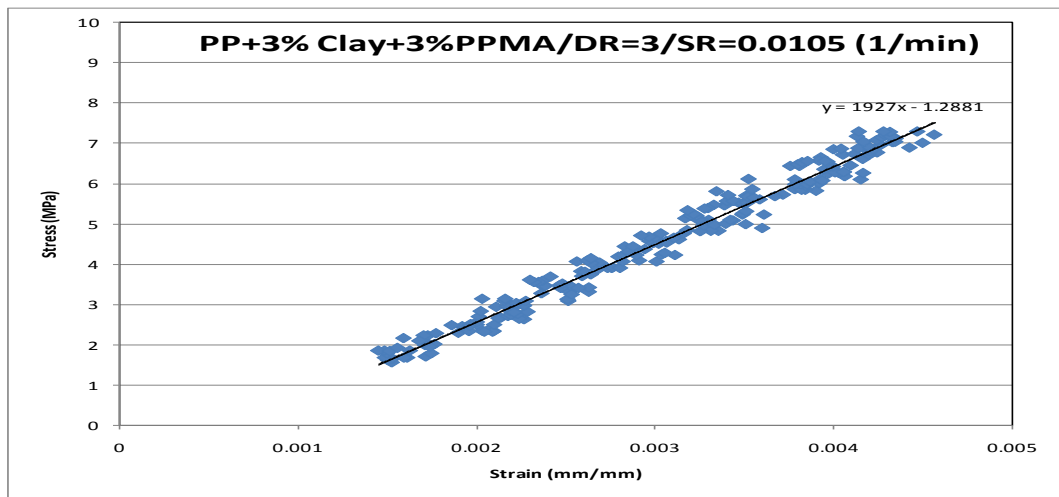


PP + 5% Clay - Draw Ratio (λ) = 3

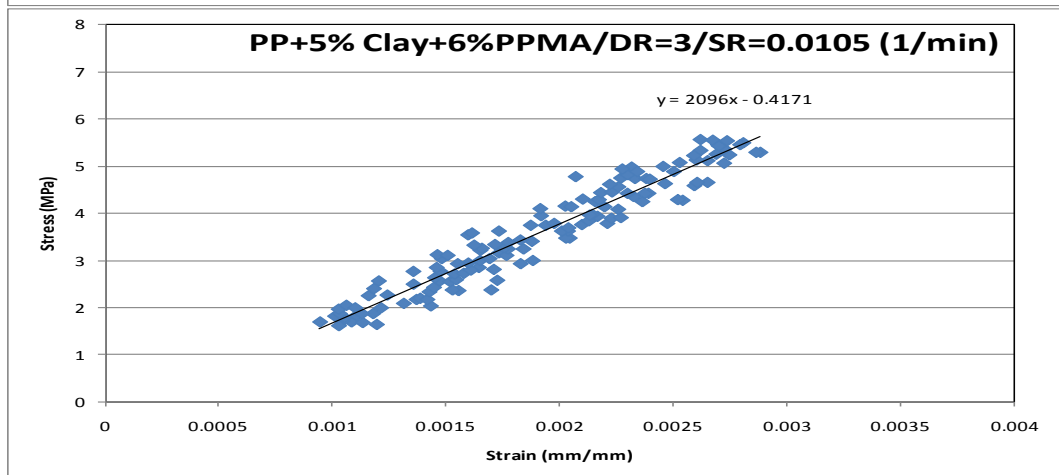
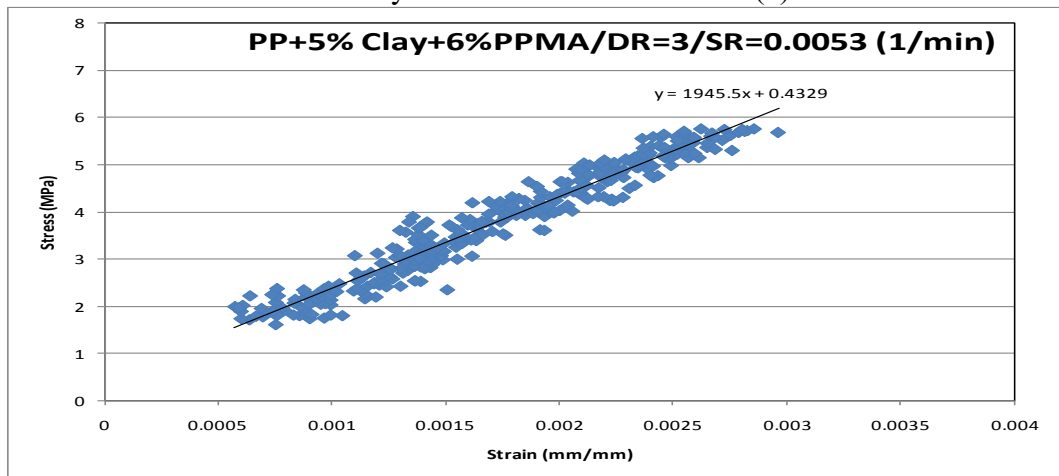


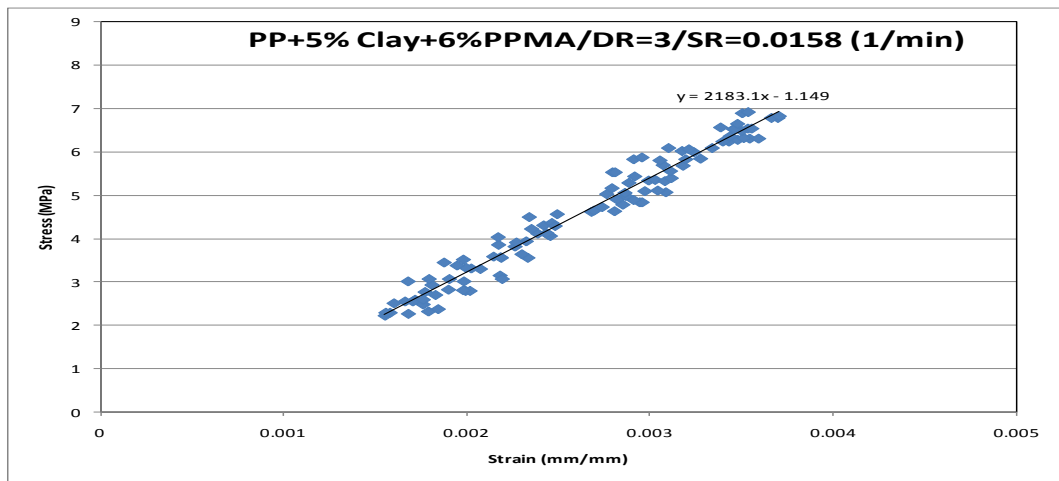
PP + 3% Clay + 3% PPMA - Draw Ratio (λ) = 3



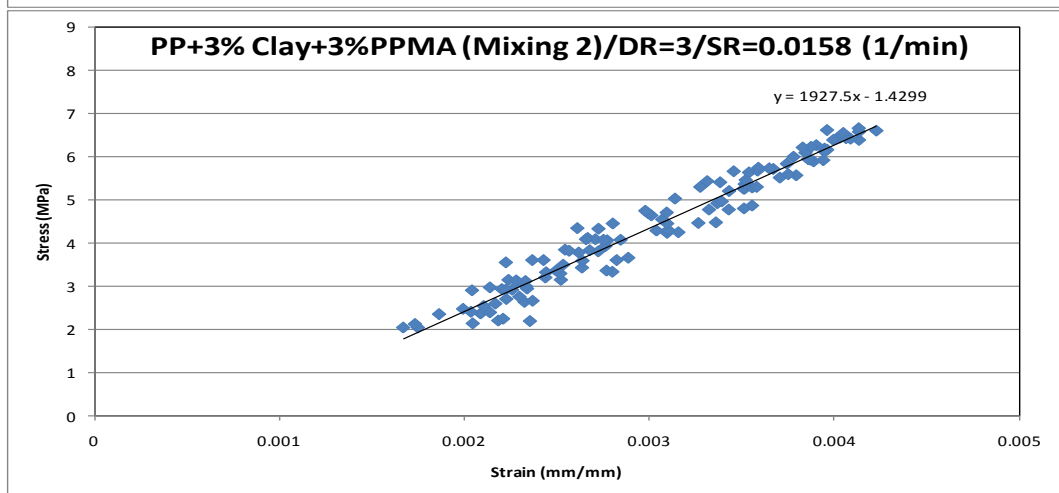
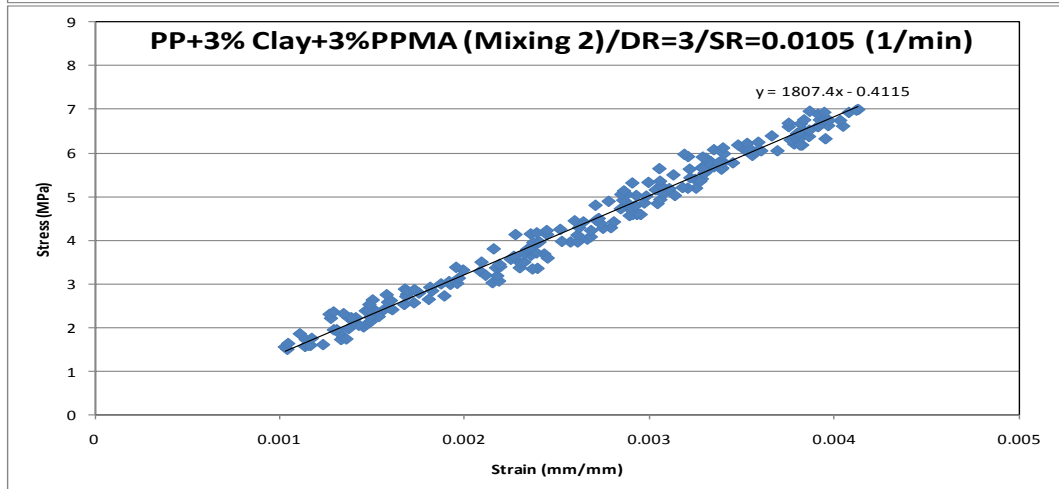
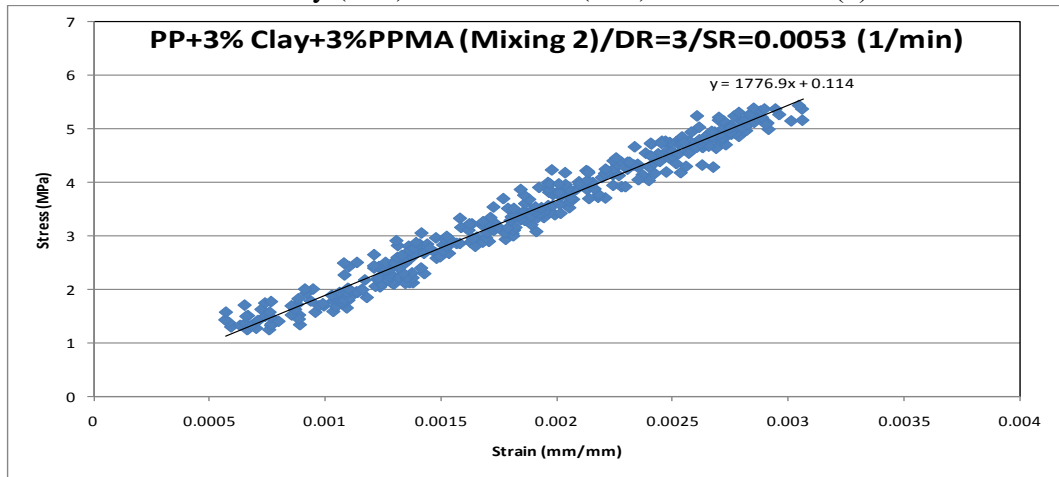


PP + 5% Clay + 6%PPMA - Draw Ratio (λ) = 3

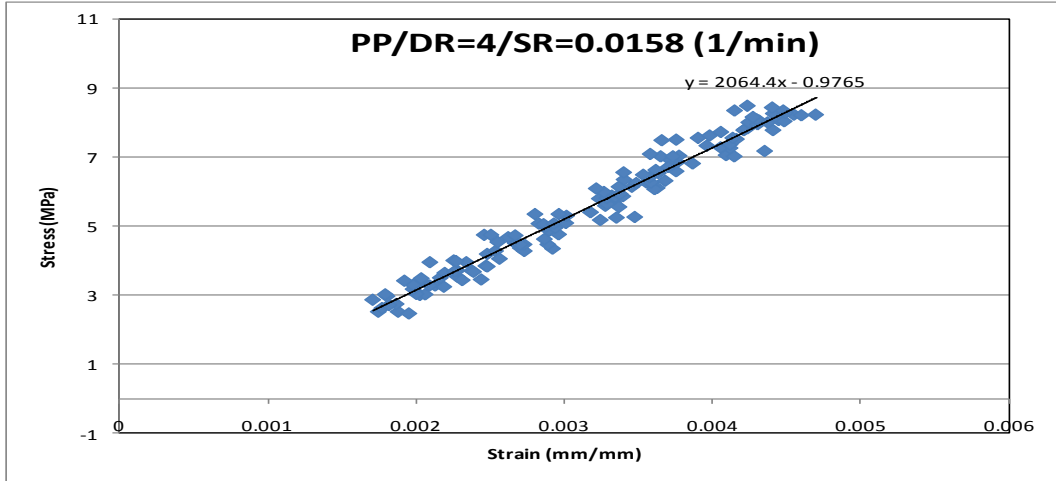
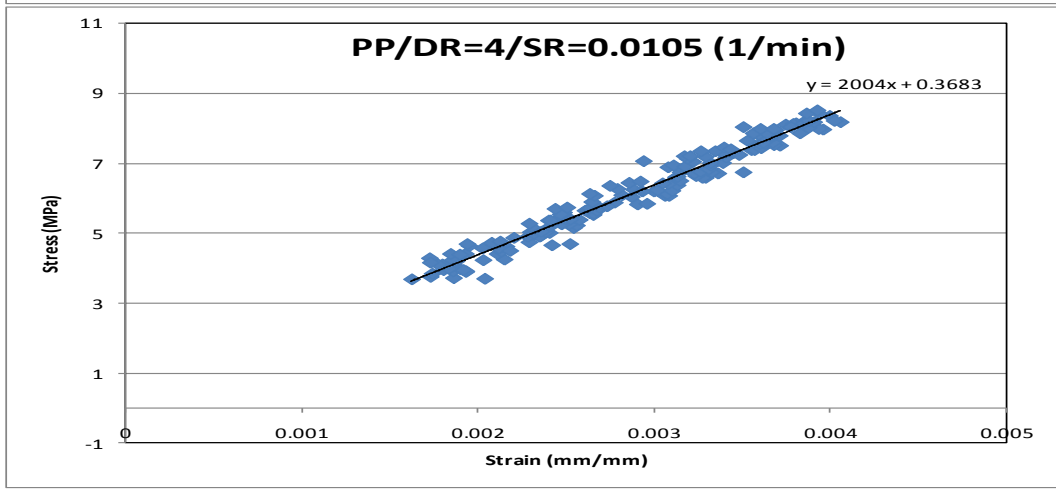
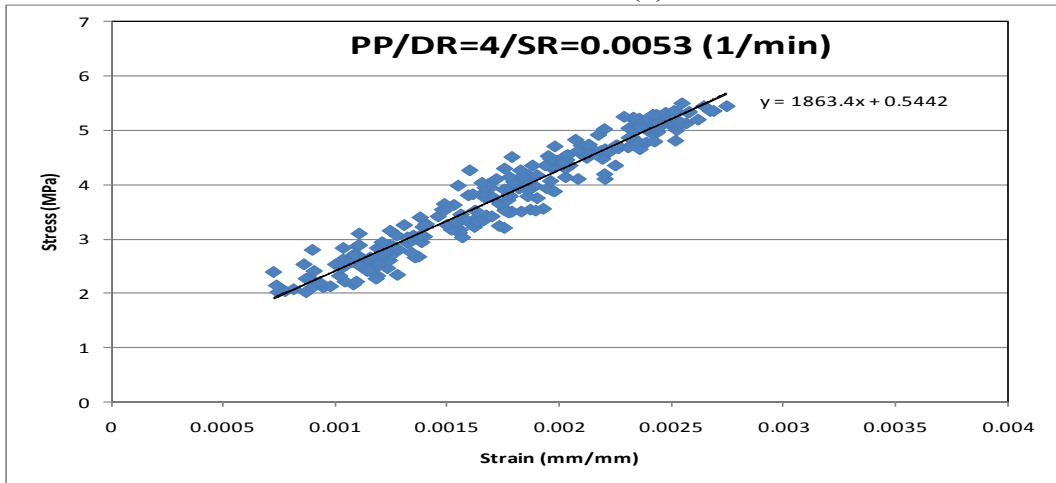




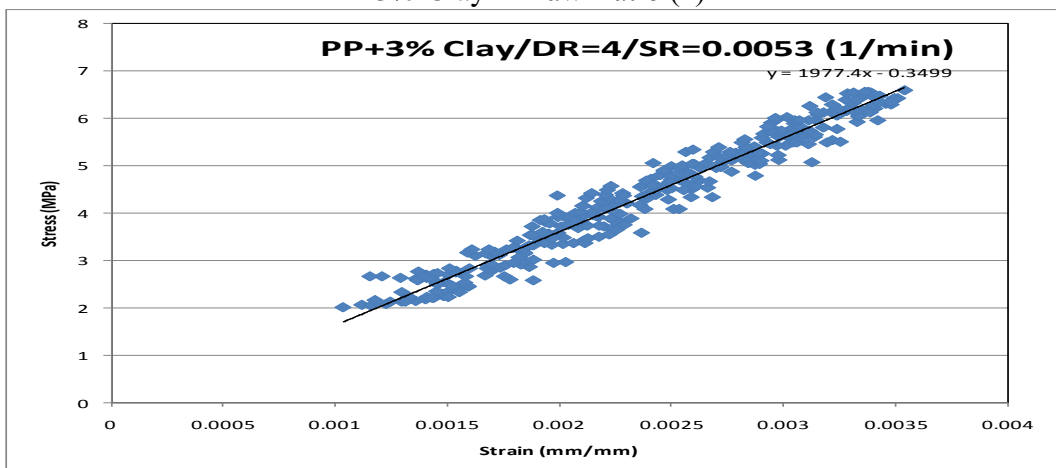
PP + 3% Clay (MB) + 3%PPMA (MB) - Draw Ratio (λ) = 3

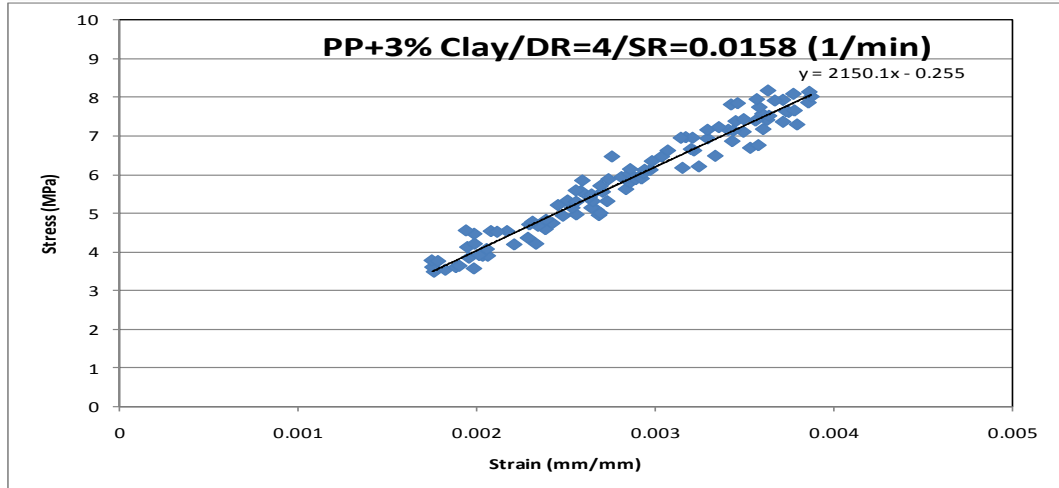
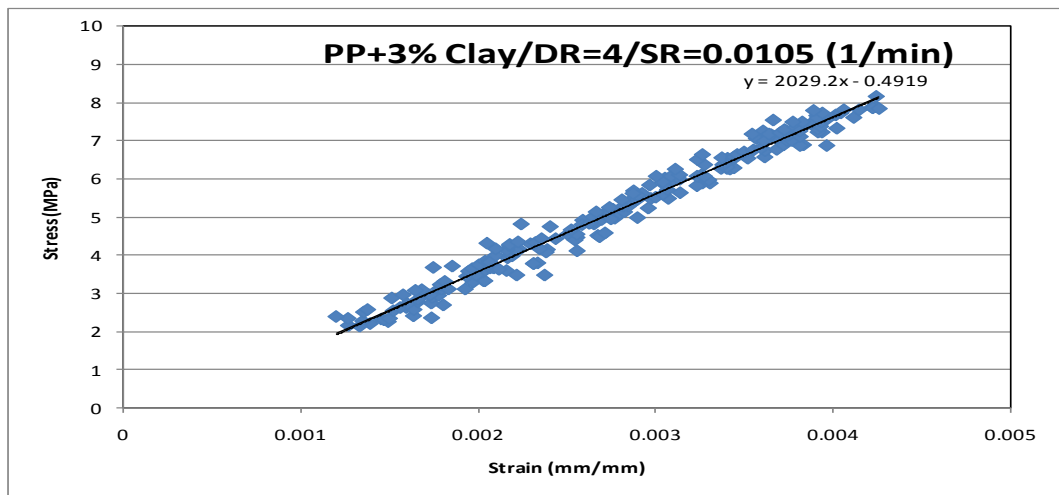


Pure PP - Draw Ratio (λ) = 4

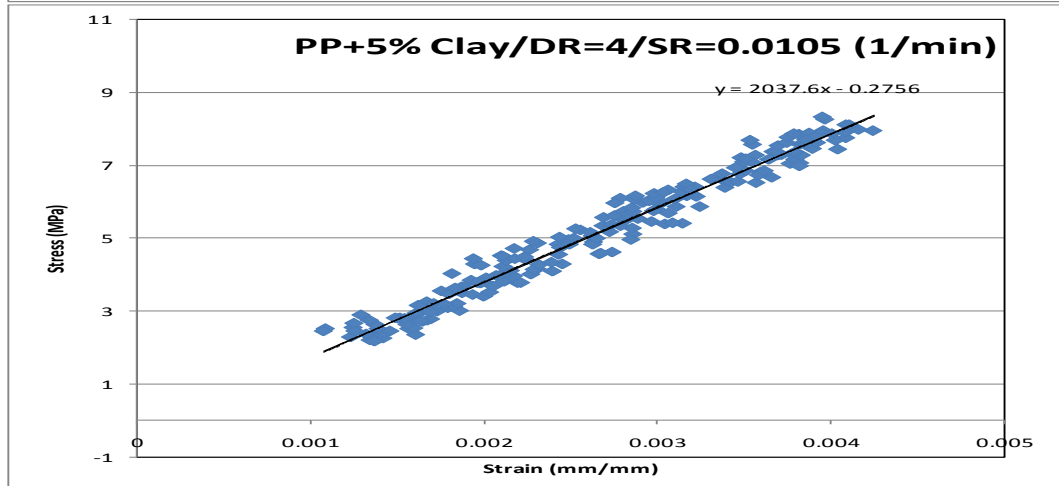
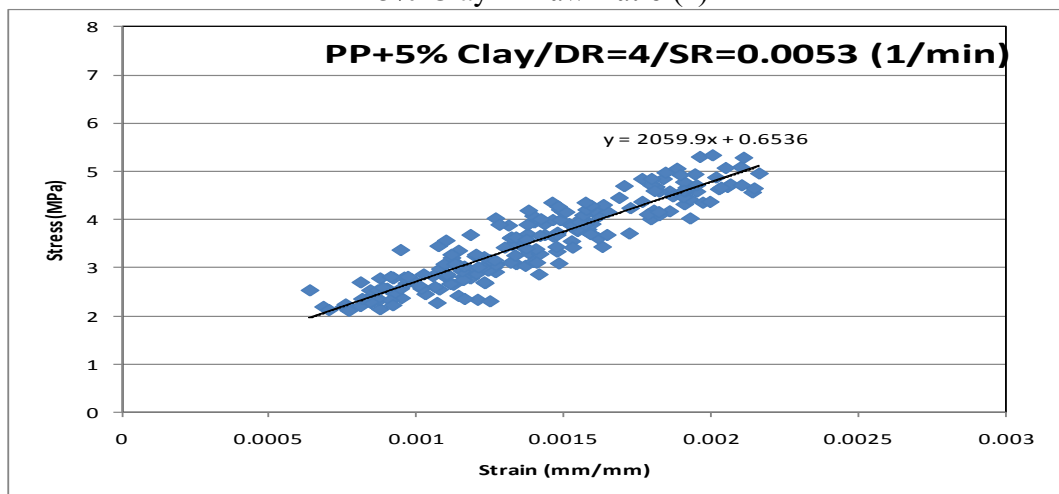


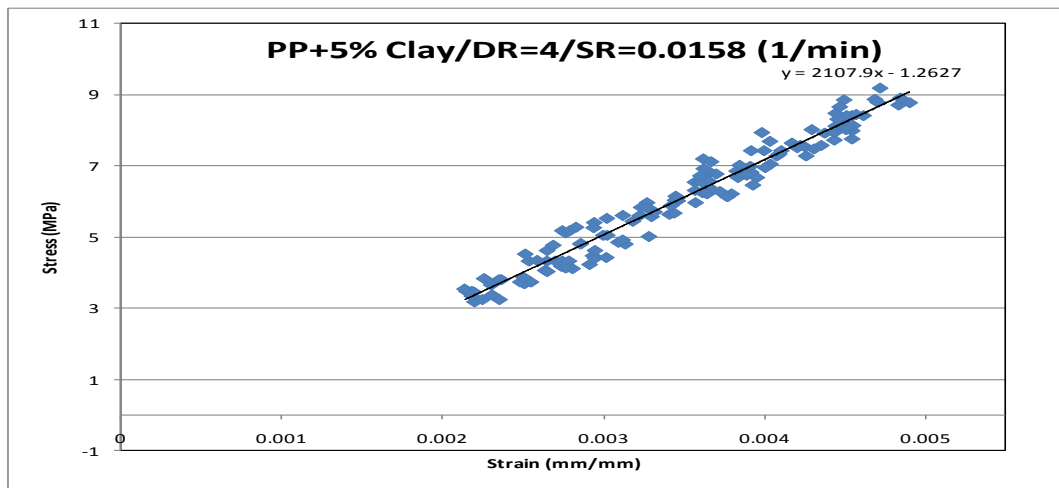
PP + 3% Clay - Draw Ratio (λ) = 4



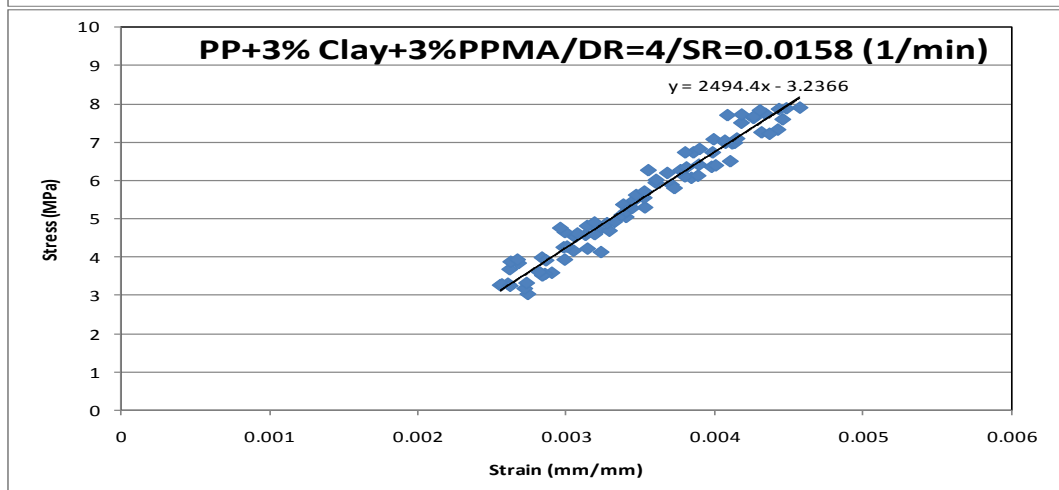
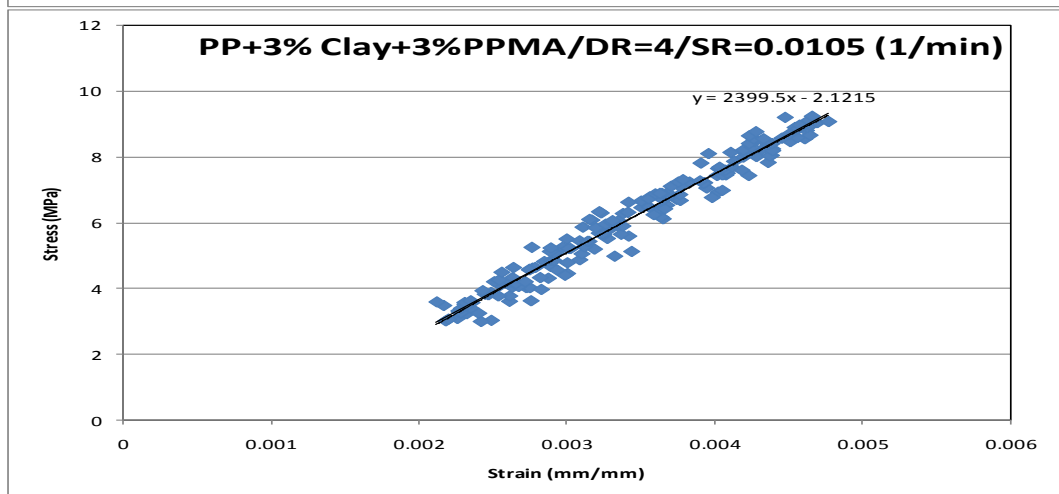
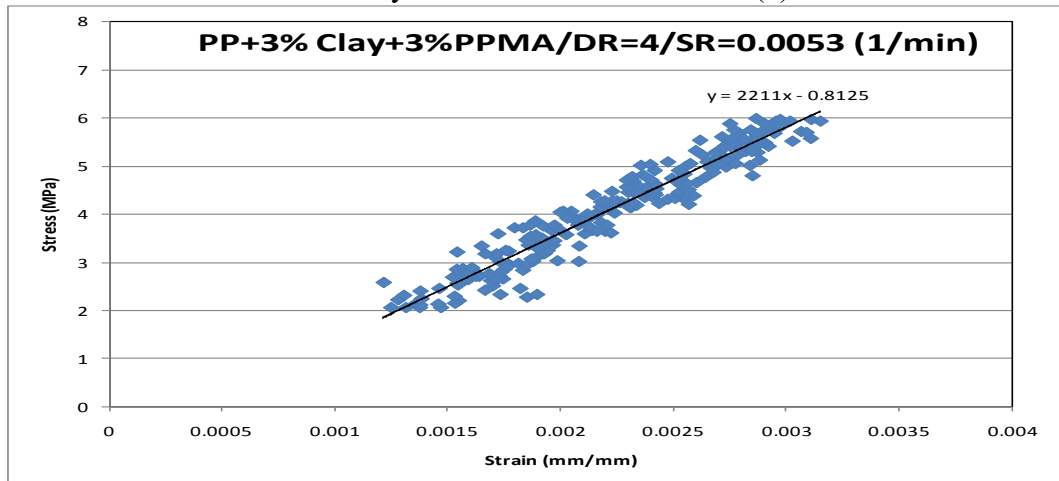


PP + 5% Clay - Draw Ratio (λ) = 4

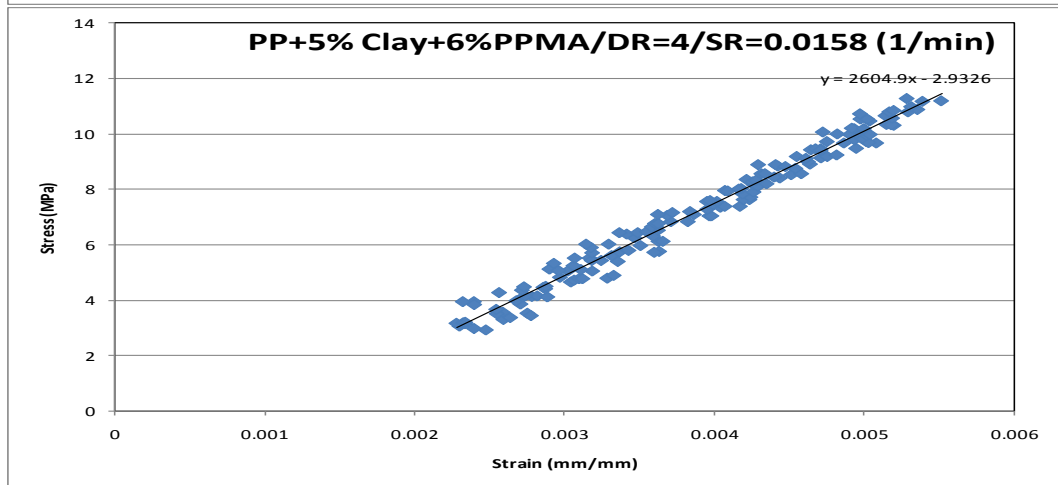
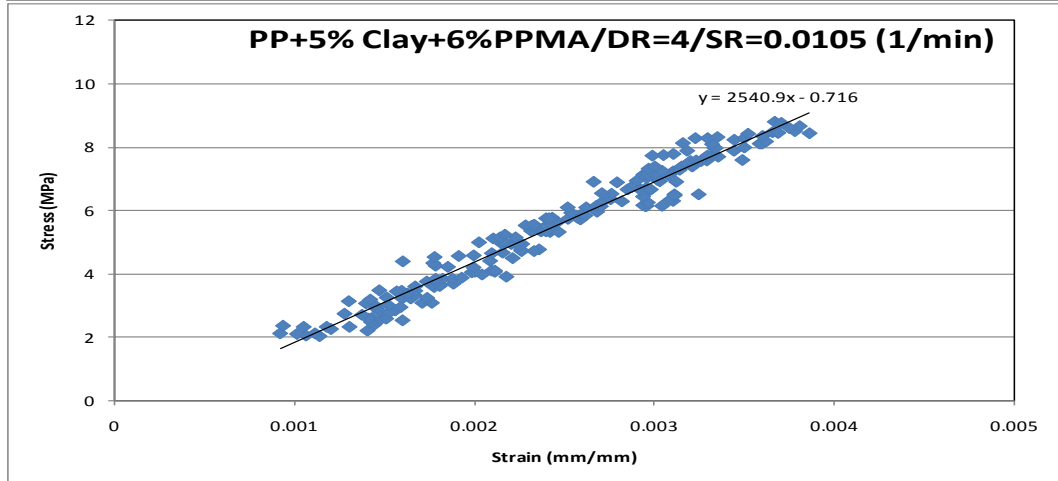
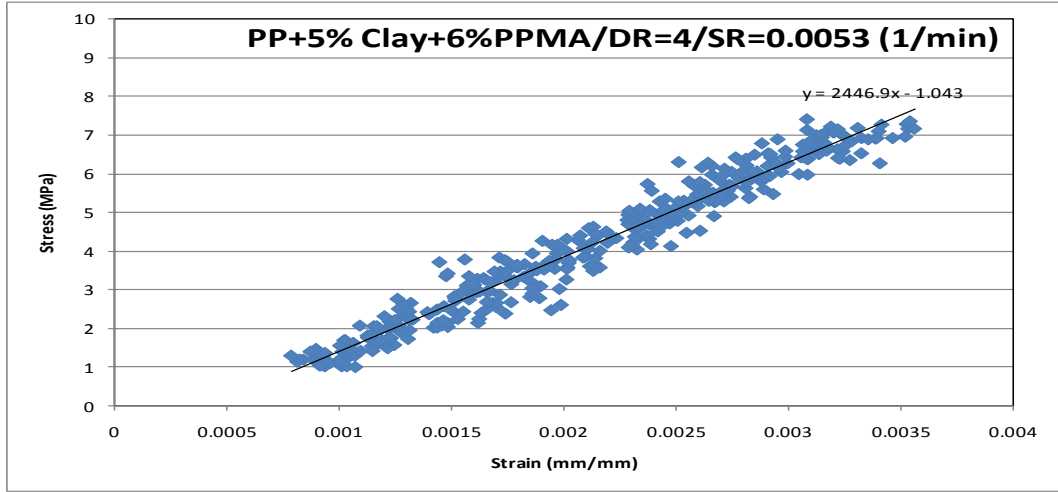




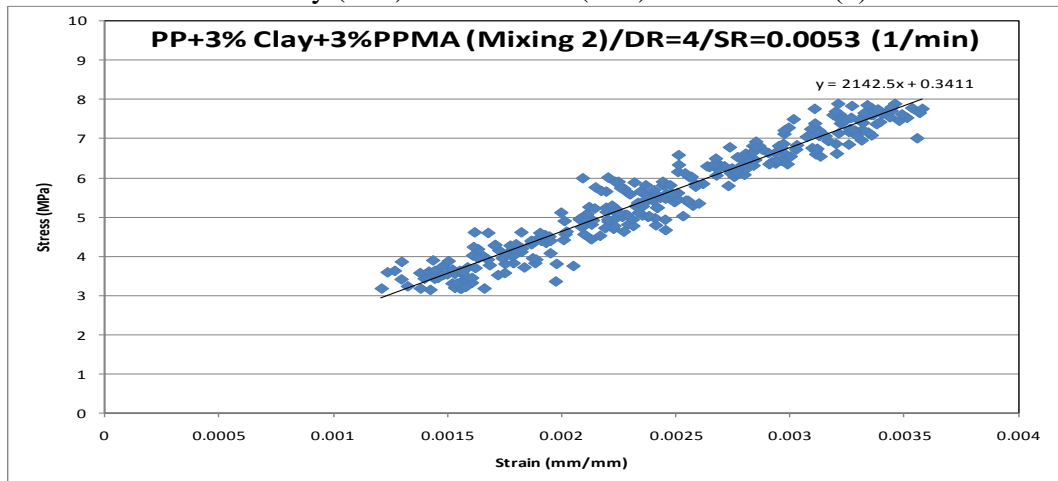
PP + 3% Clay + 3%PPMA - Draw Ratio (λ) = 4

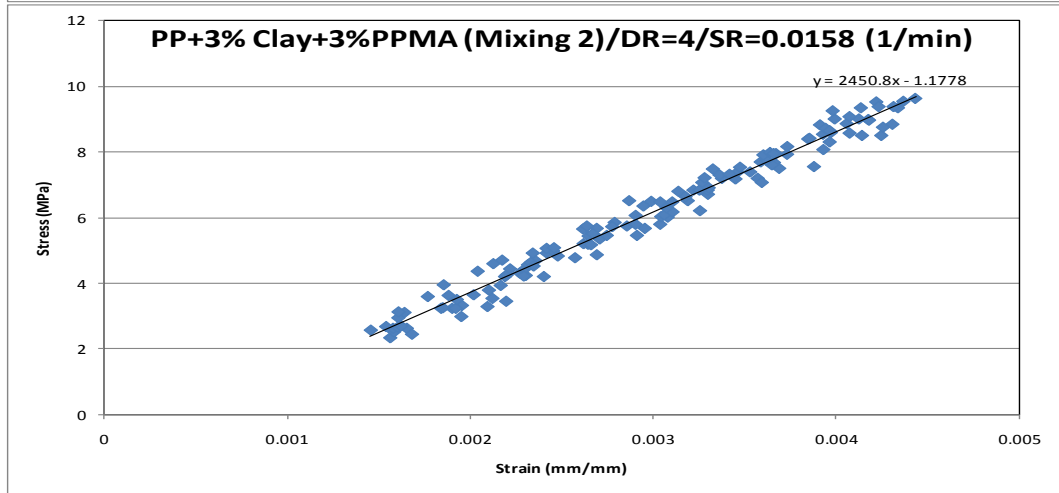
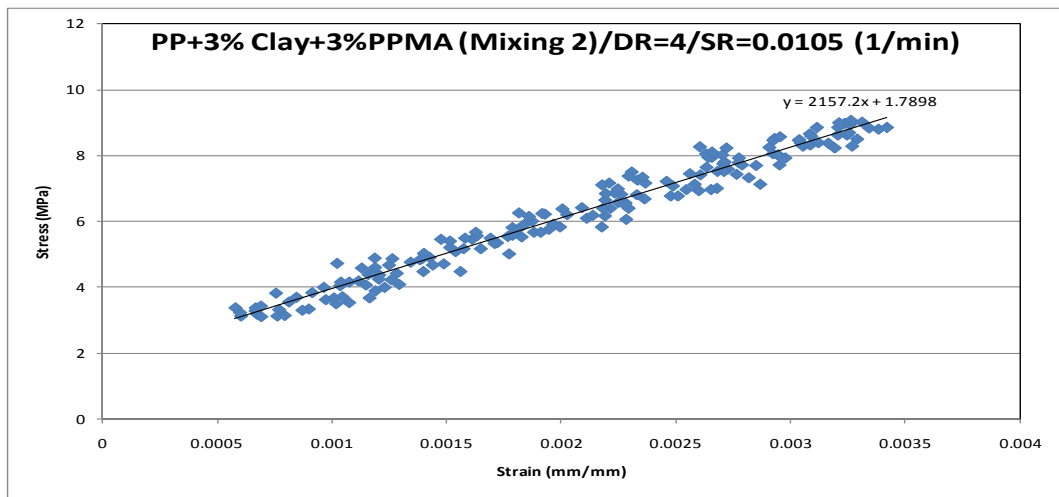


PP + 5% Clay + 6%PPMA - Draw Ratio (λ) = 4

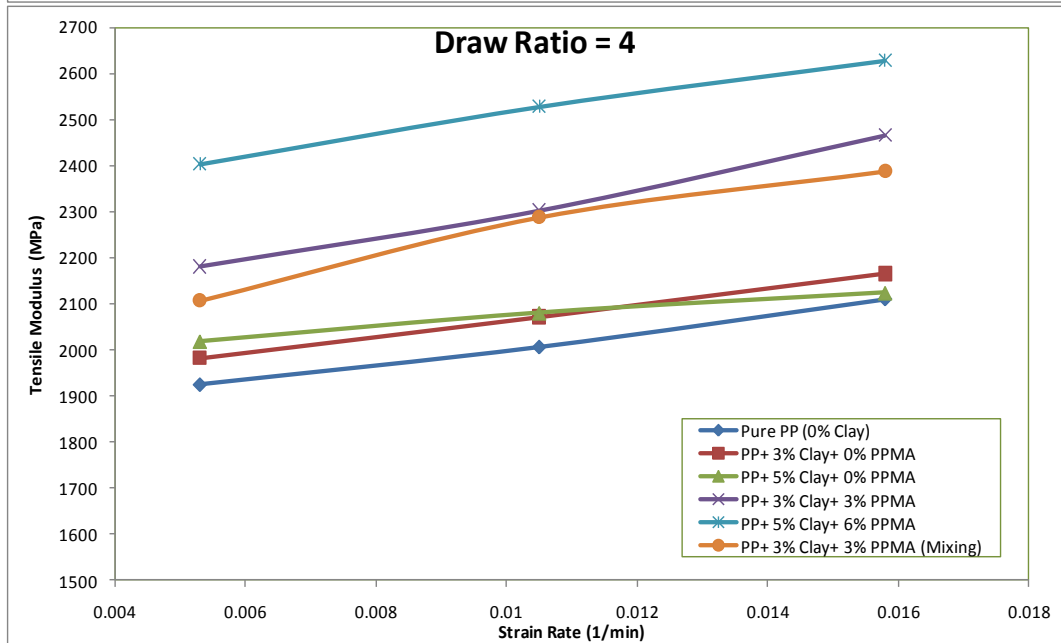
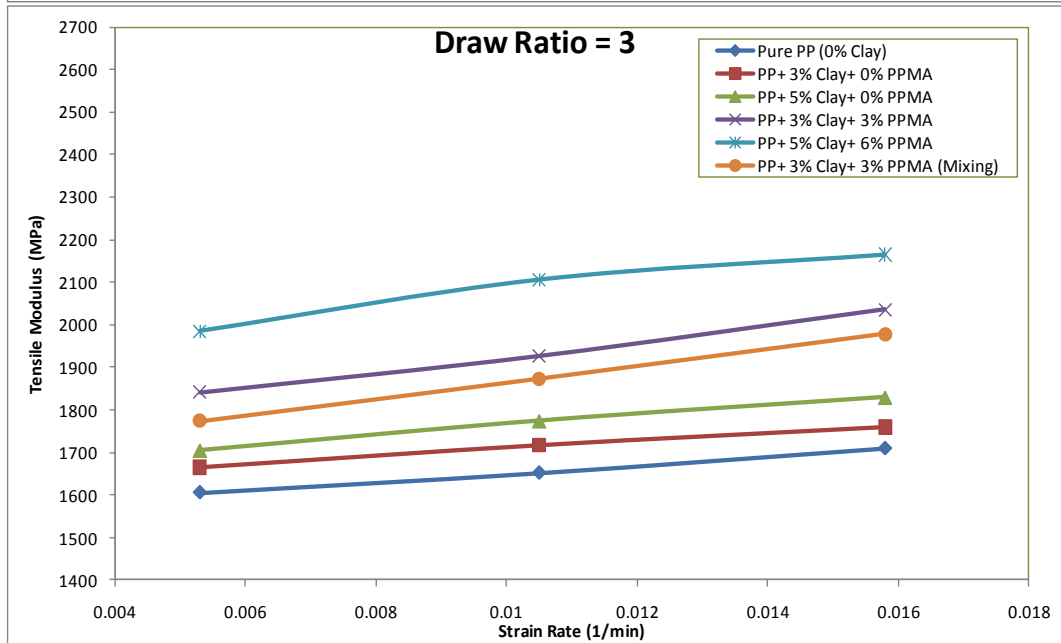
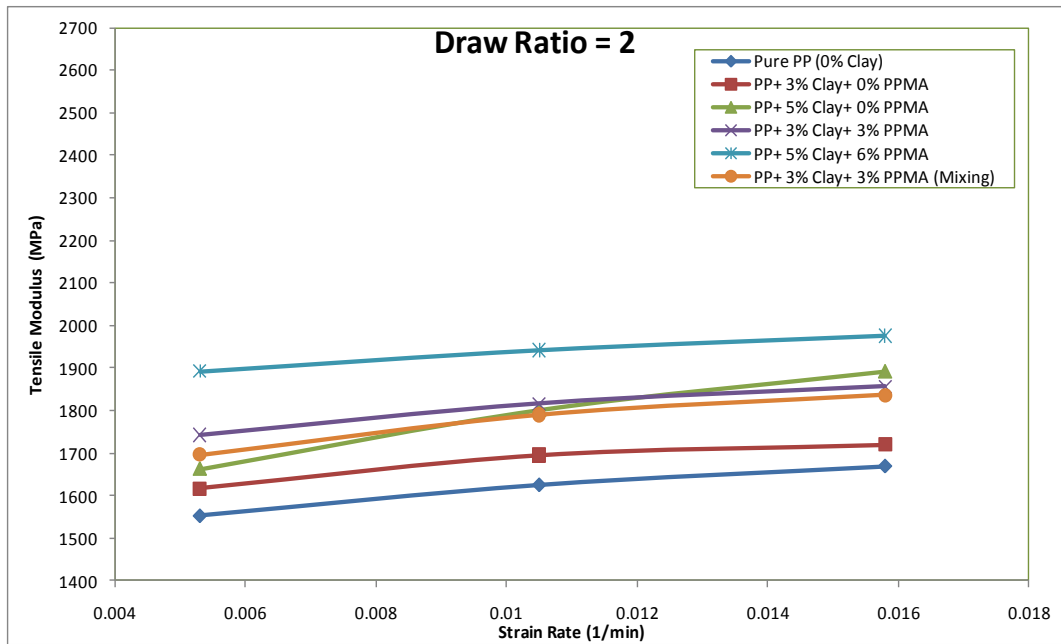


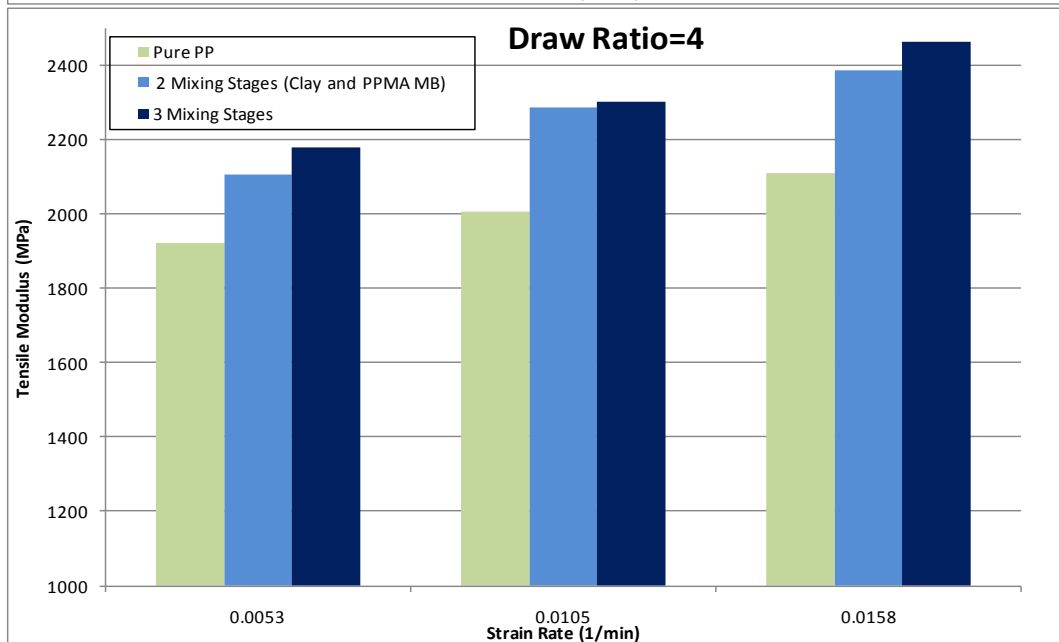
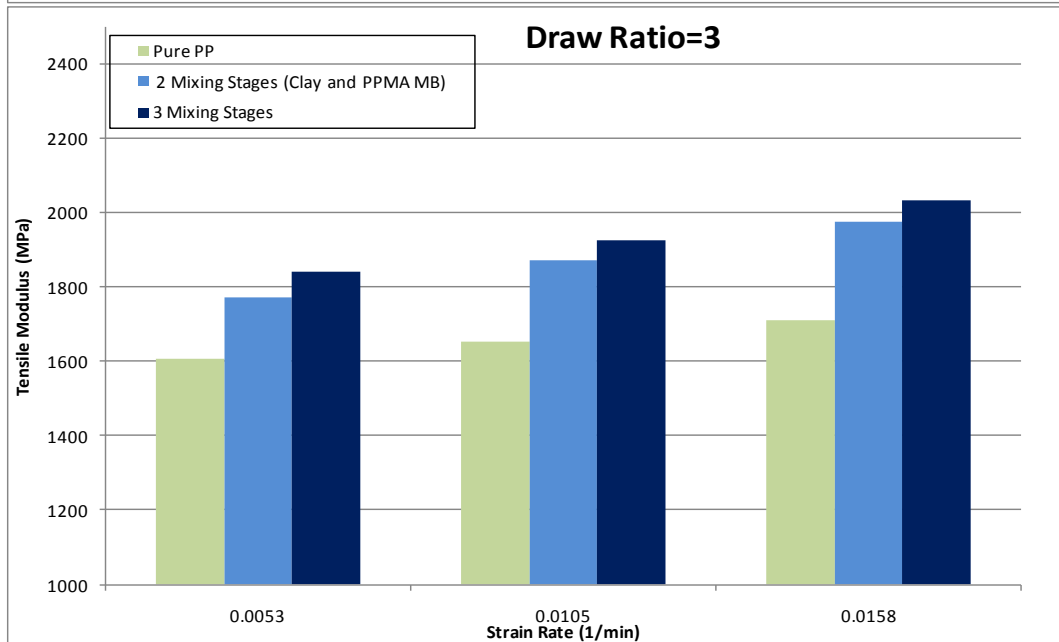
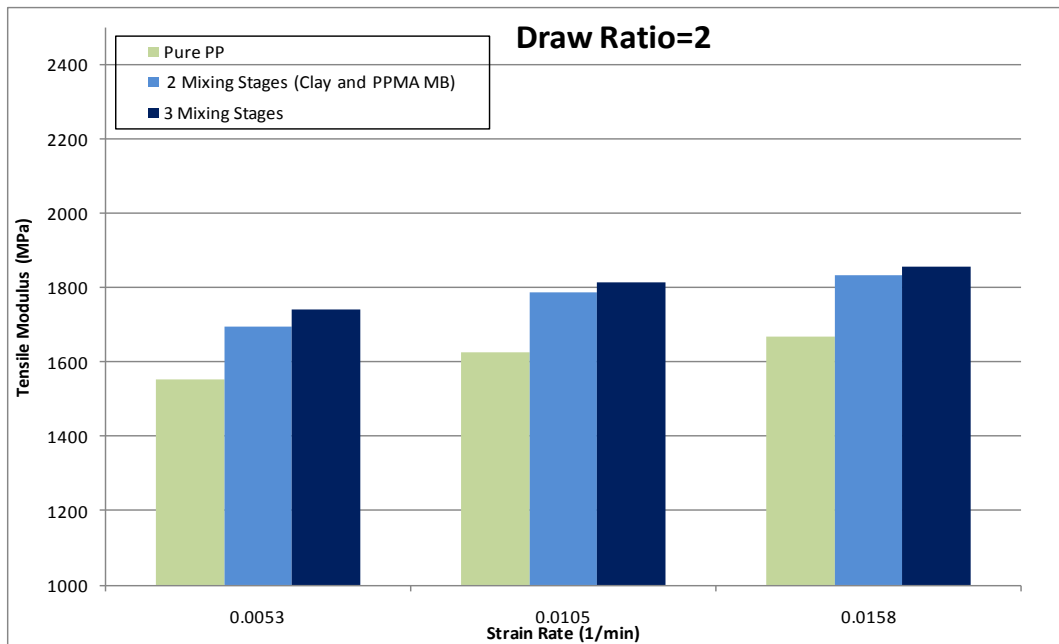
PP + 3% Clay (MB) + 3%PPMA (MB) - Draw Ratio (λ) = 4





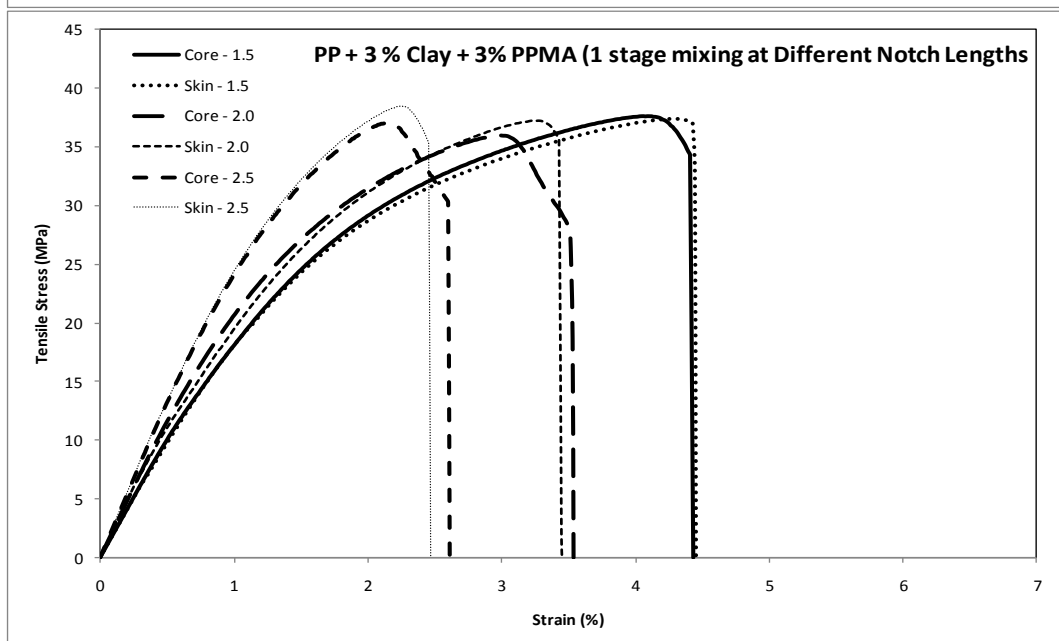
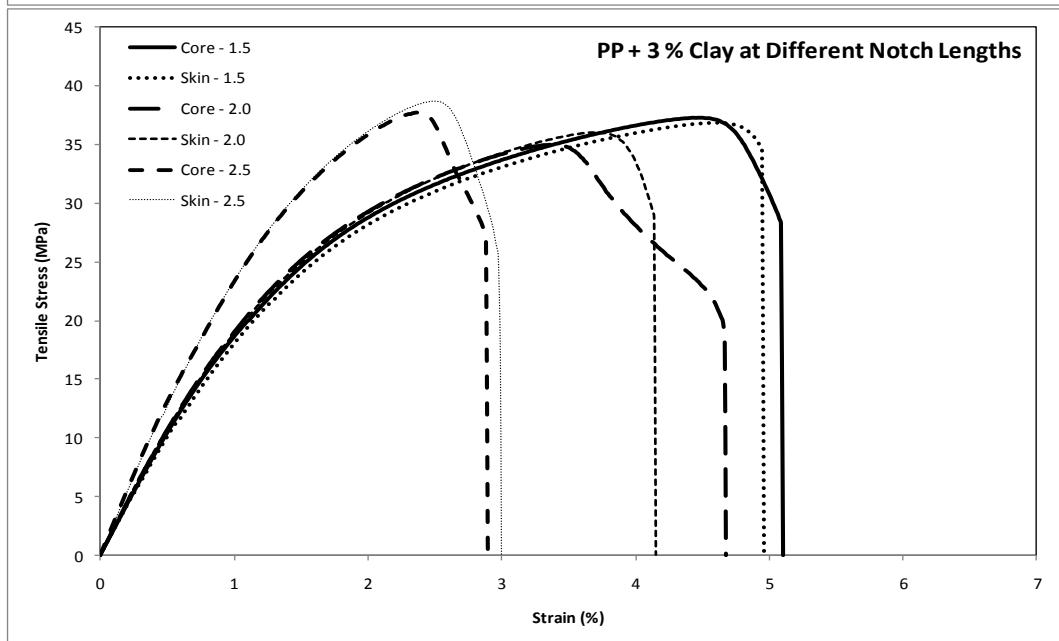
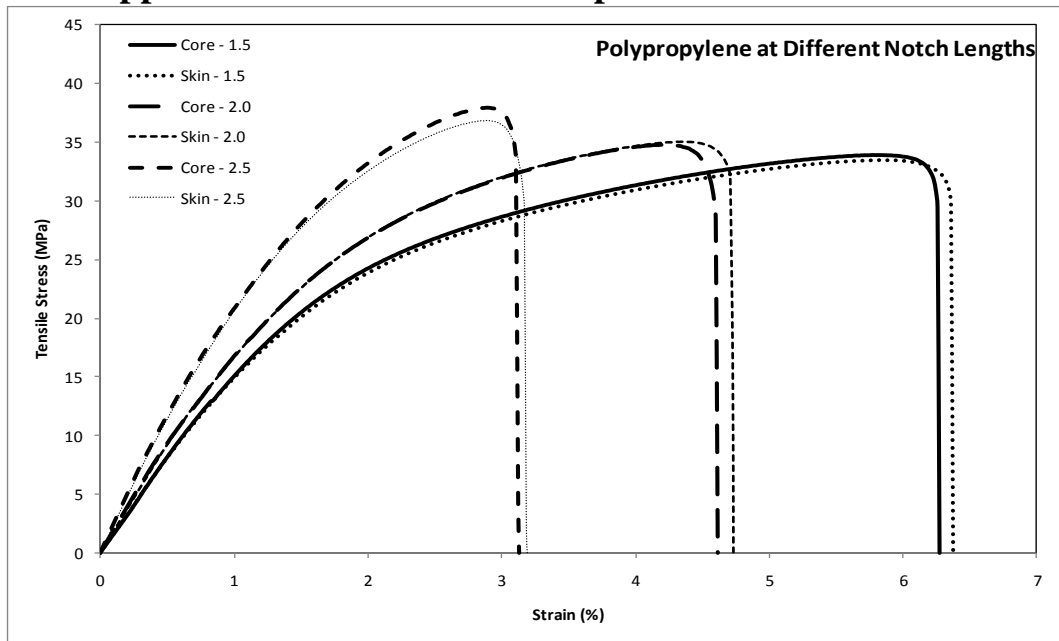
Appendix H2: Tensile Video Extensometer (Strain Rate Effect on Modulus) for Injection Moulded bars

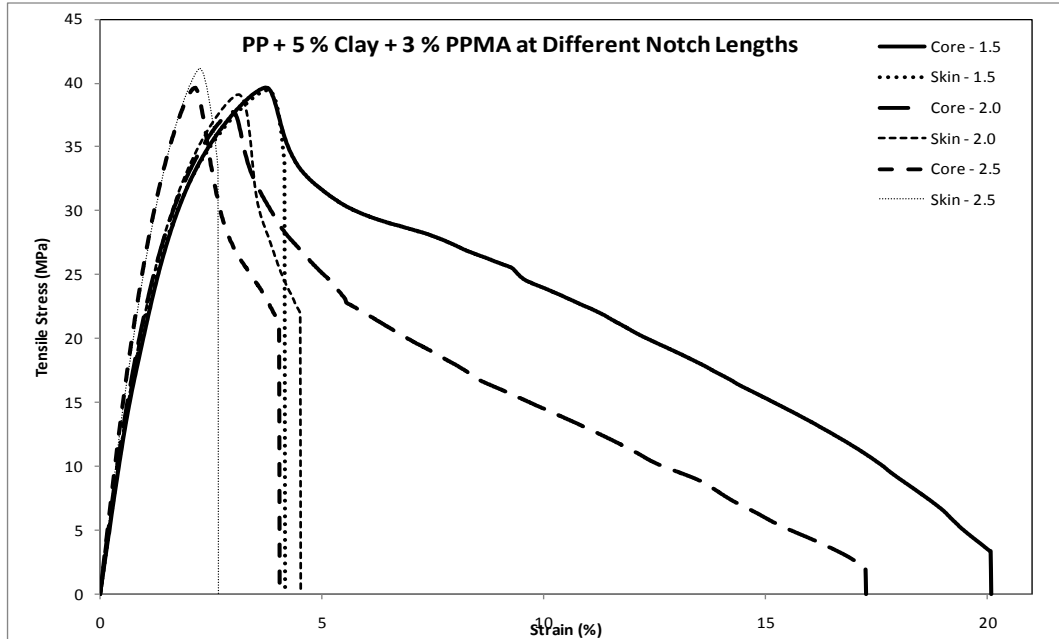
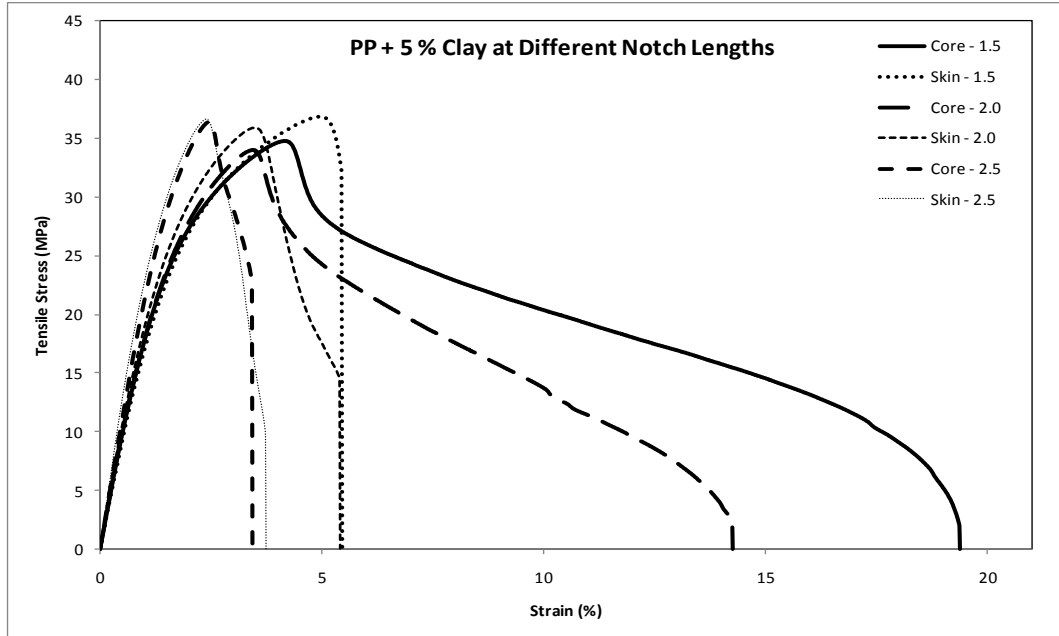
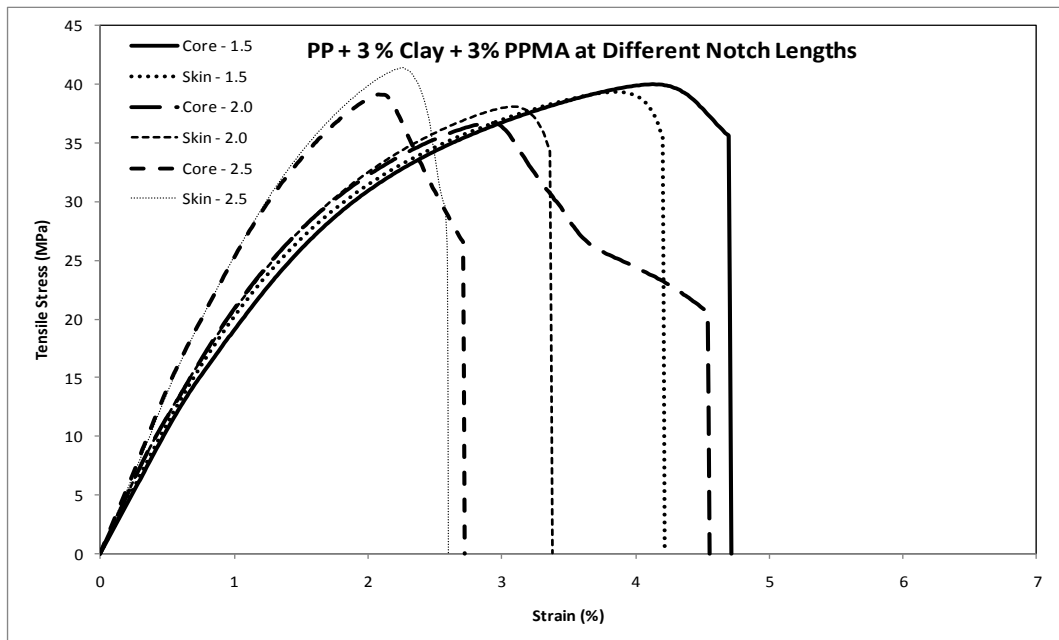


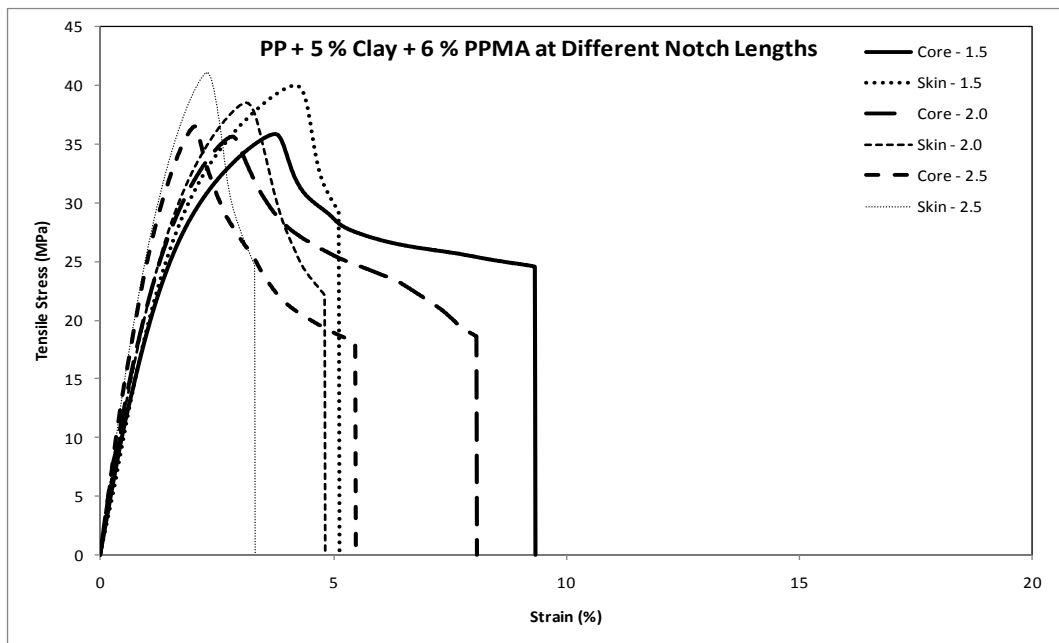


Appendix I: Tensile Fracture Stress-Strain Graphs of PPNCs

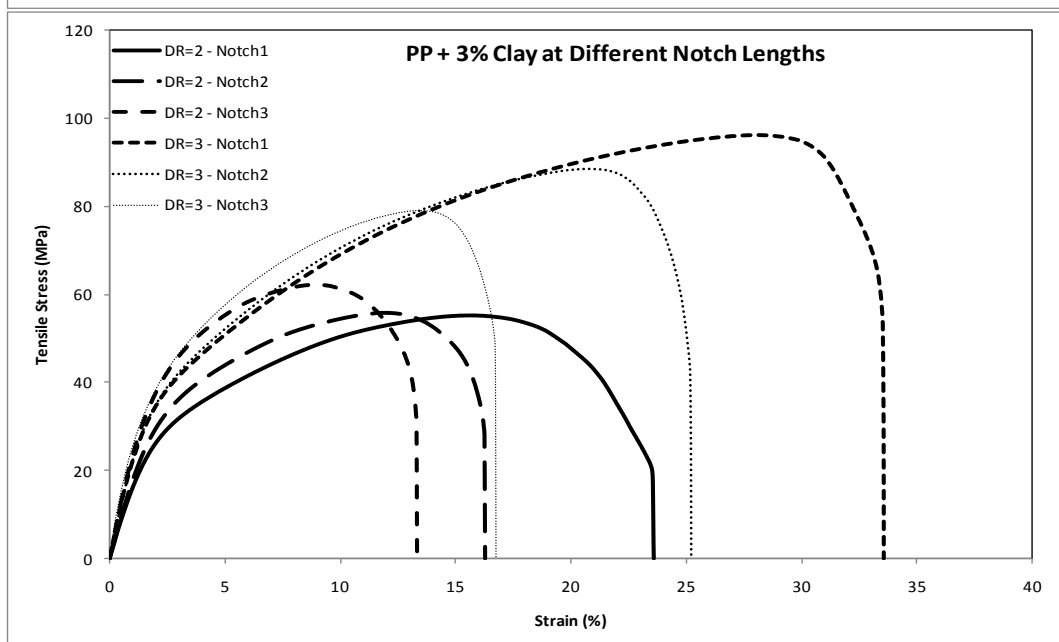
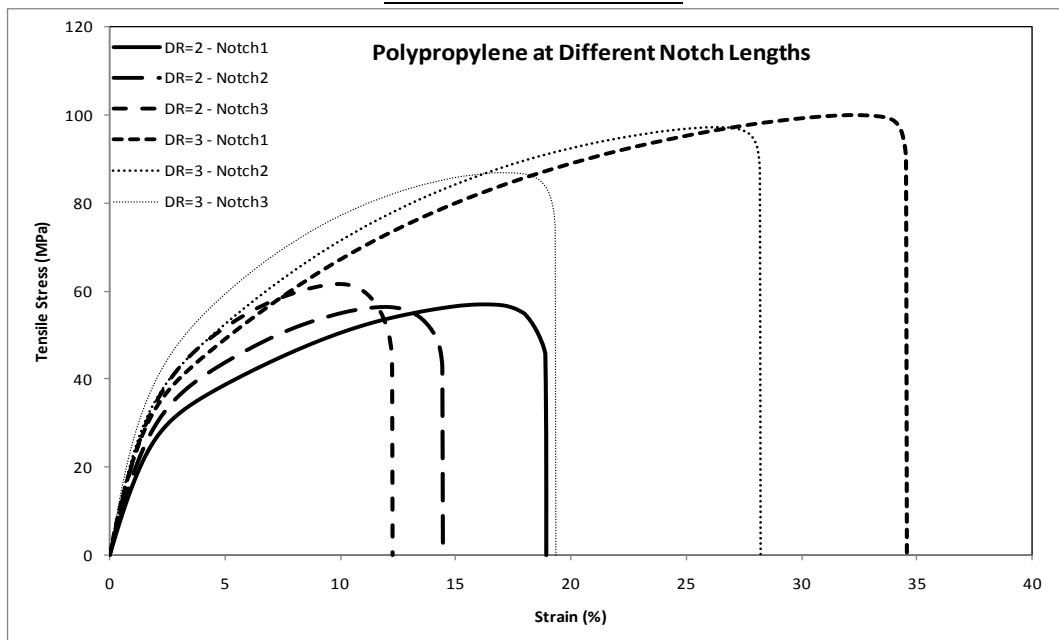
Appendix II: Stress-Strain Graphs of Undrawn PPNCs

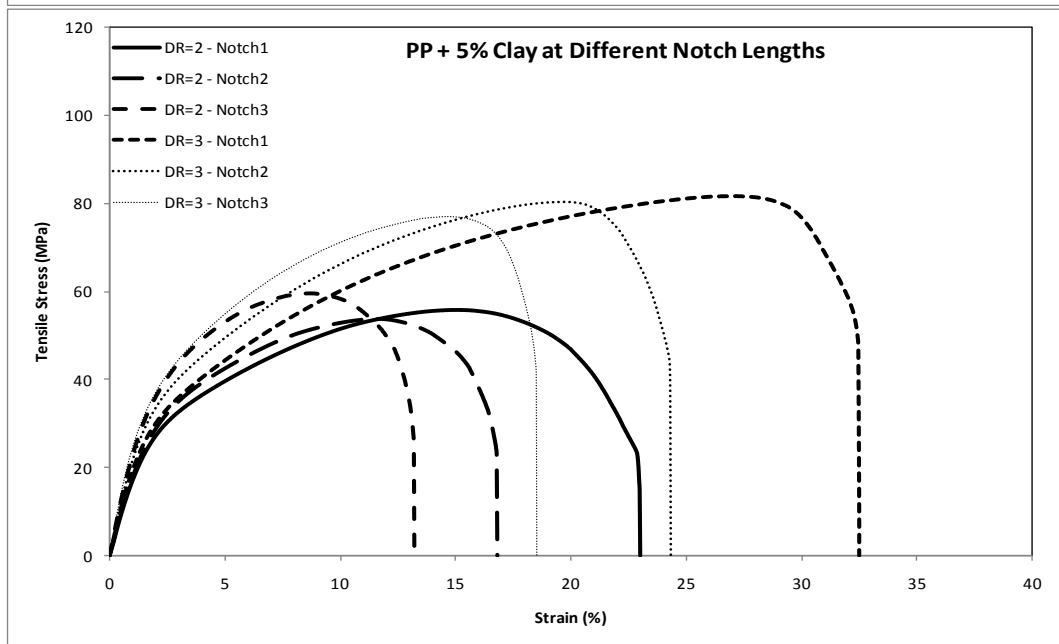
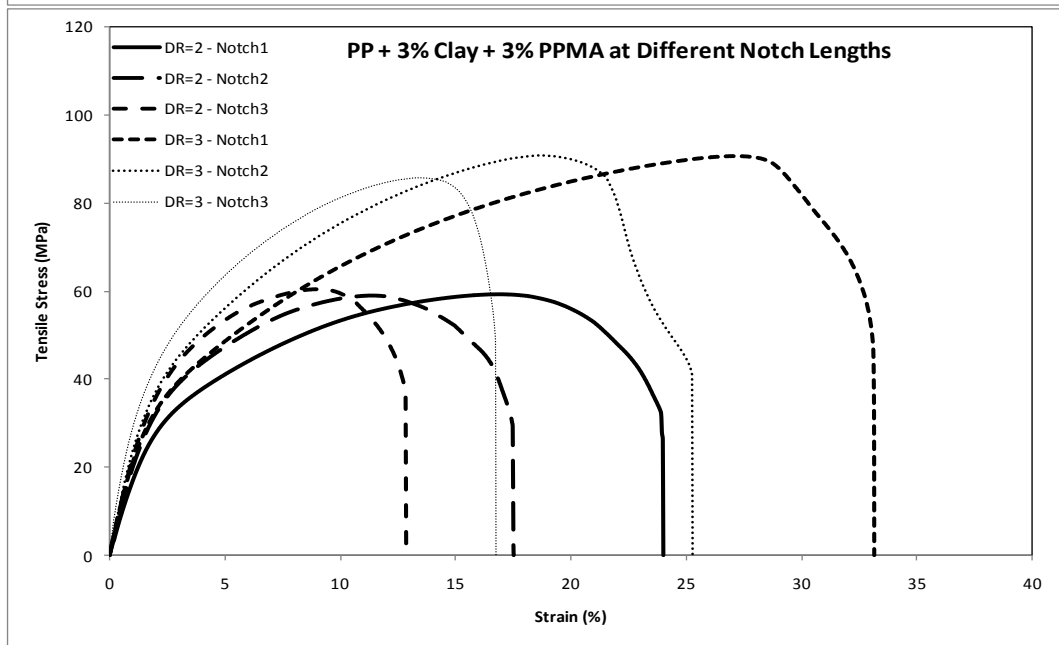
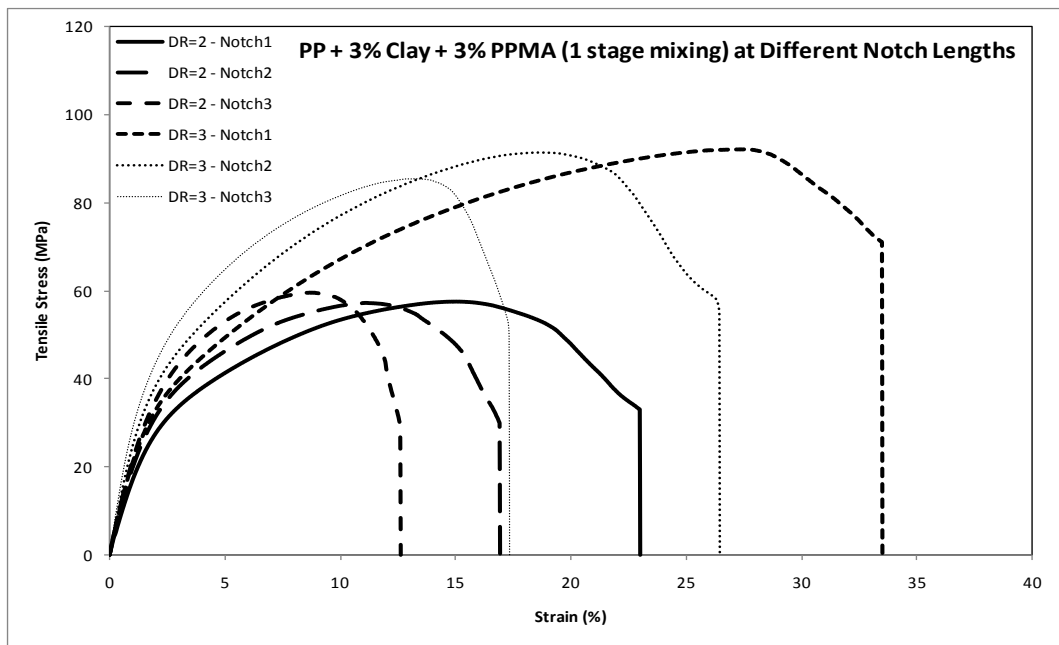


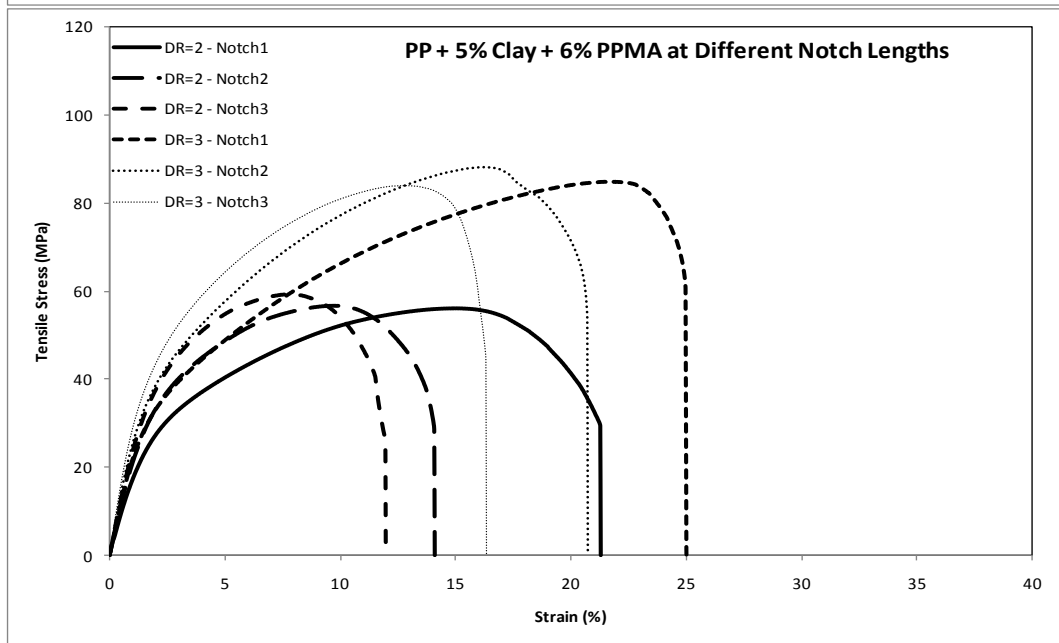
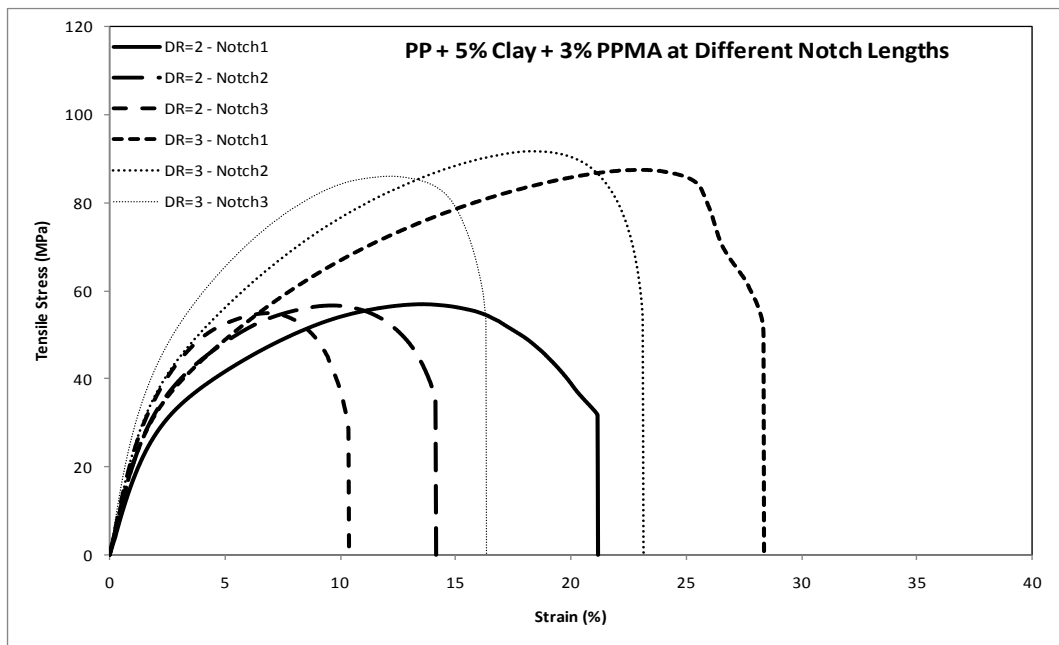




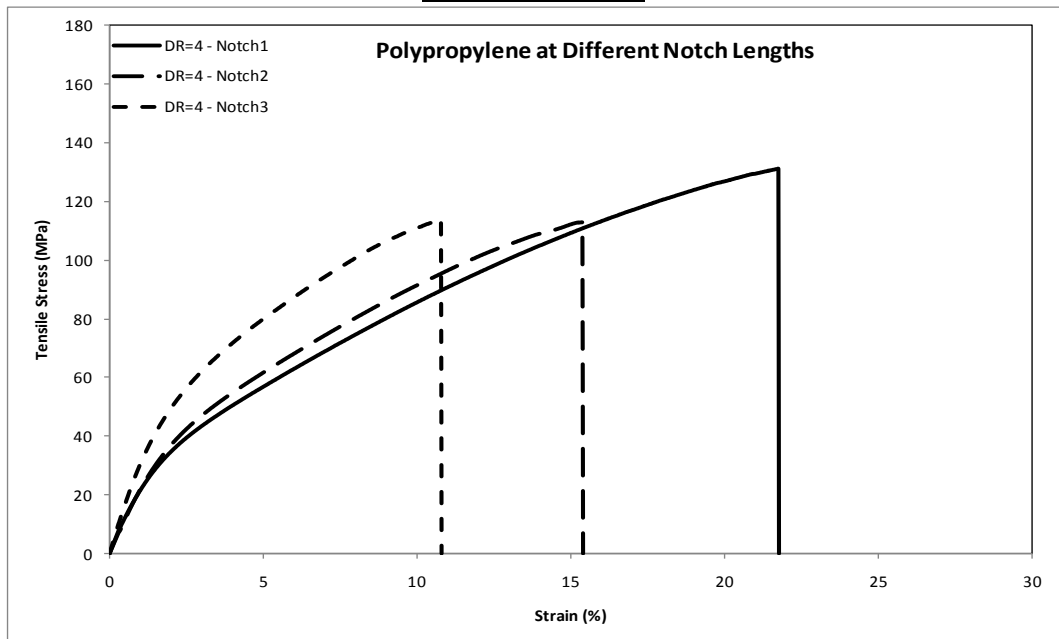
Appendix I2: Stress-Strain Graphs of Drawn PPNCs
Draw Ratio = 2 & 3

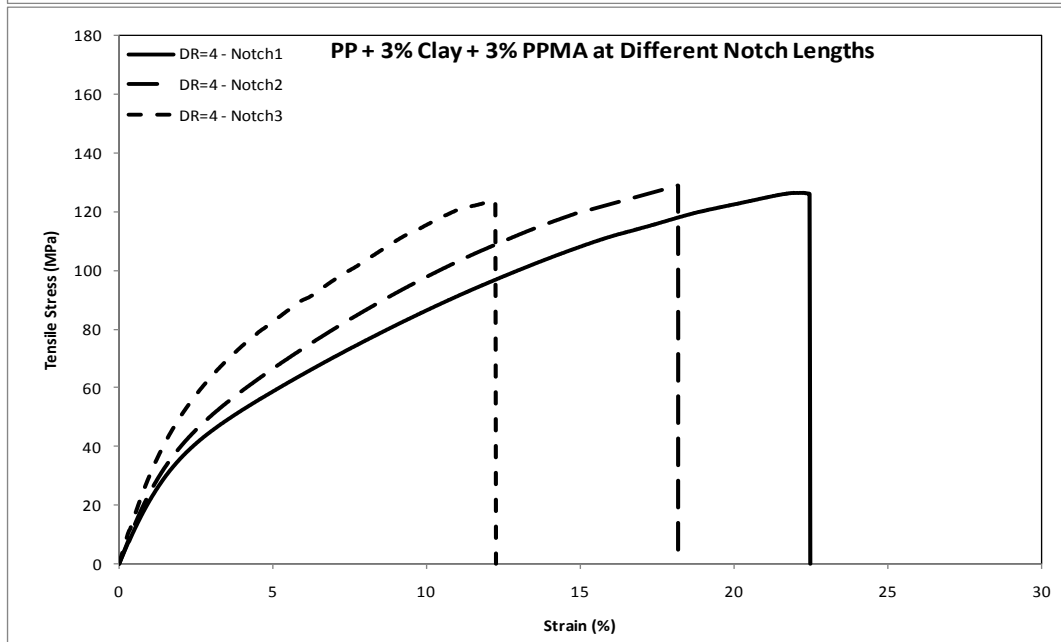
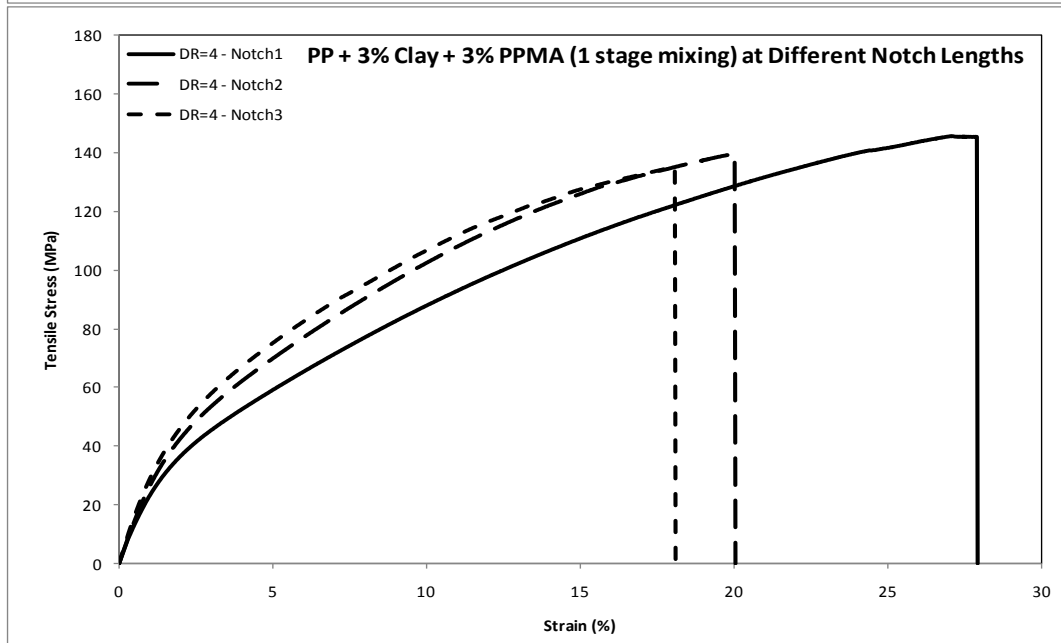
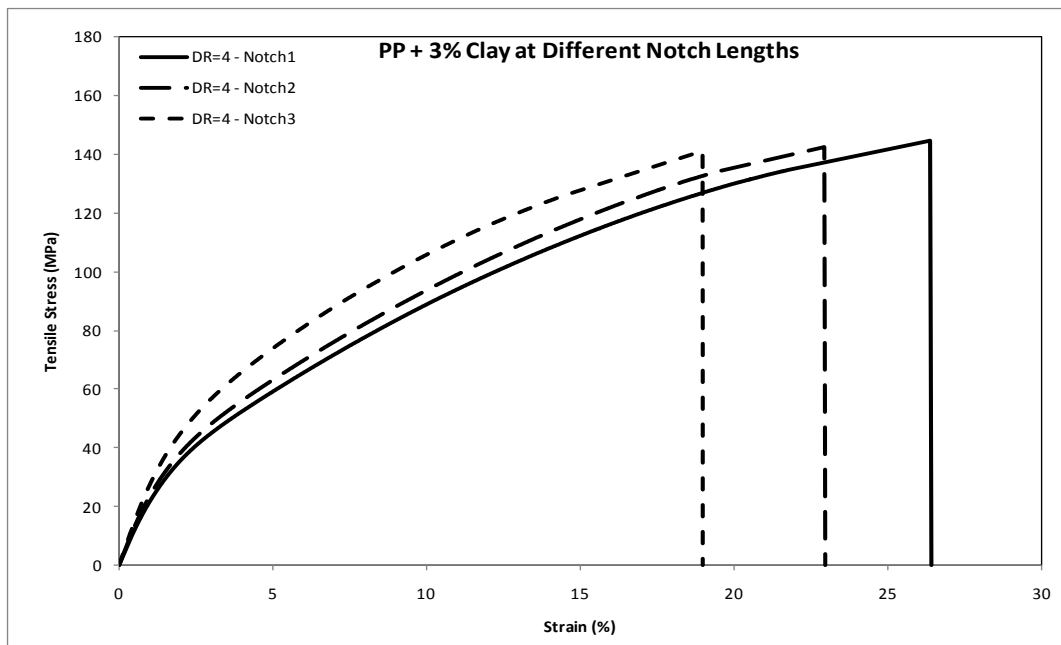


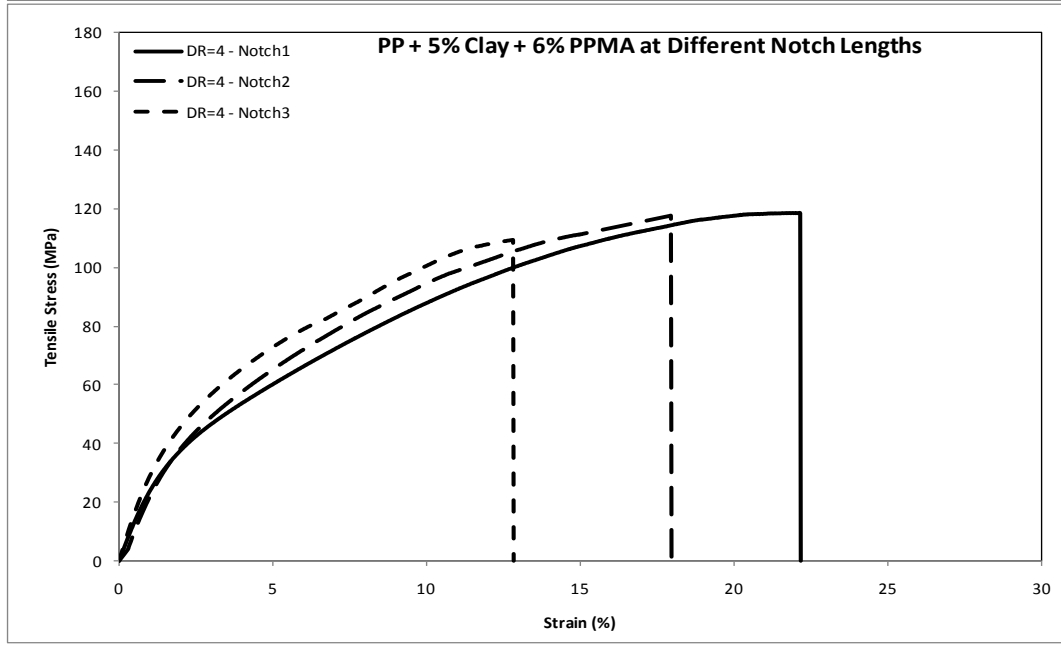
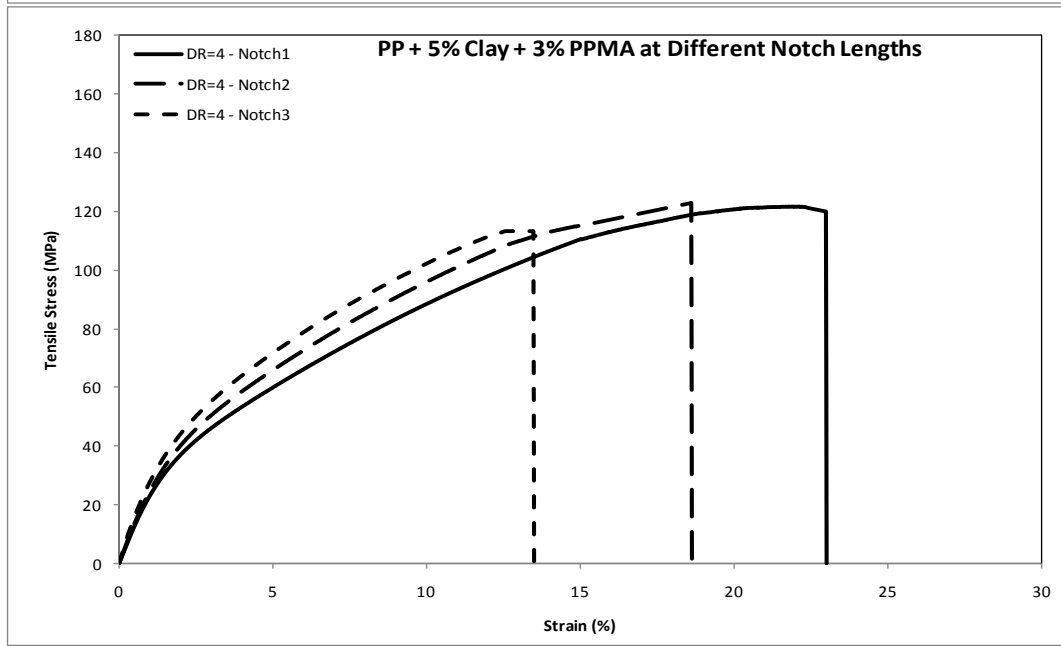
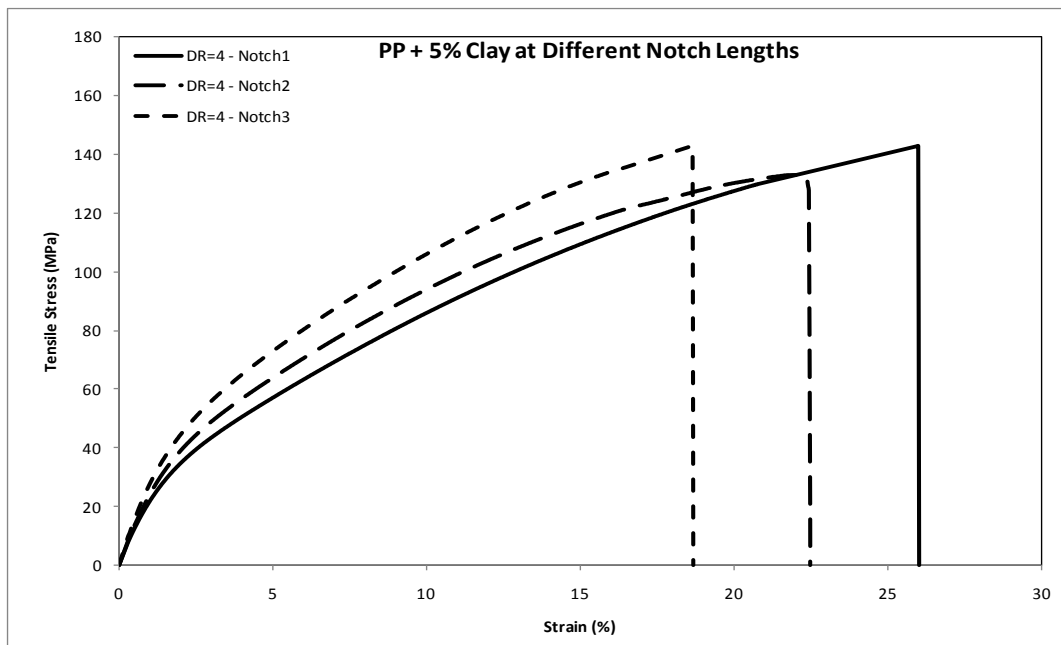




Draw Ratio =4

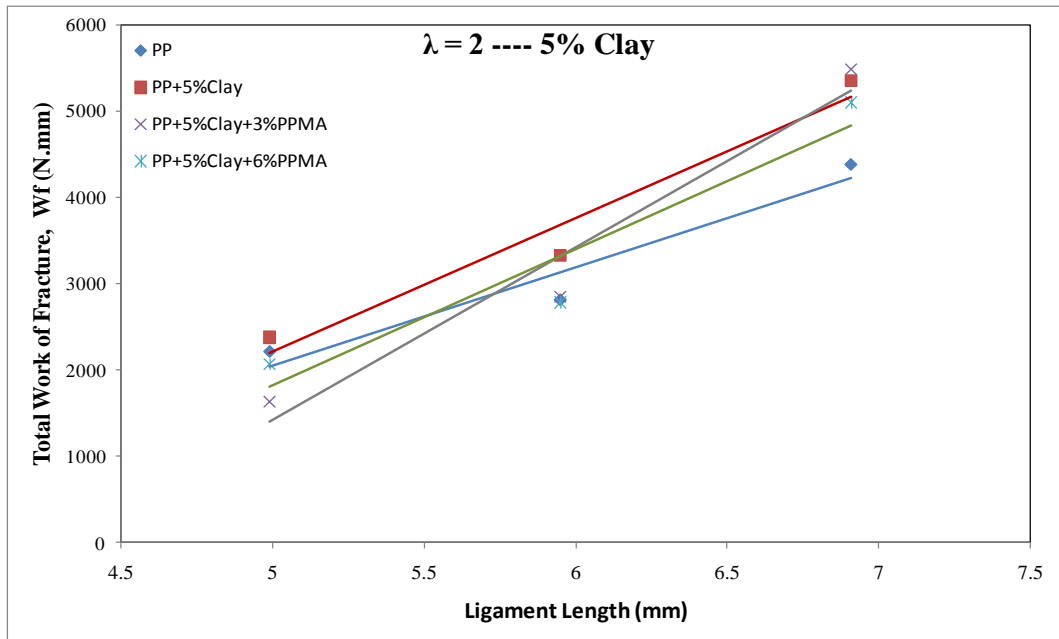
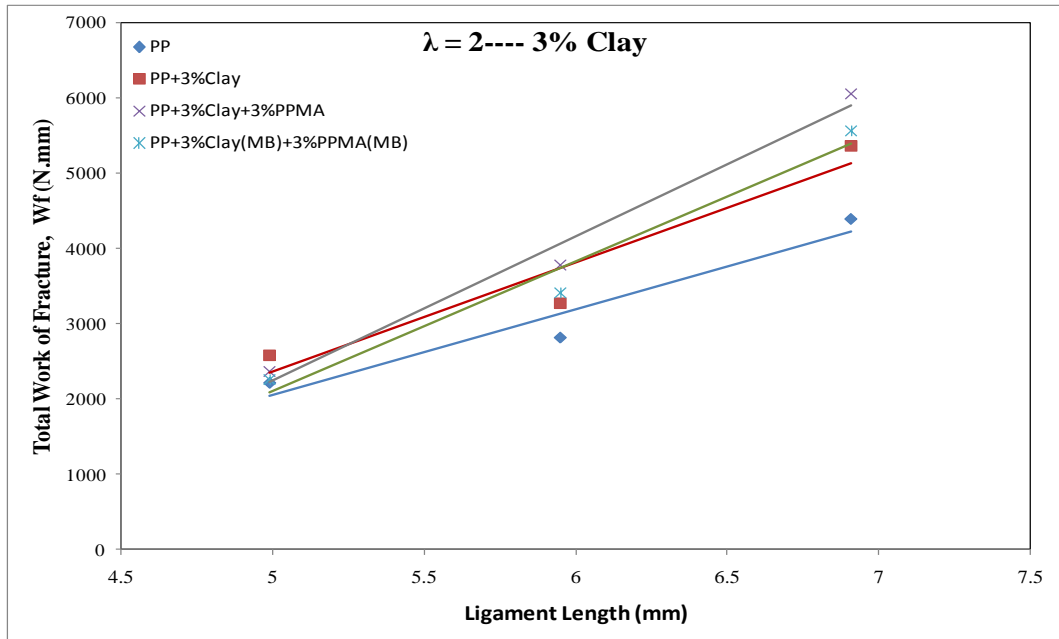


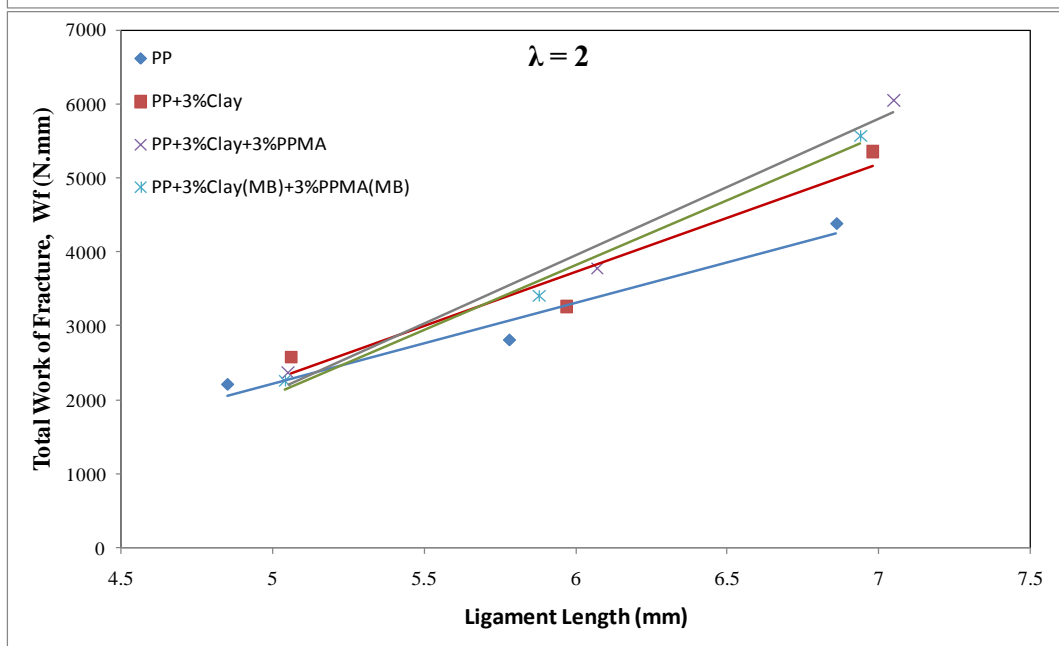
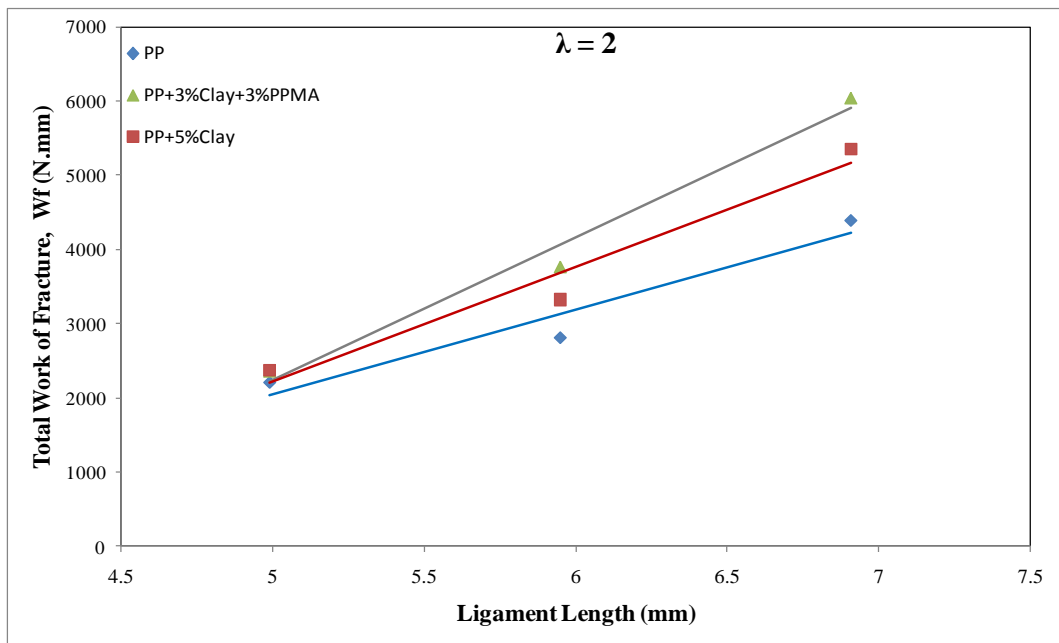




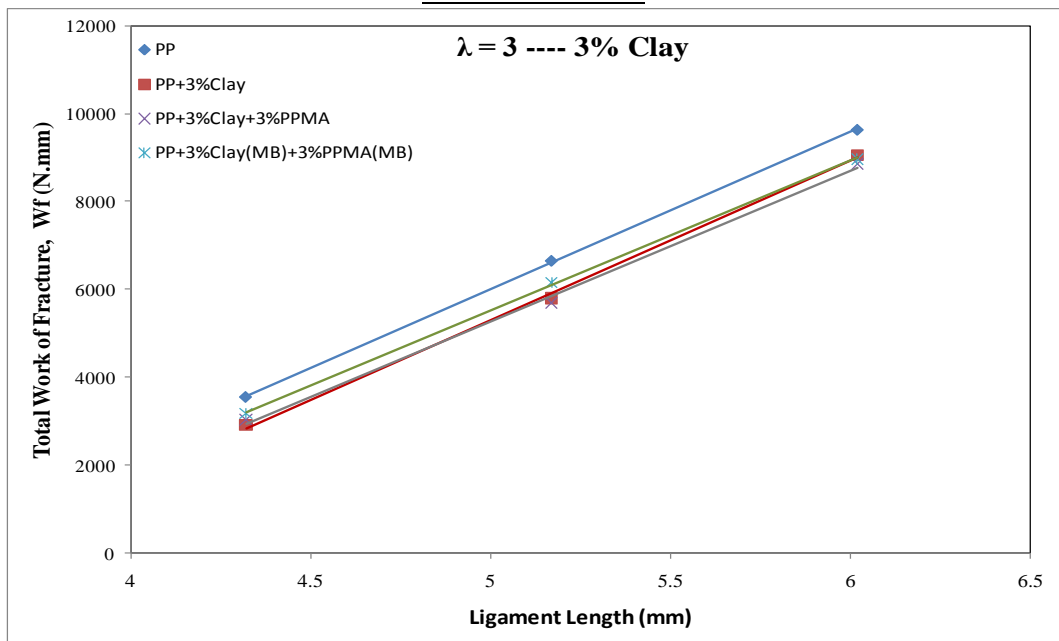
Appendix J: Total Work of Fracture for Different Ligament Lengths of PPNCs

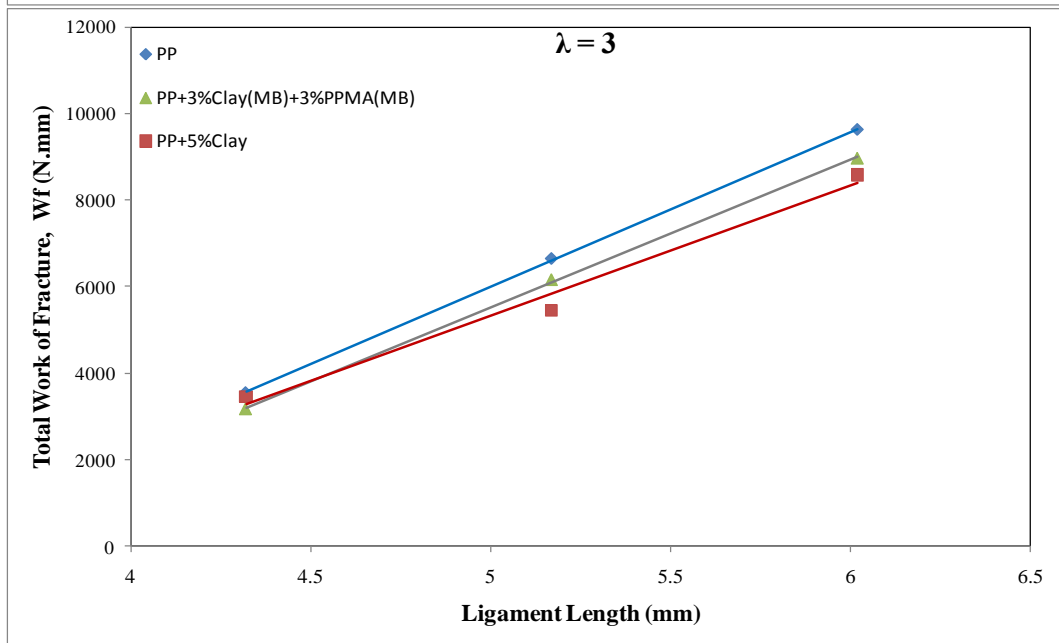
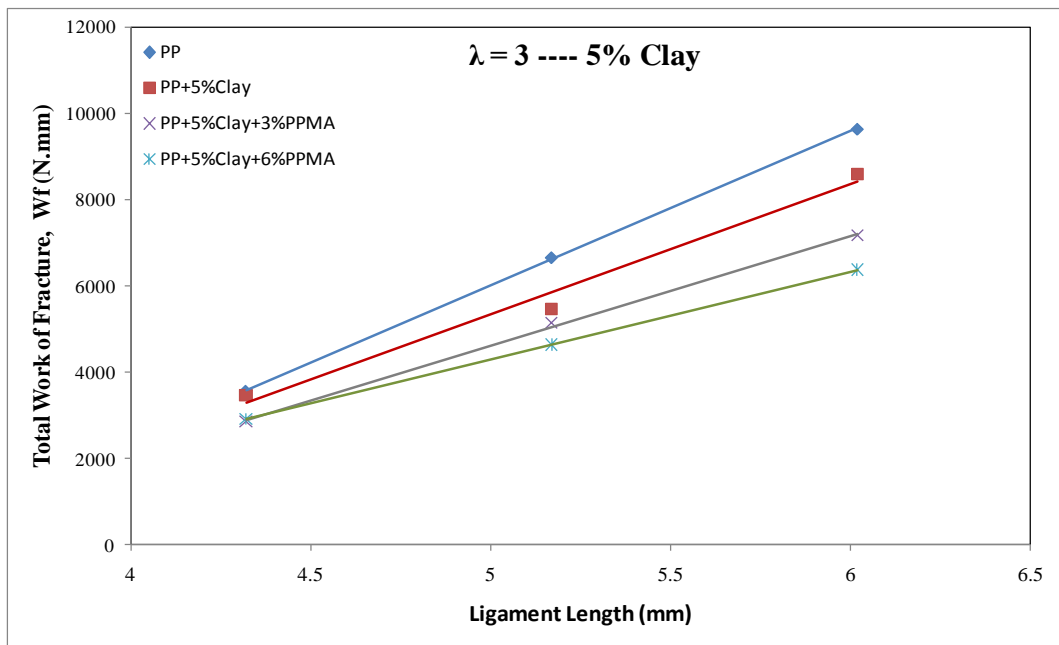
Draw Ratio = 2





Draw Ratio = 3





Draw Ratio =4

